

DEVELOPMENT OF COBALT AND RHENIUM ANTICANCER AGENTS
TARGETING THE TUMOR MICROENVIRONMENT

A Dissertation

Presented to the Faculty of the Graduate School

of Cornell University

In Partial Fulfillment of the Requirements for the Degree of

Doctor of Philosophy

by

Arthur Paden King

May 2020

© 2020 Arthur Paden King

DEVELOPMENT OF COBALT AND RHENIUM ANTICANCER AGENTS
TARGETING THE TUMOR MICROENVIRONMENT

Arthur Paden King, Ph. D.

Cornell University 2020

This work details the development of metal-based anticancer agents specifically tailored to target aspects of the tumor microenvironment. Cancerous tumors receive decreased blood and nutrient supplies relative to healthy tissues, which leads to low O₂ content, decreased pH, and increased levels of protein misfolding and DNA damage. Therapeutics may be designed to target these aspects of the tumor microenvironment, leading to increased selectivity for cancer cells over healthy cells. In particular, this work describes efforts to target two aspects of the tumor microenvironment: decreased O₂ content and higher levels of endoplasmic reticulum (ER) stress. The first chapter outlines recent advances in complexes that exploit the increased rates of protein misfolding in tumors by disrupting ER function. This chapter includes a description of the relevant pathways involved in ER stress, a summary of metal complexes that kill cancer cells via ER stress, and a wholistic analysis of trends and similarities in metal complexes that share this mechanistic feature. Chapters 2 and 3 describe the development of Co(III) complexes of biologically active ligands that may be selectively reduced to yield cytotoxic species. Chapter 2 focuses on the development of Co(III)-bis(thiosemicarbazone) complexes with powerful anticancer activity. Chapter 3 details the synthesis of Co(III) complexes bearing Schiff base ligands, and it

includes a thorough study of the ligand exchange pathways and redox reactions that lead to activation of these compounds. Chapter 4 describes the development and mechanistic investigation of the first rhenium complex that kills cancer cells via ER stress. Chapter 5 details the expansion of the original lead complex from Chapter 4 into a library of derivatives with variable activity and the investigation of the lead compound's activity in vivo. Finally, Chapter 6 describes ongoing efforts to develop conjugated rhenium complexes for molecular targeting and pull-down experiments. Together, these results provide a description of metal complexes that target the tumor microenvironment and outline a template for the development of anticancer metal complexes from synthesis to physical characterization to mechanistic studies of their anticancer activity.

BIOGRAPHICAL SKETCH

The author was born and grew up in Statenville, GA, where he lived with his parents, Paul and Shannon King, until his graduation from Echols County High School in 2011. He then attended Mercer University in Macon, GA, where he pursued Bachelor's degrees in both Chemistry and English Literature. While studying in his chemistry classes, he became interested in pursuing chemical research. He began his research career studying the use of biosurfactants for waste remediation under the tutelage of Dr. Kathryn Kloepper. After completing his studies at Mercer University, he proceeded to begin graduate school at Cornell University. While at Cornell, the author studied Bioinorganic Chemistry under the supervision of Justin Wilson. He began his studies focusing on the development of cobalt complexes as hypoxia-targeting anticancer agents. After completing his Master's degree with a focus on this topic, he began investigating rhenium complexes that treat cancer by inducing endoplasmic reticulum stress. After defending his thesis, he plans to pursue a career in chemical research, beginning with a postdoctoral position at the National Cancer Institute, where he will work with Dr. Freddy Escorcia to develop targeted radiotherapeutics for the treatment of liver cancer.

ACKNOWLEDGMENTS

First and foremost, I would like to acknowledge my parents for everything they did that helped me make it to this point. Without countless hours of help and a lot of patience, I could never have even gone to college, much less graduate school. My mom taught me the value of hard work and helped me overcome some of my bad habits, like terrible attention to details. My dad, who was self-employed for most of my life, taught me about independence and working well with others. Both of my parents showed me by example how to work with others and how to treat my co-workers, a lesson that has helped me immeasurably as I go through life.

My parents didn't raise me alone. I grew up with a huge family, and all of them have shaped my life in some way. I would like to thank my grandparents for always being there for me, for their help with my schoolwork, for the hours and days they spent taking care of me when I was young, and for my Grandma's eternal willingness to make me something to eat, even when I just ate. My extended family has also helped me throughout my life, especially my aunt, Florence, who helped introduce me to forestry, one of my favorite activities in high school, and my cousins Bobbie and Lacey, who were more like sisters to me when I was growing up.

From my time as an undergraduate, I would like to thank my research advisors, Dr. Kloepper and Dr. Davis. Dr. Kloepper taught me many of my early chemistry classes, and she was also my first research mentor. As an analytical chemist, she showed me the value of precision in my work, and she was the person who first truly introduced me to the scientific research process. Dr. Davis was my favorite English professor, and his classes and the discussions that came along with them helped form

my opinions of the world outside of the lab, which can be very easy to lose track of when pursuing a career in the sciences.

While at Cornell, I have been helped in the pursuit of my studies by dozens of people, from professors to staff to other students. My advisor, Justin Wilson, earns most of my thanks. Upon my arrival in his lab, he taught me synthetic inorganic chemistry beginning with the very basics of setting up a reaction, and he showed me how to culture cells. His patience while I was just beginning was a huge help, as I made mistakes constantly, some of them several times. Throughout my time at Cornell, his door has always been open, and I have spent many hours discussing wild ideas and unrelated science questions with him. He also taught me the writing and journal submission process, which will be a huge help as I pursue my independent career.

Several other professors have been a great help to me as well. My committee members, Kyle Lancaster and Peter Wolczanski, have both been responsible for teaching me inorganic chemistry. Kyle taught me formally in two classes, and he has always made time for me when I needed to ask him a research question outside of class. I worked with Pete as a grader for two years, and I learned almost as much as the students did in the process. I also presented my research several times for Pete at our literature lunches, and he provided fresh insight on the chemical aspects of my research.

In the process of actually completing work in the lab, I have been helped greatly by several of Cornell's staff scientists. Ivan Kereszetes and Tony Condo of the NMR facility made several of my experiments possible, and I spent hours with Ivan

going through the minute details of my spectra or setting up exotic NMR experiments that would have otherwise been impossible. Adam Wojno taught me flow cytometry, and thanks to him, Sierra and I were able to perform several flow cytometry experiments independently by the time we finished working on the cytometer. Sam MacMillan taught me how to do X-Ray crystallography. She showed me the entire process, from mounting crystals to solving structures, and she gave me an appreciation for the subtleties of the process.

Other graduate students, inside and outside the Wilson group, also helped me throughout my time at Cornell. Josh Woods, Sarah Nathan, and Jesse Spivey shared a lab space with me, and I'd like to thank them for all the times they discussed ideas with me, both large and small, about how to perform a step in a reaction or about the big picture of a project. Charlene Konkankit and Tracky Huang worked with me on the Rhenium project in our lab, and both of them provided invaluable insight into my project and helped me develop the chemistry of the rhenium isonitrile complexes that became the focus of my work. The rest of the group also helped me understand my chemistry, and showed me a lot of their own research. Aohan Hu, Kevin Knopf, William Schumacher, and Nikki Thiele all talked with me frequently about our work, and seeing the way they approached their own challenges gave me ideas about how to work through my own challenges.

Finally, I'd like to thank my wife Sierra. We met here at Cornell, and we both joined the Wilson group at the same time. Eventually, after two years in the group, we began dating, and two years later we were married. Not long after I switched my project to working on rhenium complexes, Sierra and I began to work on the same

compounds, as we both focused on different aspects of the same investigations. The way in which the two of us worked together was complementary, and without her I never would have been able to accomplish most of what I did in my research.

TABLE OF CONTENTS

Chapter 1. Endoplasmic Reticulum Stress, an Arising Target for Metal Anticancer Agents	1
Introduction	2
Background	4
Detection of ER Stress	11
Anticancer Metal Complexes that Induce ER Stress	14
Trends and Opportunities for Metal Anticancer Agents Targeting the ER	49
Chapter 2. Bis(thiosemicarbazone) Complexes of Cobalt (III): Synthesis, Characterization, and Anticancer Potential	63
Introduction	64
Results	66
Discussion	87
Conclusion	96
Experimental	97
Supporting Information	110
Chapter 3. Physical Properties, Ligand Substitution Reactions, and Biological Activity of Co(III)-Schiff Base Complexes	152
Introduction	153
Results	156
Discussion	172
Conclusion	179
Experimental	180
Supporting Information	191
Chapter 4. A Rhenium Isonitrile Complex Induces Unfolded Protein Response-Mediated Apoptosis in Cancer Cells	221
Introduction	222
Results and Discussion	223
Conclusion	232
Experimental	232
Supporting Information	245
Chapter 5. Exploring the In Vivo and In Vitro Anticancer Activity of Rhenium Isonitrile Complexes	273
Introduction	274
Results and Discussion	275
Conclusion	302
Experimental	304
Supporting Information	322
Chapter 6. Development of Conjugation Strategies for Bifunctional Rhenium Anticancer Agents	380
Introduction	381
Results and Discussion	383
Conclusion	386
Experimental	389
Supporting Information	397

Appendix 1. Novel Cobalt (III) Bis(thiosemicarbazone) Complexes	404
Appendix 2. Synthesis of [⁵⁵ Co(ATS)(NH ₃) ₂]Cl	413

LIST OF FIGURES AND TABLES

Figure 1.1. Schematic diagram of ER stress-response pathways and activation of the UPR	7
Figure 1.2. Proposed mechanism of ER stress induction by pyridine-pyrazole-based copper chelators	17
Figure 1.3. Piano-stool ruthenium complexes induce their cytotoxic effects and ER stress by producing ROS	24
Figure 1.4. Cellular response upon treatment with [Re(dmphen)(CO) ₃ (p-tol-ICN)] ⁺	29
Figure 1.5. Mammosphere formation of HMLER breast cancer stem cells in the presence or absence of the indicated anticancer compounds	32
Figure 1.6. Identification of intracellular protein targets of iridium photosensitizers	34
Figure 1.7. Schematic representation of pull-down assays performed to detect protein targets of Pt(II) agents	40
Figure 1.8. In vivo activity of 30	45
Figure 1.9. In vivo activity of 35	46
Table 1.1. Phenotypes and Examples of Induction of ER Stress by Metal Complexes	50
Chart 2.1. Structures of Cu(ATSM) and the [Co(BTSC)(L) ₂] ⁺ Complexes investigated in Chapter 2	65
Scheme 2.1. Synthesis of Cobalt(III) Bis(thiosemicarbazone) Complexes	68
Figure 2.1. X-ray crystal structures of [Co(GTS)(Im) ₂] ⁺ , [Co(GTS)(BnA) ₂] ⁺ , and [Co(ATS)(Im) ₂] ⁺	68
Table 2.1. Interatomic Distances (Å) and Angles (°) of [CoGTS(Im) ₂] ⁺ , [CoATS(Im) ₂] ⁺ , and [CoGTS(BnA) ₂] ⁺	68
Figure 2.2. ⁵⁹ Co NMR spectra of [Co(ATS)L ₂] ⁺ complexes	69
Table 2.2. ⁵⁹ Co NMR Chemical Shifts and Linewidths	71
Figure 2.3. Electronic absorption spectra of [Co(ATS)(NH ₃) ₂] ⁺ , [Co(PTS)(NH ₃) ₂] ⁺ , and [Co(GTS)(NH ₃) ₂] ⁺ complexes in pH 7.4 PBS at 25 °C	72
Table 2.3. Absorbance Maxima and Extinction Coefficients for the Complexes in pH 7.4 PBS.	72
Table 2.4. Electrochemical Properties of [Co(BTSC)(L) ₂] ⁺ Complexes	73
Figure 2.4. Cyclic voltammogram of [CoGTS(Im) ₂] ⁺ before (top) and after (bottom) addition of excess imidazole	74
Figure 2.5. Percent of [Co(BTSC)(L) ₂] ⁺ remaining in solution after 24 h incubation at 37 °C in PBS as measured by RP-HPLC	76
Table 2.5. Axial ligand substitution of [Co(BTSC)(L) ₂] ⁺ complexes by <i>N</i> -methylimidazole	77
Figure 2.6. HPLC traces of 1 mM [CoGTS(Im) ₂] ⁺ incubated with 5 mM <i>N</i> -methylimidazole immediately and 3 h after mixing	78
Figure 2.7. Uptake of [Co(BTSC)(L) ₂] ⁺ complexes in normoxic and hypoxic conditions.	80
Table 2.6. Cellular uptake of complexes in A549 cells	81
Figure 2.8. Effect of [Co(BTSC)(Im) ₂] ⁺ complex concentration on A549 cell viability as measured by the MTT assay for [Co(ATS)(Im) ₂] ⁺ , [Co(PTS)(Im) ₂] ⁺ , and [Co(GTS)(Im) ₂] ⁺ .	82
Figure 2.9. Dose-response curves of cisplatin and [Co(GTS)(NH ₃) ₂] ⁺ in MRC-5 (normal lung fibroblast) cells	84
Table 2.7. IC ₅₀ Values (μM) for [Co(BTSC)(L) ₂]NO ₃ Complexes	85

Table 2.8. Effect of TM on IC ₅₀ values (μM) in A549 Cells	86
Figure 2.10. Effect of [CoGTS(Im) ₂] ⁺ complex concentration on A549 cell viability in the presence and absence of TM	87
Table 2.9. X-ray Crystallographic Data Collection and Refinement Parameters	106
Figures S2.1–S2.9. ¹ H NMR Spectra of [Co(BTSC)(L) ₂] ⁺ Complexes	110
Figures S2.10–S2.18. ¹³ C{ ¹ H} NMR Spectra of [Co(BTSC)(L) ₂] ⁺ Complexes	114
Figures S2.19–S2.27. ⁵⁹ Co NMR Spectra of [Co(BTSC)(L) ₂] ⁺ Complexes	119
Figures S2.28–S2.36. IR Spectra of [Co(BTSC)(L) ₂] ⁺ Complexes	123
Figures S2.37–S2.45. HPLC Chromatograms of [Co(BTSC)(L) ₂] ⁺ Complexes	128
Figures S2.46–S2.54. UV-Vis Spectra of [Co(BTSC)(L) ₂] ⁺ Complexes	132
Figures S2.55–S2.63. Cyclic Voltammograms of [Co(BTSC)(L) ₂] ⁺ Complexes	137
Figure S2.64. Uptake of [Co(BTSC)(Im) ₂] ⁺ Complexes in HeLa and A549 Cells	141
Figures S2.65–S2.73. Dose-Response Curves of [Co(BTSC)(L) ₂] ⁺ Complexes	142
Figures S2.74–S2.75. ¹ H NMR Spectrum of [Co(GTS)(NH ₃) ₂] ⁺ in the Presence of Tetrathiomolybdate	146
Chart 3.1. Structures of the [Co(Schiff base)(L) ₂] ⁺ Complexes Investigated in Chapter 3	156
Figure 3.1. X-ray crystal structures of [Co(3F-salen)(3F-BnNH ₂) ₂] ⁺ , [Co(tfacen)(3F-BnNH ₂) ₂] ⁺ , and [Co(tfacen)(NH ₃) ₂] ⁺ .	158
Table 3.1. Selected Interatomic Distances (Å) and Angles (°) of [Co(3F-salen)(3F-BnNH ₂) ₂] ⁺ , [Co(tfacen)(3F-BnNH ₂) ₂] ⁺ , and [Co(tfacen)(NH ₃) ₂] ⁺	159
Table 3.2. ⁵⁹ Co NMR Chemical Shifts and Linewidths	160
Figure 3.2. ⁵⁹ Co (120 MHz) NMR of spectra of [Co(tfacen)(NH ₃) ₂] ⁺ and [Co(tfacen)(3F-BnNH ₂) ₂] ⁺	161
Table 3.3. Electrochemical Parameters of [Co(Schiff base)(L) ₂] ⁺ Complexes	162
Figure 3.3. Cyclic voltammogram of [Co(tfacen)(3F-BnNH ₂) ₂] ⁺	162
Figure 3.4. Panel I: Proposed ligand exchange pathway and NMR spectra of [Co(Schiff base)(L) ₂] ⁺ complexes interaction with MeIm	165
Table 3.4. Axial Ligand Substitution Rate Constants of [Co(Schiff base)(L) ₂] ⁺ Complexes at 37 °C and Activation Parameters Determined by Eyring Analysis	166
Figure 3.5. Representative concentration vs time data for the axial ligand substitution of [Co(3F-salen)(3F-BnNH ₂) ₂] ⁺ with MeIm at 37 °C	167
Figure 3.6. Cell viability in the presence of varying concentrations of [Co(3F-salen)(3F-BnNH ₂) ₂] ⁺ and [Co(3F-salen)(NH ₃) ₂] ⁺	170
Table 3.5. Cytotoxicity and Cellular Uptake of [Co(Schiff base)(L) ₂] ⁺ Complexes in A549 Lung Cancer Cells	171
Table 3.6. X-ray Crystallographic Data Collection and Refinement Parameters	187
Figures S3.1–S3.6. ¹ H NMR spectra of [Co(Schiff Base)(L) ₂] ⁺ complexes	191
Figures S3.7–S3.9. ¹³ C{ ¹ H} NMR spectra of [Co(Schiff Base)(L) ₂] ⁺ complexes	195
Figures S3.10–S3.13. ¹⁹ F NMR spectra of [Co(Schiff Base)(L) ₂] ⁺ complexes	196
Figures S3.14–S3.17. IR spectra of [Co(Schiff Base)(L) ₂] ⁺ complexes	198
Figures S3.18–S3.21. HPLC chromatograms of [Co(Schiff Base)(L) ₂] ⁺ complexes	200
Figures S3.22–S3.25. ⁵⁹ Co NMR spectra of [Co(Schiff Base)(L) ₂] ⁺ complexes	203
Figures S3.26–S3.29. Cyclic voltammograms of [Co(Schiff Base)(L) ₂] ⁺ complexes	205
Figures S3.30–S3.33. Concentration versus time data for [Co(Schiff Base)(L) ₂] ⁺ complexes	207
Figures S3.34–S3.35. ¹⁹ F NMR spectral overall of ligand exchange reaction products and reaction mixtures	209
Figures S3.36–S3.37. Concentration versus time data for [Co(Schiff Base)(L) ₂] ⁺ complexes with varying pH and concentrations of incoming ligand	211

Figures S3.38-S3.39. Eyring analysis of ligand substitution processes for [Co(Schiff Base)(L) ₂] ⁺ complexes	212
Figures S3.40-S3.43. Representative dose-response curves of [Co(Schiff Base)(L) ₂] ⁺ complexes	214
Figure 4.1. Diagram of TRIP and its X-ray crystal structure	224
Table 4.1. IC ₅₀ values of TRIP, Neo-Re, and cisplatin in cancer and non-cancer cell lines	226
Figure 4.2. Investigation of mitochondrial morphology of HeLa cells after TRIP treatment	228
Figure 4.3. Evaluation of ER stress induction by TRIP	230
Figure 4.4. Proposed mechanism of ER-stress and apoptosis induction by TRIP	231
Table S4.1. X-ray Crystallographic Data Collection and Refinement Parameters	245
Table S4.2. X-ray Crystal Interatomic Distances and Angles	246
Table S4.3. Photophysical Properties of TRIP	246
Table S4.4. COMPARE Analysis Results for TRIP	246
Figure S4.1. ¹ H NMR Spectrum of TRIP	247
Figure S4.2. IR Spectrum of TRIP	247
Figure S4.3. HPLC Chromatogram of TRIP	248
Figure S4.4. UV-Vis Spectrum of TRIP	248
Figure S4.5. Emission Spectrum of TRIP	248
Figure S4.6. Transient Emission Decay Profile of TRIP	249
Figure S4.7. Aqueous Stability of TRIP in PBS	249
Figure S4.8. Photoreaction of TRIP Monitored by UV-Vis	249
Figure S4.9. TRIP Stability in the Presence of Glutathione	250
Figures S4.10–S4.13. Dose-Response Curves for TRIP	250
Figures S4.14–S4.17. Dose-Response Curves for Neo-Re	252
Figures S4.18–S4.21. Dose-Response Curves for Cisplatin	253
Figure S4.22. NCI-60 Multi-dose Mean Graph	255
Figure S4.23. Dose-Response Curves for TRIP with Necrostatin-1	256
Figure S4.24. Dose-Response Curves for TRIP with Cycloheximide	256
Figure S4.25. Dose-Response Curves for TRIP with Ferrostatin-1	256
Figure S4.26. Dose-Response Curves for TRIP with Z-VAD-FMK	257
Figure S4.27. Dose-Response Curves for Cisplatin with Z-VAD-FMK	257
Figure S4.28. Western Blot of Apoptotic Markers Caspase 3 and Cleaved PARP	258
Figure S4.29. Flow Cytometry Density Plots using Annexin V/PI	258
Figure S4.30. Bar Graph for Annexin V/PI Assay	259
Figure S4.31. Histograms of Fluorescence Intensity using Cytochrome <i>c</i> Antibody	250
Figure S4.32. Confocal Fluorescence Microscope Images of HeLa Cells Stained with Transfection or Dyes	261
Figure S4.33. Confocal Fluorescence Microscope Images of HeLa Cells Illustrating Mitochondria Morphology	262
Figure S4.34. Confocal Fluorescence Microscope Images of A2780 Cells Stained with JC-1 dye	263
Figure S4.35. Bar Graph with JC-1 Results	263
Figure S4.36. Western Blot of Autophagy Marker LC3I/LC3II	264
Figure S4.37. Western Blot of UPR Response in A2780 Cell Line	264
Figure S4.38. Western Blot of UPR Response in WT and mutant S51A eIF2α MEF cells	264
Figure S4.39. Western Blot of Puromycin Labeling in WT and mutant S51A eIF2α MEF cells	265

Figure S4.40. Cell Cycle Analysis Results in A2780 Cell Line	265
Figure S4.41. Confocal Fluorescence Microscope Images of HeLa Cells Stained with Thioflavin T	266
Figure S4.42. Bar Graph with Thioflavin T Results	267
Figure S4.3. Western Blot of Markers of HSP90 Inhibition	267
Figure S4.44. Proteasome Inhibition in Cell Lysates by TRIP	268
Figure S4.45. Western Blot of Ubiquitin Inhibition	268
Figure S4.46. Dose-Response Curves for TRIP with <i>N</i> -Acetylcysteine	269
Figure S4.47. DCF-DA Assay	269
Chart 5.1. TRIP derivatives explored in Chapter 5	277
Figure 5.1. X-ray crystal structure of TRIP-2a	280
Table 5.1. Physical properties of TRIP derivatives	282
Table 5.2. IC ₅₀ values of TRIP derivatives in HeLa Cells	286
Figure 5.2. Correlation of the physical properties and cytotoxicity of TRIP derivatives	289
Figure 5.3. ER stress induction by TRIP derivatives	293
Figure 5.4. Biodistribution of TRIP-1a and TTIP	298
Figure 5.5. In vivo anticancer activity of TRIP-1a	300
Table S5.1. X-ray Crystallographic Data and Refinement Parameters	323
Table S5.2. Selected Interatomic Distances and Angles	324
Table S5.3. Mouse Treatment Schedule and Survival Times	325
Figures S5.1–S5.10. ¹ H NMR Spectra of TRIP Derivatives	326
Figures S5.11–S5.19. ¹³ C{ ¹ H} NMR Spectra of TRIP Derivatives	331
Figures S5.20–S5.29. IR Spectra of TRIP Derivatives	337
Figures S5.30–S5.39. HPLC Chromatograms of TRIP Derivatives	342
Figures S5.40–S5.45. ¹⁵ N HMBC NMR Spectra of TRIP Derivatives	345
Figures S5.46–S5.56. Cyclic Voltammograms of TRIP Derivatives	348
Figure S5.57. Scatter Plot of ¹⁵ N Chemical Shifts vs. the First Reduction Potential	354
Figures S5.58–S5.67. UV-Vis Spectra of TRIP Derivatives	354
Figures S5.68–S5.77. Emission Spectra of TRIP Derivatives	357
Figures S5.78–S5.87. Transient Emission Decay Profiles of TRIP Derivatives	361
Figures S5.88–S5.97. Dose-Response Curves of TRIP Derivatives in HeLa Cells	366
Figure S5.98. Confocal Fluorescence Microscopy Images of TRIP derivatives in HeLa cells and Bar Graph of Intracellular Luminescence	370
Figure S5.99. ThT Fluorescence Intensity of HeLa Cells Treated with TRIP Derivatives	371
Figure S5.100. Puromycin Western Blot of HeLa Cells Treated with TRIP Derivatives	372
Figure S5.101. HPLC Chromatograms of TRIP-1a and TTIP	373
Figure S5.102. Body Weight of Mice Treated with TRIP-1a	374
Scheme 6.1. Synthetic route for bifunctional TRIP complexes. See experimental section for preparation details	383
Scheme 6.2. Synthesis of Dinuclear TRIP Complex	388
Figure S6.1. ¹ H NMR spectrum of Boc-aminomethyl phenyl isocyanide	396
Figure S6.2. ¹ H NMR spectrum of TRIP-NH₂	396
Figure S6.3. ¹ H NMR spectrum of TRIP-alkyne	397
Figure S6.4. ¹ H NMR spectrum of TRIP-azide	398
Figure S6.5. ¹ H NMR spectrum of TRIP-2a	398
Figure S6.6. ¹ H NMR spectrum of TRIP-2b.	399
Figure S6.7. ¹ H NMR spectrum of TRIP-2c	399

Figure S6.8. ^1H NMR spectrum of TRIP-1	400
Figure S6.9. ^1H NMR spectrum of TRIP-3	400
Figure S6.10. ^1H NMR spectrum of TRIP-4	401
Figure S6.11. ESI-MS of TRIP-1b	401
Figure S6.12. HPLC of TRIP-1b	402
Figure A1. ^1H NMR (500 MHz) of $[\text{Co}(\text{3F-salophen})(\text{NH}_3)_2]\text{NO}_3$	408
Figure A2. ^1H NMR (500 MHz) of $[\text{Co}(\text{3F-salophen})(\text{3F-BnNH}_2)_2]\text{NO}_3$	409
Figure A3. ^1H NMR (400 MHz) of $[\text{Co}(\text{ATS})(\text{DMAP})_2]\text{NO}_3$	409
Figure A4. ^{19}F NMR (470 MHz) of $[\text{Co}(\text{3F-salophen})(\text{3F-BnNH}_2)_2]\text{NO}_3$	410
Figure A5. ^{19}F NMR (470 MHz) of $[\text{Co}(\text{3F-salophen})(\text{NH}_3)_2]\text{NO}_3$	410
Figure A6. IR (KBr, cm^{-1}) of $[\text{Co}(\text{ATS})(\text{DMAP})_2]\text{NO}_3$	411
Figure A7. IR (KBr, cm^{-1}) of $[\text{Co}(\text{3F-salophen})(\text{3F-BnNH}_2)_2]\text{NO}_3$	411
Figure A8. IR (KBr, cm^{-1}) of $[\text{Co}(\text{3F-salophen})(\text{NH}_3)_2]\text{NO}_3$	412
Figure A9. Radio-TLC of $[\text{Co}(\text{ATS})(\text{NH}_3)_2]\text{Cl}$ with variable ATS concentration	416
Figure A10. Radio-TLC demonstrating purification of $[\text{Co}(\text{ATS})(\text{NH}_3)_2]\text{Cl}$ using Chelex resin	417

CHAPTER 1

Endoplasmic Reticulum Stress, An Arising Target for Metal Anticancer Agents

Introduction

The endoplasmic reticulum (ER) is responsible for the synthesis, folding, and trafficking of cellular proteins. Thus, proper ER function is essential for cell growth and survival. In cancer cells, ER function becomes dysregulated. The rapid, uncontrolled growth of cancer cells and the hostile, nutrient-deficient tumor environment lead to an increase in protein misfolding and demand for protein synthesis. These factors ultimately contribute to heightened levels of ER stress in cancer cells relative to healthy cells.¹⁻³ To cope with this stress, cancer cells upregulate a pathway known as the unfolded protein response (UPR), which increases their ability to survive under heightened ER protein-folding burdens. Induction of the UPR is generally cytoprotective, and cancers that upregulate the UPR are often more aggressive and resistant to chemotherapy.⁴⁻⁶ Under certain conditions of prolonged or acute UPR activation, this pathway can initiate apoptosis. As such, many cancers with upregulated UPR are hypersensitive to chemotherapeutics that interfere with ER function. Recently, this sensitivity has been leveraged to develop new drugs that disrupt the UPR, such as the clinically-approved proteasome inhibitors bortezomib and carfilzomib, which interfere with endoplasmic reticulum-associated degradation (ERAD).⁷ The recent discovery of these drugs has led to a heightened interest in compounds capable of inducing ER stress as potential new anticancer drugs.⁸⁻¹³

Although the majority of known ER stress-inducing agents are organic compounds, in recent years there have been several reports that describe the potential of metal complexes as ER-targeting cancer therapeutics. These complexes range from first row transition metal complexes that operate via the catalytic production of

reactive oxygen species (ROS), to hydrophobic late transition metal complexes that interfere with ER Ca^{2+} storage, to targeted photodynamic therapy (PDT) agents that generate singlet oxygen ($^1\text{O}_2$) locally inside the ER. The wide range of accessible structures, tunable chemical reactivities, and targeting capabilities of coordination complexes make them ideal for the development of ER-targeting anticancer drugs. Despite the clear potential of the ER as a metallodrug target, this organelle is often overlooked in comparison to traditional intracellular targets, such as the nucleus and mitochondria. The vast majority of studies investigating ER stress induction by metal complexes have been conducted within the last 20 years, with only a handful performed prior to the 21st century. In this Chapter, we highlight the recent advances in developing metal complexes that target the ER and provide an overview of the relevant biological assays that can be used to detect ER stress.

The objective of this Review is to provide a comprehensive guide for researchers seeking to design ER-targeting metallodrugs. We begin with a broad introduction of the relevant biological pathways, signaling processes, and therapeutic implications of ER stress induction, especially in relation to cancer treatment. We then provide a brief summary of the common experimental methods that are used to detect ER stress induction and ER stress-mediated cell death. After discussing this background, we explore the ER stress-inducing capacities of various metal complexes and discuss relevant structural features and mechanisms of action. Finally, we provide a comparative overview, discussion, and perspective on the potential value of metal complexes for inducing ER stress in cancer cells. We note that an article on a similar topic was recently published elsewhere.¹⁴ The scope of this Review is more expansive

and comprehensive, thus filling an unmet gap in the literature.

Background

The Endoplasmic Reticulum: Structure and Function

The ER is the largest organelle in the cell, but despite its size, it was one of the last organelles to be discovered.^{15,16} This vast organelle consists of two main regions, the nuclear envelope that borders the cell nucleus and the peripheral ER that branches throughout the cell. Both the nuclear envelope and the peripheral ER contain a mixture of flat sheets and tubular structures. The sheets form flat membranes with a lumen between them, whereas the tubules connect the ER to other organelles and provide pathways for transport of lipids and proteins. The ratio of sheets to tubules varies in a manner that depends on the specific cell type and its environment, leading to wide variability in ER morphology. The peripheral ER connects directly to other organelles, including the mitochondria, Golgi apparatus, and cytoskeleton. The ER's function, while still not fully understood, may be broadly divided into three categories: protein regulation, lipid biosynthesis, and intracellular Ca²⁺ storage. Each of these functions and some of the relevant regulatory pathways are described in greater detail below.

The ER's most well-understood purpose is its role in cellular protein regulation.^{10,15,17} The ER directly synthesizes many integral membrane proteins and several cytosolic proteins. This synthesis occurs at ribosomes associated with the ER membrane in a portion of the ER known as the rough ER. Once synthesized, proteins are translocated into the ER lumen, where they are folded. After folding, cytosolic proteins are trafficked to their destination, and membrane proteins are incorporated

into their respective membranes. Occasionally, the proteins do not fold properly or aggregate.¹⁷ Once detected, misfolded or aggregated proteins are tagged with ubiquitin, most often by the SEL1L-HRD1 protein complex. After ubiquitination, proteins are translocated back through the ER to the cytosol, where they are degraded by the proteasome. This pathway, known as ERAD, is an essential component of the ER's protein homeostasis machinery, and it has recently received attention for its role in several diseases, including Alzheimer's disease¹⁸ and cancer.^{19,20}

Although the ER is most well-known for its role in protein metabolism, it also synthesizes and organizes the vast majority of cellular lipids, such as phosphatidyl choline, triacylglycerides, and cholesterol.²¹ Unlike protein synthesis, lipid synthesis occurs in either the smooth or rough ER. Once synthesized, these lipids are transferred to their desired destinations via the secretory pathway. Lipid synthesis and organization by the ER is a dynamic process, which can be altered in response to external stimuli in order to change production or to regulate the size of the ER itself.

The final major role of the ER is to regulate and store intracellular Ca^{2+} .^{15,22} The ER stores the majority of intracellular Ca^{2+} ; the Ca^{2+} concentration within the ER lumen is approximately 1 mM, in contrast to the 100 nM concentration found in the cytosol. Signaling molecules, such as inositol 1,4,5-triphosphate, induce the release of stored Ca^{2+} into the cytosol or mitochondria. Conversely, the ER may take up Ca^{2+} from the cytosol through sarco(endo)plasmic reticulum calcium ATPase (SERCA) transporters. By balancing levels of Ca^{2+} uptake and release, the ER ensures that the cytosolic Ca^{2+} remains in the nanomolar range.

Endoplasmic Reticulum Stress Pathways and the Unfolded Protein Response

When ER function becomes disrupted by insults such as toxins or environmental changes, ER stress occurs. ER stress may be broadly categorized as being due to a perturbation of one of the three major functions of the ER: protein folding/trafficking, lipid synthesis and processing, and Ca^{2+} homeostasis. These stresses result in a decreased capacity of the ER to fold proteins, leading to an increase in misfolded proteins inside the cell. The cell has machinery for resolving this stress, such as the UPR and the integrated stress response (ISR). If the cell cannot resolve the insult or reduce the resulting stress to acceptable levels, programmed cell death occurs, often via apoptosis or paraptosis.

The major hallmark of ER stress in a cell is an increase in the amount of misfolded proteins. If these proteins accumulate, they activate the UPR by binding to the ER chaperone binding immunoglobulin protein (BiP/GRP78). In a normal, unstressed state, BiP binds to and inactivates the ER stress response proteins PERK, ATF6, and IRE1 α . At higher levels of ER stress, BiP will bind to misfolded proteins, thereby leaving the three ER stress response proteins free to be activated. Once freed, PERK and IRE1 α autophosphorylate to reach their active forms, whereas free ATF6 translocates to the Golgi apparatus. All three sensors then activate their downstream pathways, as shown in **Figure 1.1**. We have provided an abbreviated description of the UPR; in-depth analysis can be found in several recent reviews of the topic.^{23–26}

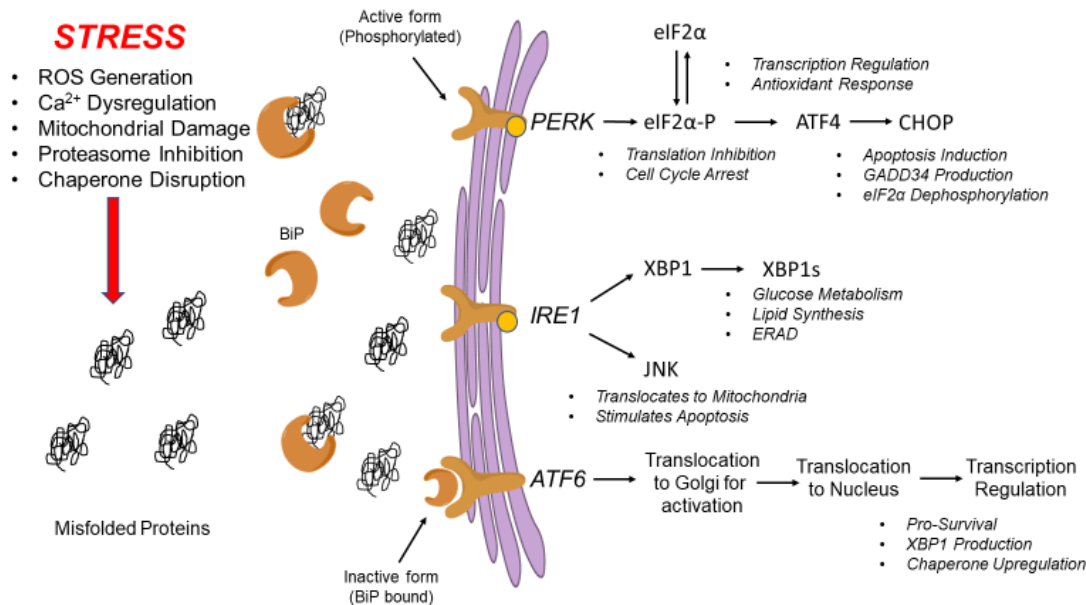


Figure 1.1. Schematic diagram of ER stress-response pathways and activation of the UPR.

The most well-established arm of the UPR is the PERK pathway. The PERK arm begins with the phosphorylation of the eukaryotic initiation factor 2 alpha (eIF2α).²⁷ eIF2α is required for protein synthesis, initiating the process by forming a critical component of the ternary translation initiation complex. Upon phosphorylation, eIF2α can no longer initiate translation, and a decrease in global protein synthesis in the cell occurs. This decrease helps reduce the protein folding load on the ER and allows the ER to devote its resources to refolding or eradicating misfolded proteins. Although global translation decreases after eIF2α phosphorylation, some stress response proteins become upregulated, including activating transcription factor 4 (ATF4) and its downstream products. ATF4 induces the transcription of proteins that ameliorate ER stress by managing ROS, amino acid synthesis, and protein export.²⁸ If these efforts succeed in reducing ER stress, eIF2α phosphorylation

levels decrease, and normal translation resumes, but if ER stress remains unresolved for an extended time or is acutely elevated to unmanageable levels, ATF4 upregulates the proapoptotic C/EPB homologous protein (CHOP), which triggers apoptosis.²⁹

The second arm of the UPR that may be activated by BiP dissociation is the IRE1 α pathway.²⁵ Once BiP dissociates, IRE1 α activates several downstream targets, including *c*-Jun N-terminal kinases (JNKs) and tumor necrosis factor receptor-associated factor 2 (TRAF2). It also cleaves part of X-box binding protein 1 (XBP1), activating this protein and allowing it to begin expression of its downstream transcripts, which regulate a variety of processes including glucose metabolism, lipid synthesis, redox homeostasis, and DNA repair. In cases of extreme ER stress, XBP1 and JNKs can also mediate apoptosis induction.³⁰

The final, least well-understood branch of the UPR is mediated by ATF6. Unlike PERK and IRE1 α , which have some proapoptotic functions, ATF6 mediates pro-survival pathways.^{31,32} After its activation, ATF6 translocates to the Golgi apparatus, where it is cleaved. The cleaved domain, a transcription factor, travels to the nucleus and begins regulating gene expression. The gene expression program induced by ATF6 includes upregulation of protein folding chaperones, such as BiP, and other ER stress-response proteins. ATF6 also causes production of antiapoptotic machinery that sequester and reduce the proapoptotic Bcl-2.

ER Stress and Cancer Progression

Recent studies have found that ER signaling and ER stress pathways undergo drastic changes in cancer cells. As such, the ER plays an integral role in cancer

aggressiveness, metastasis, and response to chemotherapy.^{33,34} Each of these aspects of the ER's role in cancer may be modulated by chemotherapeutic drugs. The role of many ER stress responses in chemotherapy is still not fully understood, and there are often conflicting reports regarding the role of specific ER pathways in cancer. Despite these knowledge gaps, several key operational changes to the ER and their implications for cancer therapy have been established.

The environment of cancer cells has several characteristics that contribute to ER stress, including low nutrient availability, hypoxia, low pH, and limited blood flow.^{1,35} Furthermore, the metabolic changes that lead to cancer, such as increased cell replication, also lead to an increased protein folding load and heightened ER stress. All these factors contribute to overactivation of the UPR in cancer cells relative to normal cells, and the upregulation of all three UPR branches is a common cancer phenotype. As in normal cells, the UPR protects cancer cells from the consequences of ER stress by managing protein translation and increasing the levels of protein-folding chaperones. As a result, UPR activation allows cancer cells to survive and proliferate even under highly unfavorable conditions. Perhaps unsurprisingly in this context, UPR activity levels have been directly linked to increased aggressiveness in tumors.^{5,36}

UPR induction does not only help cancer cells survive under harsh environmental conditions; it also conveys resistance to chemotherapy and radiation.^{5,6,37,38} Increased expression of ER stress regulators such as BiP and XBP1 have been correlated to cancer resistance both in vitro and in vivo.^{39,40} This resistance may be two-pronged, as UPR activation may protect cancer cells from the direct consequences of chemotherapy, such as increased ROS levels or DNA damage, by

upregulating ROS decomposition or DNA repair mechanisms. Alternatively, UPR induction may indirectly protect cells by inducing pro-survival pathways such as senescence or autophagy.

In addition to the role of ER stress in cancer survival, ER stress also has a strong link to cancer cell metastasis and the epithelial to mesenchymal transition (EMT).^{33,41,42} Although this link is still not fully understood, a large body of evidence points to BiP playing a significant role in metastasis during ER stress by interacting with the PI3K/AKT pathway.⁴³⁻⁴⁵ BiP attenuates PI3K, a metastasis inhibitor. Therefore, increased BiP expression correlates with increased tumor metastasis rates and poorer prognoses. As a result, elevated ER stress levels have generally been linked to increased rates of EMT,^{46,47} especially in response to chemotherapy.^{48,49} However, there is some debate regarding the relationship between ER and EMT because other studies have found that EMT sensitizes cells to ER stress-induced apoptosis.⁵⁰

Targeting the Endoplasmic Reticulum with Chemotherapy

Despite the UPR's role in promoting cancer progression and chemotherapy resistance, chemical induction of ER stress has recently garnered attention as an anticancer strategy.^{8-13,51} The high basal ER stress level in many cancer cells makes them particularly susceptible to chemotherapeutics that target the ER. This hypersensitivity has already been exploited by the FDA-approved proteasome inhibitors bortezomib and carfilzomib, which induce ER stress by preventing the degradation of unfolded proteins. The success of these drugs has led to the investigation of other ER stress-inducing agents, such as heat-shock protein 90

(HSP90) inhibitors like geldanamycin and 17-AAG,⁵² as well as BiP inhibitors such as versipelostatin.⁵³ These drugs selectively target cancer cells by disrupting their ability to remedy ER stress, leading to apoptosis. Another recently discovered therapeutic agent with high anticancer potential, salinomycin, selectively kills stem-like cancer cells via ER stress induction.⁵⁴ There have also been several reports of metal-based complexes that target the ER via mechanisms as diverse as their organic counterparts. Broadly, most ER stress induction by therapeutics may be subdivided into five causes: direct interaction with UPR machinery, disruption of protein folding chaperones, inhibition of protein degradation, interference with Ca²⁺ trafficking, or production of ROS.

Detection of ER Stress

The detection of ER stress may be accomplished by several methods, including fluorescence microscopy, histochemistry, and flow cytometry. Mechanistic information about the cause of ER stress induction may also be determined through some assays with chemical modulators of ER stress pathways. This topic has been reviewed extensively elsewhere,⁵⁵⁻⁵⁷ but we have provided a brief summary of some of the simplest and most common methods for the detection of ER stress induction, categorized by ER stress pathway. Researchers should bear in mind that ER stress induction may be a secondary or downstream effect of a compound, rather than the main target, and many compounds cause multiple types of ER stress. Also, there is no single assay to verify or negate the role ER stress plays in cell death.

The activation of one or more of the three main UPR branches is perhaps the

most obvious sign of ER stress. These pathways, which all rely on enhanced levels of specific protein marker or phosphorylation of signaling proteins, can be readily detected through Western blots.^{57,58} BiP upregulation serves as a broad indicator of ER stress, usually due to an increase in the level of misfolded proteins in the cell, which may be associated with any of the three UPR branches. The UPR branches can also be detected individually. The PERK arm of the UPR is investigated by measuring the relative levels of eIF2 α vs phosphorylated eIF2 α , with higher levels of phosphorylation indicating ER stress. If heightened phosphorylation of eIF2 α is confirmed, the role of this stress in cell death is determined by investigating increased expression of downstream pro-apoptotic proteins such as ATF4, CHOP, and NOXA. CHOP detection, in particular, is a key indicator of ER stress-mediated apoptosis. The activation of the IRE1 α arm of the UPR can be investigated by measuring the splicing of its substrate, XBP1. ATF6 activation is more difficult to detect, as it requires gene-reporter assays or transfection with fluorescent reporters for confocal microscopy.

Given the role of the proteasome in the ERAD process, measuring the proper function of this process is an important means to assay ER stress in cells. Several assays have been developed for evaluating the ubiquitin-proteasome system.^{59,60} The simplest assay for confirming proteasomal inhibition is to perform a Western blot to measure the level of ubiquitinated proteins. As the proteasome is inhibited, its substrates, marked with ubiquitin, accumulate inside the cell. An increase in the level of ubiquitinated proteins indicates a general disturbance in the proteasome system but does not confirm direct proteasome inhibition. The buildup of ubiquitinated proteins may also occur if folding chaperones, deubiquitinase enzymes, or ubiquitin ligases are

inhibited. Inhibition of the proteasome subunits may also be measured outside of cells using the purified enzyme.⁶¹ Finally, fluorescent reporter systems that label proteasomal substrates can be used, enabling the implementation of fluorescence microscopy or flow cytometry to probe proteasome function.⁶²

Because disruption of cellular Ca^{2+} trafficking may be related to ER stress, measurements of intracellular Ca^{2+} levels can provide insight on the mechanism of action of ER-targeting agents.^{63,64} For example, cell-permeable Ca^{2+} chelators can be used to probe these mechanisms. If an ER stress-inducing agent is operating through Ca^{2+} dysregulation, the addition of cell-permeable Ca^{2+} chelators is expected to alter the cytotoxicity of the compound. To more specifically evaluate the role of ER Ca^{2+} release, the SERCA pump inhibitor thapsigargin can be applied in conjunction with an ER stress-inducer in a similar manner. Intracellular Ca^{2+} fluctuations at the organelle level may also be evaluated using fluorescent Ca^{2+} sensors such as Calcium Green-5N. Lastly, Western blots can be carried out to analyze the expression levels of specific Ca^{2+} regulatory proteins, such as inositol 1,4,5-triphosphate receptors (IP3Rs).⁶⁵

Chemical modulators of ER homeostasis can also be used to detect ER stress or identify the mechanism of action of ER stress-inducing agents. Co-treating cells with antioxidants such as *N*-acetylcysteine (NAC) will decrease cytotoxic effects of compounds that act by producing ROS but should have no effect on those that do not. Thus, this agent can be used to determine if a compound induces ER stress via ROS production.^{66,67} The compound 4-phenylbutyrate aids in protein folding. If 4-phenylbutyrate decreases the cytotoxic effects of a compound, then a likely conclusion is that this compound acts via the induction of protein misfolding.⁶⁸ Chemical

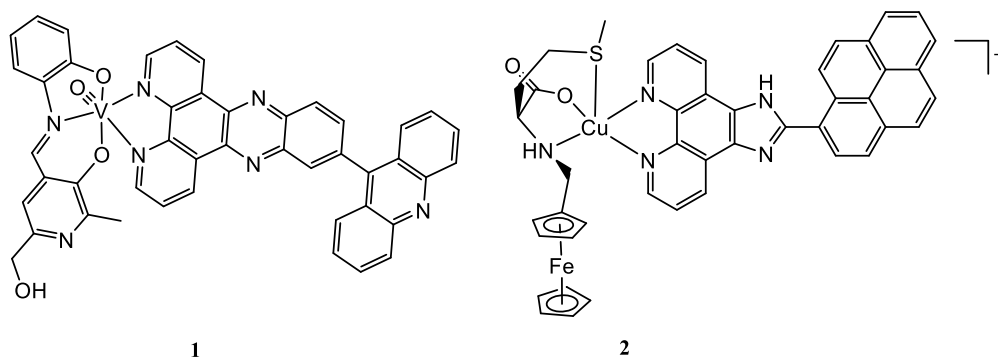
induction or downregulation of UPR pathways may also prove useful. For instance, the commercially available small molecules salubrinal and ISRIB stimulate and block the ER stress response, respectively. Salubrinal acts by preventing the dephosphorylation of eIF2 α , activating the PERK arm of the UPR and protecting cells from unfolded protein accumulation.⁶⁹ ISRIB, on the other hand, decreases eIF2 α phosphorylation levels and often sensitizes cells to ER stress.^{70,71}

Anticancer Metal Complexes that Induce ER Stress

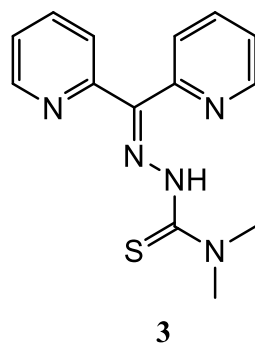
First Row Transition Metal Complexes

Relative to the reports of second and third row transition metal complexes that induce ER stress, first row complexes are comparatively rare. For this reason, first row transition metal complexes are grouped together, rather than by element, in this review. Generally, first row metal complexes have been shown to induce ER stress mediated by one of three mechanisms: photodynamic generation of ROS, disruption of intracellular metal trafficking, and proteasome inhibition. Many of these compounds operate in response to light. For example, there are reports that document ER stress induction by phototoxic vanadium (**1**)^{72,73} and bimetallic copper-ferrocene⁷⁴ (**2**) complexes. These complexes often act as photosensitizers for ³O₂, leading to the production of ¹O₂ and other ROS. The fluorescent vanadium complex **1** was shown to colocalize with ER Tracker Red via confocal microscopy experiments, and the ability of **1** and other derivatives to generate ¹O₂ was confirmed using spin-trap experiments and via the DCF-DA (dichlorofluorescein-diacetate) ROS-detection assay. Similarly, bimetallic complex **2** and related compounds exhibited colocalization with ER-

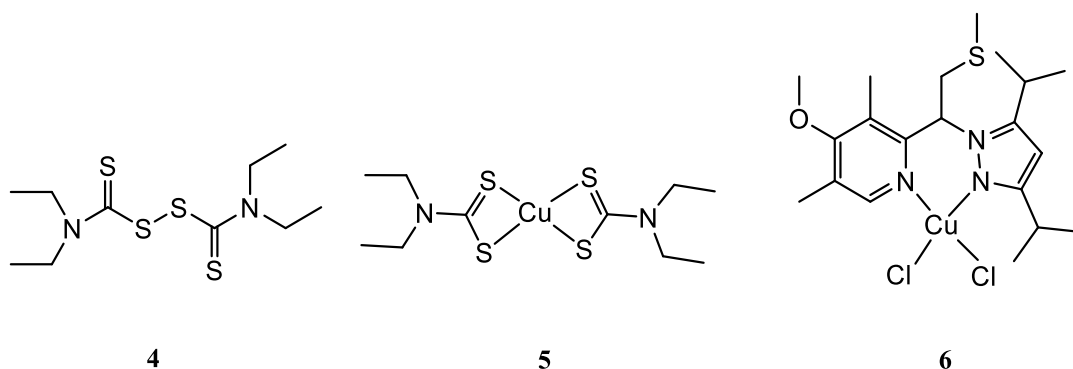
tracking dyes and induced apoptosis via ROS generation. Unlike the vanadium complex **1**, compound **2** generates ROS via a redox pathway rather than through energy transfer. All of these complexes bear extended aromatic structures such as acridine and dipyridophenazine, which likely engenders their observed ER localization due to hydrophobic interactions with the phospholipids of the ER membrane.



In addition to phototoxic ER stress mechanisms, there are several first row transition metal complexes that catalytically generate ROS via redox cycling. This family of anticancer agents includes copper and iron chelators that may be administered as the free ligand or as the pre-formed metal complex.^{75–85} These types of compounds are often selective for cancer cells over normal cells. One of the most studied iron-chelating thiosemicarbazones, di-2-pyridylketone 4,4-dimethyl-3-thiosemicarbazone (Dp44mT) (**3**), has been shown to generate ROS and activate all three branches of the UPR, eventually leading to apoptosis.⁷⁵ In the same study, it was shown that the well-known iron-chelating siderophore deferoxamine (DFO) also induces ER stress with a subtly different phenotype, indicating that iron chelation may play a more general role in this phenomenon.



Similar ER stress response occurs when cells are treated with copper ionophores such as disulfiram (**4**), the Cu-complex of disulfiram (**5**), or pyrazole-pyridines and their copper complexes, such as compound **6**. These ionophores cause intracellular copper overload, which leads to paraptotic cell death.⁸⁴ Detailed biological analyses indicate that treatment with copper chelators induces several ER stress hallmarks, including eIF2 α phosphorylation, CHOP expression, and polyubiquitinated protein accumulation. The authors conclude that these compounds share a similar mechanism in which the chelator brings extracellular Cu(II) into the cell and is then reduced to release cytotoxic free copper that leads to paraptosis, as shown in **Figure 1.2**



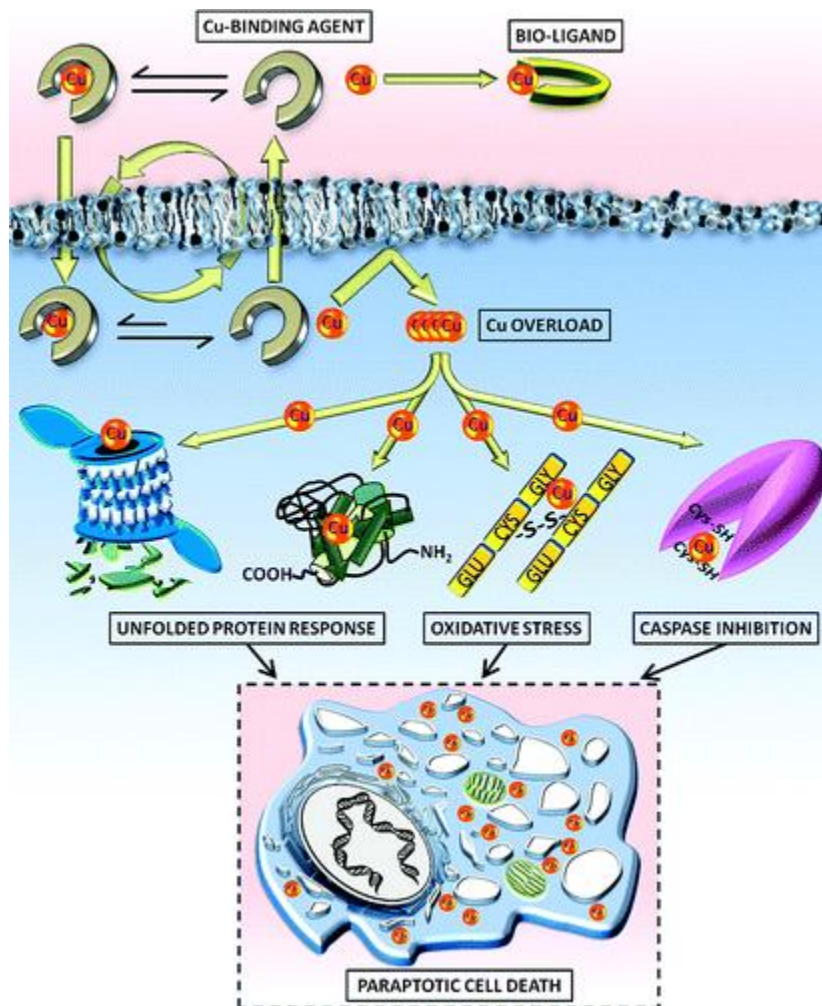


Figure 1.2. Proposed mechanism of ER stress induction by pyridine-pyrazole-based copper chelators, like that of **6**. These ligands act as ionophores for Cu(II), ultimately inducing copper overload that triggers the UPR and paraptosis. Adapted from reference 84 with permission from the American Chemical Society, copyright [2011].

Due to their capacity to act as electrophilic warheads, several first row metal complexes inhibit the nucleophilic catalytic site of the proteasome^{86–93} or ubiquitinase enzymes,⁸⁷ resulting in ER stress and apoptosis via the buildup of unfolded proteins. Due to the rapidly expanding interest in proteasome inhibitors as cancer therapeutics, the topic of metal-based proteasome inhibitors has recently been reviewed elsewhere.^{94–96} Here, we will focus on only a few examples that are pertinent to ER

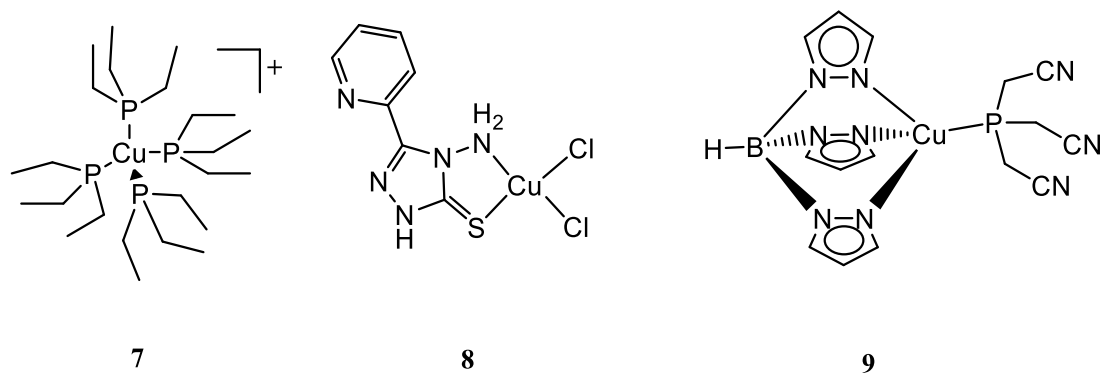
stress. One of the most relevant proteasome inhibitors is disulfiram (**4**), a drug clinically approved for alcoholism that is now being investigated as an anticancer agent. Several studies have shown that the copper complex of disulfiram and other dithiocarbamates inhibit proteasomal activity, leading to overaccumulation of misfolded proteins and apoptosis.^{88,89,97} Together, these studies highlight the potential of metal complexes as proteasome inhibitors, and support efforts to further optimize them to generate more potent, selective complexes.

Another well-investigated copper complex that induces ER stress and inhibits the proteasome is the Cu-phosphine complex **7**.^{98,99} This complex exhibits nanomolar activity against several colon and leukemia cancer cell lines, and it induces cell death by a combination of paraptosis and caspase-dependent apoptosis. Detailed mechanistic studies reveal that **7** causes increased expression of ER stress markers BiP and CHOP, as well as eventual PARP cleavage and caspase activation. The complex also effectively inhibits the ubiquitin-proteasome system and causes the accumulation of polyubiquitinated proteins. The cytotoxicity **7** is significantly attenuated in the presence of the translation inhibitor cycloheximide, indicating that protein synthesis, and possibly paraptosis, is required for this compound to exert its biological effects.

The Cu(II)-thioxotriazole complex **8** also triggers proteasome-mediated ER stress and paraptosis.¹⁰⁰ Thorough transcriptomics analysis of HT1080 cells treated with **8** revealed a marked upregulation of ER stress-related genes, especially those associated with protein folding and unfolded protein binding. Analysis via quantitative polymerase chain-reaction (qPCR) revealed upregulation of ER stress markers BiP and CHOP. The authors also observed the phosphorylation of eIF2 α , ATF4

upregulation, and XBP1 splicing, further confirming ER stress induction. Complex **8** triggers the accumulation of polyubiquitinated proteins and inhibits the activity of the proteasome in cell lysates, indicating that proteasomal inhibition may be its primary mechanism of action.

Proteasome inhibition leading to ER stress induction has also been reported for Cu(I) complexes bearing tris(pyrazolyl)borate ligands, such as compound **9**.⁹¹ Compound **9** exhibits sub-micromolar cytotoxicity against a broad panel of cancer cell lines and is selective for cancer cells over normal kidney (HEK293) cells. Treatment of ovarian cancer 2008 cells with **9** induced the accumulation of polyubiquitinated proteins and triggered increased phosphorylation of the UPR regulators PERK and IRE1. Like several other Cu complexes, the mode of cell death caused by this compound is paraptosis. Paraptosis was confirmed using cycloheximide, which attenuated the cytotoxicity of **9**, whereas caspase-dependent apoptosis was ruled out because caspase inhibitors had no effect on the activity of **9**. Compound **9** also significantly inhibited tumor growth in mice bearing murine Lewis lung carcinoma tumors without affecting their bodyweight, indicating that this compound does not give rise to acute toxicity. Given these favorable properties, compound **9** and related analogues have great promise as potential anticancer agents.



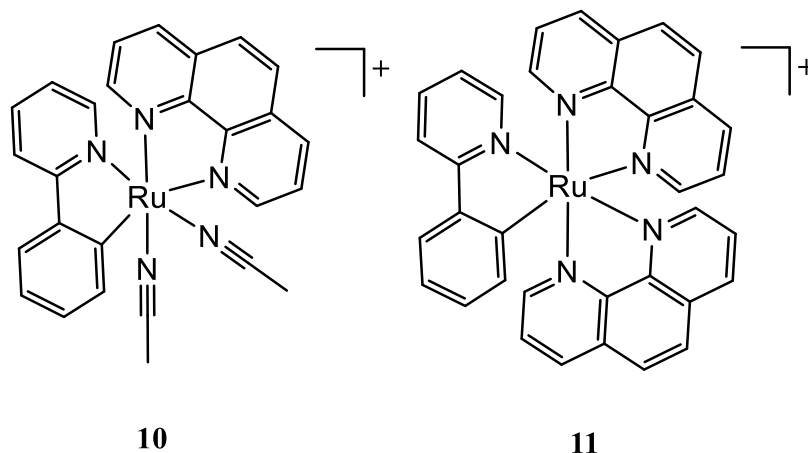
Ruthenium

Of all transition metals, ruthenium complexes have by far the most reports of ER stress-mediated anticancer activity. The ligand frameworks of Ru-based ER stress-inducing compounds vary widely. These compounds assume a range of different structural archetypes, including trispolypyridyl complexes, cyclometalated compounds, organometallic piano-stool structures, and simple coordination complexes. Despite having the same metal center, these complexes exhibit diverse mechanisms of ER stress induction.

One particularly potent and well-investigated class of Ru-based ER stress inducers are mono-cationic, cyclometalated Ru(II) complexes.^{101–103} A large library of ruthenium cyclometalated species, such as **10** and **11**, have been shown to induce ER stress and subsequent apoptosis. ER stress induction by these compounds has been extensively characterized by demonstrating hyperphosphorylation of eIF2 α , splicing of XBP1, and expression of CHOP.¹⁰² The role of CHOP in apoptosis induction was confirmed through the use of anti-CHOP siRNA. By silencing this pro-apoptotic

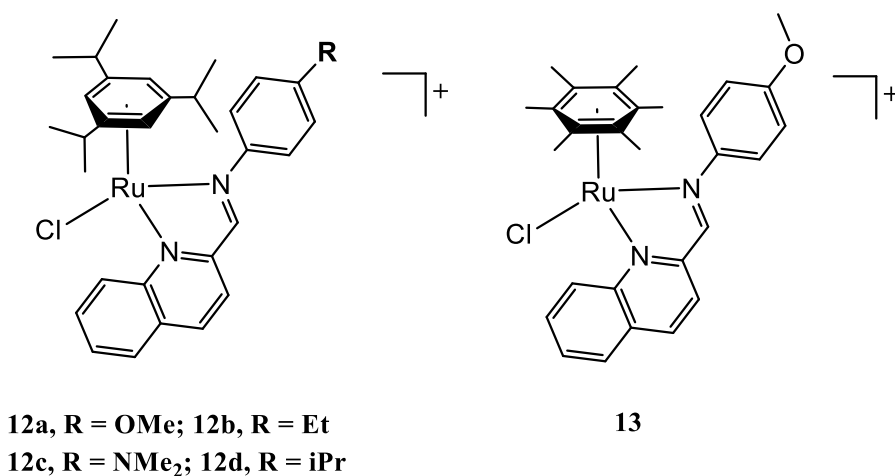
factor, the cells were significantly less sensitive to treatment by **10** and **11**. The original lead compound, **10**, also significantly inhibited tumor growth in vivo without severe side effects. Further structural optimization of **10** led to an expanded library of cyclometalated complexes with increased solubility and higher potency, with complex **11**, for instance, exhibiting low-nanomolar anticancer activity in vitro.^{104,105} Structure-activity studies revealed that complexes with relatively high lipophilicity were the most potent, and that complexes with intermediate redox potentials (0.4–0.6 V vs SCE) were most active. Based on this redox potential dependence, the authors concluded that electron transfer or oxidation of the Ru(II) center may play a role in their activity. Further investigation of the biological properties and cellular response to these compounds indicates that several of them induce both DNA damage and ER stress, whereas others act only via targeting the ER.¹⁰⁶ From a detailed analysis of cells treated with **10**, the authors found that this compound binds to histones, which ultimately lead to disruption of DNA replication.¹⁰⁷ The compound also downregulates hypoxia-inducible factor 1- α (HIF1 α) by directly interacting with the regulatory protein prolyl hydroxylase domain-containing protein 2 (PHD2), leading to hypoxia-selective anticancer activity.¹⁰⁸ Further experiments will be needed to determine whether DNA damage or ER stress is the major cause of cytotoxicity of this compound. Cellular uptake experiments revealed that **10** enters cells through iron transporters and via amino acid transporters. Genomic experiments revealed that cellular export and resistance to these compounds are mediated by the multi-drug transporter ABCB1 and by the endothelial growth factor repair (EGFR) pathway.¹⁰³ Together, these studies provide a thorough picture of the ER stress-mediated

anticancer properties of this class of compounds, which is further supported by promising in vivo activity and interesting insight on their resistance mechanisms.



In addition to cyclometalated compounds, several piano-stool ruthenium complexes have also been found to induce ER stress.^{109–113} Notably, these complexes have highly modular structures that are amenable to combinatorial synthesis. A combinatorial screening method was used to identify complexes such as **12a** to be potent ER stress-inducing anticancer agents.¹⁰⁹ In a follow-up study, the role of the arene substituent of complex **12a** was investigated by comparing the activities of **12a** and **13**, which contain the same pyridylimine ligand but different arenes. Both **12a** and **13** cause splicing of XBP1 and CHOP expression, indicating that they are ER stress inducers.¹¹⁰ Surprisingly, these two compounds induce ER stress by different mechanisms of action. Compound **12a**, bearing the 1,3,5-triisopropylbenzene ligand, causes ROS-mediated ER stress, whereas **13**, which contains the hexamethylbenzene ligand, acts via an ROS-independent mechanism. Both compounds **12a** and **13**, along

with a large number of related analogues, operate via p53-independent pathways and therefore retain their high cytotoxicity in p53-null cell lines.¹¹¹ By modifying the pyridylimine ligand of **12a**, other potent compounds like **12b-d** could be obtained. These compounds exhibit nanomolar activity against a broad panel of cancer cell lines.¹¹³ The cytotoxicity of these compounds is directly related to the π -acidity of the pyridylimine ligand, with more π -acidic ligands giving rise to more potent compounds. The ligand π -acidity is also correlated to the ROS production capabilities of these complexes. This result indicates that these compounds induce ER stress and cell death via the production of ROS. This mechanism was confirmed by showing that the cytotoxicity of these compounds is significantly reduced in the presence of the antioxidant NAC, as shown in **Figure 1.3**. Related dinuclear ruthenium arene complexes bearing diimine ligands also possess anticancer activity in the low micromolar range, and their activity arises from both DNA damage and ROS-mediated ER stress pathways.¹¹⁴ Based on the powerful anticancer activity and unique anticancer mechanisms of this class of compounds, they represent a promising new class of metallodrugs.



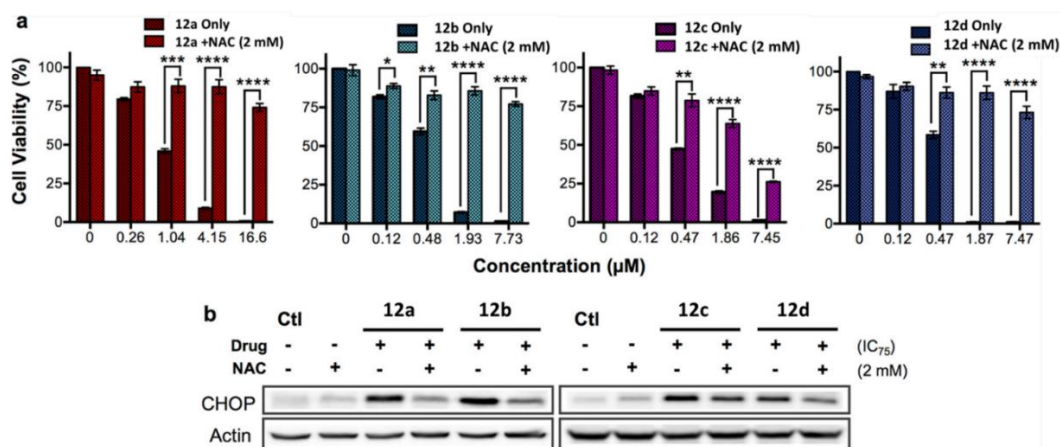
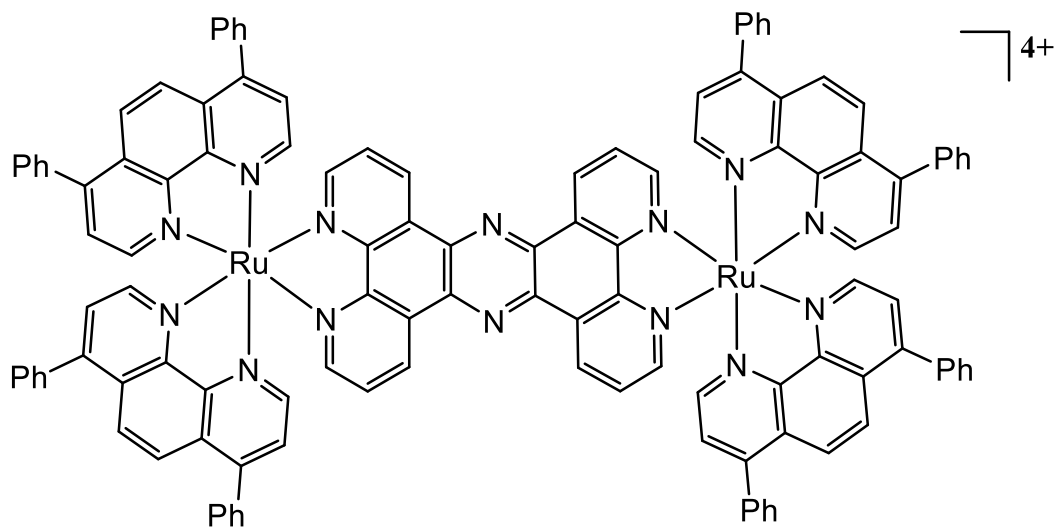


Figure 1.3. Piano-stool ruthenium complexes, like **12**, induce their cytotoxic effects and ER stress by producing ROS. (a) Cell viability of cells treated with compounds **12a-d** in the presence and absence of NAC in HCT-116 cells (2 mM). (b) CHOP expression level in HCT-166 cells treated with **12a-d** in the presence or absence of NAC (2 mM). Adapted from reference 113 with permission from the American Chemical Society, copyright [2018].

Although polypyridyl Ru(II) complexes have well-established anticancer activity,¹¹⁵ there are relatively few reports of ER stress-related anticancer mechanisms for these compounds.^{116–118} One extremely hydrophobic, dinuclear complex bearing 4,7-diphenyl-1,10-phenanthroline (DPP) ligands (**14**) exhibits low-micromolar anticancer activity. Its localization, tracked by fluorescence microscopy, confirmed that it is taken up by the ER.¹¹⁶ The complex interacts strongly with liposomes and shows environment-dependent luminescence, with greatly increased luminescence in hydrophobic media. Despite the fact that this compound localizes to the ER, experiments to probe whether it induces ER stress were not carried out. A different family of ruthenium polypyridyl complexes bearing *p*-cresol groups has been reported to induce ROS-mediated ER stress, as evidenced by CHOP induction and

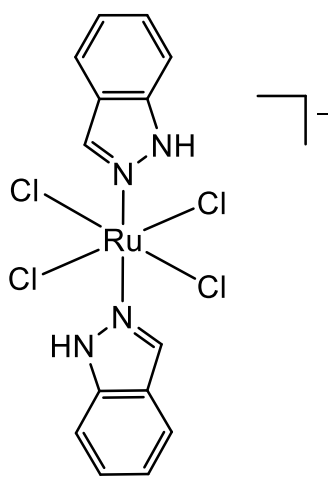
phosphorylation of eIF2 α .¹¹⁸



14

Ru(III) coordination complexes have also been linked to ER stress induction. The Ru(III)-indazole complex anion KP1019 or NKP-1339 (**15**), which has undergone clinical investigations for the treatment of cancer,^{119,120} has recently been shown to induce ER stress.¹²¹ This complex triggers several ER stress hallmarks, including phosphorylation of PERK and eIF2 α , as well as upregulation of XBP1 and CHOP. However, the IRE1 α pathway is unaffected. This complex also causes downregulation of BiP, a result that is unexpected for conventional ER stress-inducers. The authors attribute this downregulation to activation of the ERAD pathway because upregulation of ERAD has previously been shown to reduce BiP levels, and because no downregulation of BiP was found on the mRNA level. ER stress induction by **15** may arise from ROS generation, as previous reports have linked ROS generation to the anticancer activity of **15**.¹²² Another recent study has reported that **15** inhibits SERCA

transporters, which may induce ER stress by disruption of intracellular Ca^{2+} trafficking.¹²³ This mechanism explains the phenotype observed in response to this compound, as it is very similar to the thoroughly investigated organic SERCA inhibitor thapsigargin. ER stress induction by this compound may also result in immunogenic cell death (ICD), as a recent study reports that cells exposed to **15** exhibited several hallmarks of ICD, including calreticulin exposure and ATP release.¹²⁴ Taken together, this compound's in vivo activity, unorthodox mechanism of action, and potential to cause ICD in cancer cells make it a promising anticancer agent.

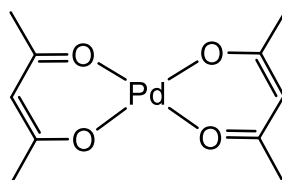


15

Palladium

Unlike its heavier congener platinum, which has been widely investigated for anticancer activity, palladium complexes remain largely unexplored. To date, only one palladium complex, $[\text{Pd}(\text{acac})_2]$ (**16**) has been shown to exhibit anticancer activity that is mediated by ER stress induction.¹²⁵ Unlike conventional platinum-based drugs, this

compound does not bind closed circular DNA. Treatment of cancer cells with **16** induced several markers of ER stress, including activation of ATF4 and XBP1, upregulation of BiP, and ER swelling. The complex also causes CHOP-dependent apoptosis, which was determined by showing that CHOP silencing with siRNA significantly rescues cells from apoptosis. Although the exact cause of ER stress induction by **16** is not confirmed, it is hypothesized to arise from interference with ER Ca^{2+} stores because treatment of cells with this compound gives rise to a dose-dependent release of stored Ca^{2+} from the ER. Complex **16** also shows activity in vivo. It significantly inhibited tumor growth in mice bearing H460 lung cancer xenografts, but no studies were performed to determine whether ER stress was also responsible for the in vivo activity of **16**. Further investigation is needed to determine whether this ER stress-inducing activity is characteristic of labile Pd(II) complexes or unique to $[\text{Pd}(\text{acac})_2]$.

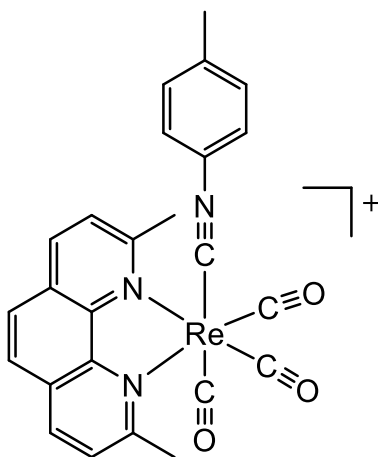


16

Rhenium

In recent years, rhenium complexes have arisen as a new promising class of metal-based anticancer agents.^{126–130} Through research efforts to explore the anticancer activities of these compounds, an ER stress-causing rhenium compound was discovered.¹³¹ Compound **17**, a Re(I) tricarbonyl complex bearing both a diimine and isonitrile ligand, induces ER stress by causing the accumulation of unfolded

proteins. This buildup of unfolded protein results in increased phosphorylation of eIF2 α , leading to the induction of ATF4 and expression of CHOP (**Figure 1.4**). The complex also induces mitochondrial fragmentation and eventual depolarization, leading to apoptosis. Unlike similar late transition metal complexes, this complex apparently does not operate via ROS induction, interference with intracellular Ca²⁺ stores, or inhibition of the ubiquitin-proteasome system. The potency of this complex is enhanced in the presence of the eIF2 α dephosphorylation inhibitor salubrinal. Because this compound does not operate via one of three canonical means of induction ER stress, further studies are needed to determine its mechanism of action to guide efforts to develop more potent analogues.



17

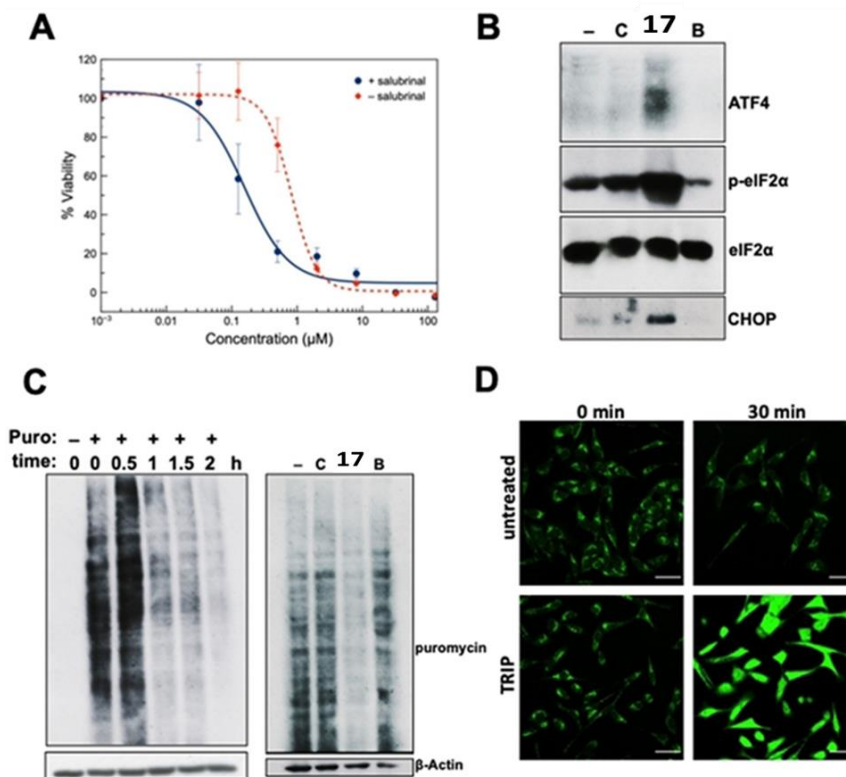


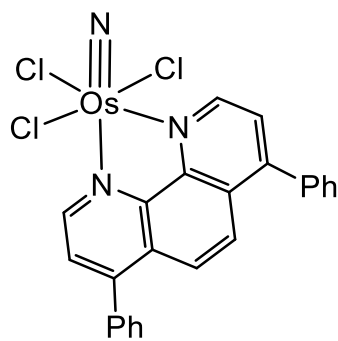
Figure 1.4. Cellular response upon treatment with **17**. (A) Dose-response curves of HeLa cells treated with **17** in the presence or absence of the eIF2 α dephosphorylation inhibitor salubrinal. (B) Western blot analysis of ER stress markers ATF4, p-eIF2 α , and CHOP upon treatment of A2780 cells with vehicle control (-), cisplatin (C), **17**, or bortezomib (B). (C) Puromycin assay indicating a decrease in A2780 cellular translation levels upon treatment with **17** (left panel) or vehicle control (-), cisplatin (C), **17**, or bortezomib (B) (right panel). (D) Confocal fluorescence microscopy images of protein aggregates formed upon treatment of HeLa cells with **17**. Protein aggregates were stained with the thioflavin T dye. Adapted from reference 131 with permission from John Wiley and Sons, copyright [2019].

Osmium

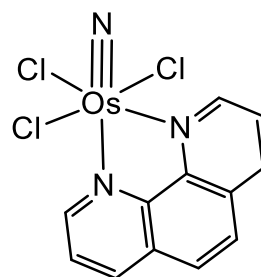
Despite the increasing the use of osmium complexes for the treatment of cancer,^{132,133} only two such complexes have been shown to induce ER stress.^{134–136} These two ER stress-inducing compounds, **18** and **19**, both contain the high oxidation state Os(VI) center with a terminal nitrido ligand. Detailed mechanistic studies using

varying shRNA sequences were performed on this class of compounds to probe their mechanisms of action. Based on the relative protective or sensitizing effects of the shRNA sequences, the cellular processes affected by the compounds could be determined. Surprisingly, the mechanisms of action of these Os-nitrido complexes depend heavily on the nature of the substituents on the supporting diimine ligand. For example, compound **18** with a DPP ligand operates via the induction of ER stress, whereas **19**, which bears 1,10-phenanthroline, causes both DNA damage and ER stress. Evidence for the fact that **18** causes ER stress was obtained by showing that eIF2 α phosphorylation and CHOP activation result when cells are treated with this compound. Furthermore, **18** gives rise to cellular apoptosis in a manner that is independent of p53. In contrast to the rhenium complex **17**, the activity of complex **18** is decreased in the presence of the ER stress mediator salubrinal. The less lipophilic complex **19**, which causes both ER stress and DNA damage, has cancer stem cell-selective activity, as shown in part by its ability to effectively reduce growth of breast cancer stem cell mammospheres (**Figure 1.5**). This high activity may arise from the ability of the compound to trigger ER stress via the eIF2 α pathway, which has been implicated as a target for selectively killing stem cells.⁵⁰ The stem cell selectivity exhibited by **19** makes it a particularly promising drug candidate because most conventional chemotherapeutic agents are ineffective against cancer stem cells.^{137,138} In addition to its in vitro activity, **19** has high activity in vivo. In an orthotopic glioblastoma mouse model, mice treated at a dose of 0.5 mg/kg with complex **19** were able to prolong mouse survival by 130% in comparison to mice treated with the vehicle control. Given their promising in vitro and in vivo activity, these stem cell-

selective, ER stress-inducing Os-nitrido compounds show great promise as anticancer agents. Because only a limited number of complexes have been analyzed thus far, more compounds should be synthesized and studied in order to develop a SAR to identify more potent analogues.



18



19

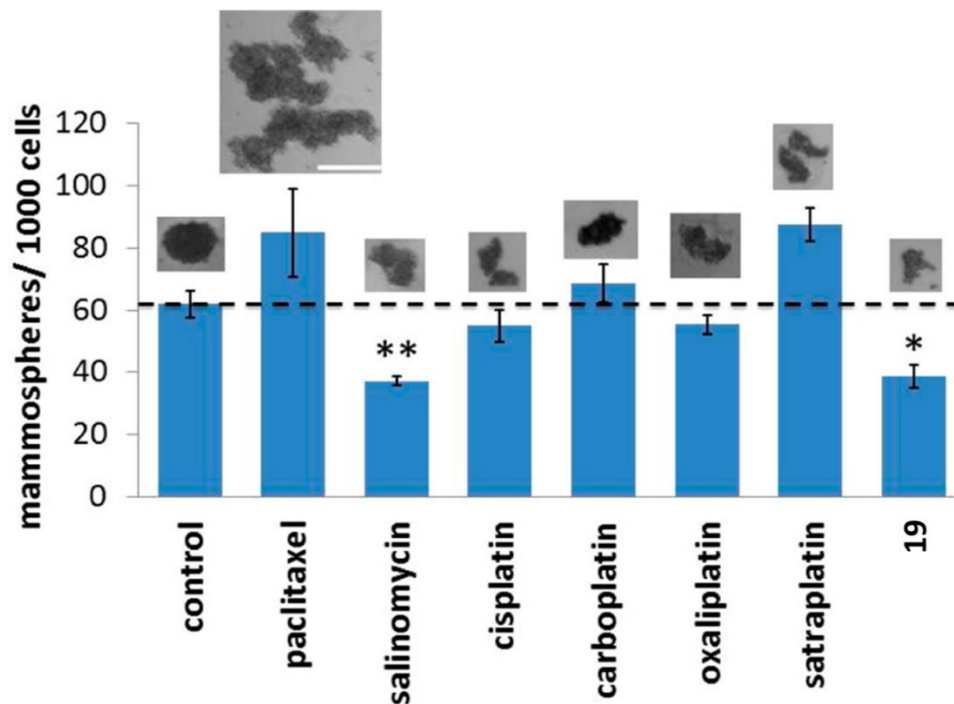


Figure 1.5. Mammosphere formation of HMLER breast cancer stem cells in the presence or absence of the indicated anticancer compounds, including **19**, at their IC₅₀ values after 5 days of treatment. Representative brightfield microscopy pictures of mammospheres treated with the indicated compounds are provided above the relevant columns. Adapted from reference 135 with permission from the American Chemical Society, copyright [2014].

Iridium

Although the majority of Ir(III) anticancer agents are based on the cyclopentadienyl piano stool structural type,¹³⁹ thus far only substitution-inert, cyclometalated polypyridyl complexes of iridium have been demonstrated to cause ER stress. Many of these complexes are luminescent with very high quantum yields, allowing determination of their intracellular localization to organelles such as the ER. Furthermore, the rich photophysical properties of this class of compounds often give rise to phototoxic effects that are mediated by the generation of ROS. If these compounds localize to the ER, the generation of ROS by light irradiation directly

damages this organelle and gives rise to ER stress-mediated apoptosis.^{140–143}

Compound **20**, for example, is a representative phototoxic ER stress-inducing agent within this class of Ir(III) cyclometalated complexes that produces both $^1\text{O}_2$ and superoxide upon irradiation. This complex was demonstrated to photo-cross link and photo-oxidize proteins via both photoinduced electron transfer and energy transfer.¹⁴²

Proteomics experiments were performed on cell lysates to identify the most commonly damaged protein targets of this compound upon irradiation, as shown in **Figure 1.6**. These targets span proteins associated with the ER, mitochondria, and membranes, indicating that widespread cellular damage is caused by the ROS released from **20**.

Based on these results, the authors propose a dual mechanism of phototoxicity from these compounds, in which superoxide causes protein crosslinking and aggregation, and $^1\text{O}_2$ oxidizes proteins. Another ER-localizing photoactive cyclometalated Ir(III) complex bearing a terpyridine ligand, compound **21**, was investigated and shown to trigger ER stress upon irradiation.¹⁴³ This compound, which has an enhancement in cytotoxicity of nearly 100-fold in the presence of light, induces an increase in cytosolic Ca^{2+} levels after irradiation, presumably due to release of Ca^{2+} from the ER. Thus, it is likely that the ROS generated by this compound directly attack the Ca^{2+} -trafficking machinery of the ER. The iridium *N*-heterocyclic carbene (NHC) complex **22** has also been shown to localize to the ER and generate ROS locally upon irradiation, but further studies are needed to characterize the full anticancer potential of this compound.¹⁴¹

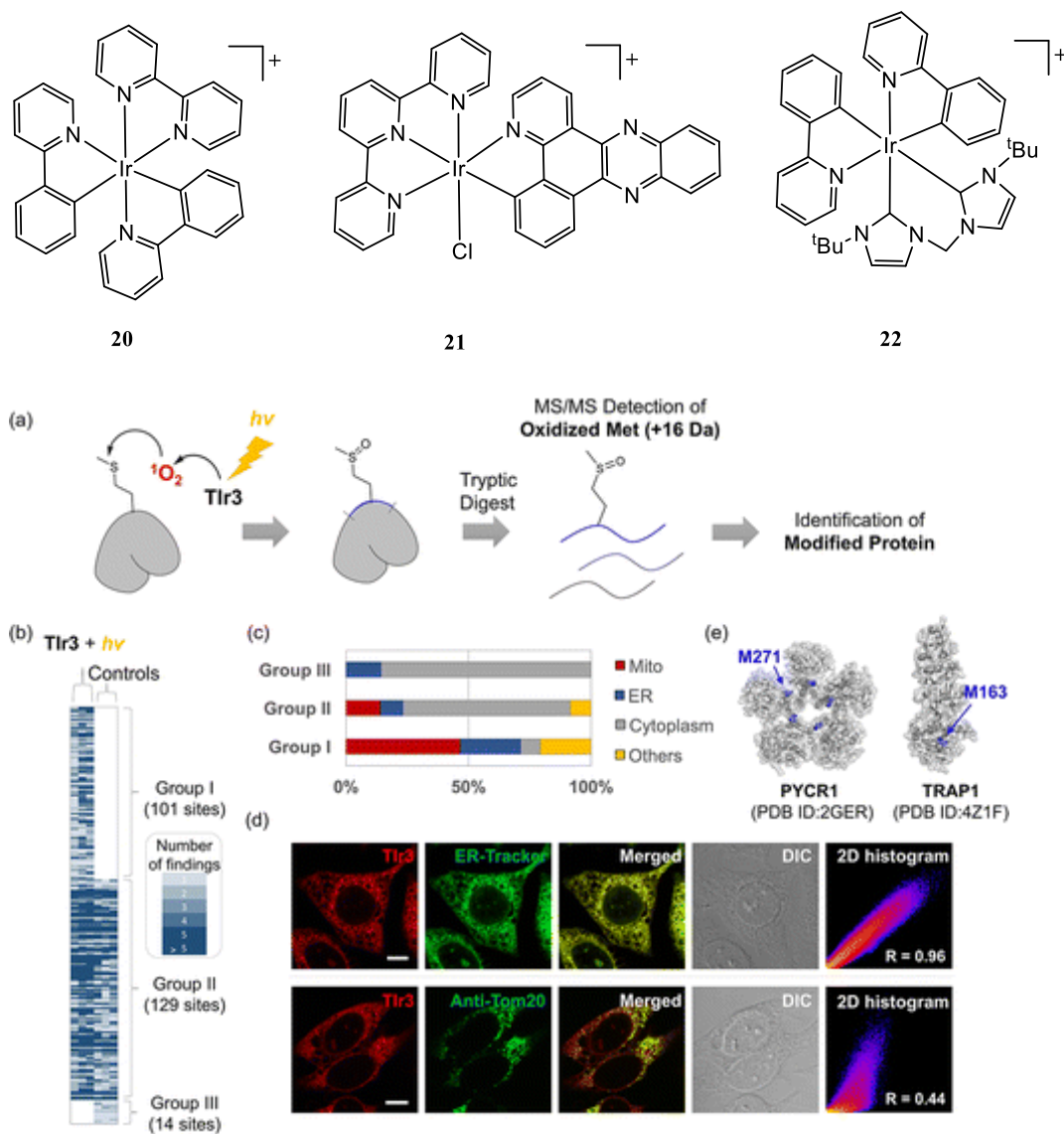
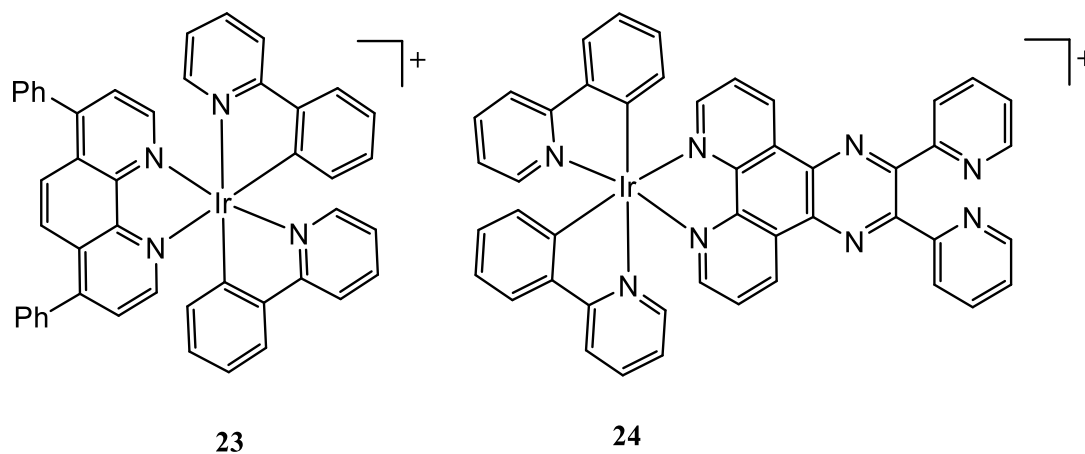


Figure 1.6. Identification of intracellular protein targets of iridium photosensitizers. (a) Pictorial representation of the method used for MS/MS detection of oxidized methionine. (b/c) Distribution of proteins oxidized by **20** upon photooxidation (Group I), relative to those oxidized by endogenous processes (Groups II and III). (d) Confocal fluorescence microscopy imaging of iridium complexes showing colocalization with ER-Tracker dye. (e) Crystal structures of selected oxidized proteins responsible for mitochondrial function. Reproduced from reference 142 with permission from the American Chemical Society, copyright [2016].

Certain members of this class of cyclometalated Ir(III) complexes are also capable of inducing ER stress in the absence of light. Complex **23** and related structural analogues, for example, cause potent cytotoxic effects in the dark. These compounds were shown to localize to cell membranes, particularly the organelle membranes of the ER. Cell death induced by these agents was accompanied by mitochondrial fragmentation, mitochondrial membrane depolarization, cytochrome *c* release from the mitochondria, and caspase 3 activation.¹⁴⁴ Complex **23** triggers expression of CHOP, indicating that ER-mediated apoptosis is operational. This compound also causes Ca²⁺ release from the ER to the cytosol, a process that precedes mitochondrial Ca²⁺ overload and the observed mitochondrial damage. Thus far, only the analog containing the DPP ligand has been studied for ER stress induction, so further studies will be needed to understand which structural properties are required to produce the observed phenotype. Complex **24**, which bears an expanded phenazine ligand, exhibits nanomolar cytotoxicity in MCF-7 breast cancer cells, which is mediated by ER stress.¹⁴⁵ This compound induces paraptotic cell death, as evidenced by activation of MAP kinases and abrogation of its anticancer activity by the protein synthesis inhibitor cycloheximide. Unlike the other cyclometalated Ir(III) ER stress inducers, this compound appears to accumulate preferentially in the mitochondria. Within the mitochondria, it has a secondary effect on the ER, due to the production of ROS that causes inhibition of the ubiquitin-proteasome system. Thus, this compound shows that ER localization is not a strict requirement for causing ER stress. A final, less well investigated class of Ir(III) compounds that deserves mention are a family of neutral complexes bearing phenylpyridine and tetrazolato ligands.¹⁴⁶ Despite not being

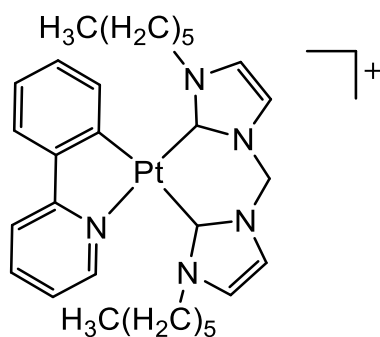
cationic like the other Ir(III) complexes discussed, these agents still localize to the ER and trigger cell death. However, few mechanistic studies have been performed that verify them to cause ER stress. Their localization to this organelle suggests that ER stress could be a likely mechanism.



Platinum

Due to their clinical success, Pt compounds are among the most thoroughly explored class of metal-based anticancer agents. Although the clinically approved Pt anticancer agents operate via DNA binding, recent studies have identified Pt complexes with novel mechanisms of action, which includes ER targeting. Within the latter category, a family of luminescent Pt(II)-NHC complexes, including complex **25**, localize to the ER and exhibit moderate phototoxicity.¹⁴⁷ Upon irradiation, these compounds induce ER stress, which was confirmed via the detection of phosphorylated PERK and eIF2 α by Western blot. Following ER stress, the usual cascade of mitochondrial depolarization, caspase activation, and apoptosis occurs. Complex **25** was found to be the most selective agent within this class of compounds. It exhibits a greater than 30-fold increase in cytotoxicity upon irradiation, reflecting

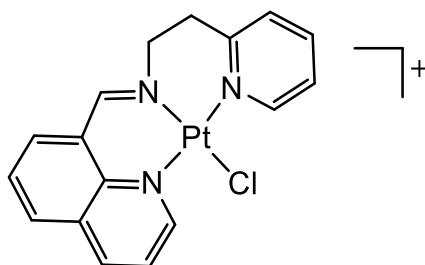
the potential of these complexes for use in PDT. Further mechanistic studies on **25** showed that this compound triggers ICD.¹⁴⁸ The ICD caused by **25** is likely a direct consequence of ER stress induction, as ER stress in general and especially eIF2 α phosphorylation is often correlated with ICD.^{149,150} The ICD triggered by **25** was detected by confirming that the “eat me” signal calreticulin is translocated to the cell membrane. The presentation of calreticulin marks the cell for phagocytosis by immune cells. Flow cytometry provided further confirmation that macrophages will phagocytose cells treated with **25**. The potential of ER stress-inducing agents, like **25**, to trigger ICD highlights the value of these compounds in the clinic.



25

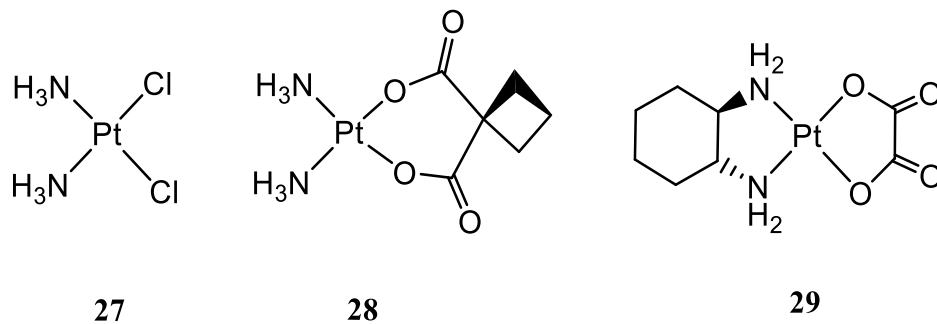
A Pt(II) complex bearing a tridentate quinoline-Schiff base ligand, **26**, has also been reported to induce ER stress.¹⁵¹ This compound localizes to the mitochondria, triggering its depolarization. The ER is affected downstream of this process, as evidenced by the phosphorylation of PERK and eIF2 α and induction of CHOP. Compound **26** was further evaluated in vivo. This compound was able to significantly reduce tumor growth in mice bearing A549 lung cancer xenografts. Despite its distinct mechanism, compound **26** was equally effective as cisplatin in this in vivo antitumor

model.

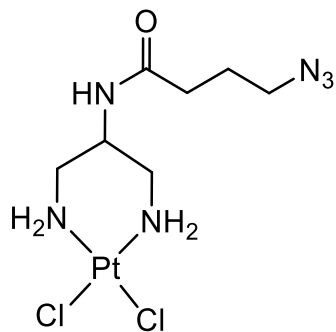


26

Recently, there has been some controversy regarding the mechanisms of action of the three FDA-approved platinum drugs cisplatin (**27**), carboplatin (**28**), and oxaliplatin (**29**). These compounds are known to act as DNA-damaging agents based on their abilities to form covalent adducts. However, recent studies have shown that ER stress can result from treatment with these drugs.^{152–156} For instance, cisplatin can induce apoptosis even in anucleated cytoplasts, cells lacking a nucleus, where DNA damage-mediated cell death cannot occur.¹⁵² The authors of this study showed using cell-permeable Ca^{2+} chelators that in these cells apoptosis induction via cisplatin was dependent on cytosolic Ca^{2+} accumulation. Cisplatin also induced upregulation of BiP and the Ca^{2+} -dependent protease calpain in these cells, confirming the role of ER stress and Ca^{2+} trafficking in apoptosis induction by cisplatin. These results support a growing body of literature indicating that platinum drugs induce ER stress in addition to DNA damage.¹⁵⁷



In a more recent study, pull-down methods were used to identify the protein targets of platinum anticancer agents in yeast cells.¹⁵⁴ Azidoplatin (**30**), a model for conventional DNA-binding platinum anticancer agents, contains an azide functional group for carrying out pulldown experiments via click chemistry. This compound was used to identify potential molecular targets of cisplatin-like Pt(II) compounds, as shown in **Fig. 7**. After treating yeast cells with **30**, click chemistry and biotin-streptavidin pull down was used to isolate covalent Pt-protein complexes. A large number of the proteins identified were related to ER stress, whereas relatively few proteins were related to DNA damage response. In particular, components of the ubiquitin-proteasome system and the protein-folding chaperone PDI were detected. Isolated PDI was used to confirm that compound **30** makes covalent adducts with this protein, leading to its inhibition. The authors also confirmed that both **30** and cisplatin induce the UPR pathway and ER stress in yeast, supporting the theory that ER protein binding is responsible for Pt-induced cell death. Further experiments are needed to elucidate whether these pathways are also operative in human cells.



30

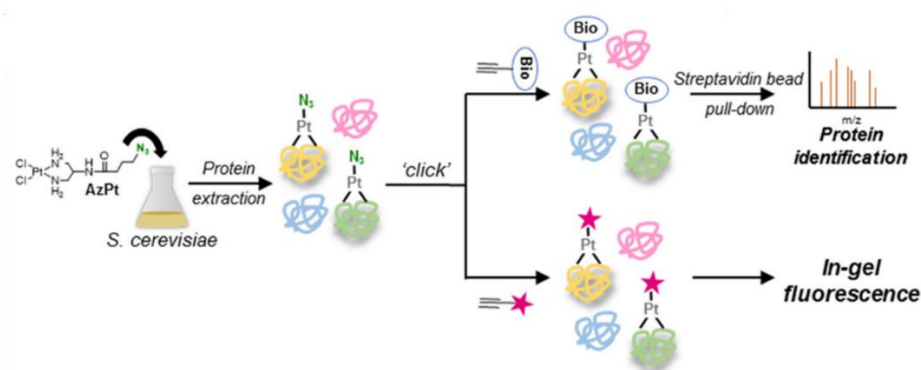
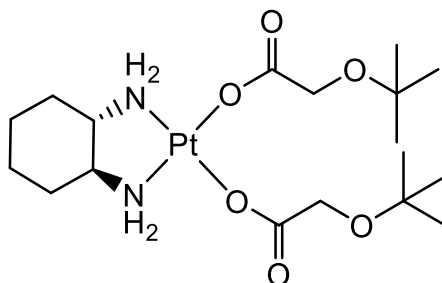


Figure 1.7. Schematic representation of pull-down assays performed using **30**, abbreviated as AzPt in this figure, to detect protein targets of Pt(II) agents. Adapted from reference 155 with permission from the American Chemical Society, copyright [2017].

ER stress and UPR induction have also been found to occur following oxaliplatin treatment. In one study, the administration of oxaliplatin gave rise to elevated ROS levels that proceeded to activate the ER stress response, which led initially to cytoprotective autophagy followed by eventual apoptosis.¹⁵³ The knockdown of CHOP with siRNA decreased the cytotoxicity of oxaliplatin, supporting the role of ER stress in apoptosis induction. The antioxidant NAC also protected cells from oxaliplatin toxicity. The interpretation of this experiment is challenging because thiols, like NAC, are known to directly bind to and deactivate

Pt(II) compounds in a manner that is independent of ROS.^{158,159} Another study also investigated the role of ER stress in the anticancer activity of oxaliplatin. The authors also show that ER stress mediates apoptosis induction by oxaliplatin. Resistance to oxaliplatin was conferred by overexpression of the multi-drug transporter ABCG2, which decreases the ER stress response.¹⁵⁵ The idea that oxaliplatin may not have DNA as a primary target is also supported by recent work using an RNAi approach to identify the cell damage profile of oxaliplatin.¹⁶⁰ The authors found that, rather than damaging DNA, oxaliplatin may instead target ribosome biogenesis.

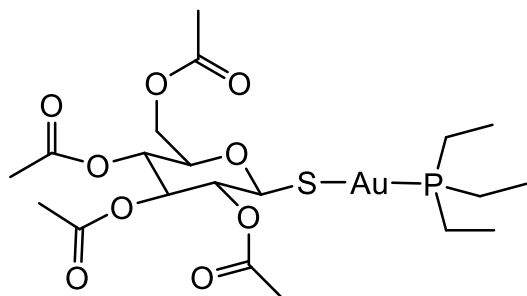
A structural analogue of oxaliplatin, compound **31**, was also recently shown to exhibit potent in vitro and in vivo anticancer activity.¹⁶¹ This compound induces mitochondrial damage and ROS generation, leading to Ca²⁺ release from the ER. The resulting cytosolic Ca²⁺ overload triggers apoptosis via the intrinsic mitochondrial pathway. This compound activates several ER stress markers, including upregulation of BiP, phosphorylation of eIF2 α , and expression of CHOP. The role of Ca²⁺ in cell death induction was confirmed by the simultaneous upregulation of IP3R and downregulation of ERp44, essential Ca²⁺ regulatory proteins associated with the ER. The activity of **31** decreased when CHOP was silenced with siRNA, confirming the role of ER stress in cell death initiation. The compound also significantly inhibited tumor growth in vivo with minimal side effects. Importantly, Western blot analysis confirmed that ER stress was responsible for the in vivo antitumor activity of **31**.



31

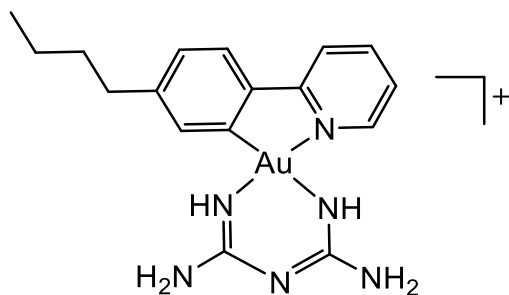
Gold

Several gold complexes exhibit ER stress-mediated anticancer activity, including the well-known rheumatoid arthritis drug auranofin (**32**), which has also been evaluated as a potential anticancer agent.^{162,163} Compound **32** triggers multiple ER stress markers in cancer cells, including XBP1 splicing, eIF2 α phosphorylation, and expression of CHOP.¹⁶⁴ The underlying cause of ER stress induced by **32** likely arises from ROS generation that results in the accumulation of misfolded proteins. This hypothesis is supported by the observation of increased levels of polyubiquitinated proteins and folding chaperones like the heat shock proteins. It has also been shown that **32** directly inhibits proteasomal deubiquitinases, a property that may be responsible for the in vivo and in vitro detection of excess polyubiquitinated proteins.^{165,166} **32** and other gold complexes also inhibit thioredoxin reductase (TRX), a selenium-containing enzyme responsible for redox homeostasis.^{167–170} TRX inhibition disrupts disulfide formation in the ER, further contributing to ER stress.¹⁷¹



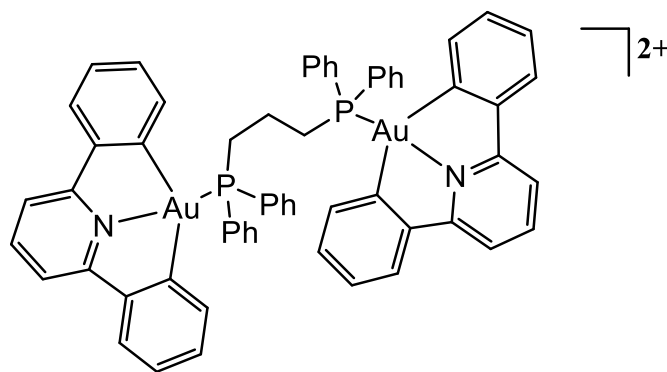
32

Although auranofin is currently the only Au(I) complex reported to induce ER stress, several anticancer complexes of Au(III) target the ER.^{172–174} For example, the cyclometalated Au(III) complex **33** induces cancer cell death and prevents angiogenesis by causing ER stress.¹⁷² Confocal fluorescence microscopy experiments of cells treated with this compound revealed ER swelling. Furthermore, upregulation of BiP and CHOP, as well as eIF2 α phosphorylation, caused by **33** was confirmed by Western blot. Unlike other ER stress inducers discussed above, the activity of compound **33** was not diminished in the presence of caspase inhibitors, indicating that it does not trigger caspase-dependent apoptosis. Instead, the translation inhibitor cycloheximide was shown to decrease the cytotoxic effects of **33**, suggesting that paraptosis is operational.



33

The dinuclear compound **34** is another example of an ER stress-inducing Au(III) complex.¹⁷³ Compound **34** is extremely potent in vitro, with IC₅₀ values in the low-nanomolar range in a variety of cancer types. Western blot analyses showed BiP upregulation, hyperphosphorylation of eIF2 α , and CHOP expression in response to this compound, confirming that it induces ER stress. The cause of ER stress triggered by **34** was attributed to the inhibition of TRX. Assays using both purified enzyme and within living cells confirmed that **34** is a potent TRX inhibitor. Compound **34** was also tested for in vivo anticancer activity in mice bearing hepatocellular carcinoma cancer xenografts. The results of these studies (**Fig. 8**) showed that this compound is more effective at inhibiting tumor growth than both cisplatin and doxorubicin. These results further support ER targeting as a strategy for the development of anticancer agents.



34

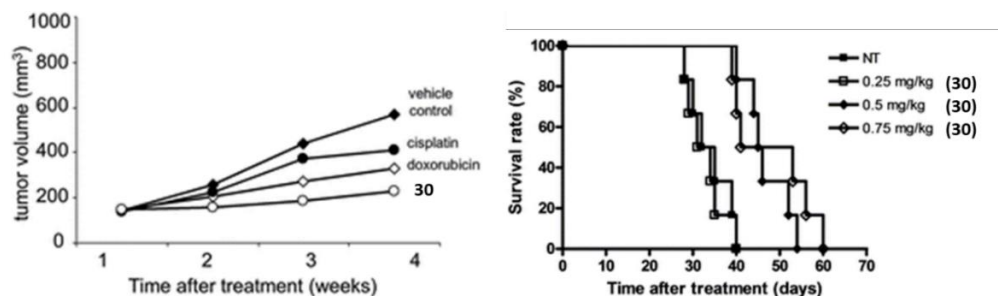
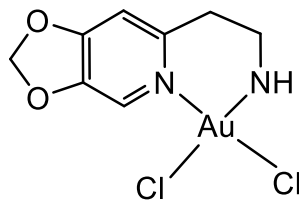


Figure 1.8. (Left) Tumor volume versus treatment time for mice bearing hepatocellular carcinoma cancer xenografts. Mice were treated with **30** and other control compounds twice weekly. (Right) Mouse survival rate versus treatment time for mice bearing orthotopic hepatocellular carcinoma tumors. Adapted from reference 173 with permission from the Royal Chemical Society, copyright [2013].

Compound **35** is another example of a Au(III) complex that has potent *in vitro* and *in vivo* anticancer activity.¹⁷⁴ Cellular uptake and organelle fractionation experiments revealed that **35** localizes preferentially to the mitochondria. Furthermore, mitochondrial ROS induction was confirmed via the DCF-DA assay. The cytotoxic effects of these mitochondrial ROS were validated by co-treatment with a mitochondria-specific superoxide scavenger, which decreased the potency of **35**. This mitochondrial damage subsequently engenders ER stress, which was evidenced by phosphorylation of PERK and eIF2 α and CHOP expression, and ultimately apoptosis. Compound **35** was also evaluated *in vivo*. This compound exhibited striking *in vivo* activity, with greater efficacy than cisplatin in mice bearing A549 lung cancer xenografts (**Figure 1.9**).



35

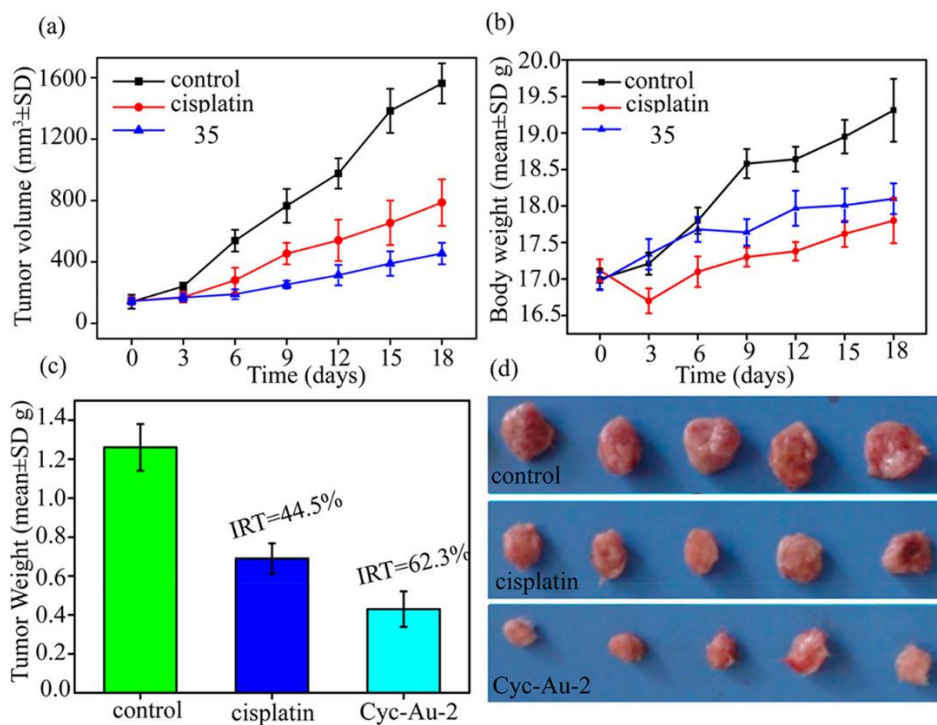


Figure 1.9. In vivo activity of **35**. (a) Tumor volume versus treatment time for mice bearing A549 xenografts. (b) Mouse body weight versus treatment time. (c) Tumor weights for mice treated with **35** or cisplatin at the end of the study. (d) Representative pictures of excised tumors from these experiments. Adapted from reference 174 with permission from the American Chemical Society, copyright [2018].

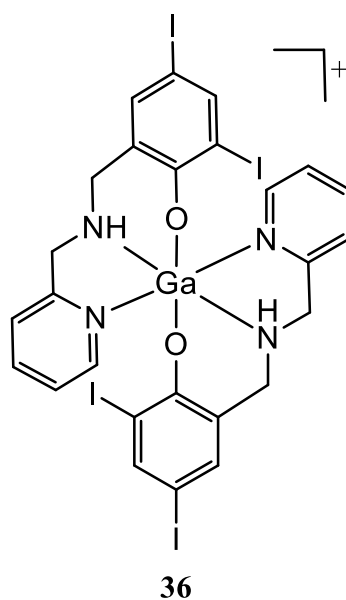
p- and f-Block Compounds

Another important family of metal-based proteasome inhibitors are Ga³⁺ complexes.^{175,176} In one study, gallium complexes bearing pyridine/polyphenol ligands like compound **36** exhibited powerful anticancer activity in vivo toward prostate

cancer xenografts, and the complexes were not cross-resistant with cisplatin.¹⁷⁵

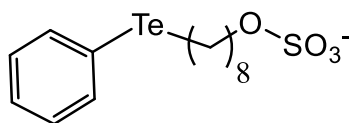
Proteasome inhibition by the lead compound was confirmed both *in vitro* and *in vivo*.

Although it is likely that this compound induces ER stress via this mechanism, this possibility has not yet been investigated.



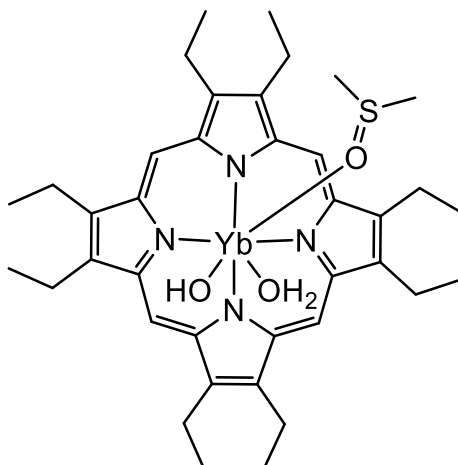
Although compounds containing tellurium have scarcely been explored for anticancer activity, there is one report of a tellurium-containing compound (**37**) that induces ER stress.¹⁷⁷ Compound **37** generates ROS, specifically superoxide, leading to ER stress-mediated apoptosis. This compound activates the ER stress marker ATF4 and phosphorylates eIF2 α , ultimately triggering expression of CHOP. Surprisingly, the analogous selenium complex is inactive in cancerous cells, highlighting the importance of tellurium in the mechanism of action of this compound. Further structure-activity relationship (SAR) experiments and mechanistic work are needed to determine whether this ER stress induction may be a more general feature of

tellurium-containing compounds.



37

Within the f-block, there has been a report describing the ER stress-inducing properties of an Yb(III) porphyrin anticancer agent (**38**).¹⁷⁸ Notably, this complex has sub-micromolar activity against several cancer cell lines. It also induces apoptosis by activating ER stress pathways. ER stress in response to **38** was confirmed via the detection of increased CHOP expression, eIF2 α phosphorylation, and ER swelling. This ER stress leads to mitochondrial swelling and dysfunction. Although the specific cause of ER stress was not conclusively determined, this compound was found to inhibit the ubiquitin-proteasome system, which provides a likely hypothesis for its observed activity. Lastly, the effect of **38** on the gene expression profile of HeLa cells was investigated. These studies revealed that **38** causes changes in gene expression that were very similar to those found for the established ER stress-inducing agents thapsigargin and gossypol. This study highlights how relatively simple metal-containing compounds can have biological properties that match those of more complex organic natural products. Furthermore, compound **38** is a rare example of a lanthanide-containing anticancer agent. Given the chemical similarity of the lanthanide ions, further studies to probe the anticancer and ER stress-inducing properties of other lanthanide porphyrin complexes is warranted.

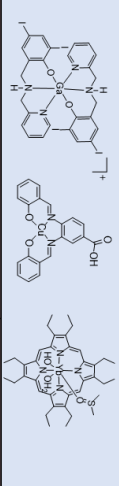
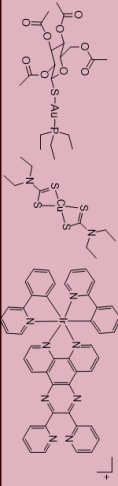
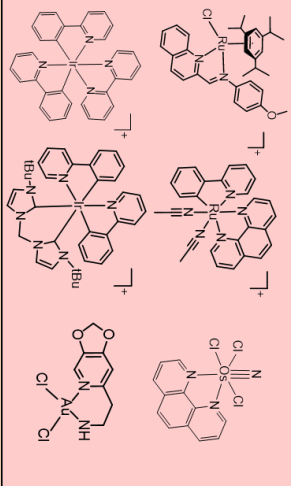
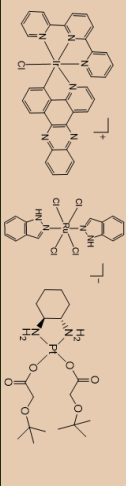
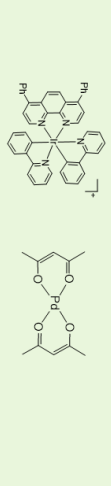


38

Trends in and Opportunities for Metal Anticancer Agents Targeting the ER

As summarized here, a diverse range of metal complexes have been demonstrated to trigger ER stress-mediated anticancer activity. To date, dozens of different metal complexes have been shown to possess this type of biological activity. The means by which these complexes cause ER stress are equally diverse; among many different possible mechanisms, these complexes can act as photosensitizers, proteasome inhibitors, modulators of Ca²⁺ trafficking, and inhibitors of essential enzymes for ER homeostasis. Despite the wide variance of ER stress induction mechanisms, some trends with respect to ligand types and isostructural compounds have become apparent. A broad overview of the types of ER stress induction, relevant metal complexes, detection methods, and an exhaustive list of references within each category is provided in **Table 1.1**.

Table 1.1. Phenotypes and Examples of Induction of ER Stress by Metal Complexes

Mode of ER Stress Induction	Representative Compounds Inducing this Phenotype	Assays for Detection	Reports of Induction by Metal Complexes
ERAD Inhibition		<ul style="list-style-type: none"> • Ubiquitin Western blot^a • In vitro assays with isolated proteasome • Fluorescent tracking of proteasome substrates 	87, 89, 94, 169, 175, 176, 178
ERAD Inhibition and ROS Generation		<p>See relevant assays for ERAD inhibition and ROS generation</p>	90–93, 164–170
ROS Generation		<ul style="list-style-type: none"> • DCF/DA assay^b • Co-treatment with NAC • Co-treatment with MitoSox • Confocal microscopy with localized ROS indicators • Nrf2-activation 	72–75, 83, 101, 102, 104–114, 118, 134–136, 140–143, 147, 151, 173, 174, 177
Ca²⁺ Disruption and ROS Generation		<p>See relevant assays ROS generation and disruption of Ca²⁺ Trafficking</p>	121–123, 143, 161
Disruption of Ca²⁺ Trafficking		<ul style="list-style-type: none"> • Measurement of ER Ca²⁺ levels^c • Co-treatment with Ca²⁺ chelators • Quantification of Ca²⁺ chaperones 	125, 144

^aFor reviews on detection of proteasome inhibition, see references 179,180. ^bFor detailed experimental description of ROS detection, see references 113,174,181. ^cFor experimental protocols to detect Ca²⁺ signaling disruption, see references 123,144.

Two ligand scaffolds have appeared frequently among these ER stress-inducing compounds. The first are polypyridyl phenanthroline derivatives. In particular, the DPP ligand appears in multiple ER stress-inducing compounds discussed here, including **10**, **11**, **14**, **17–20**, **23**, and **24**. These compounds show a proclivity for ER localization, especially for those that are mono-cationic. Despite the structural similarities between these complexes, they cause ER stress via different mechanisms, ranging from ROS generation to Ca²⁺ trafficking disruption. Thus, it is likely that these ligands and complex charge are factors that direct these complexes to the ER, whereas more subtle structural and electronic differences affect the activity of the compounds within this organelle. Another common scaffold among many ER-targeting complexes are phenylpyridine ligands, which form cyclometalated complexes. These ligands are found in compounds **10**, **11**, **20–25**, **33**, and **34**. Similarly, hydrophobicity of these ligands combined with their ability to counterbalance the high cationic charge on the metal often leads to hydrophobic, monocationic complexes. In the case of both phenanthroline and phenylpyridine, the resulting metal complexes are often saturated with inert ligands, indicating that the geometry or redox activity of the complexes, rather than their ligand substitution reactivity, may give rise to their anticancer properties.

A separate class of ER stress-inducing metal complexes comprises species with labile coordination sites. In these complexes, ligand substitution will occur readily under biological conditions, enabling the metal center to act as a potent

electrophile. Complexes in this class arise from first row transition metals such as copper complexes **5–9**, as well as platinum- and gold-containing compounds **24, 25**, and **30–35**. When ER stress induction occurs in response to these compounds, common targets are enzymes in the ubiquitin-proteasome system or redox regulatory enzymes like TRX or PDI. Furthermore, many of these complexes exhibit reduced toxicity in the presence of NAC, which can attenuate their activity via neutralizing ROS or by binding directly to the central metal atom.

Disruption of redox homeostasis is also a common feature of metal-based anticancer agents, particularly those in which the metal can easily access multiple oxidation states, such as first row transition metal or ruthenium complexes. ROS generation by photoexcited metal complexes, for example, is also a means of inducing ER stress. Furthermore, these ROS-generating complexes do not necessarily need to be localized to the ER in order to induce an ER stress phenotype, as mitochondrial damage often leads to ER stress-mediated apoptosis. Thus, researchers seeking to investigate the anticancer phenotypes caused by metal anticancer agents should investigate whether the compounds induce ER stress, even if they do not localize to the ER or if another type of cell damage is identified.

Overall, ER-targeting complexes exhibit remarkable potency, which is reflected by the large number of reports on this topic that describe compounds with nanomolar anticancer activity and significant *in vivo* tumor-reduction capabilities. These compounds also have generally high selectivity for cancer cells, which arises from the increased ER protein load and higher basal levels of ROS in the tumor microenvironment. The unorthodox mechanisms of action of these compounds allows

them to circumvent traditional resistance mechanisms, such as upregulation of DNA-repair pathways and mutation of p53. The ability of many ER-targeting complexes to induce ICD is also promising, as ICD induction has gained increased recognition as a critical hallmark of successful activity in the clinic.¹⁸²⁻¹⁸⁴ Together, these results, most of which are from only the last five years, demonstrate the tremendous potential of metal complexes as ER-targeting anticancer agents.

References

- 1 Y. P. Vandewynckel, D. Laukens, A. Geerts, E. Bogaerts, A. Paridaens, X. Verhelst, S. Janssens, F. Heindryckx and H. Van Vlierberghe, *Anticancer Res.*, 2013, **33**, 4683–4694.
- 2 R. K. Yadav, S.-W. Chae, H.-R. Kim and H. J. Chae, *J. Cancer Prev.*, 2014, **19**, 75–88.
- 3 A. Walczak, K. Gradzik, J. Kabzinski, K. Przybylowska-Sygut and I. Majsterek, *Oxid. Med. Cell. Longev.*, 2019, **2019**, 5729710.
- 4 T. Avril, E. Vauléon and E. Chevet, *Oncogenesis*, 2017, **6**, e373.
- 5 J. R. Cubillos-Ruiz, S. E. Bettigole and L. H. Glimcher, *Cell*, 2017, **168**, 692–706.
- 6 E. Bahar, J. Y. Kim and H. Yoon, *Cancers (Basel)*, 2019, **11**, 338.
- 7 E. A. Obeng, L. M. Carlson, D. M. Gutman, W. J. Harrington, K. P. Lee, L. H. Boise and L. H. Boise, *Blood*, 2006, **107**, 4907–4916.
- 8 I. Kim, W. Xu and J. C. Reed, *Nat. Rev. Drug Discov.*, 2008, **7**, 1013–1030.
- 9 S. J. M. Healy, A. M. Gorman, P. Mousavi-Shafaei, S. Gupta and A. Samali, *Eur. J. Pharmacol.*, 2009, **625**, 234–246.
- 10 Y. Liu and Y. Ye, *Cell Res.*, 2011, **21**, 867–883.
- 11 F. Martinon, *Acta Oncol. (Madr)*, 2012, **51**, 822–830.
- 12 L. Vincenz, R. Jäger, M. O’Dwyer and A. Samali, *Mol. Cancer Ther.*, 2013, **12**, 831–843.
- 13 S. Banerjee and W. Zhang, *ChemBioChem*, 2018, **19**, 2341–2343.
- 14 C. Huang, T. Li, J. Liang, H. Huang, P. Zhang and S. Banerjee, *Coord. Chem. Rev.*, 2020, **408**, 213178.
- 15 D. S. Schwarz and M. D. Blower, *Cell. Mol. Life Sci.*, 2016, **73**, 79–94.
- 16 L. M. Westrate, J. E. Lee, W. A. Prinz and G. K. Voeltz, *Annu. Rev. Biochem.*, 2015, **84**, 791–811.
- 17 L. Ellgaard and A. Helenius, *Nat. Rev. Mol. Cell Biol.*, 2003, **4**, 181–191.
- 18 K. Gadhave, N. Bolshette, A. Ahire, R. Pardeshi, K. Thakur, C. Trandafir, A. Istrate, S. Ahmed, M. Lahkar, D. F. Muresanu and M. Balea, *J. Cell. Mol. Med.*, 2016, **20**, 1392–1407.
- 19 C. L. Soave, T. Guerin, J. Liu and Q. P. Dou, *Cancer Metastasis Rev.*, 2017, **36**, 717–736.
- 20 N. A. Borg and V. M. Dixit, *Annu. Rev. Cancer Biol.*, 2017, **1**, 59–77.
- 21 J. Jacquemyn, A. Cascalho and R. E. Goodchild, *EMBO Rep.*, 2017, **18**, 1905–1921.
- 22 A. Raffaello, C. Mammucari, G. Gherardi and R. Rizzuto, *Trends Biochem. Sci.*, 2016, **41**, 1035–1049.
- 23 A. Chakrabarti, A. W. Chen and J. D. Varner, *Biotechnol. Bioeng.*, 2011, **108**, 2777–2793.
- 24 C. Hetz, *Nat. Rev. Mol. Cell Biol.*, 2012, **13**, 89–102.
- 25 C. J. Adams, M. C. Kopp, N. Larburu, P. R. Nowak and M. M. U. Ali, *Front. Mol. Biosci.*, 2019, **6**, 11.
- 26 A. Almanza, A. Carlesso, C. Chinthia, S. Creedican, D. Doultinos, B. Leuzzi,

- A. Luís, N. McCarthy, L. Montibeller, S. More, A. Papaioannou, F. Püschel, M. L. Sassano, J. Skoko, P. Agostinis, J. de Belleruche, L. A. Eriksson, S. Fulda, A. M. Gorman, S. Healy, A. Kozlov, C. Muñoz-Pinedo, M. Rehm, E. Chevet and A. Samali, *FEBS J.*, 2019, **286**, 241–278.
- 27 Z. Liu, Y. Lv, N. Zhao, G. Guan and J. Wang, *Cell Death Dis.*, 2015, **6**, e1822.
- 28 I. M. N. Wortel, L. T. van der Meer, M. S. Kilberg and F. N. van Leeuwen, *Trends Endocrinol. Metab.*, 2017, **28**, 794–806.
- 29 H. Hu, M. Tian, C. Ding and S. Yu, *Front. Immunol.*, 2019, **10**, 3083.
- 30 R. Sano and J. C. Reed, *Biochim. Biophys. Acta - Mol. Cell Res.*, 2013, **1833**, 3460–3470.
- 31 M. Li, P. Baumeister, B. Roy, T. Phan, D. Foti, S. Luo and A. S. Lee, *Mol. Cell Biol.*, 2000, **20**, 5096–5106.
- 32 F. Walter, A. O’Brien, C. G. Concannon, H. Düssmann and J. H. M. Prehn, *J. Biol. Chem.*, 2018, **293**, 18270–18284.
- 33 C. M. Limia, C. Sauzay, H. Urrea, C. Hetz, E. Chevet and T. Avril, *Cancers (Basel)*, 2019, **11**, 631.
- 34 H. Urrea, E. Dufey, T. Avril, E. Chevet and C. Hetz, *Trends in Cancer*, 2016, **2**, 252–262.
- 35 M. Bi, C. Naczki, M. Koritzinsky, D. Fels, J. Blais, N. Hu, H. Harding, I. Novoa, M. Varia, J. Raleigh, D. Scheuner, R. J. Kaufman, J. Bell, D. Ron, B. G. Wouters and C. Koumenis, *EMBO J.*, 2005, **24**, 3470–3481.
- 36 X. Chen, D. Iliopoulos, Q. Zhang, Q. Tang, M. B. Greenblatt, M. Hatzia Apostolou, E. Lim, W. L. Tam, M. Ni, Y. Chen, J. Mai, H. Shen, D. Z. Hu, S. Adoro, B. Hu, M. Song, C. Tan, M. D. Landis, M. Ferrari, S. J. Shin, M. Brown, J. C. Chang, X. S. Liu and L. H. Glimcher, *Nature*, 2014, **508**, 103–107.
- 37 T. Avril, E. Vauléon and E. Chevet, *Oncogenesis*, 2017, **6**, e373.
- 38 D. Y. A. Dadey, V. Kapoor, A. Khudanyan, F. Urano, A. H. Kim, D. Thotala and D. E. Hallahan, *Oncotarget*, 2016, **7**, 2080–2092.
- 39 C. Roller and D. Maddalo, *Front. Pharmacol.*, 2013, **4**, 10.
- 40 W. Shi, Z. Chen, L. Li, H. Liu, R. Zhang, Q. Cheng, D. Xu and L. Wu, *J. Cancer*, 2019, **10**, 2035–2046.
- 41 A. Pommier, N. Anaparthi, N. Memos, Z. Larkin Kelley, A. Gouronnec, R. Yan, C. Auffray, J. Albregues, M. Egeblad, C. A. Iacobuzio-Donahue, S. K. Lyons and D. T. Fearon, *Science*, 2018, **360**, eaao4908.
- 42 C. C. Han and F. S. Wan, *J. Breast Cancer*, 2018, **21**, 354–362.
- 43 M. M. Lizardo, J. J. Morrow, T. E. Miller, E. S. Hong, L. Ren, A. Mendoza, C. H. Halsey, P. C. Scacheri, L. J. Helman and C. Khanna, *Neoplasia (United States)*, 2016, **18**, 699–710.
- 44 P. Ren, C. Chen, J. Yue, J. Zhang and Z. Yu, *Onco. Targets. Ther.*, 2017, **10**, 617–625.
- 45 C. N. Cultrara, S. D. Kozuch, P. Ramasundaram, C. J. Heller, S. Shah, A. E. Beck, D. Sabatino and J. Zilberberg, *BMC Cancer*, 2018, **18**, 1263.
- 46 Q. Zhong, B. Zhou, D. K. Ann, P. Minoo, Y. Liu, A. Banfalvi, M. S. Krishnaveni, M. Dubourd, L. Demaio, B. C. Willis, K. J. Kim, R. M. DuBois,

- E. D. Crandall, M. F. Beers and Z. Borok, *Am. J. Respir. Cell Mol. Biol.*, 2011, **45**, 498–509.
- 47 S. Zhou, J. Yang, M. Wang, D. Zheng and Y. Liu, *Mol. Med. Rep.*, 2020, **21**, 173–180.
- 48 P. P. Shah and L. J. Beverly, *Oncotarget*, 2015, **6**, 17725–17737.
- 49 P. P. Shah, T. V. Dupre, L. J. Siskind and L. J. Beverly, *Oncotarget*, 2017, **8**, 22625–22639.
- 50 Y. X. Feng, E. S. Sokol, C. A. Del Vecchio, S. Sanduja, J. H. L. Claessen, T. A. Proia, D. X. Jin, F. Reinhardt, H. L. Ploegh, Q. Wang and P. B. Gupta, *Cancer Discov.*, 2014, **4**, 702–715.
- 51 M. Wang, M. E. Law, R. K. Castellano and B. K. Law, *Crit. Rev. Oncol. Hematol.*, 2018, **127**, 66–79.
- 52 A. Younes and G. V. Georgakis, *Futur. Oncol.*, 2005, **1**, 273–281.
- 53 H. R. Park, K. Furihata, Y. Hayakawa and K. Shin-Ya, *Tetrahedron Lett.*, 2002, **43**, 6941–6945.
- 54 P. B. Gupta, T. T. Onder, G. Jiang, K. Tao, C. Kuperwasser, R. A. Weinberg and E. S. Lander, *Cell*, 2009, **138**, 645–659.
- 55 S. Gupta, A. Samali, U. Fitzgerald and S. Deegan, *Int. J. Cell Biol.*, 2010, 830307.
- 56 L. Qi, L. Yang and H. Chen, in *Methods in Enzymology*, Academic Press Inc., 2011, vol. 490, pp. 137–146.
- 57 C. M. Oslowski and F. Urano, in *Methods in Enzymology*, Academic Press Inc., 2011, vol. 490, pp. 71–92.
- 58 A. Gupta, D. E. Read and S. Gupta, *Methods Mol. Biol.*, 2015, **1292**, 19–38.
- 59 A. T. Melvin, G. S. Woss, J. H. Park, M. L. Waters and N. L. Allbritton, *Cell Biochem. Biophys.*, 2013, **67**, 75–89.
- 60 Y. Leestemaker and H. Ovaa, *Drug Discov. Today Technol.*, 2017, **26**, 25–31.
- 61 P. Maher, *Bio. Protoc.*, 2014, **4**, 1028.
- 62 J. Gan, Y. Leestemaker, A. Sapmaz and H. Ovaa, *Front. Mol. Biosci.*, 2019, **6**, 14.
- 63 I. E. Wertz and V. M. Dixit, *J. Biol. Chem.*, 2000, **275**, 11470–11477.
- 64 P. Pinton, C. Giorgi, R. Siviero, E. Zecchini and R. Rizzuto, *Oncogene*, 2008, **27**, 6407–6418.
- 65 M. W. Harr and C. W. Distelhorst, *Cold Spring Harb. Perspect. Biol.*, 2010, **2**, a005579.
- 66 J. T. Machado, R. T. Iborra, F. B. Fusco, G. Castilho, R. S. Pinto, A. Machado-Lima, E. R. Nakandakare, A. C. Seguro, M. H. Shimizu, S. Catanози and M. Passarelli, *Atherosclerosis*, 2014, **237**, 343–352.
- 67 Y. Sun, *World J. Gastroenterol.*, 2014, **20**, 15289–15298.
- 68 S. Mimori, Y. Okuma, M. Kaneko, K. Kawada, T. Hosoi, K. Ozawa, Y. Nomura and H. Hamana, *Biol. Pharm. Bull.*, 2012, **35**, 84–90.
- 69 M. Boyce, K. F. Bryant, C. Jousse, K. Long, H. P. Harding, D. Scheuner, R. J. Kaufman, D. Ma, D. M. Coen, D. Ron and J. Yuan, *Science*, 2005, **307**, 935–939.
- 70 C. Sidrauski, D. Acosta-Alvear, A. Khoutorsky, P. Vedantham, B. R. Hearn, H.

- Li, K. Gamache, C. M. Gallagher, K. K.-H. Ang, C. Wilson, V. Okreglak, A. Ashkenazi, B. Hann, K. Nader, M. R. Arkin, A. R. Renslo, N. Sonenberg and P. Walter, *eLife*, 2013, **2**, e00498.
- 71 C. Sidrauski, A. M. McGeachy, N. T. Ingolia and P. Walter, *eLife*, 2015, e05033.
- 72 S. Banerjee, A. Dixit, R. N. Shridharan, A. A. Karande and A. R. Chakravarty, *Chem. Commun.*, 2014, **50**, 5590–5592.
- 73 S. Banerjee, A. Dixit, A. A. Karande and A. R. Chakravarty, *Dalton Trans.*, 2016, **45**, 783–796.
- 74 T. K. Goswami, S. Gadadhar, B. Balaji, B. Gole, A. A. Karande and A. R. Chakravarty, *Dalton Trans.*, 2014, **43**, 11988–11999.
- 75 A. M. Merlot, N. H. Shafie, Y. Yu, V. Richardson, P. J. Jansson, S. Sahni, D. J. R. Lane, Z. Kovacevic, D. S. Kalinowski and D. R. Richardson, *Biochem. Pharmacol.*, 2016, **109**, 27–47.
- 76 R. Trondl, L. S. Flocke, C. R. Kowol, P. Heffeter, U. Jungwirth, G. E. Mair, R. Steinborn, É. A. Enyedy, M. A. Jakupec, W. Berger and B. K. Keppler, *Mol. Pharmacol.*, 2014, **85**, 451–459.
- 77 L. Moráň, T. Pivetta, S. Masuri, K. Vašíčková, F. Walter, J. Prehn, M. Elkalaf, J. Trnka, J. Havel and P. Vaňhara, *Metallomics*, 2019, **11**, 1481–1489.
- 78 S. Hager, K. Korbula, B. Bielec, M. Grusch, C. Pirker, M. Schosserer, L. Liendl, M. Lang, J. Grillari, K. Nowikovskyy, V. F. S. Pape, T. Mohr, G. Szakács, B. K. Keppler, W. Berger, C. R. Kowol and P. Heffeter, *Cell Death Dis.*, 2018, **9**, 1052.
- 79 C. N. Hancock, L. H. Stockwin, B. Han, R. D. Divelbiss, J. H. Jun, S. V. Malhotra, M. G. Hollingshead and D. L. Newton, *Free Radic. Biol. Med.*, 2011, **50**, 110–121.
- 80 Y. Fu, Y. Liu, J. Wang, C. Li, S. Zhou, Y. Yang, P. Zhou, C. Lu and C. Li, *Oncol. Rep.*, 2017, **37**, 1662–1670.
- 81 K. Ohui, E. Afanasenko, F. Bacher, R. L. X. Ting, A. Zafar, N. Blanco-Cabra, E. Torrents, O. Dömötör, N. V. May, D. Darvasiova, É. A. Enyedy, A. Popović-Bijelić, J. Reynisson, P. Rapta, M. V. Babak, G. Pastorin and V. B. Arion, *J. Med. Chem.*, 2019, **62**, 512–530.
- 82 N. Ding and Q. Zhu, *Transl. Cancer Res.*, 2018, **7**, S495–S499.
- 83 H. Huang, Y. Liao, N. Liu, X. Hua, J. Cai, C. Yang, H. Long, C. Zhao, X. Chen, X. Lan, D. Zang, J. Wu, X. Li, X. Shi, X. Wang and J. Liu, *Oncotarget*, 2016, **7**, 2796–2808.
- 84 S. Tardito, I. Bassanetti, C. Bignardi, L. Elviri, M. Tegoni, C. Mucchino, O. Bussolati, R. Franchi-Gazzola and L. Marchiò, *J. Am. Chem. Soc.*, 2011, **133**, 6235–6242.
- 85 J. L. Kim, D. H. Lee, Y. J. Na, B. R. Kim, Y. A. Jeong, S. Il Lee, S. Kang, S. Y. Joung, S. Y. Lee, S. C. Oh and B. W. Min, *Tumor Biol.*, 2016, **37**, 9709–9719.
- 86 I. Kim, C. H. Kim, J. H. Kim, J. Lee, J. J. Choi, Z. A. Chen, M. G. Lee, K. C. Chung, C. Y. Hsu and Y. S. Ahn, *Exp. Cell Res.*, 2004, **298**, 229–238.
- 87 D. Chen, *Front. Biosci.*, 2005, **10**, 2932–2939.
- 88 D. Chen, Q. C. Cui, H. Yang and Q. P. Dou, *Cancer Res.*, 2006, **66**, 10425–

- 10433.
- 89 H. Pang, D. Chen, Q. C. Cui and Q. Ping Dou, *Int. J. Mol. Med.*, 2007, **19**, 809–816.
- 90 M. Frezza, S. S. Hindo, D. Tomco, M. M. Allard, Q. C. Cui, M. J. Heeg, D. Chen, Q. P. Dou and C. N. Verani, *Inorg. Chem.*, 2009, **48**, 5928–5937.
- 91 V. Gandin, F. Tisato, A. Dolmella, M. Pellei, C. Santini, M. Giorgetti, C. Marzano and M. Porchia, *J. Med. Chem.*, 2014, **57**, 4745–4760.
- 92 Z. Zhang, C. Bi, Y. Fan, H. Wang and Y. Bao, *Int. J. Mol. Med.*, 2015, **36**, 1143–1150.
- 93 T. Zhou, Y. Cai, L. Liang, L. Yang, F. Xu, Y. Niu, C. Wang, J. L. Zhang and P. Xu, *Bioorganic Med. Chem. Lett.*, 2016, **26**, 5780–5784.
- 94 X. Chen, Q. Yang, L. Xiao, D. Tang, Q. P. Dou and J. Liu, *Cancer Metastasis Rev.*, 2017, **36**, 655–668.
- 95 Z. Zhang, H. Wang, M. Yan, H. Wang and C. Zhang, *Mol. Med. Rep.*, 2017, **15**, 3–11.
- 96 Shagufta and I. Ahmad, *Inorg. Chim. Acta*, 2020, **506**, 119521.
- 97 K. G. Daniel, D. Chen, S. Orlu, Q. C. ind. Cui, F. R. Miller and Q. P. Dou, *Breast Cancer Res.*, 2005, **7**, 897–908.
- 98 V. Gandin, M. Pellei, F. Tisato, M. Porchia, C. Santini and C. Marzano, *J. Cell. Mol. Med.*, 2012, **16**, 142–151.
- 99 R. Bortolozzi, G. Viola, E. Porcù, F. Consolaro, C. Marzano, M. Pellei, V. Gandin and G. Basso, *Oncotarget*, 2014, **5**, 5978–5991.
- 100 S. Tardito, C. Isella, E. Medico, L. Marchiò, E. Bevilacqua, M. Hatzoglou, O. Bussolati and R. Franchi-Gazzola, *J. Biol. Chem.*, 2009, **284**, 24306–24319.
- 101 L. Leyva, C. Sirlin, L. Rubio, C. Franco, R. Le Lagadec, J. Spencer, P. Bischoff, C. Gaidon, J.-P. Loeffler and M. Pfeffer, *Eur. J. Inorg. Chem.*, 2007, **2007**, 3055–3066.
- 102 X. Meng, M. L. Leyva, M. Jenny, I. Gross, S. Benosman, B. Fricker, S. Harlepp, P. Hébraud, A. Boos, P. Wlosik, P. Bischoff, C. Sirlin, M. Pfeffer, J.-P. Loeffler and C. Gaidon, *Cancer Res.*, 2009, **69**, 5458–5466.
- 103 C. Licon, J.-B. Delhorme, G. Riegel, V. Vidimar, R. Cerón-Camacho, B. Boff, A. Venkatasamy, C. Tomasetto, P. da Silva Figueiredo Celestino Gomes, D. Rognan, J.-N. Freund, R. Le Lagadec, M. Pfeffer, I. Gross, G. Mellitzer and C. Gaidon, *Inorg. Chem. Front.*, 2020, **7**, 678–688.
- 104 L. Fetzer, B. Boff, M. Ali, M. Xiangjun, J. P. Collin, C. Sirlin, C. Gaidon and M. Pfeffer, *Dalton Trans.*, 2011, **40**, 8869–8878.
- 105 V. Vidimar, X. Meng, M. Klajner, C. Licon, L. Fetzer, S. Harlepp, P. Hébraud, M. Sidhoum, C. Sirlin, J. P. Loeffler, G. Mellitzer, G. Sava, M. Pfeffer and C. Gaidon, *Biochem. Pharmacol.*, 2012, **84**, 1428–1436.
- 106 M. Klajner, C. Licon, L. Fetzer, P. Hebraud, G. Mellitzer, M. Pfeffer, S. Harlepp and C. Gaidon, *Inorg. Chem.*, 2014, **53**, 5150–5158.
- 107 C. Licon, M. E. Spaety, A. Capuozzo, M. Ali, R. Santamaria, O. Armant, F. Delalande, A. Van Dorsselaer, S. Cianferani, J. Spencer, M. Pfeffer, G. Mellitzer and C. Gaidon, *Oncotarget*, 2017, **8**, 2568–2584.
- 108 V. Vidimar, C. Licon, R. Cerón-Camacho, E. Guerin, P. Coliat, A.

- Venkatasamy, M. Ali, D. Guenot, R. Le Lagadec, A. C. Jung, J. N. Freund, M. Pfeffer, G. Mellitzer, G. Sava and C. Gaiddon, *Cancer Lett.*, 2019, **440–441**, 145–155.
- 109 M. J. Chow, C. Licona, D. Yuan Qiang Wong, G. Pastorin, C. Gaiddon and W. H. Ang, *J. Med. Chem.*, 2014, **57**, 6043–6059.
- 110 M. J. Chow, C. Licona, G. Pastorin, G. Mellitzer, W. H. Ang and C. Gaiddon, *Chem. Sci.*, 2016, **7**, 4117–4124.
- 111 M. J. Chow, M. V. Babak, D. Y. Q. Wong, G. Pastorin, C. Gaiddon and W. H. Ang, *Mol. Pharm.*, 2016, **13**, 2543–2554.
- 112 M. J. Chow, M. Alfiean, G. Pastorin, C. Gaiddon and W. H. Ang, *Chem. Sci.*, 2017, **8**, 3641–3649.
- 113 M. J. Chow, M. V. Babak, K. W. Tan, M. C. Cheong, G. Pastorin, C. Gaiddon and W. H. Ang, *Mol. Pharm.*, 2018, **15**, 3020–3031.
- 114 J. Zhao, S. Li, X. Wang, G. Xu and S. Gou, *Inorg. Chem.*, 2019, **58**, 2208–2217.
- 115 L. Zeng, P. Gupta, Y. Chen, E. Wang, L. Ji, H. Chao and Z. S. Chen, *Chem. Soc. Rev.*, 2017, **46**, 5771–5804.
- 116 M. R. Gill, D. Cecchin, M. G. Walker, R. S. Mulla, G. Battaglia, C. Smythe and J. A. Thomas, *Chem. Sci.*, 2013, **4**, 4512–4519.
- 117 B. Purushothaman, P. Arumugam, H. Ju, G. Kulsi, A. A. S. Samson and J. M. Song, *Eur. J. Med. Chem.*, 2018, **156**, 747–759.
- 118 L. Xu, P. P. Zhang, X. Q. Fang, Y. Liu, J. Q. Wang, H. Z. Zhou, S. T. Chen and H. Chao, *J. Inorg. Biochem.*, 2019, **191**, 126–134.
- 119 R. Trondl, P. Heffeter, C. R. Kowol, M. A. Jakupec, W. Berger and B. K. Keppler, *Chem. Sci.*, 2014, **5**, 2925–2932.
- 120 H. A. Burris, S. Bakewell, J. C. Bendell, J. Infante, S. F. Jones, D. R. Spigel, G. J. Weiss, R. K. Ramanathan, A. Ogden and D. Von Hoff, *ESMO Open*, 2016, **1**, e000154.
- 121 L. S. Flocke, R. Trondl, M. A. Jakupec and B. K. Keppler, *Invest. New Drugs*, 2016, **34**, 261–268.
- 122 S. Kapitza, M. A. Jakupec, M. Uhl, B. K. Keppler and B. Marian, *Cancer Lett.*, 2005, **226**, 115–121.
- 123 F.-Z. Sadafi, L. Massai, G. Bartolommei, M. R. Moncelli, L. Messori and F. Tadini-Buoninsegni, *ChemMedChem*, 2014, **9**, 1660–1664.
- 124 D. Wernitznig, K. Kiakos, G. Del Favero, N. Harrer, H. MacHat, A. Osswald, M. A. Jakupec, A. Wernitznig, W. Sommergruber and B. K. Keppler, *Metallomics*, 2019, **11**, 1044–1048.
- 125 Y. Wang, J. Hu, Y. Cai, S. Xu, B. Weng, K. Peng, X. Wei, T. Wei, H. Zhou, X. Li and G. Liang, *J. Med. Chem.*, 2013, **56**, 9601–9611.
- 126 A. Leonidova and G. Gasser, *ACS Chem. Biol.*, 2014, **9**, 2180–2193.
- 127 K. M. Knopf, B. L. Murphy, S. N. MacMillan, J. M. Baskin, M. P. Barr, E. Boros and J. J. Wilson, *J. Am. Chem. Soc.*, 2017, **139**, 14302–14314.
- 128 E. B. Bauer, A. A. Haase, R. M. Reich, D. C. Crans and F. E. Kühn, *Coord. Chem. Rev.*, 2019, **393**, 79–117.
- 129 C. C. Konkankit, B. A. Vaughn, S. N. MacMillan, E. Boros and J. J. Wilson,

- Inorg. Chem.*, 2019, **58**, 3895-3909.
- 130 P. Collery, D. Desmaele and V. Vijaykumar, *Curr. Pharm. Des.*, 2019, **25**, 3306–3322.
- 131 A. P. King, S. C. Marker, R. V. Swanda, J. J. Woods, S. Qian and J. J. Wilson, *Chem. – A Eur. J.*, 2019, **25**, 9206–9210.
- 132 M. Hanif, M. V. Babak and C. G. Hartinger, *Drug Discov. Today*, 2014, **19**, 1640–1648.
- 133 P. Zhang and H. Huang, *Dalton Trans.*, 2018, **47**, 14841–14854.
- 134 K. Suntharalingam, T. C. Johnstone, P. M. Bruno, W. Lin, M. T. Hemann and S. J. Lippard, *J. Am. Chem. Soc.*, 2013, **135**, 14060–14063.
- 135 K. Suntharalingam, W. Lin, T. C. Johnstone, P. M. Bruno, Y.-R. Zheng, M. T. Hemann and S. J. Lippard, *J. Am. Chem. Soc.*, 2014, **136**, 14413–14416.
- 136 G. Berger, K. Grauwet, H. Zhang, A. M. Hussey, M. O. Nowicki, D. I. Wang, E. A. Chiocca, S. E. Lawler and S. J. Lippard, *Cancer Lett.*, 2018, **416**, 138–148.
- 137 M. Prieto-Vila, R. U. Takahashi, W. Usuba, I. Kohama and T. Ochiya, *Int. J. Mol. Sci.*, 2017, **18**, 2574.
- 138 L. T. H. Phi, I. N. Sari, Y.-G. Yang, S.-H. Lee, N. Jun, K. S. Kim, Y. K. Lee and H. Y. Kwon, *Stem Cells Int.*, 2018, **2018**, 5416923.
- 139 Z. Liu and P. J. Sadler, *Acc. Chem. Res.*, 2014, **47**, 1174–1185.
- 140 S. Mandal, D. K. Poria, R. Ghosh, P. S. Ray and P. Gupta, *Dalton Trans.*, 2014, **43**, 17463–17474.
- 141 C. Yang, F. Mehmood, T. L. Lam, S. L. F. Chan, Y. Wu, C. S. Yeung, X. Guan, K. Li, C. Y. S. Chung, C. Y. Zhou, T. Zou and C. M. Che, *Chem. Sci.*, 2016, **7**, 3123–3136.
- 142 J. S. Nam, M. G. Kang, J. Kang, S. Y. Park, S. J. C. Lee, H. T. Kim, J. K. Seo, O. H. Kwon, M. H. Lim, H. W. Rhee and T. H. Kwon, *J. Am. Chem. Soc.*, 2016, **138**, 10968–10977.
- 143 B. Yuan, J. Liu, R. Guan, C. Jin, L. Ji and H. Chao, *Dalton Trans.*, 2019, **48**, 6408–6415.
- 144 R. Cao, J. Jia, X. Ma, M. Zhou and H. Fei, *J. Med. Chem.*, 2013, **56**, 3636–3644.
- 145 S. K. Tripathy, U. De, N. Dehury, P. Laha, M. K. Panda, H. S. Kim and S. Patra, *Dalton Trans.*, 2016, **45**, 15122–15136.
- 146 C. Caporale, C. A. Bader, A. Sorvina, K. D. M. MaGee, B. W. Skelton, T. A. Gillam, P. J. Wright, P. Raiteri, S. Stagni, J. L. Morrison, S. E. Plush, D. A. Brooks and M. Massi, *Chem. - A Eur. J.*, 2017, **23**, 15666–15679.
- 147 T. Zou, C.-N. Lok, Y. M. E. Fung and C.-M. Che, *Chem. Commun.*, 2013, **49**, 5423–5425.
- 148 D. Y. Q. Wong, W. W. F. Ong and W. H. Ang, *Angew. Chem., Int. Ed.*, 2015, **54**, 6483–6487.
- 149 O. Kepp, M. Semeraro, J. M. Bravo-San Pedro, N. Bloy, A. Buqué, X. Huang, H. Zhou, L. Senovilla, G. Kroemer and L. Galluzzi, *Semin. Cancer Biol.*, 2015, **33**, 86–92.
- 150 L. Bezu, A. Sauvat, J. Humeau, L. C. Gomes-da-Silva, K. Iribarren, S.

- Forveille, P. Garcia, L. Zhao, P. Liu, L. Zitvogel, L. Senovilla, O. Kepp and G. Kroemer, *Cell Death Differ.*, 2018, **25**, 1375–1393.
- 151 F. Y. Wang, X. M. Tang, X. Wang, K. Bin Huang, H. W. Feng, Z. F. Chen, Y. N. Liu and H. Liang, *Eur. J. Med. Chem.*, 2018, **155**, 639–650.
- 152 A. Mandic, J. Hansson, S. Linder and M. C. Shoshan, *J. Biol. Chem.*, 2003, **278**, 9100–9106.
- 153 Y. Shi, B. Tang, P.-W. Yu, B. Tang, Y.-X. Hao, X. Lei, H.-X. Luo and D.-Z. Zeng, *PLoS One*, 2012, **7**, e51076.
- 154 R. M. Cunningham and V. J. DeRose, *ACS Chem. Biol.*, 2017, **12**, 2737–2745.
- 155 H.-H. Hsu, M.-C. Chen, R. Baskaran, Y.-M. Lin, C. H. Day, Y.-J. Lin, C.-C. Tu, V. Vijaya Padma, W.-W. Kuo and C.-Y. Huang, *J. Cell. Physiol.*, 2018, **233**, 5458–5467.
- 156 E. C. Sutton, C. E. McDevitt, M. V. Yglesias, R. M. Cunningham and V. J. DeRose, *Inorg. Chim. Acta*, 2019, **498**, 118984.
- 157 Y. Xu, C. Wang and Z. Li, *Mol. Clin. Oncol.*, 2014, **2**, 3–7.
- 158 T. Ishikawa and F. Ali-Osman, *J. Biol. Chem.*, 1993, **268**, 20116–20125.
- 159 A. De Luca, L. J. Parker, W. H. Ang, C. Rodolfo, V. Gabbarini, N. C. Hancock, F. Palone, A. P. Mazzetti, L. Menin, C. J. Morton, M. W. Parker, M. Lo Bello and P. J. Dyson, *Proc. Natl. Acad. Sci. U. S. A.*, 2019, **116**, 13943–13951.
- 160 P. M. Bruno, Y. Liu, G. Y. Park, J. Murai, C. E. Koch, T. J. Eisen, J. R. Pritchard, Y. Pommier, S. J. Lippard and M. T. Hemann, *Nat. Med.*, 2017, **23**, 461–471.
- 161 X. Wang, Q. Guo, L. Tao, L. Zhao, Y. Chen, T. An, Z. Chen and R. Fu, *Mol. Carcinog.*, 2017, **56**, 218–231.
- 162 T. Onodera, I. Momose and M. Kawada, *Chem. Pharm. Bull.*, 2019, **67**, 186–191.
- 163 C. Roder and M. J. Thomson, *Drugs R D*, 2015, **15**, 13–20.
- 164 W. Fiskus, N. Saba, M. Shen, M. Ghias, J. Liu, S. Das Gupta, L. Chauhan, R. Rao, S. Gunewardena, K. Schorno, C. P. Austin, K. Maddocks, J. Byrd, A. Melnick, P. Huang, A. Wiestner and K. N. Bhalla, *Cancer Res.*, 2014, **74**, 2520–2532.
- 165 N. Liu, X. Li, H. Huang, C. Zhao, S. Liao, C. Yang, S. Liu, W. Song, X. Lu, X. Lan, X. Chen, S. Yi, L. Xu, L. Jiang, C. Zhao, X. Dong, P. Zhou, S. Li, S. Wang, X. Shi, P. Q. Dou, X. Wang and J. Liu, *Oncotarget*, 2014, **5**, 5453–5471.
- 166 N. Liu, Z. Guo, X. Xia, Y. Liao, F. Zhang, C. Huang, Y. Liu, X. Deng, L. Jiang, X. Wang, J. Liu and H. Huang, *Eur. J. Pharmacol.*, 2019, **846**, 1–11.
- 167 V. Milacic, D. Chen, L. Ronconi, K. R. Landis-Piwowar, D. Fregona and Q. P. Dou, *Cancer Res.*, 2006, **66**, 10478–10486.
- 168 A. Bindoli, M. P. Rigobello, G. Scutari, C. Gabbiani, A. Casini and L. Messori, *Coord. Chem. Rev.*, 2009, **253**, 1692–1707.
- 169 X. Zhang, M. Frezza, V. Milacic, L. Ronconi, Y. Fan, C. Bi, D. Fregona and Q. P. Dou, *J. Cell. Biochem.*, 2010, **109**, 162–172.
- 170 K. Fidy, A. Pastorzak, A. Goral, K. Szczygiel, W. Fendler, A. Muchowicz, M. A. Bartłomieczyk, J. Madzio, J. Cyran, A. Graczyk-Jarzynka, E. Jansen, E. Patkowska, E. Lech-Maranda, D. Pal, H. Blair, A. Burdzinska, P. Pedzisz, E.

- Glodkowska-Mrowka, U. Demkow, K. Gawle-Krawczyk, M. Matysiak, M. Winiarska, P. Juszczynski, W. Mlynarski, O. Heidenreich, J. Golab and M. Firczuk, *Mol. Oncol.*, 2019, **13**, 1180–1195.
- 171 G. J. Poet, O. B. Oka, M. Lith, Z. Cao, P. J. Robinson, M. A. Pringle, E. S. Arnér and N. J. Bulleid, *EMBO J.*, 2017, **36**, 693–702.
- 172 J. J. Zhang, R. W. Y. Sun and C. M. Che, *Chem. Commun.*, 2012, **48**, 3388–3390.
- 173 R. W. Y. Sun, C. N. Lok, T. T. H. Fong, C. K. L. Li, Z. F. Yang, A. F. M. Siu and C. M. Che, *Chem. Sci.*, 2013, **4**, 1979–1988.
- 174 K.-B. Huang, F.-Y. Wang, X.-M. Tang, H.-W. Feng, Z.-F. Chen, Y.-C. Liu, Y.-N. Liu and H. Liang, *J. Med. Chem.*, 2018, **61**, 3478–3490.
- 175 R. Shakya, F. Peng, J. Liu, M. J. Heeg and C. N. Verani, *Inorg. Chem.*, 2006, **45**, 6263–6268.
- 176 D. Chen, M. Frezza, R. Shakya, Q. C. Cui, V. Milacic, C. N. Verani and Q. P. Dou, *Cancer Res.*, 2007, **67**, 9258–9265.
- 177 P. Du, N. E. B. Saidu, J. Intemann, C. Jacob and M. Montenarh, *Biochim. Biophys. Acta - Gen. Subj.*, 2014, **1840**, 1808–1816.
- 178 W.-L. Kwong, R. Wai-Yin Sun, C.-N. Lok, F.-M. Siu, S.-Y. Wong, K.-H. Low and C.-M. Che, *Chem. Sci.*, 2013, **4**, 747–754.
- 179 L. Tsvetkov, M. Nanjundan, M. Domino and K. G. Daniel, *Expert Opin. Drug Discov.*, 2010, **5**, 1221–1236.
- 180 Y. Li, R. J. Tomko and M. Hochstrasser, *Curr. Protoc. Cell Biol.*, 2015, **2015**, 67:3.43.1–3.43.20.
- 181 E. Eruslanov and S. Kusmartsev, *Methods Mol. Biol.*, 2010, **594**, 57–72.
- 182 A. Serrano-del Valle, A. Anel, J. Naval and I. Marzo, *Front. Cell Dev. Biol.*, 2019, **7**, 50.
- 183 J. Zhou, G. Wang, Y. Chen, H. Wang, Y. Hua and Z. Cai, *J. Cell. Mol. Med.*, 2019, **23**, 4854–4865.
- 184 B. L. Rapoport and R. Anderson, *Int. J. Mol. Sci.*, 2019, **20**, 959.

CHAPTER 2

Bis(thiosemicarbazone) Complexes of Cobalt (III): Synthesis, Characterization, and Anticancer Potential

Reproduced in part with permission from: A. Paden King, Hendryck A. Gellineau, Jung-Eun Ahn, Samantha N. MacMillan, and Justin J. Wilson. *Inorg. Chem.* **2017**, *56*, 6609-6623. Copyright [2017] American Chemical Society.

Introduction

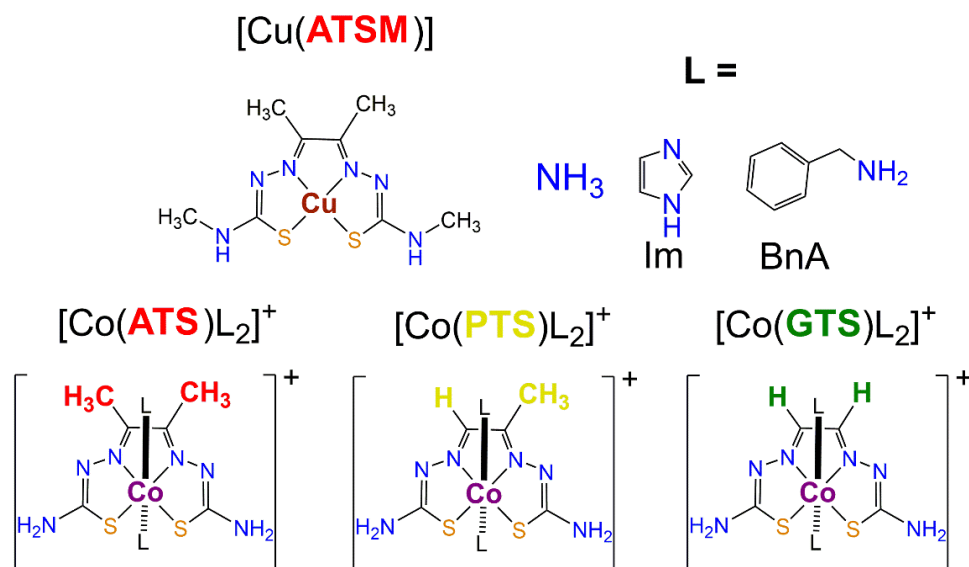
As discussed in Chapter 1, endoplasmic reticulum (ER) stress induction has emerged as a method for targeting the tumor microenvironment with metal anticancer agents. However, tumors have other characteristics that may be leveraged to selectively activate metallodrugs. The microenvironment is characterized by leaky vasculature, low extracellular pH, and hypoxia.¹⁻⁵ The hypoxic nature of tumors allows for selective activation of metal complexes via redox chemistry. This strategy has effectively been employed to target hypoxic cancers over normal tissues.⁶⁻⁹

Among the metal ion redox couples explored, those of the cobalt(III)/cobalt(II) and copper(II)/copper(I) couples are the most commonly exploited for the development of redox-activated prodrugs. Cobalt(III) complexes, which have been investigated as both hypoxia-targeting agents and as enzyme inhibitors,¹⁰⁻²⁷ are kinetically inert due to their low-spin d^6 electron configuration. Reduction to cobalt(II) yields a labile d^7 complex, facilitating the loss of ligands within the coordination sphere. In this capacity, cobalt(III) complexes can act as chaperones to deliver cytotoxic ligands selectively to hypoxic regions where metal reduction is favored.^{17,25,28}

With regard to copper(II)-based hypoxia-targeting complexes, the most well characterized class of compounds are those of the bis(thiosemicarbazone) (BTSC) ligands.²⁹⁻³² The radioactive BTSC ^{64}Cu complex $[\text{Cu}(\text{ATSM})]$ where ATSM = diacetyl-bis(N^4 -methylthiosemicarbazone) (**Chart 2.1**) is an established hypoxia imaging agent.³³ With an appropriate copper(II)/copper(I) redox potential, $[\text{Cu}(\text{ATSM})]$ is reduced selectively in hypoxic cells.³⁴⁻³⁹ The resulting Cu(I) complex is substantially less stable, and the free ATSM ligand along with the radioactive ^{64}Cu ion are released

and trapped within the cell. The accumulation of radioactive ^{64}Cu selectively in hypoxic cells gives rise to the hypoxia-imaging properties of this compound. In addition to diagnostic applications, Cu-BTSC complexes and free BTSC ligands possess well-documented anticancer activity.⁴⁰ New drug candidates based on these ligands are currently under investigation.⁴¹

Chart 2.1. Structures of Cu(ATSM) and the $[\text{Co}(\text{BTSC})(\text{L})_2]^+$ Complexes Investigated in this Work.



We aimed to combine the hypoxia-targeting properties of the cobalt(III)/cobalt(II) redox couple with the anticancer potential of the BTSC ligands in the form of nine new cobalt(III) BTSC complexes (**Chart 2.1**). We hypothesized that the octahedral coordination geometry and increased kinetic inertness of cobalt(III), compared to the square planar coordination geometry and relative lability of copper(II), would confer key advantages to these complexes as hypoxia-targeting anticancer agents.

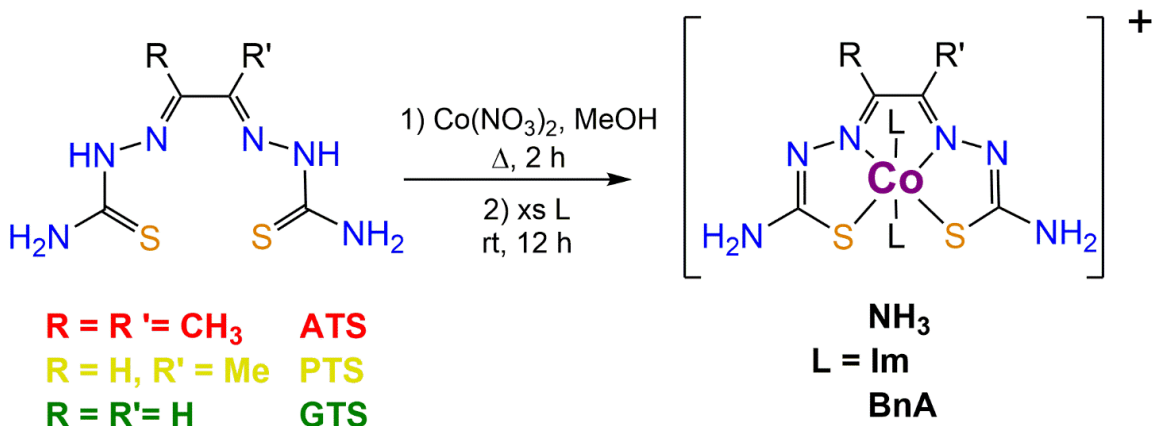
The six-coordinate geometry of cobalt(III) allows for tuning of the physiochemical properties of the compounds for biological use via modification of axial ligands. Furthermore, the greater kinetic inertness of cobalt(III) compared to copper(II) should give rise to more stable compounds before they are reduced to their active forms. Reduction of the cobalt(III) BTSC complexes may release the cytotoxic BTSC ligand and give rise to hypoxia-selective anticancer activity. We have carried out detailed characterization of the cobalt(III) BTSC complexes, studied their stabilities, and investigated their potential as hypoxia-targeting anticancer agents. The results described herein detail a structure-activity relationship for this class of compounds and provide guiding principles for the next generation of cobalt(III)-based hypoxia-targeting agents.

Results

Synthesis of Cobalt(III) Bis(thiosemicarbazone) Complexes

Nine cobalt(III) bis(thiosemicarbazone) complexes were synthesized by the method shown in **Scheme 2.1**. Heating an equimolar mixture of the free BTSC ligand and $\text{Co}(\text{NO}_3)_2$ in MeOH under reflux for approximately 30 min afforded a green solid. This uncharacterized intermediate was treated with an excess of ammonia, imidazole, or benzylamine. A color change from green to red is accompanied by the addition of the axial ligands. The compounds were isolated by filtration. Characterization by NMR spectroscopy, mass spectrometry, IR spectroscopy, and elemental analysis is consistent with the proposed structures (**Figures S2.1–S2.36**). RP-HPLC was used to verify that the compounds were isolated in greater than 95% purity (**Figures S2.37–S2.45**).

Scheme 2.1. Synthesis of Cobalt(III) Bis(thiosemicarbazone) Complexes.



X-Ray Crystallography

Single crystals, suitable for X-ray diffraction, were obtained for three [Co(BTSC)(L)₂NO₃] complexes by the vapor diffusion of Et₂O into DMF solutions. The crystal structures of the cations [CoGTS(Im)₂]⁺, [CoATS(Im)₂]⁺, and [CoGTS(BnA)₂]⁺ are shown in **Figure 2.1**, and interatomic distances and angles are given in **Table 2.1**. All three complexes exhibit the expected octahedral coordination geometry for a low-spin d⁶ Co³⁺ ion. The BTSC ligands occupy four coordination sites in the equatorial plane, requiring the nitrogen donors to be arranged in a trans orientation. Despite the presence of two methyl groups in the backbone of ATS compared to GTS, the interatomic distances between cobalt and the sulfur and nitrogen donors of these ligands are indistinguishable between the three complexes. The Co–Im bond lengths of [CoGTS(Im)₂]⁺ and [CoATS(Im)₂]⁺ range from 1.943 to 1.9616 Å, similar to those reported for a related octahedral cobalt(III) Schiff base complex bearing axial imidazole ligands.⁴² Notably, the equatorial ligand has little effect on the axial ligand bond distances. For the complex [CoGTS(BnA)₂]⁺, the benzylamine axial ligand Co–N bond

distances are 2.003(3) and 2.006(3) Å, approximately 0.04 Å longer than the imidazole Co–N distances in [CoGTS(Im)₂]⁺ and [CoATS(Im)₂]⁺.

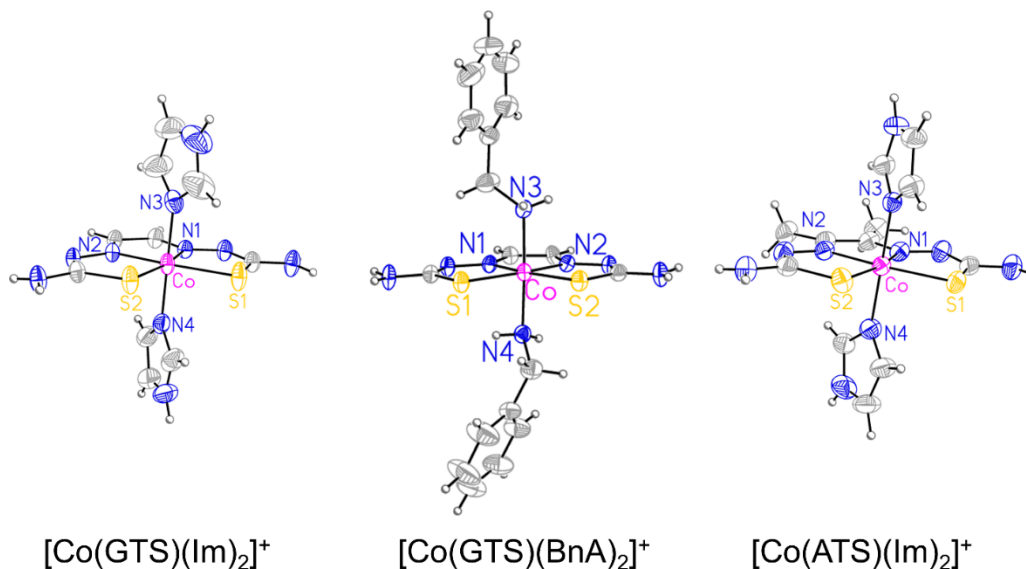


Figure 2.1. X-ray crystal structures of [Co(GTS)(Im)₂]⁺, [Co(GTS)(BnA)₂]⁺, and [Co(ATS)(Im)₂]⁺. Ellipsoids are drawn at the 50% probability level. The disordered component of the imidazole ligand in [Co(ATS)(Im)₂]⁺ is omitted for clarity.

Table 2.1. Interatomic Distances (Å) and Angles (°) of [CoGTS(Im)₂]⁺, [CoATS(Im)₂]⁺, and [CoGTS(BnA)₂]⁺.^a

Interatomic Distance	[CoGTS(Im) ₂] ⁺	[CoATS(Im) ₂] ⁺	[CoGTS(BnA) ₂] ⁺
Co–S ₁	2.2424(6)	2.2472(9)	2.2578(10)
Co–S ₂	2.2401(6)	2.2563(9)	2.2506(10)
Co–N ₁	1.8920(16)	1.898(3)	1.895(3)
Co–N ₂	1.8860(17)	1.890(2)	1.887(3)
Co–N ₃	1.9616(18)	1.943(3)	2.006(3)
Co–N ₄	1.9585(18)	1.952(3)	2.003(3)
Angle	[CoGTS(Im) ₂] ⁺	[CoATS(Im) ₂] ⁺	[CoGTS(BnA) ₂] ⁺

S ₁ –Co–S ₂	105.01(2)	106.56(3)	106.59(4)
S ₁ –Co–N ₁	85.85(5)	85.38(8)	85.17(9)
S ₁ –Co–N ₂	169.65(5)	168.00(9)	168.38(9)
S ₁ –Co–N ₃	90.32(6)	89.47(8)	90.99(10)
S ₁ –Co–N ₄	89.59(6)	90.13(9)	87.66(10)
S ₂ –Co–N ₁	169.13(5)	168.06(8)	168.23(9)
S ₂ –Co–N ₂	85.29(5)	87.75(9)	85.00(9)
S ₂ –Co–N ₃	90.23(6)	89.39(8)	89.02(9)
S ₂ –Co–N ₄	90.96(5)	87.75(9)	93.13(10)
N ₁ –Co–N ₂	83.86(7)	82.64(12)	83.23(12)
N ₁ –Co–N ₃	89.35(7)	90.49(11)	91.31(13)
N ₁ –Co–N ₄	89.43(7)	92.58(12)	86.74(13)
N ₂ –Co–N ₃	90.76(7)	91.28(11)	89.90(13)
N ₂ –Co–N ₄	89.10(7)	89.76(12)	91.05(13)
N ₃ –Co–N ₄	178.78(7)	176.87(11)	177.71(13)

^a Atoms are labeled as shown in Figure 2.1. Numbers in parentheses are the estimated standard deviations for the last significant figure.

⁵⁹Co NMR Spectroscopy

Cobalt-59 is an $I = 7/2$ nucleus with 100% natural abundance. Although linewidths may be broad due to quadrupolar relaxation, diamagnetic cobalt complexes are often amenable to characterization by ⁵⁹Co NMR spectroscopy.^{43–46} All nine of the [Co(BTSC)(L)₂]⁺ complexes were characterized by ⁵⁹Co NMR spectroscopy. Representative spectra are shown in **Figure 2.2**, and chemical shifts (δ) and linewidths ($\nu_{1/2}$) are summarized in **Table 2.2**. The remaining ⁵⁹Co NMR spectra are in Appendix 1, **Figures S2.19–S2.27**.

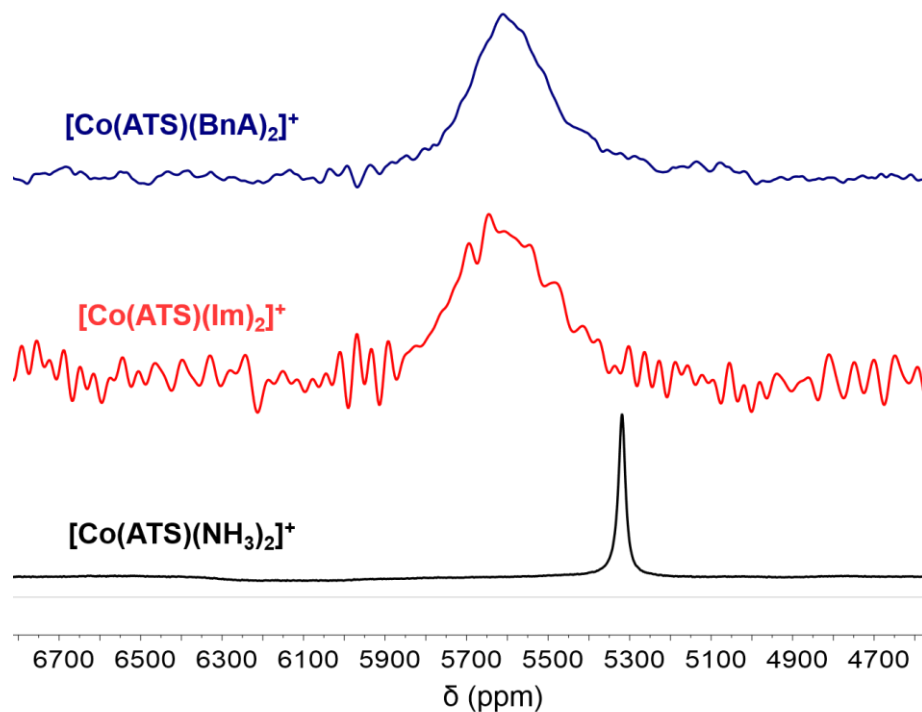


Figure 2.2. ^{59}Co NMR spectra of $[\text{Co}(\text{ATS})\text{L}_2]^+$ complexes in $\text{DMSO-}d_6$ at $25\text{ }^\circ\text{C}$ obtained at a frequency of 119 MHz. Spectra are referenced to $\text{K}_3[\text{Co}(\text{CN})_6]$ in D_2O at 0 ppm.

The chemical shift of the ^{59}Co resonance exhibits a dependence on both the equatorial and axial ligands. For a given BTSC, the chemical shift moves downfield by approximately 300 ppm as the axial ligand is altered from NH_3 to BnA or Im. Complexes of PTS and ATS exhibit chemical shifts that are within 30 ppm of each other. In contrast, the corresponding GTS complexes, which lack the electron-donating methyl groups on the ligand backbone, resonate approximately 80 ppm upfield from the PTS and ATS complexes. The linewidth of the resonance appears to correlate only with the nature of the axial ligand; complexes with axial ammonia ligands give rise to reasonably sharp signals with $\nu_{1/2} < 3000$ Hz. In contrast, axial imidazole and benzylamine ligands give rise to very broad peaks with linewidths exceeding 20,000 Hz.

Table 2.2. ^{59}Co NMR Chemical Shifts and Linewidths^a

Compound	δ (ppm)	$\nu_{1/2}$ (Hz)
$[\text{Co}(\text{ATS})(\text{NH}_3)_2]^+$	5320	2600
$[\text{Co}(\text{ATS})(\text{Im})_2]^+$	5640	33500
$[\text{Co}(\text{ATS})(\text{BnA})_2]^+$	5600	27900
$[\text{Co}(\text{PTS})(\text{NH}_3)_2]^+$	5320	1400
$[\text{Co}(\text{PTS})(\text{Im})_2]^+$	5610	30700
$[\text{Co}(\text{PTS})(\text{BnA})_2]^+$	5590	21100
$[\text{Co}(\text{GTS})(\text{NH}_3)_2]^+$	5250	1200
$[\text{Co}(\text{GTS})(\text{Im})_2]^+$	5570	30000
$[\text{Co}(\text{GTS})(\text{BnA})_2]^+$	5510	20200

^a Chemical shifts are referenced to $\text{K}_3[\text{Co}(\text{CN})_6]$ in D_2O set at $\delta = 0$ ppm.

UV-Vis Spectroscopy

The electronic structure of the cobalt bis(thiosemicarbazone) complexes was further characterized by UV-Vis spectroscopy. Representative UV-Vis spectra of the $[\text{Co}(\text{BTSC})(\text{NH}_3)_2]^+$ complexes are shown in **Figure 2.3**, and data for these and the remaining complexes are collected in **Table 2.3**. UV-Vis spectra for the other complexes are in Appendix 1, **Figures S2.46–S2.54**. All of the complexes display two distinct absorption maxima: one highly intense feature between 340 and 390 nm and another, less intense feature ranging from 499 to 530 nm. A third less well-defined band is also apparent in the range of 440 to 450 nm. The low energy transitions are red-shifted as the equatorial ligand is changed from the most electron-donating ligand ATS to the least donating GTS. The influence of the axial ligand is substantially less

pronounced.

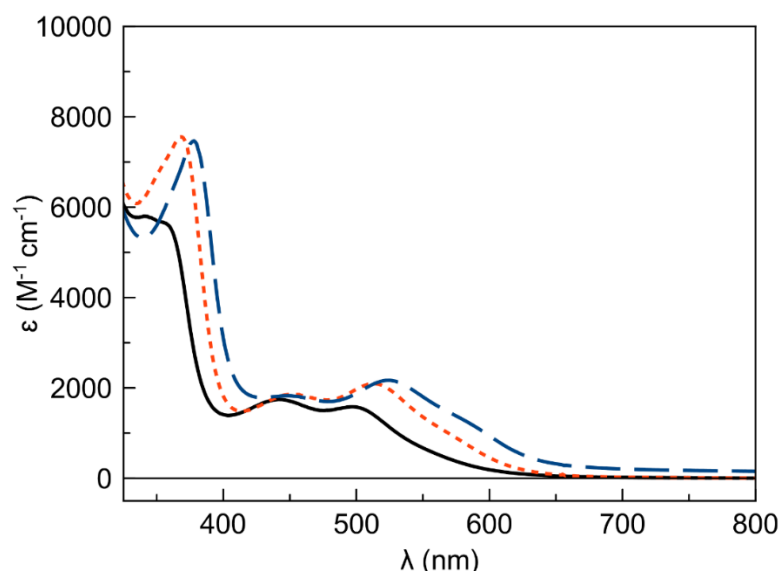


Figure 2.3. Electronic absorption spectra of $[\text{Co}(\text{ATS})(\text{NH}_3)_2]^+$ (solid black line), $[\text{Co}(\text{PTS})(\text{NH}_3)_2]^+$ (small orange dashes), and $[\text{Co}(\text{GTS})(\text{NH}_3)_2]^+$ (long blue dashes) complexes in pH 7.4 PBS at 25 °C.

Table 2.3. Absorbance Maxima and Extinction Coefficients for the Complexes in pH 7.4 PBS

Compound	λ , nm (ϵ , $\text{M}^{-1} \text{cm}^{-1}$)		
$[\text{Co}(\text{ATS})(\text{NH}_3)_2]^+$	341 (5800)	443 (1708)	499 (1566)
$[\text{Co}(\text{ATS})(\text{Im})_2]^+$	367 (5791)	446 (1705)	503 (1699)
$[\text{Co}(\text{ATS})(\text{BnA})_2]^+$	363 (7673)	447 (1520)	510 (1624)
$[\text{Co}(\text{PTS})(\text{NH}_3)_2]^+$	368 (7557)	450 (1834)	514 (2038)
$[\text{Co}(\text{PTS})(\text{Im})_2]^+$	374 (6339)	449 (1576)	516 (1842)
$[\text{Co}(\text{PTS})(\text{BnA})_2]^+$	375 (8016)	450 (1700)	524 (1870)
$[\text{Co}(\text{GTS})(\text{NH}_3)_2]^+$	377 (7456)	446 (1961)	523 (2015)
$[\text{Co}(\text{GTS})(\text{Im})_2]^+$	379 (7417)	442 (1805)	527 (2040)
$[\text{Co}(\text{GTS})(\text{BnA})_2]^+$	384 (8676)	446 (1548)	537 (1853)

Electrochemistry

The electrochemical properties of the $[\text{Co}(\text{BTSC})(\text{L})_2]^+$ complexes were analyzed by cyclic voltammetry in anhydrous DMF with 0.10 M NBu_4PF_6 as the supporting electrolyte. Results of the electrochemical studies are presented in **Table 2.4**, and representative voltammograms of the compound $[\text{Co}(\text{GTS})(\text{Im})_2]^+$ are displayed in **Figure 2.4**. Other voltammograms are shown in Appendix 1, **Figures S2.55–S2.63**.

Table 2.4. Electrochemical Properties of $[\text{Co}(\text{BTSC})(\text{L})_2]^+$ Complexes^a

Compound	$E_{1/2}, \text{Co(II/I)}$	$E_{\text{pc}}, \text{Co(III/II)}$
$[\text{Co}(\text{ATS})(\text{NH}_3)_2]^+$	-1.18	-1.10
$[\text{Co}(\text{ATS})(\text{Im})_2]^+$	-1.19	-0.86
$[\text{Co}(\text{ATS})(\text{BnA})_2]^+$	-1.18	-0.83
$[\text{Co}(\text{PTS})(\text{NH}_3)_2]^+$	-1.11	-0.92
$[\text{Co}(\text{PTS})(\text{Im})_2]^+$	-1.12	-0.84
$[\text{Co}(\text{PTS})(\text{BnA})_2]^+$	-1.14	-0.84
$[\text{Co}(\text{GTS})(\text{NH}_3)_2]^+$	-1.02	-0.95
$[\text{Co}(\text{GTS})(\text{Im})_2]^+$	-1.00	-0.72
$[\text{Co}(\text{GTS})(\text{BnA})_2]^+$	-1.00	-0.69

^a Potentials are referenced to the SCE. Data were obtained at a glassy carbon working electrode in anhydrous DMF containing 0.10 M TBAP, using a scan rate of 100 mV/s at 25 °C.

All complexes exhibited the same general features: an initial, irreversible reduction (A) followed by a quasi-reversible reduction/oxidation (B/C), and then a broad oxidation feature (D) (**Figure 2.4**). Scans after the first sweep showed a new irreversible reduction feature (E) at a more positive potential than the initial irreversible reduction peak potential. To further probe the nature of this electrochemical reactivity, excess

imidazole was added to the electrochemical cell. The addition of imidazole had three pronounced effects upon the voltammogram, as shown in **Figure 2.4**.

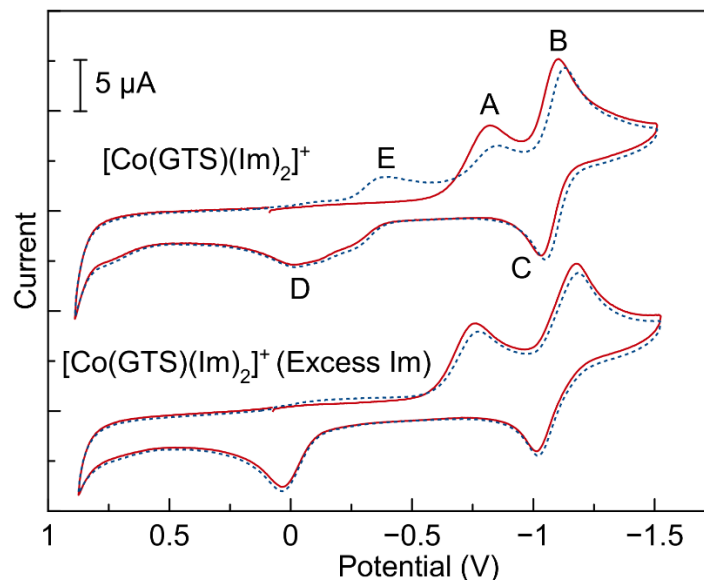


Figure 2.4. Cyclic voltammogram of $[\text{Co}(\text{GTS})(\text{Im})_2]^+$ before (top) and after (bottom) addition of excess imidazole. The first scan is shown as a solid red line, while the second scan is represented by small blue dashes. This experiment was performed at 25 °C in DMF solution with 0.10 M TBAP electrolyte at a scan rate of 100 mV/s. The potential is referenced to SCE, based on the position of the Fc/Fc⁺ couple as an internal standard.

First, the irreversible reduction event (A) does not decrease in amplitude as dramatically upon the second cycle. Second, the broad irreversible oxidation feature (D) becomes much sharper, coalescing into what appears to be a single peak. Third, the reduction peak (E), a feature that is only apparent upon the second cycle, disappears altogether. These results indicate that axial ligand exchange plays an integral role in the complexes' electrochemical behavior. We propose a mechanism in which the initial irreversible reduction peak (A) corresponds to the Co(III)/Co(II) reduction process. Population of e_g^* antibonding orbitals upon reduction of Co(III) leads to the dissociation of at least one of the axial ligands. The quasi-reversible reduction/oxidation event (B/C)

is attributed to the Co(II)/Co(I) couple of the resulting complex, which lacks axial nitrogen donor ligands. The broad oxidation event (D) corresponds to the Co(II)/Co(III) oxidation of a mixture of complexes containing either nitrogen donor axial ligands or coordinated DMF axial ligands. The new reduction event (E) is the Co(III)/Co(II) couple of complexes bearing axial DMF ligands. When excess imidazole is added, recombination of this ligand with the cobalt complex to form [CoGTS(Im)₂]⁺ occurs rapidly after feature (C). As such, feature (D) coalesces to a single oxidation event, corresponding to that of [CoGTS(Im)₂]⁺ exclusively, and feature (E), which is attributed to the complex with axial DMF ligands, is not observed. Similar electrochemical mechanisms have been reported in other Co(III) complexes.¹⁰

Stability and N-Methylimidazole Challenge Studies

The stability of the [Co(BTSC)(L)₂]⁺ complexes at 37 °C in pH 7.4 PBS was evaluated by RP-HPLC. The peak area of the intact complex was measured after a 24 h incubation period. All complexes showed significant degradation over this time course; the amount of intact complex remaining ranges from 0–70% (**Figure 2.5**). Decomposition in PBS is accompanied by formation of a precipitate as well as the appearance of new peaks on the chromatogram. For the complexes bearing BnA, one of these peaks was conclusively identified to be free BnA, indicating that axial ligand loss is a key decomposition pathway for these complexes. Characterization of the precipitate by ¹H NMR spectroscopy showed the presence of the intact complex, which may have precipitated as an insoluble phosphate or chloride salt. The nature of the axial ligand has the greatest impact on complex stability, whereas effects due to the equatorial ligand

are subtler. Complexes with axial ammonia ligands, $[\text{Co}(\text{BTSC})(\text{NH}_3)_2]^+$, exhibit the highest stability, whereas those with benzylamine axial ligands are the least stable. For the benzylamine and ammonia complexes, the GTS ligand confers greater stability than the ATS ligand.

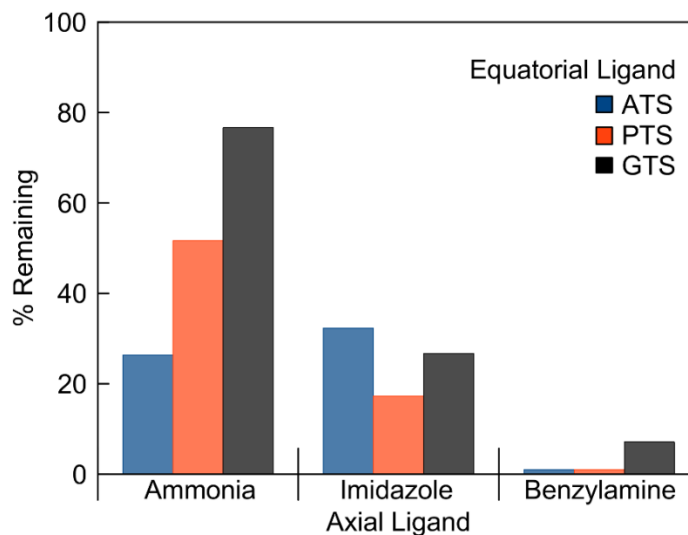


Figure 2.5. Percent of $[\text{Co}(\text{BTSC})(\text{L})_2]^+$ remaining in solution after 24 h incubation at 37 °C in PBS as measured by RP-HPLC. Values are the average of two independent experiments.

The significant dependence on the nature of the axial ligand on the complex stability may indicate that these compounds are degrading via axial ligand substitution reactions, a phenomenon that is well studied for related cobalt-based Schiff-base enzyme inhibitors.^{10,13,42} This hypothesis was further explored by treating the $[\text{Co}(\text{BTSC})(\text{L})_2]^+$ complexes with 5 molar equivalents of *N*-methylimidazole (meIm) to qualitatively examine the susceptibility of these compounds to axial ligand substitution. The stability of the complexes with respect to the meIm challenge was investigated by RP-HPLC after 24 h. Decay of the peak corresponding to the intact complex was observed in

conjunction with the appearance of two new peaks of higher retention times (**Figure 2.6**). We assign these new peaks as the monosubstituted and disubstituted complexes, $[\text{Co}(\text{BTSC})(\text{L})(\text{meIm})]^+$ and $[\text{Co}(\text{BTSC})(\text{meIm})_2]^+$ species based on their respective retention times on the column. The relative quantities of the starting complex, monosubstituted, and disubstituted complexes are shown in **Table 2.5**.

Table 2.5. Axial ligand substitution of $[\text{Co}(\text{BTSC})(\text{L})_2]^+$ complexes by *N*-methylimidazole

Compound	% Intact	% Monosubstituted	% Disubstituted
$[\text{Co}(\text{ATS})(\text{NH}_3)_2]^+$	38	27	35
$[\text{Co}(\text{ATS})(\text{Im})_2]^+$	11	43	46
$[\text{Co}(\text{ATS})(\text{BnA})_2]^+$	0	7	93
$[\text{Co}(\text{PTS})(\text{NH}_3)_2]^+$	56	22	22
$[\text{Co}(\text{PTS})(\text{Im})_2]^+$	7	39	54
$[\text{Co}(\text{PTS})(\text{BnA})_2]^+$	1	6	93
$[\text{Co}(\text{GTS})(\text{NH}_3)_2]^+$	65	15	20
$[\text{Co}(\text{GTS})(\text{Im})_2]^+$	6	37	58
$[\text{Co}(\text{GTS})(\text{BnA})_2]^+$	12	20	68

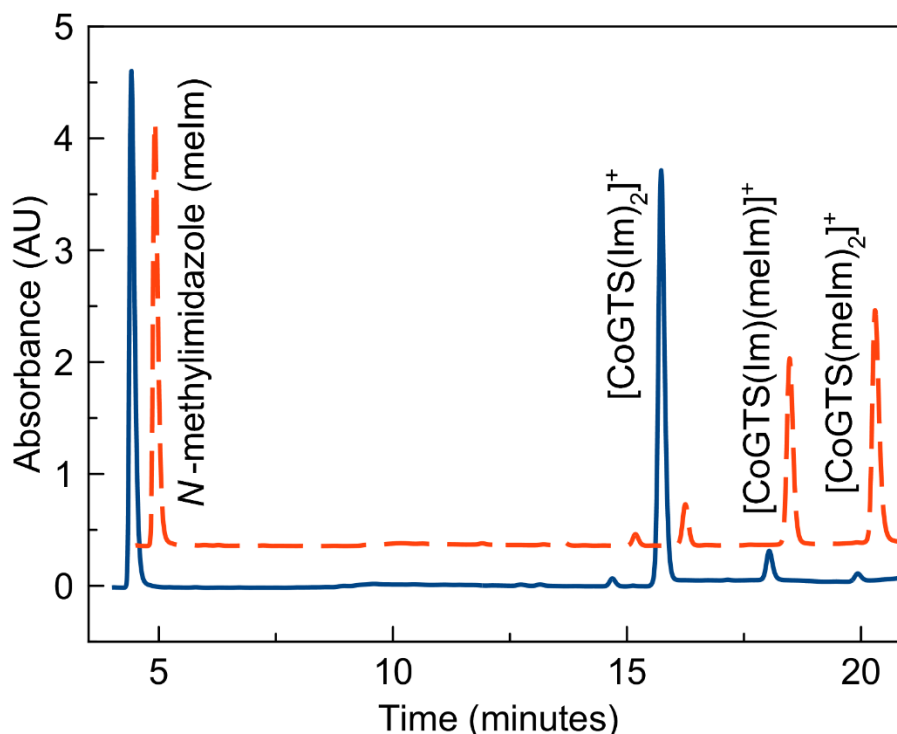


Figure 2.6. HPLC traces of 1 mM $[\text{CoGTS}(\text{Im})_2]^+$ incubated with 5 mM *N*-methylimidazole immediately (solid blue) and 3 h (red dashes) after mixing. The 3-h trace is shifted up and to the right relative to the initial trace for clarity.

The stability trends for this meIm challenge study match those observed for the stability in PBS. Namely, the susceptibility of the complex to axial ligand substitution with meIm is mostly dependent on the axial ligand. The benzylamine and Im complexes exhibit the greatest amount of substitution by meIm after 24 h, whereas the complexes bearing axial ammonia ligands are resistant to meIm substitution. This trend is opposite to that observed for the axial ligand substitution of related cobalt(III) Schiff base compounds where axial ammonia ligands exhibited faster kinetics for meIm substitution compared to Im.⁴²

Uptake Experiments

To investigate the relationship between structure and intracellular accumulation, the uptake of the cobalt bis(thiosemicarbazone) complexes in A549 cells was quantified using GFAAS in conjunction with the Bradford protein assay. To test for hypoxia selectivity, these measurements were carried out under both normoxic and hypoxic conditions. The cells were treated with 100 μM of the complexes and incubated for 24 h prior to quantification of uptake. The results of these studies are shown in **Figure 2.7**. Cellular uptake is dictated primarily by the equatorial ligand; the axial ligands only have a minor influence. Cellular uptake increases as the number of methyl groups on the equatorial ligand backbone increases. As such, the ATS complexes are taken up much more efficiently than the PTS and GTS complexes. Notably, the GTS and PTS complexes exhibit less uptake than free $\text{Co}(\text{NO}_3)_2$ itself. The efficient uptake of $\text{Co}(\text{NO}_3)_2$ by mammalian cells has been observed previously and was postulated to arise from either ion transporters or transferrin-mediated pathways.⁴⁷

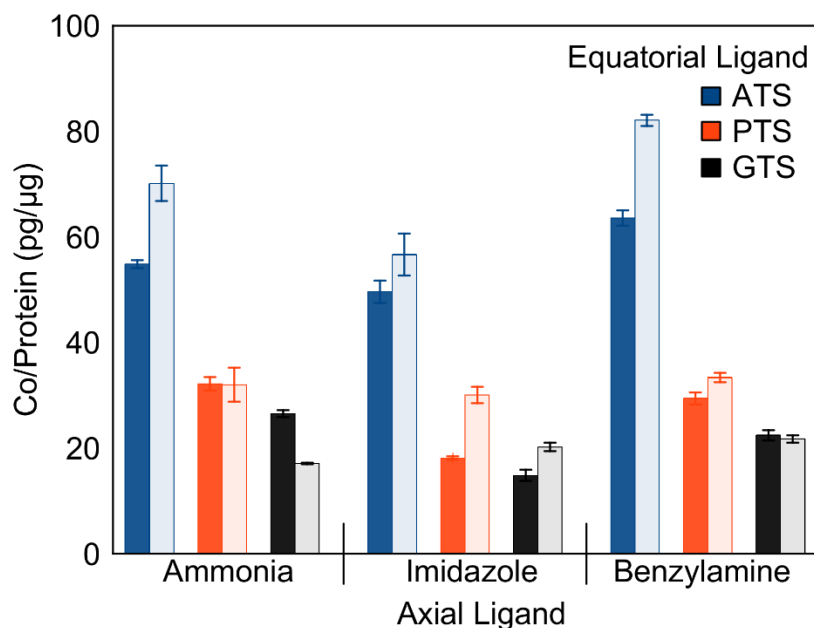


Figure 2.7. Uptake of $[\text{Co}(\text{BTSC})(\text{L})_2]^+$ complexes in normoxic (dark fill) and hypoxic (light fill) conditions. Bars indicate the mass ratio of cobalt to protein ($\text{pg}/\mu\text{g}$) in each sample after 24-h incubation with $100 \mu\text{M}$ Co complex. Results are the average of three samples for each complex.

Several complexes exhibited differential accumulation under hypoxic conditions. The ratio of uptake in normoxia and hypoxia is given in **Table 2.6**. Six out of the nine complexes showed $>10\%$ increase in uptake under hypoxic conditions. $[\text{CoGTS}(\text{NH}_3)_2]^+$, in contrast, showed decreased uptake under hypoxic conditions. In general, the less stable, hydrophobic complexes containing imidazole and benzylamine demonstrated the highest hypoxia selectivity. Compounds containing the ATS and PTS equatorial ligands exhibit higher selectivity on average than GTS complexes. This trend in selectivity matches that reported for the $\text{Cu}(\text{BTSC})$ complexes, despite the fact that the copper complexes have a much more positive reduction potential relative to the cobalt(III) bis(thiosemicarbazones).^{48,49} The observed hypoxia selectivity is of these

complexes is substantially lower than those reported for Cu(ATSM) (5× selectivity) and its derivatives.^{48,49}

Table 2.6. Cellular Uptake of Complexes in A549 Cells

Compound	Co/Protein (pg/μg) (Normoxia)	Co/Protein (pg/μg) (Hypoxia)	Hypoxia/Normoxia Ratio
Co(NO ₃) ₂	37 ± 2	33 ± 3	0.88 ± 0.09
[Co(ATS)(NH ₃) ₂] ⁺	55 ± 1	70 ± 3	1.28 ± 0.05
[Co(ATS)(Im) ₂] ⁺	50 ± 2	57 ± 4	1.10 ± 0.09
[Co(ATS)(BnA) ₂] ⁺	64 ± 1	82 ± 1	1.30 ± 0.03
[Co(PTS)(NH ₃) ₂] ⁺	32 ± 1	32 ± 3	0.99 ± 0.09
[Co(PTS)(Im) ₂] ⁺	18.0 ± 0.3	30 ± 1	1.70 ± 0.07
[Co(PTS)(BnA) ₂] ⁺	29 ± 1	33 ± 1	1.10 ± 0.04
[Co(GTS)(NH ₃) ₂] ⁺	27 ± 1	17.0 ± 0.1	0.65 ± 0.01
[Co(GTS)(Im) ₂] ⁺	15 ± 1	20 ± 1	1.40 ± 0.09
[Co(GTS)(BnA) ₂] ⁺	22 ± 1	22 ± 1	0.97 ± 0.04

In Vitro Anticancer Activity

The cytotoxic effects of the complexes and free ligands were determined under both normoxic and hypoxic conditions in HeLa and A549 cell lines using the MTT assay. The cytotoxic activity of the complexes is tabulated as 50% growth inhibitory concentration (IC₅₀) values in **Table 2.7**. In general, the activity is correlated strongly with the identity of the equatorial BTSC ligand. **Figure 2.8** shows the dose-response curves for the treatment of A549 with the three [Co(BTSC)(Im)₂]⁺ complexes. Representative dose-response curves for the other compounds and cell lines are deposited in Appendix 1, **Figures S2.64–S2.72**. **Figure 2.8** reflects the general trends

that are seen for all of the complexes; complexes bearing the GTS ligand exhibit potent cytotoxicity, whereas those bearing the ATS ligand are inactive. The dose-response curves of complexes bearing the PTS ligand indicate a dose-dependent decrease in cell viability. However, these curves display a leveling out effect at 30–50% cell viability, where beyond a certain concentration threshold the cell viability remains constant. Even at the highest concentration screened (500 μM), the cell viability does not go to zero. This leveling out effect limited our ability to determine precise IC_{50} values, as the leveling out often occurred near 50% cell viability. The trends in cytotoxicity correspond with the activities of the free ligands, as the toxicity of the free ligands increases in the order $\text{ATS} < \text{PTS} \approx \text{GTS}$. Notably, the activity of free PTS and GTS ligands exceeds that of the cobalt(III) complexes, indicating that coordination to cobalt(III) significantly attenuates their cytotoxicity. All the cobalt(III) complexes are also less active than the established metal-based anticancer drug cisplatin.

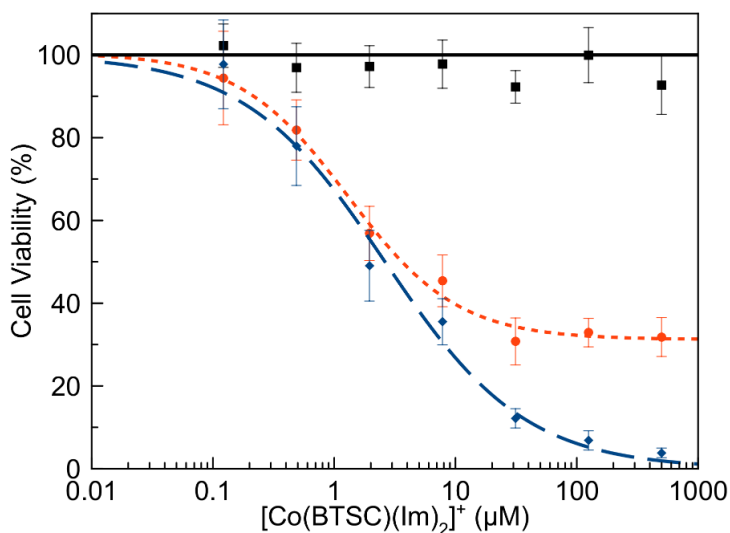


Figure 2.8. Effect of $[\text{Co}(\text{BTSC})(\text{Im})_2]^+$ complex concentration on A549 cell viability as measured by the MTT assay for $[\text{Co}(\text{ATS})(\text{Im})_2]^+$ (solid black line, square marker),

$[\text{Co}(\text{PTS})(\text{Im})_2]^+$ (small-dashed orange line, circle marker), and $[\text{Co}(\text{GTS})(\text{Im})_2]^+$ (broad blue dashed line, diamond marker).

The axial ligands show less pronounced effects on the cytotoxicity. In general, complexes containing benzylamine and imidazole are slightly more potent than those with ammonia, but this trend does not hold for all nine complexes. The complexes were also tested in HeLa cells (**Table 2.7**). The activity of these complexes and the free BTSC ligands was greater than that observed in A549 cells, but the trends in activity remain the same. The cytotoxicity was also evaluated in MRC-5 normal lung fibroblasts as a model for non-cancerous cells (**Figure 2.9, Table 2.7**). Like the free BTSC ligands, the cobalt complexes are inactive in this cell line, suggesting that they may possess a favorable therapeutic index. As such, the cytotoxicity of the complexes exhibits a distinct cell line dependence with the most potent activity in A549 cells, less activity in HeLa cells, and no substantial cytotoxicity in MRC-5 cells. Notably, cisplatin exhibits less cell-line dependence and is cytotoxic in the micromolar range against normal MRC-5 cells (**Figure 2.9**).

Most complexes showed no statistically significant increase in cytotoxicity under hypoxic conditions. Only a modest decrease in the IC_{50} values of the PTS and GTS complexes was observed under hypoxia. In contrast, the free PTS and GTS ligands exhibited decreased activity in hypoxia. Among the GTS complexes, $[\text{CoGTS}(\text{Im})_2]^+$ displayed the greatest hypoxia selectivity, with a hypoxia selectivity index ($\text{IC}_{50}\text{Norm}/\text{IC}_{50}\text{Hyp}$) of 2.0 in HeLa cells. Tirapazamine, a well-characterized hypoxia-selective cytotoxic agent, was used as a positive control.^{50,51} This compound displayed a hypoxia selectivity index of 3.3 in HeLa cells in our lab; this value is lower than the

typical hypoxia selectivity index of 10 that is observed for this compound in other studies.^{52,53} Cisplatin exhibited no difference in activity under hypoxic versus normoxic conditions.

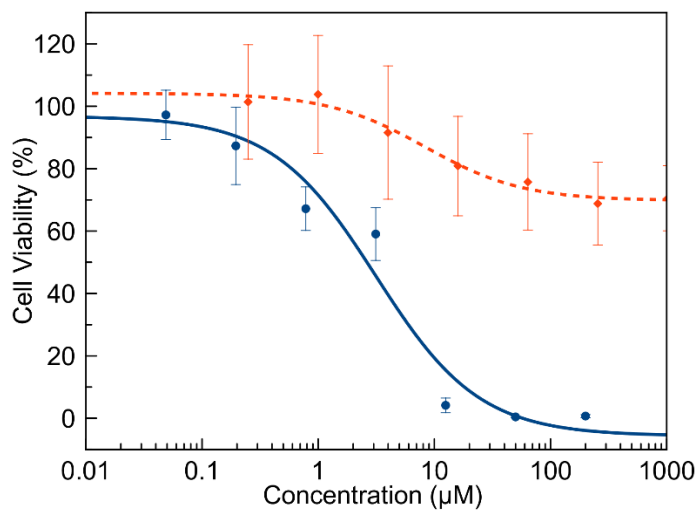


Figure 2.9. Dose-response curves of cisplatin (solid blue line, circular marker) and [Co(GTS)(NH₃)₂]⁺ (orange dashes, diamond marker) in MRC-5 (normal lung fibroblast) cells.

Table 2.7: IC₅₀ Values (μM) for [Co(BTSC)(L)₂]NO₃ Complexes

Compound	HeLa		A549		MRC-5
	Normoxia	Hypoxia	Normoxia	Hypoxia	Normoxia
Cisplatin	1.7 ± 0.07	1.7 ± 0.21	5.5 ± 3.2	5.2 ± 2.4	3.5 ± 1.2
Tirapazamine	44 ± 19	13 ± 4.2	60 ± 5.4	11 ± 6.5	n.d. ^b
ATS	>20	>20	16.4 ± 0.87	17.5 ± 2.7	n.d. ^b
PTS	0.027 ± 0.002	0.055 ± 0.001	0.06 ± 0.03	0.09 ± 0.03	n.d. ^b
GTS	0.067 ± 0.008	0.094 ± 0.010	0.02 ± 0.01	0.04 ± 0.01	>20
Co(NO ₃) ₂	>500	>500	>500	>500	>500
[Co(ATS)(NH ₃) ₂] ⁺	>500	>500	>500	>500	n.d. ^b
[Co(ATS)(Im) ₂] ⁺	>500	>500	>500	>500	n.d. ^b
[Co(ATS)(BnA) ₂] ⁺	>500	>500	>500	>500	n.d. ^b
[Co(PTS)(NH ₃) ₂] ⁺	≈22 ^a	≈15 ^a	≈16.9 ^a	≈21.8 ^a	n.d. ^b
[Co(PTS)(Im) ₂] ⁺	≈28 ^a	≈17 ^a	≈4.2 ^a	≈8.6 ^a	n.d. ^b
[Co(PTS)(BnA) ₂] ⁺	≈8.6 ^a	≈8.8 ^a	≈7.1 ^a	≈27 ^a	n.d. ^b
[Co(GTS)(NH ₃) ₂] ⁺	21 ± 2.9	15 ± 4.6	12 ± 1.4	9.2 ± 1.4	>250
[Co(GTS)(Im) ₂] ⁺	7.4 ± 2.4	3.7 ± 2.3	2.6 ± 0.4	2.9 ± 0.7	>250
[Co(GTS)(BnA) ₂] ⁺	7.3 ± 1.5	6.3 ± 0.76	5.8 ± 0.95	8.2 ± 1.9	>250

^a Accurate IC₅₀ values could not be obtained for these compounds because the dose-response curves level off near 50% cell viability. These values represent the average concentration at which the beginning of this leveling effect is observed in the dose-response curves. ^b n.d. = not determined.

Cytotoxicity Experiments with Tetrathiomolybdate

The correlation in activity of the complexes with their BTSC ligands suggests that they may be operating by similar mechanisms of action. The BTSC ligands induce their cytotoxic effects in a copper ion-dependent manner.⁴⁰ These ligands act as ionophores for copper, shuttling Cu(BTSC) complexes into cells where they generate cytotoxic reactive species that induce cell death.⁵⁴ Treatment of cells with

tetrathiomolybdate (TM) decreases the cytotoxic effects of these ligands by depleting the available copper pool.^{40,55,56} To test whether the $[\text{Co}(\text{GTS})(\text{L})_2]^+$ complexes operate via a similar mechanism, A549 cells were treated with both $[\text{Co}(\text{GTS})(\text{L})_2]^+$ complexes and TM. The IC_{50} values increased by a factor of 10 when cells were treated with TM, as shown in **Table 2.8** and **Figure 2.10**. This result indicates that the complexes operate via a copper-dependent mechanism. To confirm that TM does not react with the $[\text{Co}(\text{BTSC})(\text{L})_2]^+$ complexes, $[\text{Co}(\text{GTS})(\text{NH}_3)_2]\text{NO}_3$ and TM (1:1) were co-incubated in $\text{DMSO-}d_6$ and monitored by NMR spectroscopy. Only intact $[\text{Co}(\text{GTS})(\text{NH}_3)_2]\text{NO}_3$ is detected, indicating that TM does not remove the cobalt(III) ion (**Figures S2.73–S2.74**).

Table 2.8. Effect of TM on IC_{50} values (μM) in A549 Cells

Compound	Without TM	With 5 μM TM
GTS	0.02 ± 0.01	3.93 ± 0.85
$[\text{Co}(\text{GTS})(\text{NH}_3)_2]^+$	12 ± 1.4	290 ± 105
$[\text{Co}(\text{GTS})(\text{Im})_2]^+$	2.6 ± 0.4	68 ± 23
$[\text{Co}(\text{GTS})(\text{BnA})_2]^+$	5.8 ± 1.0	99 ± 20

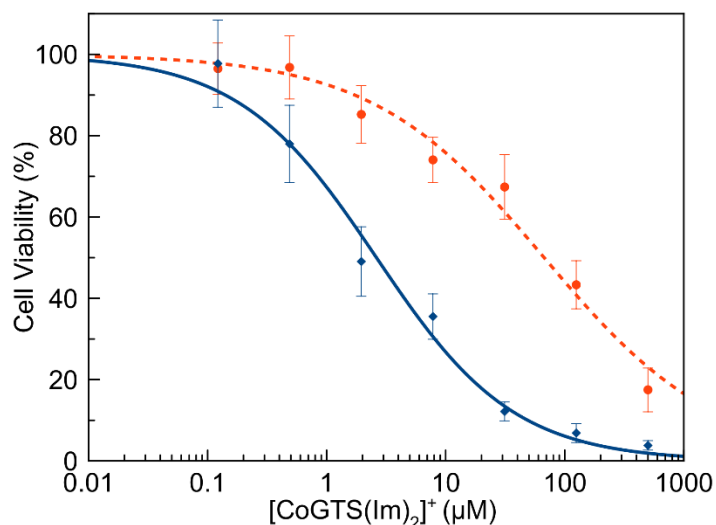


Figure 2.10. Effect of $[\text{CoGTS}(\text{Im})_2]^+$ complex concentration on A549 cell viability in the presence (dashed line, circular marker) and absence (solid blue line, diamond marker) of TM.

Discussion

The anticancer potential of cobalt(III) complexes is currently a topic of significant interest, which has prompted the investigation of numerous different cobalt(III) coordination complexes.^{14,23,27} Additionally, the BTSC ligands are well-characterized, biomedically active agents.^{41,57,58} Although there are a few reports of cobalt(II) complexes of BTSCs,^{59,60} there is surprisingly no prior investigation on the cobalt(III) analogues. In this study, we were interested in combining the biological effects of the BTSC ligands with the hypoxia-targeting properties of cobalt(III) complexes, premised on the hypothesis that reductive activation of these complexes would give rise to hypoxia-selective anticancer agents. We synthesized a small library comprising nine $[\text{Co}(\text{BTSC})(\text{L})_2]^+$ complexes to elucidate structure-activity relationships for this class of compounds. The results of this study may be compared to related and well-established anticancer cobalt(III) Schiff base complexes¹³ and

Cu(BTSC) compounds⁶¹ in order to provide a comprehensive picture regarding relationships between metal complex structure and biological activity.

The synthesis of the compounds proceeds by the sequential reaction of $\text{Co}(\text{NO}_3)_2$ with the BTSC followed by the addition of the axial ligand (**Scheme 2.1**). The reaction takes place with the aerobic oxidation of the cobalt(II) to cobalt(III). A green intermediate observed prior to addition of the axial ligands is hypothesized to be a cobalt(II) complex of the BTSC ligand. The cobalt(III) compounds were isolated as dark red solids. In contrast to the Cu(BTSC) complexes, the cobalt(III) analogues exhibit good water solubility; stock solutions of the compounds in mM concentrations in pure water could be readily made. These complexes were characterized and verified to be pure via NMR spectroscopy, X-ray crystallography, and HPLC. The NMR spectra of the nine complexes display no signs of paramagnetism, consistent with the expected diamagnetic nature of a low-spin cobalt(III) complex. Upon coordination to cobalt(III), the ^1H NMR resonances of the BTSC ligands shift upfield, and the acidic azomethine proton resonance disappears. Analysis of these complexes by HR-ESI-MS revealed molecular ion peaks with masses matching those expected for the general formulae $[\text{Co}(\text{BTSC})(\text{L})_2]^+$. The crystal structures of $[\text{Co}(\text{GTS})(\text{Im})_2]^+$, $[\text{Co}(\text{GTS})(\text{BnA})_2]^+$, and $[\text{Co}(\text{ATS})(\text{Im})_2]^+$ (**Figure 2.1**) reveal the expected octahedral coordination geometry at the cobalt(III) center. The equatorial Co–BTSC ligand distances are relatively invariant in the three complexes. The axial Co–Im and Co–BnA distances are different; the Co–BnA distances are approximately 0.04 Å longer than the Co–Im distances, a feature that may be attributed to steric crowding at the cobalt(III) center by the large benzylamine ligands.

Further characterization of these compounds was accomplished by electronic absorption spectroscopy, ^{59}Co NMR spectroscopy, and cyclic voltammetry. Absorbance bands in the UV-Vis spectra in the ranges of 340 to 390 nm and 499 to 530 nm shift depending on the nature of the equatorial ligand (**Figure 2.3**, **Table 2.3**). Both bands blue-shift following the sequence $\text{GTS} < \text{PTS} < \text{ATS}$. A smaller blue-shift is also apparent as the axial ligand is varied from either benzylamine or imidazole to ammonia. The low energy absorbance bands in the 499 to 530 nm range are assigned as a metal-to-ligand charge transfer (MLCT) transitions, and the higher energy feature in the 340 to 390 nm range is assigned as an intraligand $\pi-\pi^*$ transition. These assignments are made based on their large molar absorptivities and relative energies. The assignments are also consistent with the observed trends. As the equatorial ligand shifts from weakly electron donating (GTS) to strongly electron donating (ATS), the ligand-based π^* orbital increases in energy leading to a concomitant increase in energy of both the MLCT and ligand-based transitions. These absorbance spectra are qualitatively similar to those of previously reported cobalt(III) Schiff base complexes, for which the major features were a low-energy MLCT and a high energy $\pi-\pi^*$ transition.¹⁰

The cyclic voltammograms show a clear relationship between ligand donor-capacity and the complex reduction potential. The initial reductive sweep in all complexes produces an irreversible reduction, which we assign to the Co(III)/Co(II) coupled with axial ligand loss, followed by a quasi-reversible Co(II)/Co(I) reduction of the remaining complex bearing only the equatorial BTSC ligand (**Figure 2.4**). As such, the reduction potential of the Co(II)/Co(I) couple is independent of the nature of the axial ligand (**Table 2.4**). As the equatorial ligands are altered from ATS to PTS to GTS

the reduction potential of the Co(II/I) couple shifts by approximately +100 mV. This trend is consistent with that observed in the Cu(BTSC) complexes, which decrease in reduction potential by approximately 60 mV as methyl groups are added to the ligand backbone.⁶¹ ATS with two electron-donating methyl groups renders reduction of the cobalt center less favorable, giving rise to a more negative redox potential. The Co(III)/Co(II) redox couple, arguably the more important redox process for hypoxia targeting, is reflected by an irreversible peak potential. This peak potential is sensitive to both equatorial and axial ligands. The equatorial ligand effects follow the expected trend as for the Co(II)/Co(I) couple. For the same BTSC ligand, the benzylamine and imidazole complexes had more positive reduction potentials than the corresponding ammonia complexes, as expected based on the relative donating abilities of the ligands.⁶² The most positive reduction potential observed for the Co(III)/Co(II) couple is -0.69 V for [CoGTS(BnA)₂]⁺, substantially more negative than the value reported for the established hypoxia-imaging agent CuATSm, -0.59 V.⁶¹ The reduction potentials of the cobalt(III) BTSC complexes lie on the edge of the range needed for hypoxia selectivity (-0.75 to -0.35 V vs SCE).^{7,23,63} Notably, irreversible reduction feature (E) (**Figure 2.4**) corresponds to the Co(III)/Co(II) couple of the complex with axial DMF ligands, which is generated electrochemically after the irreversible reduction of the intact complex. This reduction feature is 500 mV more positive than the Co(III)/Co(II) couples of the intact complexes, feature (A). This result suggests that ligand substitution of the axial ligands by an oxygen donor may shift the reduction potential to a region more suitable for reduction in the cellular environment.

The ^{59}Co NMR spectra (**Figure 2.2**) corroborate the trends observed in UV-Vis spectra and cyclic voltammograms. The ^{59}Co chemical shifts move upfield as the equatorial ligand is altered from ATS to PTS to GTS, and as the axial ligand is changed from Im to BnA to NH_3 (**Table 2.2**). As discussed above, the linewidth of the resonances depends only on the axial ligand with the NH_3 complexes displaying the sharpest signals. The linewidth of quadrupolar nuclei depends on the nuclear quadrupole coupling constant, the asymmetry of the electric field gradient, and on the rotational correlation time of the complex.⁴³ Because the complexes are all roughly the same size, their rotational correlation time should be similar, and the difference in linewidth observed for the ammonia complex most likely arises from the smaller nuclear quadrupolar coupling constant and electric field gradient conferred by this ligand. The ammonia complexes give resonances that are shifted upfield by approximately 300 ppm relative to the corresponding benzylamine and imidazole complexes, signifying an increase in the shielding of the cobalt nucleus by ammonia.^{44,45} The chemical shifts of ^{59}Co nuclei correlate linearly with the lowest energy d–d transition corrected for the nephelauxetic ratio of the ligands.^{46,43} In this case, the downfield chemical shift of the ammonia complexes is consistent with the stronger field nature of ammonia relative to imidazole.⁶⁴ The weaker field nature of benzylamine relative to ammonia in this case may be a consequence of steric crowding of the metal center, as evidenced from the crystal structure, which minimizes metal-ligand orbital overlap and decreases the ligand field splitting energy.

The stability of the complexes in aqueous solution may be a key factor in their anticancer activity, and establishing trends in complex stability facilitates the design of

improved analogues. We find that the axial ligand plays a large role in the stability of the complex. Complexes with axial ammonia ligands are more stable in pH 7.4 PBS than those with imidazole or benzylamine (**Figure 2.5**). This trend also holds when the complexes are challenged with *N*-methylimidazole as a competing ligand (**Figure 2.6, Table 2.5**). We hypothesize that the decrease in stability of the imidazole and benzylamine complexes arises due to weaker ligand donor strength and unfavorable steric interactions, respectively. Octahedral cobalt(III) complexes undergo ligand substitution reactions primarily via interchange dissociative-type mechanisms, processes that are accelerated by such factors.⁶⁵ These results support the hypothesis that axial ligand identity is integral to complex stability, and the complexes are sufficiently labile to degrade even under normoxic conditions.

Cellular uptake of the complexes in both normoxic and hypoxic conditions was measured in A549 cells. These studies show a large dependence of the cellular uptake on the nature of the equatorial ligand (**Figure 2.7, Table 2.6**). Cellular uptake increases in the order GTS<PTS<ATS. In contrast, the axial ligand has only a minor influence on the overall cell uptake. This result is somewhat surprising, especially for complexes bearing the axial benzylamine ligand. This lipophilic ligand should facilitate uptake of the complex via passive diffusion. The lack of significant axial ligand dependence may indicate that the axial ligands dissociate before the complex enters the cell or may suggest that more complex uptake pathways are operative. The presence of O₂ also influenced the uptake in some cases, as ATS complexes showed mildly increased uptake under hypoxic conditions, while PTS and GTS complexes generally showed no selectivity or normoxic selectivity.

Cytotoxicity of the complexes in cancer cells, like uptake, is primarily dependent on the nature of the equatorial ligand (**Table 2.7**). GTS complexes are the most cytotoxic, and ATS complexes are essentially inactive. This trend follows that observed for the free ligands and for the corresponding copper(II) complexes, where GTS and PTS are the most cytotoxic and ATS is the least.^{40,66} The IC₅₀ values of the cobalt(III) complexes are at least a factor of 10 higher than those of the free ligand and copper complexes, indicating that coordination to this inert ion acts to attenuate the cytotoxicity of the ligand. With respect to cytotoxic activity, the importance of the axial ligand is less than that of the equatorial ligand. In general, the complexes bearing axial ammonia ligands are less active than the corresponding imidazole and benzylamine complexes. Because the axial ligands primarily affect the stabilities of the complexes, this trend suggests that there is an inverse dependence on complex stability and cytotoxicity. The cell uptake studies indicate that the ATS complexes are taken up much more effectively than those of PTS and GTS. This inverse relationship between cell uptake and cytotoxicity indicates that different factors are important for these properties. The more lipophilic nature of ATS compared to GTS may lead to its increased uptake. However, the lack of cytotoxicity of the ATS complexes is consistent with the lack of activity of the free ligand. This result suggests that the cytotoxicity of the cobalt(III) complexes is mediated by that of the free ligand itself; the greater cell uptake of the [Co(ATS)(L)₂]⁺ complexes cannot compensate for the lack of cytotoxic activity of the ATS ligand. As such, it is likely that the cobalt(III) complexes are acting as chaperones for the cytotoxic bis(thiosemicarbazones). Although the PTS complexes exhibit cytotoxic activity, they fail to kill 100% of the cells even at concentrations exceeding

100 μM . As such, the dose-response curves (**Figure 2.8**) level out at high concentrations. This leveling out effect has also been observed in the dose-response curves of related BTSC ligand and their corresponding copper complexes.⁶⁷ This behavior for cytotoxic compounds is previously described and is attributed to cell-to-cell variability and is often observed in compounds that inhibit the cell cycle at a specific phase.^{68,69}

With respect to hypoxic cytotoxicity, only moderate increases in activity—1.2 to 1.4-fold—are observed when the cells are incubated under conditions of hypoxia. The lack of significant increases in hypoxic cytotoxicity is consistent with the very negative reduction potentials of the cobalt(III) complexes that fall outside the window that is typically necessary for hypoxia targeting. Although not directly useful for therapeutic applications, the small increases in hypoxic activity suggest that further ligand tuning may give access to cobalt(III) BTSC complexes with suitable properties for hypoxia targeting. The observed lack of correlation between hypoxic uptake and reduction potential matches that observed for a class of cobalt(III)–cyclam complexes, which were proposed to be trapped intracellularly via ligand substitution rather than reduction.⁷⁰

The GTS complexes exhibit minimal cytotoxic effects in the non-cancerous lung fibroblast cell line MRC-5 (**Figure 2.9**). The result indicates that such complexes may possess a beneficial therapeutic index for the selective killing of cancer cells. This property is also shared by the free BTSC ligands and the corresponding copper(II) complexes. The fact that this selectivity for cancerous over non-cancerous cell lines is maintained in the cobalt(III) complexes further supports the hypothesis that these complexes are acting as chaperones for the active BTSC ligand. The free BTSC ligands

induce cytotoxicity by acting as copper(II) ionophores. These agents form copper(II) complexes which enter the cell and generate reactive-oxygen species, killing the cell.^{40,71} As such, treating cells with the copper-depleting agent TM protects them from BTSC-induced cytotoxicity. Treatment of A549 cells with 5 μ M TM also inhibited the cytotoxic activity of $[\text{Co}(\text{GTS})(\text{L})_2]^+$ complexes (**Figure 2.10**). The IC_{50} values increased by a factor of 10 in the presence of TM (**Table 2.8**). This result indicates that these cobalt(III) complexes operate via a similar mechanism of action as the free BTSC ligand, which involves copper(II) ions, and is consistent with the fact that the cytotoxic activity of the cobalt(III) complexes correlates directly with that of the free ligands.

Based on the physical properties, uptake, and cytotoxicity of the complexes, we propose a mechanism in which the cobalt complex acts as a prodrug that breaks down upon a combination of reduction and ligand substitution to yield the cytotoxic BTSC ligand. The more labile imidazole and benzylamine complexes undergo substitution, yielding complexes with more positive reduction potentials in line with the cyclic voltammetric studies. Reduction to cobalt(II) may favor transmetalation of the BTSC ligand with copper(II), forming a cytotoxic agent. Transmetalation of a zinc(II) thiosemicarbazone complex with copper(II) has been observed,⁷² and the ability of copper(II) to transmetalate a cobalt(II) complex is expected thermodynamically on the basis of the Irving-Williams series.⁷³ The more inert ammonia complexes are less cytotoxic, consistent with the proposed mechanism. These results indicate that compounds' toxicity may be modified directly by changing the (BTSC) ligand, or indirectly by modifying the axial ligand, thus affecting the rate of release.

Conclusion

Nine $[\text{Co}(\text{BTSC})(\text{L})_2]\text{NO}_3$ complexes have been synthesized and characterized. A detailed investigation of their physical and biochemical properties enabled us to determine structure-activity relationships for this class of compounds. We find that the overall stability of the complex is modulated by the nature of the axial ligand, whereas the redox potential is primarily dictated by the nature of the equatorial ligand. The cytotoxicity of the complexes depends largely on the equatorial (BTSC) ligand, with toxicity increasing in the order $\text{ATS} < \text{PTS} \approx \text{GTS}$, following the correlation expected for the free ligands and copper(II) complexes. The cellular uptake of these complexes, in contrast, follows the opposite trend where ATS complexes are taken up more efficiently than the corresponding PTS and GTS complexes. Poor hypoxia selectivity with respect to both cell uptake and cytotoxicity was observed, which we attribute to the highly negative redox potentials of the complexes. By using TM as a copper-depleting agent, we showed that the complexes kill cancer cells via a copper-dependent mechanism in a similar fashion as the free BTSC ligands. Collectively these results suggest a mechanism where cobalt complexes enter the cell, engage in ligand substitution reactions that increase the redox potential, undergo reduction, and then transmetalate with copper(II) or release free cytotoxic BTSC ligands. Thus, structural modification of the axial ligands may be used to tune the kinetics of substitution of the prodrug complex. These results serve as a guide for the development of second generation anticancer cobalt-based prodrugs.

Experimental

Materials and Methods

$\text{Co}(\text{NO}_3)_2 \cdot 6\text{H}_2\text{O}$ was obtained from Strem Chemicals (Newburyport, MA). Imidazole (Im) and benzylamine (BnA) were obtained from Alfa Aesar and used as received. The bis(thiosemicarbazone) ligands diacetyl bis(thiosemicarbazone) (ATS), pyruvaldehyde bis(thiosemicarbazone) (PTS), and glyoxal bis(thiosemicarbazone) (GTS) were synthesized as previously described.³¹ Solvents were of ACS grade or higher. CHAPS (3-[(3-cholamidopropyl)dimethylammonio]-1-propanesulfonate) lysis buffer was prepared using 1% CHAPS by mass, 5 mM ethylenediamine tetraacetic acid (EDTA), 50 mM tris(hydroxymethyl)aminomethane (Tris), and 110 mM NaCl; the pH was adjusted to 7.4 using dilute HCl or NaOH as necessary. All reactions were carried out under ambient atmospheric conditions without any efforts to exclude oxygen or water.

Physical Measurements

NMR samples were prepared with DMSO- d_6 as the solvent. Spectra were acquired on a 500 MHz Bruker AV 3HD spectrometer equipped with a broadband Prodigy cryoprobe. ^1H and $^{13}\text{C}\{^1\text{H}\}$ NMR spectra were referenced to the residual solvent peak of DMSO at 2.50 and 39.52 ppm, respectively.⁷⁴ ^{59}Co NMR spectra were referenced to $\text{K}_3[\text{Co}(\text{CN})_6]$ in D_2O at 0 ppm.⁴⁶ UV-Vis spectra were acquired using an Agilent Cary 8454 UV-Visible spectrophotometer. IR spectra were acquired on a Bruker Hyperion ATIR with ZnSe ATR attachment for solid powders. Graphite furnace atomic absorption spectroscopy (GFAAS) measurements were performed with a PerkinElmer PinAAcle 900z instrument. Electrochemical measurements were

carried out using a Pine WaveNow potentiostat with a three-electrode setup consisting of a glassy carbon working electrode, a platinum counter electrode, and Ag wire quasi-reference electrode. Complexes were dissolved in anhydrous DMF with 0.10 M (Bu₄N)(PF₆) (TBAP) as the supporting electrolyte. Potentials were referenced using an internal standard of the ferrocene/ferricenium couple at 0.45 V vs the saturated calomel electrode (SCE).^{63,75} The sample cell was deoxygenated by bubbling nitrogen gas through the solution prior to analysis, and maintained under a blanket of nitrogen during the experiment. Analytical high-performance liquid chromatography (HPLC) was performed using a Shimadzu LC20-AT HPLC with an Ultra Aqueous C18 column, 100 Å, 5 µm, 250 mm x 4.6 mm (Restek, Bellefonte, PA) and an SPD-20AV UV/Vis detector monitoring at 220 and 260 nm. The flow rate for all HPLC analyses was 1 mL/min. Gradient elution was carried out as follows: 10% MeOH in water containing 0.1% TFA for 5 min, followed by linear gradient to 100% MeOH containing 0.1% TFA over 20 min. High-resolution mass spectra (HRMS) were recorded on an Exactive Orbitrap mass spectrometer in positive ESI mode (ThermoFisher Scientific, Waltham, MA). Elemental analyses (CHN) were performed by Atlantic Microlab Inc., Norcross, GA, USA.

[CoATS(NH₃)₂]NO₃

ATS (0.30 g, 1.5 mmol) was suspended in MeOH (10 mL) and added to a solution of CoNO₃·6H₂O (0.43 g, 1.5 mL) in MeOH (10 mL), resulting in an immediate color change to dark green. The mixture was heated under reflux for 3 h, and 30% aqueous NH₄OH (3 mL) was added. The mixture was left stirring at room temperature

for 16 h. The resulting bright red solid was isolated via vacuum filtration and washed with MeOH and Et₂O. Yield 0.41 g (71%). ¹H NMR (DMSO-*d*₆, 500 MHz): δ 7.60 (s, 4H), 2.35 (s, 6H), 2.12 (s, 6H). ¹³C{¹H}NMR (DMSO-*d*₆, 125 MHz): δ 179.9, 155.4, 15.9. IR (ATR, cm⁻¹): 3486 w, 3360 w, 3281 w, 3136 m, 2949 w, 2945 w, 2850 w, 1753 w, 1622 m, 1591 m, 1568 m, 1545 m, 1514 w, 1477 m, 1425 s, 1350 s, 1323 s, 1256 m, 1229 s, 1171 s, 1125 s, 1101 s, 1063 s, 998 w, 935 m, 918 m, 845 m, 825 s, 746 s, 708 s, 665 s, 655 s, 615 s. HR-ESI-MS (positive ion mode): *m/z* 323.0269 ([M]⁺, calcd. 323.0271). Anal. Calcd. for [Co(ATS)(NH₃)₂](NO₃) (C₆H₁₆CoN₉O₃S₂): C, 18.70; H, 4.19; N, 32.72. Found: C, 18.99; H, 4.07; N, 32.45.

[CoATS(Im)₂](NO₃)

ATS (0.31 g, 1.5 mmol) was suspended in MeOH (10 mL) and added to a solution of CoNO₃·6H₂O (0.42 g, 1.4 mmol) in MeOH (10 mL), resulting in an immediate color change to dark green. The mixture was heated under reflux for 2 h, and imidazole (1.00 g, 14.7 mmol) was added. After stirring at room temperature for 16 h, the resulting solution was concentrated to dryness under vacuum, and the remaining red residue was dissolved in approximately 2 mL of MeOH. The solution was cooled in an ice bath for 15 min, resulting in the precipitation of a bright red solid, which was collected by filtration and washed with Et₂O. Yield 0.41 g (58%). ¹H NMR (DMSO-*d*₆, 500 MHz): δ 12.67 (br s, *N*-H), 7.69 (m, 6H), 7.14 (s, 2H), 6.75 (s, 2H), 2.46 (s, 6H). ¹³C{¹H}NMR (DMSO-*d*₆, 125 MHz): δ 181.4, 155.5, 137.8, 127.6, 117.5, 16.0. IR (ATR, cm⁻¹): 3485 w, 3358 m, 3270 m, 3136 m, 3049 w, 2951 w, 2851 w, 2611 w, 2390 w, 1753 w, 1626 m, 1589 m, 1566 m, 1537 w, 1486 w, 1429 m, 1356 m, 1323 s, 1300

m, 1256 m, 1227 s, 1175 m, 1124 m, 1101 m, 1063 s, 999 w, 935 m, 916 m, 845 m, 826 m, 745 s, 665 s. HR-ESI-MS (positive ion mode): m/z 425.0490 ($[M]^+$, calcd. 425.0489). Anal. Calcd. for $[\text{CoATS}(\text{Im})_2]\text{NO}_3 \cdot \text{MeOH}$ ($\text{C}_{13}\text{H}_{22}\text{CoN}_{11}\text{O}_4\text{S}_2$): C, 30.06; H, 4.27; N, 29.66. Found: C, 30.04; H, 4.13; N, 29.59.

[CoATS(BnA)₂]NO₃

ATS (0.16 g, 0.69 mmol) and $\text{CoNO}_3 \cdot 6\text{H}_2\text{O}$ (0.20 g, 0.69 mmol) were suspended in 3 mL of MeOH. The resulting dark green solution was heated under reflux for 1 h, and benzylamine (0.50 mL, 4.7 mmol) was added. The mixture was allowed to stir at room temperature for 16 h. The resulting dark red solid was isolated via vacuum filtration and washed with MeOH and Et_2O . Yield: 0.23 g (57%). ^1H NMR ($\text{DMSO-}d_6$, 500 MHz): δ 7.81 (s, 4H), 7.27 (m, 6H), 7.20 (m, 4H), 3.08 (s, 8H), 2.27 (s, 6H). $^{13}\text{C}\{^1\text{H}\}$ NMR ($\text{DMSO-}d_6$, 125 MHz): δ 180.3, 157.1, 138.3, 128.3 (2C overlapping), 127.4, 46.5, 16.2. IR (ATR, cm^{-1}): 3279 w, 3107 w, 1651 w, 1616 w, 1582 w, 1553 w, 1526 w, 1483 w, 1442 s, 1386 w, 1356 m, 1323 s, 1306 s, 1221 s, 1171 m, 1134 m, 1072 m, 1003 w, 972 s, 928 m, 846 m, 827 m, 758 s, 750 s, 706 m 694 s, 660 s, 619 s. HR-ESI-MS (positive ion mode): m/z 503.1204 ($[M]^+$, calcd. 503.1210). Anal. Calcd. for $[\text{CoATS}(\text{BnA})_2]\text{NO}_3 \cdot \text{H}_2\text{O}$ ($\text{C}_{20}\text{H}_{30}\text{CoN}_9\text{O}_4\text{S}_2$): C, 41.16; H, 5.18; N, 21.60. Found: C, 41.31; H, 5.09; N, 21.83.

[CoPTS(NH₃)₂]NO₃

PTS (0.21 g, 0.96 mmol) was added as a suspension in MeOH (7 mL) to a red solution of $\text{CoNO}_3 \cdot 6\text{H}_2\text{O}$ (0.27 g, 0.92 mmol) in MeOH (7 mL), which immediately resulted in a dark green mixture. The mixture was heated under reflux for 1 h. An

aqueous solution comprising 30% NH_4OH (2 mL) was added, and the mixture was stirred at room temperature for 16 h. The resulting dark red solid was isolated via vacuum filtration and washed with MeOH and Et_2O . Yield 0.25 g (73%). ^1H NMR ($\text{DMSO-}d_6$, 500 MHz): δ 7.80 (s, 2H), 7.65 (s, 1H), 7.63 (s, 2H), 2.32 (s, 3H), 2.22 (s, 6H). $^{13}\text{C}\{^1\text{H}\}$ NMR ($\text{DMSO-}d_6$, 125 MHz): δ 182.3, 180.0, 154.6, 146.9, 15.7. IR (ATR, cm^{-1}): 3464 w, 3399 w, 3321 w, 3279 w, 3165 w, 3124 w, 1616 m, 1595 m, 1574 m, 1522 m, 1476 m, 1416 s, 1375 m, 1314 s, 1280 s, 1244 m, 1192 s, 1163 s, 1052 m, 932 w, 870 m, 824 w, 752 m, 700 s, 652 m. HR-ESI-MS (positive ion mode): m/z 309.0110 ($[\text{M}]^+$, calcd. 309.0115). Anal. Calcd. for $[\text{CoPTS}(\text{NH}_3)_2]\text{NO}_3$ ($\text{C}_5\text{H}_{14}\text{CoN}_9\text{O}_3\text{S}_2$): C, 16.18; H, 3.80; N, 33.95. Found: C, 16.44; H, 3.65; N, 33.91.

[CoPTS(Im)₂]₂NO₃

PTS (0.20 g, 0.92 mmol) was suspended in MeOH (4 mL) and added to a solution of $\text{CoNO}_3 \cdot 6\text{H}_2\text{O}$ (0.27 g, 0.92 mmol) in MeOH (4 mL), which immediately resulted in a dark green mixture. The mixture was heated under reflux for 1 h. Imidazole (0.63 g, 9.16 mmol) was added, and the mixture was stirred at room temperature for 16 h. The resulting dark red solid was isolated via vacuum filtration and washed with MeOH and Et_2O . Yield 0.27 g (60%). ^1H NMR ($\text{DMSO-}d_6$, 500 MHz): δ 12.72 (br s, N-H), 7.90 (s, 2H), 7.80 (s, 1H), 7.77 (br s, 2H), 7.74 (s, 2H), 7.17 (s, 2H), 6.82 (s, 2H), 2.40 (s, 3H). $^{13}\text{C}\{^1\text{H}\}$ NMR ($\text{DMSO-}d_6$, 125 MHz): δ 183.3, 181.5, 154.7, 147.2, 138.0, 127.8, 117.8, 15.8. IR (ATR cm^{-1}): 3305 m, 3192 m, 3138 m, 3080 m, 2963 m, 1630 m, 1570 m, 1548 w, 1508 w, 1425 s, 1377 w, 1344 w, 1306 s, 1260 w, 1242 w, 1165 s, 1109 w, 1097 w, 1066 s, 1029 w, 1014 w, 926 s, 862 m, 825 m, 762 m, 735 s, 719 s,

687 m, 654 s, 606 s. HR-ESI-MS (positive ion mode): m/z 411.0334 ($[M]^+$, calcd. 411.0333). Anal. Calcd. for $[\text{CoPTS}(\text{Im})_2]\text{NO}_3 \cdot 1.1\text{H}_2\text{O}$ ($\text{C}_{11}\text{H}_{18.2}\text{CoN}_{11}\text{O}_{4.1}\text{S}_2$): C, 26.79; H, 3.72; N, 31.24. Found: C, 27.27; H, 3.81; N, 30.82.

[CoPTS(BnA)₂]₂NO₃

PTS (0.15 g, 0.69 mmol) and $\text{CoNO}_3 \cdot 6\text{H}_2\text{O}$ (0.20 g, 0.69 mmol) were suspended in 1 mL of MeOH. The mixture was heated under reflux for 1 h to yield a dark green solution. Benzylamine (0.15 mL, 1.4 mmol) was added, and the mixture was stirred at room temperature for 16 h. The resulting dark red solid was isolated via vacuum filtration and washed with MeOH and Et_2O . Yield 0.22 g (54%). ^1H NMR ($\text{DMSO}-d_6$, 500 MHz): δ 7.99 (s, 2H), 7.83 (s, 2H), 7.67 (s, 1H), 7.21–7.38 (m, 10H), 3.13–3.22 (m, 8H), 2.31 (s, 3H). $^{13}\text{C}\{^1\text{H}\}$ NMR ($\text{DMSO}-d_6$, 125 MHz): δ 182.3, 180.0, 156.0, 148.0, 138.2, 128.5, 128.20, 127.5, 46.4, 15.8. IR (ATR, cm^{-1}): 3420 w, 3281 w, 3107 m, 2945 w, 1622 m, 1574 m, 1439 s, 1312 s, 1244 w, 1159 s, 1070 w, 972 m, 928 m, 864 w, 827 w, 758 s, 698 s. HR-ESI-MS (positive ion mode): m/z 489.1051 ($[M]^+$, calcd. 489.1054). Anal. Calcd. for $[\text{CoPTS}(\text{BnA})_2]\text{NO}_3 \cdot 2\text{H}_2\text{O}$ ($\text{C}_{19}\text{H}_{30}\text{CoN}_9\text{O}_5\text{S}_2$): C, 38.84; H, 5.15; N, 21.46. Found: C, 38.55; H, 5.11; N, 21.65.

[CoGTS(NH₃)₂]₂NO₃

GTS (0.1 g, 0.50 mmol) was suspended in MeOH (3 mL) and added to a solution of $\text{CoNO}_3 \cdot 6\text{H}_2\text{O}$ (0.15 g, 0.50 mmol) in MeOH (3 mL), which immediately resulted in a dark brown mixture. The mixture was refluxed for 1 h, and 30% aqueous NH_4OH (1.5 mL) was added. The mixture was left stirring at room temperature for 2 h. The resulting

dark purple solid was isolated via vacuum filtration and washed with MeOH and Et₂O. Yield: 0.12 g (64%). ¹H NMR (DMSO-*d*₆, 500 MHz): δ 7.82 (s, 4H), 7.56 (s, 2H), 2.28 (s, 6H). ¹³C{¹H} NMR (DMSO-*d*₆, 125 MHz): δ 182.0, 144.2. IR (ATR, cm⁻¹): 3420 w, 3292 w, 3111 m, 1649 m, 1614 m, 1555 w, 1520 w, 1425 s, 1331 s, 1296 s, 1259 m, 1209 s, 1194 s, 1065 m, 970 w, 854 m, 816 s, 708 s, 675 m. HR-ESI-MS (positive ion mode): *m/z* 294.9960 ([M]⁺, calcd. 294.9958). Anal. Calcd. for [CoGTS(NH₃)₂]NO₃·H₂O (C₄H₁₄CoN₉O₄S₂): C, 12.80, H, 3.76; N, 33.59. Found: C, 12.67; H, 3.70; N, 33.42.

[CoGTS(Im)₂]NO₃

GTS (0.25 g, 1.2 mmol) was suspended in MeOH (5 mL) and added to a solution of CoNO₃·6H₂O (0.36 g, 1.3 mmol) in MeOH (3 mL), which immediately resulted in a dark brown mixture. The mixture was heated under reflux for 1.5 h. Imidazole (1.18 g, 19 mmol) in a solution of 3 mL MeOH was added, resulting in a color change to purple. The mixture was left stirring at room temperature for 16 h. The resulting dark purple solid was isolated via vacuum filtration and washed with MeOH and Et₂O. Yield: 0.43 g (73%). ¹H NMR (DMSO-*d*₆, 300 MHz): δ 12.77 (s, 2H), 7.92 (s, 4H), 7.80 (s, 2H), 7.72 (s, 2H), 7.19 (s, 2H), 6.88 (s, 2H). ¹³C{¹H} NMR (DMSO-*d*₆, 125 MHz): δ 183.1, 144.8, 137.9, 127.8, 117.9. IR (ATR, cm⁻¹): 3283 w, 3152 w, 3122 w, 2941 w, 1624 m, 1548 w, 1510 w, 1423 s, 1328 m, 1309 m, 1258 m, 1184 s, 1101 m, 1070 s, 1020 m, 1006 m, 902 m, 847 m, 810 s, 756 s, 710 s, 656 s, 634 m. HR-ESI-MS (positive ion mode): *m/z* 397.0179 ([M]⁺, calcd. 397.0176). Anal. Calcd. for

[CoGTS(Im)₂]NO₃·0.75MeOH (C_{10.75}H₁₇CoN₁₁O_{3.75}S₂): C, 26.71; H, 3.55; N, 31.87.

Found: C, 26.79; H, 3.42; N, 32.29.

[CoGTS(BnA)₂]NO₃

GTS (0.28 g, 1.37 mmol) and CoNO₃·6H₂O (0.40 g, 1.37 mmol) were suspended in 4 mL of MeOH, which immediately resulted in formation of a dark brown solution. The mixture was heated under reflux for 2 h, and benzylamine (1.5 mL, 13.7 mmol) was added. The mixture was left stirring at room temperature for 16 h. The resulting dark red solid was collected by filtration and washed with MeOH and Et₂O. Yield: 0.41 g (56%). ¹H NMR (DMSO-*d*₆, 500 MHz): δ 7.99 (s, 4H), 7.67 (s, 2H), 7.26 (m, 10H), 3.32 (m, obscured by H₂O peak), 3.16 (m, 4H). ¹³C{¹H} NMR (DMSO-*d*₆ 125 MHz): δ 181.9, 145.4, 138.1, 128.6, 128.2, 127.5, 46.3. IR (ATR, cm⁻¹): 3389 w, 3310 w, 3284 w, 3144 m, 3065 w, 1643 m, 1628 m, 1587 w, 1551 w, 1522 w, 1495 w, 1435 s, 1410 s, 1393 s, 1310 s, 1192 s, 1052 m, 978 m, 922 m, 854 m, 812 s, 750 s, 698 s, 613 m. HR-ESI-MS (positive ion mode): *m/z* 475.0898 ([M]⁺, calcd. 475.0897). Anal. Calcd. for [CoGTS(BnA)₂]NO₃ (C₁₈H₂₈CoN₉O₅S₂): C, 40.22; H, 4.50; N, 23.45. Found: C, 40.44; H, 4.54; N, 23.64.

X-Ray Crystallography

Single crystals were grown via the vapor diffusion of diethyl ether into a solution of the complexes in DMF. Low-temperature (223 K) X-ray diffraction data for [Co(GTS)(Im)₂]NO₃·DMF, [Co(ATS)(Im)₂]NO₃, and [Co(GTS)(BnA)₂]NO₃·DMF were collected on a Bruker X8 Kappa diffractometer coupled to an ApexII CCD detector

with graphite-monochromated Mo K α radiation ($\lambda = 0.71073 \text{ \AA}$). The structures were solved through intrinsic phasing using SHELXT⁷⁶ and refined against F^2 on all data by full-matrix least squares with SHELXL⁷⁷ following established refinement strategies⁷⁸. All non-hydrogen atoms were refined anisotropically. Positions of hydrogen atoms bound to carbon atoms were geometrically calculated and refined using a riding model. Hydrogen atoms bound to nitrogen were located in the difference Fourier synthesis and subsequently refined semi-freely with the help of distance restraints. The isotropic displacement parameters of all hydrogen atoms were fixed to 1.2 times the U value of the atoms they are linked to (1.5 times for methyl groups). In the structure of [Co(GTS)(Im)₂]NO₃·DMF, the DMF molecule and nitrate counterion exhibited disorder about their respective locations in the crystal lattice. The two disordered components of the DMF molecules were refined with appropriate similarity restraints, allowing the occupancy of each component to refine freely with net occupancy of both components summing to one. The nitrate counterion was handled in the same manner. Likewise, in the structure of [Co(ATS)(Im)₂]NO₃, the nitrate counterion exhibited similar disorder that was refined as described above. One of the axial imidazole ligands in [Co(ATS)(Im)₂]NO₃ was rotationally disordered about the Co–N axis. The two disordered components were refined as described above. Details of the data quality and a summary of the residual values of all the refinements are listed in **Table 2.9**.

Table 2.9. X-ray Crystallographic Data Collection and Refinement Parameters

	[Co(GTS)(Im) ₂]NO ₃ ·DMF	[Co(ATS)(Im) ₂]NO ₃	[Co(GTS)(BnA) ₂]NO ₃ ·DMF
formula	C ₁₃ H ₂₁ CoN ₁₂ O ₄ S ₂	C ₁₂ H ₁₈ CoN ₁₁ O ₃ S ₂	C ₂₁ H ₃₁ CoN ₁₀ O ₄ S ₂
fw	532.47	487.42	610.61
space group	<i>P</i> 2 ₁ / <i>n</i>	<i>P</i> 2 ₁ / <i>n</i>	<i>P</i> 2 ₁ / <i>n</i>
<i>a</i> , Å	13.8070(7)	8.4179(8)	9.2715(5)
<i>b</i> , Å	11.2235(6)	9.3561(7)	11.2627(6)
<i>c</i> , Å	14.7344(7)	24.287(2)	26.5823(17)
β , deg	104.089(2)	90.303(6)	98.548(3)
<i>V</i> , Å ³	2214.6(2)	1912.8(3)	2744.9(3)
<i>Z</i>	4	4	4
ρ_{calcd} g·cm ⁻³	1.597	1.693	1.478
<i>T</i> , K	223(2)	223(2)	223(2)
μ (Mo <i>K</i> α), mm ⁻¹	1.012	1.158	0.825
θ range, deg	1.813 to 26.372	2.333 to 26.369	1.967 to 25.349
completeness to θ , %	100.0	100.0	100.0
total no. of data	21018	17792	23249
no. of unique data	4524	3913	5029
no. of param	434	284	369
no. of restraints	533	94	8
R1 ^a , %	4.25	6.21	7.77
wR2 ^b , %	9.97	13.33	13.70
GoF ^c	1.055	1.035	1.039
max, min peaks e·Å ⁻¹	0.840, -0.235	0.813, -0.623	0.735, -0.600

^a $R_1 = \sum ||F_o| - |F_c|| / \sum |F_o|$ for all data. ^b $wR_2 = \{\sum [w(F_o^2 - F_c^2)^2] / \sum [w(F_o^2)^2]\}^{1/2}$ for all data. ^c $GoF = \{\sum [w(F_o^2 - F_c^2)^2] / (n - p)\}^{1/2}$, where *n* is the number of data and *p* is the number of refined parameters.

Stability and *N*-methylimidazole Challenge Studies

[Co(BTSC)(L)₂]⁺ complexes were dissolved in pH 7.4 phosphate-buffer saline (PBS) to a final concentration of 1 mM in both the absence and presence of 5 mM *N*-methylimidazole as a competing ligand. Immediately after preparation, the solutions were analyzed via RP-HPLC. The solutions were then incubated at 37 °C for 24 h and

analyzed again using the same HPLC conditions. The stability was characterized by the peak area remaining of the starting complex.

Cell Lines and Culture Conditions

HeLa (human cervical cancer), A549 (human lung cancer), and MRC-5 (human lung fibroblast) cells were obtained from American Type Culture Collection (ATCC). All cell lines were cultured as adherent monolayers in an incubator at 37 °C with a humidified atmosphere of 5% CO₂. A549 and HeLa cell lines were maintained in Dulbecco's Modified Eagle's Medium (DMEM) supplemented with 10% fetal bovine serum (FBS). MRC-5 cells were cultured in Minimum Essential Media (MEM) containing 10% FBS. Cells were checked for mycoplasma contamination monthly using the Plasmotest™ mycoplasma detection kit from InvivoGen.

Cytotoxicity Assay

The colorimetric MTT assay was used to evaluate cytotoxicity.⁷⁹ Trypsinized cells were plated at 2000 cells/well in 100 µL/well in a 96-well plate and incubated for 24 h. The media was removed and replaced with 200 µL of growth media containing varying concentrations of the complexes, ranging from 0 to 500 µM. For hypoxia/normoxia comparative studies, two plates were simultaneously dosed with the complex of interest; one plate was incubated under normoxic conditions, and the other was incubated in a hypoxia chamber (Billips-Rothenburg, Inc., Del Mar, CA, USA), which was purged with an atmosphere of 95% N₂ and 5% CO₂. After 24 h, the culture medium containing the complex was removed, 200 µL of fresh media was added, and

both plates were allowed to incubate an additional 48 h under normoxic conditions. After this time, the media was removed again, and a solution of thiazolyl blue tetrazolium bromide (MTT) in DMEM (200 μ L, 1 mg/mL) was added to each well. Upon incubation for 4 h, the DMEM/MTT solutions were aspirated, and the purple formazan crystals were dissolved in 200 μ L of an 8:1 mixture of DMSO: pH 10 glycine buffer. The absorbance of each well at 570 nm was measured using a microplate reader. Absorbance values were normalized to the untreated wells and plotted as concentration of cobalt complex versus % viability. The resulting dose-response curves were analyzed using a logistic sigmoid function.⁶⁸ Reported IC₅₀ values represent the average of three independent experiments, each carried out with six replicates per concentration level. Stock solutions of the cobalt complexes were prepared fresh in 18.2 M Ω ·cm H₂O prior to serial dilution in the cell culture medium.

Uptake Experiments

Cellular uptake of cobalt was determined by implementing slight modifications to previously reported protocols.^{47,80} Trypsinized cells (2×10^6) were seeded in six 75 cm² culture dishes and incubated for 24 h. The media was removed, and the cells were treated with either 0 or 100 μ M cobalt complex and placed under normoxic or hypoxic conditions, as described above, for 24 h. Dishes containing no cells were also incubated with 100 μ M of the cobalt complex to correct for non-specific adsorption of cobalt to the plastic. Media was removed from all dishes, and the cells were rinsed with 3 mL PBS and detached with trypsin (3 mL). The cells were centrifuged at 1000 rpm for 10 min. The supernatant was discarded, and the pellet was resuspended in 1 mL PBS.

Samples were centrifuged and resuspended twice more using the same conditions to remove extracellular cobalt, and centrifuged a final time to pellet cells. The pellet was resuspended in ice-cold, ultrapure 1× CHAPS lysis buffer, and samples were gently agitated 30 min. The protein concentration in each sample was then determined using the Thermo Fisher Bicinchoninic Acid Protein Assay Kit according to the manufacturer's instructions. The cobalt concentration in each sample was determined using GFAAS. Results were reported as the mass ratio of cobalt to protein (pg/μg) in each sample.

Supporting Information

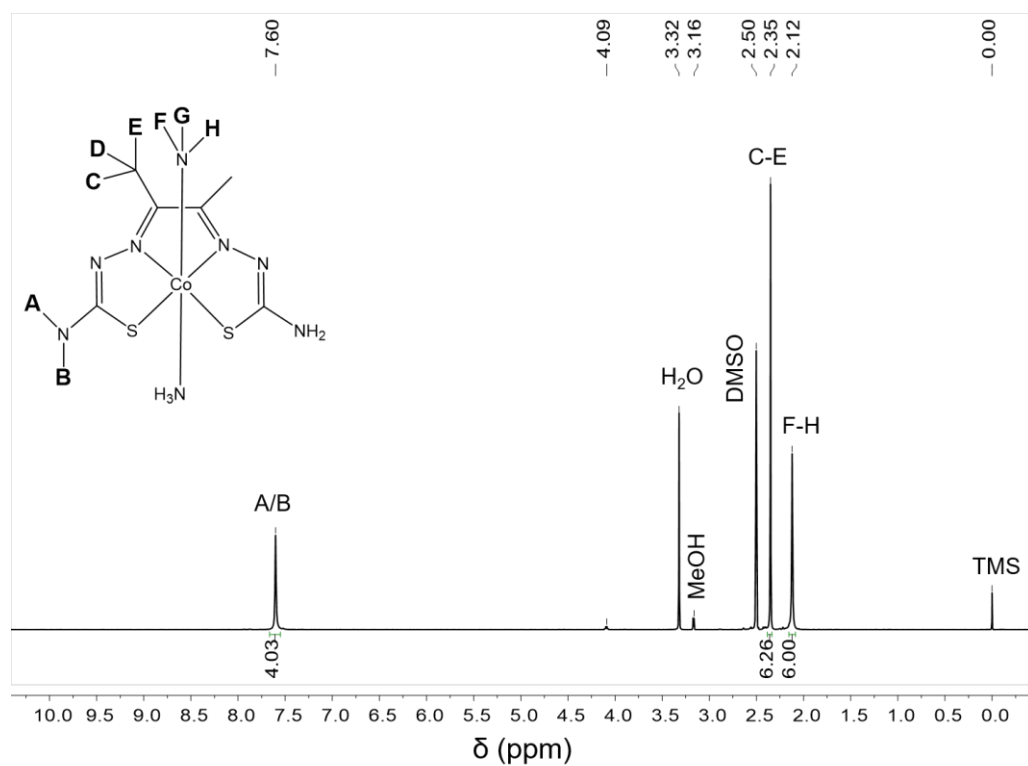


Figure S2.1. ^1H NMR spectrum of $[\text{Co}(\text{ATS})(\text{NH}_3)_2]^+$ (DMSO- d_6 , 500 MHz, 298 K)

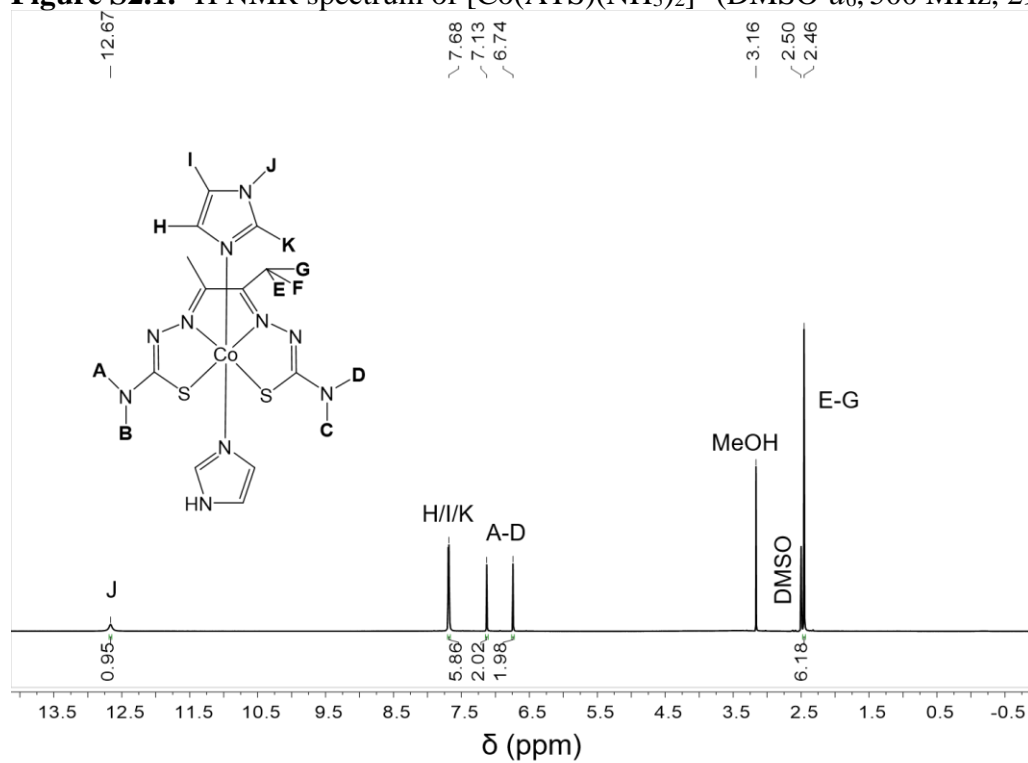


Figure S2.2. ^1H NMR spectrum of $[\text{Co}(\text{ATS})(\text{Im})_2]^+$ (DMSO- d_6 , 500 MHz, 298 K)

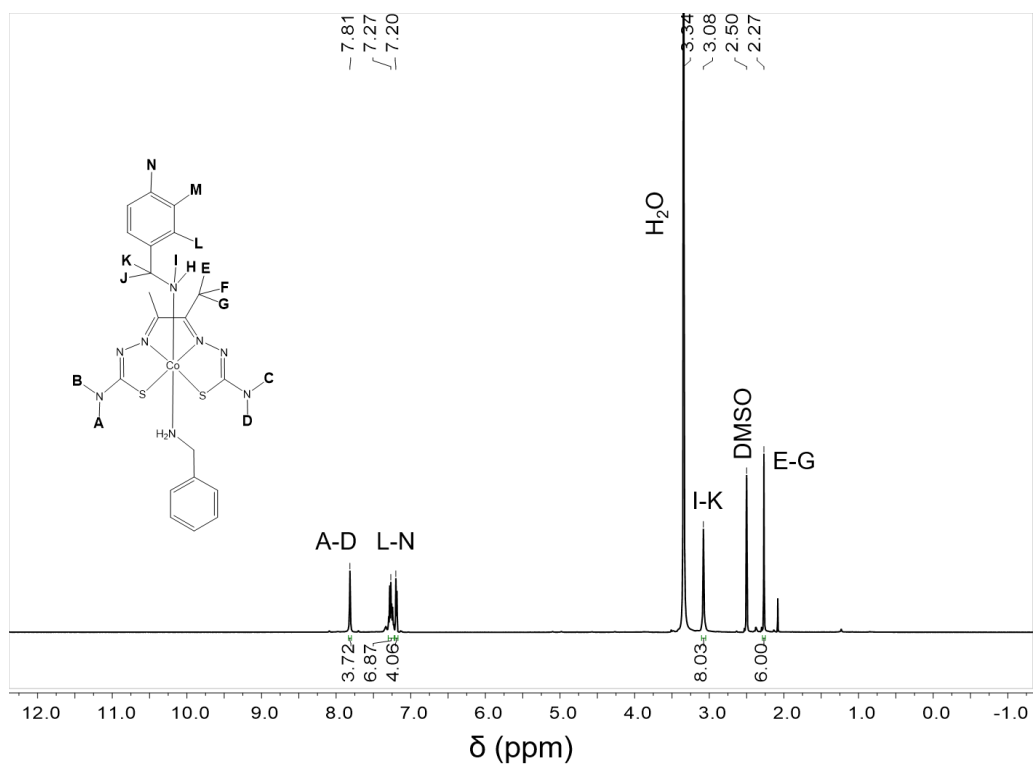


Figure S2.3. ^1H NMR spectrum of $[\text{Co}(\text{ATS})(\text{BnA})_2]^+$ (DMSO- d_6 500 MHz, 298 K)

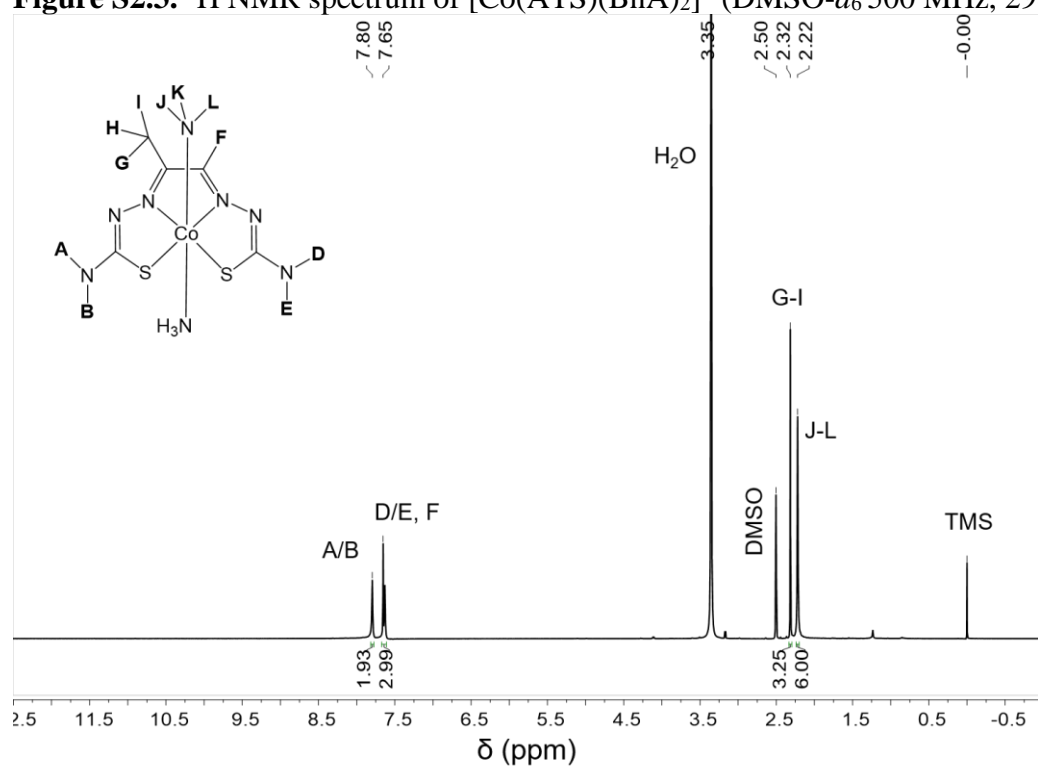


Figure S2.4. ^1H NMR spectrum of $[\text{Co}(\text{PTS})(\text{NH}_3)_2]^+$ (DMSO- d_6 500 MHz, 298 K)

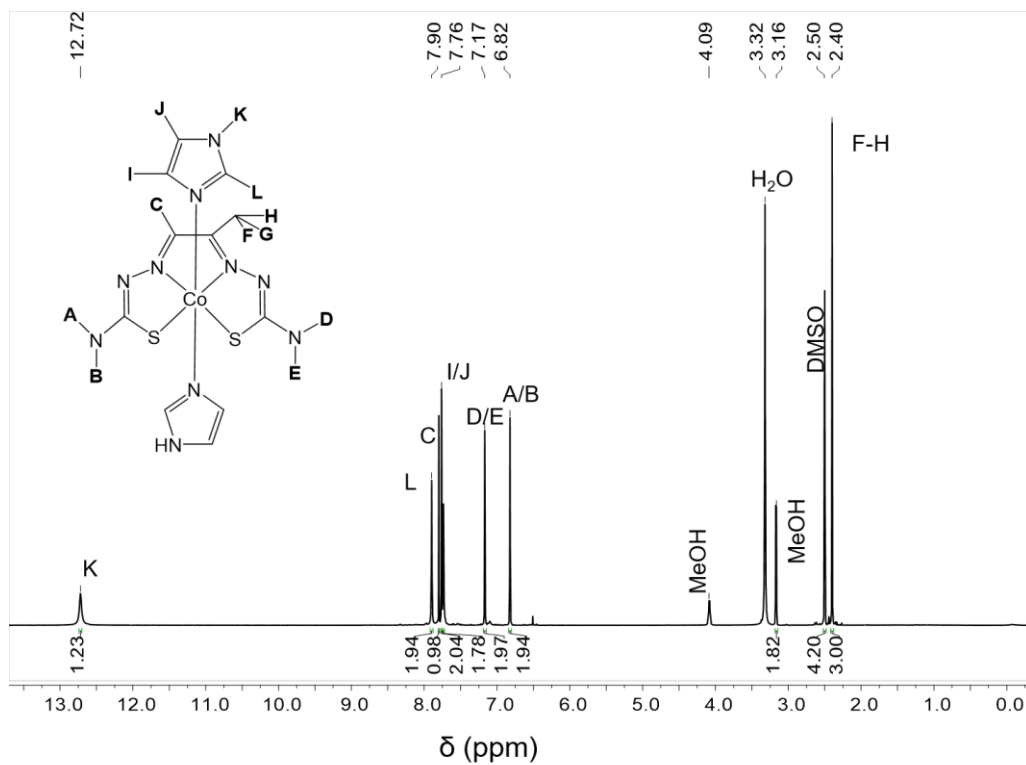


Figure S2.5. ^1H NMR spectrum of $[\text{Co}(\text{PTS})(\text{Im})_2]^+$ ($\text{DMSO-}d_6$ 500 MHz, 298 K)

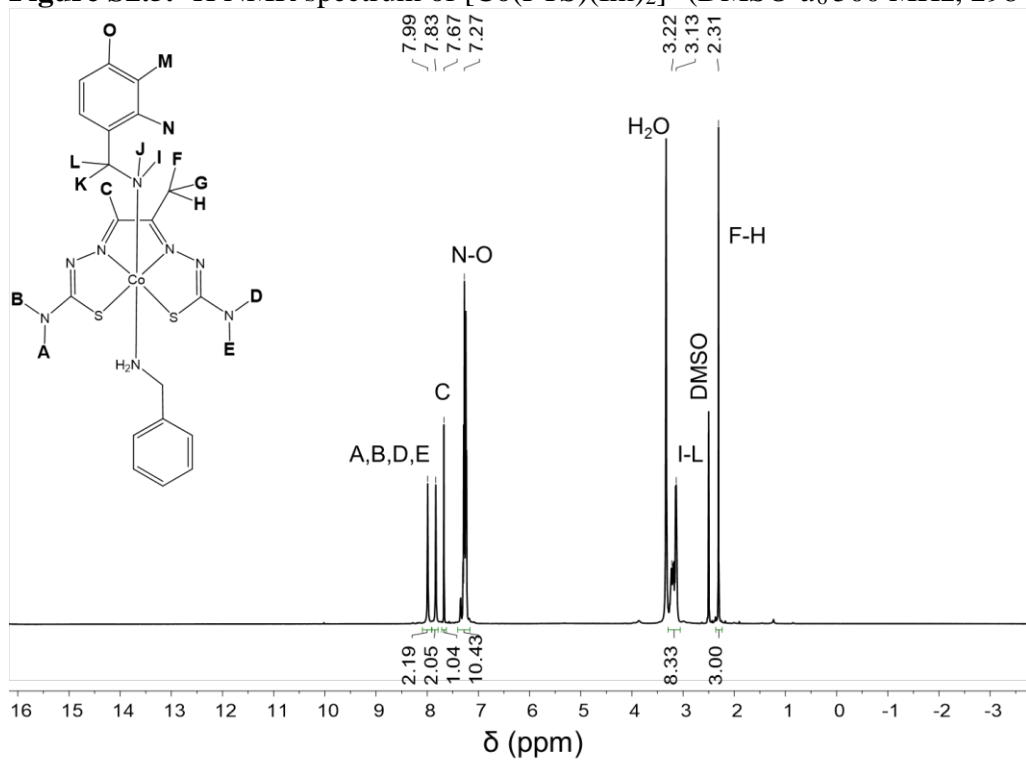


Figure S2.6. ^1H NMR spectrum of $[\text{Co}(\text{PTS})(\text{BnA})_2]^+$ ($\text{DMSO-}d_6$ 500 MHz, 298 K)

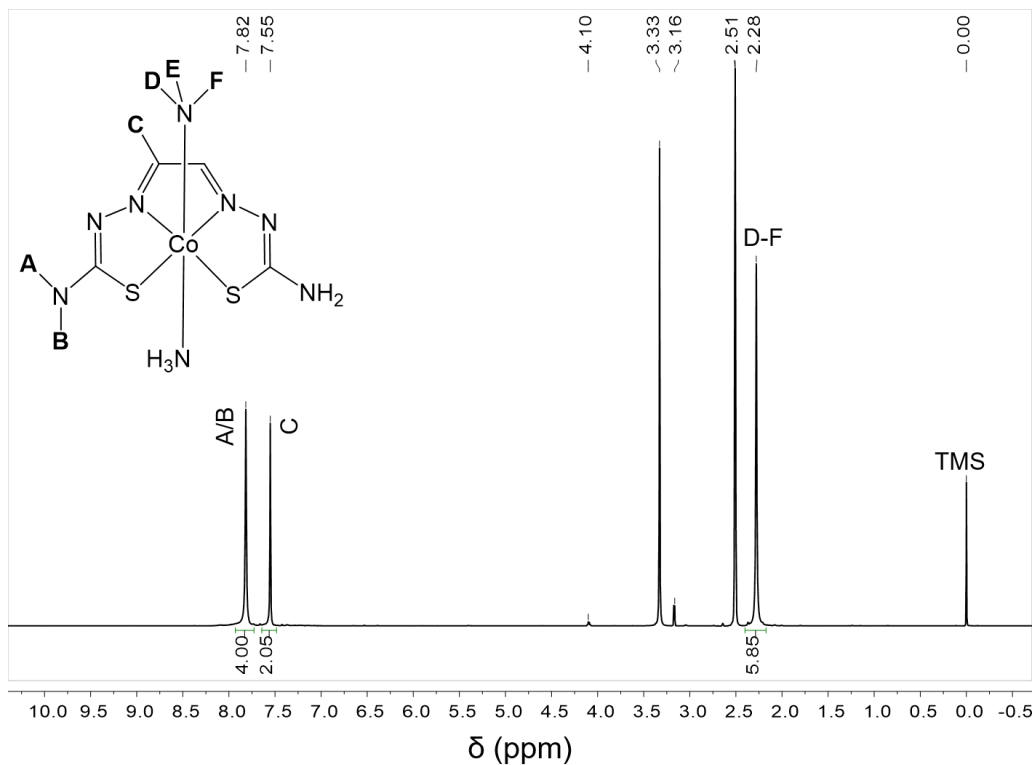


Figure S2.7. ^1H NMR spectrum of $[\text{Co}(\text{GTS})(\text{NH}_3)_2]^+$ ($\text{DMSO-}d_6$ 500 MHz, 298 K)

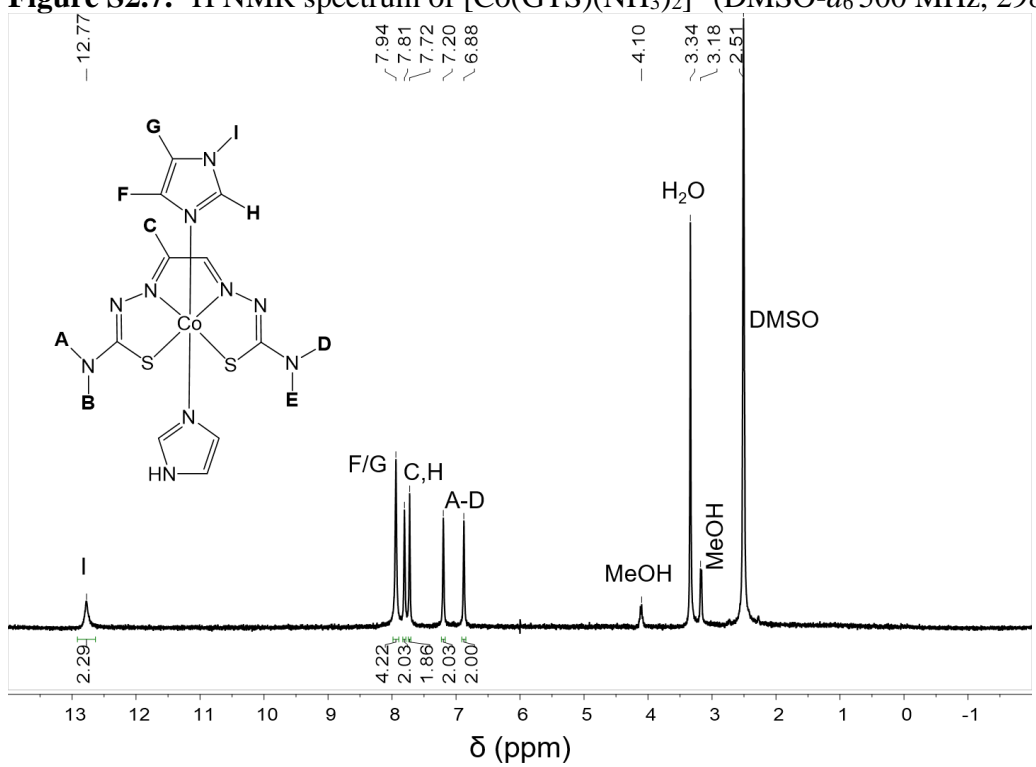


Figure S2.8. ^1H NMR spectrum of $[\text{Co}(\text{GTS})(\text{Im})_2]^+$ ($\text{DMSO-}d_6$ 500 MHz, 298 K)

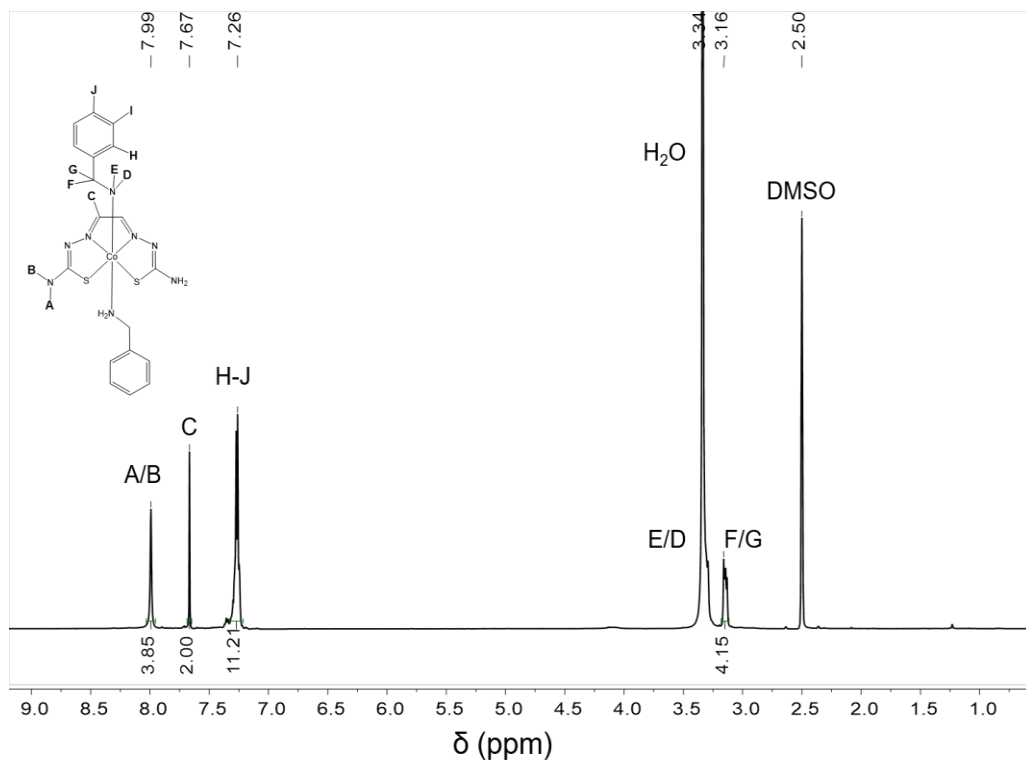


Figure S2.9. ^1H NMR spectrum of $[\text{Co}(\text{GTS})(\text{BnA})_2]^+$ ($\text{DMSO-}d_6$ 500 MHz, 298 K)

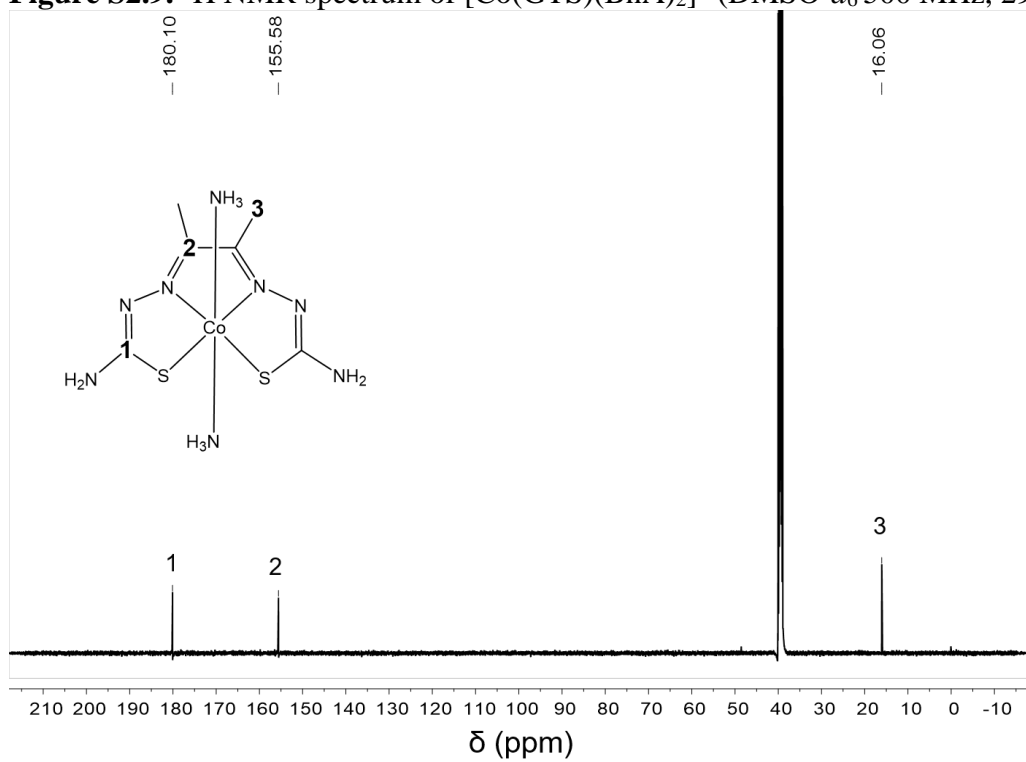


Figure S2.10. $^{13}\text{C}\{^1\text{H}\}$ NMR spectrum of $[\text{Co}(\text{ATS})(\text{NH}_3)_2]^+$ ($\text{DMSO-}d_6$, 125 MHz, 298 K)

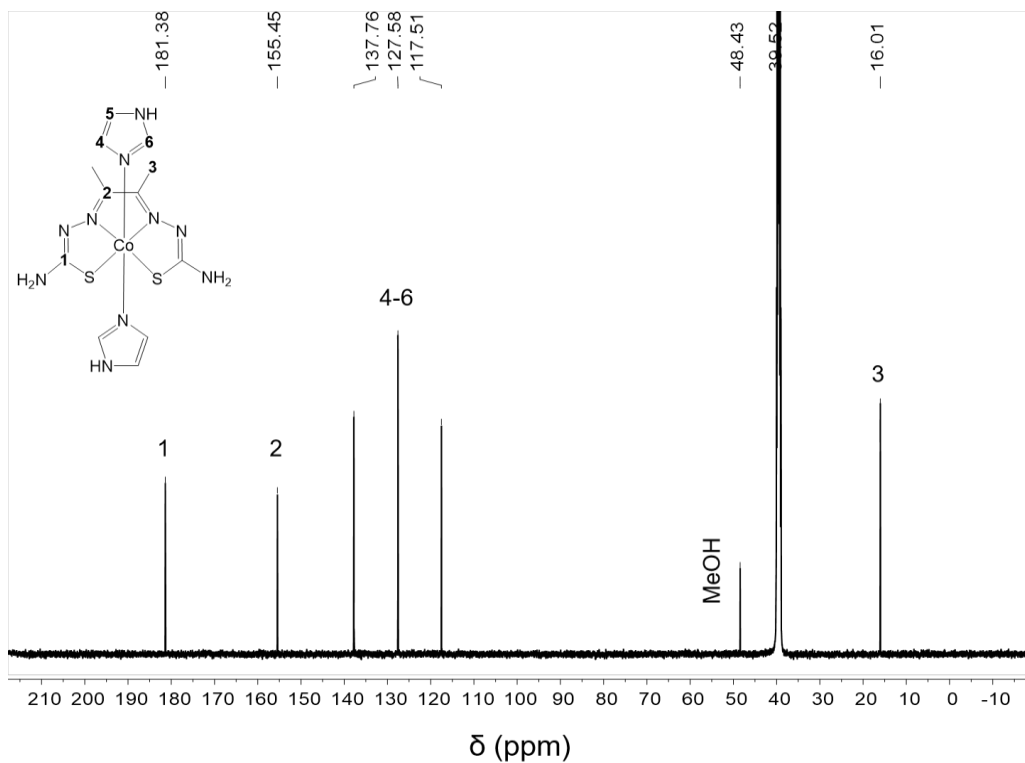


Figure S2.11. $^{13}\text{C}\{^1\text{H}\}$ NMR spectrum of $[\text{Co}(\text{ATS})(\text{Im})_2]^+$ (DMSO- d_6 125 MHz, 298 K)

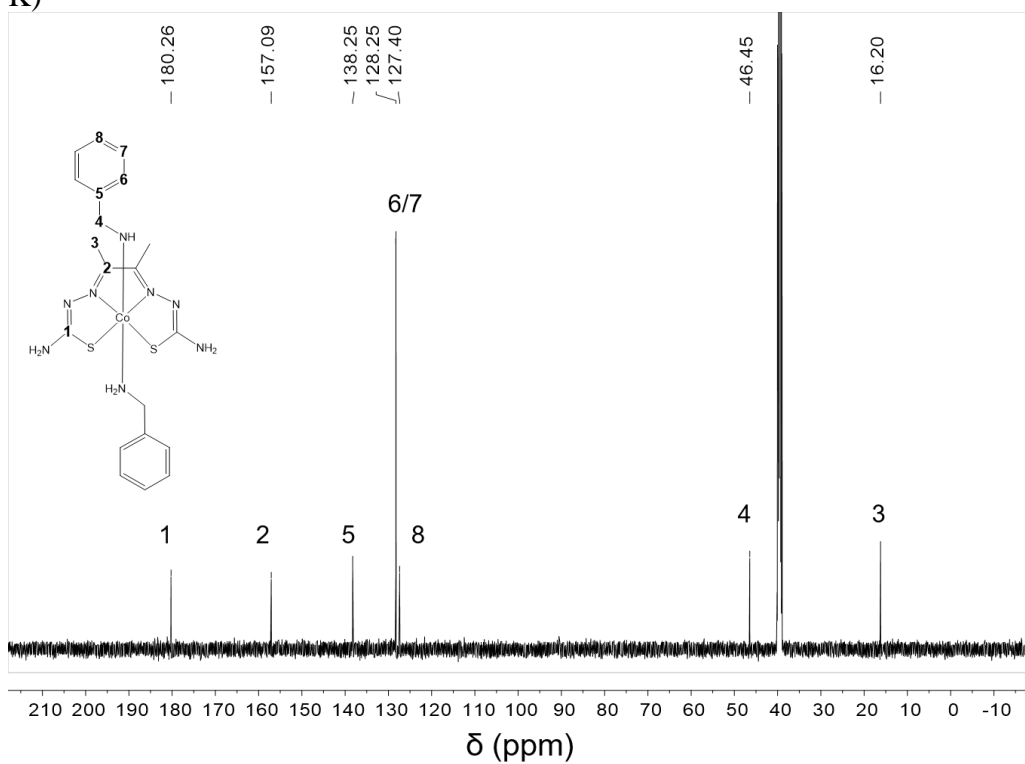


Figure S2.12. $^{13}\text{C}\{^1\text{H}\}$ NMR spectrum of $[\text{Co}(\text{ATS})(\text{BnA})_2]^+$ (DMSO- d_6 125 MHz, 298 K)

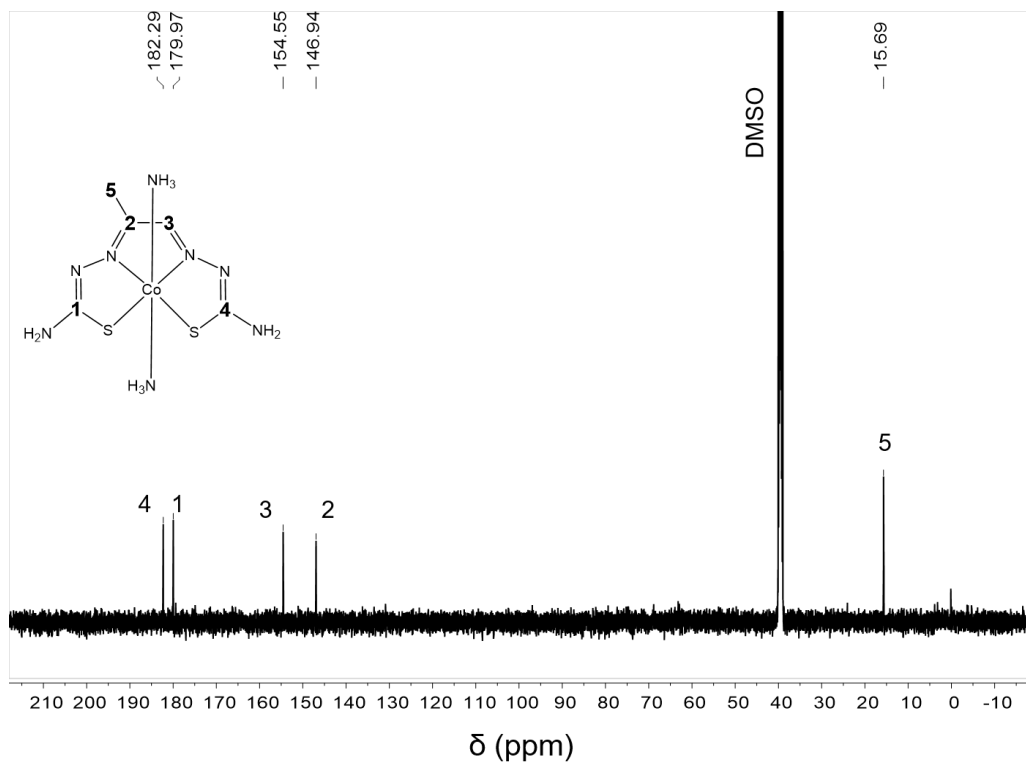


Figure S2.13. $^{13}\text{C}\{^1\text{H}\}$ NMR spectrum of $[\text{Co}(\text{PTS})(\text{NH}_3)_2]^+$ ($\text{DMSO-}d_6$ 125 MHz, 298 K)

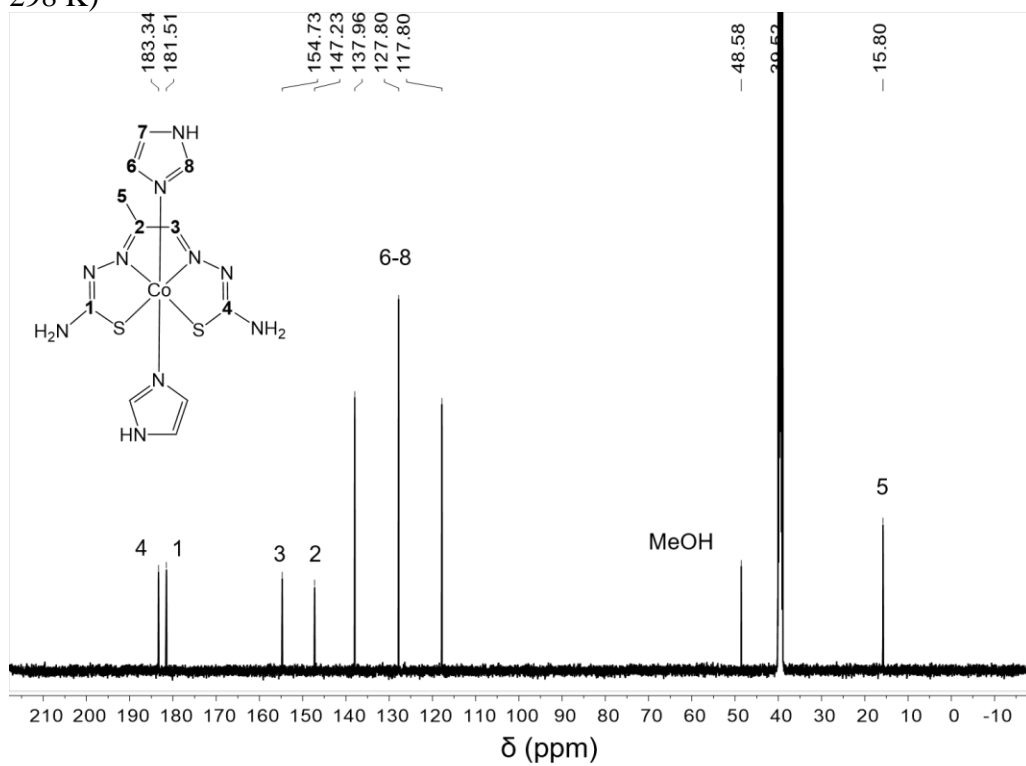
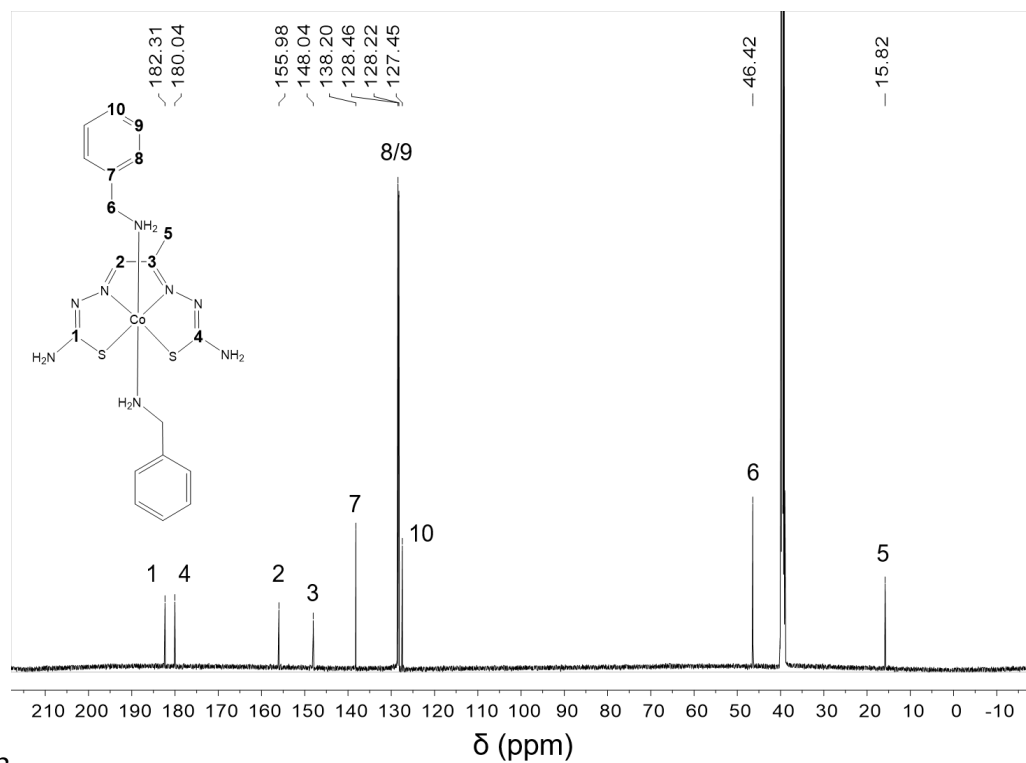


Figure S2.14. $^{13}\text{C}\{^1\text{H}\}$ NMR spectrum of $[\text{Co}(\text{PTS})(\text{Im})_2]^+$ ($\text{DMSO-}d_6$ 125 MHz, 298 K)



3
Figure S2.15. $^{13}\text{C}\{^1\text{H}\}$ NMR spectrum of $[\text{Co}(\text{PTS})(\text{BnA})_2]^+$ (DMSO- d_6 125 MHz, 298 K)

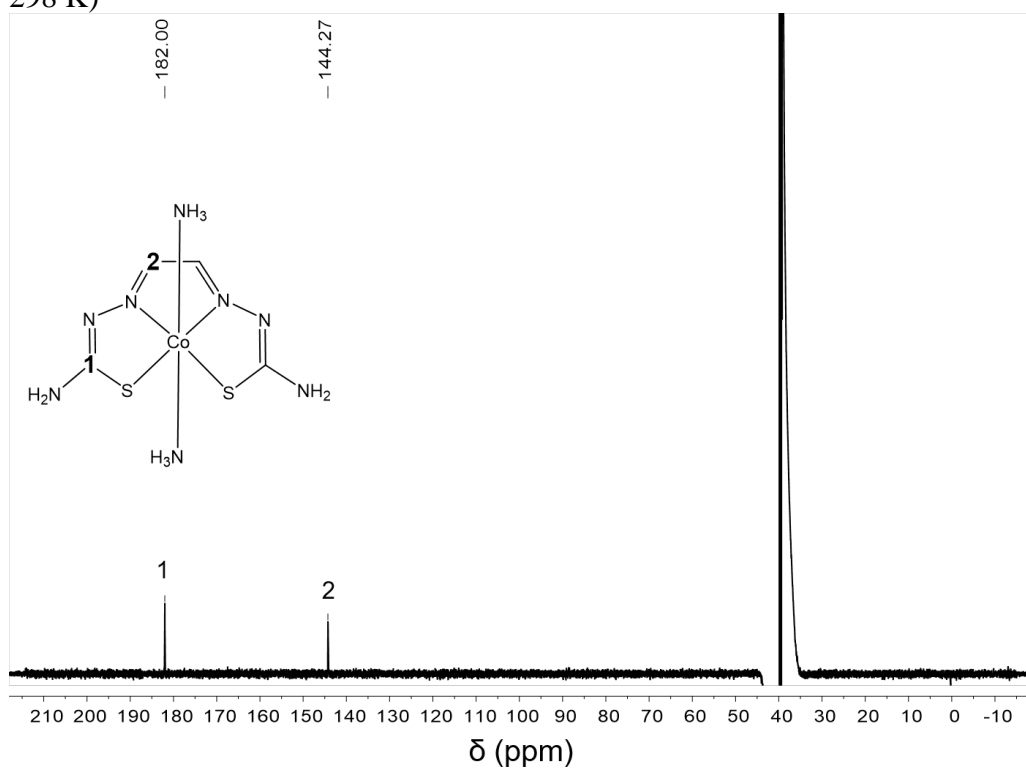


Figure S2.16. $^{13}\text{C}\{^1\text{H}\}$ NMR spectrum of $[\text{Co}(\text{GTS})(\text{NH}_3)_2]^+$ (DMSO- d_6 125 MHz,

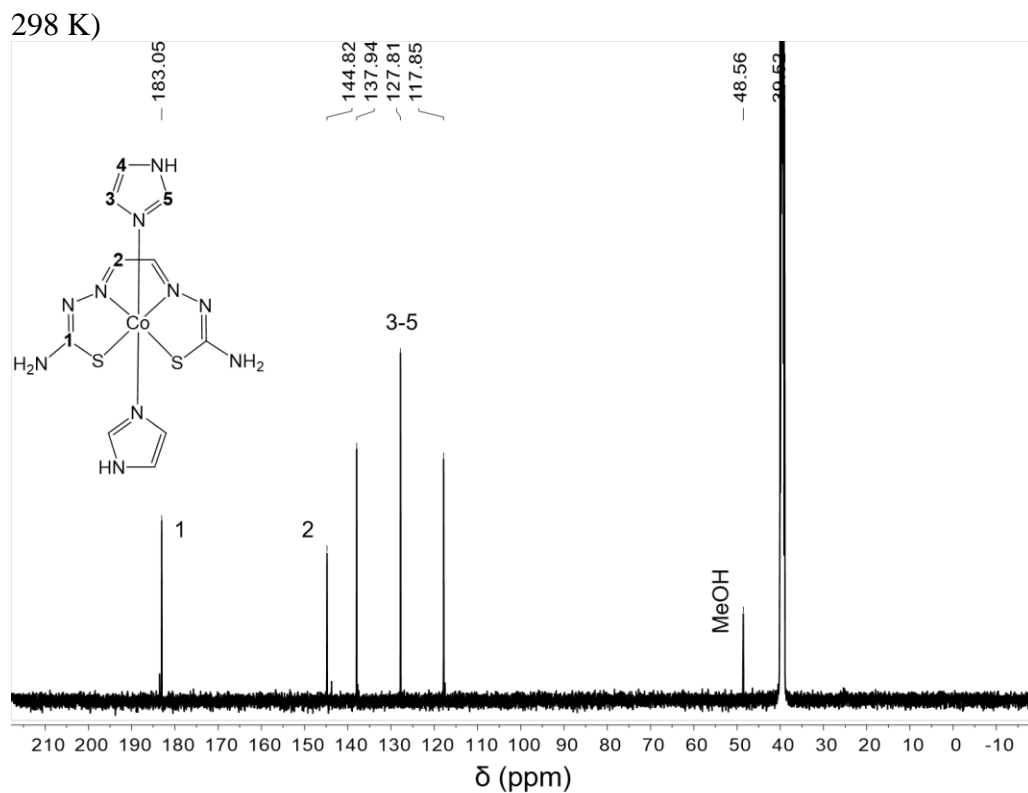


Figure S2.17. $^{13}\text{C}\{^1\text{H}\}$ NMR spectrum of $[\text{Co}(\text{GTS})(\text{Im})_2]^+$ (DMSO- d_6 125 MHz, 298 K)

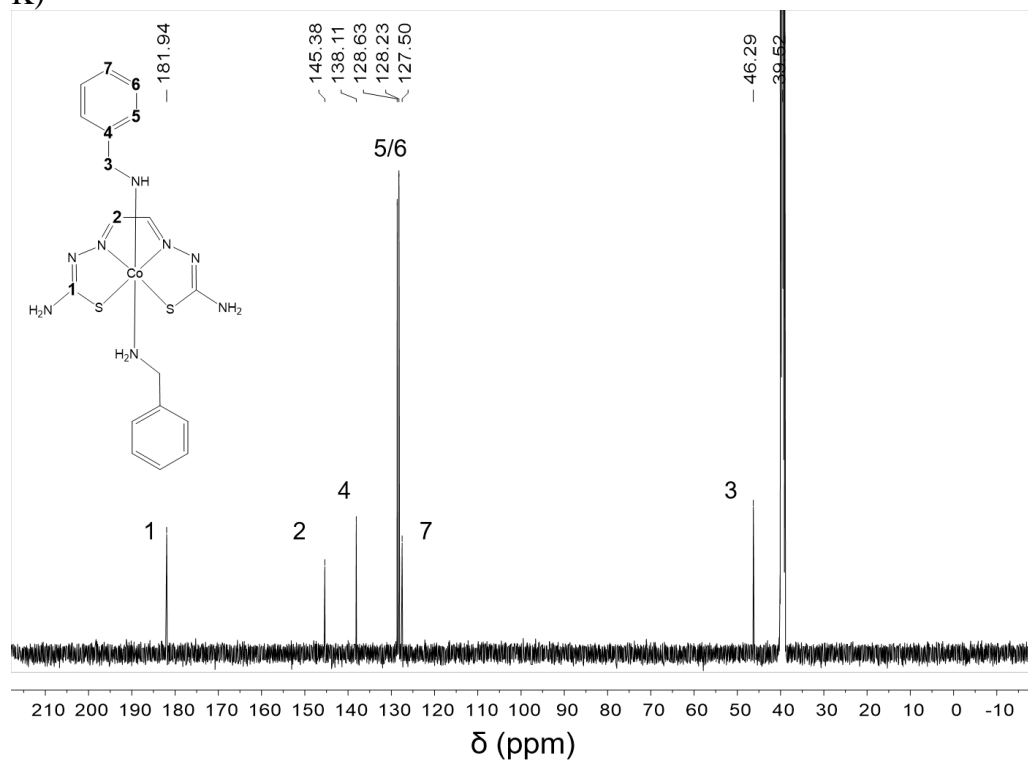


Figure S2.18. $^{13}\text{C}\{^1\text{H}\}$ NMR spectrum of $[\text{Co}(\text{GTS})(\text{BnA})_2]^+$ (DMSO- d_6 125 MHz,

298 K)

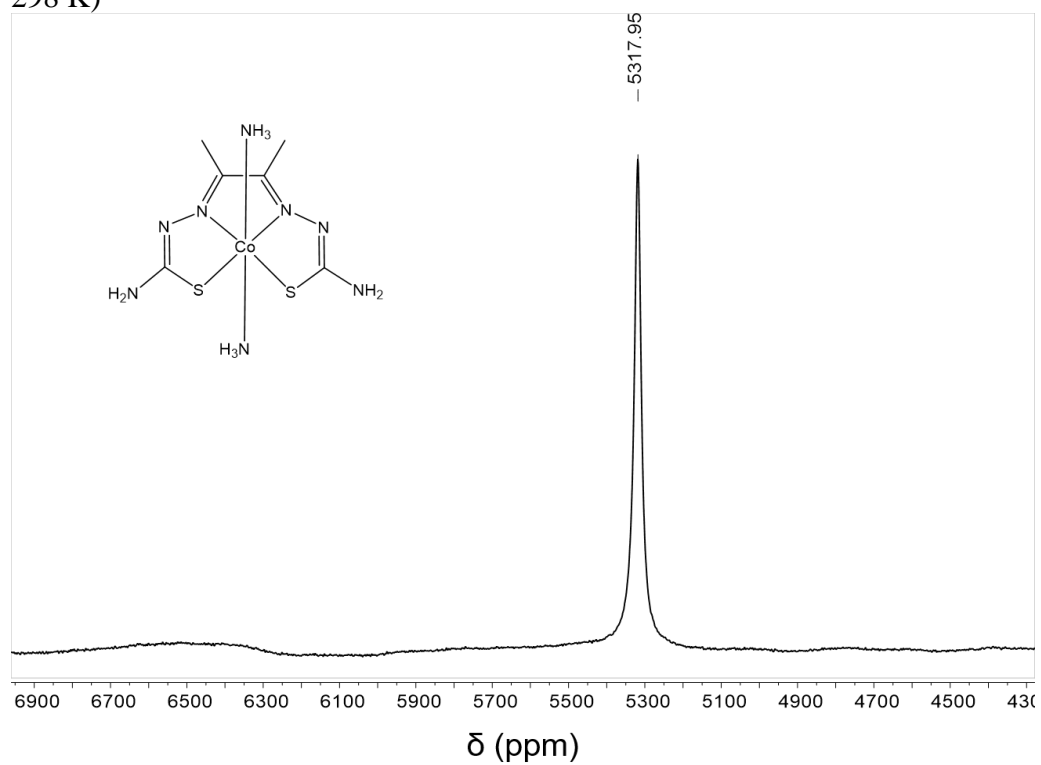


Figure S2.19. ^{59}Co NMR spectrum of $[\text{Co}(\text{ATS})(\text{NH}_3)_2]^+$ (DMSO- d_6 , 119 MHz, 298 K)

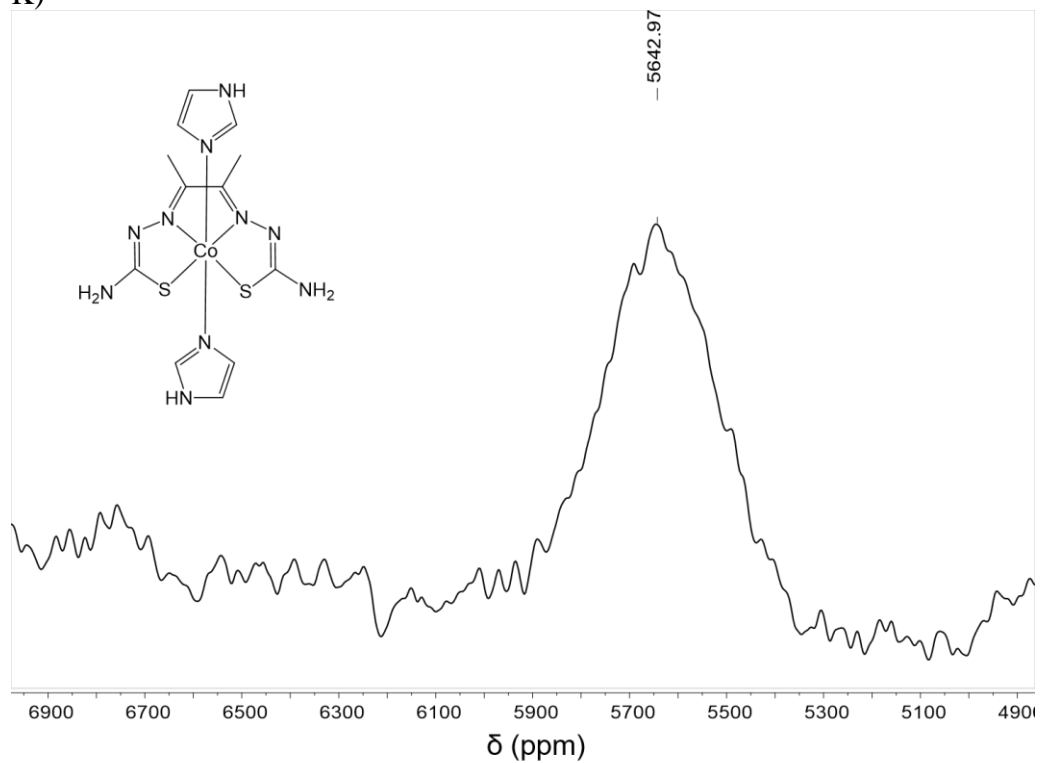


Figure S2.20. ^{59}Co NMR spectrum of $[\text{Co}(\text{ATS})(\text{Im})_2]^+$ (DMSO- d_6 , 119 MHz, 298 K)

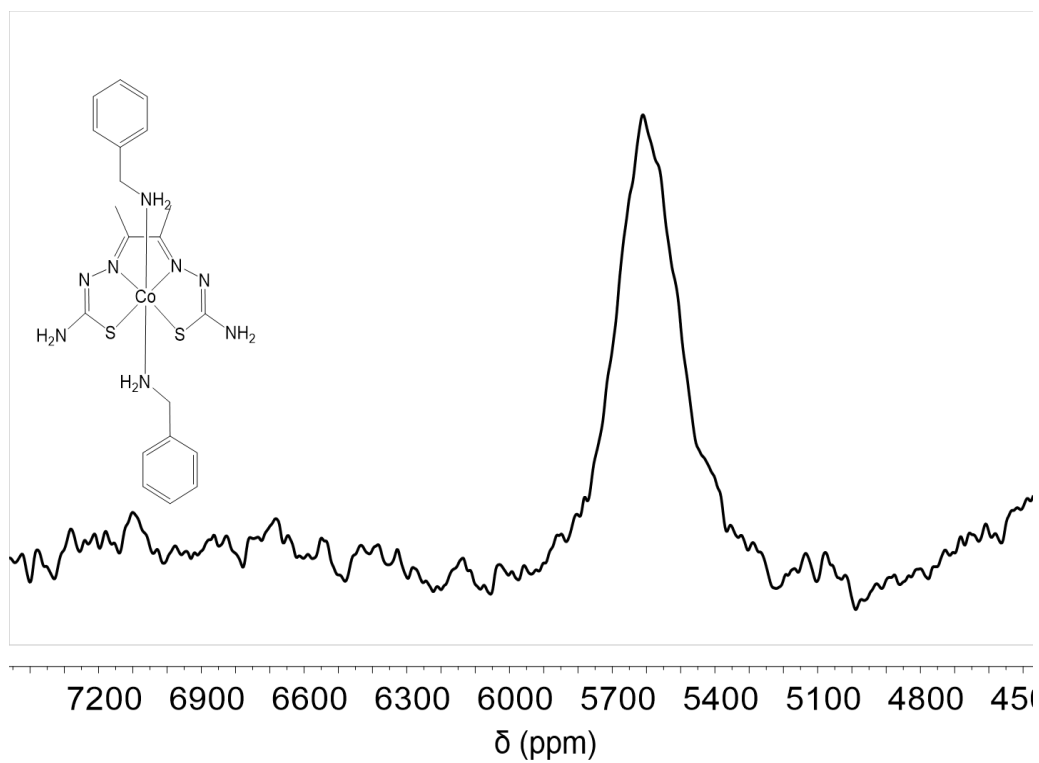


Figure S2.21. ^{59}Co NMR spectrum of $[\text{Co}(\text{ATS})(\text{BnA})_2]^+$ (DMSO- d_6 119 MHz, 298

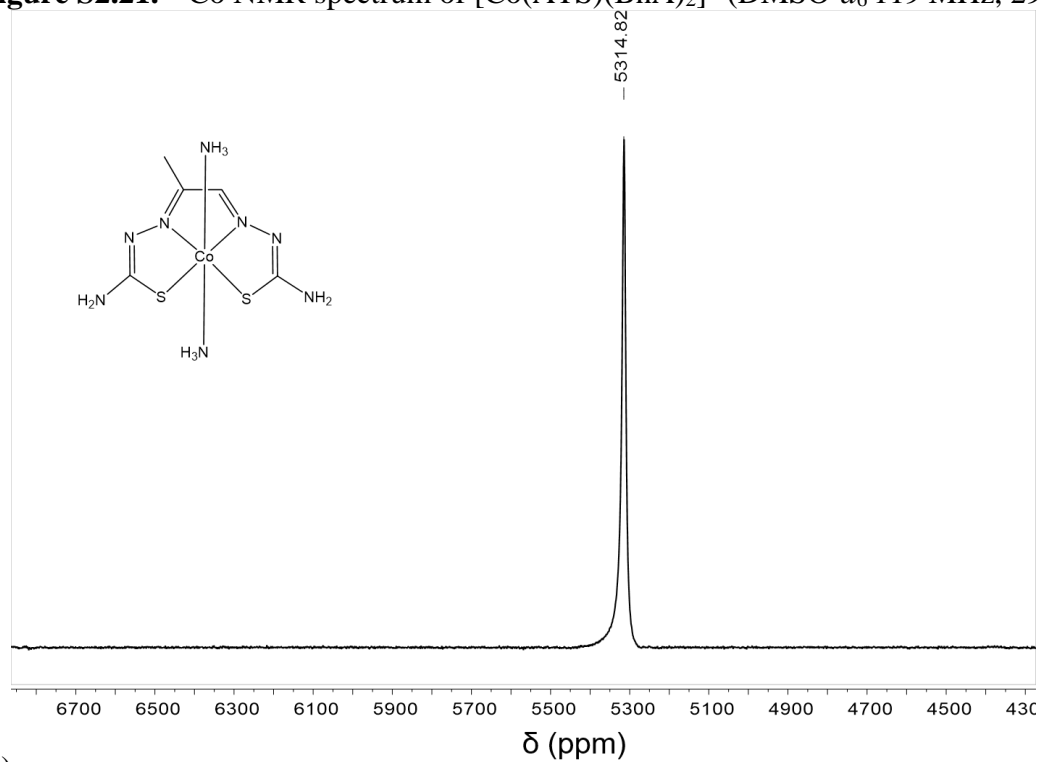


Figure S2.22. ^{59}Co NMR spectrum of $[\text{Co}(\text{PTS})(\text{NH}_3)_2]^+$ (DMSO- d_6 119 MHz, 298 K)

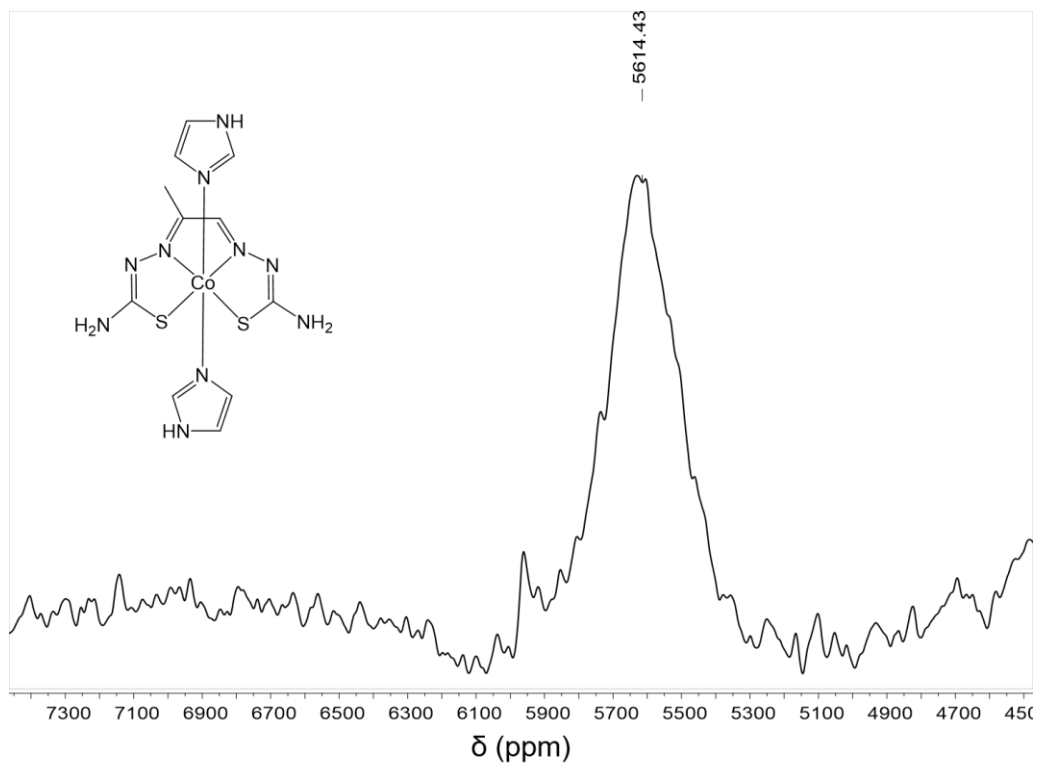


Figure S2.23. ^{59}Co NMR spectrum of $[\text{Co}(\text{PTS})(\text{Im})_2]^+$ (DMSO- d_6 119 MHz, 298 K)

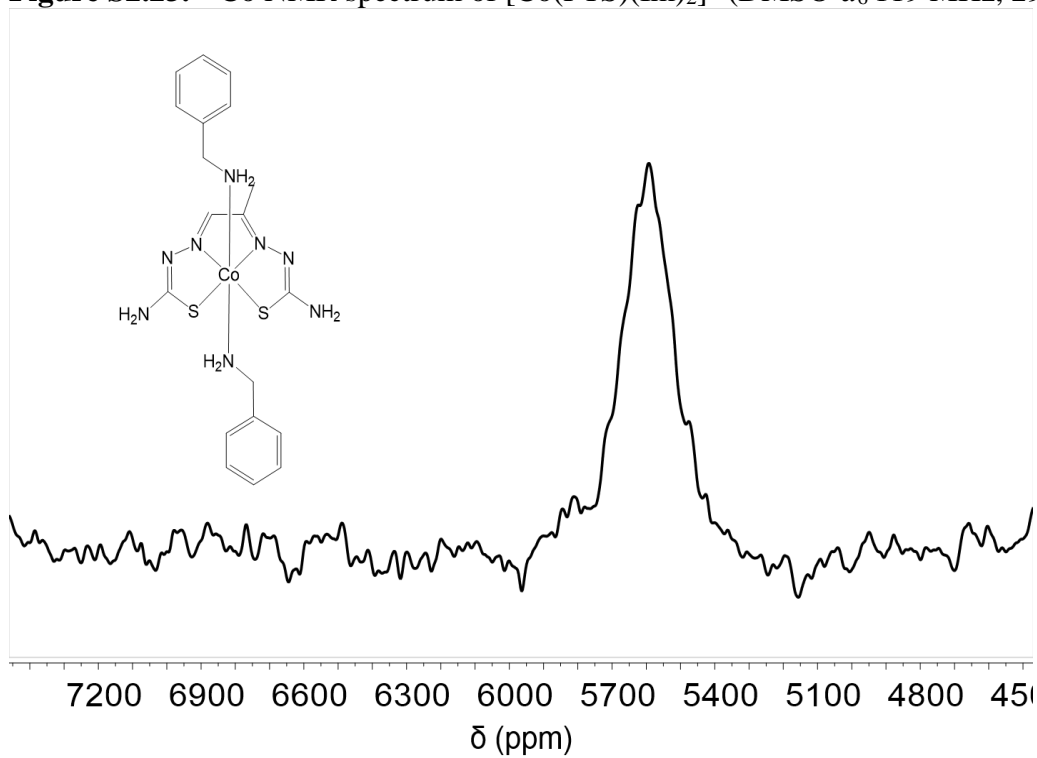


Figure S2.24. ^{59}Co NMR spectrum of $[\text{Co}(\text{PTS})(\text{BnA})_2]^+$ (DMSO- d_6 119 MHz, 298 K)

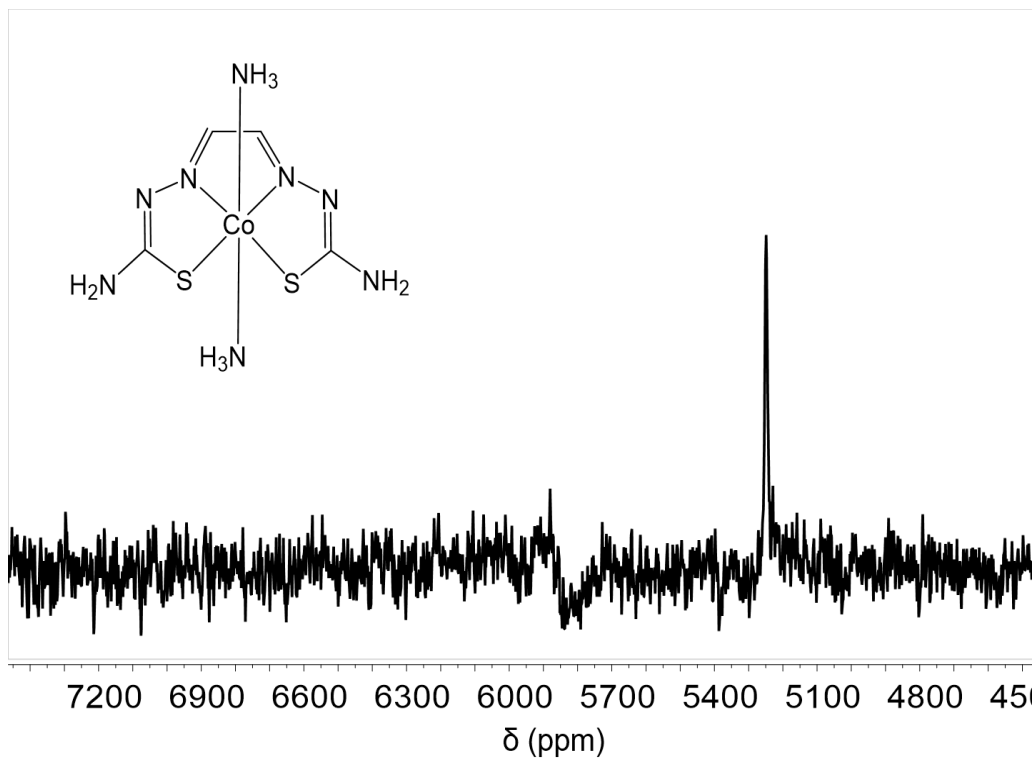


Figure S2.25. ^{59}Co NMR spectrum of $[\text{Co}(\text{GTS})(\text{NH}_3)_2]^+$ (DMSO- d_6 119 MHz, 298 K)

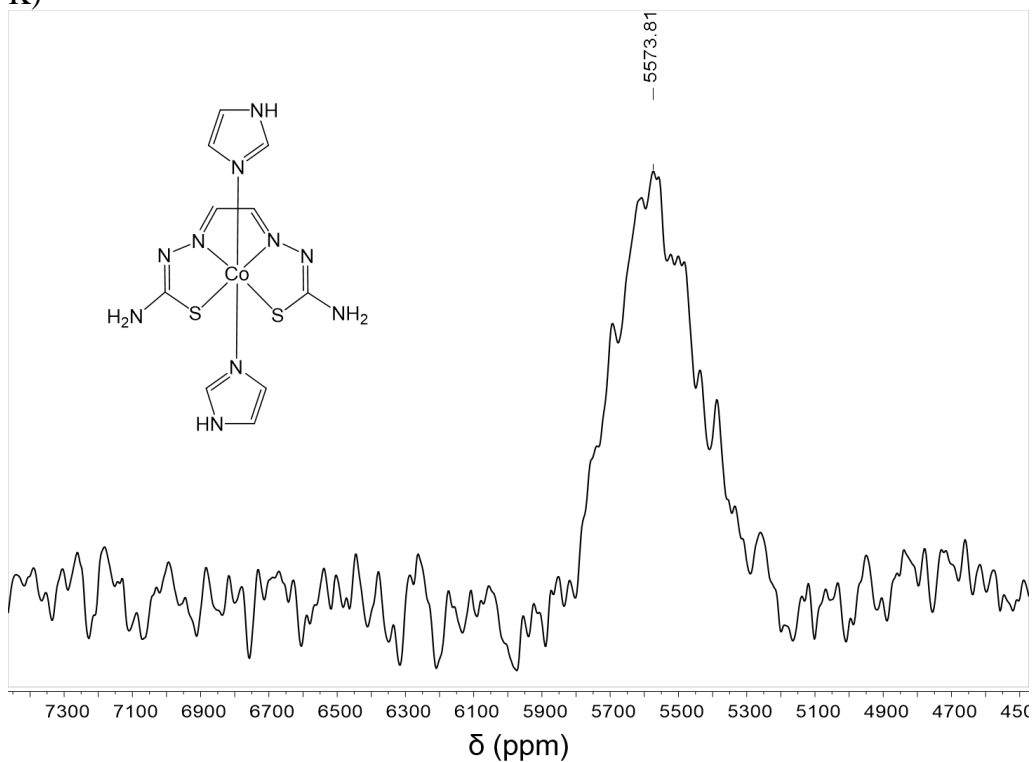


Figure S2.26. ^{59}Co NMR spectrum of $[\text{Co}(\text{GTS})(\text{Im})_2]^+$ (DMSO- d_6 119 MHz, 298 K)

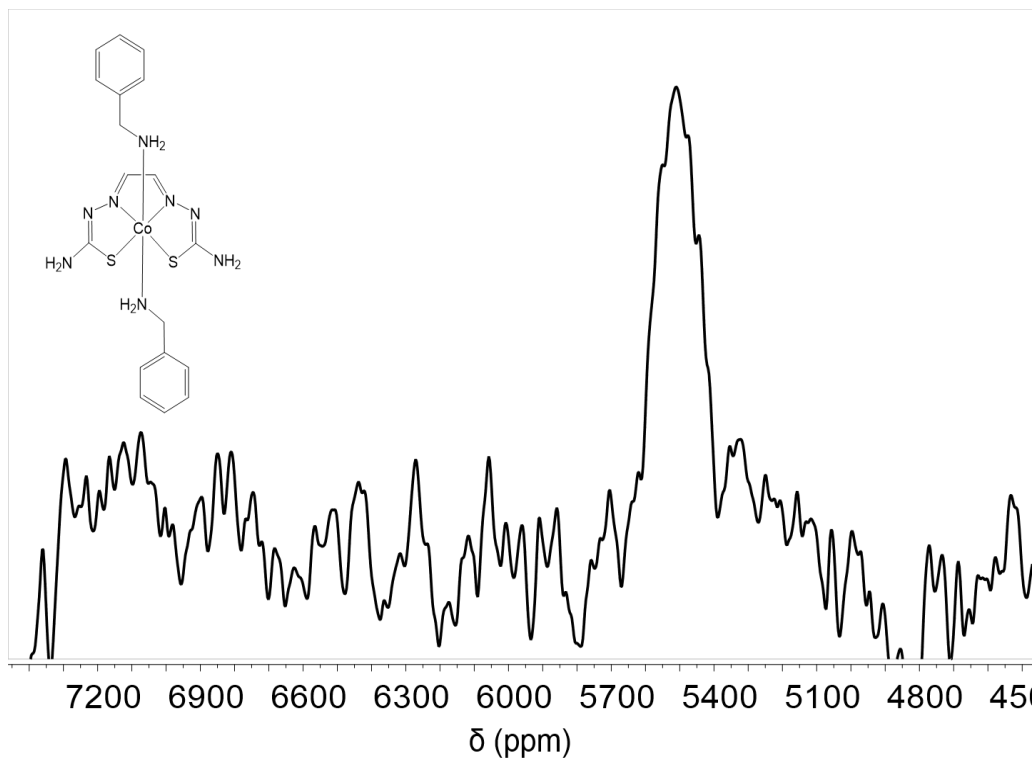


Figure S2.27. ^{59}Co NMR spectrum of $[\text{Co}(\text{GTS})(\text{BnA})_2]^+$ (DMSO- d_6 119 MHz, 298 K)

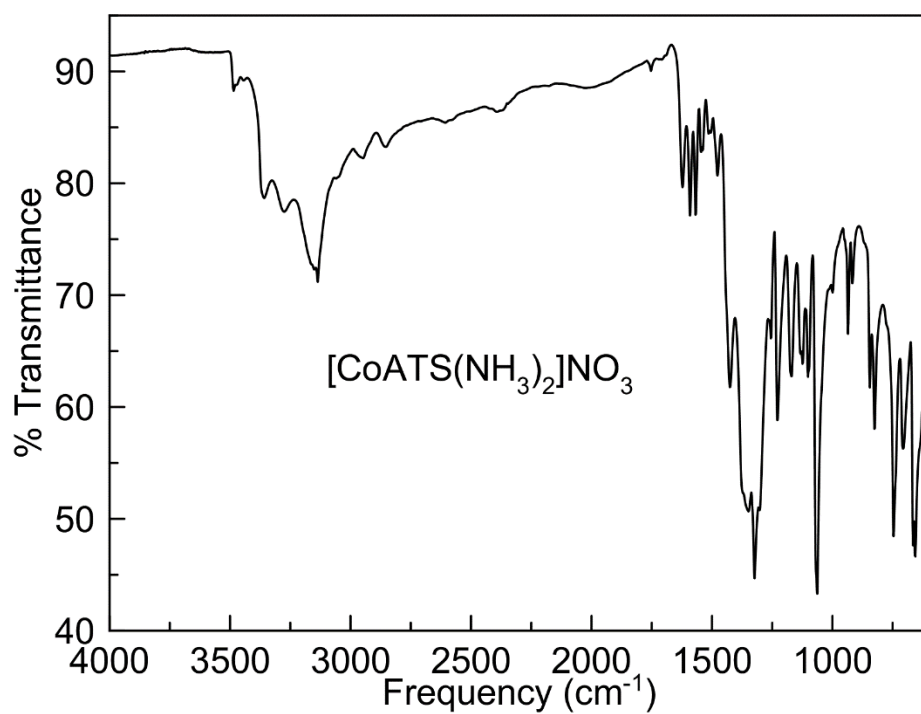


Figure S2.28. IR Spectrum of $[\text{Co}(\text{ATS})(\text{NH}_3)_2](\text{NO}_3)$.

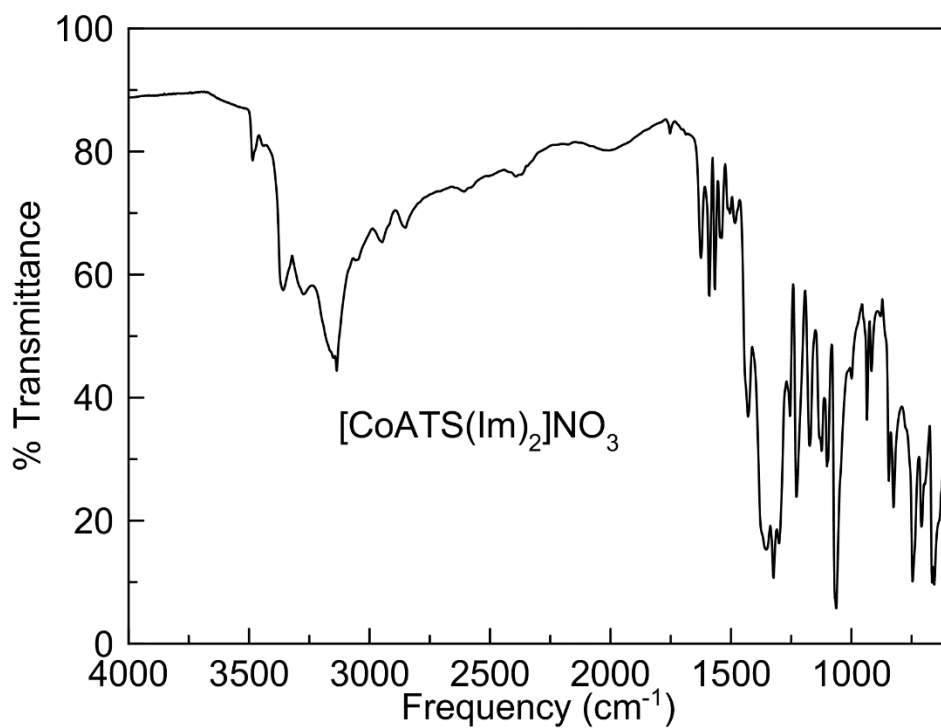


Figure S2.29. IR Spectrum of [Co(ATS)(Im)₂](NO₃).

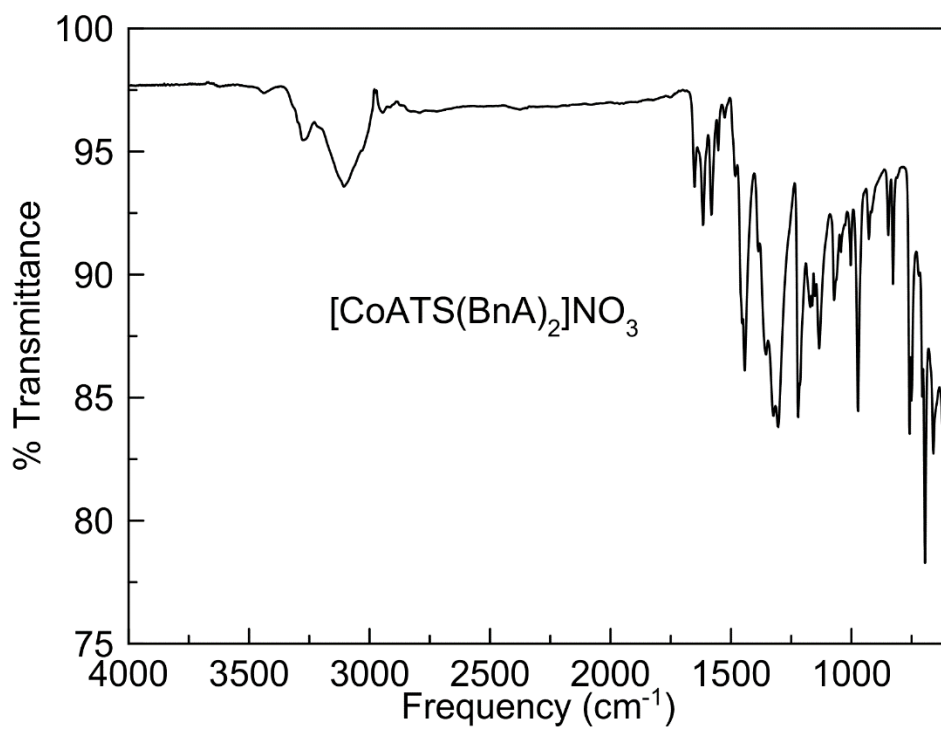


Figure S2.30. IR Spectrum of [Co(ATS)(BnA₂)](NO₃).

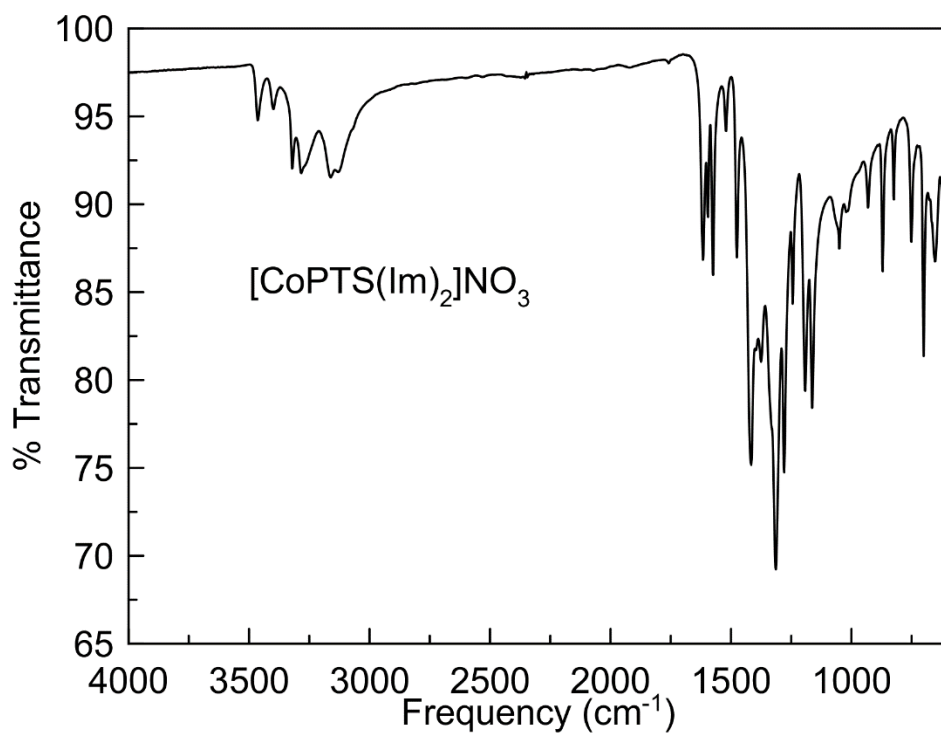


Figure S2.31. IR Spectrum of $[\text{Co}(\text{PTS})(\text{NH}_3)_2](\text{NO}_3)$.

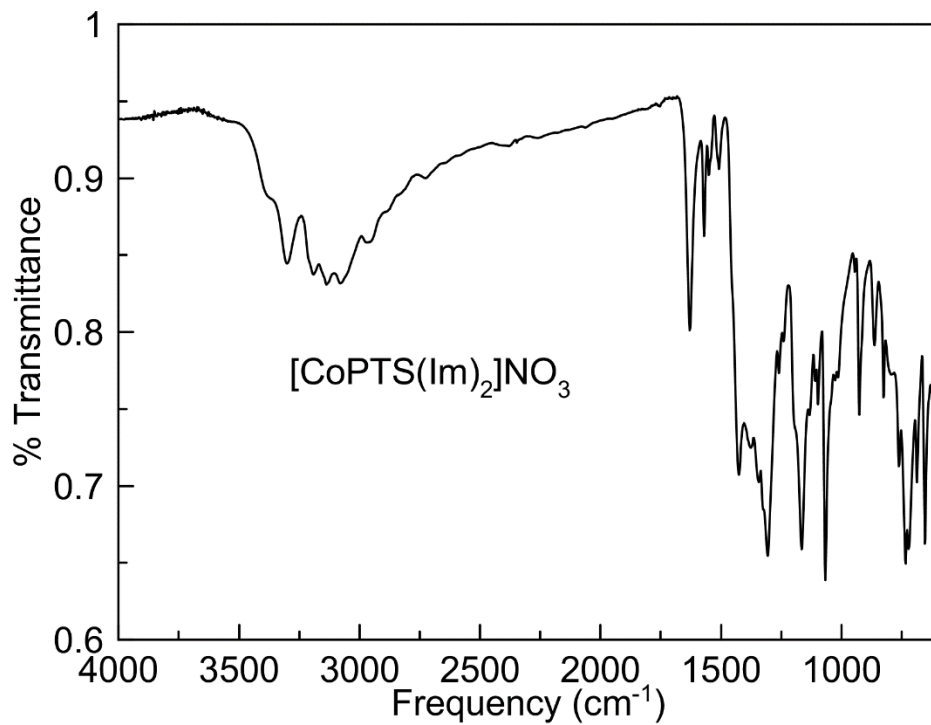


Figure S2.32. IR Spectrum of $[\text{Co}(\text{PTS})(\text{Im})_2](\text{NO}_3)$.

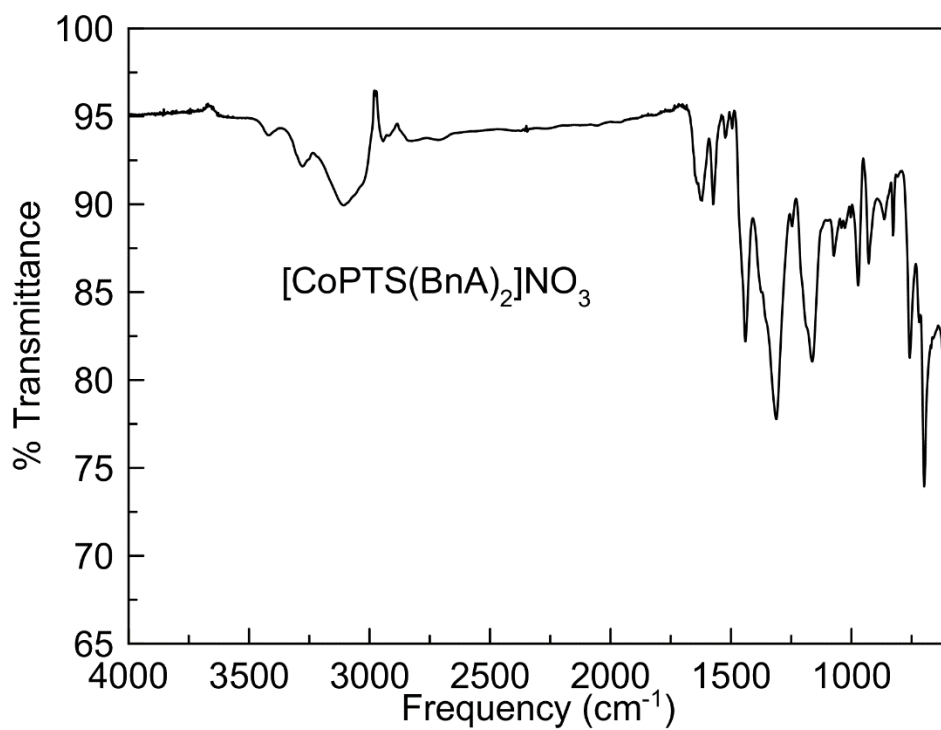


Figure S2.33. IR Spectrum of [Co(PTS)(BnA)₂](NO₃).

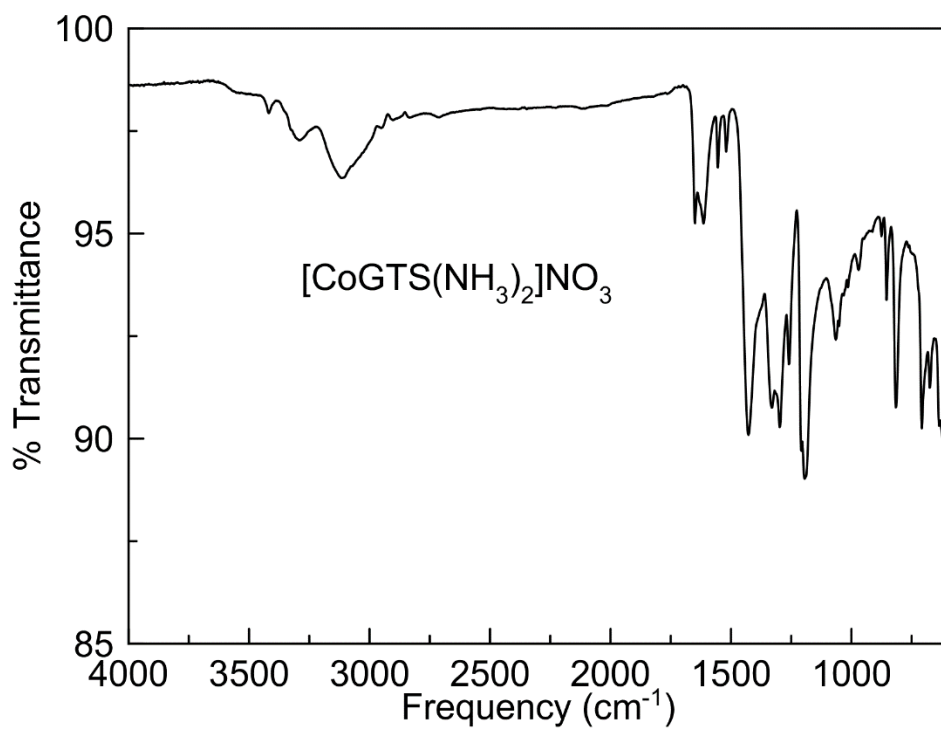


Figure S2.34. IR Spectrum of [Co(GTS)(NH₃)₂](NO₃).

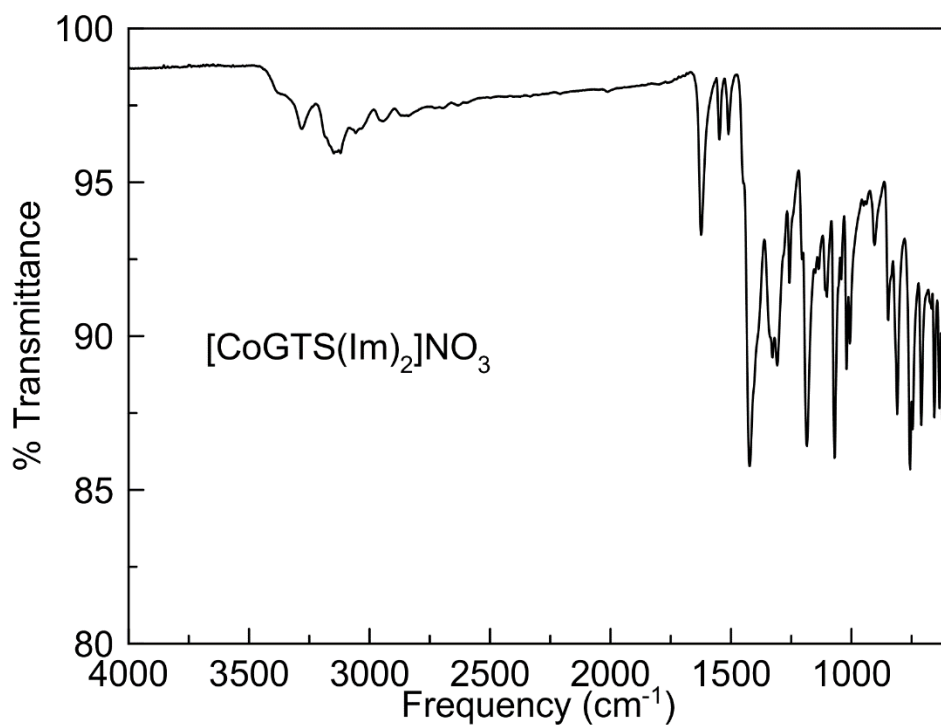


Figure S2.35. IR Spectrum of [Co(GTS)(Im)₂]₂(NO₃).

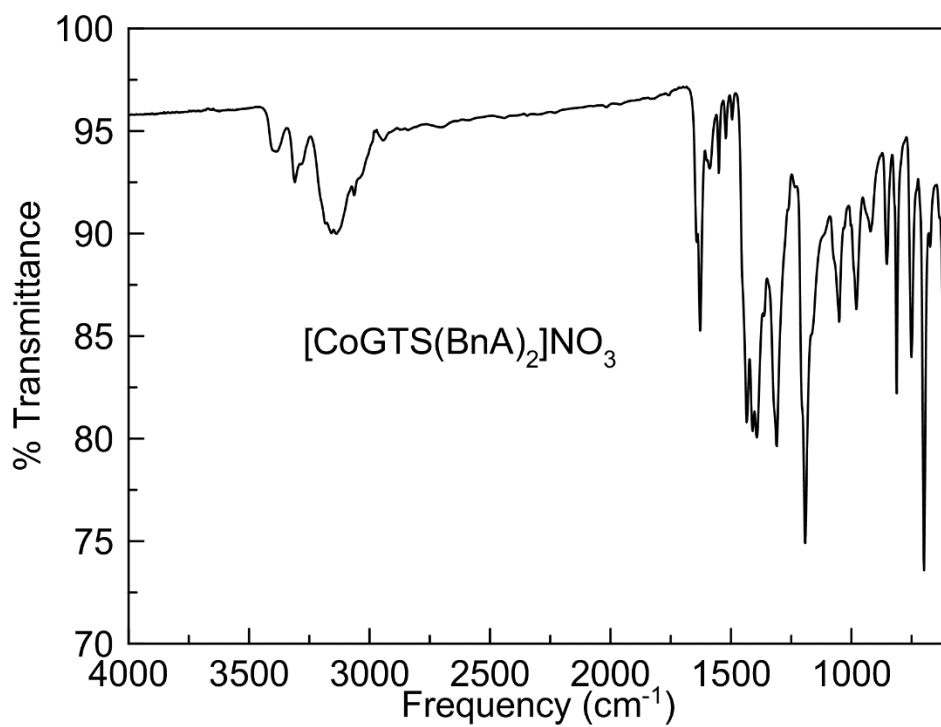


Figure S2.36. IR Spectrum of [Co(GTS)(BnA)₂]₂(NO₃).

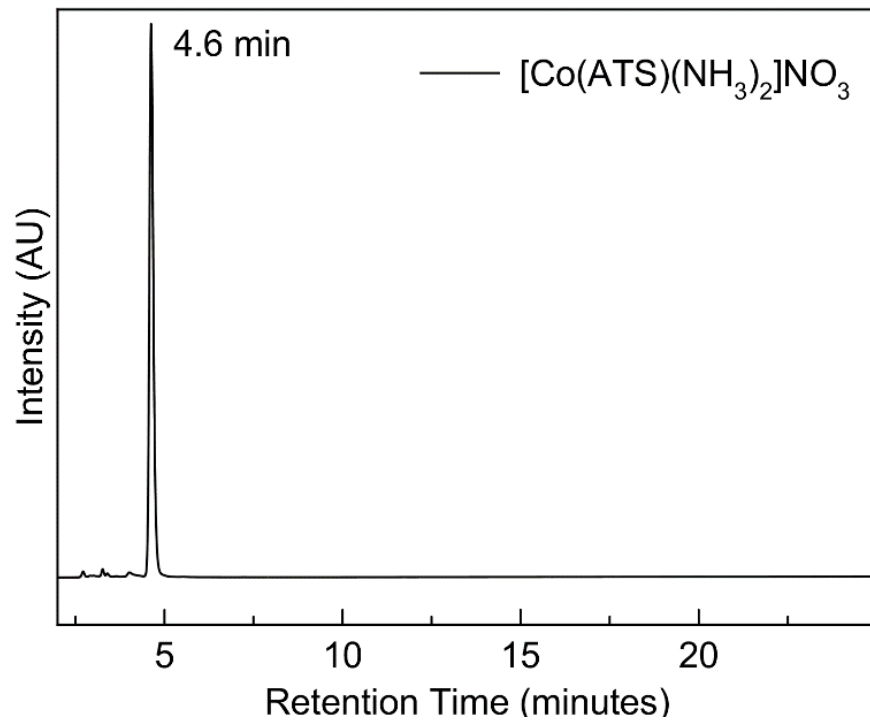


Figure S2.37. HPLC Chromatogram of $[\text{Co}(\text{ATS})(\text{NH}_3)_2]^+$

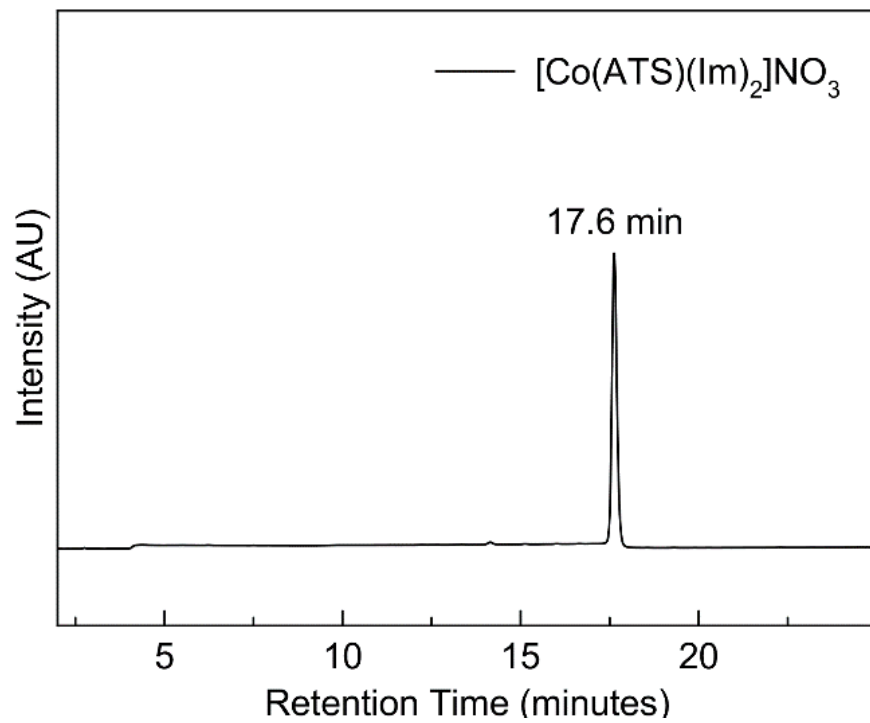


Figure S2.38. HPLC Chromatogram of $[\text{Co}(\text{ATS})(\text{Im})_2]^+$

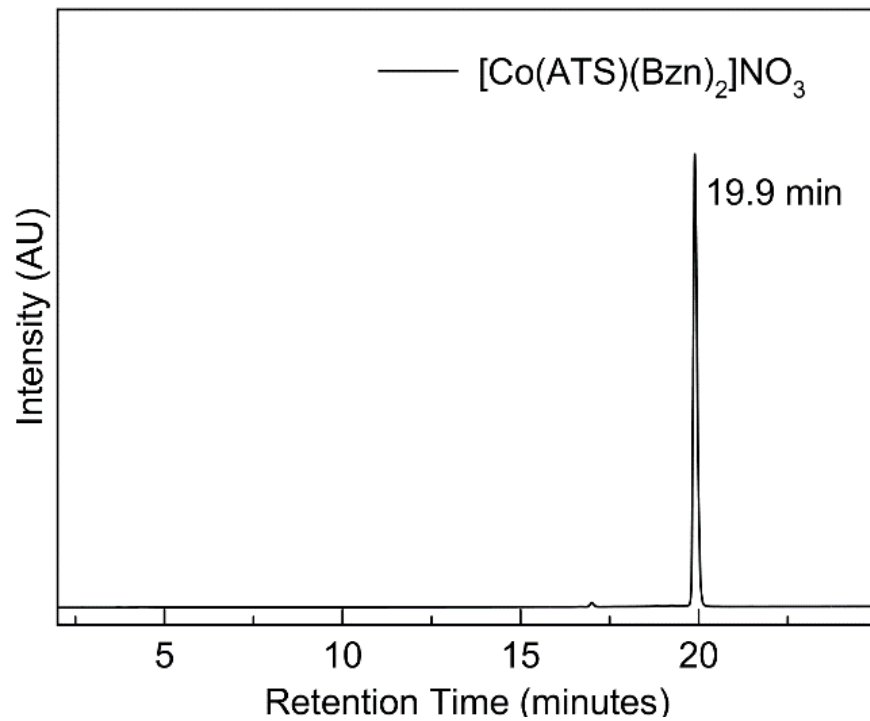


Figure S2.39. HPLC Chromatogram of $[\text{Co}(\text{ATS})(\text{BnA})_2]^+$

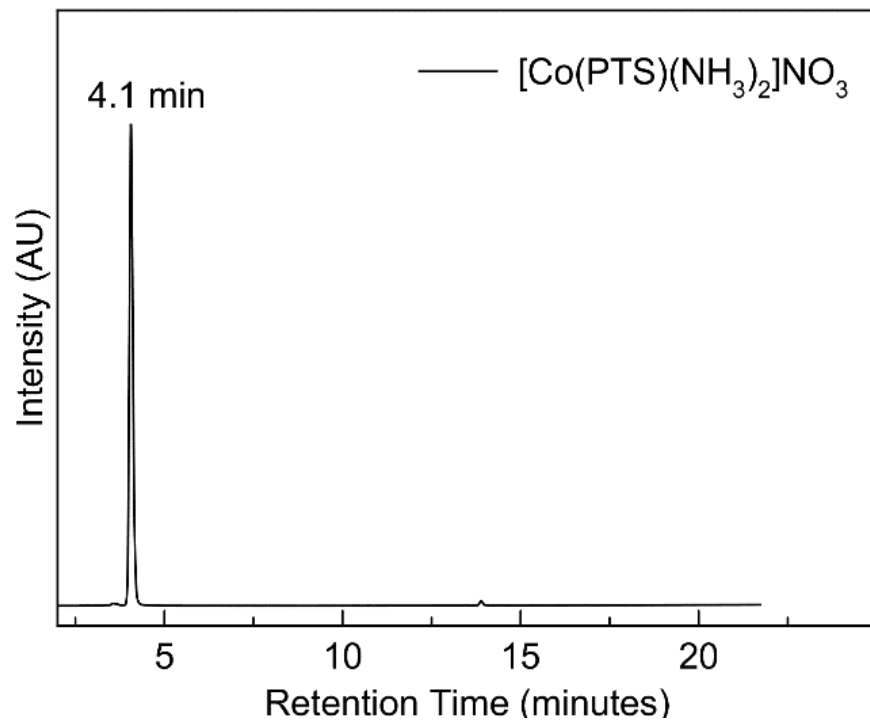


Figure S2.40. HPLC Chromatogram of $[\text{Co}(\text{PTS})(\text{NH}_3)_2]^+$

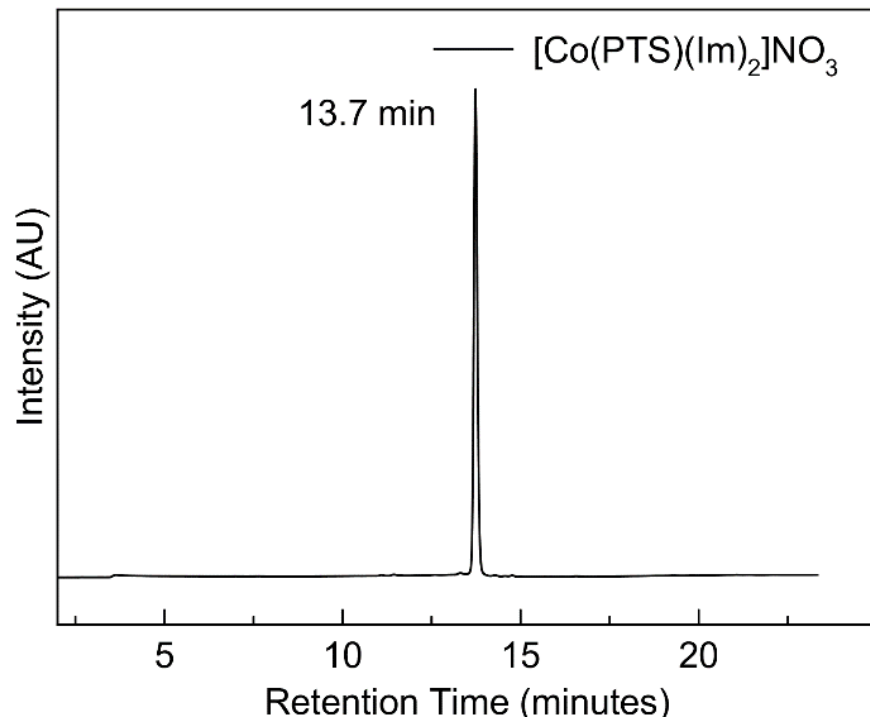


Figure S2.41. HPLC Chromatogram of $[\text{Co}(\text{PTS})(\text{Im})_2]^+$

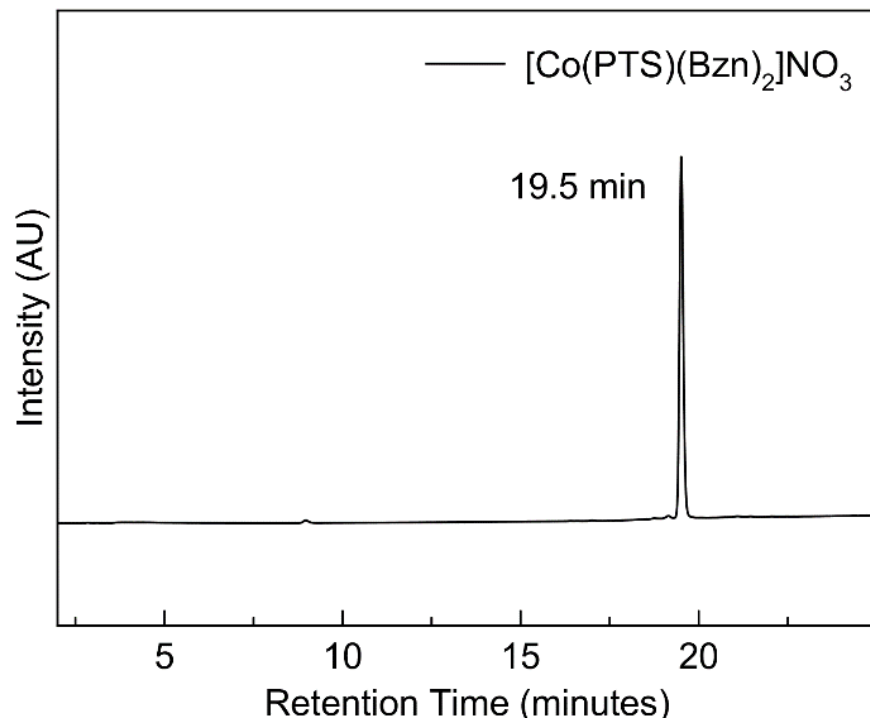


Figure S2.42. HPLC Chromatogram of $[\text{Co}(\text{PTS})(\text{BnA})_2]^+$

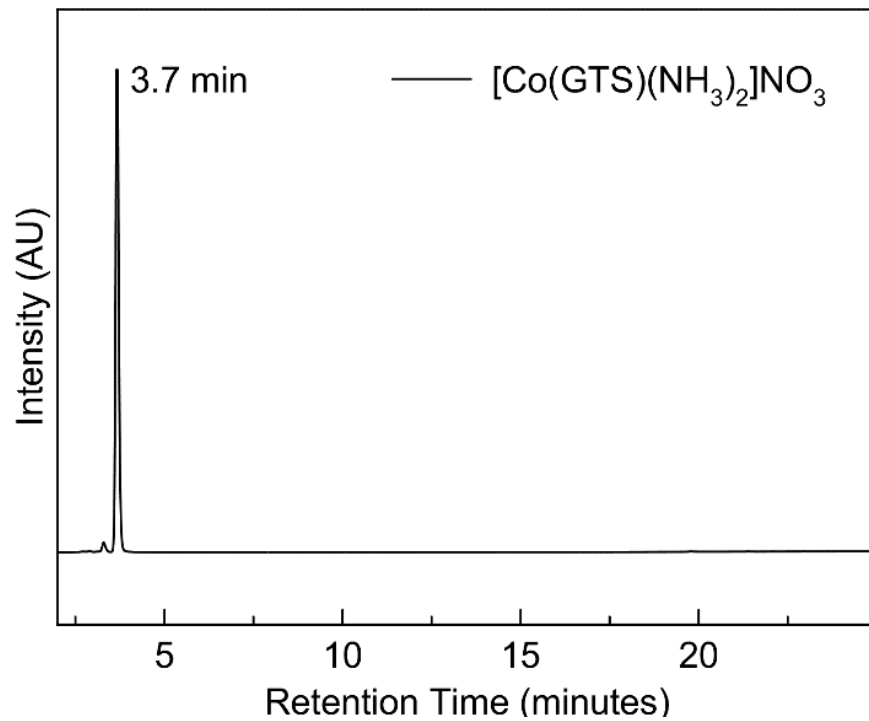


Figure S2.43. HPLC Chromatogram of $[\text{Co}(\text{GTS})(\text{NH}_3)_2]^+$

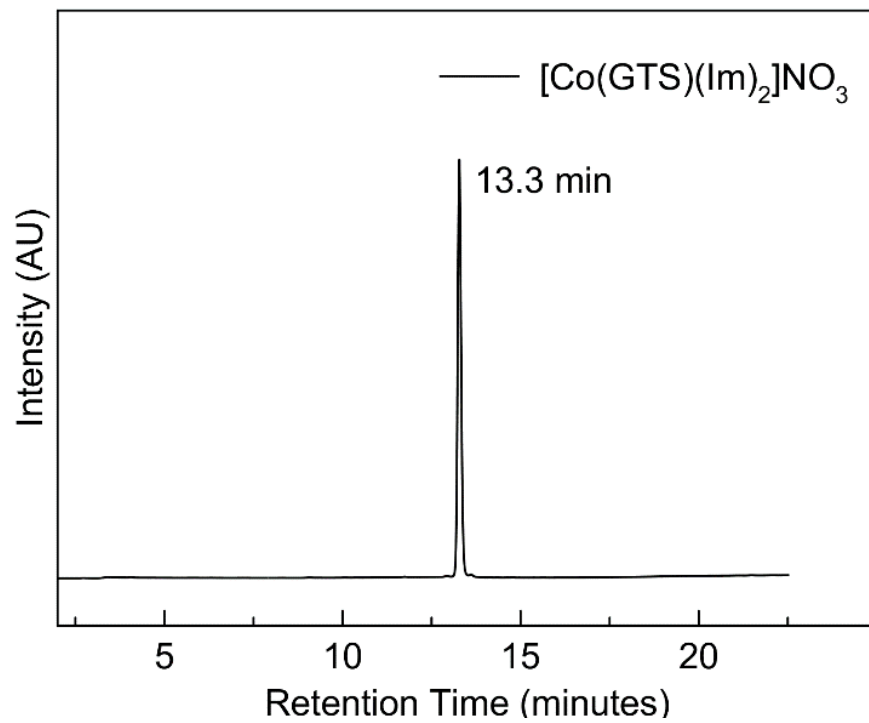


Figure S2.44. HPLC Chromatogram of $[\text{Co}(\text{GTS})(\text{Im})_2]^+$

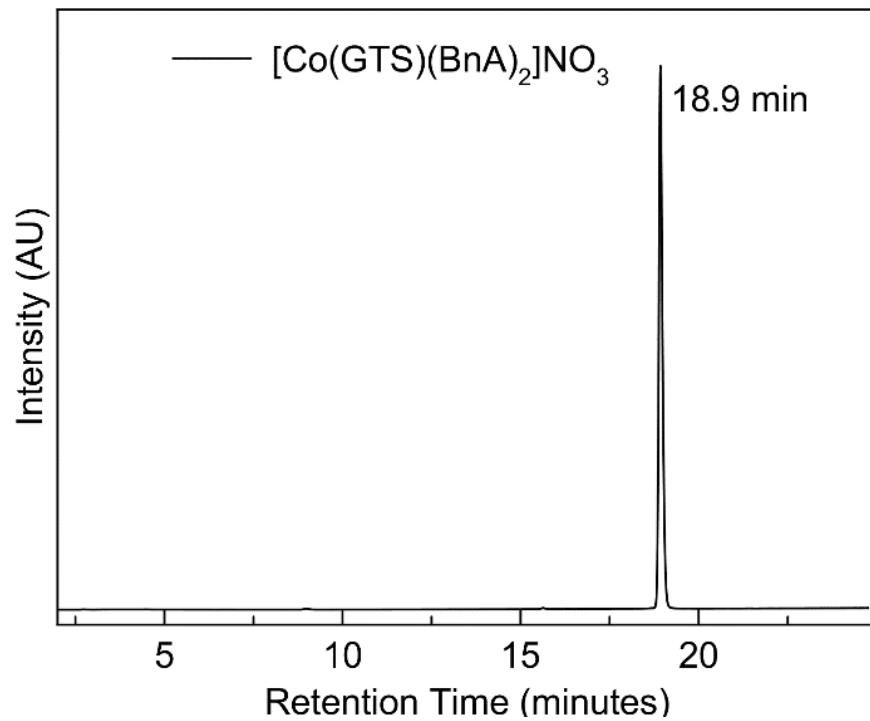


Figure S2.45. HPLC Chromatogram of $[\text{Co}(\text{GTS})(\text{BnA})_2]^+$

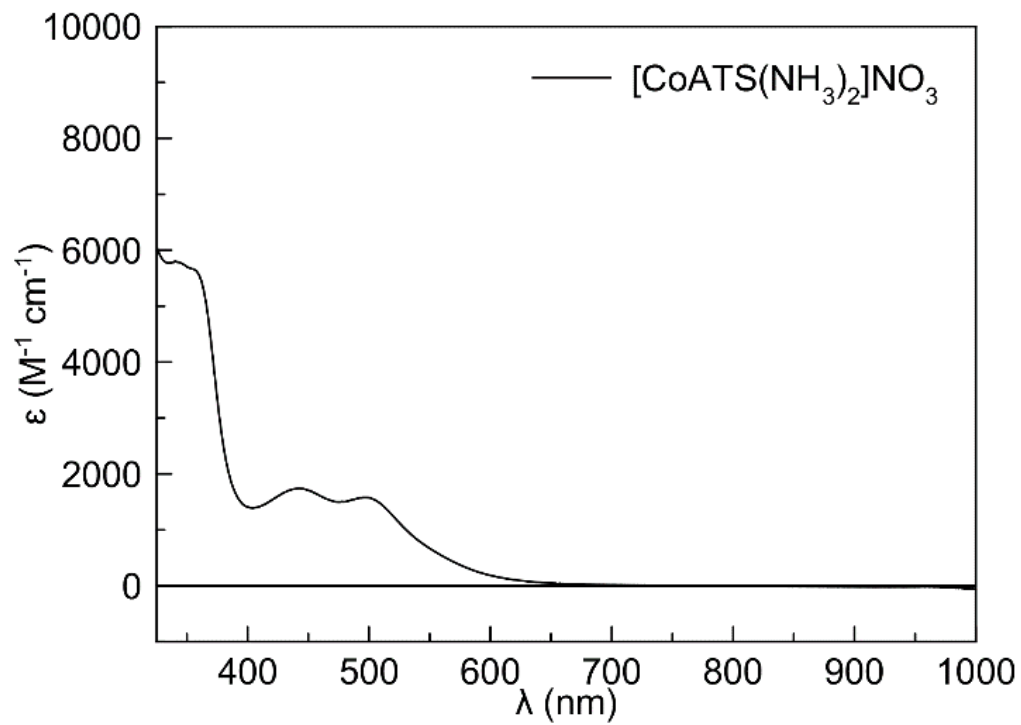


Figure S2.46. UV-Vis Spectrum of $[\text{Co}(\text{ATS})(\text{NH}_3)_2]^+$ in pH 7.4 phosphate-buffered saline.

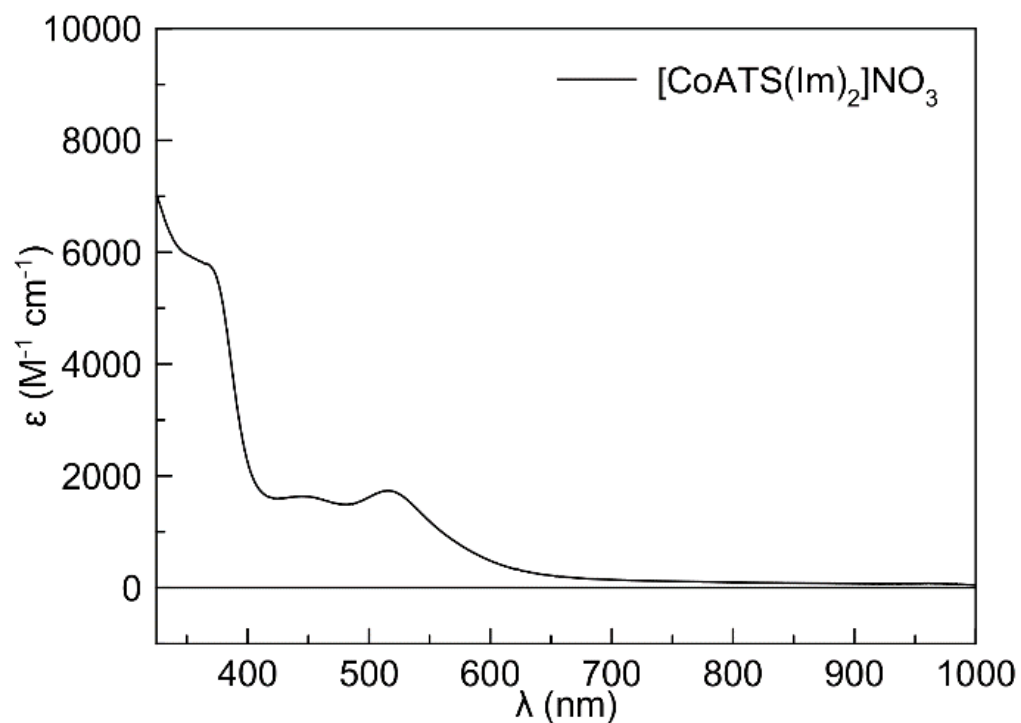


Figure S2.47. UV-Vis Spectrum of $[\text{CoATS}(\text{Im})_2]^+$ in pH 7.4 phosphate-buffered saline.

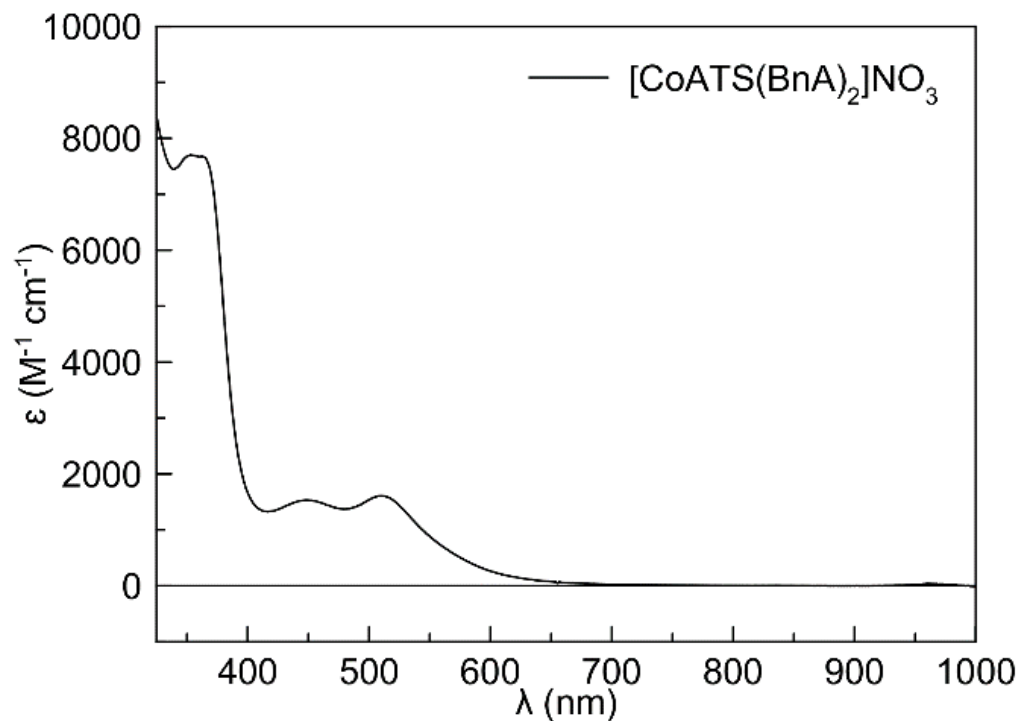


Figure S2.48. UV-Vis Spectrum of $[\text{CoATS}(\text{BnA})_2]^+$ in pH 7.4 phosphate-buffered saline.

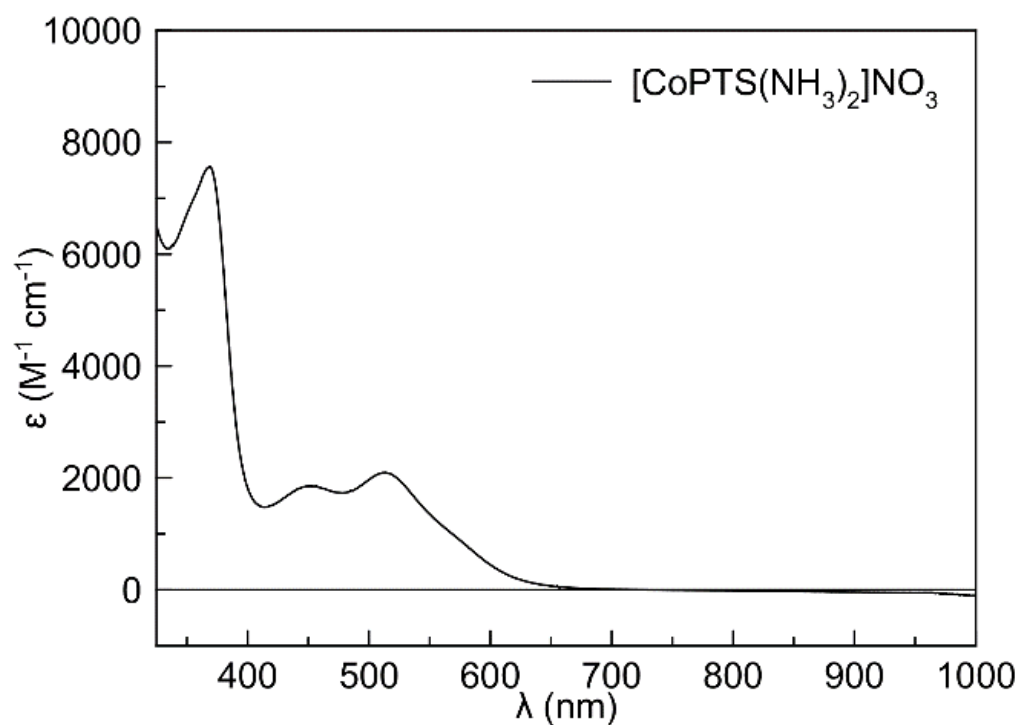


Figure S2.49. UV-Vis Spectrum of $[\text{CoPTS}(\text{NH}_3)_2]^+$ in pH 7.4 phosphate-buffered saline.

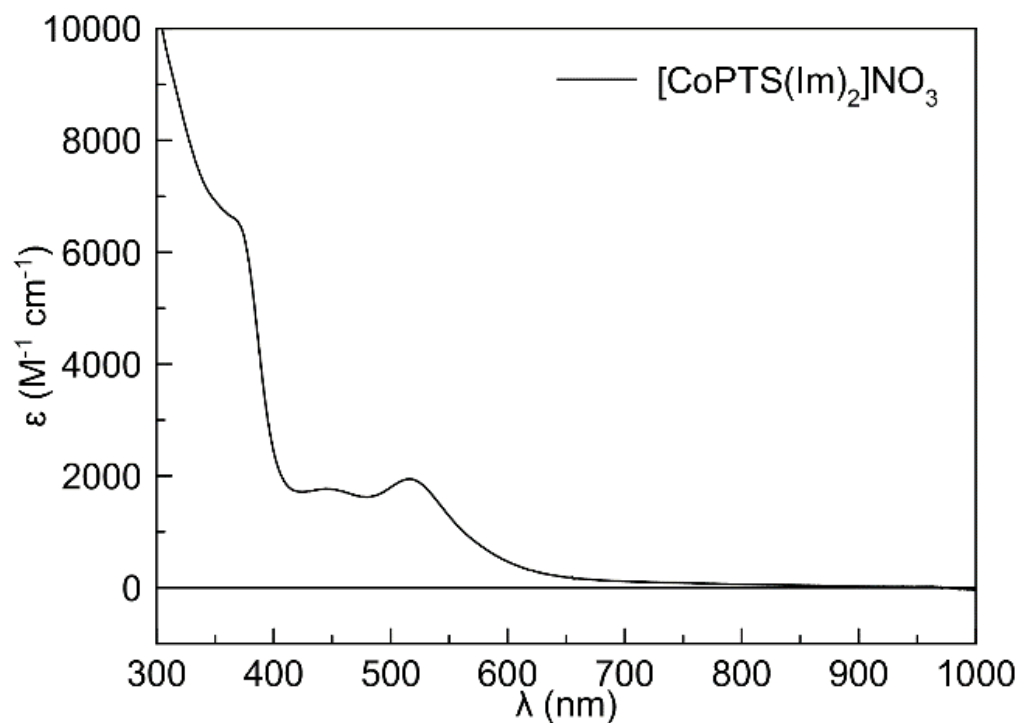


Figure S2.50. UV-Vis Spectrum of $[\text{CoPTS}(\text{Im})_2]^+$ in pH 7.4 phosphate-buffered saline.

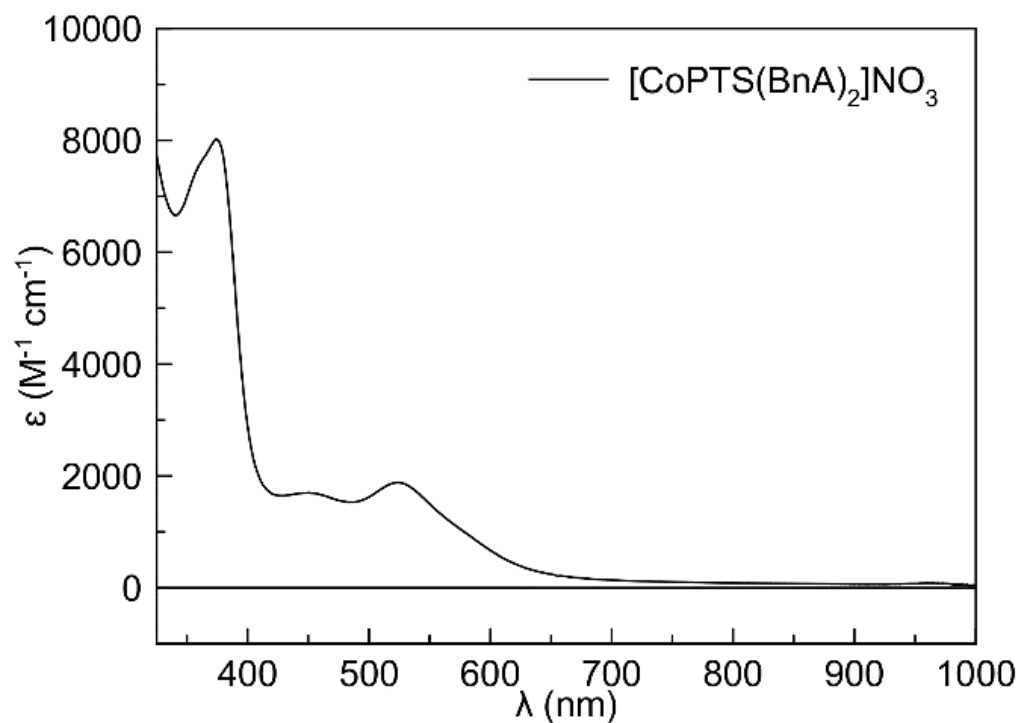


Figure S2.51. UV-Vis Spectrum of $[\text{Co}(\text{PTS})(\text{BnA})_2]^+$ in pH 7.4 phosphate-buffered saline.

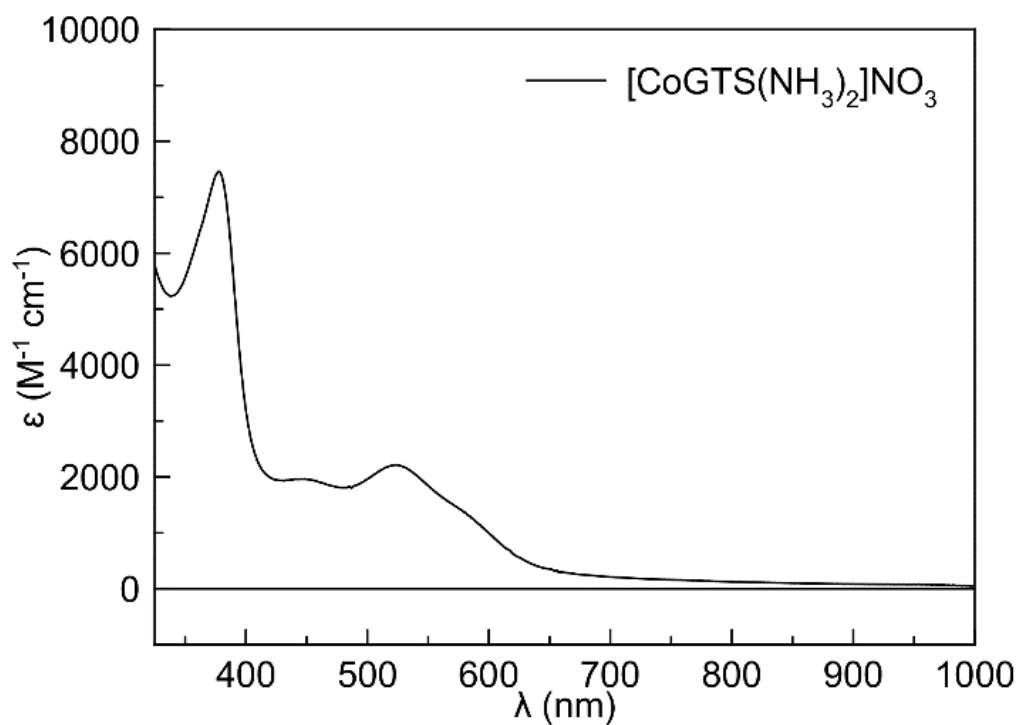


Figure S2.52. UV-Vis Spectrum of $[\text{Co}(\text{GTS})(\text{NH}_3)_2]^+$ in pH 7.4 phosphate-buffered

saline.

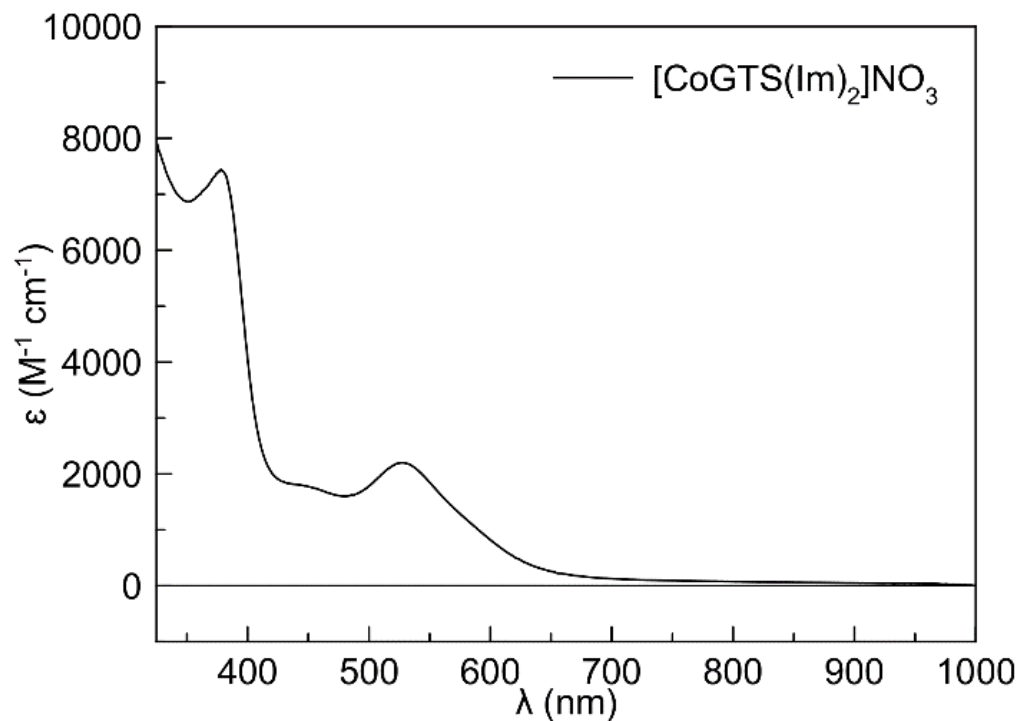


Figure S2.53. UV-Vis Spectrum of $[\text{Co}(\text{GTS})(\text{Im})_2]^+$ in pH 7.4 phosphate-buffered saline.

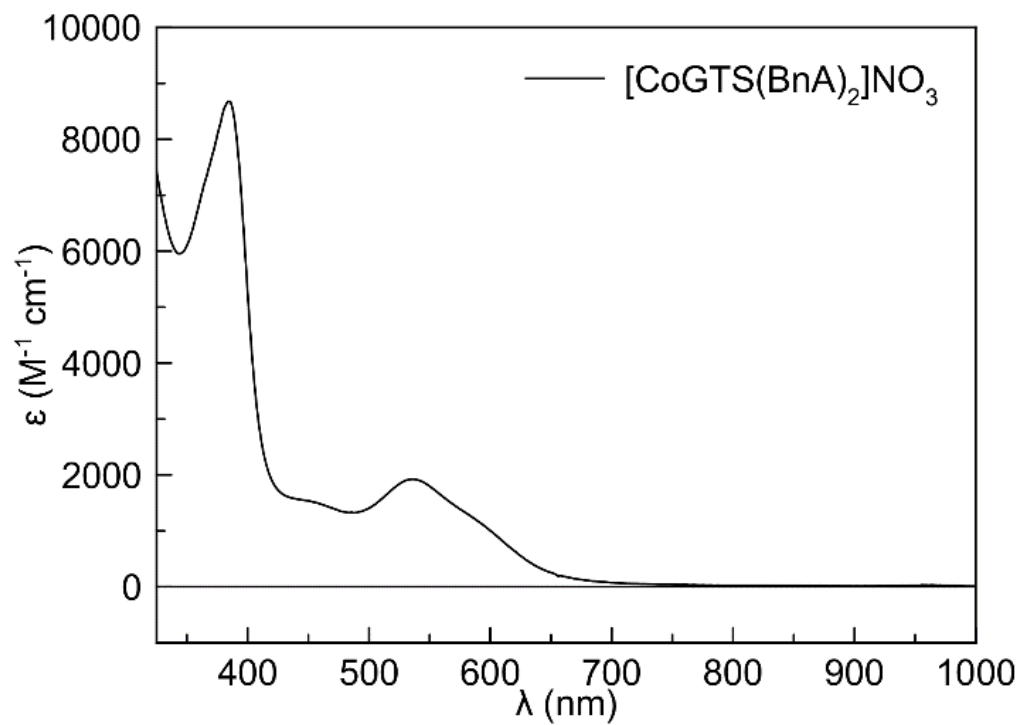


Figure S2.54. UV-Vis Spectrum of $[\text{Co}(\text{GTS})(\text{BnA})_2]^+$ in pH 7.4 phosphate-buffered

saline.

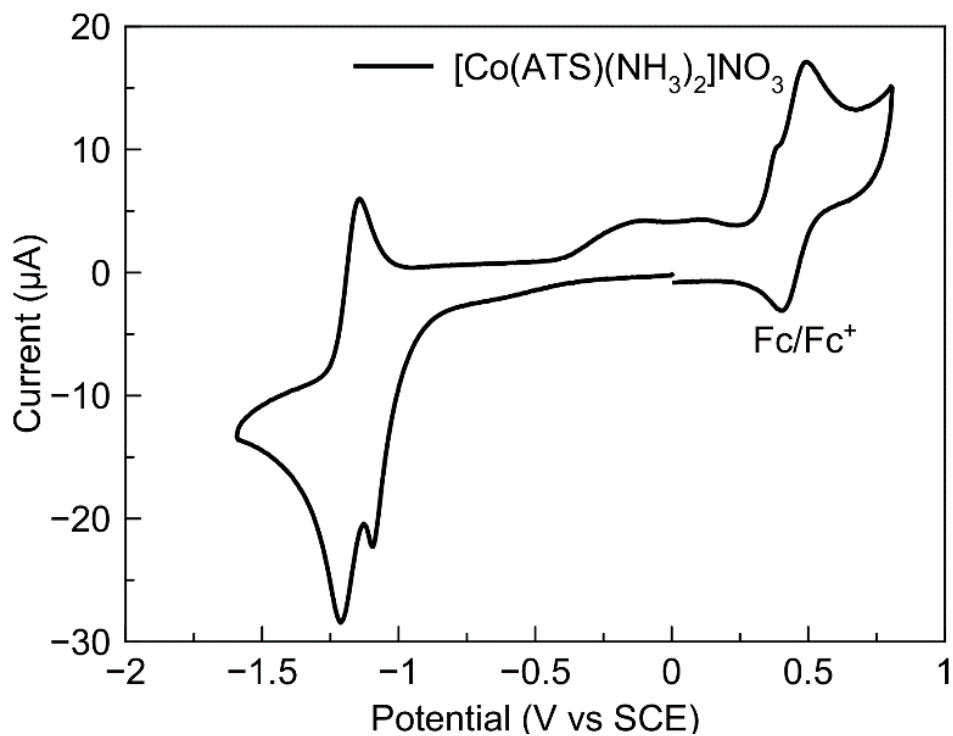


Figure S2.55. CV of $[\text{Co}(\text{ATS})(\text{NH}_3)_2]^+$ in DMF with $0.1 \text{ M } [\text{N}(\text{Bu})_4]\text{PF}_6$

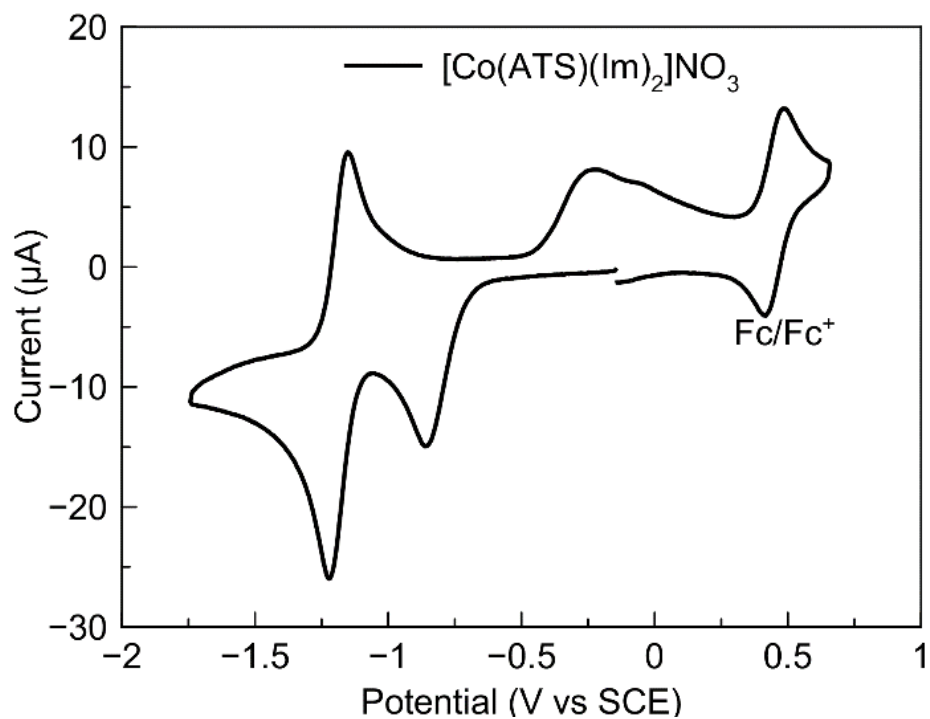


Figure S2.56. CV of $[\text{Co}(\text{ATS})(\text{Im})_2]^+$ in DMF with $0.1 \text{ M } [\text{N}(\text{Bu})_4]\text{PF}_6$

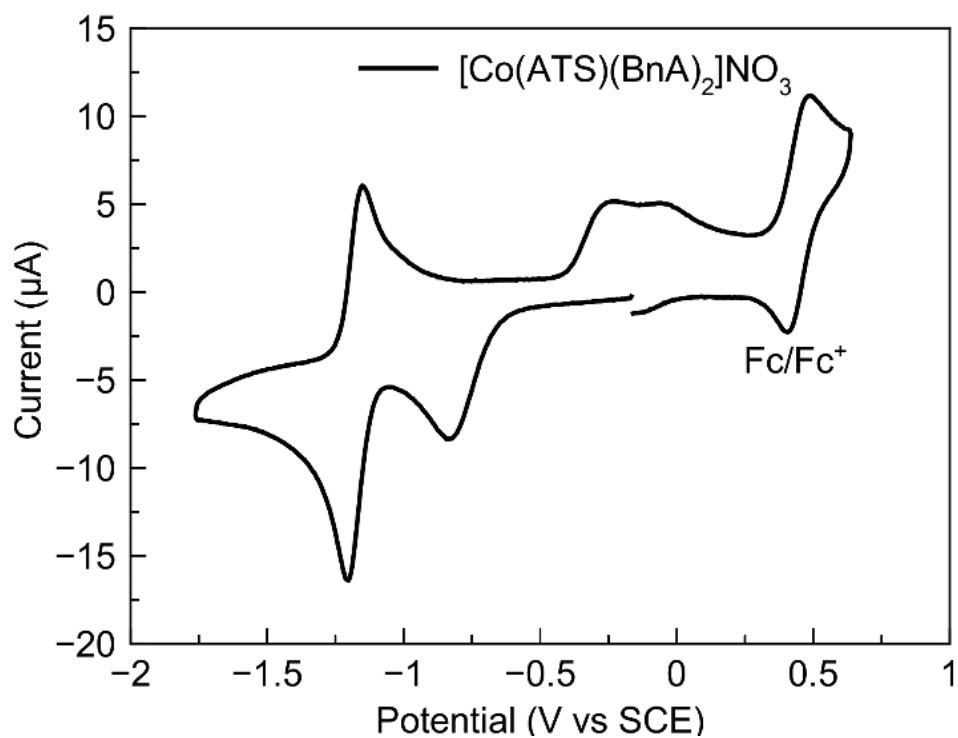


Figure S2.57. CV of $[\text{Co}(\text{ATS})(\text{BnA})_2]^+$ in DMF with $0.1 \text{ M } [\text{N}(\text{Bu})_4]\text{PF}_6$

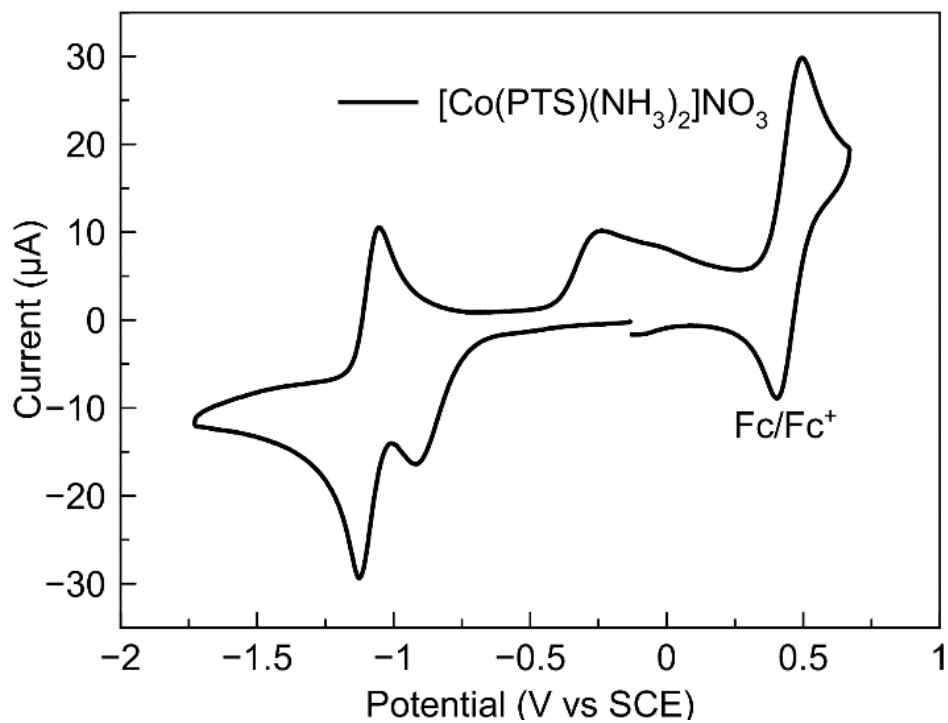


Figure S2.58. CV of $[\text{Co}(\text{PTS})(\text{NH}_3)_2]^+$ in DMF with $0.1 \text{ M } [\text{N}(\text{Bu})_4]\text{PF}_6$

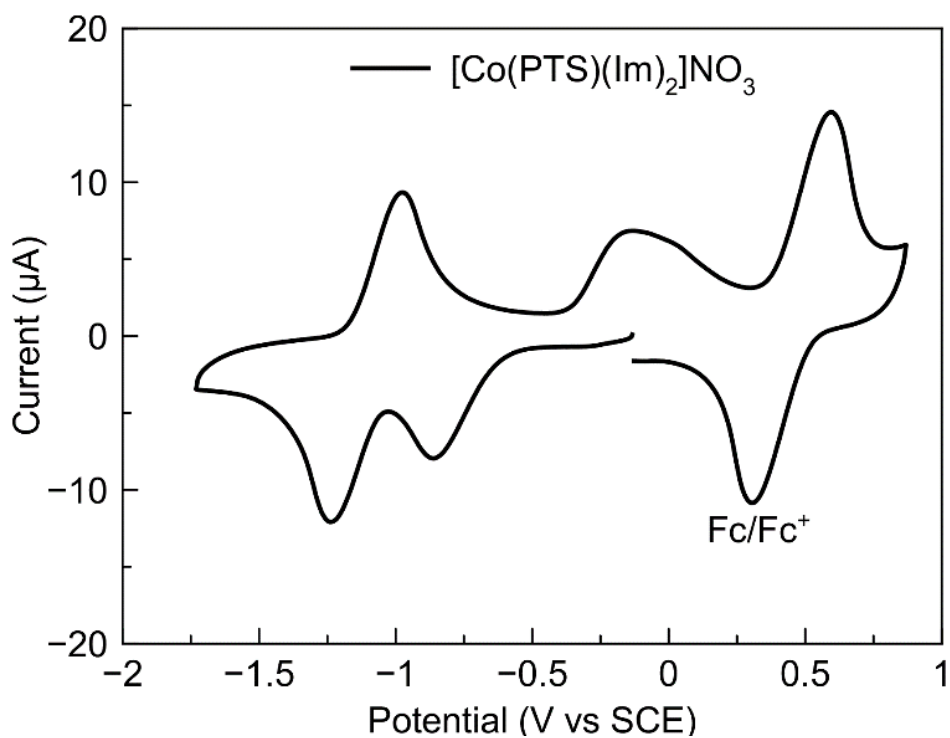


Figure S2.59. CV of $[\text{Co}(\text{PTS})(\text{Im})_2]^+$ in DMF with 0.1 M $[\text{N}(\text{Bu})_4]\text{PF}_6$

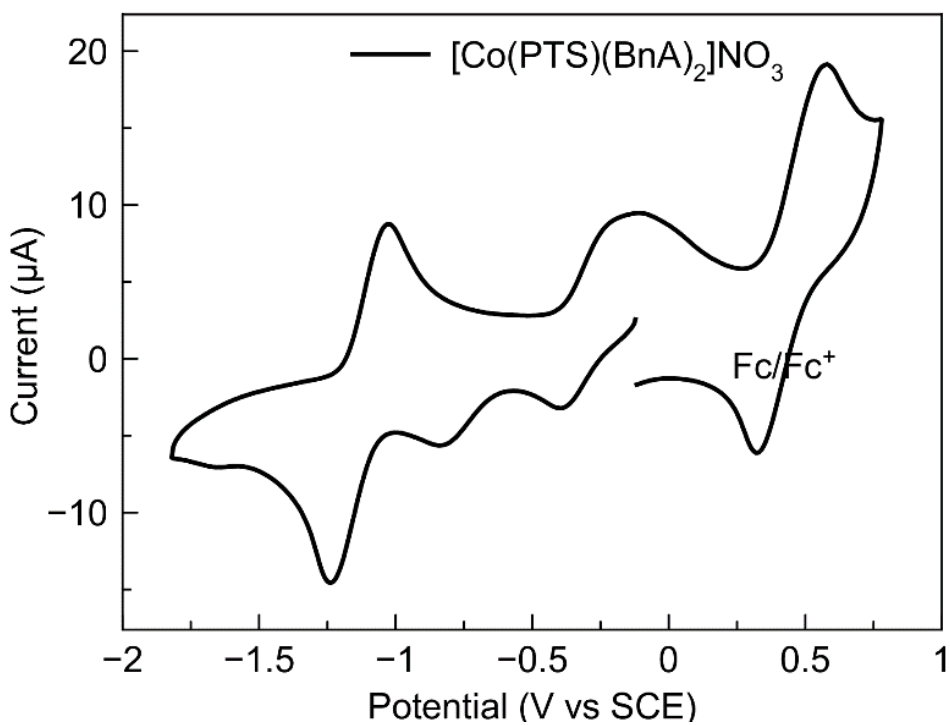


Figure S2.60. CV of $[\text{Co}(\text{PTS})(\text{BnA})_2]^+$ in DMF with 0.1 M $[\text{N}(\text{Bu})_4]\text{PF}_6$

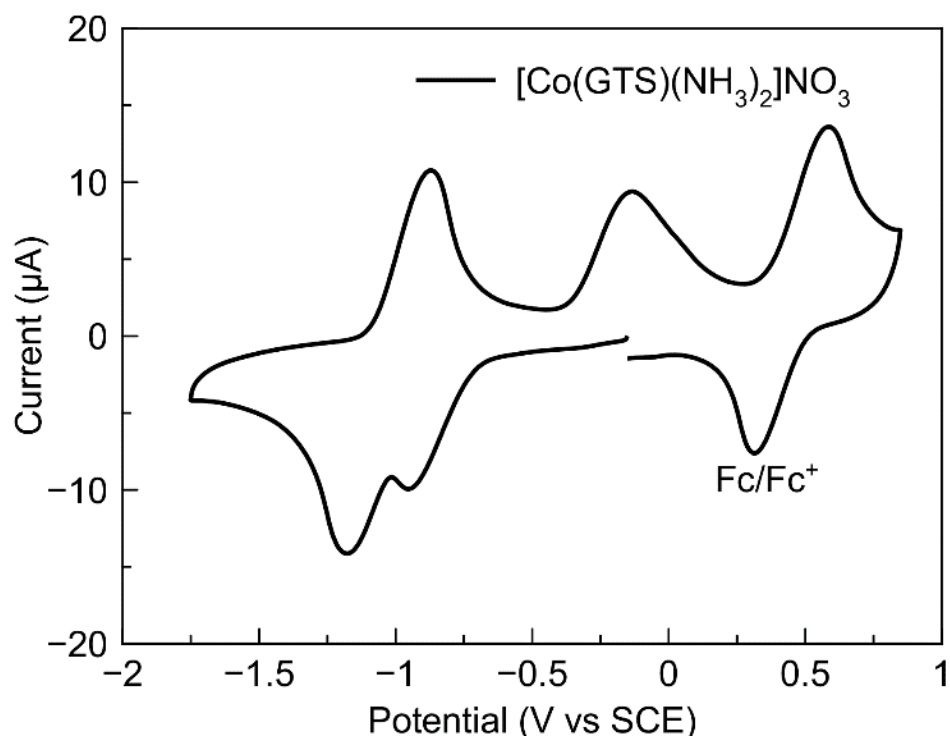


Figure S2.61. CV of $[\text{Co}(\text{GTS})(\text{NH}_3)_2]^+$ in DMF with 0.1 M $[\text{N}(\text{Bu})_4]\text{PF}_6$

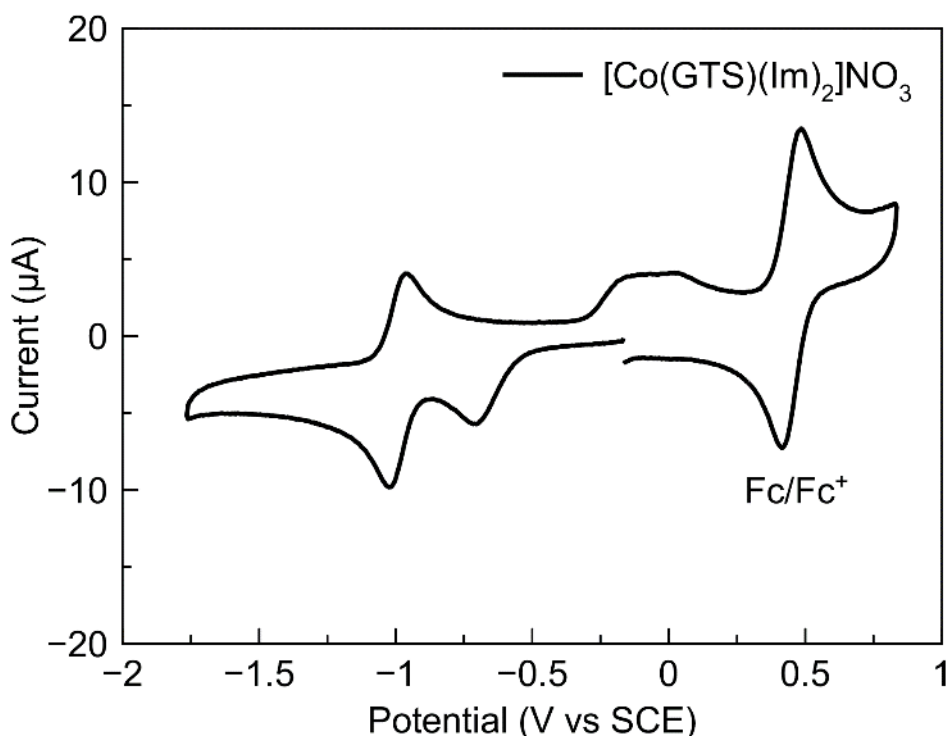


Figure S2.62. CV of $[\text{Co}(\text{GTS})(\text{Im})_2]^+$ in DMF with 0.1 M $[\text{N}(\text{Bu})_4]\text{PF}_6$

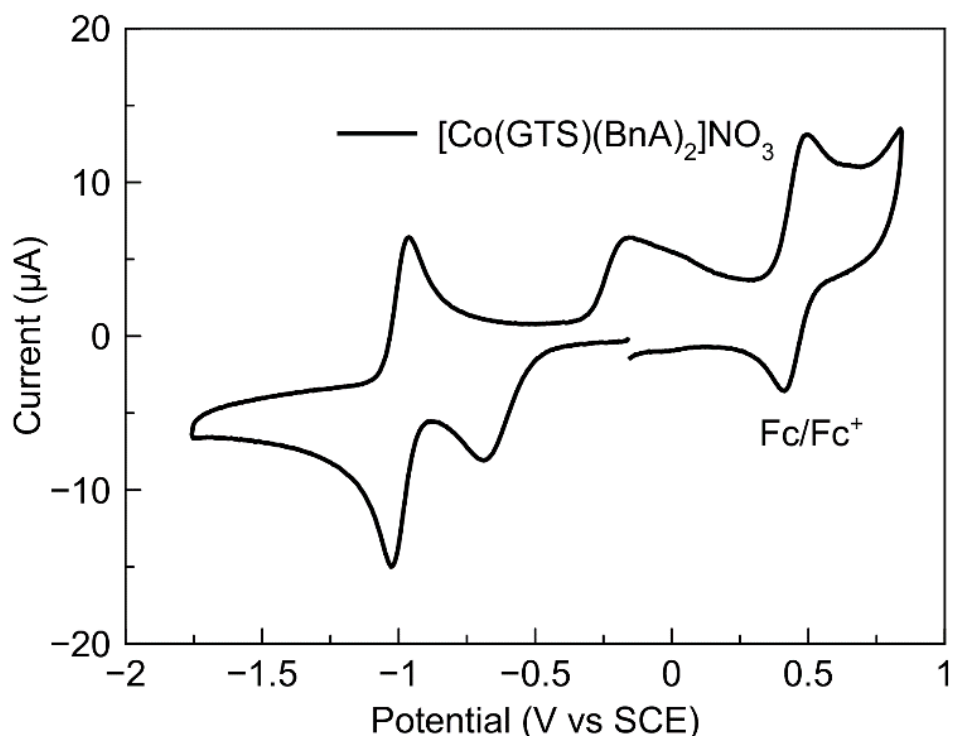


Figure S2.63. CV of $[\text{Co}(\text{GTS})(\text{BnA})_2]^+$ in DMF with 0.1 M $[\text{N}(\text{Bu})_4]\text{PF}_6$

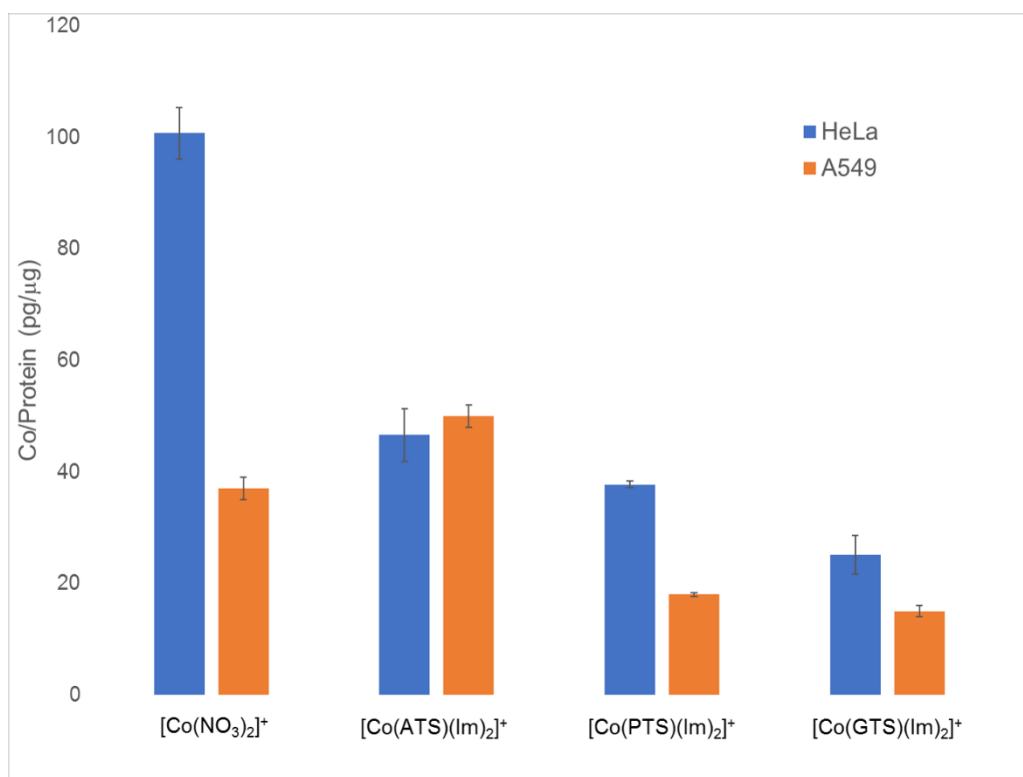


Figure S2.64. Uptake of $[\text{Co}(\text{BTSC})(\text{Im})_2]^+$ Complexes in HeLa and A549 Cells

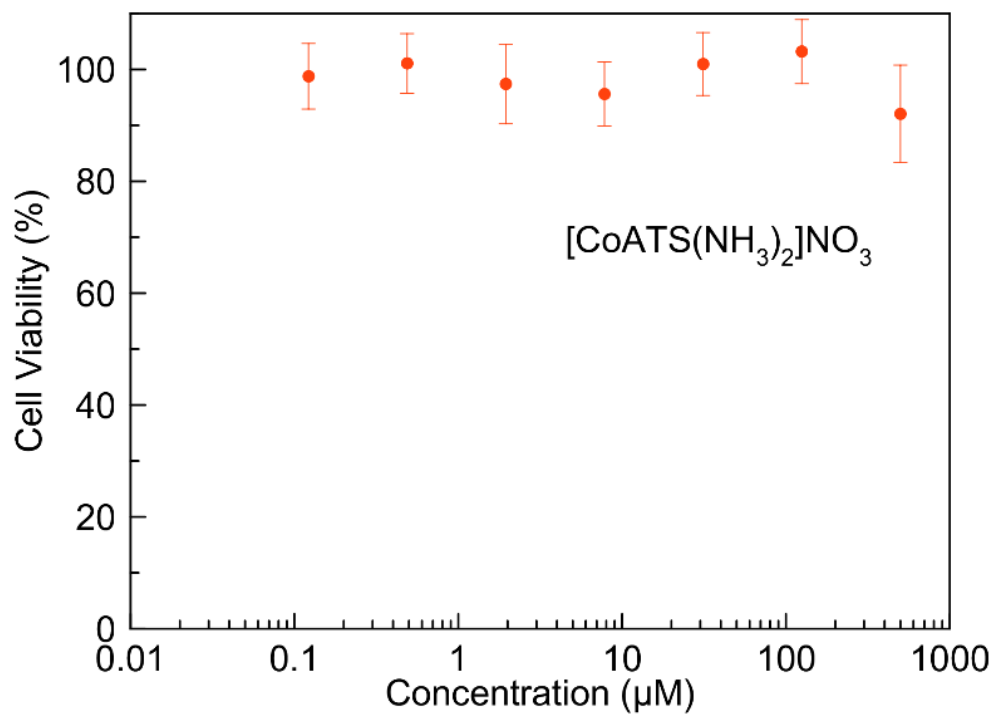


Figure S2.65. Dose-Response Curve of $[\text{Co}(\text{ATS})(\text{NH}_3)_2]^+$ in A549 Cells

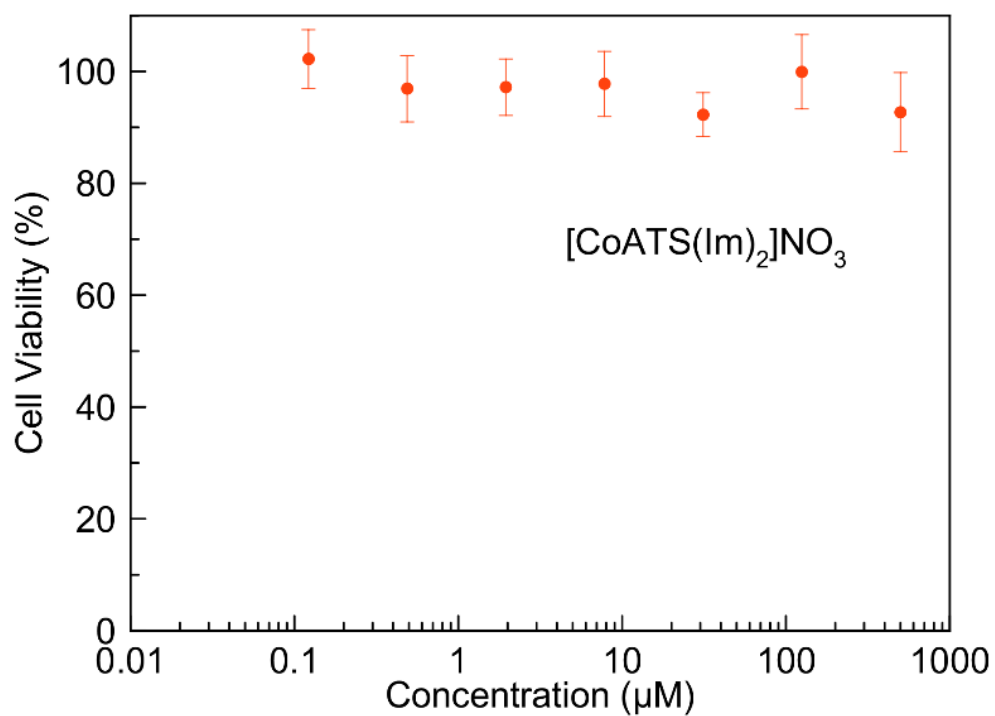


Figure S2.66. Dose-Response Curve of $[\text{Co}(\text{ATS})(\text{Im})_2]^+$ in A549 Cells

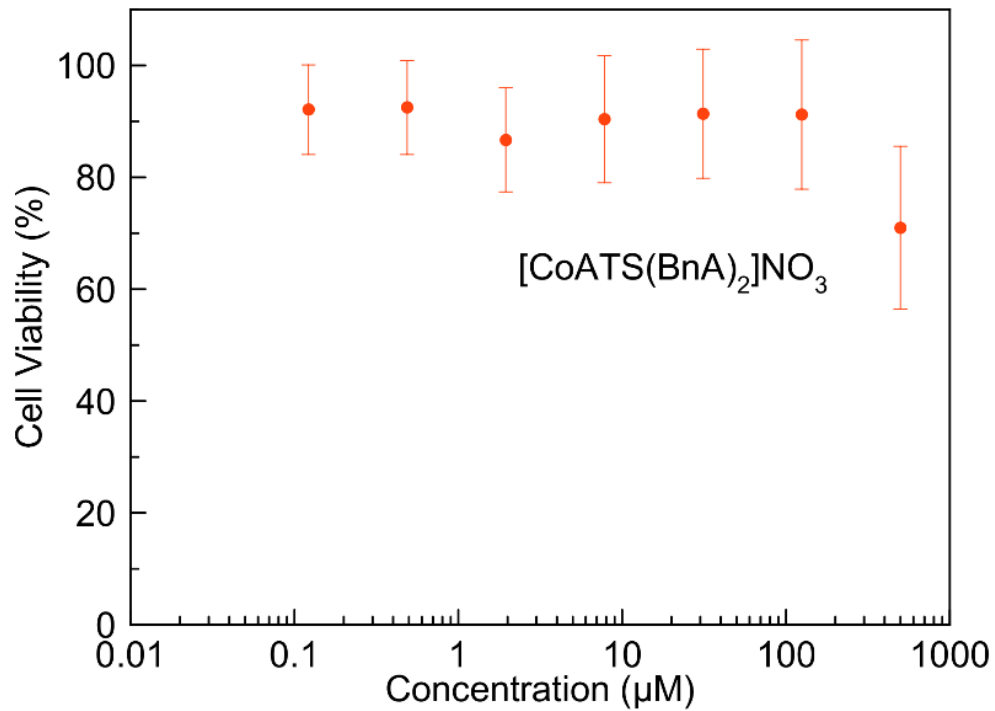


Figure S2.67. Dose-Response Curve of $[\text{Co}(\text{ATS})(\text{BnA})_2]^+$ in A549 Cells

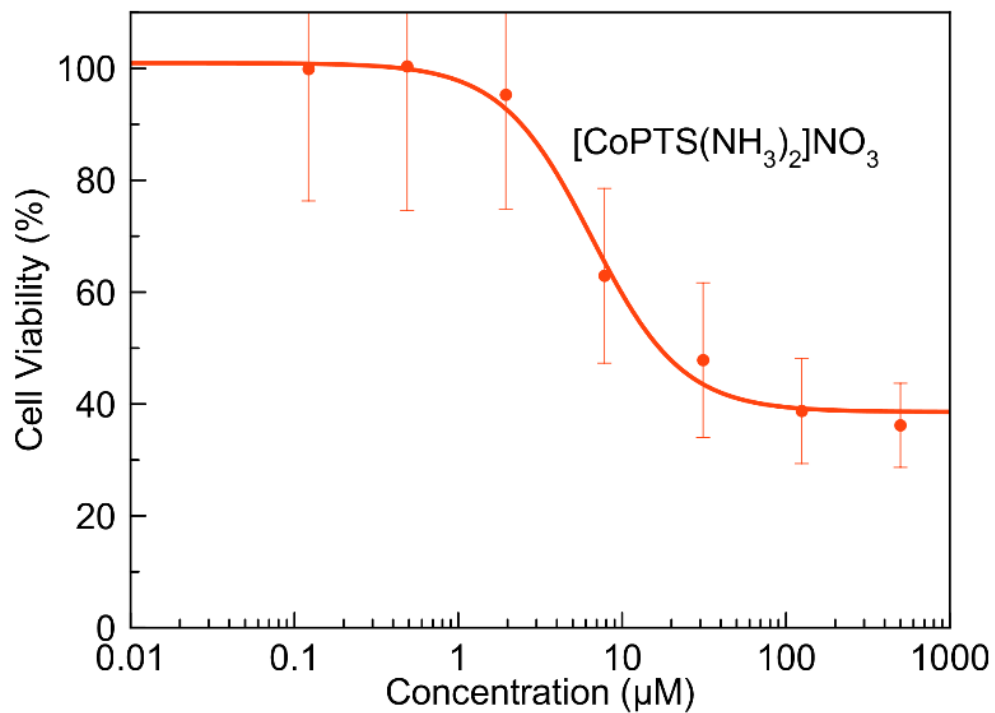


Figure S2.68. Dose-Response Curve of $[\text{Co}(\text{PTS})(\text{NH}_3)_2]^+$ in A549 Cells

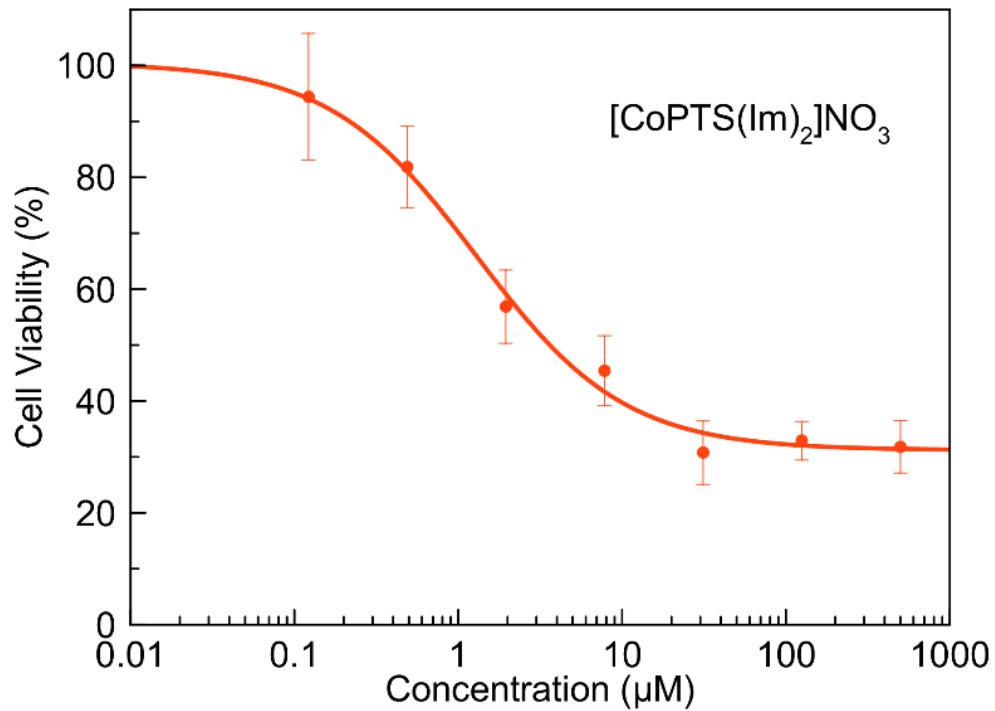


Figure S2.69. Dose-Response Curve of $[\text{Co}(\text{PTS})(\text{Im})_2]^+$ in A549 Cells

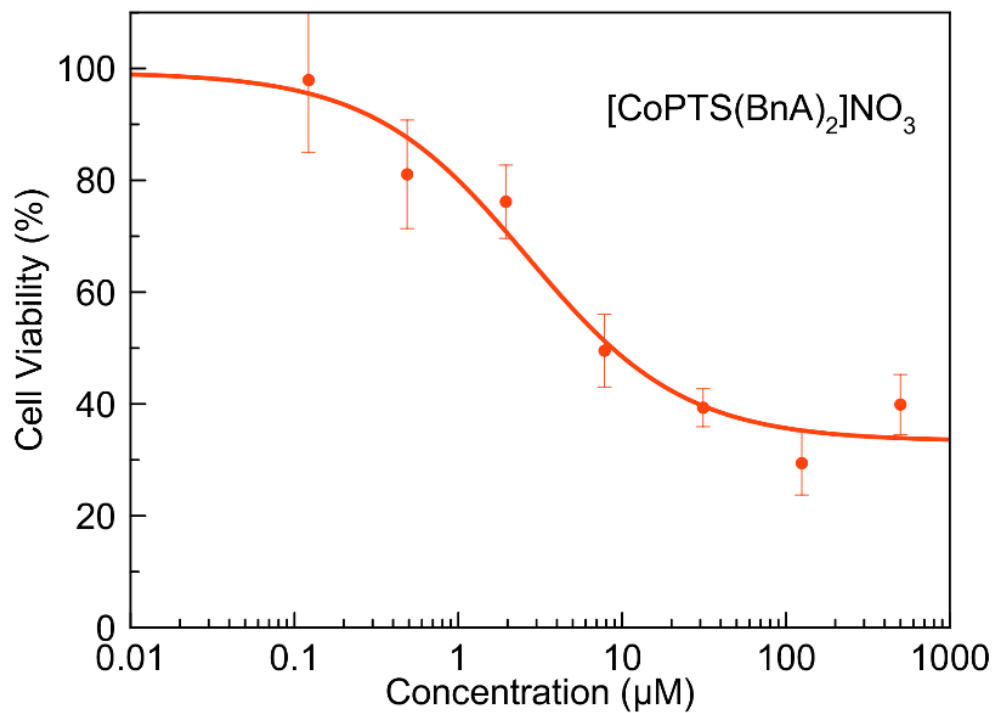


Figure S2.70. Dose-Response Curve of $[\text{Co}(\text{PTS})(\text{BnA})_2]^+$ in A549 Cells

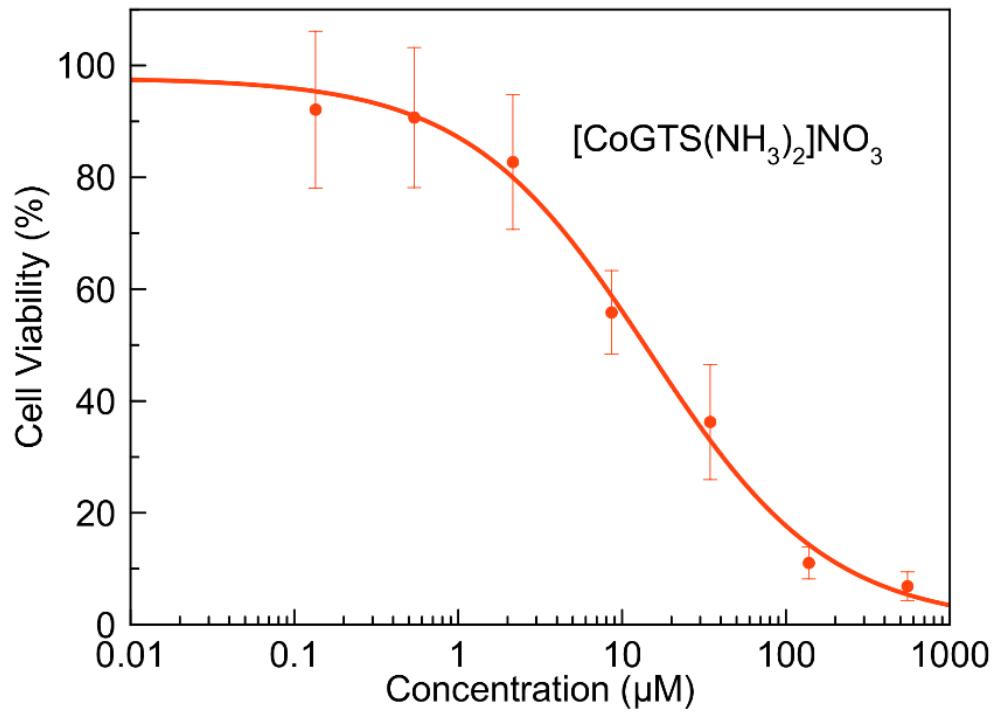


Figure S2.71. Dose-Response Curve of [Co(GTS)(NH₃)₂]⁺ in A549 Cells

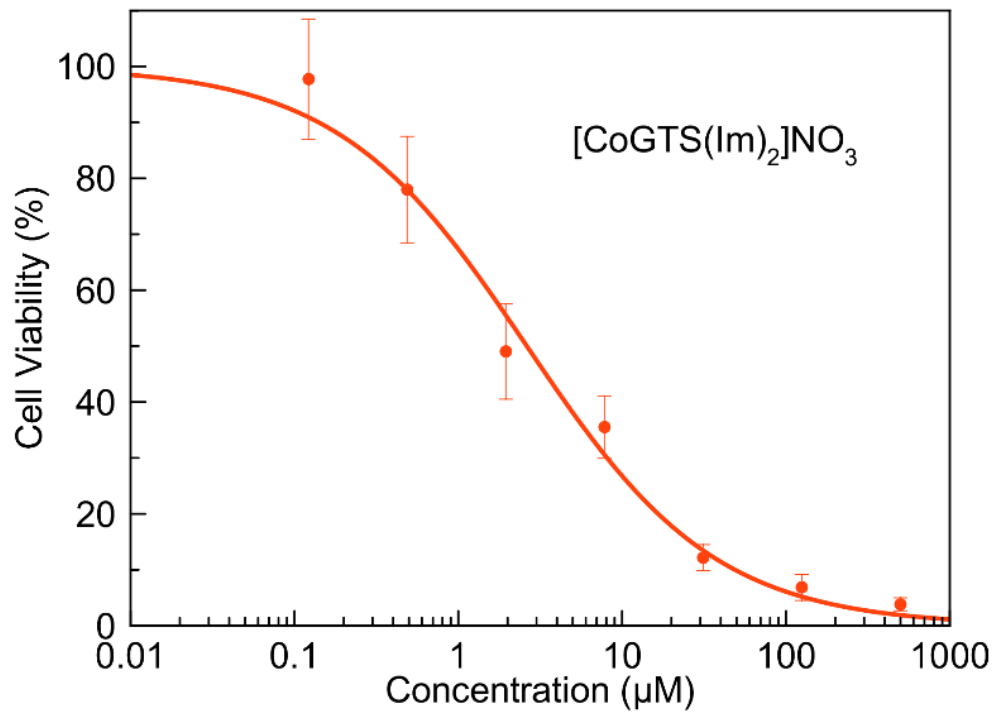


Figure S2.72. Dose-Response Curve of [Co(GTS)(Im)₂]⁺ in A549 Cells

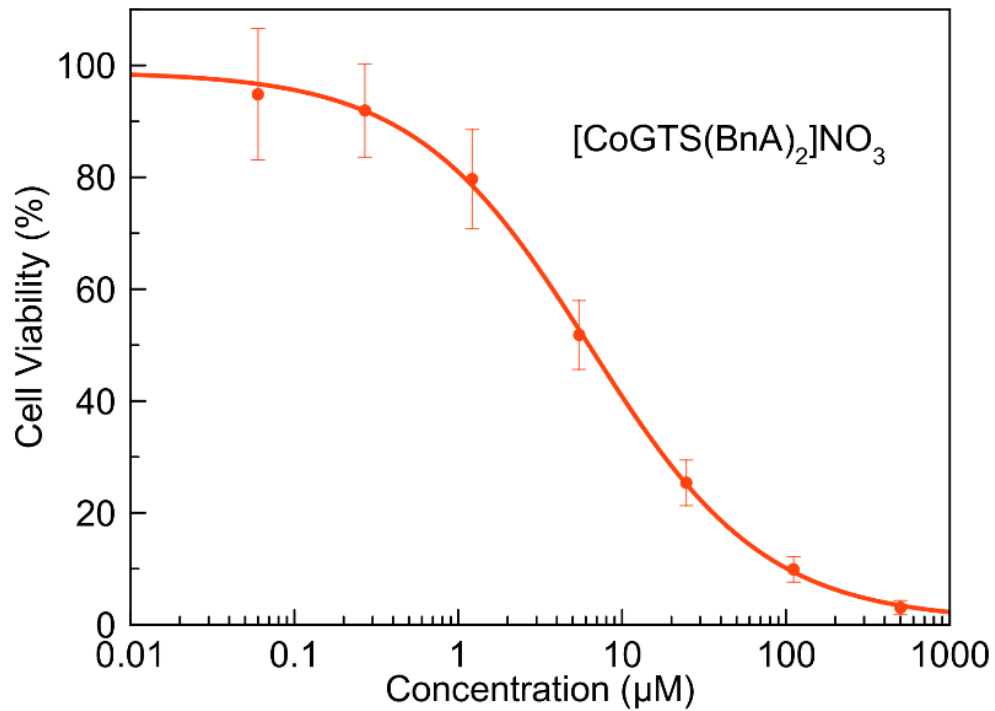


Figure S2.73. Dose-Response Curve of $[\text{Co}(\text{GTS})(\text{BnA})_2]^+$ in A549 Cells

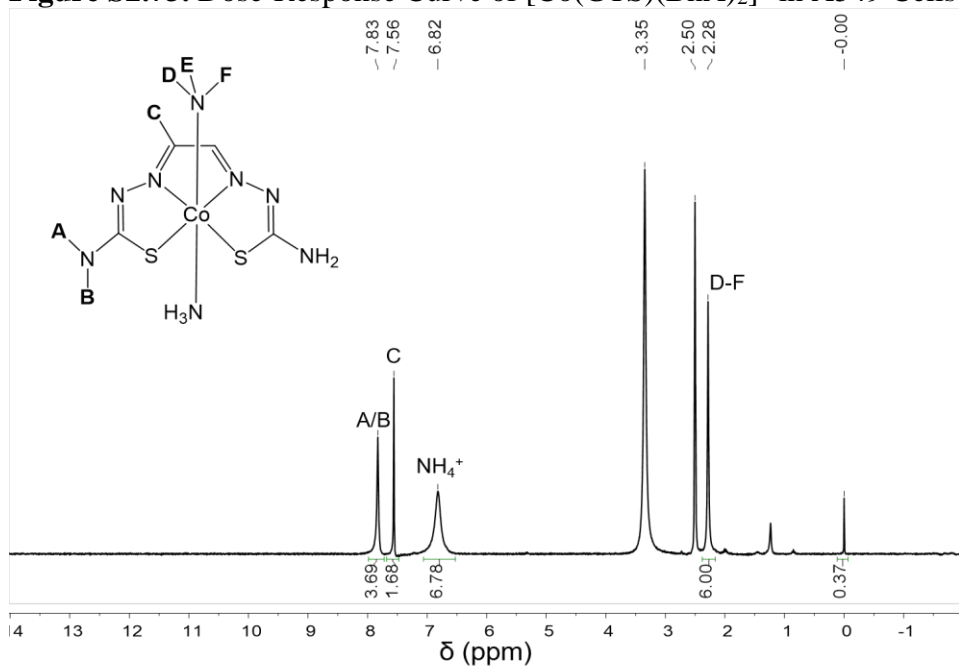


Figure S2.74. ^1H NMR spectrum of $[\text{Co}(\text{GTS})(\text{NH}_3)_2]^+$ and ammonium tetrathiomolybdate immediately after mixing ($\text{DMSO}-d_6$, 400 MHz, 298 K)

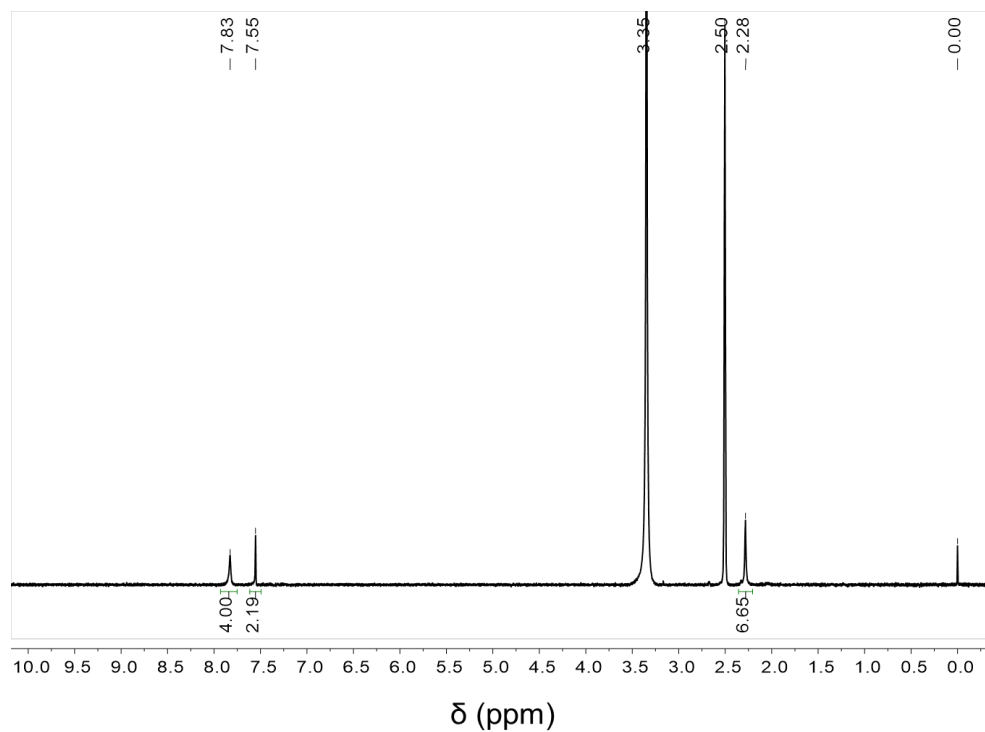


Figure S2.75. ^1H NMR spectrum of $[\text{Co}(\text{GTS})(\text{NH}_3)_2]^+$ and ammonium tetrathiomolybdate 1 day after mixing ($\text{DMSO-}d_6$, 400 MHz, 298 K)

References

- 1 J. A. Joyce, *Cancer Cell*, 2005, **7**, 513–520.
- 2 T. W. Hambley, *Aust. J. Chem*, 2008, **61**, 647–653.
- 3 Q.-T. Le and D. Courter, *Cancer Metastasis Rev.*, 2008, **27**, 351–62.
- 4 W. R. Wilson and M. P. Hay, *Nat. Rev. Cancer*, 2011, **11**, 393–410.
- 5 J. W. Wojtkowiak, D. Verduzco, K. J. Schramm and R. J. Gillies, *Mol. Pharm.*, 2011, **8**, 2032–2038.
- 6 M. D. Hall, T. W. Failes, N. Yamamoto and T. W. Hambley, *Dalton Trans.*, 2007, 3983–3990.
- 7 E. Reisner, V. B. Arion, B. K. Keppler and A. J. L. Pombeiro, *Inorg. Chim. Acta*, 2008, **361**, 1569–1583.
- 8 U. Jungwirth, C. R. Kowol, B. K. Keppler, C. G. Hartinger, W. Berger and P. Heffeter, *Antioxid. Redox Signal.*, 2011, **15**, 1085–1127.
- 9 N. Graf and S. J. Lippard, *Adv. Drug Deliv. Rev.*, 2012, **64**, 993–1004.
- 10 A. Böttcher, T. Takeuchi, K. I. Hardcastle, T. J. Meade, H. B. Gray, D. Cwikel, M. Kapon and Z. Dori, *Inorg. Chem.*, 1997, **36**, 2498–2504.
- 11 T. Takeuchi, A. Böttcher, C. M. Quezada, M. I. Simon, T. J. Meade and H. B. Gray, *J. Am. Chem. Soc.*, 1998, **120**, 8555–8556.
- 12 A. K. Renfrew, N. S. Bryce and T. W. Hambley, *Chem. Sci.*, 2013, **4**, 3731–3739.
- 13 M. C. Heffern, V. Reichova, J. L. Coomes, A. S. Harney, E. A. Bajema and T. J. Meade, *Inorg. Chem.*, 2015, **54**, 9066–9074.
- 14 C. R. Munteanu and K. Suntharalingam, *Dalton Trans.*, 2015, **44**, 13796–13808.
- 15 A. K. Renfrew, N. S. Bryce and T. Hambley, *Chem. - A Eur. J.*, 2015, **21**, 15224–15234.
- 16 P. B. Cressey, A. Eskandari, P. M. Bruno, C. Lu, M. T. Hemann and K. Suntharalingam, *ChemBioChem*, 2016, **17**, 1713–1718.
- 17 I. C. A. de Souza, L. V. Faro, C. B. Pinheiro, D. T. G. Gonzaga, F. de C. da Silva, V. F. Ferreira, F. da S. Miranda, M. Scarpellini and M. Lanznaster, *Dalton Trans.*, 2016, **45**, 13671–13674.
- 18 C. V. Garcia, G. L. Parrilha, B. L. Rodrigues, P. J. S. Barbeira, R. M. Clarke, T. Storr and H. Beraldo, *Polyhedron*, 2017, **124**, 86–95.
- 19 T. R. Todorović, J. Vukašinović, G. Portalone, S. Suleiman, N. Gligorijević, S. Bjelogrić, K. Jovanović, S. Radulović, K. Anđelković, A. Cassar, N. R. Filipović and P. Schembri-Wismayer, *Med. Chem. Commun.*, 2017, **8**, 103–111.
- 20 T. Takeuchi, A. Böttcher, C. M. Quezada, T. J. Meade and H. B. Gray, *Bioorg. Med. Chem.*, 1999, **7**, 815–819.
- 21 A. S. Harney, J. Lee, L. M. Manus, P. Wang, D. M. Ballweg, C. LaBonne and T. J. Meade, *Proc. Natl. Acad. Sci. U. S. A.*, 2009, **106**, 13667–72.
- 22 J. Y.-C. Chang, R. J. Stevenson, G.-L. Lu, P. J. Brothers, G. R. Clark, W. A. Denny and D. C. Ware, *Dalton Trans.*, 2010, **39**, 11535–50.
- 23 B. J. Kim, T. W. Hambley and N. S. Bryce, *Chem. Sci.*, 2011, **2**, 2135–2142.
- 24 R. R. Hurtado, A. S. Harney, M. C. Heffern, R. J. Holbrook, R. A. Holmgren

- and T. J. Meade, *Mol. Pharm.*, 2012, **9**, 325–333.
- 25 N. Yamamoto, A. K. Renfrew, B. J. Kim, N. S. Bryce and T. W. Hambley, *J. Med. Chem.*, 2012, **55**, 11013–11021.
- 26 J. Y.-C. Chang, G.-L. Lu, R. J. Stevenson, P. J. Brothers, G. R. Clark, K. J. Botting, D. M. Ferry, M. Terceel, W. R. Wilson, W. A. Denny and D. C. Ware, *Inorg. Chem.*, 2013, **52**, 7688–7698.
- 27 M. C. Heffern, N. Yamamoto, R. J. Holbrook, A. L. Eckermann and T. J. Meade, *Curr. Opin. Chem. Biol.*, 2013, **17**, 189–96.
- 28 A. K. Renfrew, *Metallomics*, 2014, **6**, 1324–35.
- 29 F. A. French and B. L. Freedlander, *Cancer Res.*, 1958, **18**, 1290–1300.
- 30 F. A. French and B. L. Freedlander, *Cancer Res.*, 1960, **20**, 505–538.
- 31 B. A. Gingras, T. Suprunchuk and C. H. Bayley, *Can. J. Chem.*, 1962, **40**, 1053–1059.
- 32 P. J. Jansson, T. Yamagishi, A. Arvind, N. Seebacher, E. Gutierrez, A. Stacy, S. Maleki, D. Sharp, S. Sahni and D. R. Richardson, *J. Biol. Chem.*, 2015, **290**, 9588–603.
- 33 A. L. Vāvere and J. S. Lewis, *Dalton Trans.*, 2007, 4893–4902.
- 34 A. Obata, E. Yoshimi, A. Waki, J. S. Lewis, N. Oyama, M. J. Welch, H. Saji, Y. Yonekura and Y. Fujibayashi, *Ann. Nucl. Med.*, 2001, **15**, 499–504.
- 35 R. I. Maurer, P. J. Blower, J. R. Dilworth, C. A. Reynolds, Y. Zheng and G. E. D. Mullen, *J. Med. Chem.*, 2002, **45**, 1420–31.
- 36 Z. Xiao, P. S. Donnelly, M. Zimmermann and A. G. Wedd, *Inorg. Chem.*, 2008, **47**, 4338–4347.
- 37 K. A. Price, P. J. Crouch, I. Volitakis, B. M. Paterson, S. Lim, P. S. Donnelly and A. R. White, *Inorg. Chem.*, 2011, **50**, 9594–9605.
- 38 P. S. Donnelly, J. R. Liddell, S. Lim, B. M. Paterson, M. A. Cater, M. S. Savva, A. I. Mot, J. L. James, I. A. Trounce, A. R. White and P. J. Crouch, *Proc. Natl. Acad. Sci. U. S. A.*, 2012, **109**, 47–52.
- 39 D. Xie, T. L. King, A. Banerjee, V. Kohli and E. L. Que, *J. Am. Chem. Soc.*, 2016, **138**, 2937–2940.
- 40 C. Stefani, Z. Al-Eisawi, P. J. Jansson, D. S. Kalinowski and D. R. Richardson, *J. Inorg. Biochem.*, 2015, **152**, 20–37.
- 41 B. M. Paterson and P. S. Donnelly, *Chem. Soc. Rev.*, 2011, **40**, 3005–3018.
- 42 L. M. Manus, R. J. Holbrook, T. A. Atesin, M. C. Heffern, A. S. Harney, A. L. Eckermann and T. J. Meade, *Inorg. Chem.*, 2013, **52**, 1069–1076.
- 43 A. Yamasaki, *J. Coord. Chem.*, 1991, **24**, 211–260.
- 44 J. Mason, *Chem. Rev.*, 1987, **87**, 1299–1312.
- 45 A. Medek, V. Frydman and L. Frydman, *Proc. Natl. Acad. Sci. U. S. A.*, 1997, **94**, 14237–14242.
- 46 R. Bramley, M. Brorson, A. M. Sargeson and C. E. Schaeffer, *J. Am. Chem. Soc.*, 1985, **107**, 2780–2787.
- 47 S. I. Kirin, I. Ott, R. Gust, W. Mier, T. Weyhermüller and N. Metzler-Nolte, *Angew. Chemie Int. Ed.*, 2008, **47**, 955–959.
- 48 J. L. Dearling, J. S. Lewis, D. W. McCarthy, M. J. Welch and P. J. Blower, *Chem. Commun.*, 1998, 2531–2532.

- 49 P. Burgman, J. A. O'Donoghue, J. S. Lewis, M. J. Welch, J. L. Humm and C. C. Ling, *Nucl. Med. Biol.*, 2005, **32**, 623–630.
- 50 E. M. Zeman, J. M. Brown, M. J. Lemmon, V. K. Hirst and W. W. Lee, *Int. J. Radiat. Oncol. Biol. Phys.*, 1986, **12**, 1239–42.
- 51 S. B. Reddy and S. K. Williamson, *Expert Opin. Investig. Drugs*, 2009, **18**, 77–87.
- 52 M. Ahmadi, Z. Ahmadihosseini, S. J. Allison, S. Begum, K. Rockley, M. Sadiq, S. Chintamaneni, R. Lokwani, N. Hughes and R. M. Phillips, *Br. J. Pharmacol.*, 2014, **171**, 224–36.
- 53 S. Strese, M. Fryknäs, R. Larsson and J. Gullbo, *BMC Cancer*, 2013, **13**, 331–342.
- 54 K. Y. Djoko, P. S. Donnelly and A. G. Mcewan, *Metallomics*, 2014, **6**, 2250–2259.
- 55 D. B. Lovejoy, P. J. Jansson, U. T. Brunk, J. Wong, P. Ponka and D. R. Richardson, *Cancer Res.*, 2011, **71**, 5871–5880.
- 56 G. J. Brewer, R. D. Dick, D. K. Grover, V. LeClaire, M. Tseng, M. Wicha, K. Pienta, B. G. Redman, T. Jahan, V. K. Sondak, M. Strawderman, G. LeCarpentier and S. D. Merajver, *Clin. Cancer Res.*, 2000, **6**, 1–10.
- 57 D. S. Kalinowski, P. Quach and D. R. Richardson, *Future Med. Chem.*, 2009, **1**, 1143–1151.
- 58 J. R. Dilworth and R. Hueting, *Inorg. Chim. Acta*, 2012, **389**, 3–15.
- 59 X. Zhong, J. Yi, J. Sun, H.-L. Wei, W.-S. Liu and K.-B. Yu, *Eur. J. Med. Chem.*, 2006, **41**, 1090–1092.
- 60 A. S. El-Tabl, M. M. A. El-wahed and A. M. S. M. Rezk, *Spectrochim. Acta Part A Mol. Biomol. Spectrosc.*, 2014, **117**, 772–788.
- 61 J. L. Dearling, J. S. Lewis, G. E. Mullen, M. J. Welch and P. J. Blower, *J. Biol. Inorg. Chem.*, 2002, **7**, 249–259.
- 62 A. B. P. Lever, *Inorg. Chem.*, 1990, **29**, 1271–1285.
- 63 V. V Pavlishchuk and A. W. Addison, *Inorg. Chim. Acta*, 2000, **298**, 97–102.
- 64 G. Navon and R. Panigel, *Inorg. Chem.*, 1989, **28**, 1405–1407.
- 65 L. Helm and A. E. Merbach, *Chem. Rev.*, 2005, **105**, 1923–1960.
- 66 D. Palanimuthu, S. Vijay Shinde, K. Somasundaram and A. G. Samuelson, *J. Med. Chem.*, 2013, **56**, 722–734.
- 67 F. N. Akladios, S. D. Andrew and C. J. Parkinson, *J. Biol. Inorg. Chem.*, 2016, **21**, 931–944.
- 68 X. Xia, M. S. Owen, R. E. C. Lee and S. Gaudet, *Cell Death Dis.*, 2014, **5**, e1261.
- 69 M. Fallahi-Sichani, S. Honarnejad, L. M. Heiser, J. W. Gray and P. K. Sorger, *Nat. Chem. Biol.*, 2013, **9**, 708–714.
- 70 N. Yamamoto, S. Danos, P. D. Bonnitcha, T. W. Failes, E. J. New and T. W. Hambley, *J. Biol. Inorg. Chem.*, 2008, **13**, 861–871.
- 71 D. R. Richardson, P. C. Sharpe, D. B. Lovejoy, D. Senaratne, D. S. Kalinowski, M. Islam and P. V. Bernhardt, *J. Med. Chem.*, 2006, **49**, 6510–6521.
- 72 A. E. Stacy, D. Palanimuthu, P. V. Bernhardt, D. S. Kalinowski, P. J. Jansson and D. R. Richardson, *J. Med. Chem.*, 2016, **59**, 4965–4984.

- 73 H. Irving and R. J. P. Williams, *J. Chem. Soc.*, 1953, 3192–3210.
- 74 G. R. Fulmer, A. J. M. Miller, N. H. Sherden, H. E. Gottlieb, A. Nudelman, B. M. Stoltz, J. E. Bercaw and K. I. Goldberg, *Organometallics*, 2010, **29**, 2176–2179.
- 75 N. G. Connelly and W. E. Geiger, *Chem. Rev.*, 1996, **96**, 877–910.
- 76 G. M. Sheldrick, *Acta Cryst.*, 2015, **A71**, 3–8.
- 77 G. M. Sheldrick, *Acta Cryst.*, 2008, **A64**, 112–122.
- 78 P. Müller, *Crystallogr. Rev.*, 2009, **15**, 57–83.
- 79 R. I. Freshney, *Culture of Animal Cells*, John Wiley & Sons, Inc., Hoboken, NJ, USA, 5th edn., 2005.
- 80 A. E. Egger, C. Rappel, M. A. Jakupec, C. G. Hartinger, P. Heffeter and B. K. Keppler, *J. Anal. At. Spectrom.*, 2009, **24**, 51–61.

CHAPTER 3

Physical Properties, Ligand Substitution Reactions, and Biological Activity of Co(III)-Schiff Base Complexes

Reproduced in part with permission from: A. Paden King, Hendryck A. Gellineau, Samantha N. MacMillan, and Justin J. Wilson. *Dalton Trans.* **2019**, 48, 5987-6002.

Reproduced by permission of The Royal Society of Chemistry.

Introduction

In Chapter 2, we reported a family of cobalt(III)-bis(thiosemicarbazone) (BTSC) complexes with powerful anticancer activity. We found that these complexes operate by first undergoing ligand substitution to yield a copper-BTSC complex that is the cytotoxic agent. However, despite the complexes' redox activity in the biologically relevant window, these compounds do not display a large difference in activity in cells cultured in hypoxic environments versus cells cultured in normal conditions. In order to improve the hypoxia selectivity of these and other Co(III) compounds, it is necessary to understand their activation pathways and ligand exchange behavior. The electrochemical and thermal reactivity of cobalt have been extensively investigated in previous works. In the +3 oxidation state, this ion is kinetically inert, undergoing ligand substitution reactions on a much slower timescale than its neighbors on the periodic table.¹⁻³ In contrast, the +2 oxidation state of cobalt is labile. The dichotomy between the inertness of these two oxidation states has enabled the development of Co(III) prodrugs that undergo reduction in biological systems to form labile Co(II) complexes, which subsequently release their ligands as a cytotoxic payload.⁴⁻⁷ This reductive release strategy has been investigated for several different classes of Co(III) complexes with the ultimate objective of selectively targeting hypoxic environments.⁸⁻¹⁷

In addition to exploiting the Co(III) redox properties for developing redox-activated prodrugs, the slow ligand exchange kinetics of Co(III) have been used to design enzyme inhibitors.^{18,19} Within this class of Co(III) complexes, the most studied are those of the general structural formula $[\text{Co}(\text{acacen})(\text{L})_2]^+$ where acacen = *N,N'*-bis(acetylaceton)ethylenediamine and L is usually a neutral N-donor ligand. These

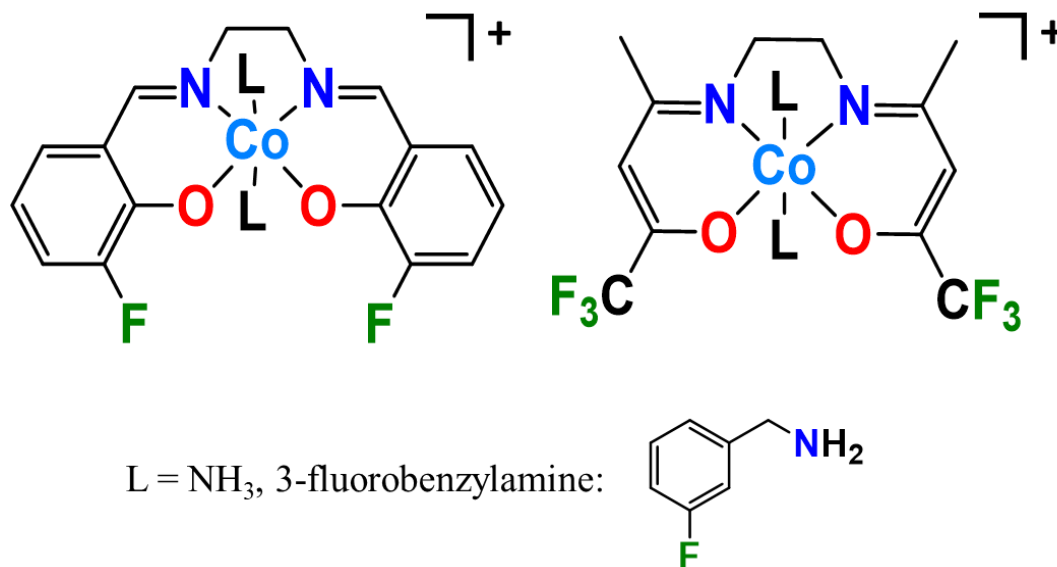
octahedral $[\text{Co}(\text{acacen})(\text{L})_2]^+$ complexes undergo ligand substitution reactions with histidine residues in the active sites of proteins to irreversibly inhibit them.^{20–24} Because of their efficacy against serine proteases, these complexes have been explored for the treatment of viruses, such as HIV and herpes, which rely heavily on these enzymes.^{25–27} For example, the compound $[\text{Co}(\text{acacen})(2\text{-methylimidazole})_2]^+$ is currently in clinical trials for the treatment of herpes.^{28,29} Functionalization of the ligand scaffold of these complexes allows for fine tuning of the ligand substitution rate, which can dramatically affect their enzyme-inhibitory activities.^{30–32} Furthermore, the facile synthesis of these complexes has allowed for the design of light-activated^{33,34} and targeted versions of these inhibitors to improve their selectivity.^{18,20,35}

In this Chapter, we aimed to investigate the physical properties, ligand exchange kinetics, and biological activity of a small subset of $[\text{Co}(\text{Schiff base})(\text{L})_2]^+$ complexes with the objective of understanding ligand substitution processes in this class of compounds and discern how they might be modified to give rise to hypoxia selectivity. The complexes shown in **Chart 3.1**, bearing either 3-fluorosalicylaldehyde ethylenediamine- (3F-salen) or trifluoroacetylacetone ethylenediamine- (tfacen) based equatorial ligands and NH_3 or 3-fluorobenzylamine (3F-BnNH₂) axial ligands, were chosen to investigate the role of both the equatorial and axial ligands on their activation mechanisms. The use of these fluorinated ligands was motivated by several reasons. First, the presence of fluorine in these complexes provides a useful NMR handle for studying their speciation in solution via ¹⁹F NMR spectroscopy.^{36–40} Second, equatorial ligands containing electron-withdrawing groups, such as fluorine, give rise to Co(III) complexes with slow ligand substitution kinetics,²³ which may be

more therapeutically useful. Finally, novel imaging opportunities are available for fluorine-containing compounds via ^{19}F magnetic resonance imaging or ^{18}F positron emission tomography.^{36,39–43} The enhanced metabolic stability of C–F bonds also make the use of this element in drugs ideal, as reflected by the fact that over 20% of currently administered drugs contain fluorine.⁴⁴

After synthesizing the complexes and confirming their basic structure and stability, the complexes were analyzed via cyclic voltammetry to ascertain the favorability and reversibility of reduction, and their ligand exchange rates, activation parameters, and reaction mechanisms were evaluated. These properties were then correlated with the relative cytotoxicity and uptake of the complexes in cancer cells. The combined results provide valuable insight into the both the thermal and electrochemical reactivity of this class of complexes and may help future researchers to design Co(III) complexes as enzyme inhibitors or cytotoxic agents.

Chart 3.1. Structures of the $[\text{Co}(\text{Schiff base})(\text{L})_2]^+$ Complexes Investigated in This Chapter



Results

Synthesis of $[\text{Co}(\text{Schiff base})(\text{L})_2]\text{Cl}$ Complexes

The four complexes, shown in **Chart 3.1**, were targeted to study the effects of both the equatorial and axial ligands on the nature of the biological activity of this class of $[\text{Co}(\text{Schiff base})(\text{L})_2]^+$ complexes. The syntheses were straightforward, following closely with procedures found in the literature for related complexes.⁴⁵ Briefly, a mixture of $\text{CoCl}_2 \cdot 6\text{H}_2\text{O}$ and 1 equiv of the Schiff base ligand was heated to reflux in methanol for 1 h to yield a dark green solution. This dark green solution, which contains an uncharacterized intermediate, was treated with an excess of the axial ligand to form the desired red-brown Co(III) complexes. As observed during the synthesis of related Co(III) complexes, the oxidation of the initial Co(II) starting material is most likely mediated by atmospheric oxygen. The low-spin diamagnetic nature of these complexes was confirmed by ^1H NMR spectroscopy, which showed

sharp resonances within the range of 0 to 10 ppm. Further characterization of these complexes was provided by mass spectrometry, showing the expected ion peaks for the intact cationic complexes. $^{13}\text{C}\{^1\text{H}\}$ NMR spectroscopy further confirmed the structure and symmetry of the complexes. No suitable $^{13}\text{C}\{^1\text{H}\}$ NMR spectrum could be obtained for $[\text{Co}(\text{3F-salen})(\text{NH}_3)_2]^+$ due to its poor solubility. In addition to these spectroscopic methods, elemental analysis and HPLC further verified these compounds to be greater than 95% pure. (**Figures S3.1–S3.21**).

X-Ray Crystallography

The complexes $[\text{Co}(\text{3F-salen})(\text{3F-BnNH}_2)_2]^+$, $[\text{Co}(\text{tfacen})(\text{3F-BnNH}_2)_2]^+$, and $[\text{Co}(\text{tfacen})(\text{NH}_3)_2]^+$ were further characterized by single-crystal X-ray diffraction. The crystal structures are shown in **Figure 3.1**, and selected interatomic distances and angles are collected in **Table 3.2**. The Co(III) center attains the expected pseudo-octahedral geometry comprising the four donor atoms of the Schiff base ligand in the equatorial plane and two of the monodentate nitrogen donors in a trans arrangement. In these three structures, the equatorial ligand does not reside in a perfectly planar configuration, a feature that is most notable for $[\text{Co}(\text{3F-salen})(\text{3F-BnNH}_2)_2]^+$. The equatorial Co–N and Co–O distances vary slightly among the three complexes. These distances are longest for $[\text{Co}(\text{tfacen})(\text{NH}_3)_2]^+$, which range from 1.904 to 1.910 Å, and shortest for $[\text{Co}(\text{3F-salen})(\text{3F-BnNH}_2)_2]^+$, with values between 1.894 to 1.899 Å. The longer distances observed for $[\text{Co}(\text{tfacen})(\text{NH}_3)_2]^+$ may be a result of the strong electron donating character of the axial NH_3 ligand, which decreases the Lewis acidity of the metal center.⁴⁶ In comparing the axial ligand distances, this trend is the

opposite. Namely, the axial Co–N distances of $[\text{Co}(\text{tfacen})(3\text{F-BnNH}_2)_2]^+$ (1.972 Å) are longer than those of $[\text{Co}(\text{tfacen})(\text{NH}_3)_2]^+$ (1.967 and 1.961 Å). The smaller steric profile of the NH_3 may partly account for the shorter Co–N_{axial} distances in $[\text{Co}(\text{tfacen})(\text{NH}_3)_2]^+$ compared to $[\text{Co}(\text{tfacen})(3\text{F-BnNH}_2)_2]^+$.

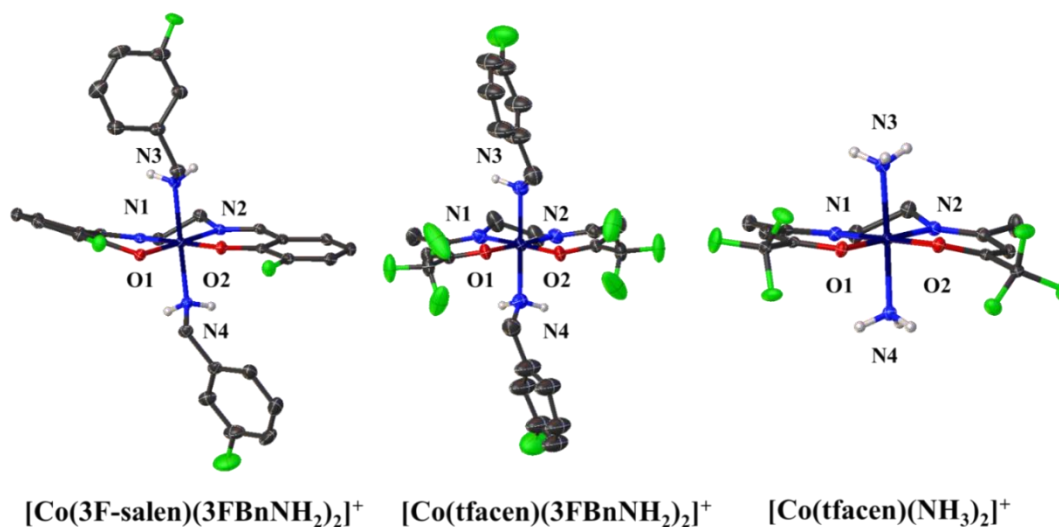


Figure 3.1. X-ray crystal structures of $[\text{Co}(3\text{F-salen})(3\text{F-BnNH}_2)_2]^+$, $[\text{Co}(\text{tfacen})(3\text{F-BnNH}_2)_2]^+$, and $[\text{Co}(\text{tfacen})(\text{NH}_3)_2]^+$. Ellipsoids are drawn at the 50% probability level. Non-acidic hydrogen atoms, counterions, and solvent molecules are omitted for clarity.

Table 3.1. Selected Interatomic Distances (Å) and Angles (°) of [Co(3F-salen)(3F-BnNH₂)₂]⁺, [Co(tfacen)(3F-BnNH₂)₂]⁺, and [Co(tfacen)(NH₃)₂]⁺^a

Interatomic Distance	[Co(3F-salen)(3F-BnNH ₂) ₂] ⁺	[Co(tfacen)(3F-BnNH ₂) ₂] ⁺ ^b	[Co(tfacen)(NH ₃) ₂] ⁺
Co–O ₁	1.8966(9)	1.898(3)	1.9106(9)
Co–O ₂	1.8938(9)		1.9069(10)
Co–N ₁	1.8942(11)	1.902(4)	1.9044(12)
Co–N ₂	1.8990(11)		1.9056(11)
Co–N ₃	1.9762(12)	1.972(4)	1.9670(12)
Co–N ₄	1.9803(12)		1.9614(12)
Angle	[Co(3F-salen)(3F-BnNH ₂) ₂] ⁺	[Co(tfacen)(3F-BnNH ₂) ₂] ⁺	[Co(tfacen)(NH ₃) ₂] ⁺
O ₁ –Co–O ₂	86.98(4)	84.17(19)	84.08(4)
O ₁ –Co–N ₁	93.25(4)	178.40(15)	95.35(4)
O ₁ –Co–N ₂	178.48(5)	94.74(15)	178.66(5)
O ₁ –Co–N ₃	89.76(5)	90.47(16)	88.81(5)
O ₁ –Co–N ₄	89.68(4)	87.95(15)	88.72(5)
O ₂ –Co–N ₁	179.13(5)		179.07(5)
O ₂ –Co–N ₂	94.50(5)		94.61(5)
O ₂ –Co–N ₃	90.24(5)		90.75(5)
O ₂ –Co–N ₄	88.52(5)		89.11(5)
N ₁ –Co–N ₂	85.27(5)	86.3(3)	85.97(5)
N ₁ –Co–N ₃	90.60(5)	90.88(16)	89.96(5)
N ₁ –Co–N ₄	90.63(5)	90.67(16)	90.15(5)
N ₂ –Co–N ₃	89.90(5)		90.94(5)
N ₂ –Co–N ₄	90.69(5)		91.54(5)
N ₃ –Co–N ₄	178.67(5)	177.9(2)	177.52(5)

^a Atoms are labeled as indicated in Fig. 1. ^b This molecule resides on a crystallographic 2-fold rotation axis. Redundant distances and angles are omitted from the table.

⁵⁹Co NMR Spectroscopy

All four complexes were characterized by ⁵⁹Co NMR spectroscopy. The quadrupolar ⁵⁹Co nucleus is characterized by a ground state nuclear spin of $I = 7/2$ and is 100% naturally abundant. By virtue of its large quadrupole moment, this nucleus gives rise to broad NMR signals with linewidths ranging from a few hundred to over 20,000 Hz.⁴⁷ Both the chemical shift and linewidth of ⁵⁹Co NMR spectra convey valuable information about properties of the complex being measured, such as ligand field splitting and reduction potential.^{47–53} In particular, upfield chemical shifts arise from complexes with larger ligand field splitting, indicating that the chemical shift is a useful parameter for quantifying the donor strength of a given set of ligands. The

signal linewidth is dictated by the quadrupolar relaxation rate of the ^{59}Co nucleus, which is a function of the solution tumbling time and electric field gradient imposed by the ligand environment.⁵⁴ The ^{59}Co NMR chemical shifts and linewidths of all complexes are reported in **Table 3.2**, and representative ^{59}Co NMR spectra are shown in **Figure 3.2**. Other spectra are deposited in the **Supporting Information (Figure S322–S325)**.

Table 3.2. ^{59}Co NMR Chemical Shifts and Linewidths^a

Complex	δ (ppm)	$\nu_{1/2}$ (Hz)
$[\text{Co}(\text{3F-salen})(\text{NH}_3)_2]^{+b}$	8340	4900
$[\text{Co}(\text{3F-salen})(\text{3F-BnNH}_2)_2]^{+c}$	8600	10000
$[\text{Co}(\text{tfacen})(\text{NH}_3)_2]^{+b}$	8540	3800
$[\text{Co}(\text{tfacen})(\text{3F-BnNH}_2)_2]^{+c}$	8740	5800

^aChemical shifts are referenced to $\text{K}_3[\text{Co}(\text{CN})_6]$ in D_2O at 0 ppm. ^bObtained in D_2O .

^cObtained in $\text{MeOD-}d_4$.

In comparison to complexes bearing axial 3F-BnNH₂ ligands, those with axial NH₃ ligands give rise to signals that have narrower linewidths and are shifted approximately 200 ppm upfield. This upfield shift reflects the greater ligand donor strength of NH₃ compared to 3F-BnNH₂. The equatorial ligands have an equally important effect upon the chemical shift. The ^{59}Co resonance of complexes containing the 3F-salen equatorial ligand are shifted approximately 200 ppm upfield and have broader linewidths compared with their tfacen counterparts.

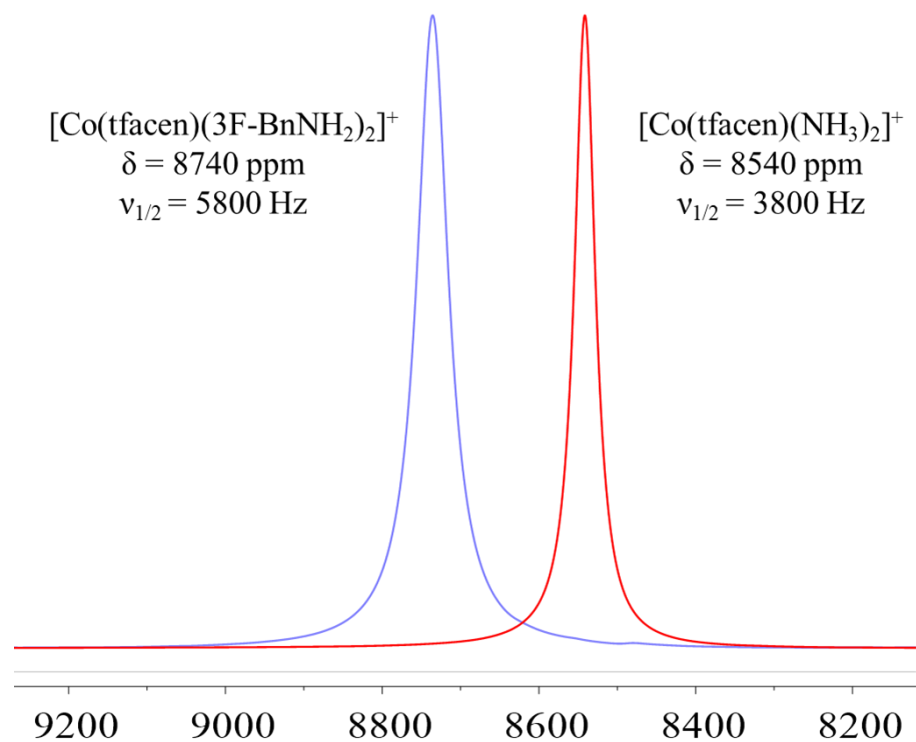


Figure 3.2. ^{59}Co (120 MHz) NMR spectra of $[\text{Co}(\text{tfacen})(\text{NH}_3)_2]^+$ (red) and $[\text{Co}(\text{tfacen})(3\text{F-BnNH}_2)_2]^+$ (blue), obtained in D_2O and $\text{MeOD-}d_4$, respectively at 295 K. Chemical shifts are reported relative to $\text{K}_3[\text{Co}(\text{CN})_6]$ in D_2O at 0 ppm.

Cyclic Voltammetry

Because of the potential importance of redox activation for this class of compounds, the electrochemical properties of the complexes were analyzed by cyclic voltammetry. The cyclic voltammograms of all complexes were obtained in DMF solution containing 0.1 M TBAP as the supporting electrolyte. A representative voltammogram of the complex $[\text{Co}(\text{tfacen})(3\text{F-BnNH}_2)_2]^+$ with redox features labeled is shown in **Figure 3.3**, and relevant reduction potentials for the complexes are reported in **Table 3.3**. Cyclic voltammograms of all complexes are shown in **Fig. S3.26-S3.29**.

Table 3.3. Electrochemical Parameters of [Co(Schiff base)(L)₂]⁺ Complexes^a

Complex	E _{pc} Co(III)/Co(II)	E _{1/2} Co(II)/Co(I)
[Co(3F-salen)(NH ₃) ₂] ⁺	-0.73	-1.07
[Co(3F-salen)(3F-BnNH ₂) ₂] ⁺	-0.58	-1.10
[Co(tfacen)(NH ₃) ₂] ⁺	-0.81	-1.31
[Co(tfacen)(3F-BnNH ₂) ₂] ⁺	-0.67	-1.31

^aPotentials are referenced to the SCE. Data were obtained in anhydrous DMF with 0.1 M TBAP using a glassy carbon working electrode. The scan rate was 0.1 V/s, and all data were obtained at 25 °C.

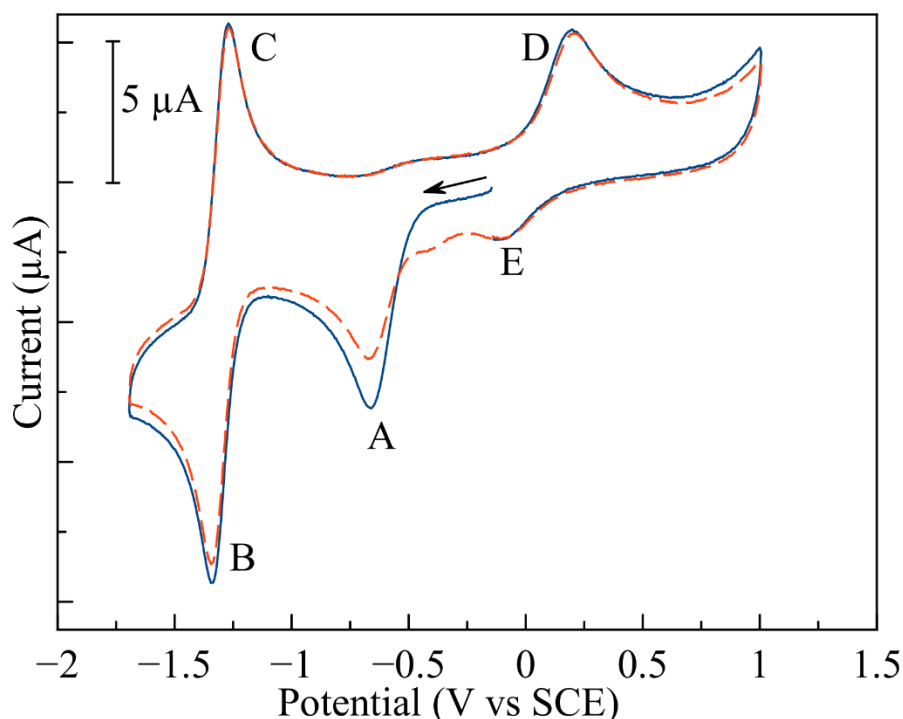


Figure 3.3. Cyclic voltammogram of [Co(tfacen)(3F-BnNH₂)₂]⁺ in DMF with 0.1 M TBAP supporting electrolyte. Potential is referenced to the SCE based on ferrocene (E_{1/2} 0.45 V vs SCE) as internal standard. The first scan is shown as a solid blue line, while the second scan is shown as a dashed, red line.

The electrochemical properties of these complexes are comparable to previously studied Co(III) Schiff base complexes.^{45,55} Upon scanning cathodically, an initial, irreversible reduction (A) is observed. The irreversibility of this feature, which corresponds to the Co(III)/Co(II) couple, arises from the concomitant loss of axial

ligands upon the reduction of Co(III). At more negative potentials, a quasi-reversible redox event, corresponding to the Co(II)/Co(I) couple (**B/C**) is detected. Because at this point the Co(II) complex has lost its axial ligands, the potential of couple **B/C** is only dependent on the equatorial Schiff base ligand. Scanning anodically, oxidation back to Co(III) (**D**) results in the formation of a new species, presumed to be the solvent adduct $[\text{Co}(\text{Schiff base})(\text{DMF})_2]^+$. Subsequent reduction of this solvent-bound species on following scans gives rise to a new reduction event (**E**), which occurs at a more positive potential compared to the intact complex.

The peak potential of the Co(III)/Co(II) couple is approximately 100 mV more negative for the tfacen complexes compared to those with the 3F-salen ligand. The axial ligands play a more pronounced role in modifying this couple; NH_3 complexes are 150 mV more negative than the corresponding 3F-Bn NH_2 complexes. As mentioned above, the Co(II)/Co(I) (**B/C**) feature is independent of the axial ligands. This couple is approximately 200 mV more negative for the tfacen complexes than the 3F-salen complexes.

Stability and Ligand Exchange

To assess the kinetic lability of the complexes, they were challenged with 25 equiv of MeIm, a model for a protein histidine side chain, and the ensuing axial ligand substitution reactions were monitored by ^{19}F NMR spectroscopy and RP-HPLC. Under these conditions, all of the complexes exhibit the same general behavior, undergoing two sequential stepwise axial ligand substitution reactions with MeIm (**Figure 3.4**). These reactions are conveniently monitored by ^{19}F NMR spectroscopy,

capitalizing on the sensitivity of the ^{19}F resonance of the equatorial Schiff base ligand with respect to the nature of the axial ligands. In monitoring the ^{19}F NMR spectrum over time, an initial new species, the monosubstituted complex, is detected, followed by the much slower formation of the disubstituted product. Representative plots of the concentration of all species over time are shown the ESI (**Figure S3.30-S3.33**). To confirm that the final products of these reactions were the disubstituted MeIm complexes $[\text{Co}(\text{3F-salen})(\text{MeIm})_2]\text{Cl}$ and $[\text{Co}(\text{tfacen})(\text{MeIm})_2]\text{Cl}$, we synthesized them independently and verified that their NMR spectroscopic signatures match those observed in our kinetics experiments (**Figure S3.34 and S3.35**). Complexes bearing axial 3F-BnNH₂ ligands, which contain fluorine, could also be monitored by the shift in the ^{19}F NMR signal of the 3F-BnNH₂. The rate of formation of the ^{19}F resonance of free 3F-BnNH₂ is consistent with the rate of decay of the corresponding resonance for the equatorial ligand of the starting complex. HPLC chromatograms of these reactions at different time points reveal the presence of three species, which are assigned to starting material, monosubstituted complex, and disubstituted complex. The relative peak integrations determined by NMR spectroscopy and HPLC are consistent, indicating that both methods are viable for determining the reaction rates.

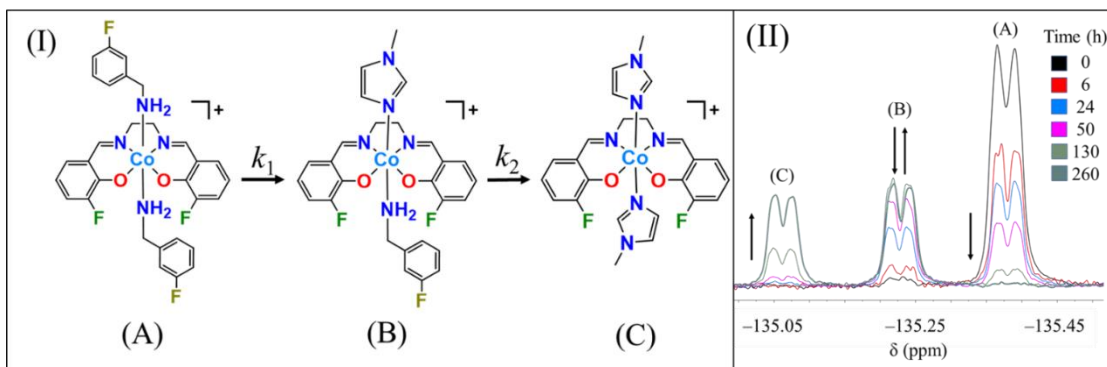


Figure 3.4. Panel I: Proposed ligand exchange pathway of $[\text{Co}(\text{Schiff base})(\text{L})_2]^+$ complexes by MeIm. Panel II: ^{19}F NMR spectra of $[\text{Co}(3\text{F-salen})(3\text{F-BnNH}_2)_2]^+$ over time. Chemical shifts are referenced to 0.5 mM NaTFA internal standard at -75.51 ppm.

Changing the concentration of MeIm while maintaining pseudo first-order conditions does not affect the rate of the reaction, indicating that the rate law for this reaction is zero-order with respect to this incoming ligand. For example, incubating with 200 equiv of MeIm rather than 25 equiv yields essentially the same rate constant (**Figure S3.36**). The observed pseudo first-order rate constants for the decay of the starting material are within an order of magnitude of those reported for Co(III) pentammine halide complexes.¹ The independence of the reaction rate on the concentration of MeIm is consistent with a dissociative ligand substitution pathway, a mechanism that has been observed for related $[\text{Co}(\text{acacen})(\text{L})_2]^+$ complexes.^{23,30,31} Co(III) ammine complexes are also known to undergo ligand substitution via the conjugate-base mechanism, which requires deprotonation of an ammine ligand to labilize the trans leaving group.² For this mechanism, the reaction rate is accelerated at higher pH values. When the substitution reaction was carried out at pH 8.3 instead of pH 7.4, no increase in the reaction rate was observed, indicating that the conjugate-base mechanism is not operative within this pH range (**Figure S3.37**).

Table 3.4. Axial Ligand Substitution Rate Constants of [Co(Schiff base)(L)₂]⁺ Complexes at 37 °C and Activation Parameters Determined by Eyring Analysis

Complex	$k_1 \times 10^7$ (s ⁻¹) (37 °C)	$k_2 \times 10^7$ (s ⁻¹) (37 °C)	$k_1 \Delta H^\ddagger$ (kJ/mol) ^a	$k_1 \Delta S^\ddagger$ (J · mol ⁻¹ · K ⁻¹) ^a	$k_2 \Delta H^\ddagger$ (kJ/mol) ^a	$k_2 \Delta S^\ddagger$ (J · mol ⁻¹ · K ⁻¹) ^a
[Co(3F-salen)(NH ₃) ₂] ⁺	64.5 ± 0.6	33.5 ± 0.2	115.3 ± 1.8	27.6 ± 0.9	130.1 ± 2.9	69.9 ± 2.3
[Co(3F-salen)(3F-BnNH ₂) ₂] ⁺	734 ± 40	164 ± 9	115.7 ± 3.7	50.2 ± 2.4	119.3 ± 1.8	49.3 ± 1.8
[Co(tfacen)(NH ₃) ₂] ⁺	39.6 ± 0.2	7.98 ± 0.7	115.6 ± 0.7	24.0 ± 0.2	137.4 ± 3.4	78.9 ± 2.9
[Co(tfacen)(3F-BnNH ₂) ₂] ⁺	172 ± 1.0	22.5 ± 0.7	115.0 ± 3.0	35.8 ± 1.3	129.4 ± 4.6	66.0 ± 3.7

^aValues obtained from Eyring-style plots of reaction rate constant versus temperature. The reported errors are the standard errors based on the least square regression analysis of the data.

The rate constants of these ligand substitution processes were determined by plotting the relative ¹⁹F NMR or HPLC peak areas of the starting complex and products versus time and fitting this data to a series of first-order integrated rate laws for a sequential A → B → C reaction pathway. (**Equation 3.1, Figure S3.30–S3.33**).^{56,57} The resulting pseudo first-order rate constants are given in **Table 3.4**, and representative data demonstrating the concentrations of all species over time are shown in **Figure 3.5**. The rate constant for the second ligand substitution step was determined by fitting the concentration vs time data for the monosubstituted complex, [Co(Schiff base)(L)(MeIm)]⁺, to **Equation 3.2**. After solving for the rate constants k_1 and k_2 using **Equations 3.1** and **3.2**, **Equation 3.3** was used to calculate the predicted product concentration over time. The comparison between the product concentration calculated using **Equation 3.3** and the actual product concentration was used to verify the validity of the calculated rate constants, as shown in **Figure 3.5**. In these equations, A, B, and C refer to the species shown in **Figure 3.4**.

Equation 3.1:

$$[A] = [A]_0 \exp(-k_1 t)$$

Equation 3.2:

$$[B] = [B]_0 \exp(-k_2 t) + \frac{[A]_0 k_1}{(k_2 - k_1)} \{ \exp(-k_1 t) - \exp(-k_2 t) \}$$

Equation 3.3:

$$[C] = [C]_0 + [B]_0 \{ 1 - \exp(-k_2 t) \} + [A]_0 \left(1 + \frac{k_1 \exp(-k_2 t) - k_2 \exp(-k_1 t)}{k_2 - k_1} \right)$$

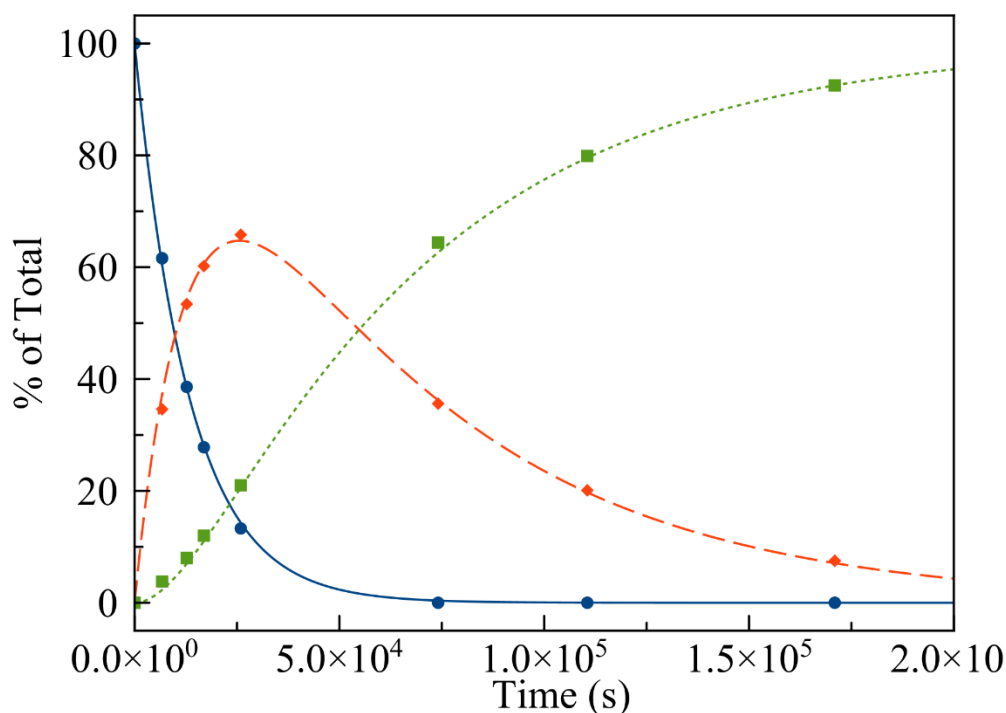


Figure 3.5. Representative concentration vs time data for the axial ligand substitution of $[\text{Co}(\text{3F-salen})(\text{3F-BnNH}_2)_2]^+$ with MeIm at 37 °C. Concentrations of species (A) (solid blue line, circular marker), (B) (broad dashed orange line, diamond marker), and (C) (short dashed green line, square marker) were fit to equations 1, 2, and 3, respectively. Here, (A), (B), and (C) refer to ligand substitution reactants and products shown in **Figure 3.4**.

The resulting rate constants are strongly dependent on both the axial and equatorial ligands. The complexes with 3F-salen equatorial ligands undergo substitution reactions faster than the analogous tfacen complexes. Likewise, complexes with axial 3F-BnNH₂ ligands are more labile than the analogous complexes with NH₃ axial ligands. The relative inertness of the NH₃ complexes is in contrast to similar acacen complexes,³⁰ which were found to undergo fairly rapid substitution. Related bis(thiosemicarbazone) Co(III) complexes are similar to the Schiff base complexes in this Chapter because they are also more stable with axial NH₃ ligands compared to benzylamine ligands.⁵⁵ The axial ligands have a more pronounced effect on the substitution rate constants compared to the equatorial ligands. This result is expected for the proposed dissociative mechanism because the rate of substitution for this mechanistic pathway primarily depends on the strength of the M–L bond of the dissociating ligand. For all complexes, the substitution of the second axial ligand with MeIm is substantially slower than that of the first axial ligand.

The activation parameters for these reactions were determined via Eyring analysis. These values are given in Table 5, and plots of $\ln(k/T)$ vs $1/T$ are shown in **Figure S3.38** and **S3.39**. The magnitudes of the enthalpies of activation and the positive values of the entropies of activation observed for all compounds are consistent with a dissociative ligand exchange mechanism.⁵⁸ In comparing the complexes, the enthalpies of activation for the first step (k_1) are all similar, sitting near a value of 115 kJ/mol. The entropies of activation vary more widely in a manner that is dependent on both the equatorial and axial ligands. Complexes with 3F-BnNH₂ axial ligand exhibit higher entropies of activation than the analogous NH₃ complexes.

Likewise complexes with equatorial 3F-salen ligands have a larger entropy of activation than tfacen complexes. In all cases, the enthalpy of activation for the second step (k_2) is greater than that for the first step.

The ligand exchange reactions were also evaluated in the presence of ascorbic acid in order to determine the effects of a reducing environment on the ligand exchange pathway. In all cases, the addition of ascorbic acid to the reaction mixture only minimally accelerated the initial decay of the starting material (species A). However, ascorbic acid had a much more pronounced effect on the formation of the final product (species C). Species C, the disubstituted product, accumulates rapidly, and the buildup of species B, the monosubstituted intermediate, is greatly diminished. This change in the reaction mechanism indicates that the loss of one axial ligand is required for reduction by ascorbic acid.

Cytotoxicity

The cytotoxicity of all complexes and the free ligands were evaluated in A549 lung cancer cells using the MTT assay. The 50% growth inhibitory concentration (IC_{50}) values for all complexes, free ligands, and relevant control compounds are listed in **Table 3.5**. Representative dose-response curves for $[Co(3F-salen)(3F-BnNH_2)_2]^+$ and $[Co(3F-salen)(NH_3)_2]^+$ are shown in **Figure 3.6**. Additional dose-response curves are deposited in the Supporting Information (**Figure S3.40–S3.43**).

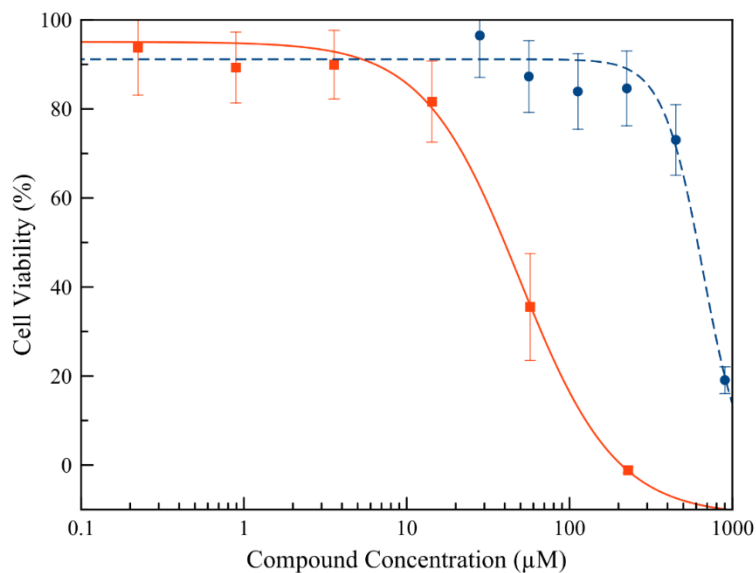


Figure 3.6. Cell viability in the presence of varying concentrations of $[\text{Co}(\text{3F-salen})(\text{3F-BnNH}_2)_2]^+$ (solid red line, square marker) and $[\text{Co}(\text{3F-salen})(\text{NH}_3)_2]^+$ (dashed blue line, circular marker) as measured by the MTT assay.

The complexes $[\text{Co}(\text{3F-salen})(\text{NH}_3)_2]^+$ and $[\text{Co}(\text{tfacen})(\text{NH}_3)_2]^+$ are effectively inactive against this cancer cell line. In contrast, complexes bearing axial 3F-BnNH₂ ligands $[\text{Co}(\text{3F-salen})(\text{3F-BnNH}_2)_2]^+$ and $[\text{Co}(\text{tfacen})(\text{3F-BnNH}_2)_2]^+$ exhibit moderate activity, as characterized by IC₅₀ values of 50 and 60 µM, respectively. This result indicates that the axial ligand plays the major role in determining the activities of this class of complexes, implicating ligand exchange mechanisms as an important component to their activities. The tfacen ligand is non-toxic, and 3F-salen is substantially less potent than the complex $[\text{Co}(\text{3F-salen})(\text{3F-BnNH}_2)_2]^+$, indicating that the toxic effects are not arising from dissociation of the equatorial ligands.

Table 3.5. Cytotoxicity and Cellular Uptake of [Co(Schiff base)(L)₂]⁺ Complexes in A549 Lung Cancer Cells

Compound	IC ₅₀ (μM)	Cobalt/Protein (pg/μg)
[Co(3F-salen)(NH ₃) ₂] ⁺	>500	43.0 ± 8.4
[Co(3F-salen)(3F-BnNH ₂) ₂] ⁺	50 ± 16	175 ± 19
[Co(tfacen)(NH ₃) ₂] ⁺	>500	26.7 ± 2.2
[Co(tfacen)(3F-BnNH ₂) ₂] ⁺	60 ± 17	697 ± 13
Co(NO ₃) ₂ ^a	>500	37 ± 2
Tfacen	>200	NA
3F-salen	97 ± 9.2	NA
cisplatin ^a	5.5 ± 3.2	NA

^aReported in reference 16.

Cobalt Uptake

To evaluate the relationship between complex structure and cellular uptake, the cobalt uptake of all complexes by A549 cells was measured. Cells were treated with 100 μM cobalt complexes for 24 h, and the uptake was quantified by the ratio of cobalt to protein in the cell samples (pg/μg), which were determined by GFAAS and the Bicinchonic Acid Assay, respectively. Cobalt uptake for Co(NO₃)₂, measured previously in our lab, was used as a control to probe the effects of supporting ligands.⁵⁵ Results of the uptake experiments are shown in **Table 3.5**. In general, complexes with the axial ligand 3F-BnNH₂ are taken up by cells much more effectively than those with axial NH₃ ligands. However, no clear dependence on the equatorial ligands is evidenced. For example, [Co(3F-salen)(NH₃)₂]⁺ is taken up more effectively than [Co(tfacen)(NH₃)₂]⁺, but [Co(3F-salen)(3F-BnNH₂)₂]⁺ is taken up less effectively than [Co(tfacen)(3F-BnNH₂)₂]⁺. For related [Co(bis(thiosemicarbazone))(L)₂]⁺ complexes a similar marked dependence on the axial ligand on cell uptake was noted.⁵⁵ The uptake of all complexes except [Co(tfacen)(NH₃)₂]⁺ was greater than that of free Co²⁺, administered in the form of

Co(NO₃)₂, which enters cells through both ion transporters and by transferrin-mediated pathways.^{59,60}

Discussion

Co(III) Schiff base complexes have been employed for a wide range of biological applications, utilizing their enzyme inhibitory,^{18,22,35} antiviral,^{26,27,61} and anticancer^{9,10,55,62–64} properties. These complexes have also been studied as reduction-activated prodrugs.^{46,65} Despite these previous investigations, few studies have systematically evaluated the general activity of the [Co(Schiff base)(L)₂]⁺ scaffold. In this Chapter, a small set of [Co(Schiff base)(L)₂]⁺ complexes was prepared and thoroughly investigated.. Two families of Co(III) Schiff base complexes, bearing either ammonia (NH₃) or 3-fluorobenzylamine (3F-BnNH₂) axial ligands, were studied. These efforts are specifically focused on how ligand substitution and reduction pathways are affected by both the equatorial and axial ligands, and how these properties manifest in biological activity. The data obtained in this Chapter provides useful insight on the mechanisms of activation of Co(III) drug candidates.

The syntheses of the four complexes followed a method that was previously reported.⁴⁵ This procedure calls for the reaction of the Schiff base ligand and Co(NO₃)₂, followed by the addition of an excess of axial ligand. Atmospheric oxygen is presumed to be the oxidant for this reaction, affording the diamagnetic Co(III) complexes. Although [Co(3F-salen)(3F-BnNH₂)₂]Cl precipitated from the reaction mixture as the analytically pure product, the other three complexes required additional purification via precipitation from solution with NaPF₆. The PF₆⁻ counterion was then replaced with Cl⁻ using anion exchange resin. The identity and purity of the

complexes were verified by ^1H , ^{19}F , and $^{13}\text{C}\{^1\text{H}\}$ NMR spectroscopy, HPLC, elemental analysis, and X-ray crystallography. The X-ray crystal structures of $[\text{Co}(\text{3F-salen})(\text{3F-BnNH}_2)_2]^+$, $[\text{Co}(\text{tfacen})(\text{3F-BnNH}_2)_2]^+$, and $[\text{Co}(\text{tfacen})(\text{NH}_3)_2]^+$ (**Figure 3.1**) reveal the expected octahedral coordination geometries. A notable feature of these structures was the shorter $\text{Co-N}_{\text{axial}}$ distances of $[\text{Co}(\text{tfacen})(\text{NH}_3)_2]^+$ compared to those for $[\text{Co}(\text{3F-salen})(\text{3F-BnNH}_2)_2]^+$ and $[\text{Co}(\text{tfacen})(\text{3F-BnNH}_2)_2]^+$. All complexes are mono-cationic, water soluble at millimolar concentrations, and stable with respect to ambient air and light for at least several months.

The complexes were further characterized by cyclic voltammetry and ^{59}Co NMR spectroscopy. Cyclic voltammetry is a useful method that has been employed to investigate the reduction of biologically active Co(III) complexes. Both the relative potential and reversibility of redox processes in Co(III) complexes are key parameters that dictate the suitability of a compound for hypoxia-targeting.^{11,66} These properties are also important for Co(III) complexes that are intended for activation by ligand substitution; if the redox potential is too positive, undesired reduction to Co(II) may occur, drastically reducing the stability of the complex and possibly generating reactive oxygen species via redox cycling.^{67,68} The cyclic voltammograms of the four complexes all reveal an initial irreversible reduction from Co(III) to Co(II). The irreversible nature of this redox process is a consequence of dissociation of the axial ligands, which occurs upon population of the σ^* d_{z^2} orbital upon reduction. This electrochemical process has been observed for related Co(III) complexes.^{45,55,65} Consistent with the d_{z^2} LUMO, the potential of the Co(III)/Co(II) couple is most strongly dependent on the nature of the axial ligand, a phenomenon that has been

documented for similar complexes.^{69,70} As expected, the more electron-donating NH₃ ligands give rise to more negative reduction potentials compared to the analogous 3F-BnNH₂ complexes.⁷¹

NMR spectroscopy of NMR-active transition metal nuclei relays important information on the chemical environment of the metal center. Under some circumstances, chemical shifts can be correlated to ligand field splitting,^{49,52,72} thermodynamic stability,⁷³ and ligand exchange rates.^{47,50,74–76} For ⁵⁹Co, a 100% naturally abundant nucleus with $I = 7/2$, the chemical shift of the ⁵⁹Co NMR signal is related to the energy of the lowest excited state, which is a major contributor to the paramagnetic shielding term. The linewidth of ⁵⁹Co NMR signals is a consequence of quadrupolar relaxation and is therefore a function of the electric field gradient at the nucleus and the rotational correlation time of the complex.^{54,77} For tetragonal complexes, the ⁵⁹Co chemical shift exhibits an inverse, linear correlation with the ligand field splitting of the complex after adjusting for the nephelauxetic effect of the ligands.^{48,49,51,52} Thus, ⁵⁹Co NMR spectroscopy provides a method to probe both the electron donating capacity and the nephelauxetic properties of the ligand scaffolds. Furthermore, these properties that dictate the ⁵⁹Co NMR chemical shift may also relate to chemical reactivity patterns, enabling correlations between this chemical shift and catalytic activity, for example.^{78,79} The four complexes studied in this work give rise to clean ⁵⁹Co NMR spectra. The chemical shifts of these complexes range from 8340 to 8740 ppm, a relatively narrow span considering that a 16,000 ppm window exists for octahedral Co(III) complexes.⁵⁰ Complexes with axial 3F-BnNH₂ ligands resonate approximately 200 ppm downfield from their NH₃ counterparts. Per

correlations found in the literature,⁴⁹ this downfield shift reflects weaker ligand field strength of the 3F-BnNH₂ complexes compared to the NH₃ complexes,^{80,81} a feature that is most likely a consequence of the greater steric hindrance of the larger 3F-BnNH₂ ligand. Because the axial ligands are exclusively sigma-donors, this shift also indicates that the metal-ligand bond is stronger in the NH₃ complexes than in the 3F-BnNH₂ complexes. The equatorial Schiff base ligands also contribute to the observed chemical shifts. The tfacen complexes resonate approximately 200 ppm downfield from the 3F-salen complexes. The upfield shift of the 3F-salen complexes relative to the tfacen complexes may be due to increased delocalization of the HOMO on the aromatic rings of the 3F-salen ligand. The delocalization reflects the larger nephelauxetic effect of the π -aromatic 3F-salen ligands compared to tfacen, which expands the apparent valence d-electron radius. This property gives rise to greater shielding of the ⁵⁹Co nucleus.^{48,50,72}

Many bioactive Co(III) Schiff base complexes are proposed to be activated by ligand exchange rather than reduction.^{10,23,30} To assess the role of ligand substitution in the activation of the four Schiff base complexes in this Chapter the relative rates of this process and activation parameters were determined. The complexes were challenged with an excess of MeIm to drive formation of [Co(Schiff Base)(MeIm)₂]⁺, and this process was followed by ¹⁹F NMR spectroscopy or HPLC. Varying the concentration of MeIm had no effect on the rate of the reaction. The zero-order dependence of this incoming ligand is consistent with a dissociative mechanism.⁸² A conjugate base mechanism, whereby the acidic NH protons of the axial NH₃ or 3F-BnNH₂ ligand are first deprotonated, was ruled out by virtue of the fact that there was

no acceleration of the reaction rate at a higher pH.² As expected for a dissociative mechanism, the rate of ligand substitution is highly dependent on the departing axial ligand.¹ The more strongly donating NH₃ complexes exhibit much slower exchange rates than the 3F-BnNH₂ complexes. These results may also be due to steric effects, as dissociation of the bulkier 3F-BnNH₂ ligands will be more favorable.⁸³ Although the effect of the equatorial Schiff base is less pronounced, the 3F-salen complexes were consistently more reactive than their tfacen counterparts. In all cases, the rate constant for the first exchange step (k_1) was at least three times greater than that for the second (k_2). This behavior has been observed previously for the acacen family of complexes, and it may indicate greater stabilization of the monosubstituted intermediate relative to the starting complex.^{30,31}

Eyring analysis of the ligand exchange reactions was performed by measuring the rate constants for each reaction at different temperatures. In all cases, the entropies of activation are positive, a feature that is consistent with a dissociative ligand substitution mechanism^{58,84,85} The magnitude of the enthalpies of activation are also consistent with a dissociative mechanism, where the Co–N bond is weakened in the transition state.⁸⁶ These values for ΔH^\ddagger and ΔS^\ddagger are similar to those reported for structurally related Co(III) haloammine complexes and Co(III)-*trans* dioximes,^{87–89} which are known to undergo dissociative ligand substitution.

Trends are apparent in comparing the relative enthalpies and entropies of activation of the complexes. Complexes bearing the bulkier 3F-BnNH₂ axial ligands have higher ΔS^\ddagger values than those with NH₃ axial ligands. The larger entropy of activation of the 3F-BnNH₂ complexes may be a consequence of conformational

restriction of these large ligands when bound to the complexes that is relieved as they dissociate from the inner coordination sphere. Likewise, the 3F-salen complexes have higher ΔS^\ddagger values than the corresponding tfacen complexes. As observed in the crystal structures, the 3F-salen ligands can deviate significantly from planarity when bound to Co(III), whereas the tfacen ligand remain strictly planar. As such, we hypothesize that the larger ΔS^\ddagger of these complexes compared to tfacen complexes arises from the ability of these ligands to access more conformations, manifested as deviations from planarity, as the axial ligand departs. The enthalpies of activation for the first ligand substitution step are very similar for all four complexes. In considering the similar pK_a values of fluorobenzylammonium and ammonium (9.1 and 9.3, respectively)^{90,91}, their donor strengths as ligands are most likely comparable. Hence the enthalpies of activation, which are expected to be related to the donor strengths of the departing ligand, are also quite similar, and the relative reaction rates are predominantly dictated by the entropy of activation of ligand dissociation. For the substitution of the second axial ligand with MeIm, there is more variation in the ΔH^\ddagger values. In this second step, 3F-BnNH₂ complexes exhibit lower ΔH^\ddagger values than the corresponding NH₃ complexes, and 3F-salen complexes exhibit lower ΔH^\ddagger values than their tfacen analogues. In all cases, the ΔH^\ddagger values for k_2 are greater than those for k_1 , suggesting that the slower rates for the second ligand substitution step arise from enthalpic, rather than entropic, effects. The larger ΔH^\ddagger values for the monosubstituted complex may arise from the weaker *trans*-effect induced by MeIm compared to the NH₃ and 3F-BnNH₂ ligands.

Due to their tendency to undergo irreversible reduction to Co(II), many Co(III)

complexes are believed to be activated by reductive mechanism in biological systems. Because the Co-Schiff base complexes studied in this work have moderately high reduction potentials, we considered that reduction might also be a potential mechanism of activation for these complexes. In order to probe the effects of a reducing environment on the ligand exchange kinetics, we performed the ligand exchange assays in the presence of an excess of ascorbic acid, a mild, biologically relevant reductant.

The structural, electrochemical, and kinetic data described above reveal useful correlations between these properties. The Co–N_{axial} distances measured in the crystal structures scale directly with the axial ligand exchange rates. These long Co–N_{axial} distances, in turn, may be related to weaker coordinative bonds. Because the rate-determining step of dissociative ligand substitution is cleavage of the M–L bond, the rates of these reactions will be related to the M–L coordinative bond energy. Another correlation between the Co(III)/Co(II) reduction potential and the ligand substitution rate is observed. Complexes with more negative reduction potentials undergo slower ligand exchange rates compared to complexes with more positive reduction potentials. Although correlations have been reported between reduction potential and electron transfer rate for Co(III) complexes,⁶⁹ no related examples correlating ligand substitution kinetics and reduction potentials have been reported. Although the origins of this correlation warrant further investigation, it may arise as a consequence of the similarity between the transition state of dissociative ligand substitution pathway and the one-electron reduced compound. Both of these species should attain geometries with substantially elongated axial ligand bond distances.

The role of the physical properties of these four Schiff base complexes on their biological activities was investigated. The *in vitro* anticancer activity of these complexes in A549 lung cancer cells was evaluated, revealing a disparate range of IC_{50} values from 50 μM to higher than 500 μM . The NH_3 complexes are all inactive, whereas the 3F-Bn NH_2 complexes are moderately toxic. With respect to cellular uptake, the complexes bearing NH_3 ligands were taken up by cells to a much smaller extent than the 3F-Bn NH_2 . Presumably, this lower cell uptake is a consequence of the lower lipophilicity of the NH_3 ligand compared to 3F-Bn NH_2 . The lower toxicity of the NH_3 complexes, therefore, may be a factor of both diminished cell uptake and slower ligand exchange kinetics. The increased toxicity of the 3F-Bn NH_2 complexes may be due to intracellular reduction; related Co(II) salen complexes oxidatively cleave DNA *in vitro*.⁹² Although the overall cytotoxicity of these four complexes is poor, it should be emphasized that the 3F-Bn NH_2 complexes are more active than related Co Schiff base complexes⁹³ and unmodified Co(II) salen complexes, which are inactive.⁹⁴

Conclusion

Four $[Co(\text{Schiff base})(L)_2]^+$ complexes were synthesized and characterized. The complexes undergo ligand exchange in aqueous solution by a dissociative mechanism. Eyring analysis indicates that the relative reaction rates are primarily dictated by differences in the entropy of activation for the complexes. The rate of ligand exchange correlates with the Co(III)/Co(II) reduction potential of the complexes. The ligand exchange reaction mechanism is altered in the presence of ascorbate, leading to more

rapid formation of the final disubstituted product. The anticancer activity of the complexes depends heavily on the axial ligand, with the more labile, easily reduced 3F-BnNH₂ complexes showing over an order of magnitude higher activity than the inert NH₃ complexes.

Experimental

Materials and Methods

CoCl₂·6H₂O, IRA410(Cl) anion exchange resin, and *N*-methylimidazole (MeIm) were obtained from Alfa Aesar (Tewksbury, MA) and used as received. The compound 3-fluorobenzylamine was obtained from Oakwood Chemical (Estill, SC) and used as received. The Schiff base ligands 3F-salen⁹⁵ and tfacen²³ were synthesized according to previously published procedures. The Co(III) complexes, [Co(3F-salen)(MeIm)₂]Cl and [Co(tfacen)(MeIm)₂]Cl, were synthesized following a previously described procedure.⁴⁵ These complexes were used only to confirm the identities of the final products obtained in our ligand substitution kinetic studies. Solvents were of ACS grade or higher. CHAPS (3-[(3-chloamidopropyl)dimethylammonio]-1-propanesulfonate) lysis buffer was prepared using 1% CHAPS buffer by mass, 5 mM ethylenediaminetetraacetic acid (EDTA), 50 mM tris(hydroxymethyl)aminomethane (Tris), and 110 mM NaCl; the pH was adjusted to 7.4 using dilute HCl or NaOH as necessary. Ultrapure 3-(*N*-morpholino)propanesulfonic acid (MOPS) buffer was obtained from VWR Life Sciences (Radnor, PA). All reactions were performed under ambient atmospheric conditions without any attempts to exclude oxygen or water.

Physical Measurements

NMR spectra were acquired on a 500 MHz Bruker AV 3HD-spectrometer equipped with a broadband Prodigy cryoprobe. ^1H and $^{13}\text{C}\{^1\text{H}\}$ NMR spectra in MeOD- d_4 were referenced to the residual solvent peaks at 3.31 and 49.00 ppm, respectively, and ^1H and $^{13}\text{C}\{^1\text{H}\}$ NMR spectra in D_2O were referenced to a *p*-dioxane internal standard at 3.75 and 67.19 ppm, respectively.⁹⁶ ^{19}F NMR spectra were referenced internally to sodium trifluoroacetate (NaTFA) in H_2O at -75.51 ppm,^{97,98} and ^{59}Co NMR spectra were referenced to an external standard of $\text{K}_3[\text{Co}(\text{CN})_6]$ in D_2O at 0 ppm.⁴⁷ Samples for IR spectroscopy were prepared as KBr pellets and were analyzed on a Nicolet Avatar 370 DTG FTIR spectrometer. Graphite furnace atomic absorption spectroscopy (GFAAS) measurements were performed with a PerkinElmer PinAAcle 900z instrument. Electrochemical measurements were carried out using a Pine WaveNow potentiostat with a three-electrode setup consisting of a glassy carbon working electrode, a platinum counter electrode, and an Ag wire quasi-reference electrode. Complexes were dissolved in anhydrous DMF with 0.10 M $[\text{Bu}_4\text{N}][\text{PF}_6]$ (TBAP) as the supporting electrolyte. Potentials were referenced using an internal standard of the ferrocene/ferricenium couple at 0.45 V vs the saturated calomel electrode (SCE).^{99,100} The sample cell was deoxygenated by bubbling nitrogen gas through the solution prior to analysis and maintained under a blanket of nitrogen during the experiment. Analytical high-performance liquid chromatography (HPLC) was performed using a Shimadzu LC20-AT HPLC with an Ultra Aqueous C18 column, 100 Å, 5 μm, 250 mm x 4.6 mm (Restek, Bellefonte, PA) and an SPD-20AV UV/vis detector monitoring at 220 and 260 nm. The flow rate for all HPLC analyses

was 1 mL/min. Gradient elution for purity analysis was performed as follows: 10% methanol in water containing 0.1% TFA to 100% methanol containing 0.1% TFA over 20 min. Gradient elution for kinetics experiments was performed using 10% methanol in water containing 0.1% TFA to 100% methanol containing 0.1% TFA over 15 min, then continuing at 100% methanol for 10 minutes. High-resolution mass spectra (HRMS) were recorded on an Exactive Orbitrap mass spectrometer in positive electrospray ionization (ESI) mode (ThermoFisher Scientific, Waltham, MA). Elemental analyses (CHN) were performed by Atlantic Microlab Inc., Norcross, GA, USA.

[Co(3F-salen)(3F-BnNH₂)₂]Cl

Solid CoCl₂·6H₂O (0.203 g, 0.854 mmol) was added to a suspension of 3F-salen (0.26 g, 0.854 mmol) in isopropanol (10 mL). The yellow suspension of 3F-salen immediately turned dark green, and the mixture was heated at 70 °C with stirring for 1 h. The axial ligand 3F-BnNH₂ (0.63 mL, 5.5 mmol) was added, and the mixture was heated with stirring for 2 h, during which time it slowly turned red. The resulting red-brown suspension was cooled to room temperature, and the precipitate was collected by filtration. The solid product was washed with water, isopropanol, and diethyl ether and dried under vacuum to yield a dark red solid. Yield 0.15 g (27%). ¹H NMR (500 MHz, MeOD-*d*₄) δ 8.25 (s, 2H), 7.16-7.28 (m, 6H), 6.92 (td, 2H, J = 8.6, 2.5 Hz), 6.86 (d, 2H, J = 8 Hz), 6.82 (d, 2H, J = 10 Hz), 6.61-6.67 (m, 2H), 4.05 (s, 4H), 3.27 (s, 2H). ¹⁹F NMR (470 MHz, H₂O) δ -113.26 (m, 2F), -135.64 (d, 2F, J_{H-F} = 12 Hz). ¹³C{¹H} NMR (126 MHz, MeOD-*d*₄) δ 170.9 (d, J_{F-C} = 3 Hz), 164.2 (d, J_{F-C} =

248 Hz), 157.7 (d, $J_{F-C} = 243$ Hz), 155.0 (d, $J_{F-C} = 13$ Hz), 141.60 (d, $J_{F-C} = 7$ Hz), 141.57 (d, $J_{F-C} = 7$ Hz), 131.5 (d, $J_{F-C} = 8$ Hz), 131.2 (d, $J_{F-C} = 4$ Hz), 125.5 (d, $J_{F-C} = 3$ Hz), 122.0 (d, $J_{F-C} = 5$ Hz), 121.0 (d, $J_{F-C} = 19$ Hz), 116.4 (d, $J_{F-C} = 21$ Hz), 115.8 (d, $J_{F-C} = 7$ Hz), 115.6 (d, $J_{F-C} = 21$ Hz), 59.6, 45.8. IR (KBr, cm^{-1}): 3338 w, 3271 w, 3100 m, 2944 w, 2907 m, 2857 w, 1636 s, 1614 m, 1551 w, 1453 s, 1409 w, 1395 w, 1337 w, 1351 w, 1307 s, 1298 s, 1240 s, 1099 m, 1057 m, 865 m, 778 m, 734 s. ESI-MS (positive ion mode): m/z $[M]^+$ 611.147, calcd 611.148. Anal. Calcd for $[\text{Co}(3\text{F-salen})(3\text{F-BnNH}_2)_2]\text{Cl}$ ($\text{C}_{30}\text{H}_{28}\text{N}_4\text{O}_2\text{F}_4\text{CoCl}$): C, 55.70; H, 4.36; N, 8.66. Found: C, 55.44; H, 4.63; N, 8.83.

[Co(3F-salen)(NH₃)₂Cl]

$\text{CoCl}_2 \cdot 6\text{H}_2\text{O}$ (0.52 g, 2.17 mmol) was added to 3F-salen (0.66 g, 2.17 mmol) in methanol (35 mL). The yellow suspension of 3F-salen immediately turned dark green, and the mixture was heated at 60 °C with stirring for 1 h. Concentrated NH_4OH (1 mL, 18 mmol) was added, and the mixture was stirred at room temperature for 2 h. The resulting red solution was filtered, and excess aqueous NaPF_6 was added to the filtrate, which resulted in the precipitation of a red-brown solid. The solid was washed sequentially with water and diethyl ether, dissolved in methanol (20 mL), and stirred with approximately 5 g of anion exchange resin at room temperature for 2 h. The dark red solution was filtered to remove resin. The filtrate was evaporated to dryness and further dried under high vacuum to yield a dark red solid. Yield 0.31 g (33%). ^1H NMR (500 MHz, D_2O) δ 8.23 (s, 2H), 7.21 (d, 2H $J_{H-H} = 7.9$ Hz), 6.97 (m, 2H), 6.58 (m, 2H), 4.07 (s, 4H). ^{19}F NMR (470 MHz, H_2O) δ -135.97 (d, 2F, $J_{H-F} = 9.7$ Hz). IR

(KBr, cm^{-1}): 3300 w, 3017 w, 1652 m, 1629 s, 1587 w, 1453 s, 1324 m, 1312 m, 1241 m, 1227 m, 871 w, 792 w, 738 m. ESI-MS (positive ion mode): m/z $[\text{M}]^+$ 395.072, calcd 395.073. Anal. Calcd for $[\text{Co}(\text{3F-salen})(\text{NH}_3)_2]\text{Cl}\cdot 0.2\text{H}_2\text{O}$ ($\text{C}_{16}\text{H}_{18.4}\text{N}_4\text{O}_{2.2}\text{F}_2\text{CoCl}$): C, 44.25; H, 4.27; N, 12.90. Found: C, 44.02; H, 4.25; N, 12.99.

[Co(tfacen)(3F-BnNH₂)₂]Cl

$\text{CoCl}_2\cdot 6\text{H}_2\text{O}$ (0.265 g, 1.11 mmol) was added to tfacen (0.37 g, 1.11 mmol) in methanol (10 mL). The white suspension of tfacen immediately turned dark green, and the mixture was heated at 60 °C with stirring for 1 h. The axial ligand 3F-BnNH₂ (0.6 mL, 5.2 mmol) was added, and the mixture was stirred at room temperature overnight. The resulting red solution was filtered, and excess aqueous NaPF_6 was added to the filtrate, which resulted in the precipitation of a red-brown solid. The solid was washed with water and diethyl ether, then dissolved in methanol (20 mL) and stirred with approximately 5 g anion exchange resin at room temperature for 2 h. The dark red solution was filtered to remove resin, evaporated to dryness, and further dried under high vacuum to yield a light brown solid. Yield 0.35 g (47%). ^1H NMR (500 MHz, $\text{MeOD-}d_4$) δ 7.34 (m, 2H), 7.03 (m, 6H), 5.78 (s, 2H), 3.68 (s, 4H). ^{19}F NMR (470 MHz, H_2O) δ -72.33 (s, 6F), -113.13 (m, 2F). $^{13}\text{C}\{^1\text{H}\}$ NMR (126 MHz, $\text{MeOD-}d_4$) δ 175.41, 164.30 (d, $J_{\text{F-C}} = 245.3$ Hz), 161.05 (q, $J_{\text{F-C}} = 32.5$ Hz), 141.63 (d, $J_{\text{F-C}} = 7.2$ Hz), 131.65 (d, $J_{\text{F-C}} = 8.3$ Hz), 125.65 (d, $J_{\text{F-C}} = 2.8$ Hz), 118.83 (d, $J_{\text{F-C}} = 280.6$ Hz), 116.54 (d, $J_{\text{F-C}} = 21.8$ Hz), 115.75 (d, $J_{\text{F-C}} = 21.3$ Hz), 96.54, 54.77, 45.49, 23.96. IR (KBr, cm^{-1}): 3440 br m, 3052 br m, 1617 s, 1584 m, 1543 m, 1470 m, 1361 w, 1287 s,

1248 s, 1187 s, 1200 s, 900 m, 780 m, 800 m. ESI-MS (positive ion mode): m/z $[M]^+$ 639.141, calcd 639.142. Anal. Calcd for $[\text{Co}(\text{tfacen})(3\text{F-BnNH}_2)_2]\text{Cl}$ ($\text{C}_{26}\text{H}_{28}\text{N}_4\text{O}_2\text{F}_8\text{CoCl}$): C, 46.27; H, 4.18; N, 8.30. Found: C, 46.00; H, 4.29; N, 8.14.

$[\text{Co}(\text{tfacen})(\text{NH}_3)_2]\text{Cl}$

$\text{CoCl}_2 \cdot 6\text{H}_2\text{O}$ (0.269 g, 1.13 mmol) was added to tfacen (0.375 g, 1.13 mmol) in methanol (15 mL). The white suspension of tfacen immediately turned dark green, and the mixture was heated at 60 °C with stirring for 1 h. Concentrated NH_4OH (0.5 mL, 9 mmol) was added, and the mixture was stirred at room temperature for 2 h. The resulting solution was filtered, and excess aqueous NaPF_6 was added to the filtrate, which resulted in the precipitation of a red-brown solid. The solid was washed with water and diethyl ether, then dissolved in methanol (10 mL) and stirred with approximately 5 g anion exchange resin at room temperature for 2 h. The dark red solution was filtered to remove resin, evaporated to dryness, and further dried under high vacuum to yield a light brown solid. Yield 0.20 g (39%). ^1H NMR (500 MHz, D_2O) δ 8.23 (s, 2H), 7.21 (d, $J = 8.0$ Hz, 2H), 7.03 – 6.96 (m, 2H), 6.60 (td, $J = 7.9, 4.5$ Hz, 4H), 4.07 (s, 4H), 3.76 (s). ^{19}F NMR (470 MHz, H_2O) δ -72.37 (s, 6F). $^{13}\text{C}\{^1\text{H}\}$ NMR (126 MHz, D_2O): δ 187.59, 172.35 (q, $J_{\text{F-C}} = 32.6$ Hz), 131.09 (q, $J_{\text{F-C}} = 280.0$ Hz), 109.52 (q, $J_{\text{F-C}} = 3.1$ Hz), 80.33, 36.46. IR (KBr, cm^{-1}): 3682 w, 3513 w, 3304 w, 3104 w, 1635 m, 1543 m, 1461 m, 1304 s, 1187 s, 1117 s, 900 s, 787 s. ESI-MS (positive ion mode): m/z $[M]^+$ 423.066, calcd 423.067. Anal. Calcd for $[\text{Co}(\text{tfacen})(\text{NH}_3)_2]\text{Cl} \cdot 1.3\text{H}_2\text{O}$ ($\text{C}_{12}\text{H}_{20.6}\text{N}_4\text{O}_{3.3}\text{F}_6\text{CoCl}$): C, 29.90; H, 4.31; N, 11.62. Found: C, 30.40; H, 4.16; N, 11.14.

X-ray Crystallography

Single crystals of the tfacen complexes were obtained by vapor diffusion of diethyl ether into methanol solutions of these compounds. Diffusion of diethyl ether into a dimethylformamide (DMF) solution of $[\text{Co}(\text{3F-salen})(\text{3F-BnNH}_2)_2]\text{Cl}$ afforded suitable crystals for single-crystal X-ray diffraction studies. Low-temperature X-ray diffraction data for $[\text{Co}(\text{3F-salen})(\text{3F-BnNH}_2)_2]\text{Cl}$, $[\text{Co}(\text{tfacen})(\text{3F-BnNH}_2)_2]\text{Cl}$, and $[\text{Co}(\text{tfacen})(\text{NH}_3)_2]\text{Cl}$ were collected on a Rigaku XtaLAB Synergy diffractometer coupled to a Rigaku HyPix detector with Mo $K\alpha$ radiation ($\lambda = 0.71073 \text{ \AA}$) from a PhotonJet micro-focus X-ray source at 100 K. The structures were solved through intrinsic phasing using SHELXT¹⁰¹ and refined against F^2 on all data by full-matrix least squares with SHELXL¹⁰² following established refinement strategies.¹⁰³ All non-hydrogen atoms were refined anisotropically. All hydrogen atoms bound to carbon were included in the model at geometrically calculated positions and refined using a riding model. Hydrogen atoms bound to nitrogen were located in the difference Fourier synthesis map and subsequently refined semi-freely with the help of distance restraints. The isotropic displacement parameters of all hydrogen atoms were fixed to 1.2 times the U_{eq} value of the atoms they are linked to (1.5 times for CH_3 or NH_3 groups). The structure of $[\text{Co}(\text{3F-salen})(\text{3F-BnNH}_2)_2]\text{Cl}$ contained a disordered DMF molecule; the two disordered components were refined with appropriate similarity restraints, allowing the occupancy of each component to refine freely with net occupancy of both components summing to one. Likewise, in the structure of $[\text{Co}(\text{3F-salen})(\text{3F-BnNH}_2)_2]\text{Cl}$, one of the axial 3F-BnNH₂ ligands is rotationally disordered

about the Co–N axis. The two disordered components were refined as described above. The complex $[\text{Co}(\text{tfacen})(3\text{F-BnNH}_2)_2]^+$ resides on a crystallographic 2-fold axis. Additionally, this compound crystallized in a chiral space group. Refinement of the absolute structure revealed a Flack parameter of $-0.006(8)$, indicating that this crystal was enantiomerically pure, rather than a racemic twin. Details of the data quality and a summary of the residual values of the refinements are listed in **Table 3.6**.

Table 3.6. X-ray Crystallographic Data Collection and Refinement Parameters

	$[\text{Co}(3\text{F-salen})(3\text{F-BnNH}_2)_2]\text{Cl}\cdot\text{DMF}$	$[\text{Co}(\text{tfacen})(3\text{F-BnNH}_2)_2]\text{Cl}\cdot\text{Et}_2\text{O}$	$[\text{Co}(\text{tfacen})(\text{NH}_3)_2]\text{Cl}\cdot\text{MeOH}$
formula	$\text{C}_{33}\text{H}_{35}\text{CoN}_5\text{O}_3\text{F}_4\text{Cl}$	$\text{C}_{30}\text{H}_{38}\text{CoN}_4\text{O}_3\text{F}_8\text{Cl}$	$\text{C}_{13}\text{H}_{32}\text{CoN}_4\text{O}_3\text{F}_6\text{Cl}$
fw	720.04	749.02	490.72
space group	$P2_1/n$	$P 4_22_1$	$P\bar{1}$
a , Å	10.9482(2)	15.4493(3)	7.9661(2)
b , Å	22.6458(5)	15.4493(3)	11.0108(2)
c , Å	13.1929(3)	14.4740(5)	11.9024(2)
α , deg	90	90	65.768(2)
β , deg	100.046(2)	90	89.306(2)
γ , deg	90	90	82.092(2)
V , Å ³	3220.78(12)	3454.67(18)	941.82(4)
Z	4	4	2
ρ_{calcd} g·cm ⁻³	1.485	1.440	1.730
T , K	100.00(10)	100.00(10)	100.00(10)
$\mu(\text{Mo K}\alpha)$, mm ⁻¹	0.682	0.654	1.133
θ range, deg	2.092 to 26.373	2.336 to 27.103	1.879 to 29.128
completeness to θ , %	100.0	99.9	100.0
total no. of data	32486	16169	23740
no. of unique data	6588	3800	5022
no. of param	496	217	277
no. of restraints	196	483	7
$R1^a$, %	2.95	5.92	3.31
$wR2^b$, %	7.06	15.47	6.75
GoF ^c	1.053	1.048	1.058
max, min peaks e ⁻ ·Å ⁻¹	0.577, -0.271	0.790, -0.520	0.499, -0.406

^a $R1 = \sum||\text{Fo}| - |\text{Fc}||/\sum|\text{Fo}|$ for all data. ^b $wR2 = \{\sum[w(\text{Fo}^2 - \text{Fc}^2)^2]/\sum[w(\text{Fo}^2)^2]\}^{1/2}$ for all data. ^c $\text{GoF} = \{\sum[w(\text{Fo}^2 - \text{Fc}^2)^2]/(n - p)\}^{1/2}$, where n is the number of data and p is the number of refined parameters.

Ligand Exchange Experiments

To probe the axial ligand substitution of these complexes, solutions were

prepared to contain 0.5 mM Co complex, 0.5 mM NaTFA, 100 mM MOPS buffer (pH 7.4), and 12.5 mM MeIm as an entering ligand. The pH of the resulting solutions was measured to verify that the MOPS buffer fixed it at 7.4. Immediately after preparation, samples were analyzed via ^{19}F NMR spectroscopy using the NaTFA signal as an internal standard or by HPLC using the relative integration of each peak. ^{19}F NMR spectra or HPLC chromatograms were acquired periodically to monitor the ligand substitution reaction with MeIm. For reactions carried out at temperatures greater than 37 °C, aliquots were removed and flash-frozen prior to analysis by HPLC. Pseudo first-order rate constants for the decay of the starting complex were calculated by plotting the peak integration vs time and fitting these data to the appropriate first-order integrated rate law using the Magic Plot Pro software. Rate constants for the reaction of the intermediate species were calculated using the appropriate integrated rate laws for this process.^{56,57} The reported values at 18 and 37 °C are the average of at least three independent replicates, whereas data at higher temperatures were collected for a single kinetics run.

Cell Culture Conditions

A549 (human lung cancer) cells were obtained from American Type Culture Collection (ATCC). Cells were cultured as adherent monolayers in an incubator at 37 °C with a humidified atmosphere of 5% CO₂. The cells were maintained in Dulbecco's Modified Eagle's Medium (DMEM) supplemented with 10% fetal bovine serum (FBS). Cells were checked for mycoplasma contamination monthly using the Plasmotest™ mycoplasma detection kit from InvivoGen.

Cytotoxicity Assay

The colorimetric MTT assay was used to evaluate cytotoxicity.¹⁰⁴ Trypsinized cells were plated at 2000 cells/well with 100 μL /well in a 96-well plate and incubated for 24 h. The media was then removed and replaced with 200 μL of growth media containing varying concentrations of the complexes. After 24 h, the culture medium containing the complex was removed, 200 μL of fresh media was added, and plates were incubated an additional 48 h. After this time, the media was removed again, and a solution of thiazolyl blue tetrazolium bromide (MTT) in DMEM (200 μL , 1 mg/mL) was added to each well. Upon incubation for 4 h, the DMEM/MTT solutions were aspirated, and the purple formazan crystals were dissolved in 200 μL of an 8:1 mixture of DMSO: pH 10 glycine buffer. The absorbance of each well at 570 nm was measured using a BioTek Synergy HT platereader. Absorbance values were normalized to the untreated wells and plotted as concentration of cobalt complex vs % viability. The resulting dose-response curves were analyzed using a logistic sigmoid function.¹⁰⁵ Reported IC_{50} values represent the average of three independent experiments, each carried out with six replicates per concentration level. Stock solutions of the cobalt complexes were prepared fresh in 18.2 $\text{M}\Omega\cdot\text{cm}$ H_2O prior to serial dilution in the cell culture medium. Stock solutions of free ligands were prepared in DMSO and diluted to less than 1% DMSO by volume with cell culture medium.

Uptake Experiments

Cellular uptake of cobalt was determined by implementing slight modifications to previously reported protocols.^{106,107} Trypsinized cells (2×10^6) were seeded in six 75 cm² culture dishes and incubated for 24 h. The media was removed, and the cells were treated with either 0 or 100 μ M cobalt complex for 24 h. Dishes containing no cells were also incubated with 100 μ M of the cobalt complex to correct for non-specific adsorption of cobalt to the plastic. Media was removed from all dishes, and the cells were rinsed with 3 mL PBS and detached with trypsin (3 mL). The cells were centrifuged at 1000 rpm for 10 min. The supernatant was discarded, and the pellet was resuspended in 1 mL PBS. Samples were centrifuged and resuspended twice more using the same conditions to remove extracellular cobalt and centrifuged a final time to pellet cells. The pellet was resuspended in ice-cold, ultrapure 1 \times CHAPS lysis buffer, and samples were gently agitated for 30 min. The protein concentration in each sample was then determined using the Thermo Fisher Bicinchoninic Acid Protein Assay Kit according to the manufacturer's instructions. The cobalt concentration in each sample was determined using GFAAS. Results were reported as the mass ratio of cobalt to protein (pg/ μ g) in each sample.

Supporting Information

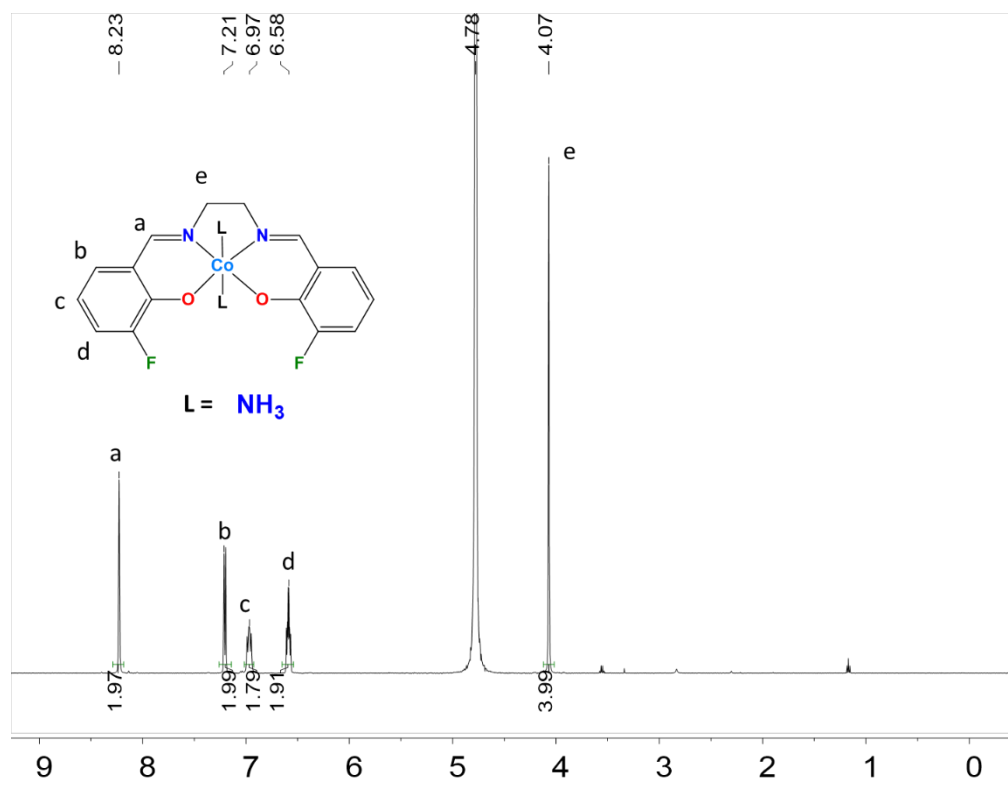


Figure S3.1. ^1H NMR (500 MHz) spectrum of $[\text{Co}(\text{3F-salen})(\text{NH}_3)_2]^+$ in $\text{MeOD-}d_4$ at 298 K.

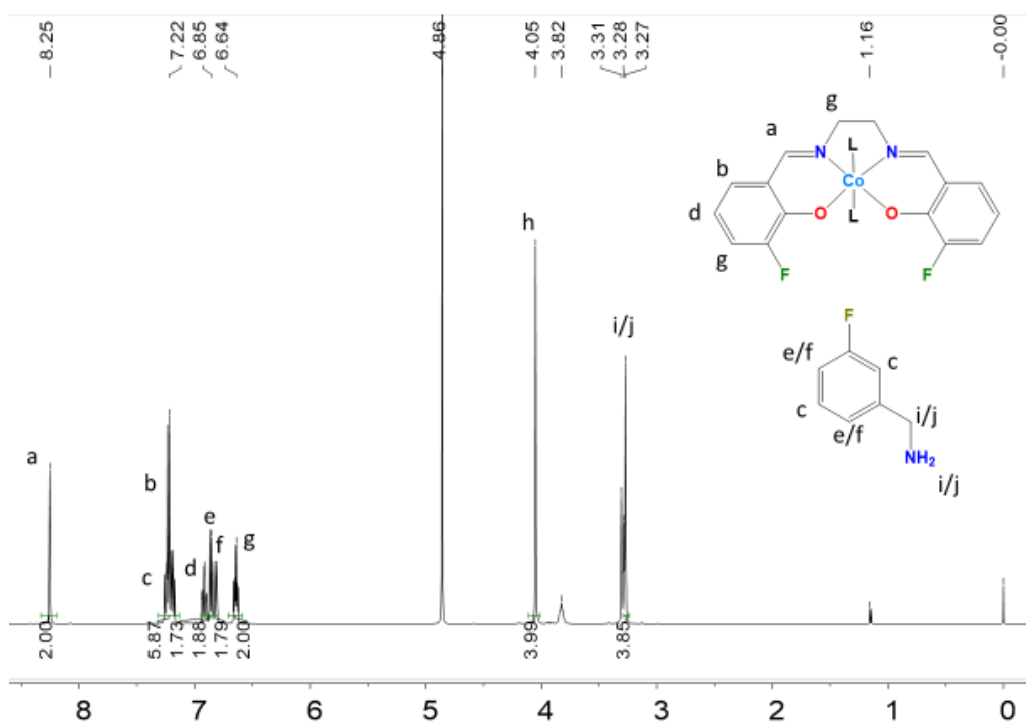


Figure S3.2. ^1H NMR (500 MHz) spectrum of $[\text{Co}(\text{3F-salen})(\text{3F-BnNH}_2)]^+$ in $\text{MeOD-}d_4$ at 298 K.

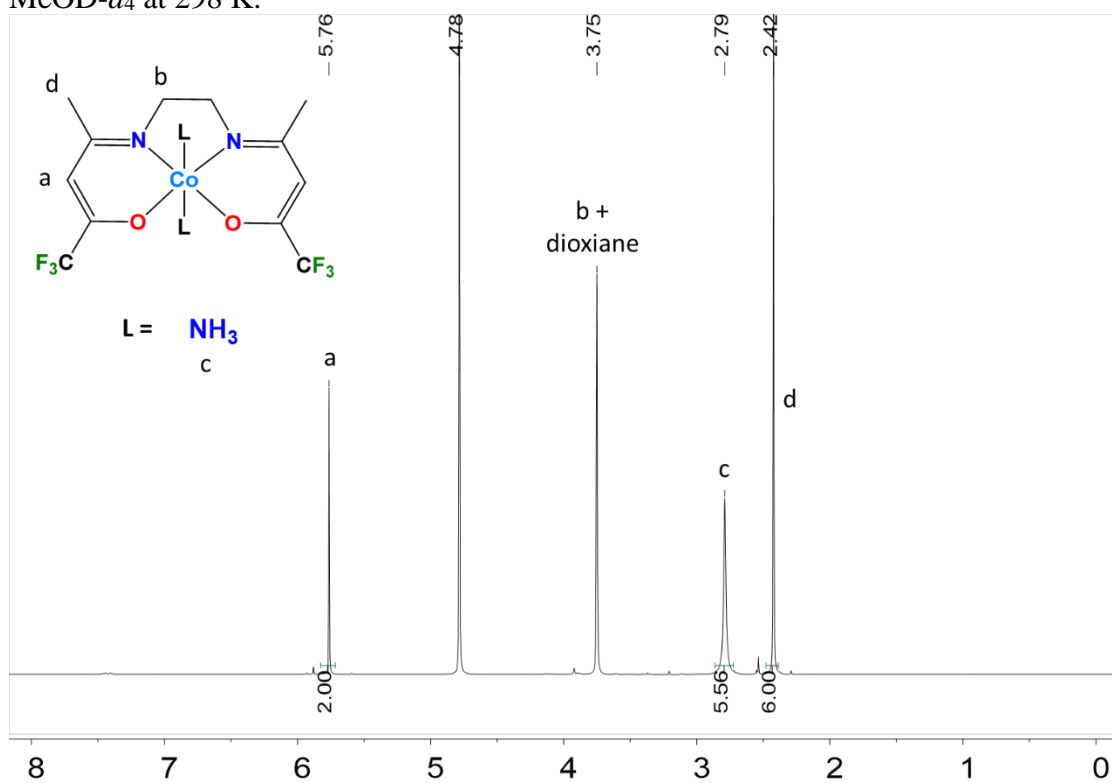


Figure S3.3. ^1H NMR (500 MHz) spectrum of $[\text{Co}(\text{tfacn})(\text{NH}_3)_2]^+$ in D_2O at 298 K.

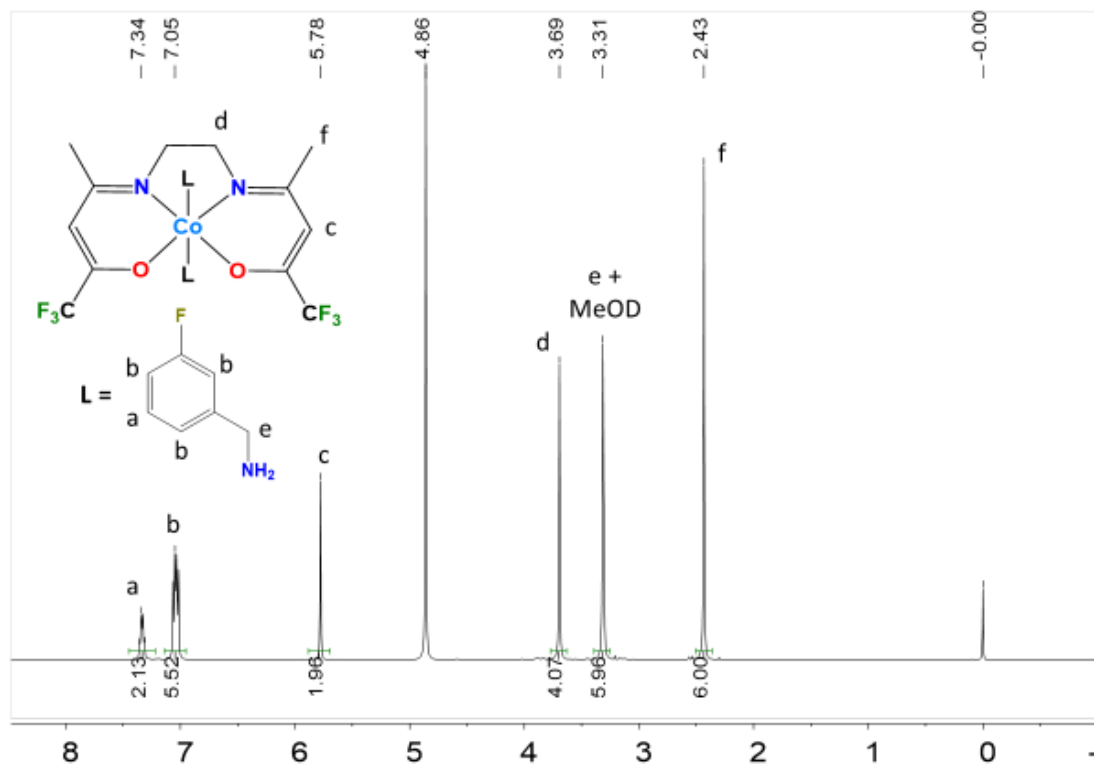


Figure S3.4. ^1H NMR (500 MHz) spectrum of $[\text{Co}(\text{tfacen})(3\text{F-BnNH}_2)_2]^+$ in $\text{MeOD-}d_4$ at 298 K.

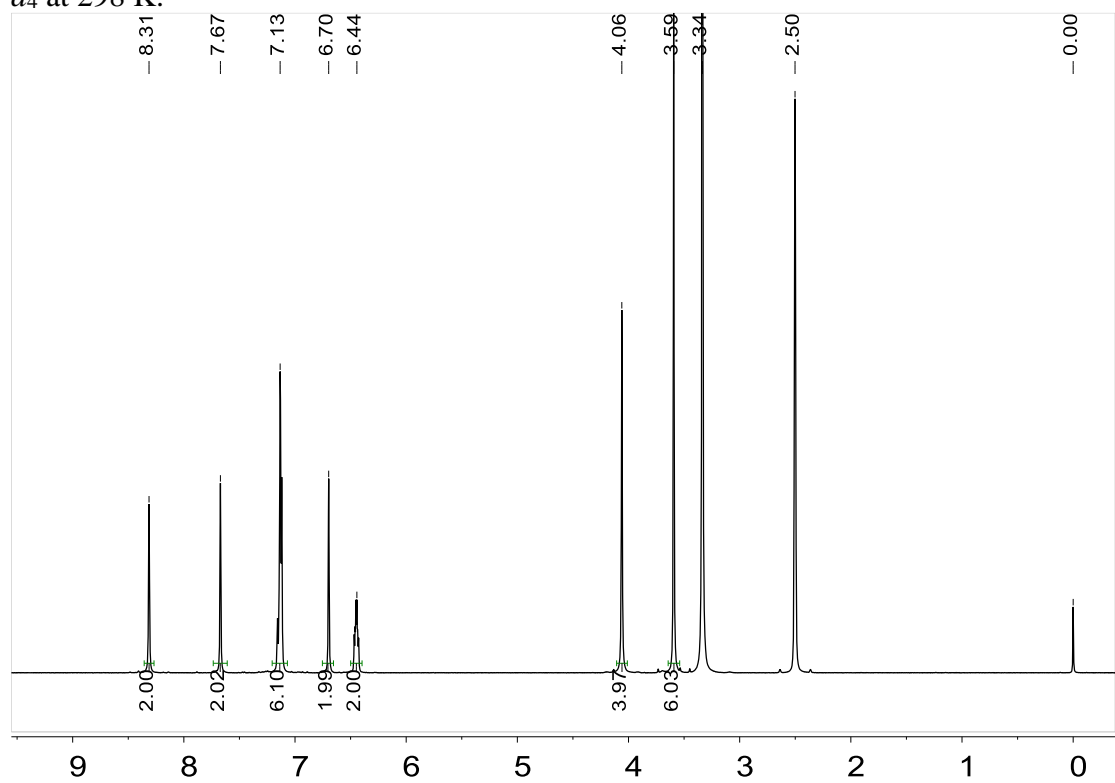


Figure S3.5. ^1H NMR (500 MHz) spectrum of $[\text{Co}(\text{3F-salen})(\text{MeIm})_2]^+$ in $\text{DMSO-}d_6$ at 298 K.

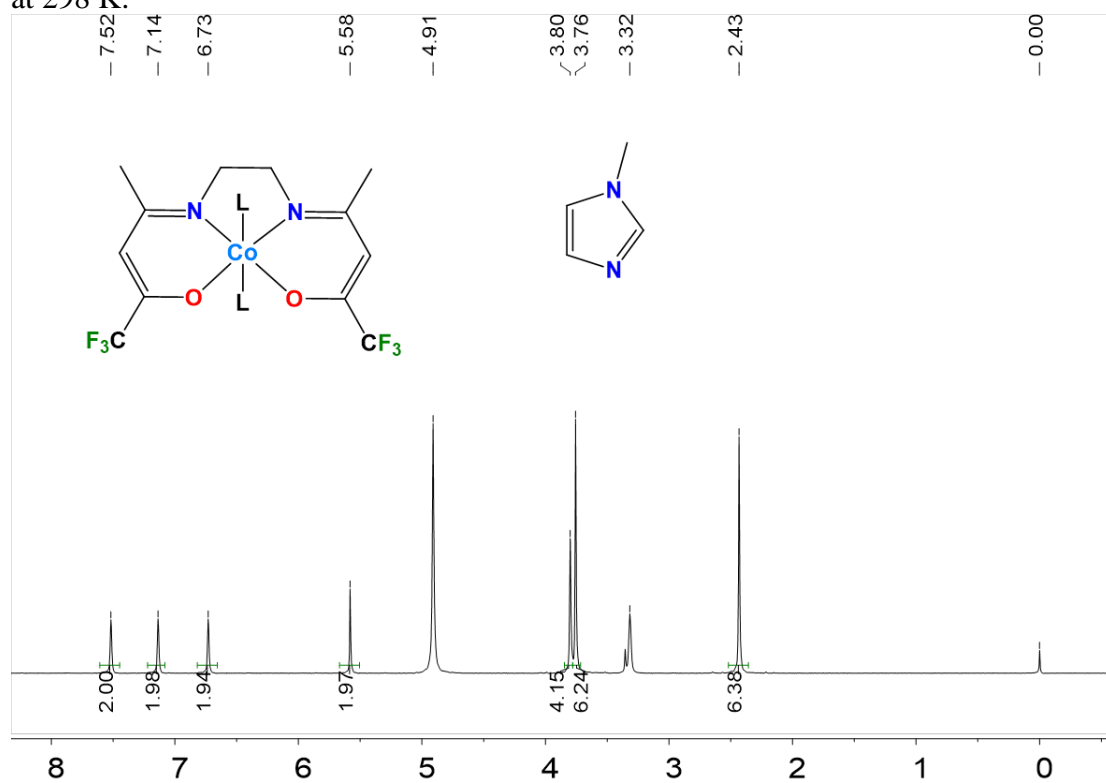


Figure S3.6. ^1H NMR (500 MHz) spectrum of $[\text{Co}(\text{tfacen})(\text{MeIm})_2]^+$ in $\text{MeOD-}d_4$ at 298 K.

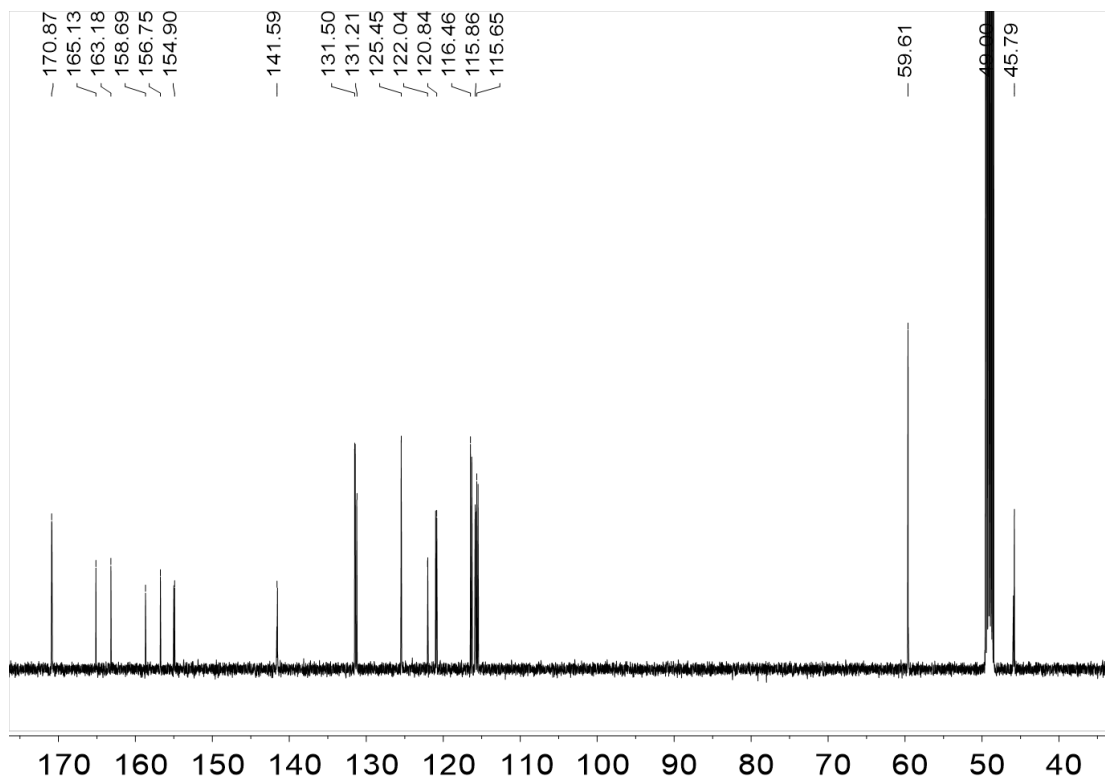


Figure S3.7. $^{13}\text{C}\{^1\text{H}\}$ NMR (126 MHz) spectrum of $[\text{Co}(\text{3F-salen})(\text{3F-BnNH}_2)_2]^+$ in $\text{MeOD-}d_4$ at 298 K.

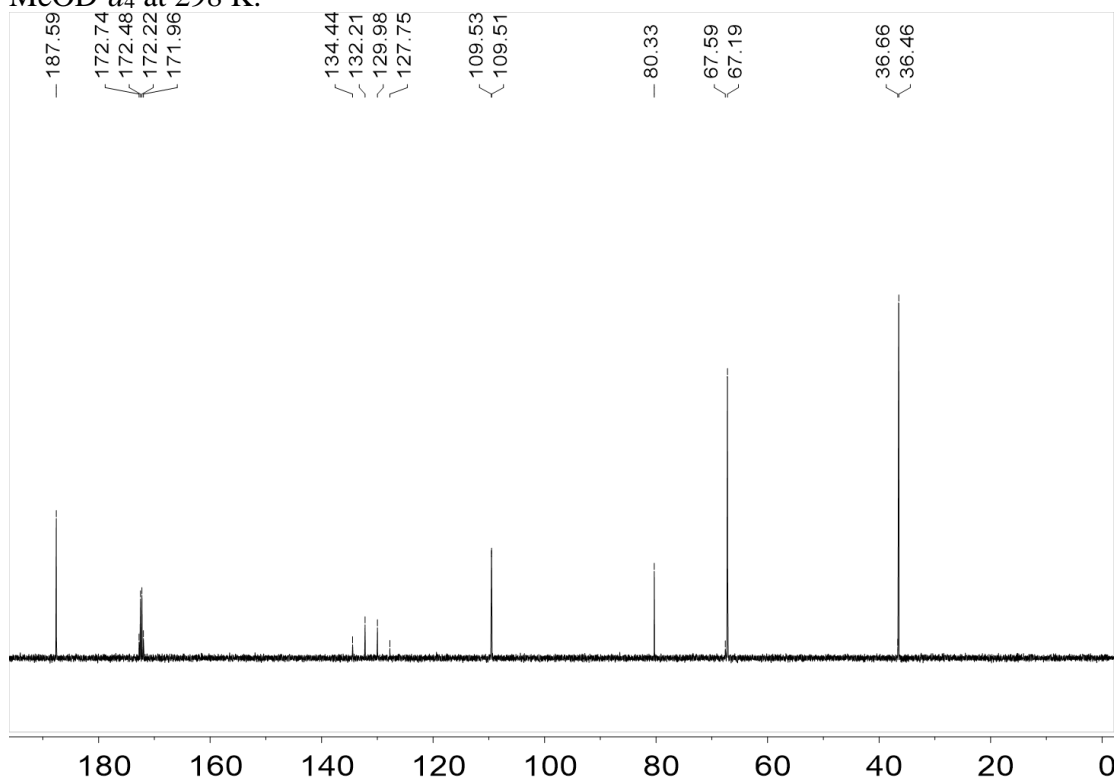


Figure S3.8. $^{13}\text{C}\{^1\text{H}\}$ NMR (126 MHz) spectrum of $[\text{Co}(\text{tfacn})(\text{NH}_3)_2]^+$ in D_2O at 298 K.

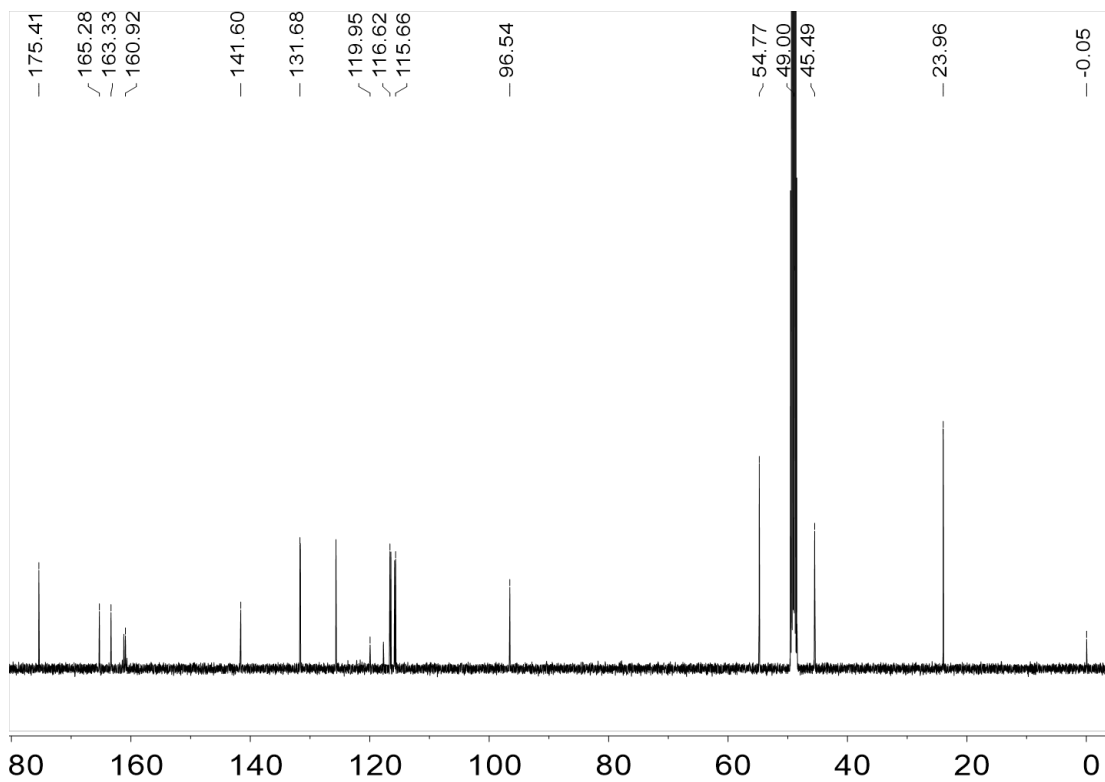


Figure S3.9. $^{13}\text{C}\{^1\text{H}\}$ NMR (126 MHz) spectrum of $[\text{Co}(\text{tfacn})(3\text{F-BnNH}_2)_2]^+$ in $\text{MeOD-}d_4$ at 298 K.

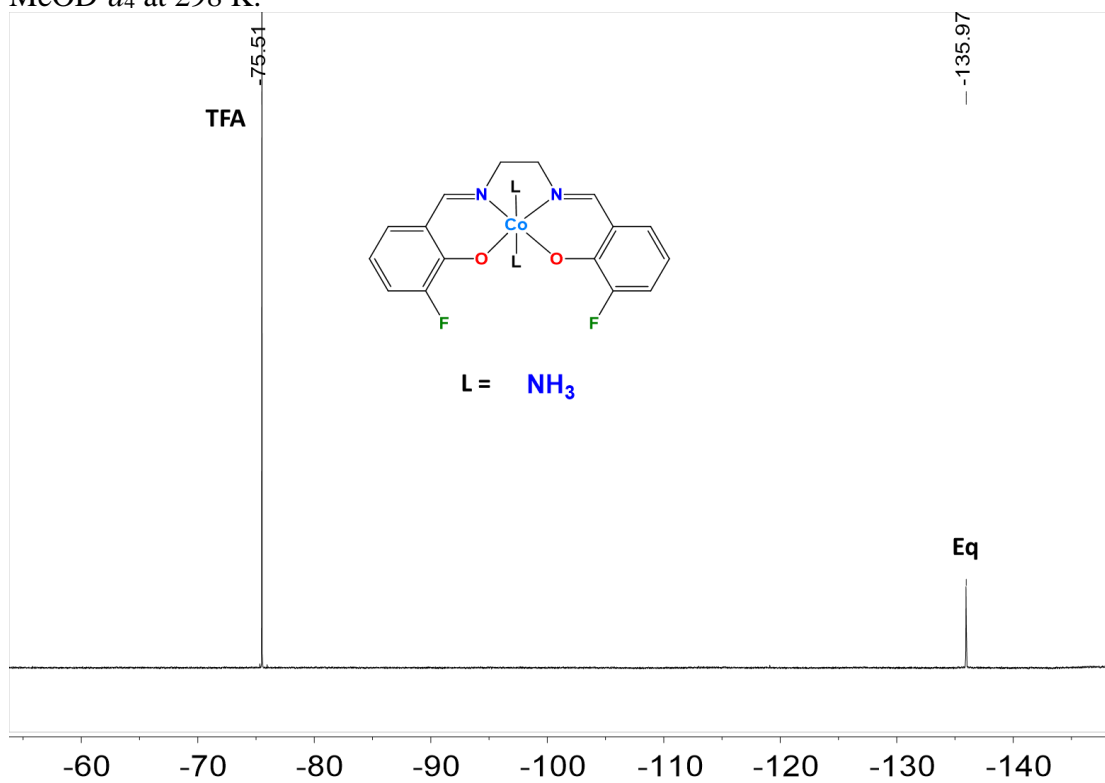


Figure S3.10. ^{19}F NMR (470 MHz) spectrum of $[\text{Co}(3\text{F-salen})(\text{NH}_3)_2]^+$ in H_2O at 298 K.

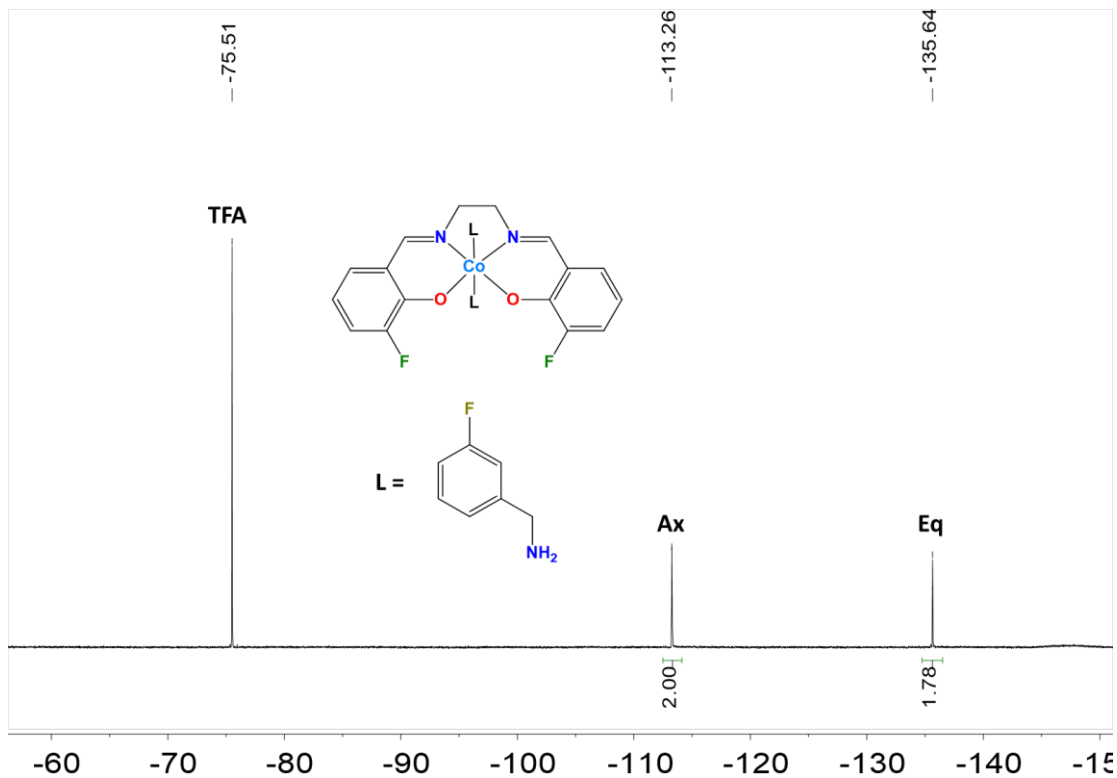


Figure S3.11. ^{19}F NMR (470 MHz) spectrum of $[\text{Co}(\text{3F-salen})(\text{3F-BnNH}_2)_2]^+$ in H_2O at 298 K.

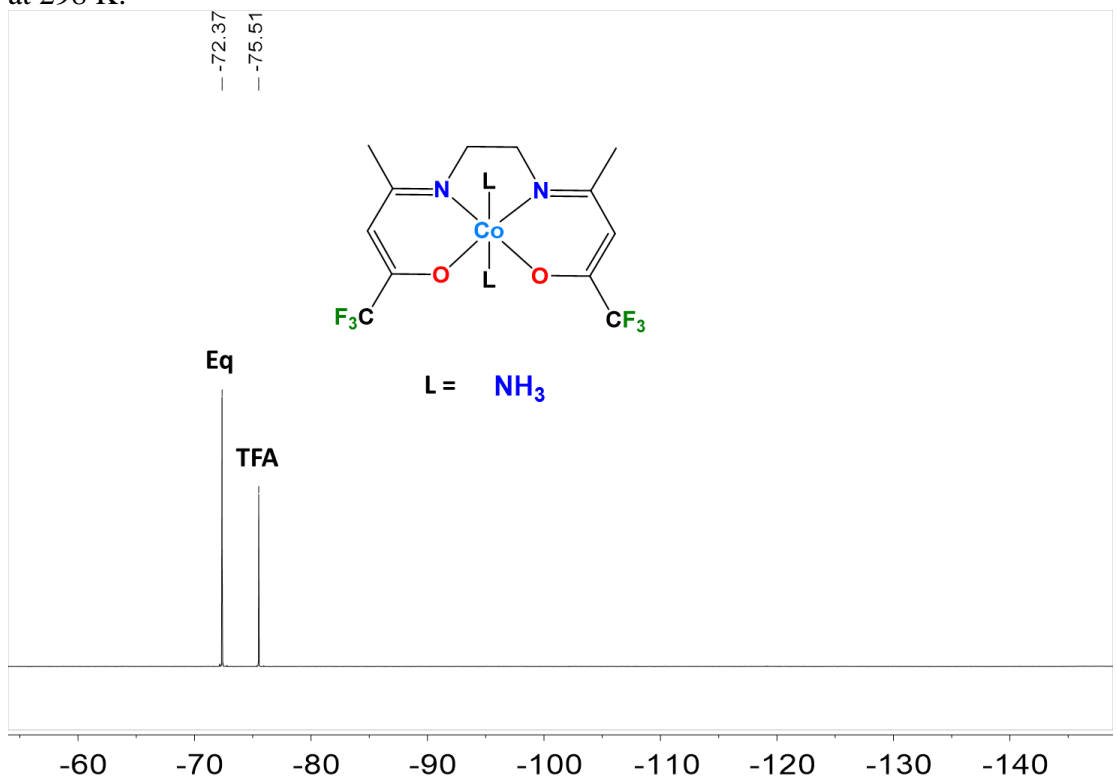


Figure S3.12. ^{19}F NMR (470 MHz) spectrum of $[\text{Co}(\text{tfacen})(\text{NH}_3)_2]^+$ in H_2O at 298 K.

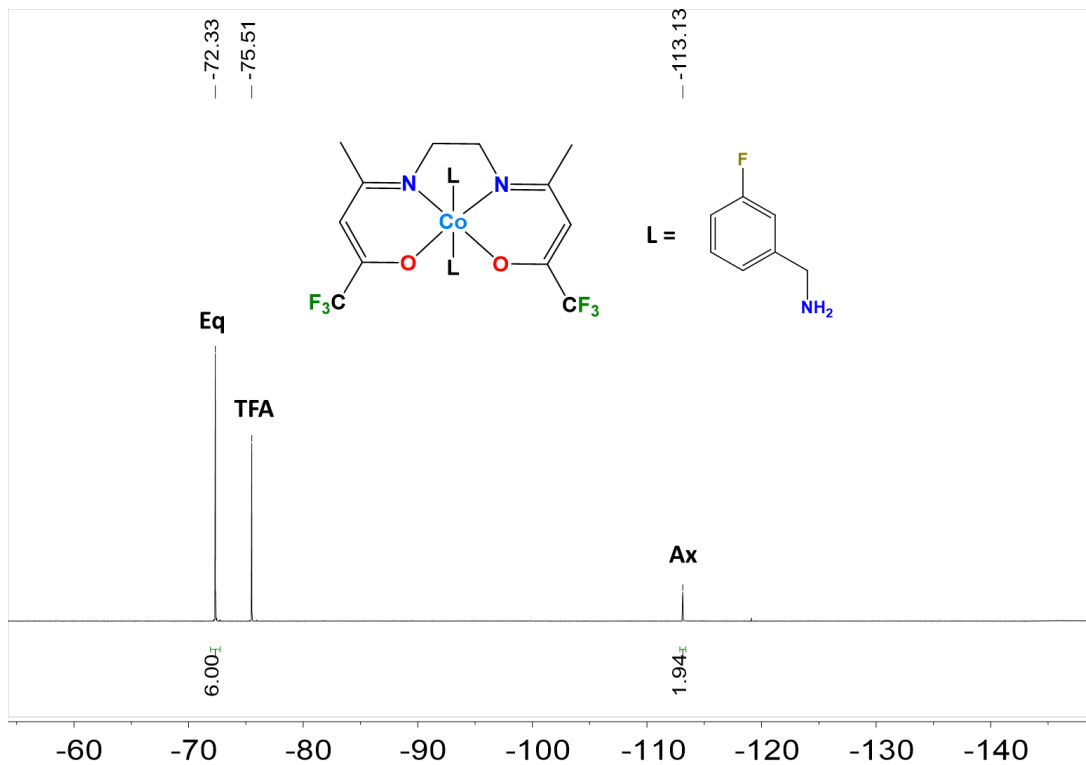


Figure S3.13. ^{19}F NMR (470 MHz) spectrum of $[\text{Co}(\text{tfacen})(3\text{F-BnNH}_2)_2]^+$ in H_2O at 298 K.

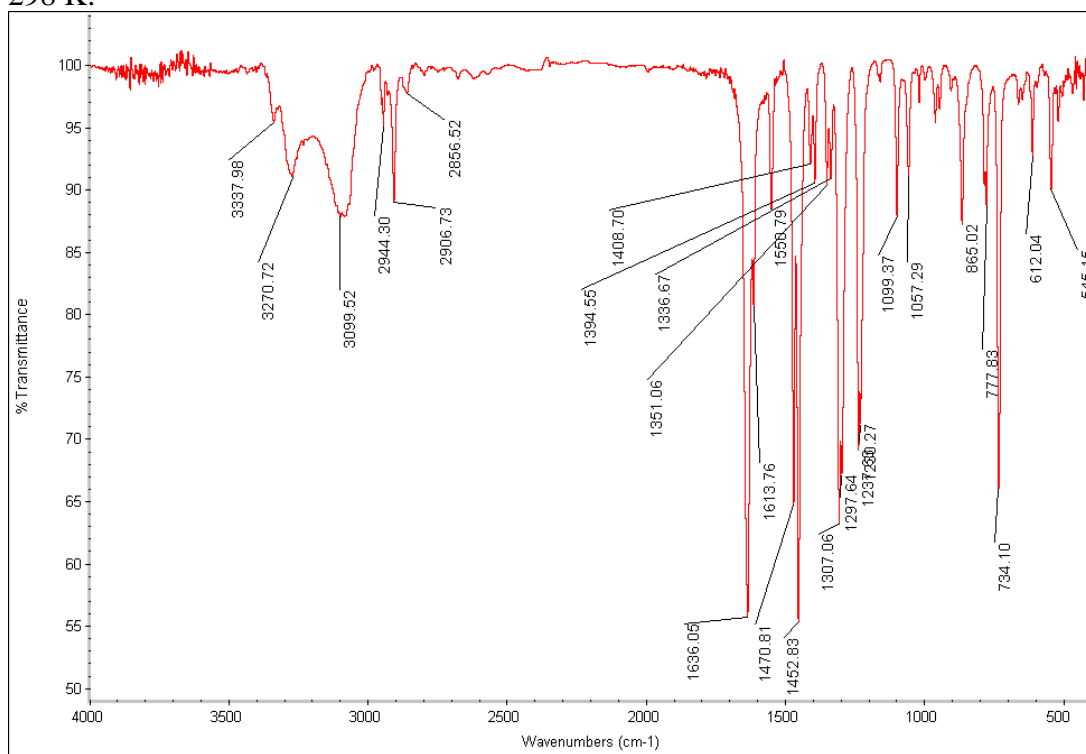


Figure S3.14. IR spectrum of $[\text{Co}(3\text{F-salen})(\text{NH}_3)_2]^+$

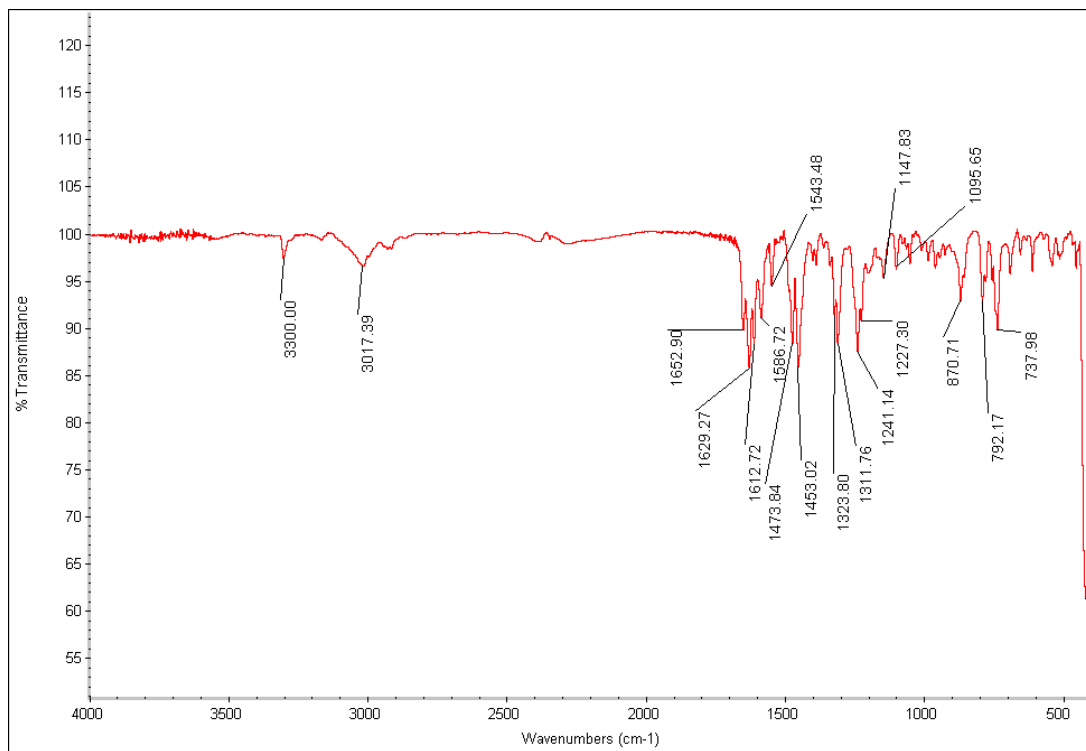


Figure S3.15. IR spectrum of $[\text{Co}(\text{3F-salen})(\text{3F-BnNH}_2)_2]^+$

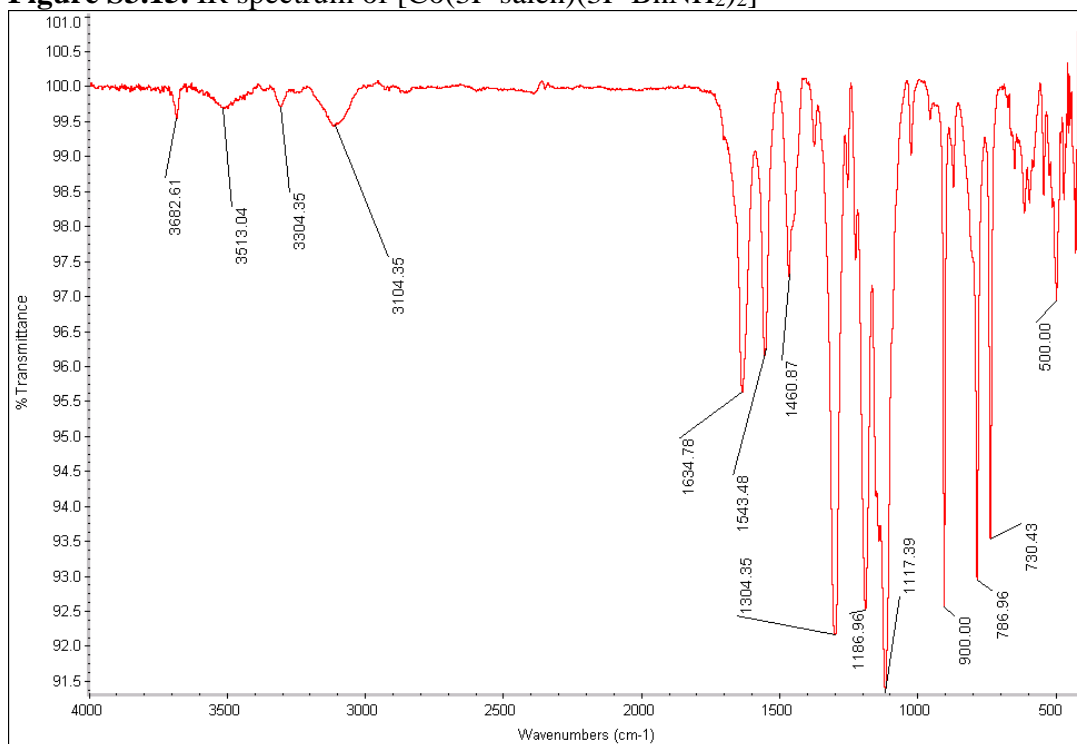


Figure S3.16. IR spectrum of $[\text{Co}(\text{tfacn})(\text{NH}_3)_2]^+$

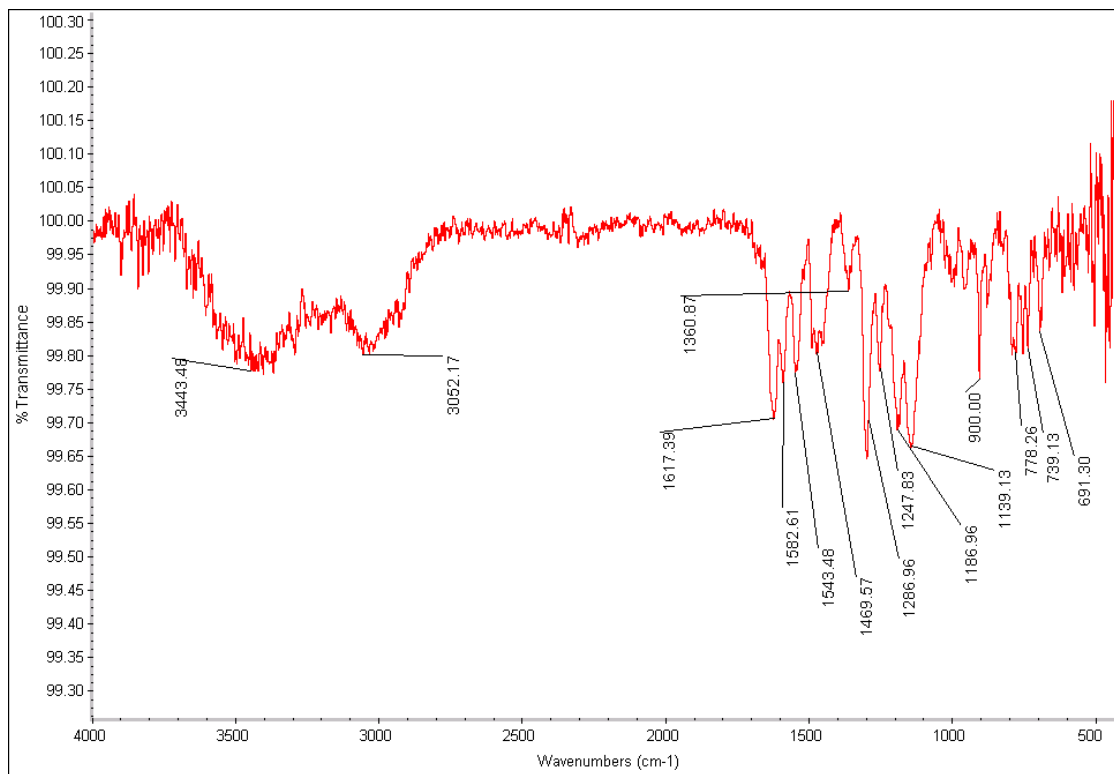


Figure S3.17. IR spectrum of $[\text{Co}(\text{tfacen})(3\text{F-BnNH}_2)_2]^+$

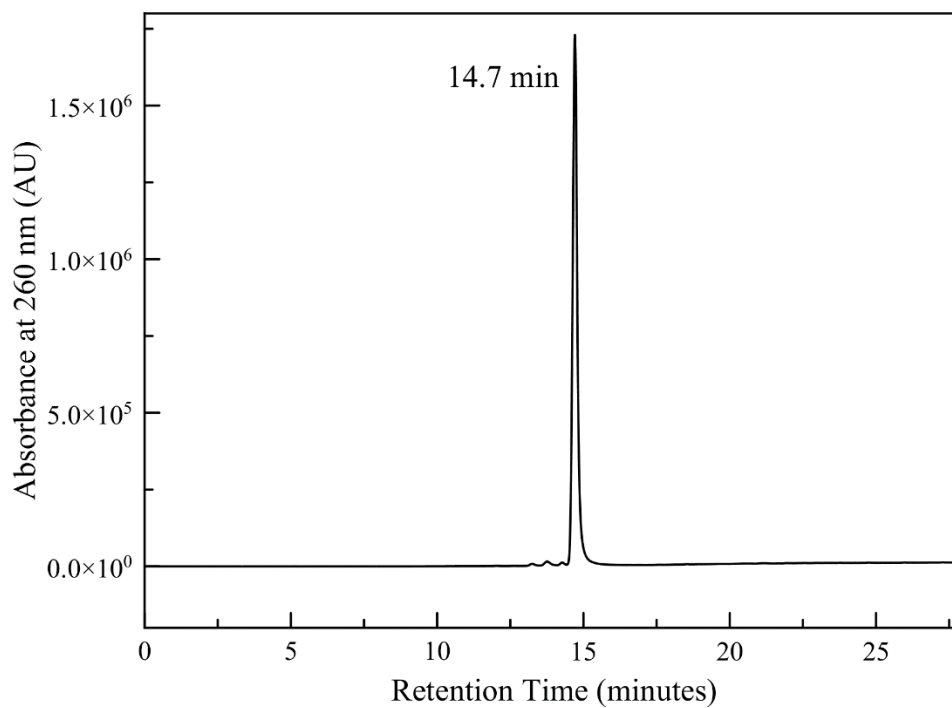


Figure S3.18. HPLC chromatogram of $[\text{Co}(3\text{F-salen})(\text{NH}_3)_2]^+$

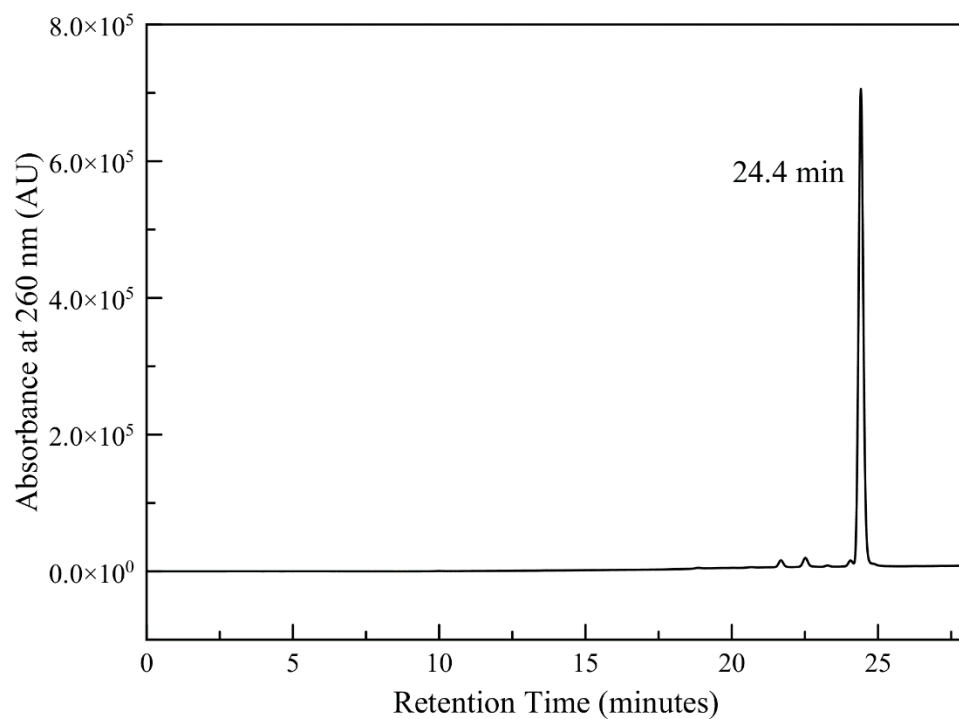


Figure S3.19. HPLC chromatogram of $[\text{Co}(\text{3F-salen})(\text{3F-BnNH}_2)_2]^+$

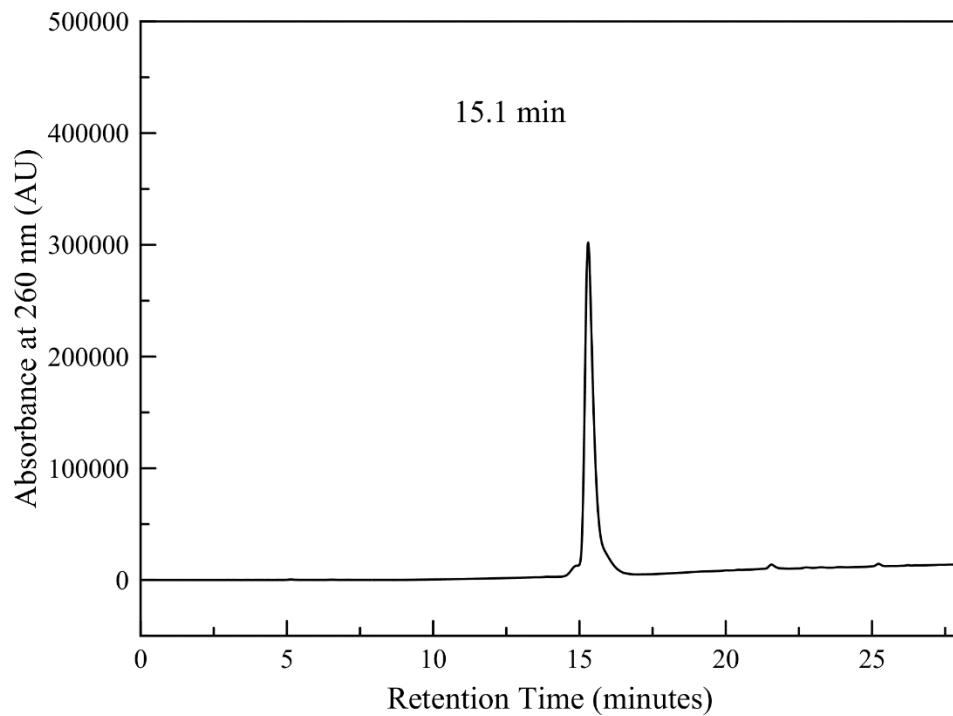


Figure S3.20. HPLC chromatogram of $[\text{Co}(\text{tfacn})(\text{NH}_3)_2]^+$

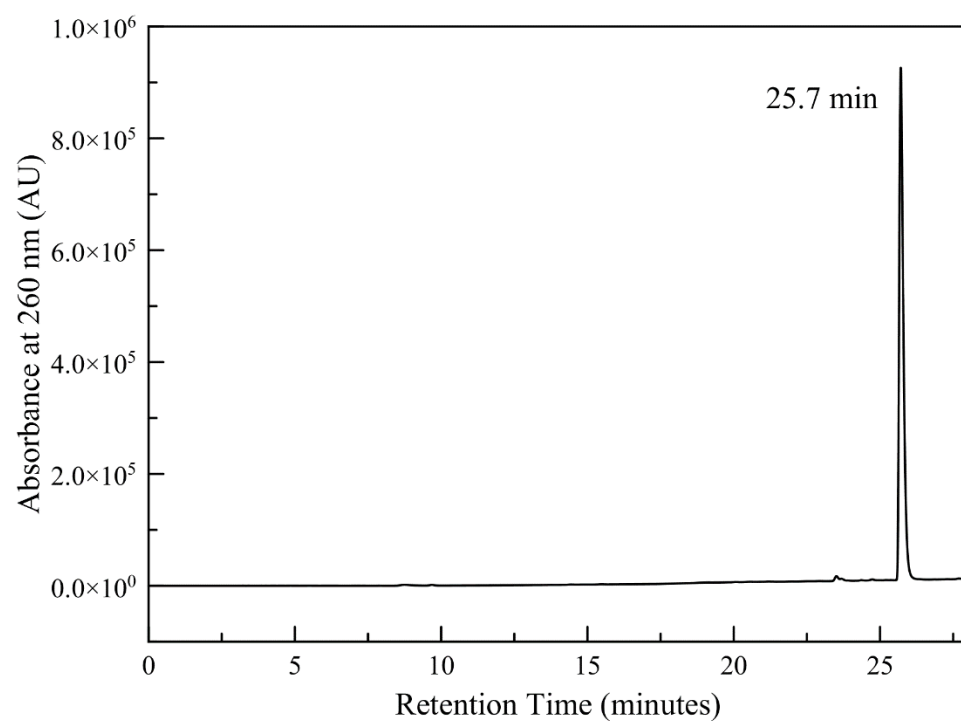


Figure S3.21. HPLC chromatogram of $[\text{Co}(\text{tfacen})(3\text{F-BnNH}_2)_2]^+$

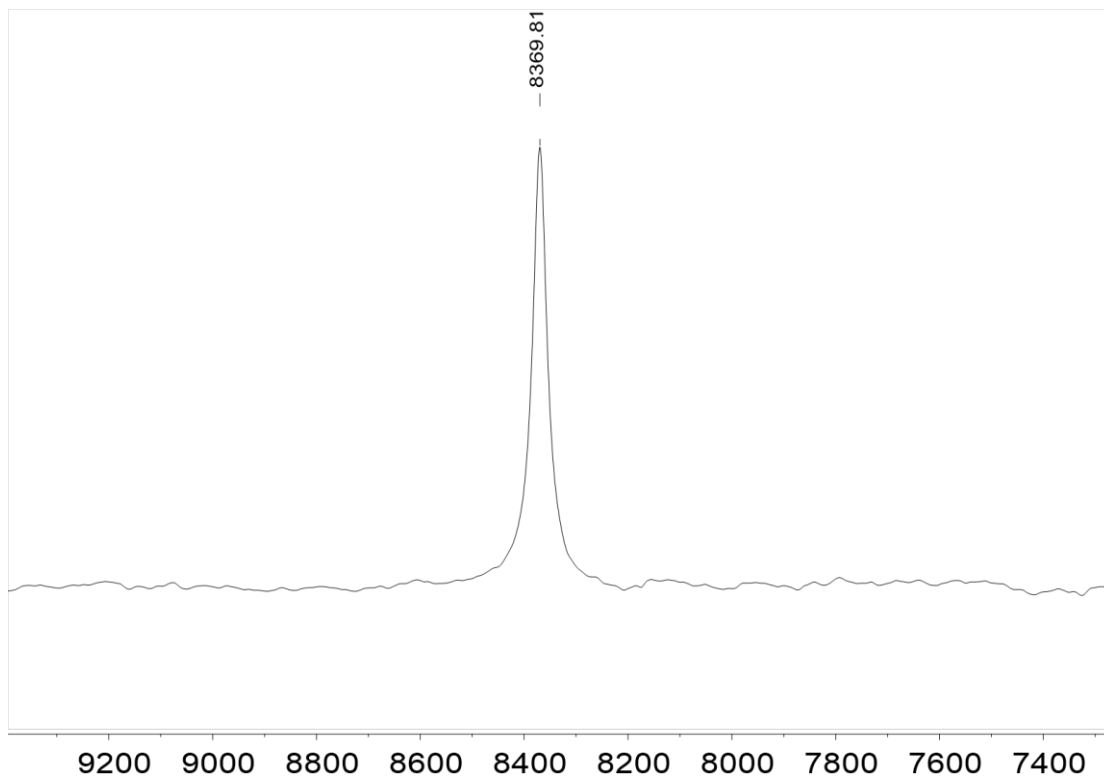


Figure S3.22. ^{59}Co NMR (120 MHz) spectrum of $[\text{Co}(\text{3F-salen})(\text{NH}_3)_2]^+$ in D_2O at 298 K.

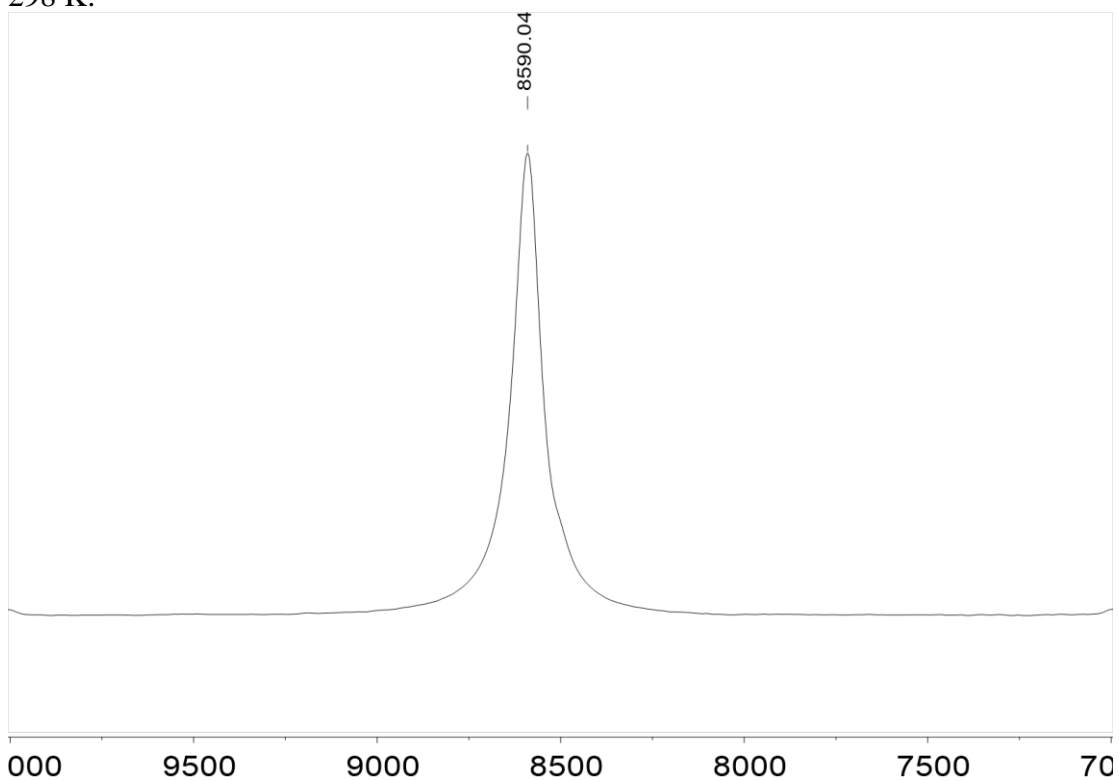


Figure S3.23. ^{59}Co NMR (120 MHz) spectrum of $[\text{Co}(\text{3F-salen})(\text{3F-BnNH}_2)_2]^+$ in $\text{MeOD-}d_4$ at 298 K.

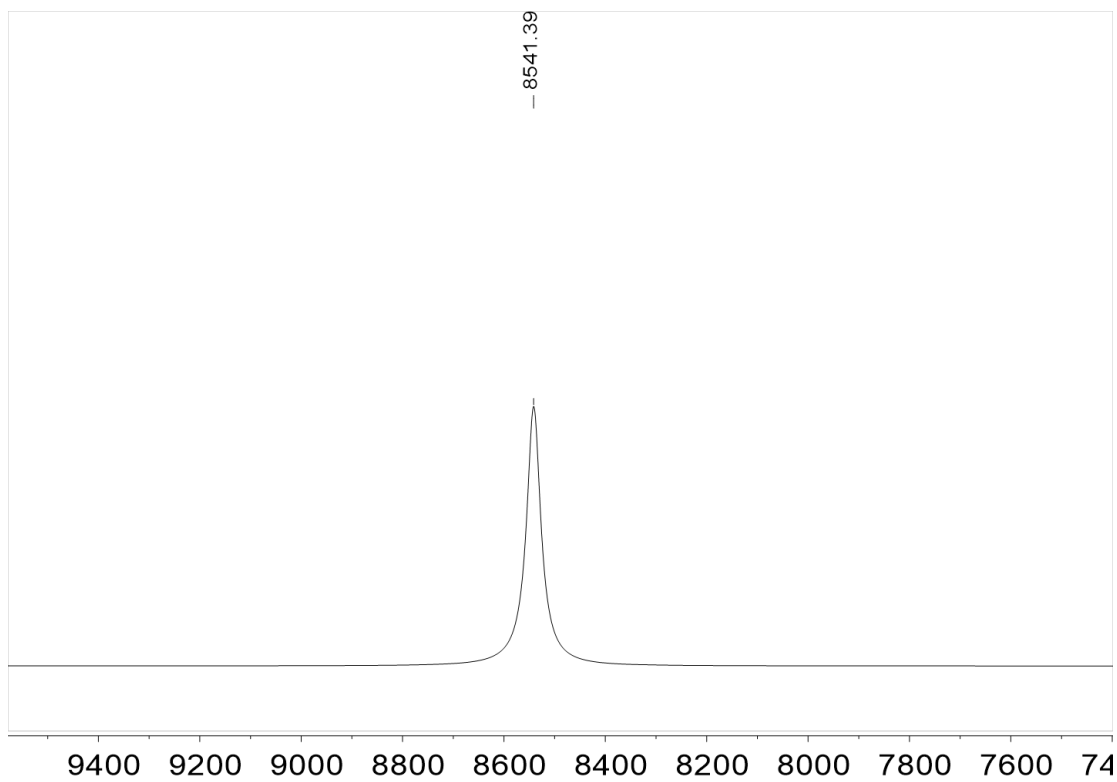


Figure S3.24. ^{59}Co NMR (120 MHz) spectrum of $[\text{Co}(\text{tfacn})(\text{NH}_3)_2]^+$ in D_2O at 298 K.

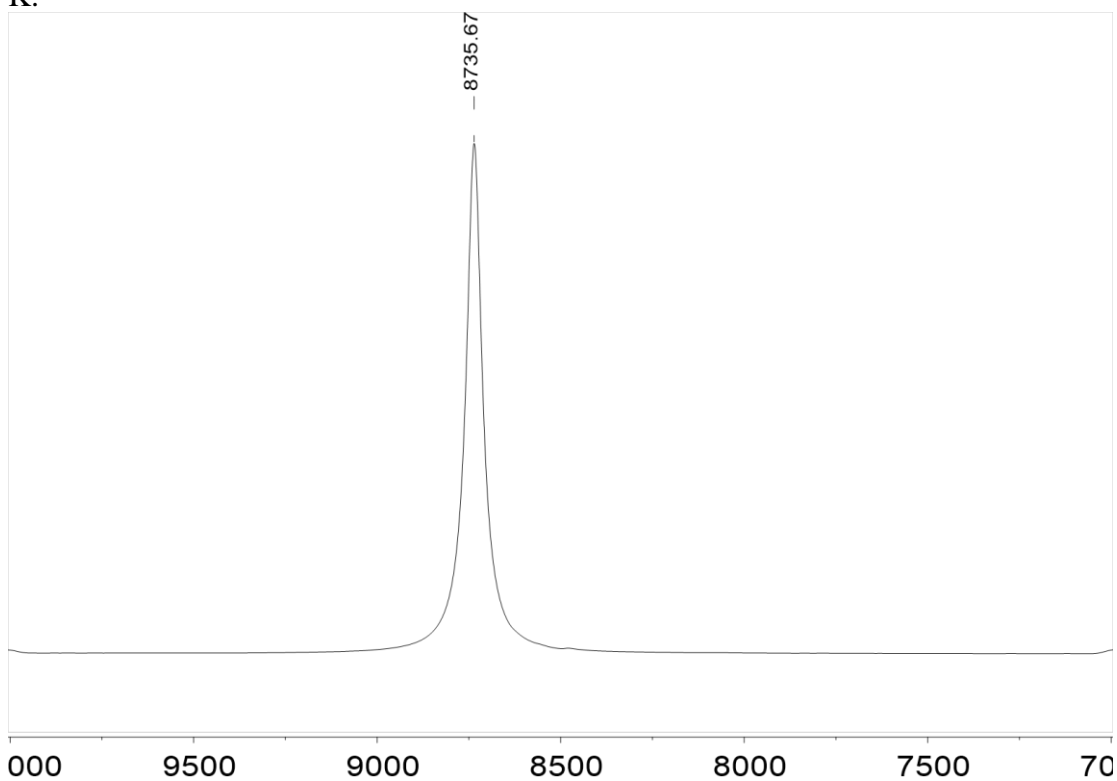


Figure S3.25. ^{59}Co NMR (120 MHz) spectrum of $[\text{Co}(\text{tfacn})(3\text{F-BnNH}_2)_2]^+$ in $\text{MeOD-}d_4$ at 298 K.

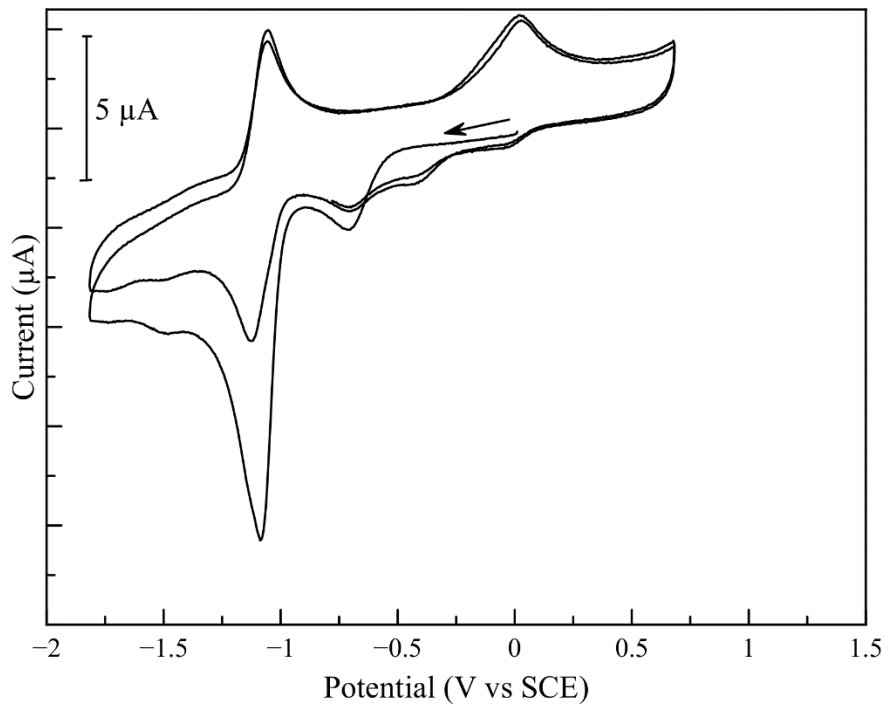


Figure S3.26. Cyclic voltammogram of $[\text{Co}(\text{3F-salen})(\text{NH}_3)_2]^+$ in DMF with 0.1 M TBAP at 298 K and 0.1 V/s scan rate.

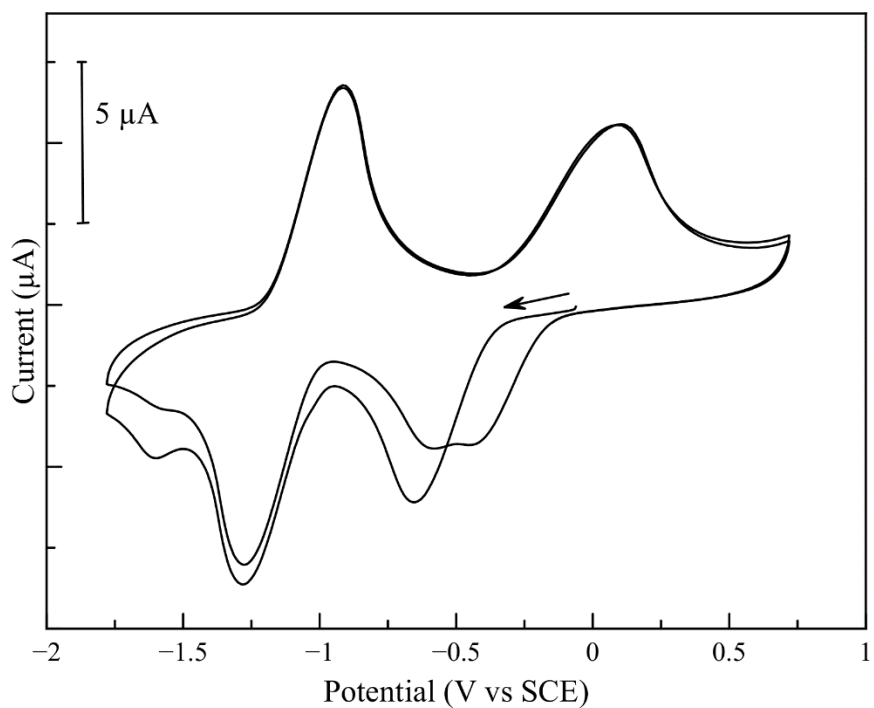


Figure S3.27. Cyclic voltammogram of $[\text{Co}(\text{3F-salen})(\text{3FBnNH}_2)_2]^+$ in DMF with 0.1 M TBAP at 298 K and 0.1 V/s scan rate.

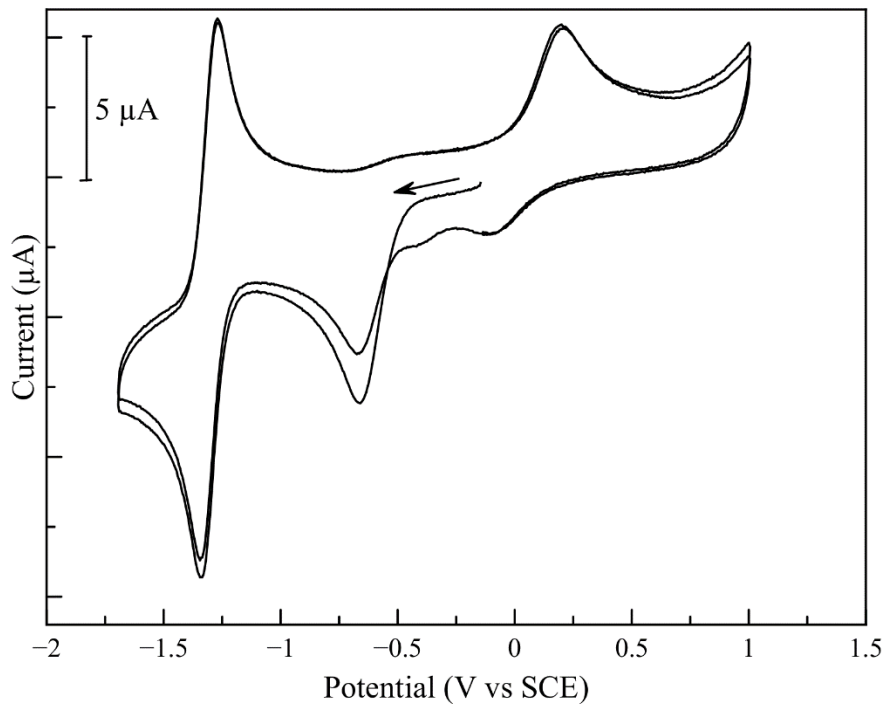


Figure S3.28. Cyclic voltammogram of $[\text{Co}(\text{tfacen})(\text{NH}_3)_2]^+$ in DMF with 0.1 M TBAP at 298 K and 0.1 V/s scan rate.

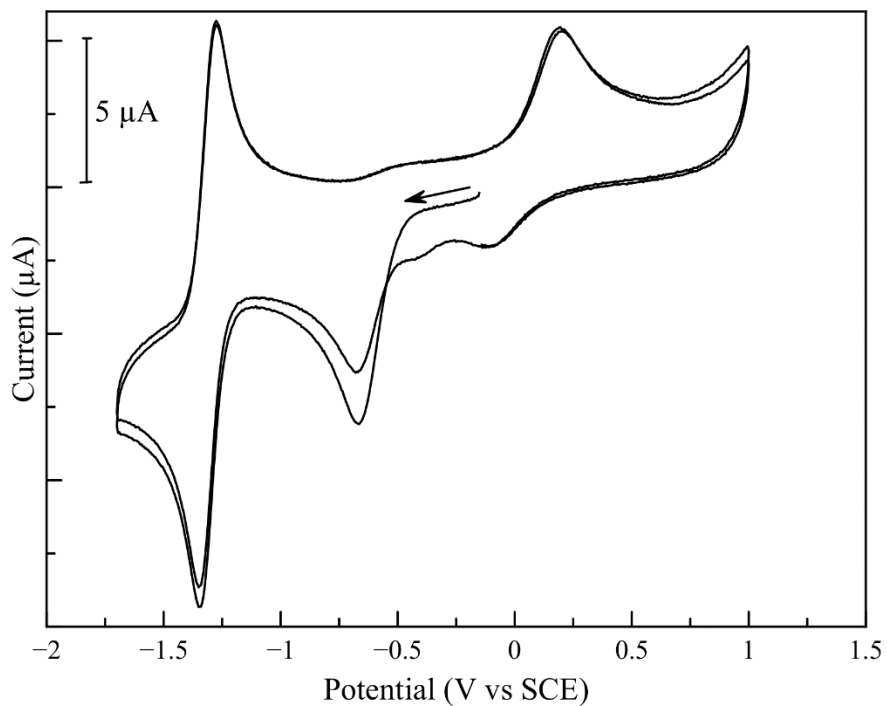


Figure S3.29. Cyclic voltammogram of $[\text{Co}(\text{tfacen})(3\text{FBnNH}_2)_2]^+$ in DMF with 0.1 M TBAP at 298 K and 0.1 V/s scan rate.

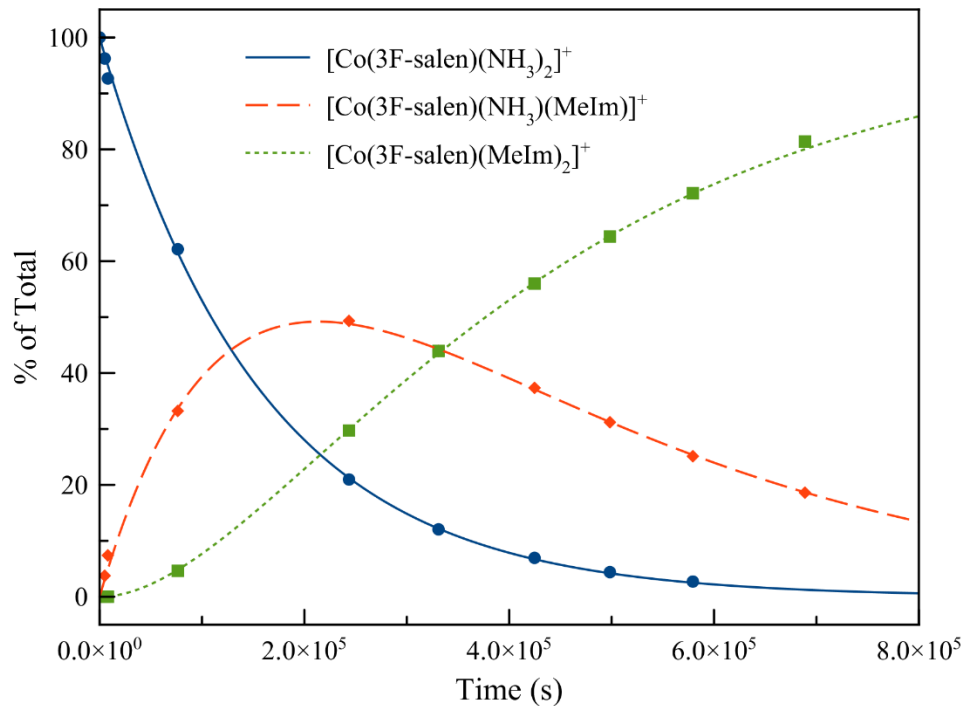


Figure S3.30. Concentration versus time plot for ligand exchange of $[\text{Co}(\text{3F-salen})(\text{NH}_3)_2]^+$ by *N*-methylimidazole in 100 mM MOPS (pH 7.4) at 335 K.

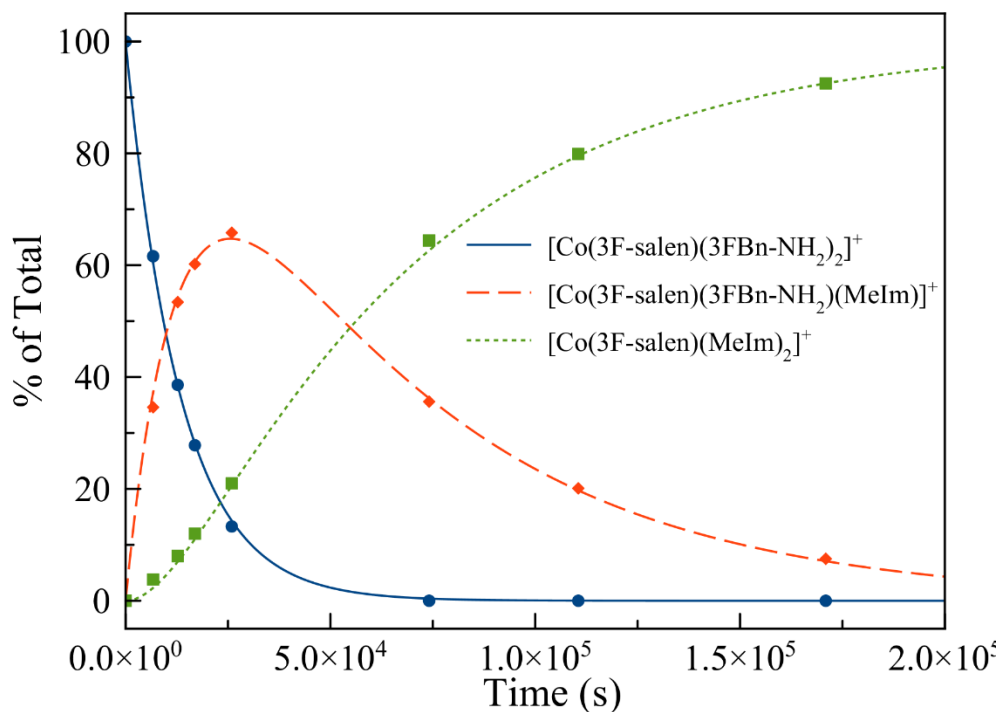


Figure S3.31. Concentration versus time plot for ligand exchange of $[\text{Co}(\text{3F-salen})(\text{3FBnNH}_2)_2]^+$ by *N*-methylimidazole in 100 mM MOPS (pH 7.4) at 335 K.

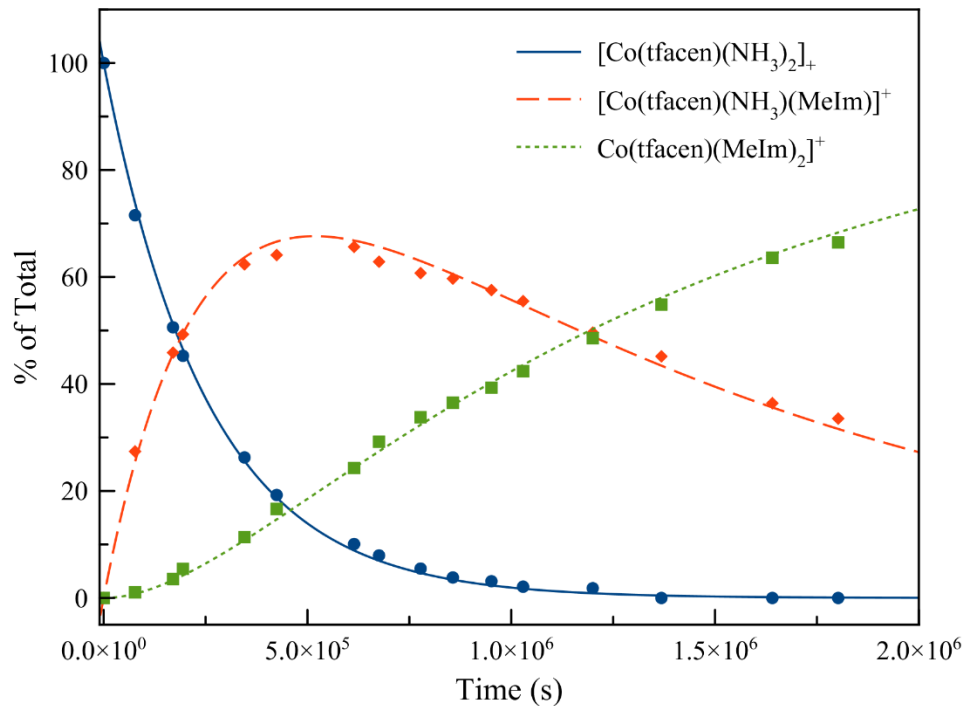


Figure S3.32. Concentration versus time plot for ligand exchange of $[\text{Co}(\text{tfacn})(\text{NH}_3)_2]^+$ by *N*-methylimidazole in 100 mM MOPS (pH 7.4) at 335 K.

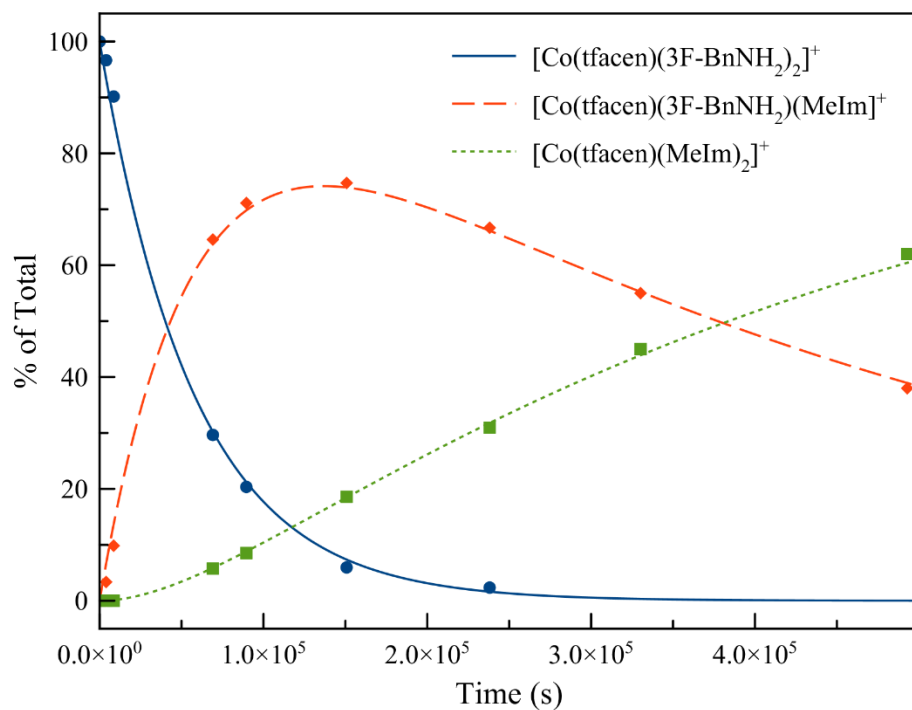


Figure S3.33. Concentration versus time plot for ligand exchange of $[\text{Co}(\text{tfacn})(3\text{F-BnNH}_2)_2]^+$ by *N*-methylimidazole in 100 mM MOPS (pH 7.4) at 335 K.

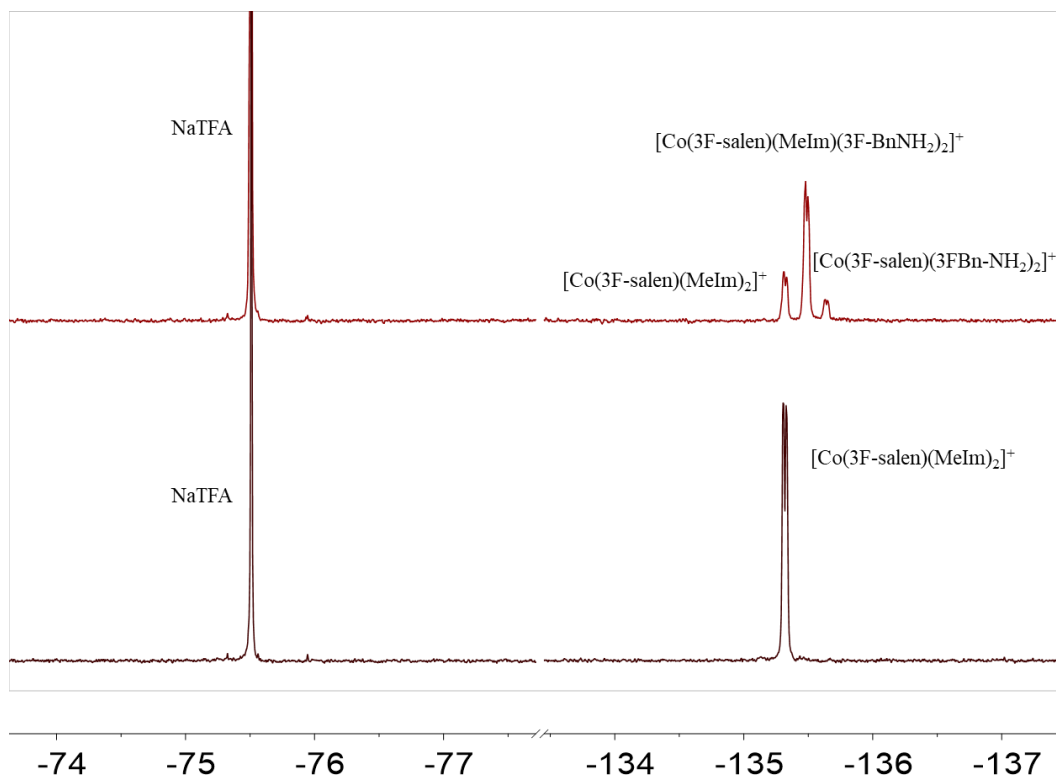


Figure S3.34. ^{19}F NMR (470 MHz) spectra in MOPS buffer (pH 7.4) of the ligand exchange reaction of $[\text{Co}(\text{3F-salen})(\text{3FBnNH}_2)_2]^+$ (top trace) and a solution of $[\text{Co}(\text{3F-salen})(\text{MeIm})_2]^+$ (bottom trace). The overlay of the spectra confirms $[\text{Co}(\text{3F-salen})(\text{MeIm})_2]^+$ as the product.

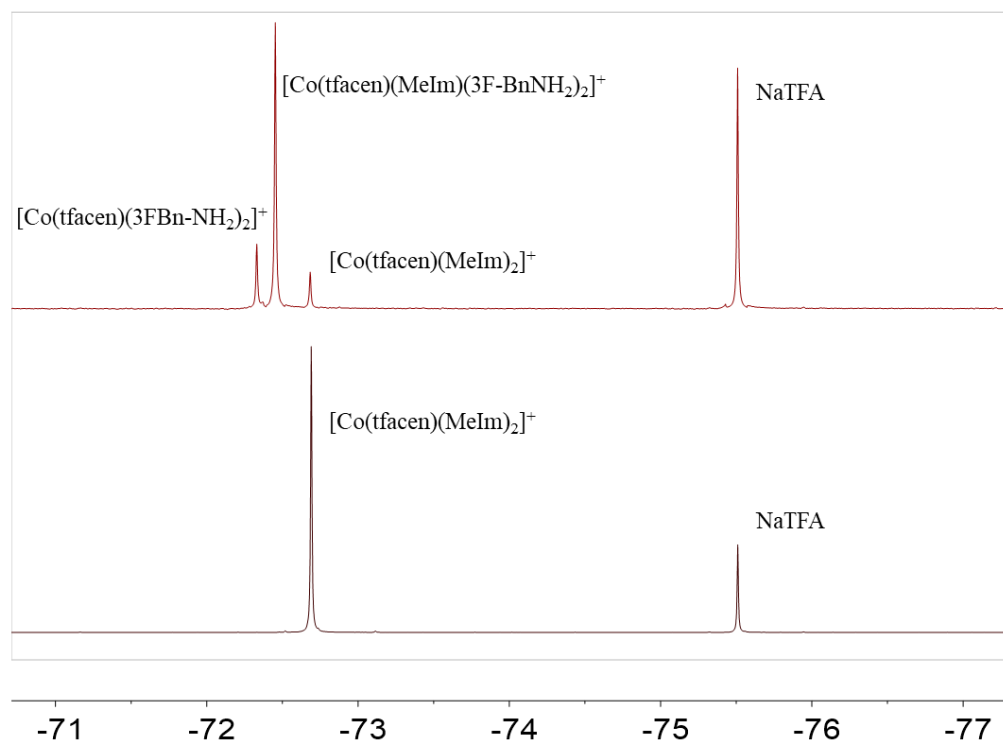


Figure S3.35. ^{19}F NMR (470 MHz) spectra in MOPS buffer (pH 7.4) of the ligand exchange reaction of $[\text{Co}(\text{tfacen})(3\text{FBnNH}_2)_2]^+$ (top trace) and a solution of $[\text{Co}(\text{tfacen})(\text{MeIm})_2]^+$ (bottom trace). The overlay of the spectra confirms $[\text{Co}(\text{tfacen})(\text{MeIm})_2]^+$ as the product.

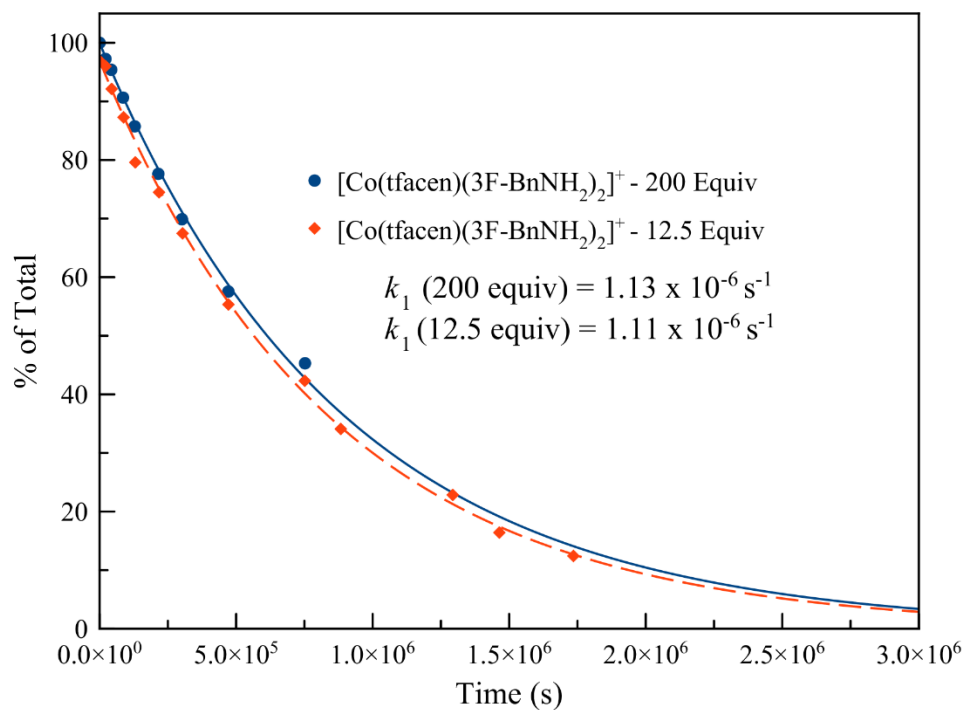


Figure S3.36. Concentration versus time plot for ligand exchange of $[\text{Co}(\text{tfacn})(3\text{F-BnNH}_2)_2]^+$ by 200 equivalents of *N*-methylimidazole in 100 mM MOPS (pH 7.4) at 291 K. The calculated pseudo first-order rate constant is the same within the error for that determined with only 25 equiv of MeIm, suggesting a zero-order dependence on MeIm.

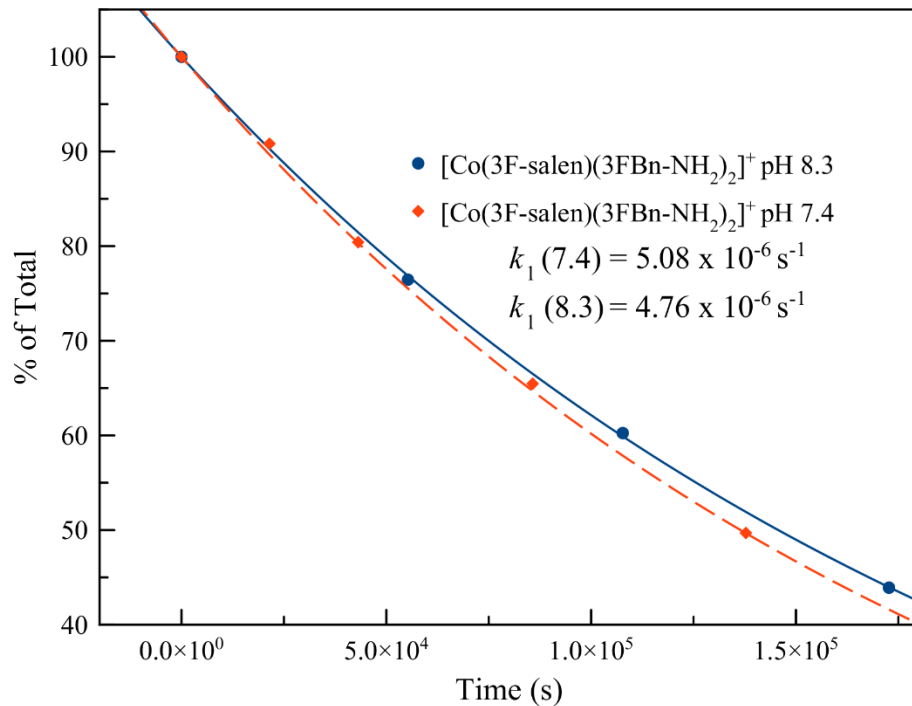


Figure S3.37. Concentration versus time plot for ligand exchange of $[\text{Co}(\text{3F-salen})(\text{3F-BnNH}_2)_2]^+$ by N-methylimidazole in 100 mM MOPS (pH 8.3) at 291 K. The calculated rate constant is the same within the error for that determined at pH 7.4, suggesting that this reaction is not accelerated by this higher pH value.

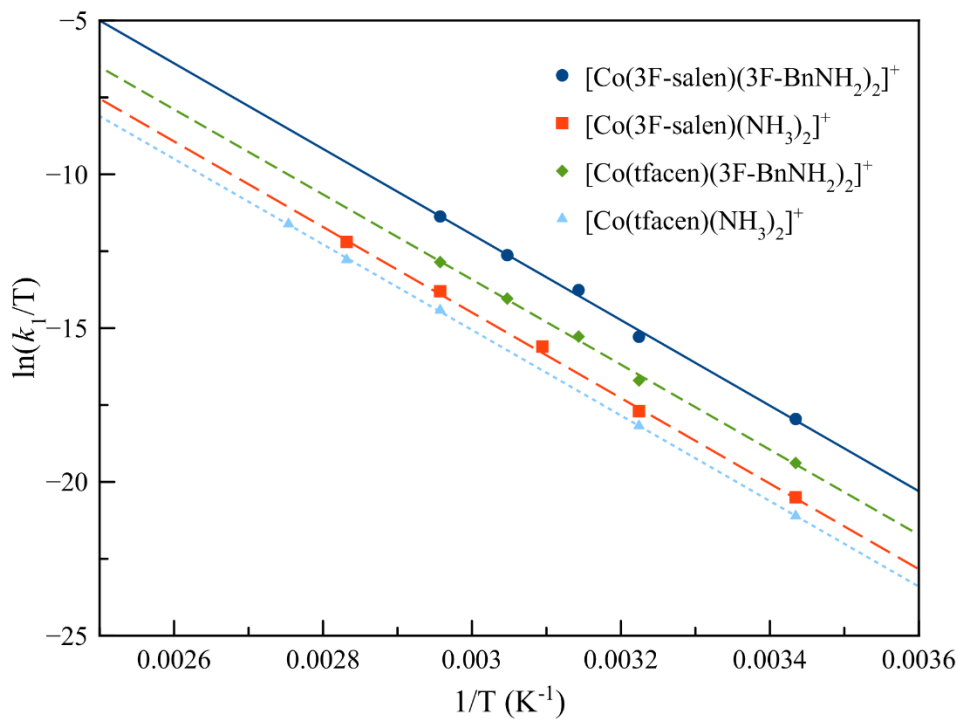


Figure S3.38. Eyring analysis plots demonstrating the dependence of the rate constant for the 1st ligand substitution step (k_1) on temperature.

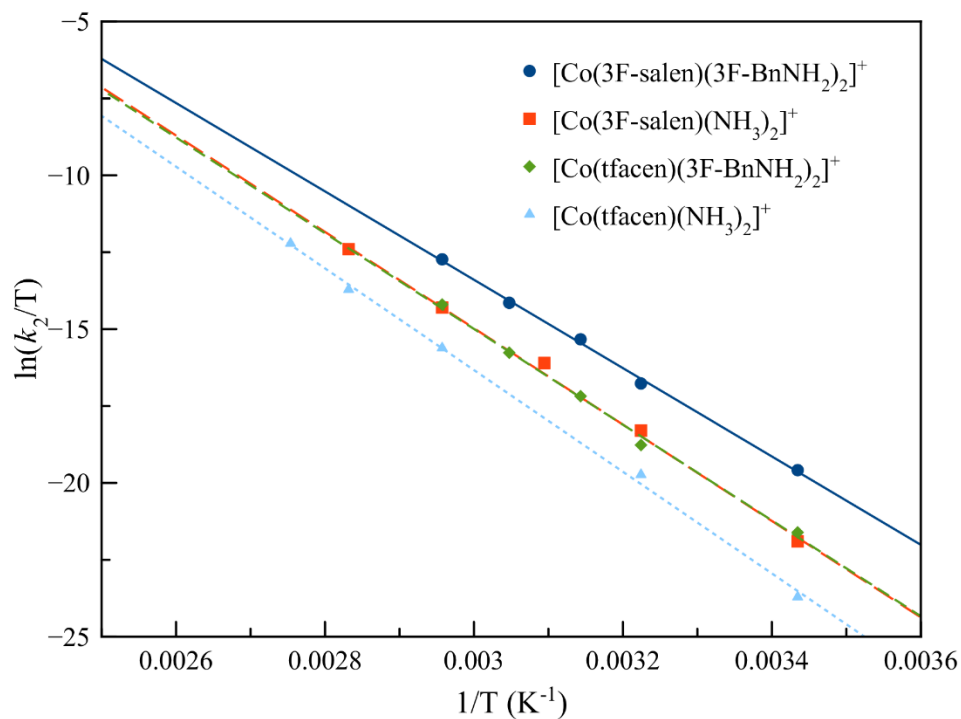


Figure S3.39. Eyring analysis plots demonstrating the dependence of the rate constant for the 2nd ligand substitution step (k_2) on temperature.

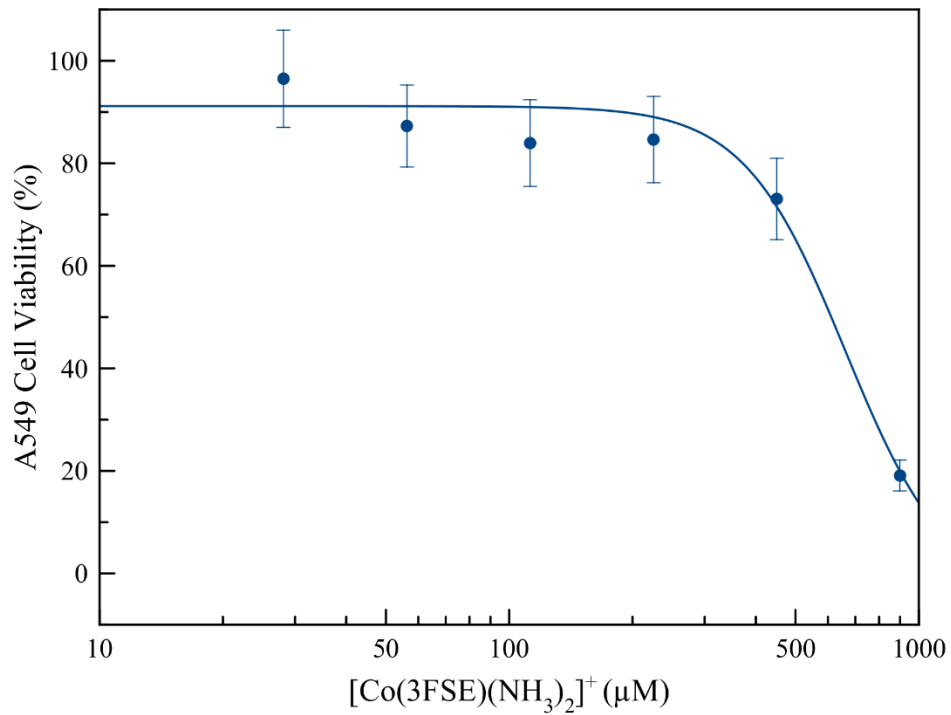


Figure S3.40. Dose-response curve for $[\text{Co}(\text{3FSE})(\text{NH}_3)_2]^+$ in A549 cells.

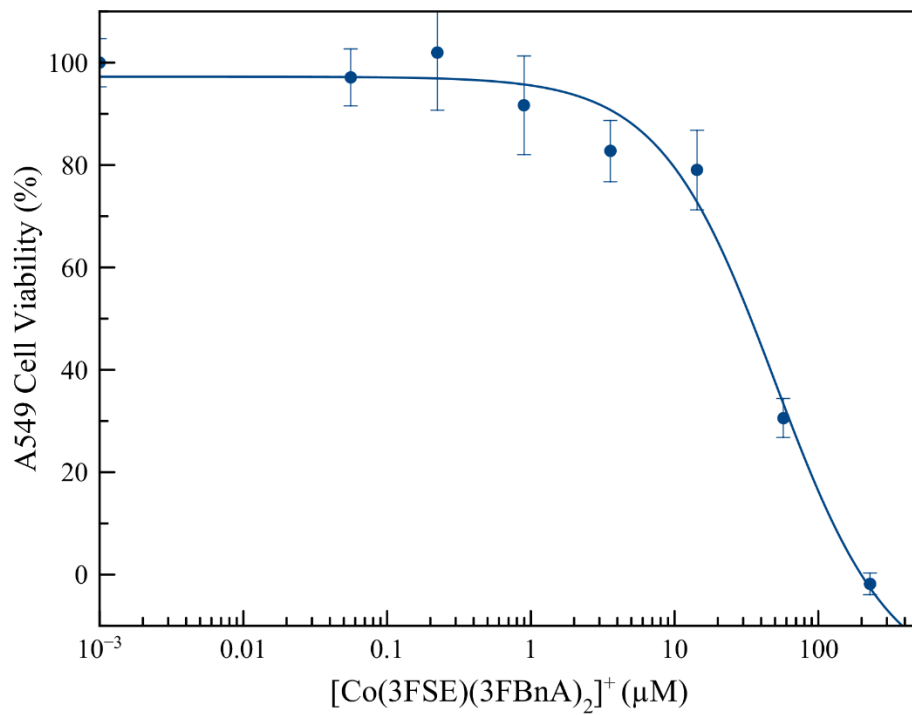


Figure S3.41. Dose-response curve for $[\text{Co}(\text{3FSE})(\text{3FBnA})_2]^+$ in A549 cells

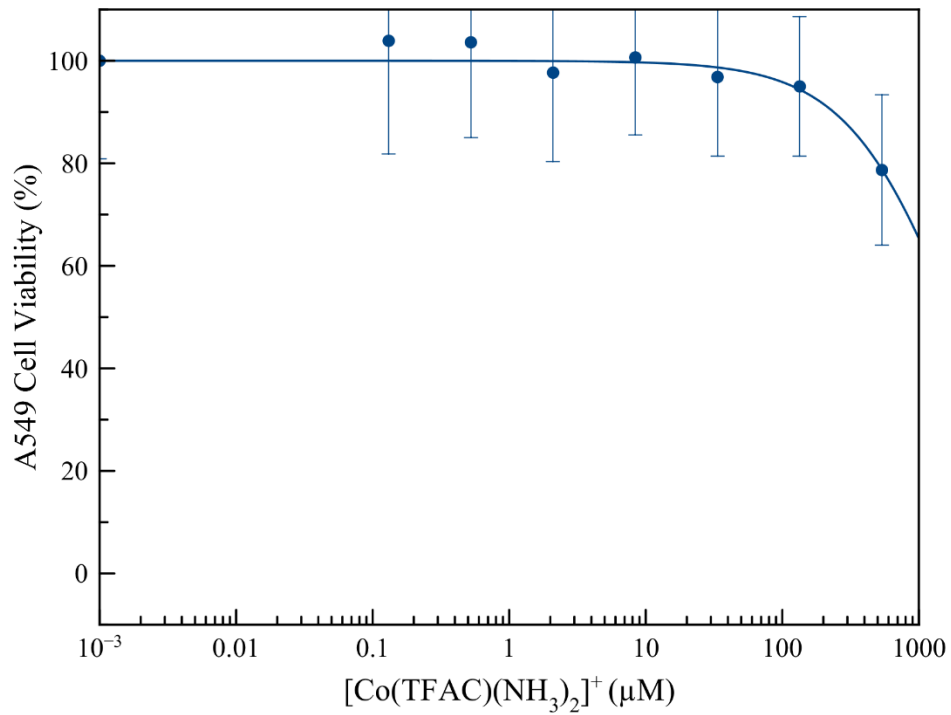


Figure S3.42. Dose-response curve for [Co(tfacen)(NH₃)₂]⁺ in A549 cells

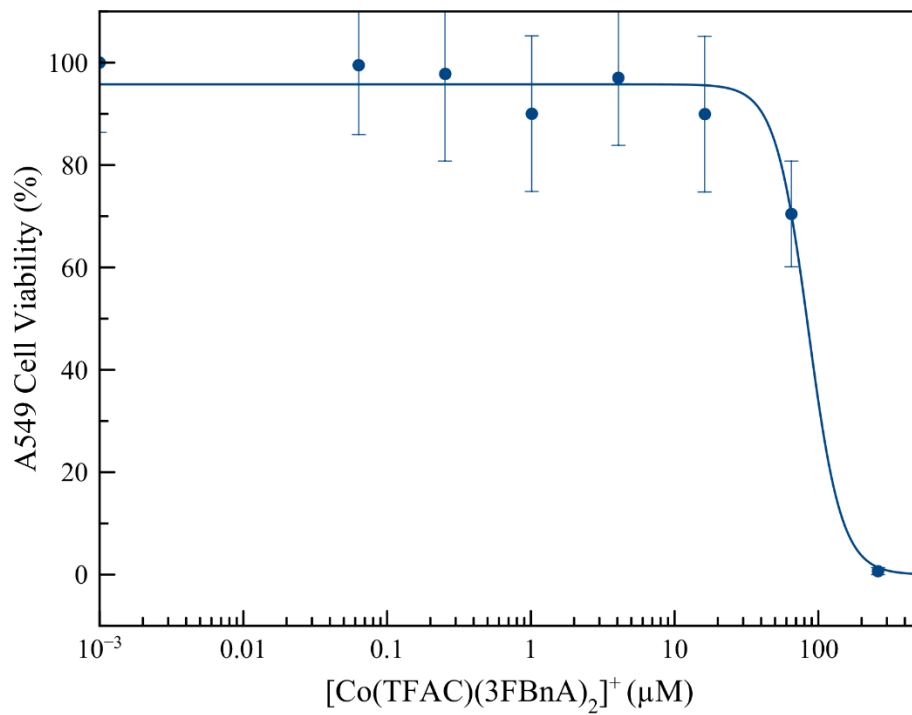


Figure S3.43. Dose-response curve for [Co(tfacen)(3F-BnNH₂)₂]⁺ in A549 cells

References

- 1 H. B. Langford, Cooper H.; Gray, *Ligand Substitution Processes*, W. A. Benjamin, Inc., New York, NY, 1966.
- 2 D. T. Richens, *Chem. Rev.*, 2005, **105**, 1961–2002.
- 3 S. V Wegner and J. P. Spatz, *Angew. Chem. Int. Ed.*, 2013, **52**, 7593–6.
- 4 M. D. Hall, T. W. Failes, N. Yamamoto and T. W. Hambley, *Dalton Trans.*, 2007, 3983–3990.
- 5 E. Reisner, V. B. Arion, B. K. Keppler and A. J. L. Pombeiro, *Inorg. Chim. Acta*, 2008, **361**, 1569–1583.
- 6 U. Jungwirth, C. R. Kowol, B. K. Keppler, C. G. Hartinger, W. Berger and P. Heffeter, *Antioxid. Redox Signal.*, 2011, **15**, 1085–1127.
- 7 N. Graf and S. J. Lippard, *Adv. Drug Deliv. Rev.*, 2012, **64**, 993–1004.
- 8 B. J. Kim, T. W. Hambley and N. S. Bryce, *Chem. Sci.*, 2011, **2**, 2135–2142.
- 9 C. Karnthaler-Benbakka, D. Groza, K. Kryeziu, V. Pichler, A. Roller, W. Berger, P. Heffeter and C. R. Kowol, *Angew. Chemie Int. Ed.*, 2014, **53**, 12930–12935.
- 10 N. Yamamoto, A. K. Renfrew, B. J. Kim, N. S. Bryce and T. W. Hambley, *J. Med. Chem.*, 2012, **55**, 11013–11021.
- 11 D. C. Ware, B. D. Palmer, W. R. Wilson and W. A. Denny, *J. Med. Chem.*, 1993, **36**, 1839–1846.
- 12 E. S. O’Neill, A. Kaur, D. P. Bishop, D. Shishmarev, P. W. Kuchel, S. M. Grieve, G. A. Figtree, A. K. Renfrew, P. D. Bonnitcha and E. J. New, *Inorg. Chem.*, 2017, **56**, 9860–9868.
- 13 W. A. Denny and W. R. Wilson, *Cancer Metastasis Rev.*, 1993, **12**, 135–151.
- 14 D. C. Ware, P. J. Brothers, G. R. Clark, W. A. Denny, B. D. Palmer and W. R. Wilson, *J. Chem. Soc. Dalt. Trans.*, 2000, 925–932.
- 15 J. Y.-C. Chang, R. J. Stevenson, G.-L. Lu, P. J. Brothers, G. R. Clark, W. A. Denny and D. C. Ware, *Dalton Trans.*, 2010, **39**, 11535–50.
- 16 J. Y.-C. Chang, G.-L. Lu, R. J. Stevenson, P. J. Brothers, G. R. Clark, K. J. Botting, D. M. Ferry, M. Tercel, W. R. Wilson, W. A. Denny and D. C. Ware, *Inorg. Chem.*, 2013, **52**, 7688–7698.
- 17 A. K. Renfrew, N. S. Bryce and T. W. Hambley, *Chem. Sci.*, 2013, **4**, 3731–3739.
- 18 T. Takeuchi, A. Böttcher, C. M. Quezada, M. I. Simon, T. J. Meade and H. B. Gray, *J. Am. Chem. Soc.*, 1998, **120**, 8555–8556.
- 19 D. Tomco, S. Schmitt, B. Ksebati, M. J. Heeg, Q. P. Dou and C. N. Verani, *J. Inorg. Biochem.*, 2011, **105**, 1759–1766.
- 20 A. S. Harney, J. Lee, L. M. Manus, P. Wang, D. M. Ballweg, C. LaBonne and T. J. Meade, *Proc. Natl. Acad. Sci. U. S. A.*, 2009, **106**, 13667–72.
- 21 M. C. Heffern, J. W. Kurutz and T. J. Meade, *Chem. - A Eur. J.*, 2013, **19**, 17043–17053.
- 22 A. Y. Louie and T. J. Meade, *Proc. Natl. Acad. Sci. U. S. A.*, 1998, **95**, 6663–8.

- 23 T. Takeuchi, A. Böttcher, C. M. Quezada, T. J. Meade and H. B. Gray, *Bioorg. Med. Chem.*, 1999, **7**, 815–819.
- 24 M. C. Heffern, P. T. Velasco, L. M. Matosziuk, J. L. Coomes, C. Karras, M. A. Ratner, W. L. Klein, A. L. Eckermann and T. J. Meade, *ChemBioChem*, 2014, **15**, 1584–1589.
- 25 R. M. Asbell, P. A.; Epstein Seth P.; Wallace, James A.; Epstein, Donald; Stewart, Claudia C.; Burger, *Cornea*, 1998, **17**, 550–557.
- 26 O. S. Burger, Richard M.; Stewart, C. C.; Winicov, I.; Bourne, N.; Stanberry, L. R.; Bonnez, W.; Weislow, *AIDS*, 2001, **15**, 1.
- 27 J. A. Schwartz, E. K. Lium and S. J. Silverstein, *J. Virol.*, 2001, **75**, 4117–28.
- 28 C. R. Munteanu and K. Suntharalingam, *Dalton Trans.*, 2015, **44**, 13796–13808.
- 29 M. C. Heffern, N. Yamamoto, R. J. Holbrook, A. L. Eckermann and T. J. Meade, *Curr. Opin. Chem. Biol.*, 2013, **17**, 189–96.
- 30 L. M. Manus, R. J. Holbrook, T. A. Atesin, M. C. Heffern, A. S. Harney, A. L. Eckermann and T. J. Meade, *Inorg. Chem.*, 2013, **52**, 1069–1076.
- 31 L. M. Matosziuk, R. J. Holbrook, L. M. Manus, M. C. Heffern, M. A. Ratner and T. J. Meade, *Dalton Trans.*, 2013, **42**, 4002–4012.
- 32 M. C. Heffern, V. Reichova, J. L. Coomes, A. S. Harney, E. A. Bajema and T. J. Meade, *Inorg. Chem.*, 2015, **54**, 9066–9074.
- 33 R. J. Holbrook, D. J. Weinberg, M. D. Peterson, E. A. Weiss and T. J. Meade, *J. Am. Chem. Soc.*, 2015, **137**, 3379–3385.
- 34 M. D. Peterson, R. J. Holbrook, T. J. Meade and E. A. Weiss, *J. Am. Chem. Soc.*, 2013, **135**, 13162–13167.
- 35 R. R. Hurtado, A. S. Harney, M. C. Heffern, R. J. Holbrook, R. A. Holmgren and T. J. Meade, *Mol. Pharm.*, 2012, **9**, 325–333.
- 36 M. Yu, D. Xie, K. P. Phan, J. S. Enriquez, J. J. Luci and E. L. Que, *Chem. Commun.*, 2016, **52**, 13885–13888.
- 37 T. Tenggel, T. Fex, H. Emtenäs, F. Almqvist, I. Sethson and J. Kihlberg, *Org. Biomol. Chem.*, 2004, **2**, 725–731.
- 38 J. B. Jordan, L. Poppe, X. Xia, A. C. Cheng, Y. Sun, K. Michelsen, H. Eastwood, P. D. Schnier, T. Nixey and W. Zhong, *J. Med. Chem.*, 2012, **55**, 678–687.
- 39 D. Xie, T. L. King, A. Banerjee, V. Kohli and E. L. Que, *J. Am. Chem. Soc.*, 2016, **138**, 2937–2940.
- 40 D. Xie, S. Kim, V. Kohli, A. Banerjee, M. Yu, J. S. Enriquez, J. J. Luci and E. L. Que, *Inorg. Chem.*, 2017, **56**, 6429–6437.
- 41 M. J. Adam and D. S. Wilbur, *Chem. Soc. Rev.*, 2005, **34**, 153.
- 42 S. M. Ametamey, M. Honer and P. A. Schubiger, *Chem. Rev.*, 2008, **108**, 1501–1516.
- 43 T. K. Venkatachalam, G. K. Pierens, P. V. Bernhardt, D. H. R. Stimson, R. Bhalla, L. Lambert and D. C. Reutens, *Aust. J. Chem.*, 2016, **69**, 1033.
- 44 Y. Zhou, J. Wang, Z. Gu, S. Wang, W. Zhu, J. L. Aceña, V. A. Soloshonok, K. Izawa and H. Liu, *Chem. Rev.*, 2016, **116**, 422–518.
- 45 A. Böttcher, T. Takeuchi, K. I. Hardcastle, T. J. Meade, H. B. Gray, D. Cwikel,

- M. Kapon and Z. Dori, *Inorg. Chem.*, 1997, **36**, 2498–2504.
- 46 C. V. Garcia, G. L. Parrilha, B. L. Rodrigues, P. J. S. Barbeira, R. M. Clarke, T. Storr and H. Beraldo, *Polyhedron*, 2017, **124**, 86–95.
- 47 A. Yamasaki, *J. Coord. Chem.*, 1991, **24**, 211–260.
- 48 N. Juranic, *Inorg. Chem.*, 1980, **19**, 1093–1095.
- 49 R. Bramley, M. Brorson, A. M. Sargeson and C. E. Schaeffer, *J. Am. Chem. Soc.*, 1985, **107**, 2780–2787.
- 50 J. Mason, *Chem. Rev.*, 1987, **87**, 1299–1312.
- 51 N. Juranic, *J. Am. Chem. Soc.*, 1988, **110**, 8341–8343.
- 52 N. Juranić, *Coord. Chem. Rev.*, 1989, **96**, 253–290.
- 53 A. Medek, V. Frydman and L. Frydman, *Proc. Natl. Acad. Sci. U. S. A.*, 1997, **94**, 14237–14242.
- 54 C. F. S. Au-Yeung and D. R. Eaton, *J. Magn. Reson.*, 1983, **52**, 366–373.
- 55 A. P. King, H. A. Gellineau, J.-E. Ahn, S. N. MacMillan and J. J. Wilson, *Inorg. Chem.*, 2017, **56**, 6609–6623.
- 56 P. W. Pilling, Michael J.; Seakins, *Reaction Kinetics*, Oxford University Press, New York, NY, 1995.
- 57 G. I. Gellene, *J. Chem. Educ.*, 1995, **72**, 196.
- 58 A. V. Ablov and N. M. Samus, *Coord. Chem. Rev.*, 1975, **17**, 253–279.
- 59 Z. Chikh, M. Hémadi, G. Miquel, N.-T. Ha-Duong and J.-M. El Hage Chahine, *J. Mol. Biol.*, 2008, **380**, 900–916.
- 60 L. O. Simonsen, H. Harbak and P. Bennekou, *Blood Cells, Mol. Dis.*, 2011, **47**, 214–225.
- 61 S. P. Epstein, Y. Y. Pashinsky, D. Gershon, I. Winicov, C. Srivilasa, K. J. Kristic and P. A. Asbell, *BMC Ophthalmol.*, 2006, **6**, 1–14.
- 62 T. W. Failes, C. Cullinane, C. I. Diakos, N. Yamamoto, J. G. Lyons and T. W. Hambley, *Chem. - A Eur. J.*, 2007, **13**, 2974–2982.
- 63 S. Jagadeesan, V. Balasubramanian, P. Baumann, M. Neuburger, D. Häussinger and C. G. Palivan, *Inorg. Chem.*, 2013, **52**, 12535–12544.
- 64 P. B. Cressey, A. Eskandari, P. M. Bruno, C. Lu, M. T. Hemann and K. Suntharalingam, *ChemBioChem*, 2016, **17**, 1713–1718.
- 65 C. Zhang, M. Sutherland, K. Herasymchuk, R. M. Clarke, J. R. Thompson, L. Chiang, C. J. Walsby and T. Storr, *Can. J. Chem.*, 2018, **96**, 110–118.
- 66 D. C. Ware, H. R. Palmer, F. B. Pruijn, R. F. Anderson, P. J. Brothers, W. A. Denny and W. R. Wilson, *Anticancer Drug Des.*, 1998, **13**, 81–103.
- 67 P. T. Chandel, N.S.; Maltepe, E.; Goldwasser, E.; Mathieu, C.E.; Simon, M.C.; Schumacker, *Proc. Natl. Acad. Sci. U. S. A.*, 1998, **95**, 11715–11720.
- 68 P. T. Chandel, Navdeep S.; McClintock, David S.; Feliciano, Carlos E.; Wood, Teresa M.; Melendez, J. A.; Schumaker, *J. Biol. Chem.*, 2000, **275**, 25130–25138.
- 69 R. C. Rillema, D. Paul; Endicott, John F.; Patel, *J. Am. Chem. Soc.*, 1972, **94**, 394–401.
- 70 J. R. Rillema, Paul D.; Endicott, John F.; Barber, *J. Am. Chem. Soc.*, 1973, **95**, 6987–6992.
- 71 A. B. P. Lever, *Inorg. Chem.*, 1990, **29**, 1271–1285.

- 72 N. Juranic, *Inorg. Chem.*, 1983, **22**, 521–525.
- 73 L. Öhrström, *Comments Inorg. Chem.*, 1996, **18**, 305–323.
- 74 M. Koller and W. von Philipsborn, *Organometallics*, 1992, **11**, 467–469.
- 75 W. von Philipsborn, *Chem. Soc. Rev.*, 1999, **28**, 95–105.
- 76 J. Kramer and K. R. Koch, *Inorg. Chem*, 2007, **46**, 7466–7476.
- 77 K. K. W. Ho, W. Y. Choy, C. Yu-Xin and S. C. F. Au-Yeung, *J. Magn. Reson. Ser. A*, 1994, **108**, 196–200.
- 78 H. Bönemann, W. Brijoux, R. Brinkmann, W. Meurers, R. Mynott, W. von Philipsborn and T. Egolf, *J. Organomet. Chem.*, 1984, **272**, 231–249.
- 79 H. Bönemann, *Angew. Chemie Int. Ed.*, 1985, **24**, 248–262.
- 80 I. Gănescu, M. Teodorescu and C. I. Lepădatu, *Zeitschrift für Phys. Chemie*, 1971, **74**, 11–16.
- 81 D. R. Brown and R. R. Pavlis, *J. Chem. Educ.*, 1985, **62**, 807–808.
- 82 F. Basolo and R. G. Pearson, *Adv. Inorg. Chem. Radiochem.*, 1961, **3**, 1–89.
- 83 D. J. Darensbourg, *Adv. Organomet. Chem.*, 1982, **21**, 113–150.
- 84 O. F. Wendt, A. Robert J. Deeth and L. I. Elding, *Inorg. Chem*, 2000, **39**, 5271–5276.
- 85 D. Hill, C. Delaney, M. Clark, M. Eaton, B. Hassan, O. Hendricks, D. K. Dang and R. U. Kirss, *RSC Adv.*, 2017, **7**, 34425–34434.
- 86 L. Helm and A. E. Merbach, *Chem. Rev.*, 2005, **105**, 1923–1960.
- 87 C. K. Poon, *Coord. Chem. Rev.*, 1973, **10**, 1–35.
- 88 A. V. Ablov and N. M. Samus, *Coord. Chem. Rev.*, 1975, **17**, 253–279.
- 89 F. Benzo, P. V. Bernhardt, G. González, M. Martinez and B. Sienra, *J. Chem. Soc. Dalt. Trans.*, 1999, 3973–3979.
- 90 L. F. Blackwell, A. Fischer, I. J. Miller, R. D. Topsom and J. Vaughan, *J. Chem. Soc.*, 1964, 3588.
- 91 M. Maeda and K. Kato, *J. Chem. Eng. Data*, 1995, **40**, 253–256.
- 92 S. Bhattacharya and S. S. Mandal, *J. Chem. Soc., Chem. Commun.*, 1995, 2489–2490.
- 93 S. J. Kirubavathy, R. Velmurugan, R. Karvembu, N. S. P. Bhuvanesh, K. Parameswari and S. Chitra, *Russ. J. Coord. Chem.*, 2015, **41**, 345–352.
- 94 R. Gust, I. Ott, D. Posselt and K. Sommer, *J. Med. Chem.*, 2004, **47**, 5837–5846.
- 95 S. R. Doctrow, K. Huffman, C. B. Marcus, G. Tocco, E. Malfroy, C. A. Adinolfi, H. Kruk, Keith Baker, N. Lazarowych, J. Mascarenhas and B. Malfroy, *J. Med. Chem*, 2002, **45**, 4549–4558.
- 96 G. R. Fulmer, A. J. M. Miller, N. H. Sherden, H. E. Gottlieb, A. Nudelman, B. M. Stoltz, J. E. Bercaw and K. I. Goldberg, *Organometallics*, 2010, **29**, 2176–2179.
- 97 J.-X. Yu, R. R. Hallac, S. Chiguru and R. P. Mason, *Prog. Nucl. Magn. Reson. Spectrosc.*, 2013, **70**, 25–49.
- 98 C. P. Rosenau, B. J. Jelier, A. D. Gossert and A. Togni, *Angew. Chemie Int. Ed.*, 2018, **57**, 9528–9533.
- 99 V. V Pavlishchuk and A. W. Addison, *Inorg. Chim. Acta*, 2000, **298**, 97–102.
- 100 N. G. Connelly and W. E. Geiger, *Chem. Rev.*, 1996, **96**, 877–910.

- 101 G. M. Sheldrick, *Acta Cryst.*, 2008, **A64**, 112–122.
- 102 G. M. Sheldrick, *Acta Cryst.*, 2015, **A71**, 3–8.
- 103 P. Müller, *Crystallogr. Rev.*, 2009, **15**, 57–83.
- 104 R. I. Freshney, *Culture of Animal Cells*, John Wiley & Sons, Inc., Hoboken, NJ, USA, 5th edn., 2005.
- 105 X. Xia, M. S. Owen, R. E. C. Lee and S. Gaudet, *Cell Death Dis.*, 2014, **5**, e1261.
- 106 S. I. Kirin, I. Ott, R. Gust, W. Mier, T. Weyhermüller and N. Metzler-Nolte, *Angew. Chemie Int. Ed.*, 2008, **47**, 955–959.
- 107 A. E. Egger, C. Rappel, M. A. Jakupec, C. G. Hartinger, P. Heffeter and B. K. Keppler, *J. Anal. At. Spectrom.*, 2009, **24**, 51–61.

CHAPTER 4

A Rhenium Isonitrile Complex Induces Unfolded Protein Response-Mediated Apoptosis in Cancer Cells

Reproduced in part with permission from: A. Paden King,* Sierra C. Marker,* Robert V. Swanda, Shu-Bing Qian, and Justin J. Wilson. *Chem. Eur. J.* **2019**, 25, 9206-9210.

*Denotes Equal Contribution

Introduction

As discussed in detail in Chapter 1, the endoplasmic reticulum (ER) is a major regulator of cancer cell proliferation, metastasis, angiogenesis, and chemotherapy resistance.¹ Cancer cells often exhibit higher rates of protein synthesis than non-cancer cells, which raises their ER protein load and leads to higher basal levels of ER stress.² To handle this ER stress, cancer cells often employ the unfolded protein response (UPR). The UPR is typically cytoprotective, and its increased activation in cancer cells can cause them to be more virulent and more resistant to chemotherapy.³ However, acute inductions of high levels of ER stress can shift the UPR to activate apoptosis.⁴ The higher basal ER stress levels of cancer cells makes them more susceptible than normal cells to apoptosis induction via overactivation of the UPR. Thus, the development of new chemotherapeutic agents that target the ER is a promising strategy for the treatment of cancer.⁵ Recently, several transition metal complexes bearing polypyridyl ligands have been discovered to induce anticancer activity via ER stress and the UPR, suggesting that the exploration of these non-traditional scaffolds may give rise to promising drug candidates.⁶⁻¹¹ In this context, our group has been exploring the anticancer activity of polypyridyl rhenium(I) tricarbonyl complexes.¹²⁻¹⁵ Certain members of this class of compounds exhibit potent cytotoxic activity that can be leveraged for their use as anticancer agents.¹⁶⁻²³ Here, we describe our investigation of a new rhenium(I) tricarbonyl complex bearing a chelating polypyridyl ligand and an axial isonitrile ligand as a potent anticancer agent. Our efforts to understand the mechanism of action of this tricarbonyl rhenium isonitrile

polypyridyl (TRIP) complex have revealed that it is an effective ER stress-inducing agent with significant antiproliferative activity.

Results and Discussion

TRIP was synthesized by treating the previously reported complex $[\text{Re}(\text{CO})_3(\text{dmphen})\text{OTf}]$ with excess 4-methylphenyl isonitrile in tetrahydrofuran (**Figure 4.1**). TRIP was fully characterized using ^1H NMR and IR spectroscopy, HR-MS, and X-ray diffraction (**Figures S4.1 and S4.2, Tables S4.1 and S4.2**). The purity of the complex was verified via elemental analysis and HPLC (**Figure S4.3, Table S4.3**). The water-soluble complex is luminescent upon irradiation with UVA and blue light and exhibits a luminescence quantum yield of 3% and a lifetime of 1.05 μs in aqueous, air-equilibrated phosphate buffer (**Figures S4.4–S4.6**). The complex is stable indefinitely as a solid and in aqueous solution for over one week (**Figures S4.7 and S4.8**). TRIP is also stable in the presence of millimolar concentrations of glutathione (**Figure S4.9**). Based on TRIP's favorable physical properties and high stability, we evaluated its potential as an anticancer agent in vitro.

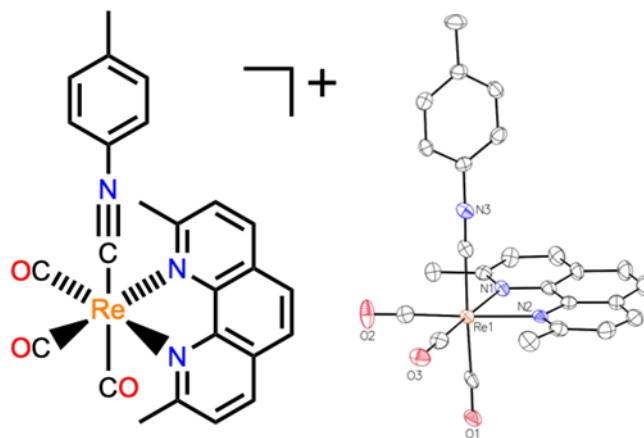


Figure 4.1. Diagram of TRIP (left) and its X-ray crystal structure (right). Ellipsoids are drawn at 50% probability. Hydrogen atoms and the counterion are omitted for clarity.

The cytotoxicity of TRIP was investigated in a panel of cancer and non-cancer cell lines to determine its potential as a therapeutic agent. For comparison, we also evaluated the activities of the established metal-based anticancer drug cisplatin and another potent rhenium anticancer agent that we have previously investigated in our lab, $[\text{Re}(\text{CO})_3(\text{dmphen})(\text{OH}_2)]^+$ (Neo-Re).^{12,15} The concentrations of these complexes required to reduce cell viability to 50% of the control (IC_{50}) are shown in **Table 4.1**. In comparison to cisplatin and Neo-Re, TRIP has comparable or greater toxicity in all cancer cell lines tested (**Figures S4.10–S4.21**). Based on its promising anticancer activity, we submitted TRIP for screening in the National Cancer Institute (NCI)-60 cell line panel (**Figure S4.22**).²⁴ The results indicate that TRIP is most potent in melanoma and breast cancer cells lines and least effective in lung and renal cancer cell lines. The activity of TRIP in this cell line panel was compared to drugs in the NCI database via the COMPARE algorithm, which compares the toxicity profiles of drugs to reveal correlations in their activity.²⁵ Highest correlations were observed for DNA-

binding agents chromomycin A3 and actinomycin D and the translation inhibitors pyllanthoside, bruceantin, and didemnin B (**Table S4.4**). Notably, the spectrum of activity of TRIP was not correlated to any of the platinum-based drugs, and it exhibits only a moderate correlation (PCC = 0.403) to Neo-Re. The high correlations to established transcription and translation inhibitors indicates that TRIP may act similarly.

Table 4.1. IC₅₀ values of TRIP, Neo-Re, and cisplatin in cancer and non-cancer cell lines.

Compound	IC ₅₀ (μM)				
	A2780	A2780	HeLa	A549	HEK293
TRIP	1.7 ± 0.7	1.9 ± 1	1.4 ± 0.2	1.4 ± 0.6	1.9 ± 0.2
Neo-Re	5.7 ± 0.6	6.0 ± 0.2	4.4 ± 1.3	7.7 ± 2.4	9.0 ± 0.3
Cisplatin	1.3 ± 0.1	12 ± 3	6.6 ± 0.7	5.6 ± 0.5	1.7 ± 0.2

To determine the type of cell death induced by TRIP, the cytotoxicity of this compound in A2780 cells was evaluated in the presence of inhibitors of various established cell death pathways. Inhibitors of necroptosis, paraptosis, and ferroptosis did not alter TRIP's activity, but the pan-caspase inhibitor Z-VAD-FMK significantly decreased TRIP's cytotoxicity (**Figures S4.23–S4.27**). Because the activation of caspases is often critical for the execution of apoptosis, this result indicates that TRIP may be inducing apoptosis. To confirm that TRIP induces caspase-dependent apoptosis, we first performed western blots to detect apoptosis markers caspase 3 and cleaved PARP (**Figure S4.28**). We further verified this cell death pathway by performing the annexin V assay, which selectively stains apoptotic cells (**Figures S4.29 and S4.30**). To determine whether TRIP induced apoptosis by the intrinsic pathway, the release of cytochrome *c* from the mitochondria was tracked using flow cytometry (**Figure S4.31**). Cytochrome *c* release occurs on the same time scale as apoptosis induction by TRIP, indicating that TRIP induces intrinsic apoptosis.

Given the promising activity of TRIP in a variety of cancer cell lines and its ability to induce intrinsic apoptosis, we explored its intracellular localization and early

cellular effects. The localization of TRIP was probed by measuring the colocalization of TRIP luminescence with organelle-specific fluorescent small molecules or fusion proteins. Partial colocalization was observed with the LysoTracker Red dye and GalT-dsRed fusion protein, but the majority of TRIP luminescence was cytosolic (**Figure S4.32**). While performing these colocalization studies, we observed that the mitochondrial morphology was noticeably altered in TRIP-treated cells. The mitochondria were significantly rounded and punctate after TRIP treatment, in contrast to the tubular, elongated morphology within untreated cells. Time-lapse microscopy experiments revealed that TRIP induces these changes after only 30 min of treatment in HeLa cells (**Figures 4.2** and **S4.33**). Although TRIP-treated mitochondria were visually different, mitochondrial polarization experiments with the ratiometric sensor JC-1 indicated that the mitochondria remained functional (**Figures S3.34** and **S3.35**), demonstrating that the observed changes might be controlled mitochondrial fission rather than fragmentation. These morphology changes were curtailed in the presence of Mdivi-1, which inhibits dynamin-related protein 1 (Drp1), an essential mediator of fission, confirming that this process is due to mitochondrial fission (**Figure 4.2**).²⁶ Because mitochondrial fission is often associated with autophagy,²⁷ we examined the expression of LC3, an autophagosome marker,²⁸ in A2780 cells upon treatment with TRIP. After 24 h, a large increase in LC3II expression relative to LC3I was observed in cells treated with TRIP (**Figure S4.36**). Based on these results, it is clear that TRIP induces both autophagy and apoptosis. Because TRIP does not depolarize the mitochondria or cause release of cytochrome *c*

on short time scales, we hypothesized that a different organelle, such as the ER, may be the key target of this compound.

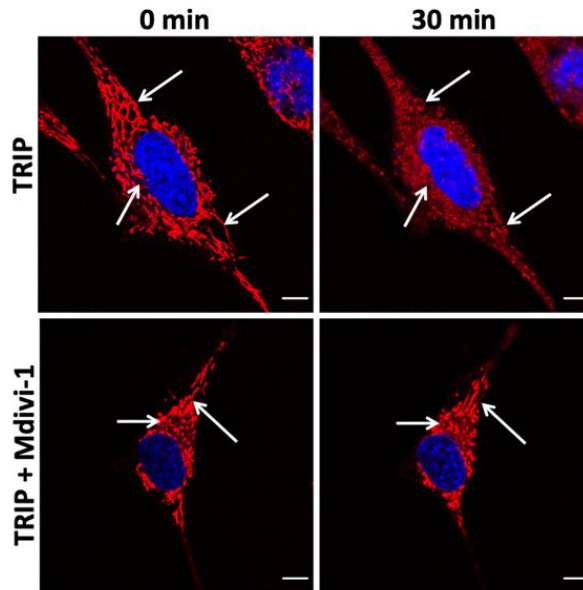


Figure 4.2. HeLa cells stained with MitoTracker Red and Hoechst dye treated with TRIP (5 μ M) for 0 and 30 min (top panels). HeLa cells stained with MitoTracker Red and Hoechst dye cotreated with TRIP (5 μ M) and Mdivi-1 (50 μ M) for 0 and 30 min (bottom panels). Scale bar = 10 μ m.

Because of the potential connections between mitochondrial fission, autophagy, and ER stress, we explored the effects of the ER stress modulator salubrinal on the cytotoxicity of TRIP in A2780 cells.²⁹ Salubrinal operates by inhibiting dephosphorylation of the master regulatory protein eukaryotic initiation factor 2 α (eIF2 α), an integral component of the UPR.²⁹⁻³² The presence of salubrinal increases the activity of TRIP by a factor of 4 (**Figure 4.3A**). Based on this synergy, we explored the possibility that TRIP was acting to cause phosphorylation of eIF2 α . Western blot analysis of A2780 cells treated with TRIP confirms the induction of

eIF2 α phosphorylation as little as 2 h after exposure (**Figures 4.3B** and **S4.37**), indicating that this process is one of the first cellular responses. Next, we explored the downstream effects of eIF2 α phosphorylation. The most immediate and pronounced effect of eIF2 α phosphorylation is the inhibition of translation.³³ To probe whether the levels of phosphorylation induced by TRIP were sufficient to inhibit protein translation, we measured endogenous global translation levels using the puromycin incorporation assay.³⁴ As early as 2 h post incubation, A2780 cells treated with TRIP incorporated substantially less puromycin compared to the untreated controls, indicating much lower rates of translation (**Figure 4.3C**). The role of eIF2 α in these processes was confirmed by testing TRIP in a mutant MEF cell line incapable of eIF2 α phosphorylation. The mutant cells showed no changes in translation levels after TRIP treatment (**Figures S4.38** and **S4.39**).

Hyperphosphorylation of eIF2 α can lead to apoptosis via upregulation of the stress-related transcription factors ATF4 and CHOP.³⁵ We measured the upregulation of these proteins in response to TRIP treatment and found that both ATF4 and CHOP were upregulated (**Figure 4.3B**), linking the observed eIF2 α phosphorylation and apoptosis. Phosphorylation of eIF2 α also results in cell cycle arrest in the G1 phase.³⁶ Cells treated with TRIP showed an 18% increase in the population of cells in the G1 phase and a corresponding decrease in the number of cells in the S phase as opposed to untreated cells (**Figure S4.40**). Thus, the ability of TRIP to stall cells in the G1 phase is fully consistent with its induction of eIF2 α phosphorylation. These results indicate that TRIP induces ER stress, triggering eIF2 α phosphorylation and the resulting downstream effects, culminating in cellular apoptosis.

Phosphorylation of eIF2 α often occurs due to the accumulation of misfolded proteins. To determine whether the observed phosphorylation was due to protein misfolding, the extent of misfolded protein accumulation induced by TRIP was evaluated using the dye Thioflavin T, (ThT) which fluoresces in the presence of protein aggregates.³⁷ The fluorescence intensity of ThT increased significantly in HeLa cells treated with TRIP in comparison to untreated cells within 30 min (**Figures 4.3D, S4.41 and S4.42**). Given the observation of fast protein aggregation upon treatment with TRIP, the induction of protein misfolding is most likely the cause of the ER stress and activation of the UPR.

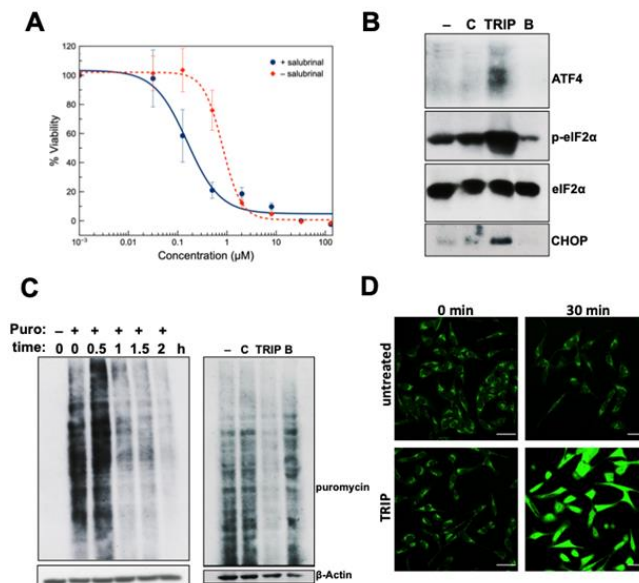


Figure 4.3. (A) Dose-response curve of A2780 cells treated with TRIP in the presence of 25 μ M salubrinal (blue) or absence of salubrinal (red). (B) Western blot of untreated (-), cisplatin (C, 10 μ M), TRIP (5 μ M), or bortezomib (B, 25 nM) for 24 h in A2780 cells. (C) Western blot of A2780 cells incubated with TRIP (5 μ M) over 0, 0.5, 1, 1.5, and 2 h with puromycin (10 min, left blot) and A2780 cells untreated (-), cisplatin (C, 10 μ M), TRIP (5 μ M), or bortezomib (B, 25 nM) treated for 24 h with puromycin (10 min, right blot). (D) Confocal microscopy images of HeLa cells treated with ThT (5 μ M) at 0 and 30 min in the absence (top panels) and the presence (bottom panels) of TRIP (5 μ M) at 0 and 30 min. Scale bar = 50 μ m.

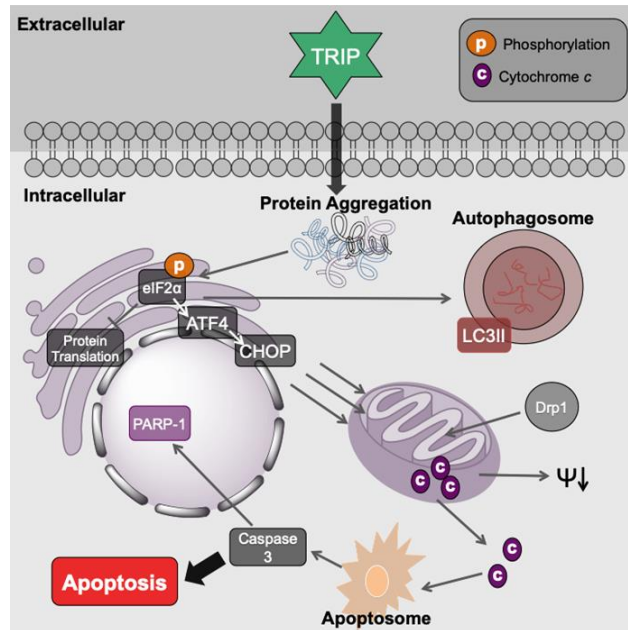


Figure 4.4. Proposed mechanism of ER-stress and apoptosis induction by TRIP.

A summary of our current understanding of TRIP's mechanism of ER stress induction and the subsequent cellular response is shown in **Figure 4.4**. TRIP induces ER stress in less than 30 min after exposure due to the accumulation of misfolded proteins. Misfolded protein accumulation leads to the phosphorylation of eIF2 α , which initiates autophagy, shuts down global protein translation, and upregulates ATF4. Prolonged eIF2 α phosphorylation and upregulation of ATF4 leads to expression of the proapoptotic protein CHOP, which induces mitochondrial membrane depolarization and release of cytochrome *c*. Cytochrome *c* release then results in caspase activation and initiation of apoptosis. Although we have investigated potential causes of eIF2 α phosphorylation, including proteasome inhibition, HSP90 inhibition, and reactive oxygen species generation, we found no evidence that TRIP triggers protein misfolding via these pathways (**Figures S4.43–S4.47**). Recently, a range of diverse

metal complexes have been shown to induce ER stress.^{7-11,38-47} The major mechanism of action proposed for these agents is through the production of ROS. Only a few studies have discovered metal complexes that induce ER stress in the absence of ROS generation.^{9,38,39,48} TRIP's ability to induce ER stress independent of ROS generation indicates that it operates via a different mechanism than many other metallodrugs targeting the ER.

Conclusions

Collectively, these results establish TRIP as a promising anticancer agent that kills cells by causing the accumulation of misfolded proteins. TRIP's favorable physical and photophysical properties, as well as its high potency, make it a candidate for future studies and a platform for the design of more potent analogues. Our current efforts are directed toward synthesizing a variety of related complexes in order to develop a structure-activity relationship and performing proteomics studies to identify TRIP's molecular mechanism of action.

Experimental

Methods and Materials

Rhenium carbonyl was purchased from Pressure Chemicals (Pittsburgh, Pennsylvania, USA). $\text{Re}(\text{CO})_5\text{Cl}$ was synthesized as previously described.¹³ The diimine ligand 2,9-dimethyl-1,10-phenanthroline (dmphen) was purchased from Cayman Chemical (Ann Arbor, MI). $[\text{Re}(\text{CO})_3(\text{dmphen})\text{Cl}]$ was synthesized using a previously reported procedure.^{49,50} The isonitrile ligand, *p*-tolyl-isonitrile was

synthesized from *p*-tolyl-formamide using a previously reported procedure.⁵¹ All solvents were ACS grade or higher. All reactions were carried out under ambient atmospheric conditions without any effort to exclude water or oxygen.

Physical Measurements

NMR samples were prepared as solutions using D₂O as the solvent. NMR spectra were acquired on a Varian Inova 400 MHz spectrometer. ¹H NMR chemical shifts were referenced to 1,4-dioxane at 3.75 ppm in D₂O. Samples for IR spectroscopy were prepared as KBr pellets and were analyzed on a Nicolet Avatar 370 DTGS (ThermoFisher Scientific, Waltham, MA). Analytical chromatography was carried out on a LC-20AT pump with a SPD-20AV UV-vis detector monitored at 270 and 220 nm (Shimadzu, Japan) using an Ultra Aqueous C18 column (100 Å, 5 μm, 250 mm × 4.6 mm, Restek, Bellefonte, PA) at a flow rate of 1 mL/min with a mobile phase containing 0.1% trifluoroacetic acid (TFA) in H₂O or MeOH. The method consisted of 5 min at 10% MeOH, followed by a linear gradient to 100% MeOH over 20 min. High-resolution mass spectra (HRMS) were recorded on an Exactive Orbitrap mass spectrometer in positive ESI mode (ThermoFisher Scientific, Waltham, MA) with samples injected as acetonitrile/water solutions with 1% formic acid. Elemental analyses (C, H, N) were performed by Atlantic Microlab Inc. (Norcross, Georgia, USA). UV-visible spectra were recorded on a Cary 8454 UV-vis (Agilent Technologies, Santa Clara, CA) or a Beckman Coulter DU800 UV-vis using 1-cm quartz cuvettes. Lifetime measurements were collected as described below. The photoreaction of TRIP was monitored by UV-vis and performed using a Newport

Mercury/Xenon Arc Lamp. The light output was modulated using a combination of a Newport heat absorbing glass filter (50.8 × 50.8 mm) with infrared cut-off (Schott KG5 filter glass), a Newport mercury line bandpass filter (25.4 mm, center wavelength 365.0 ± 2 nm), and a Newport visible absorbing filter (50.8 × 50.8 mm, center wavelength 340 nm) made of dark optical glass to isolate monochromatic 365 nm light. Luminescence quantum yield measurements were carried out on a Beckman Coulter DU800 UV-vis and Varian Eclipse Fluorometer.

X-ray Crystallography

X-ray quality crystals of TRIP were grown by slow evaporation of a methanol solution of the complex. Low temperature X-ray diffraction (100 K) data was collected on a Rigaku XtaLAB Synergy diffractometer equipped with a 4-circle Kappa goniometer and HyPix 6000HE Hybrid Photon Counting (HPC) detector with monochromated Mo K α radiation ($\lambda = 0.7107 \text{ \AA}$). Diffraction images were processed using the CrysAlisPro⁵² software. The structure was solved through intrinsic phasing using SHELXT⁵³ and refined against F^2 on all data by full-matrix least-squares with SHELXL^{54,55} following established strategies.⁵⁶ All non-hydrogen atoms were refined anisotropically. Hydrogen atoms bound to carbon were included in the model at geometrically calculated positions and refined using a riding model with the isotropic displacement parameters of all hydrogen atoms fixed at 1.2 times the U value of the atoms they are linked to. The complex was refined as a two component twin and was refined using the TWIN function in Olex^{2,57} (Twin law: -1 0 0, 0 -1 0, 0 0 1; BASF 0.00086). Details of the structure refinement details and selected interatomic distances

and angles are reported in **Table S1** and **S2**.

Synthesis of [Re(CO)₃(dmphen)(p-tol-ICN)]Cl (TRIP)

Re(CO)₃(dmphen)Cl (0.266 g, 0.52 mmol) is dissolved in THF and AgOTf (0.133 g, 0.52 mmol) is added. The mixture is heated at reflux for 3 h, after which the resulting yellow suspension is filtered. To the filtrate, *p*-tolyl-isonitrile (0.2 g, 1.7 mmol) is added, and the mixture is heated at reflux overnight. The resulting orange solution is evaporated to dryness, and the residue is dissolved in a minimum amount of methanol (≈ 5 mL). Saturated ammonium hexafluorophosphate (5 mL) is added, and the resulting suspension is filtered after 10 min. The pale yellow solid product is washed with diethyl ether and is recrystallized by slow addition of water to a saturated methanolic solution. The pure solid, as a PF₆⁻ salt, is then dissolved in acetonitrile (15 mL) and stirred with IRA-410(Cl) anion exchange resin (≈5 g) overnight. The mixture is filtered, and the resin is washed with acetonitrile (10 mL). The combined acetonitrile filtrate is then evaporated to dryness to yield the product as a pale yellow solid. Yield: 61%. ¹H NMR (400 MHz, D₂O) δ 8.56 (d, J = 8.6 Hz, 2H), 8.00 (s, 2H), 7.94 (d, J = 8.4 Hz, 2H), 7.06 (d, J = 7.3 Hz, 2H), 6.84 (d, J = 9.0 Hz, 2H), 3.28 (s, 6H), 2.21 (s, 3H). IR (KBr, cm⁻¹): 2176 m, 2040 s, 1946 s, 1923 s. HR-ESI-MS (positive ion mode): *m/z* 596.095 ([M]⁺, calcd 596.098). Anal. Calcd for [Re(CO)₃(dmphen)(*p*-tol-ICN)]Cl·2.5H₂O (ReC₂₅H₂₄N₃O_{5.5}Cl): C, 44.41; H, 3.58; N, 6.20. Found: C, 44.02; H, 3.71; N, 6.21.

Emission Quantum Yield

The luminescence quantum yields were measured relative to the standard quinine sulfate ($\Phi = 0.52$, 0.05 M H₂SO₄), which was cross-referenced in our lab to harmaline ($\Phi = 0.32$, 0.05 M H₂SO₄).⁵⁸ An excitation wavelength of 350 nm was used for the samples and standards. The compound was measured as a solution in pH 7.4 PBS with the absorbance maintained below 0.1 to prevent inner filter effects.⁵⁸ At least five different concentrations of the samples and standards were measured by UV-vis and fluorescence spectroscopy, and the absorbance at 350 nm was plotted versus the integrated emission intensity. The slopes of the resulting lines were used in the equation:

$$(1) \quad \Phi_{sample} = \Phi_{ref} \frac{S_{sample} \eta_{sample}^2}{S_{ref} \eta_{ref}^2}$$

where Φ_{ref} is the quantum yield of the reference, quinine sulfate, and S is the slope of either the sample or the reference, and η is the refractive index.

Lifetime Measurements

Laser excitation for the phosphorescence lifetime measurements was provided by pulsing the 405 nm laser line from a four-line iChrome MLE laser (Toptica Photonics AG, Munich, Germany). The diode laser in the iChrome was triggered by a DG535 Digital Delay/Pulse Generator (Stanford Research, Sunnyvale, CA) at 100 KHz and delivered 100 ns FWHM 405 nm excitation pulses. The 405 nm pulses were fiber-delivered to a sample-filled cuvette and phosphorescence was collected at 90

degrees through second fiber for delivery to a Bialkali photomultiplier tube (HC125, Hamamatsu, Bridgewater, NJ) through a 470 nm long pass filter (HQ470lp, Chroma Technology, Bellows Falls, VT). The time-resolved photon counts were collected in 40 ns time bins using a SR430 Multi-channel scaler (Stanford Research, Sunnyvale, CA). Data was transferred to a PC via the SR430 GPIB bus and fit to the standard exponential decay model. Measurements were collected in PBS solutions at 1000 μM . For deoxygenated measurements, nitrogen gas was bubbled into the PBS solutions for 15 min and then the lifetime was determined.

Stability Measurements

A 500 μM sample of TRIP was prepared in PBS and incubated at 37 °C for over 9 days. The total peak area and retention time of the sample were monitored periodically via HPLC.

Photoreactivity

Photochemical reactions were monitored by UV-vis spectroscopy. The stock solution of the rhenium compound at 1–2 mM concentrations in water were diluted in PBS (pH 7.4) to a final volume of 3 ml at a concentration of approximately 40–150 μM . The absorbance of these samples was between 0.1 and 0.5 at 365 nm. The solution was stirred in a 1-cm quartz cuvette and irradiated with 365 nm light using the Newport Mercury/Xenon Arc Lamp described above. At different time points, the UV-vis spectra were acquired. The photoreaction was deemed complete when no further changes in the UV-vis spectra were observed.

Cell Culture and Cytotoxicity

HeLa (cervical cancer) and A549 (lung cancer) cell lines were obtained from American Type Culture Collection (ATCC) and cultured using Dulbecco's Modified Eagle's Medium (DMEM) supplemented with 10% fetal bovine serum (FBS). A2780 (ovarian cancer) and A2780CP70 (cisplatin-resistant ovarian cancer) cell lines were provided by the Cell Culture Facility of Fox Chase Cancer Center⁵⁹ (Philadelphia, PA). These cells were cultured as monolayers with Roswell Park Memorial Institute (RPMI)-1640 culture media supplemented with 10% FBS. HEK295 (healthy kidney) cell line was obtained from ATCC and cultured using Modified Eagle's Medium (MEM) supplemented with 10% FBS. Knock-in loss-of-function eIF2 α mutant (eIF2 α , A/A) and isogenic wild-type (eIF2 α , S/S) MEF cells were supplied by Dr. Randal Kaufman (Sanford-Burnham Medical Research Institute, La Jolla, CA, USA). Wild-type (S/S) and eIF2 α (A/A) MEFs were cultured in DMEM, pH 7.4, containing 1 mM pyruvate and 4 mM glutamine and supplemented with 1 \times non-essential amino acid mix (Gibco/Invitrogen), 100 units/mL penicillin and 100 μ g/mL streptomycin (pen/strep; Gibco/Invitrogen) and 10% FBS. All cell lines were grown in a humidified incubator at 37 °C with an atmosphere of 5% CO₂. Cells were passed at 80–90% confluence using trypsin/EDTA. Cells were tested monthly for mycoplasma contamination with the Plasmotest™ mycoplasma detection kit from InvivoGen.

All compounds were dissolved in PBS at pH 7.4 to prepare 1–2 mM stock solutions. For cell viability studies all cells were grown to 80–90% confluence, detached with trypsin/EDTA, seeded in 96-well plates at 4000–8000 cells/well in 100

μL of growth media, and incubated for 24 h. The medium was removed and replaced with fresh medium (200 μL) containing varying dilutions of either the rhenium compounds, cisplatin, or media. The cells were then incubated for 48 h. The medium was removed from the wells, and 3-(4,5-dimethylthiazol-2-yl)-2,5-tetrazolium bromide (MTT) in DMEM, RPMI, or MEM (200 μL , 1 mg/mL) was added. The additional 48 h incubation was performed to ensure that the cells were in the logarithmic growth phase and that the cells had adequate time to regrow after exposure to the complexes. After 4 h, the MTT/DMEM, RPMI, or MEM solution was removed, and the formazan crystals were dissolved in 200 μL of an 8:1 mixture of DMSO and pH 10 glycine buffer. The absorbance at 570 nm in each well was measured using a BioTek Synergy HT plate reader. Cell viability was determined by normalizing the absorbance of the treated wells to untreated wells. The % viability data shown is an average of three independent experiments with six replicates per concentration.

Cytotoxicity with Cell Death Inhibitors

The effect various inhibitors of cellular processes had on TRIP toxicity was also examined using the MTT assay. A2780 cells were seeded in 96-well plates at 4000 cells/well in 100 μL of growth media and incubated for 24 h. The medium was removed and replaced with fresh medium (100 μL) containing a single concentration of inhibitor (2 mM *N*-acetylcysteine, 50 μM Z-VAD-FMK, 2 μM ferostatin-1, 60 μM necrostatin-1, or 1 μM cycloheximide). The cells were incubated at 37 °C for 1 h. After incubation, 100 μL of media containing serial dilutions of TRIP was added, and the MTT assay were performed after 48 h treatment as described above. The results of

the assay were compared to parallel measurements of toxicity in the absence of inhibitors.

Immunoblotting

A2780 or WT and mutant MEF cells were treated with vehicle control (water), TRIP (5 μ M), cisplatin (10 μ M), bortezomib (25 nM), or geldanamycin (20 μ M) for the indicated time periods. Cells were lysed in TBS buffer (50 mM Tris, pH7.5, 150 mM NaCl, 1 mM EDTA) containing 1% Triton X-100, 2 U/ml DNase and protease inhibitor cocktail tablet (Cell Signaling). The lysates were incubated on ice for 30 min, followed by heating for 10 min in SDS-PAGE sample buffer (50 mM Tris (pH6.8), 100 mM dithiothreitol, 2% SDS, 0.1% bromophenol blue, 10% glycerol). Proteins were separated on SDS-PAGE and transferred to PVDF membranes (Fisher). Membranes were blocked in TBS containing 5% non-fat milk and 0.1 % Tween-20 for 1 hr, followed by incubation with primary antibodies (PARP-1 (Cell Signaling), caspase 3 (intact and cleaved, Cell Signaling), ATF4 (Cell Signaling), eIF2 α (Cell Signaling), p-eIF2 α (Cell Signaling), CHOP (Cell Signaling), puromycin (DSHB), LC3I/II (Novus), AKT (Cell Signaling), HSP70 (Enzo), and ubiquitin (Santa Cruz)) overnight at 4 °C. After incubation with horseradish peroxidase-coupled secondary antibodies at room temperature for 1 hr, immunoblots were visualized using enhanced chemiluminescence (ECLPlus, GE Healthcare) and β -Actin antibody (Sigma-Aldrich) was used to quantify β -actin as a loading control.

Flow Cytometry

A2780 cells were grown for the indicated times with either media or media containing the indicated compounds. Cells were harvested as detailed below and then analyzed using a Beckman-Coulter XL flow cytometer. All results are an average of at least three independent experiments. All data was analyzed using FCS Express and MagicPlot Pro. Due to TRIP's luminescence upon excitation at 405 nm, control experiments were performed in which TRIP alone was incubated with A2780 cells for 24 h. The cells were harvested, washed, and analyzed via flow cytometry. No significant increase in luminescence intensity was observed, indicating that luminescence from TRIP does not interfere with the following assays.

Annexin V/PI by Flow Cytometry

A2780 cells were grown to confluency, then left untreated or treated with TRIP (5 μ M) for 12 or 24 h or etoposide (100 μ M) for 24 h. The media was removed, cells were washed with 1 ml PBS (pH 7.4), and trypsinized. Once cells were detached, they were rescued with fresh media and centrifuged down. The media was aspirated and the cells were washed by resuspending in PBS and centrifuging. The PBS was removed and 100 μ l of annexin binding buffer (ABB) containing 12 μ l of annexin V and 4 μ l of propidium iodide (PI) were added to each sample and the cells incubated at room temperature for 25 min. The samples were then diluted with 400 μ l of ABB and the cells were analyzed for annexin V and PI fluorescence by flow cytometry.

Cytochrome c Assay by Flow Cytometry

A2780 cells were treated with media or media containing TRIP (5 μ M) for 4 or 24 h or staurosporine (1 μ M) for 4 h. After the indicated treatment times, the cells were harvested using the FlowCelect Cytochrome *c* Kit by Millipore according to the manufacturer's instructions. The samples were then analyzed for fluorescence intensity by flow cytometry.

Confocal Fluorescence Microscopy

A total of 1×10^5 HeLa or A2780 cells were seeded onto 35 mm glass bottom dishes. After 24 h, the cells were treated with the rhenium compound or the specific dye in DMEM or RPMI media. After the indicated time, the media was removed and the cells were washed with PBS and fresh media was added. Right before imaging, the media was removed and imaging buffer was added (20 mM HEPES pH 7.4, 135 mM NaCl, 5 mM KCl, 1.8 mM CaCl₂, 1 mM MgCl₂, 1 mg/mL glucose, and 1 mg/mL bovine serum albumin). The cells were imaged with a Zeiss LSM 800 or Zeiss LSM 880 confocal laser-scanning microscope. All images were processed using ImageJ software.

Colocalization using Confocal Fluorescence Microscopy

A total of 1×10^5 HeLa or A2780 cells were seeded onto 35 mm glass bottom dishes. After 24 h, the cells were treated with the rhenium compound or the specific dye in DMEM or RPMI media. After the indicated time, the media was removed and the cells were washed with PBS and fresh media was added. Right before imaging, the media was removed and imaging buffer was added (20 mM HEPES pH 7.4, 135 mM

NaCl, 5 mM KCl, 1.8 mM CaCl₂, 1 mM MgCl₂, 1 mg/mL glucose, and 1 mg/mL bovine serum albumin). The cells were imaged with a Zeiss LSM 800 or Zeiss LSM 880 confocal laser-scanning microscope. The rhenium complex was imaged using a 405 nm laser excitation with a 410–550 nm emission filter and images were processed using ImageJ software. For transfections, a solution of 2 µL Lipofectamine 2000 in 150 µL Transfectagro was prepared for each dish. In a separate tube, 1 µg of plasmid DNA was diluted to 150 µL of Transfectagro. After 5 min, the two solutions were mixed, and after 20 min, they were added to the cells in 2 mL Transfectagro with 10% FBS. After 3 h, the Transfectagro was replaced with regular growth medium (DMEM with 10% FBS), and the cells were imaged 1 day later with the indicated treatment. For LysoTracker Red DND-99 treatment, 1 µL of 100 µM dye was added to 3 mL of medium 30 min prior to imaging.

Mitochondria Morphology Experiment using Confocal Fluorescence Microscopy

For time-lapse experiments, HeLa cells were incubated with MitoTracker Red FM (1 µL of 1 mM dye) and Hoechst 33342 (1 µL of 20 mM dye) for 30 and 15 min, respectively. After incubation with the dyes, the media was removed and the cells were washed with PBS and fresh media was added. At the microscope, the rhenium compound was diluted in imaging buffer to reach a final concentration of 5 µM and the cells were imaged over 2 min increments for a maximum of 30 min. MitoTracker Red FM was excited with a 561 nm laser with an emission filter from 630–700 nm. Hoechst 33342 was excited with a 405 nm laser with an emission filter of 410–550 nm. The same conditions for imaging were used for staurosporine, cisplatin, and

bortezomib.

JC-1 Assay using Confocal Fluorescence Microscopy

A total of approximately 1×10^5 A2780 cells were seeded onto 35 mm glass bottom dishes. After 24 h, the cells were treated with the rhenium compound for 4 or 24 h. The media was removed and replaced with fresh media containing 10 μ M JC-1 dye and the cells were incubated for 30 minutes. The media was then removed and the cells were washed once with 1 ml of PBS (pH 7.4) and 1 ml of fresh media was added to the dishes. The cells containing the rhenium compound and the JC-1 dye only were imaged in 1 ml of imaging buffer. For the positive control dishes, at the microscope, the cells were dosed with 50 μ M of carbonyl cyanide m-chlorophenyl hydrazine (CCCP) in imaging buffer, and the cells were imaged without removing CCCP. The cells were imaged using a 488 nm laser excitation with a 400–545 nm green emission filter and 575–700 nm red emission filter. The cellular images were analyzed using ImageJ software and the corrected total cell fluorescence (CTCF) was determined using the following formula:

$$(2) \text{ CTCF} = \text{Integrated density} - (\text{area of cell} \times \text{mean fluorescence of background reading})$$

The average of at least ten cells was used to determine the average CTCF and the red/green ratio.

Supporting Information

Table S4.1. X-ray Crystallographic Data and Refinement Parameters.^a

Compound	TRIP
Empirical Formula	H ₁₉ C ₂₅ N ₃ O ₃ RePF ₆
Formula Weight	740.60
<i>a</i> (Å)	10.1121(2)
<i>b</i> (Å)	14.4891(4)
<i>c</i> (Å)	17.0882(4)
α (°)	90
β (°)	92.443(2)
γ (°)	90
<i>V</i> (Å ³)	2501.41(10)
<i>Z</i>	4
Crystal System	Monoclinic
Space Group	P2 ₁ / <i>n</i>
ρ_{calc} (Mg/m ³)	1.967
μ (mm ⁻¹)	5.001
<i>T</i> (K)	100.00(10)
2 θ range (°)	2.386 – 27.103
Independent Reflections	5501
<i>R</i> _{int}	0.0862
Number of Parameters	356
Largest diff. peak and hole	1.787/-1.409
GoF	1.08
<i>R</i> 1/ <i>wR</i> 2 (all data)	0.0383/0.0895
<i>R</i> 1/ <i>wR</i> 2 (>2 θ)	0.0328/0.0873

^aMo K α λ =0.7107; *R*₁= $\Sigma||F_o|-|F_c||/\Sigma|F_o|$; *wR*2 = $\{\Sigma[w(F_o^2-F_c^2)^2]/\Sigma_w[(F_o^2)^2]\}^{1/2}$

GoF = $\{\Sigma[w(F_o^2-F_c^2)^2]/(n-p)\}^{1/2}$, where *n* is the number of data and *p* is the number of refined parameters.

Table S4.2. Selected Interatomic Distances (Å) and Angles (°).^a

Selected Interatomic Distances (Å)			
Re(1)-N(1)	2.216(3)	Re(1)-C(23)	1.960(4)
Re(1)-N(2)	2.221(3)	Re(1)-C(24)	1.908(4)
Re(1)-C(15)	2.083(4)	Re(1)-C(25)	1.931(4)
Selected Interatomic Angles (°)			
N(1)-Re(1)-N(2)	75.98(12)	N(2)-Re(1)-C(24)	177.11(14)
N(1)-Re(1)-C(15)	84.48(13)	N(2)-Re(1)-C(25)	101.60(15)
N(1)-Re(1)-C(23)	94.34(14)	C(15)-Re(1)-C(23)	177.92(14)
N(1)-Re(1)-C(24)	101.27(14)	C(15)-Re(1)-C(24)	92.01(16)
N(1)-Re(1)-C(25)	177.55(15)	C(15)-Re(1)-C(25)	95.03(16)
N(2)-Re(1)-C(15)	86.88(13)	C(23)-Re(1)-C(24)	89.90(17)
N(2)-Re(1)-C(23)	91.16(14)	C(24)-Re(1)-C(25)	84.14(17)

^aAtoms are labeled as shown in Figure 1 of the main text.

Table S4.3. Photophysical Properties of TRIP

λ , nm (ϵ , M ⁻¹ cm ⁻¹)	Φ_{lum} , % (λ , nm)	τ (μ s)	τ (nitrogen, μ s) ^a
230 (39900 \pm 2000), 261 (44800 \pm 2200), 282 (33800 \pm 1600), 306 (21000 \pm 900), 369 (2000 \pm 100)	3.08 \pm 0.26 (505)	1.05	3.46

^aNitrogen gas was bubbled into a solution of TRIP in PBS (pH 7.4) 15 min prior to taking lifetime measurement.

Table S4.4. COMPARE Analysis Results for **TRIP** Based on NCI-60 Screening Data.

Pearson Correlation Coefficient (PCC)	Compound	NSC number
0.661	chromomycin A3	S58514
0.628	phyllanthoside	S328426
0.595	actinomycin D	S3053
0.587	chromomycin A3	S58514
0.579	macbecin II	S330500
0.571	bruceantin	S165563
0.564	actinomycin D	S3053
0.561	chromomycin A3	S58514
0.547	didemnin B	S325319
0.542	anthrapyrazole	S355644

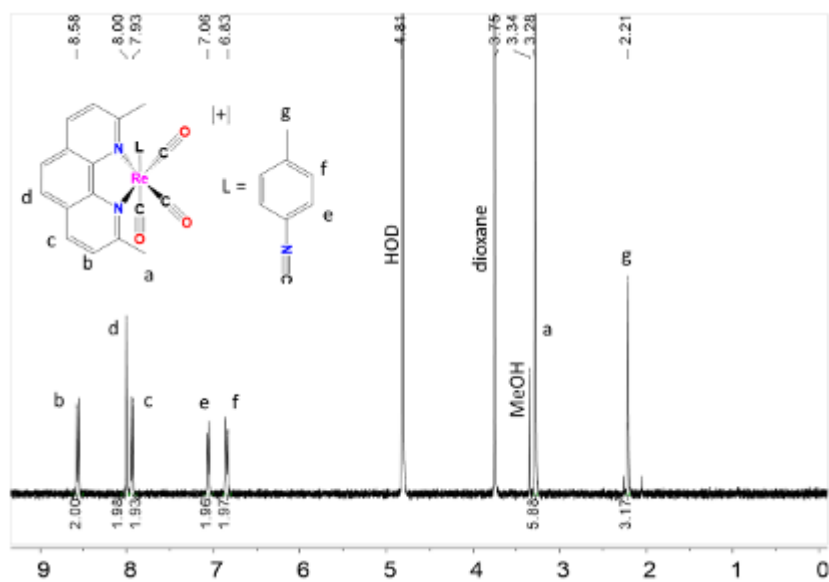


Figure S4.1. ^1H NMR spectrum of TRIP (D_2O , 400 MHz) at 25 °C. Chemical shifts are referenced to 1,4-dioxane at 3.75 ppm versus TMS.

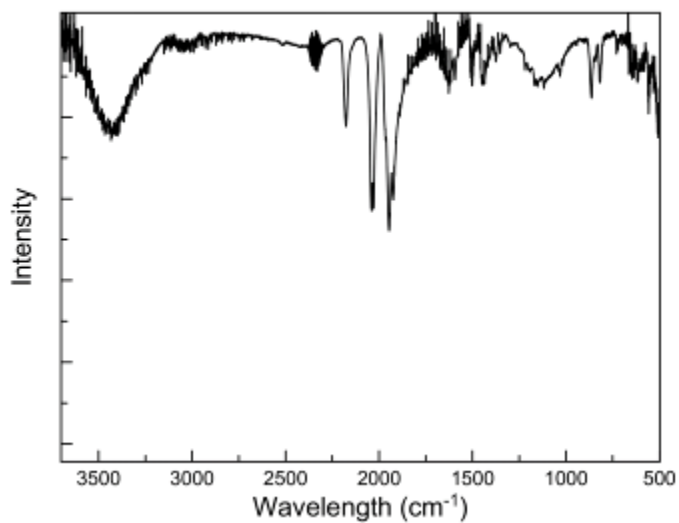


Figure S4.2. IR spectrum of TRIP.

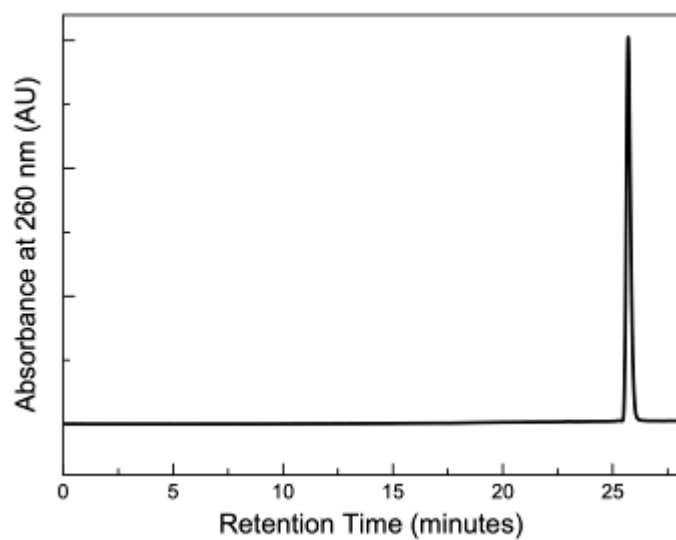


Figure S4.3. HPLC chromatogram of TRIP.

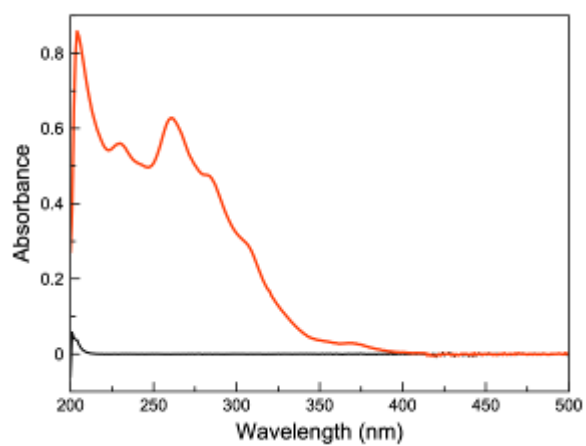


Figure S4.4. UV-vis spectrum of TRIP (10 μ M) in PBS at 25 $^{\circ}$ C.

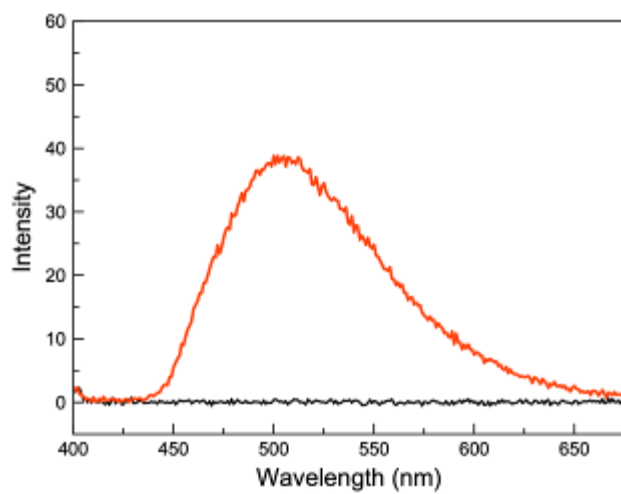


Figure S4.5. Emission spectrum of TRIP (10 μM) in PBS at 25 $^{\circ}\text{C}$.

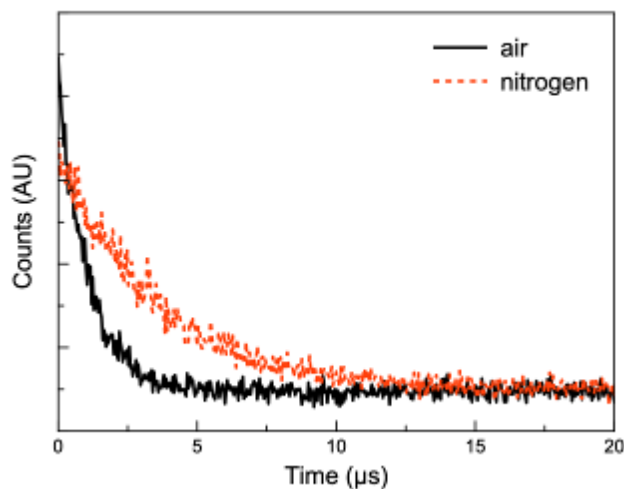


Figure S4.6. Transient emission decay profile of TRIP (1000 μM) in PBS under ambient conditions (black, solid) and under nitrogen (red, dashed).

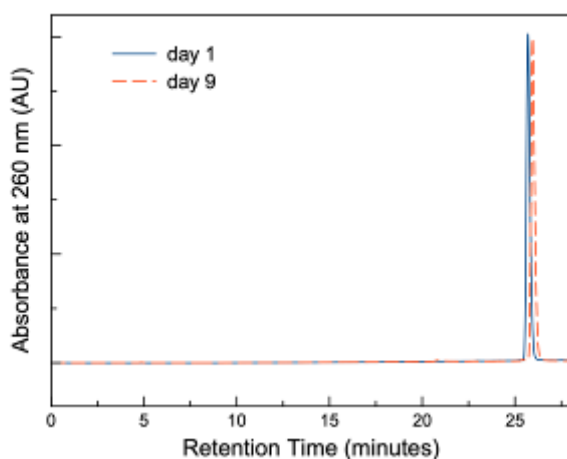


Figure S4.7. Aqueous stability of TRIP in PBS (1.5 mM) at 25 $^{\circ}\text{C}$ from day 1 (blue trace) to day 9 (red trace).

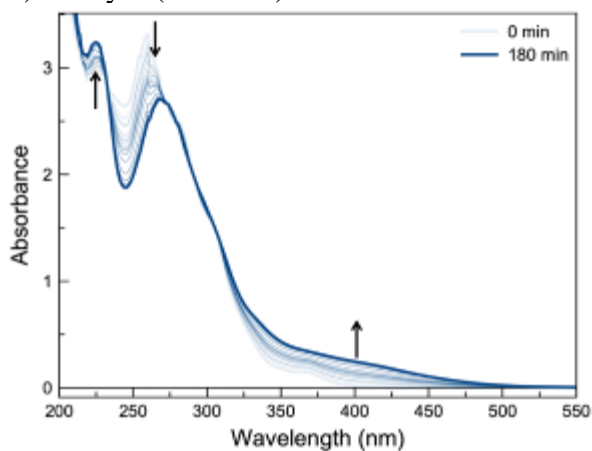


Figure S4.8. Series of UV-vis spectrum over the course of the photoreaction of TRIP

upon irradiation at 365 nm in PBS (70 μM) at 25 $^{\circ}\text{C}$.

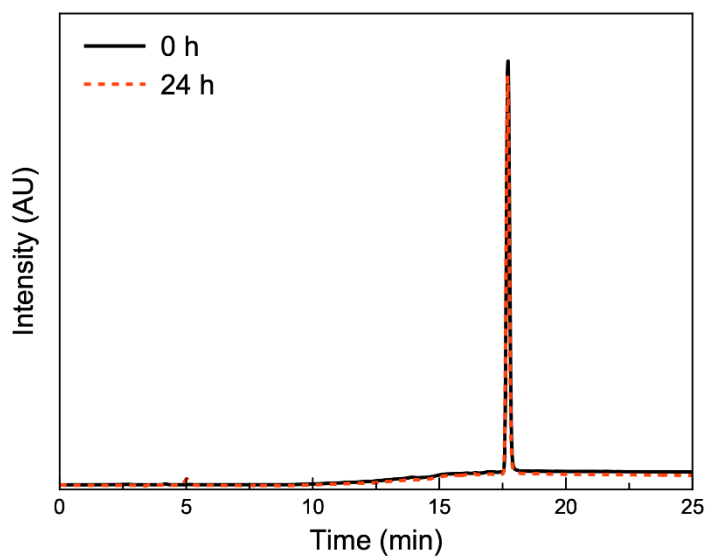


Figure S4.9. TRIP (300 μM) in the presence of glutathione (5 mM) in 100 mM MOPS buffer (pH 7.4) at 37 $^{\circ}\text{C}$ over the course of 24 h.

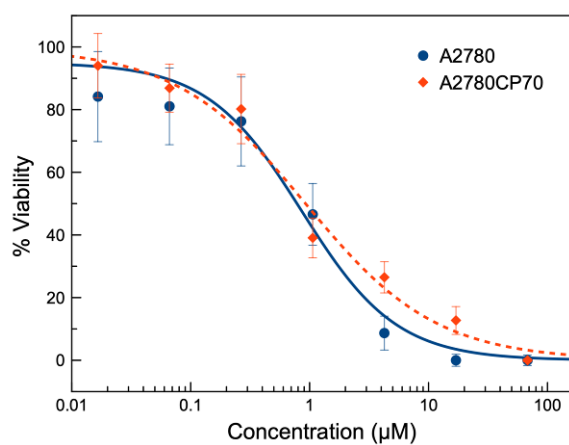


Figure S4.10. Dose-response curve of TRIP in A2780 (blue, solid) and A2780CP70 (red, dashed) cells.

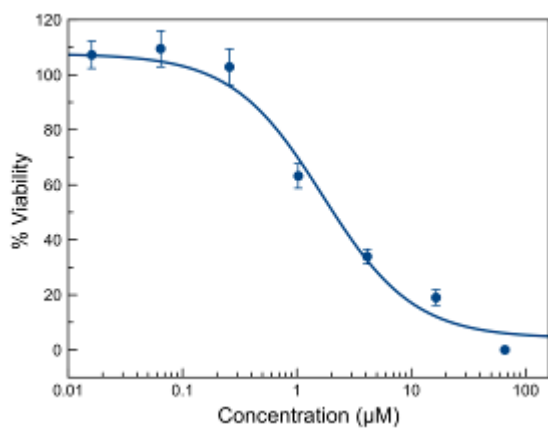


Figure S4.11. Dose-response curve of TRIP in HeLa cells.

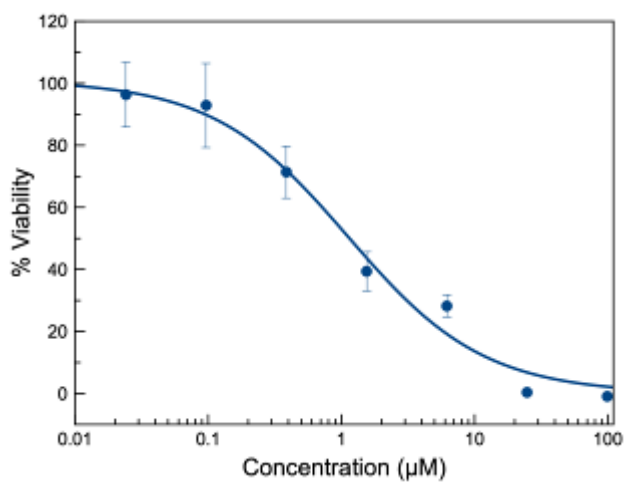


Figure S4.12. Dose-response curve of TRIP in A549 cells.

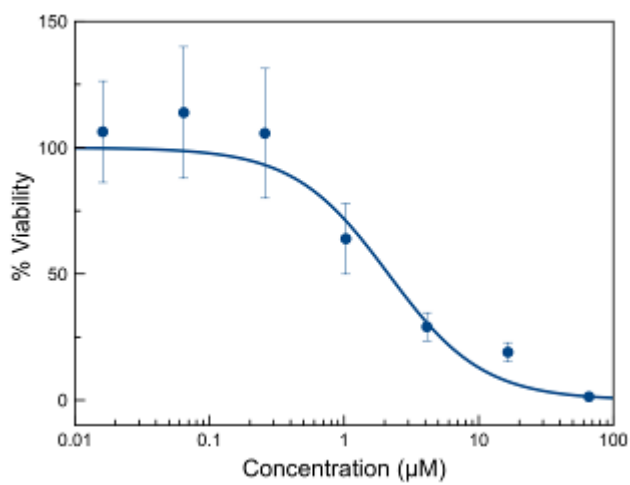


Figure S4.13. Dose-response curve of TRIP in HEK293 cells.

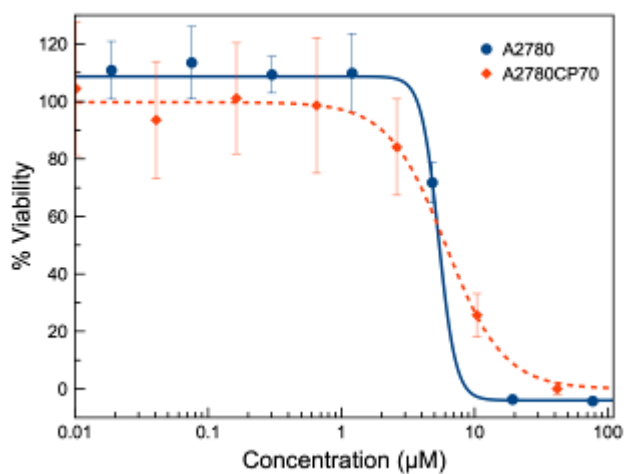


Figure S4.14. Dose-response curve of Neo-Re in A2780 (blue, solid) and A2780CP70 (red, dashed) cells.

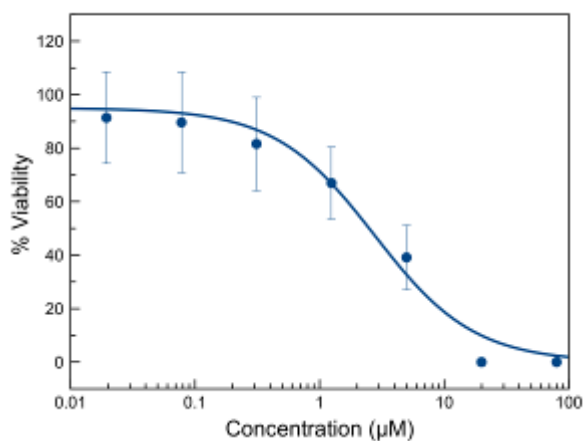


Figure S4.15. Dose-response curve of Neo-Re in HeLa cells.

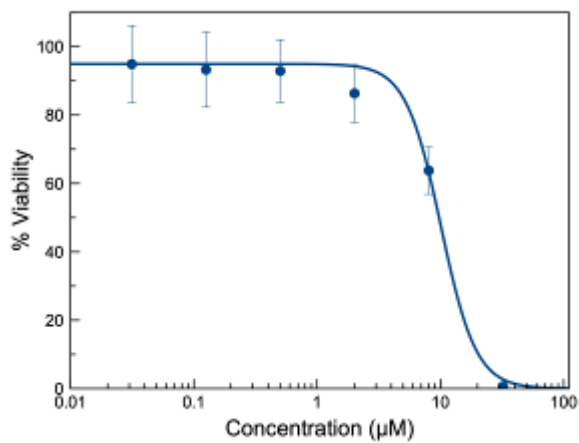


Figure S4.16. Dose-response curve of Neo-Re in A549 cells.

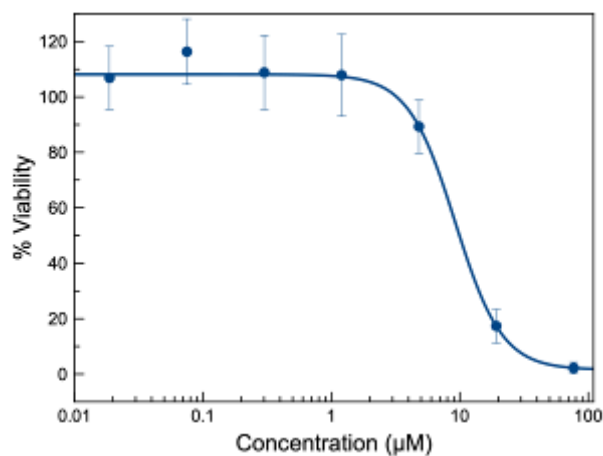


Figure S4.17. Dose-response curve of Neo-Re in HEK293 cells.

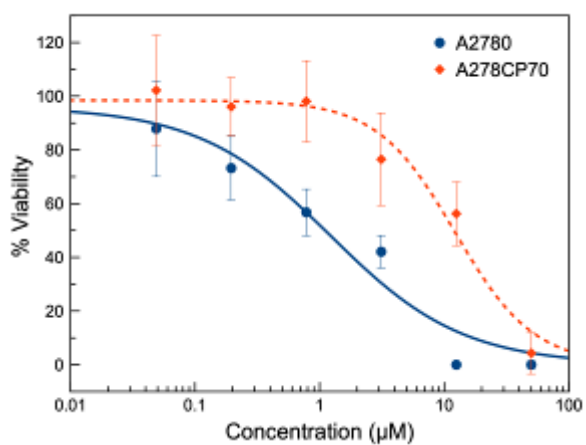


Figure S4.18. Dose-response curve of cisplatin in A2780 (blue, solid) and A2780CP70 (red, dashed) cells.

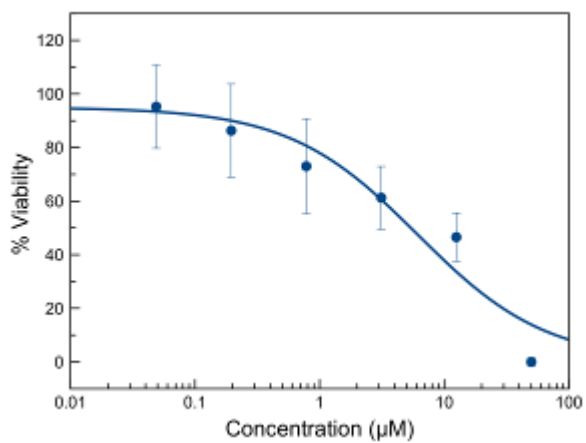


Figure S4.19. Dose-response curve of cisplatin in HeLa cells.

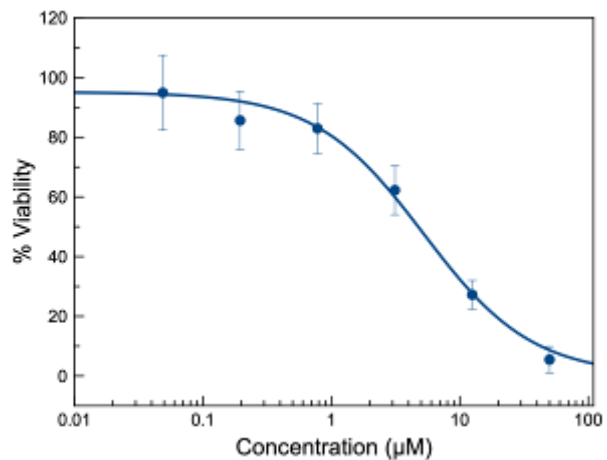


Figure S4.20. Dose-response curve of cisplatin in A549 cells.

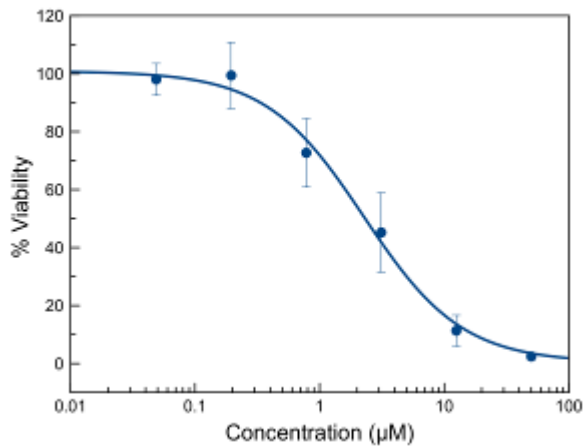


Figure S4.21. Dose-response curve of cisplatin in HEK293 cells.

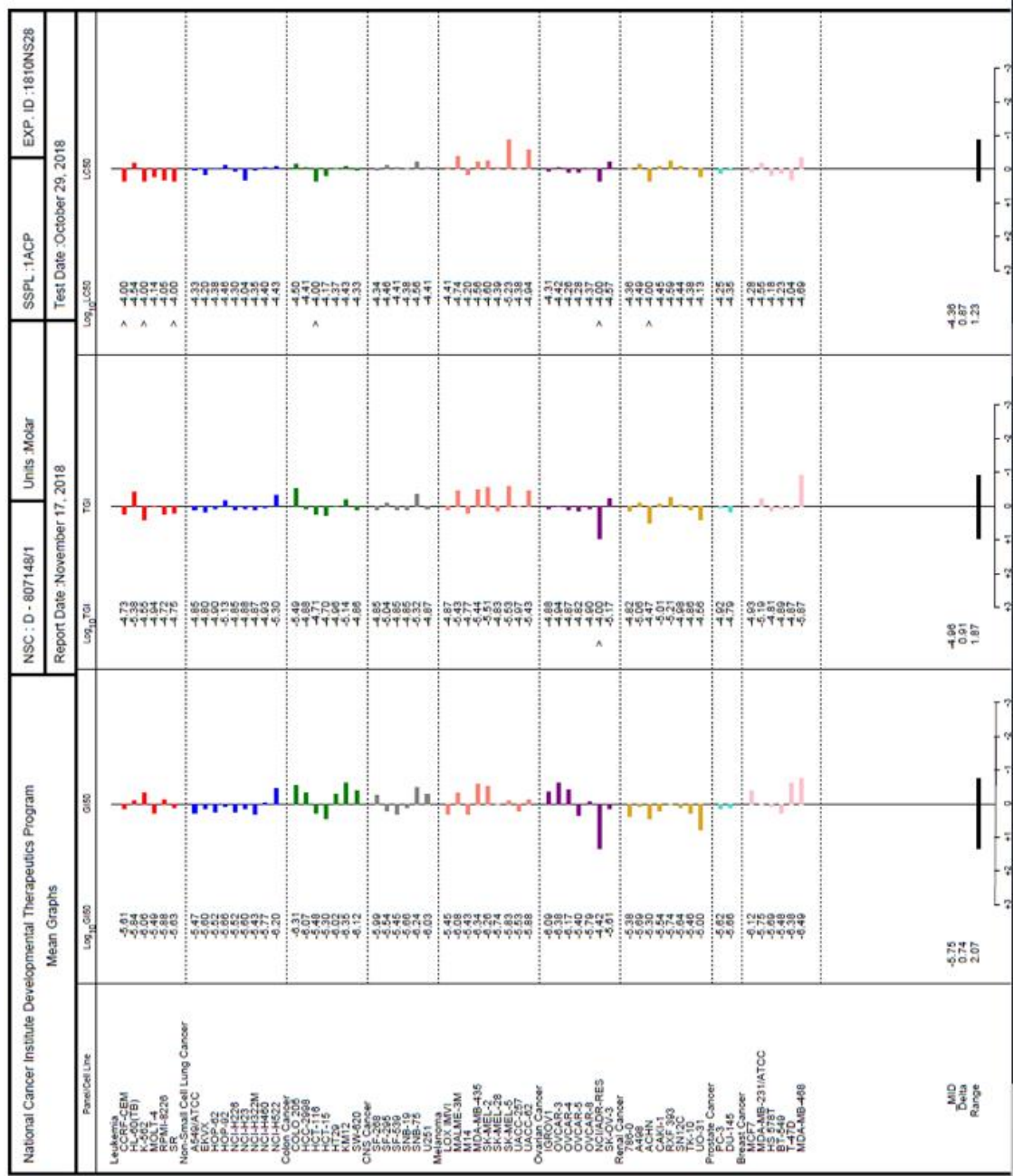


Figure S4.22. NCI-60 multi-dose mean graph for TRIP.

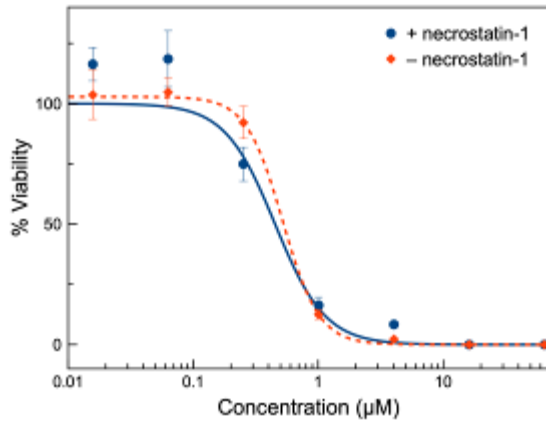


Figure S4.23. Dose-response curve of TRIP in A2780 cells with (blue, solid) and without necrostatin-1, inhibitor of necroptosis (red, dashed).

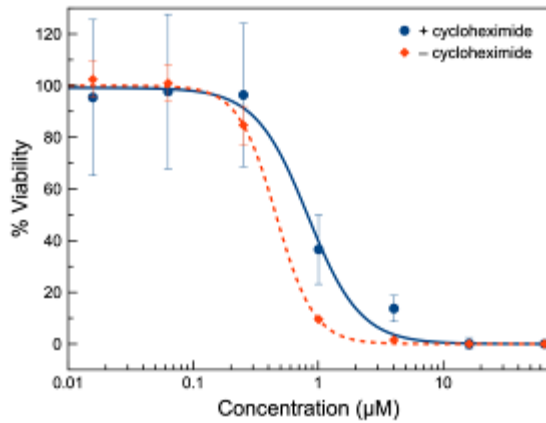


Figure S4.24. Dose-response curve of TRIP in A2780 cells with (blue, solid) and without cycloheximide, inhibitor of paraptosis (red, dashed).

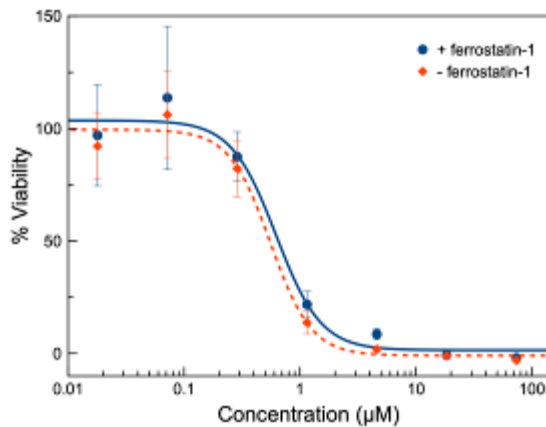


Figure S4.25. Dose-response curve of TRIP in A2780 cells with (blue, solid) and without ferrostatin-1, inhibitor of ferroptosis (red, dashed).

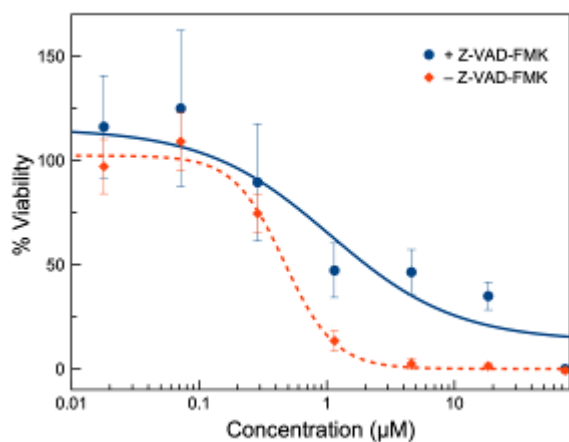


Figure S4.26. Dose-response curve of TRIP in A2780 cells with (blue, solid) and without Z-VAD-FMK (red, dashed).

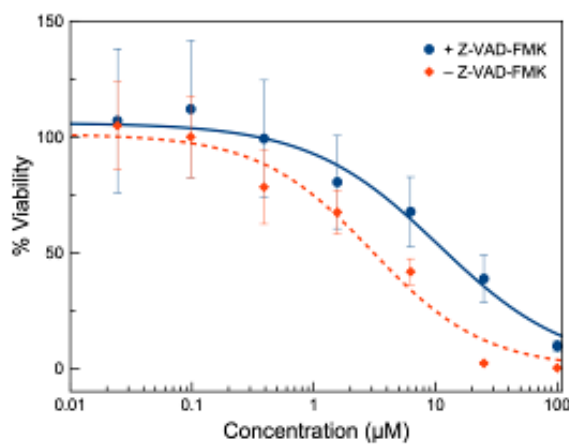


Figure S4.27. Dose-response curve of cisplatin in A2780 cells with (blue, solid) and without Z-VAD-FMK (red, dashed).

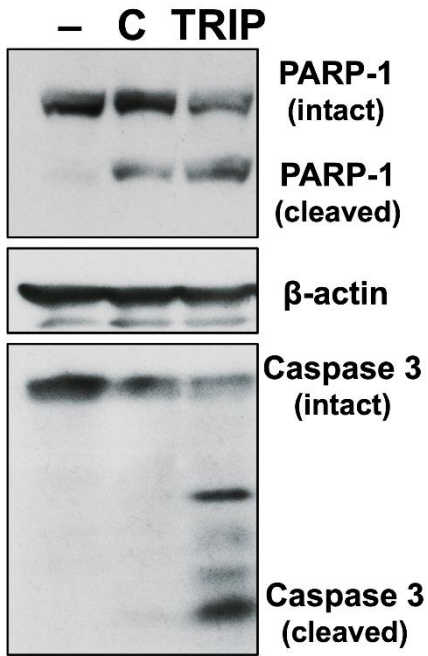


Figure S4.28. Western blot of A2780 cells untreated (–) or treated with cisplatin (C, 10 μ M), or TRIP (5 μ M) for 24 h.

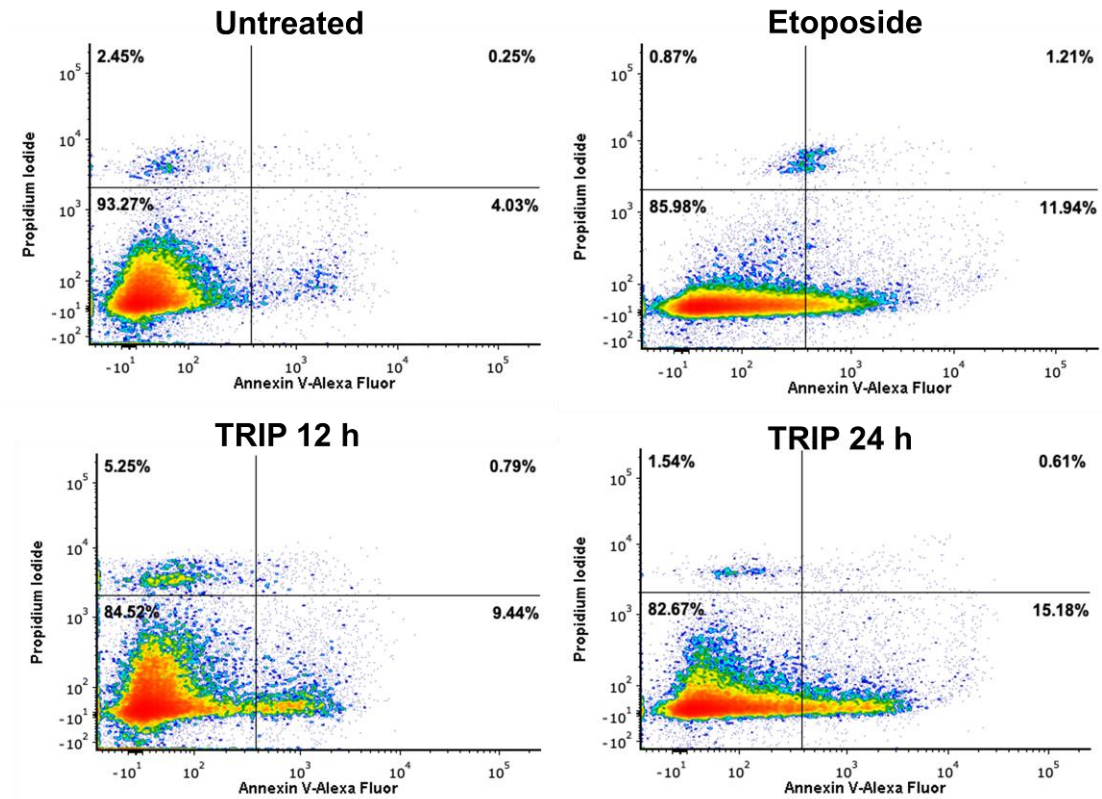


Figure S4.29. Annexin V/PI density plot of A2780 cells untreated (top left), treated with etoposide for 24 h (positive control, 100 μ M, top right), TRIP for 12 h (5 μ M, bottom left), and TRIP for 24 h (5 μ M, bottom right).

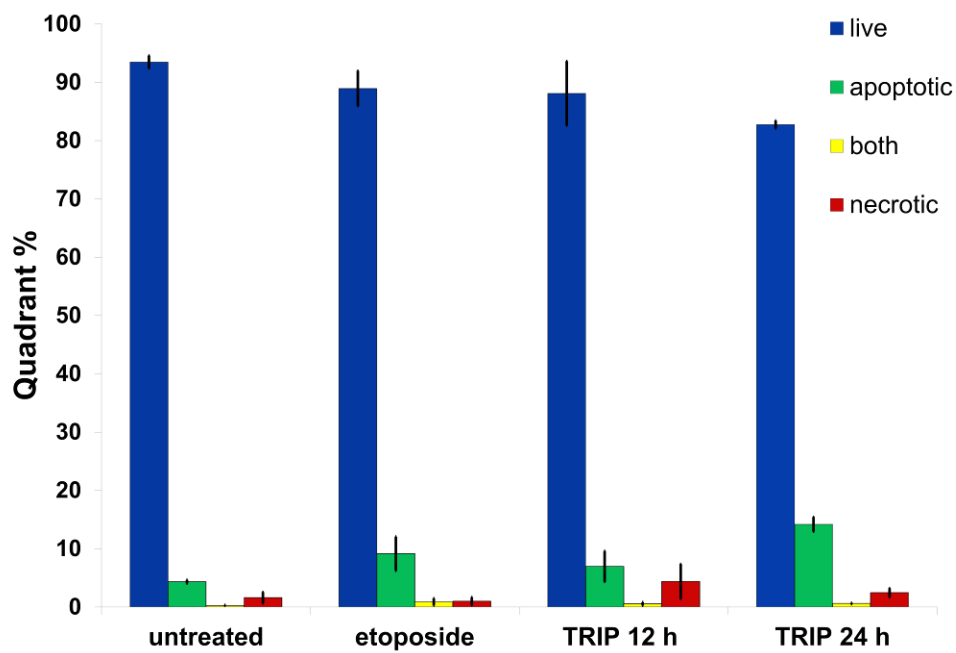


Figure S4.30. Summary of annexin V/PI data from **Figure S28** (minimum of 3 replicates).

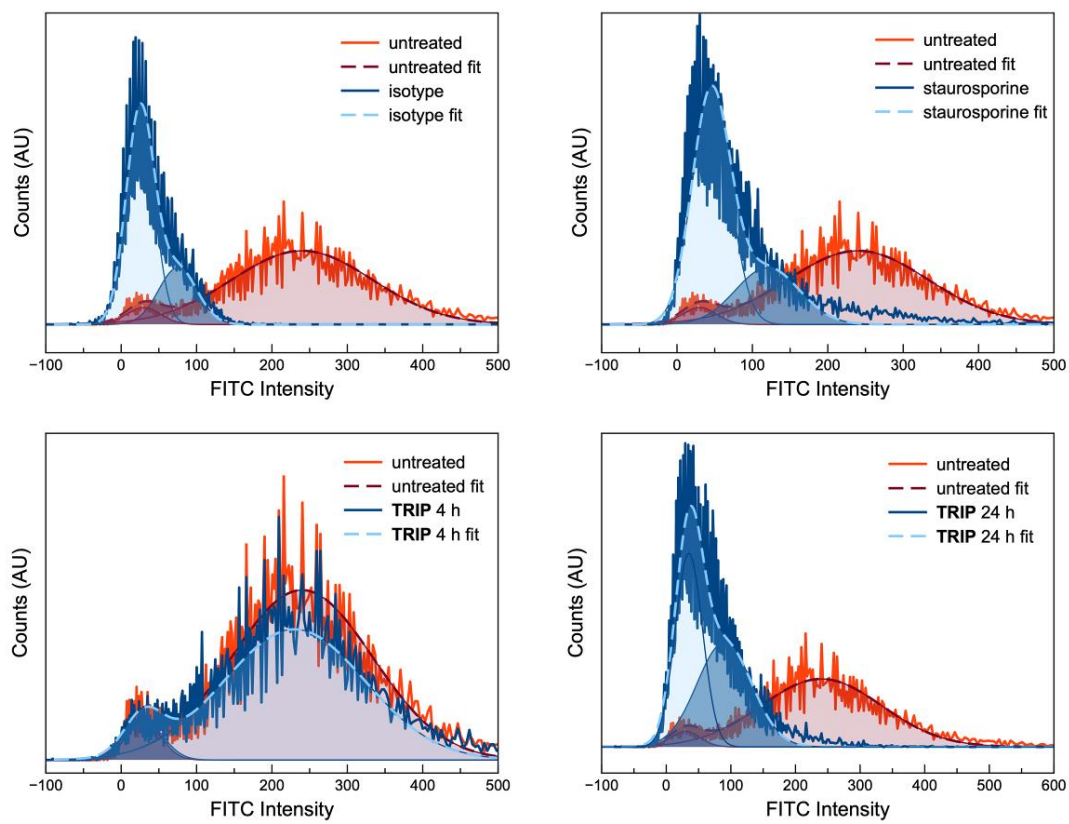


Figure S4.31. Histogram of fluorescence intensity of the cytochrome *c* antibody conjugated to FITC. Untreated cells (red, fit red dash) and cells treated with isotype control (blue, top left), staurosporine for 4 h (1 μ M, blue, top right), TRIP for 4 h (5 μ M, blue, bottom left), and TRIP for 24 h (5 μ M, blue, bottom right).

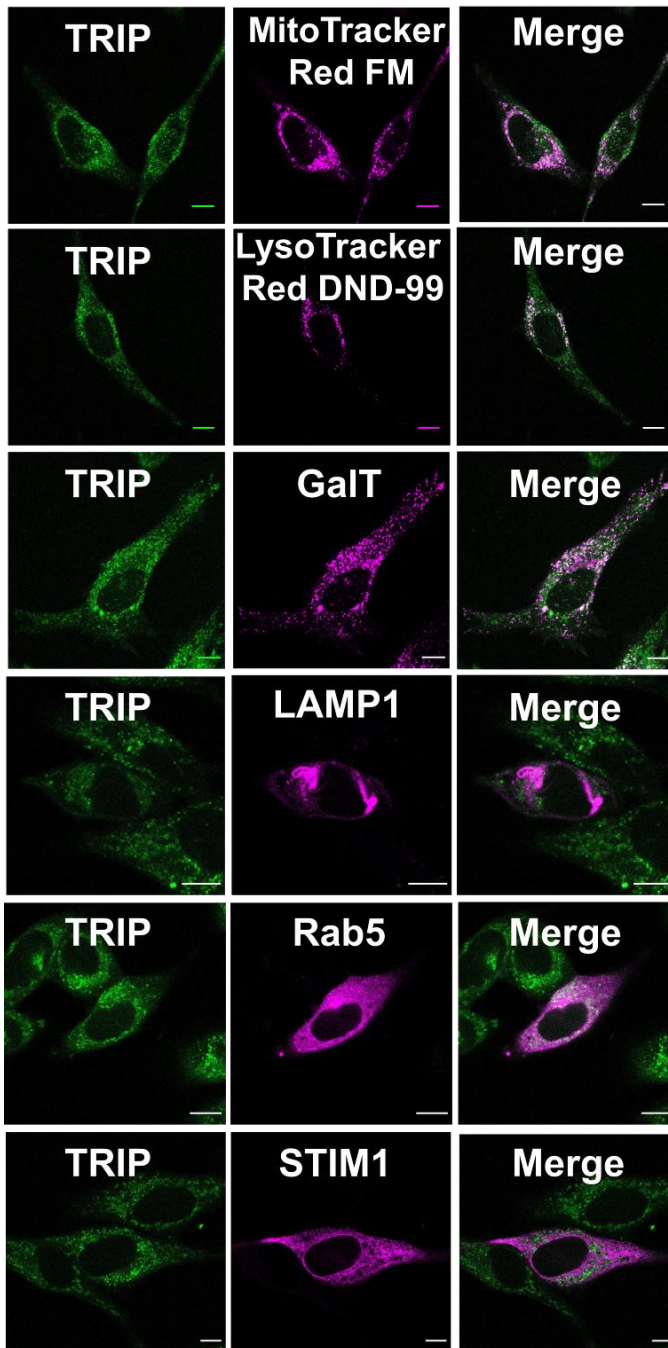


Figure S4.32. Confocal fluorescent microscope images of HeLa cells treated with TRIP (5 μ M, 4 h). Cells were additionally stained with the indicated transfection or dye. Transfected GalT-dsRed (galactosyltransferase 1) colocalizes with the Golgi apparatus, LAMP1-mRFP (Lysosomal Associated Membrane Protein 1) colocalizes with lysosomes and late endosomes, Rab5-mRFP (Ras-associated binding 5) colocalizes with early endosomes, and STIM1-mRFP (Stromal Interaction Molecule 1) colocalizes with the ER. Scale bar = 10 μ m.

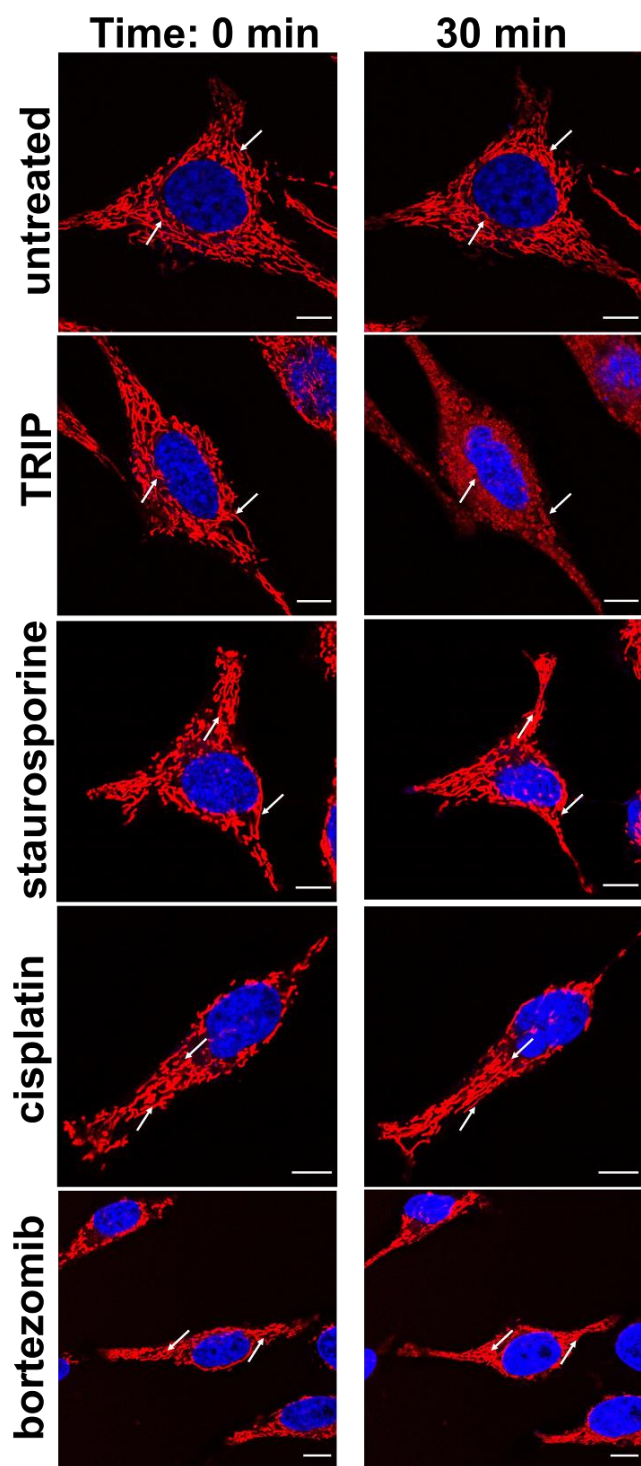


Figure S4.33. Confocal fluorescence microscope images of HeLa cells treated with no compound, TRIP (5 μM), staurosporine (1 μM), cisplatin (10 μM), and bortezomib (25 nM). Cells were stained 15 and 30 min prior to compound treatment with Hoechst dye (blue) and MitoTracker Red (red), respectively.

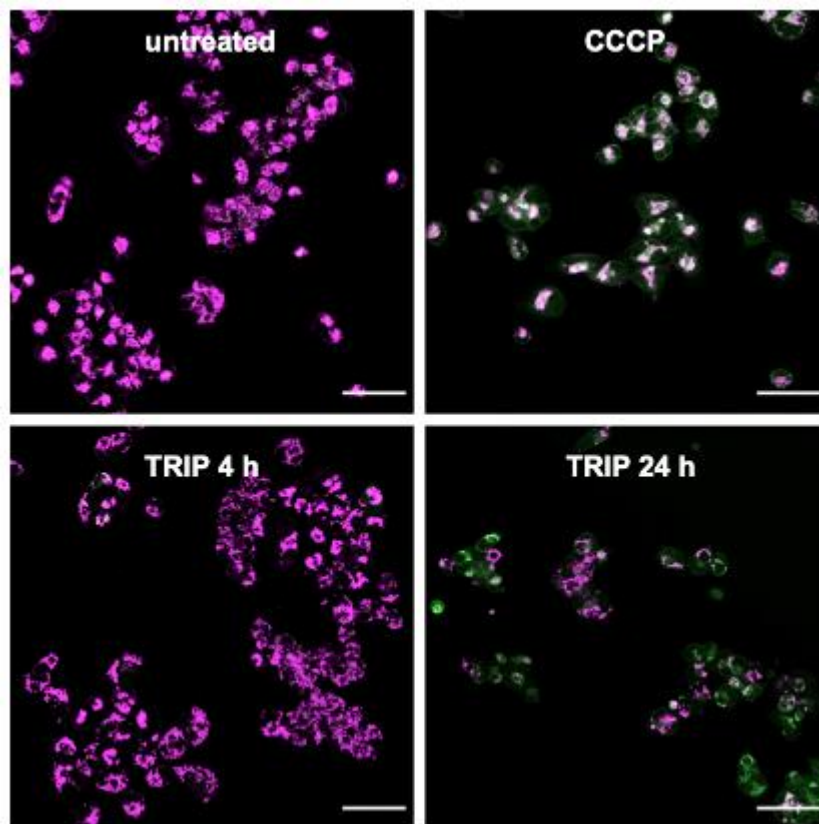


Figure S34. Confocal fluorescence microscope images of A2780 cells treated with JC-1 dye (10 μ M) and no compound (top left), CCCP (50 μ M, top right), TRIP for 4 h (5 μ M, bottom left), and TRIP for 24 h (bottom right). Scale bar = 50 μ m.

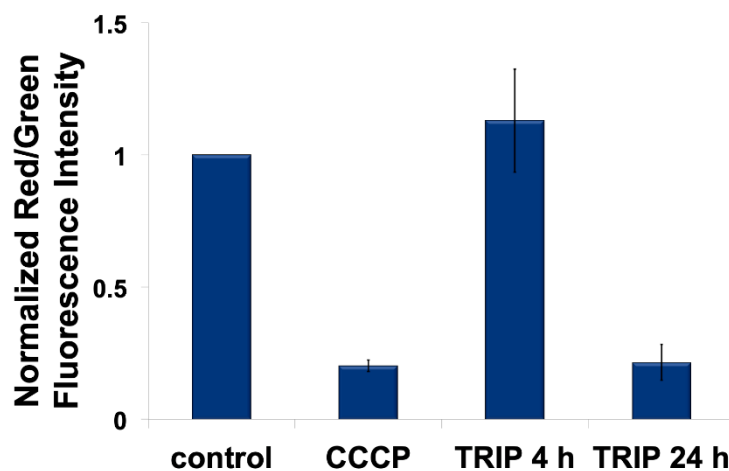


Figure S4.35. Bar graph depicting the normalized red/green fluorescence intensity of A2780 cells after treatment with the corresponding compounds.

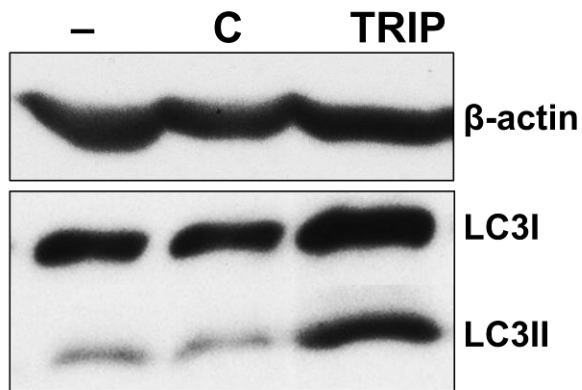


Figure S4.36. Western blot of A2780 cells untreated (-) or treated with cisplatin (C, 10 μ M), or TRIP (5 μ M) for 24 h.

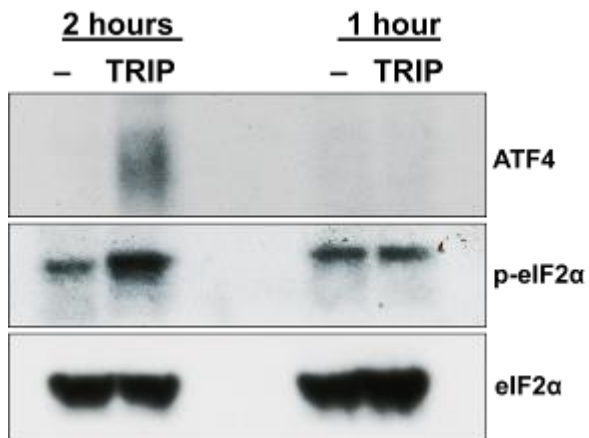


Figure S4.37. Western blot of A2780 cells untreated (-) or treated with TRIP (5 μ M) for 1 or 2 h.

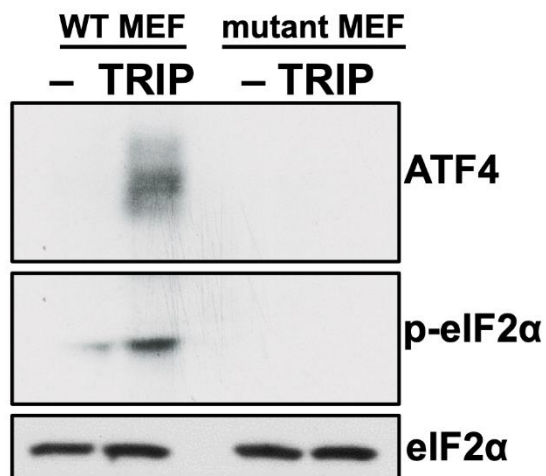


Figure S4.38. Western blot of WT and mutant S51A eIF2 α MEF cells untreated (-) or treated with TRIP (5 μ M) for 2 h.



Figure S4.39. Western blot of WT and mutant S51A eIF2 α MEF cells untreated (-) or treated with TRIP (5 μ M) for 2 h and puromycin labeled (10 min).

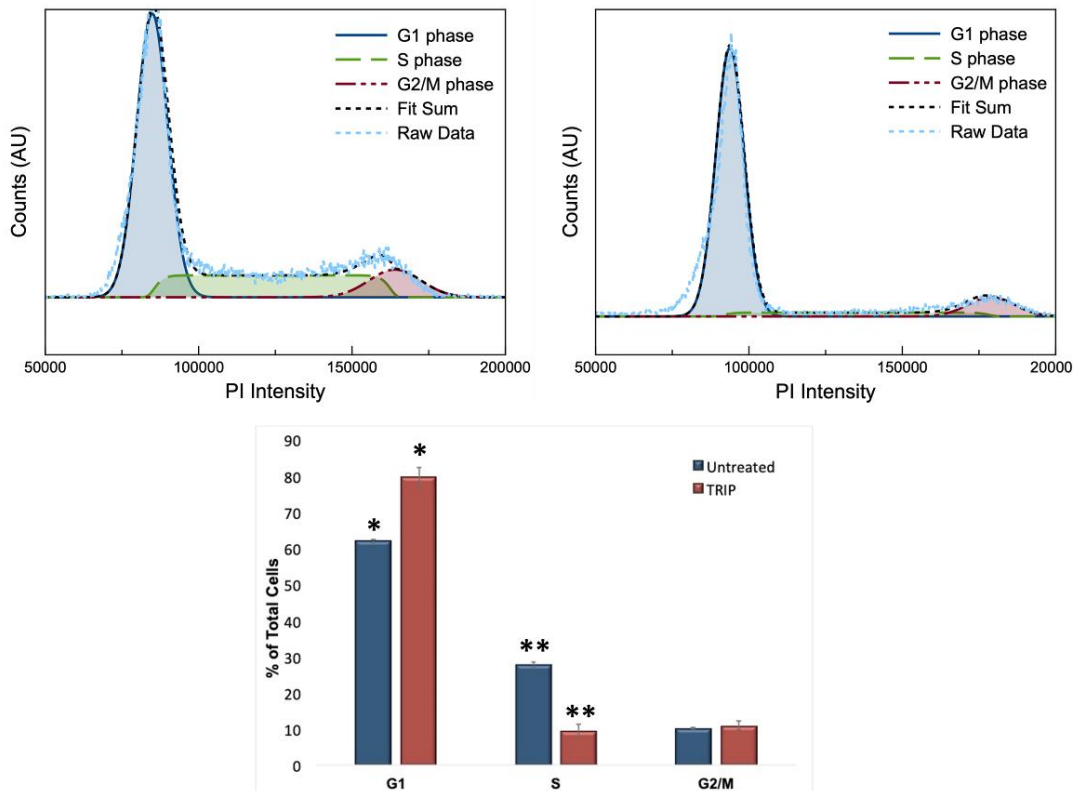


Figure S4.40. A2780 cells stained with propidium iodide and treated with no compound (left) or TRIP (5 μ M, right) for 24 h.

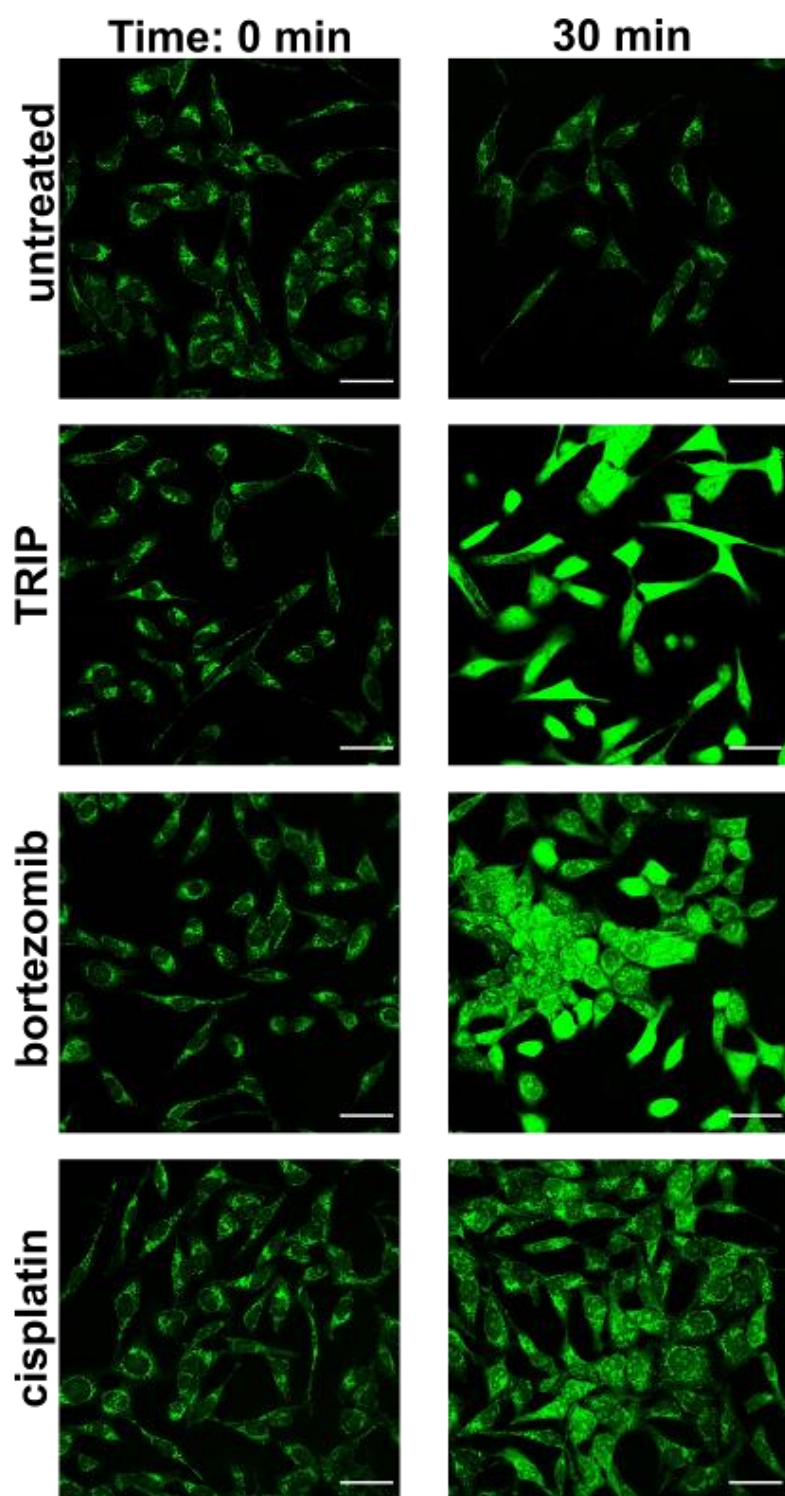


Figure S4.41. Confocal fluorescence microscope images of HeLa cells stained with Thioflavin T (5 μ M, 4 h) and treated with no compound, TRIP (5 μ M), bortezomib (25 nM), and cisplatin (10 μ M) over the course of 30 min. Scale bars = 50 μ m.

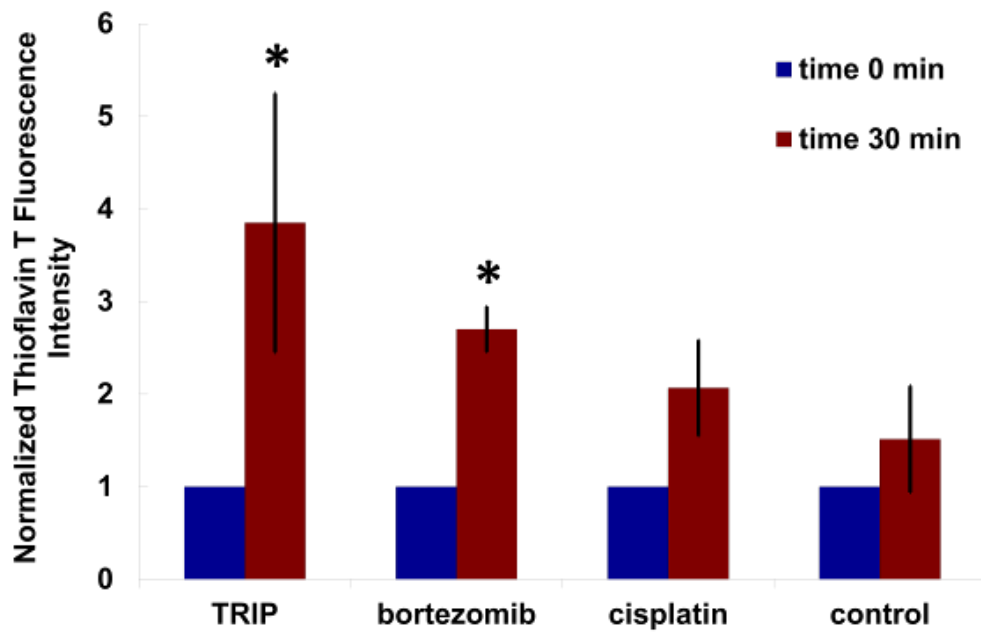


Figure S4.42. Bar graph depicting the change in Thioflavin T fluorescence intensity over the course of 30 min after treatment with the corresponding compounds.

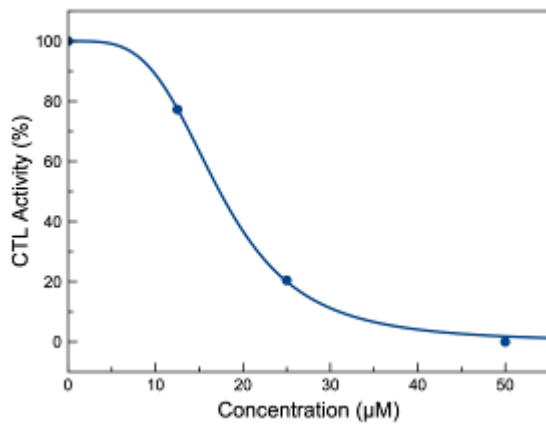


Figure S4.43. Proteasome inhibition in cell lysates by TRIP.

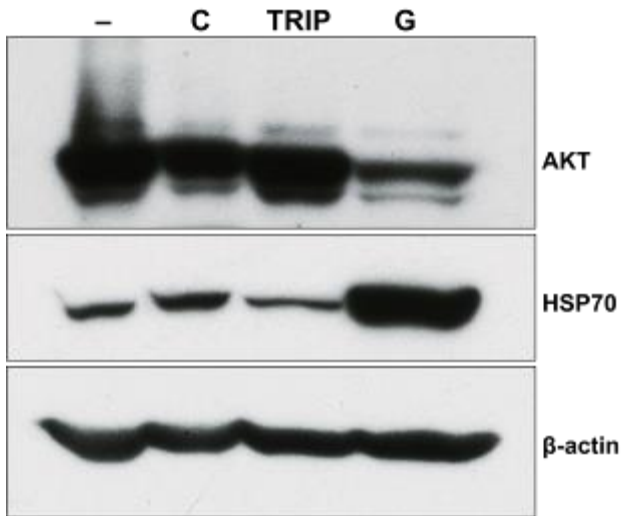


Figure S4.44. Western blot of A2780 cells treated with vehicle control (-), cisplatin (C, 10 μ M), TRIP (5 μ M), and geldanamycin (G, 20 μ M) for 24 h.

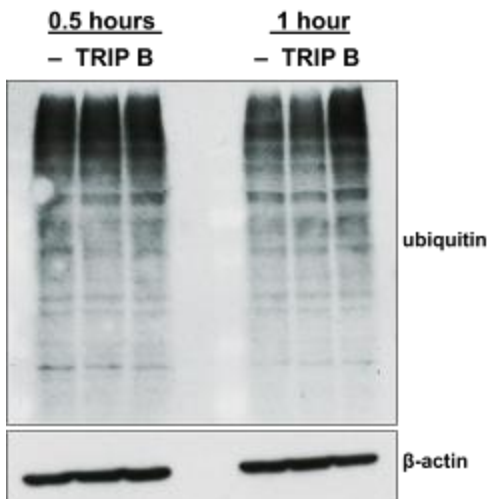


Figure S4.45. Western blot of A2780 cells treated with vehicle control (-), TRIP (5 μ M), and bortezomib (B, 25 nM) for 0.5 and 1 h.

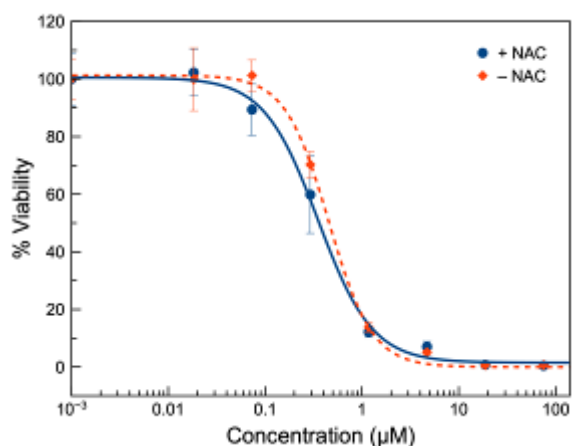


Figure S4.46. Dose-response curve of TRIP in A2780 cells with (blue, solid) and without *N*-acetylcysteine (NAC, red, dashed).

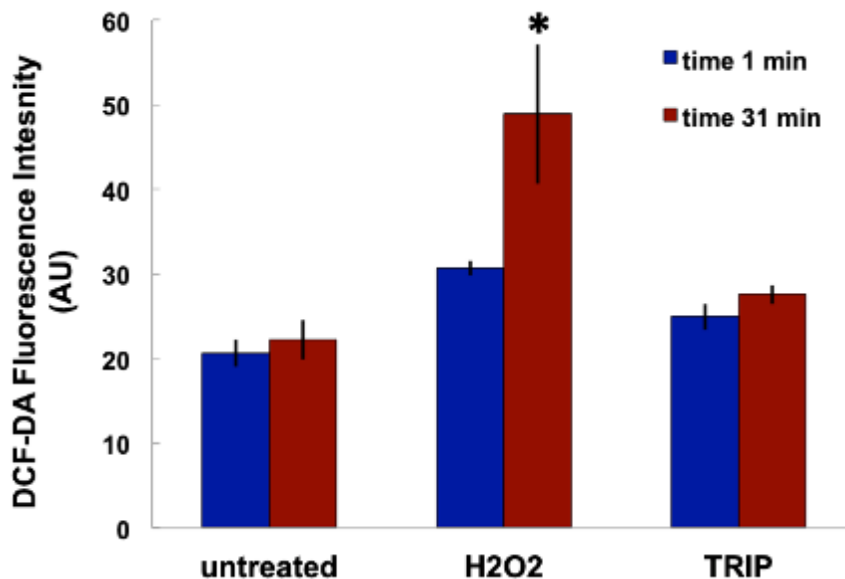


Figure S4.47. HeLa cells stained with 10 μM DCF-DA for 30 min and then treated with H₂O₂ (25 μM) or TRIP (5 μM) over the course of 30 min. The fluorescence intensity was monitored using a fluorescence plate reader.

References

- 1 H. Urra, E. Dufey, T. Avril, E. Chevet and C. Hetz, *Trends in Cancer*, 2016, **2**, 252–262.
- 2 Y.-P. Vandewynckel, D. Laukens, A. Geerts, E. Bogaerts, A. Paridaens, X. Verhelst, S. Janssens, F. Heindryckx and H. Van Vlierberghe, *Anticancer Res.*, 2013, **33**, 4683–4694.
- 3 M. J. Mann and L. M. Hendershot, *Cancer Biol. Ther.*, 2006, **5**, 736–740.
- 4 R. Sano and J. C. Reed, *Biochim. Biophys. Acta - Mol. Cell Res.*, 2013, **1833**, 3460–3470.
- 5 R. Ojha and R. K. Amaravadi, *Pharmacol. Res.*, 2017, **120**, 258–266.
- 6 J. Pracharova, G. Vigueras, V. Novohradsky, N. Cutillas, C. Janiak, H. Kostrhunova, J. Kasparkova, J. Ruiz and V. Brabec, *Chem. - A Eur. J.*, 2018, **24**, 4607–4619.
- 7 R. Cao, J. Jia, X. Ma, M. Zhou and H. Fei, *J. Med. Chem.*, 2013, **56**, 3636–3644.
- 8 T. Zou, C.-N. Lok, Y. M. E. Fung and C.-M. Che, *Chem. Commun.*, 2013, **49**, 5423–5425.
- 9 X. Meng, M. L. Leyva, M. Jenny, I. Gross, S. Benosman, B. Fricker, S. Harlepp, P. Hébraud, A. Boos, P. Wlosik, P. Bischoff, C. Sirlin, M. Pfeffer, J.-P. Loeffler and C. Gaidon, *Cancer Res.*, 2009, **69**, 5458–5466.
- 10 J. S. Nam, M.-G. Kang, J. Kang, S.-Y. Park, S. J. C. Lee, H.-T. Kim, J. K. Seo, O.-H. Kwon, M. H. Lim, H.-W. Rhee and T.-H. Kwon, *J. Am. Chem. Soc.*, 2016, **138**, 10968–10977.
- 11 K. Suntharalingam, T. C. Johnstone, P. M. Bruno, W. Lin, M. T. Hemann and S. J. Lippard, *J. Am. Chem. Soc.*, 2013, **135**, 14060–14063.
- 12 K. M. Knopf, B. L. Murphy, S. N. MacMillan, J. M. Baskin, M. P. Barr, E. Boros and J. J. Wilson, *J. Am. Chem. Soc.*, 2017, **139**, 14302–14314.
- 13 S. C. Marker, S. N. MacMillan, W. R. Zipfel, Z. Li, P. C. Ford and J. J. Wilson, *Inorg. Chem.*, 2018, **57**, 1311–1331.
- 14 C. C. Konkankit, B. A. Vaughn, S. N. MacMillan, E. Boros and J. J. Wilson, *Inorg. Chem.*, 2019, **58**, 3895–3909.
- 15 C. C. Konkankit, A. P. King, K. M. Knopf, T. L. Southard and J. J. Wilson, *ACS Med. Chem. Lett.*, 2019, **10**, 822–827.
- 16 C. C. Konkankit, S. C. Marker, K. M. Knopf and J. J. Wilson, *Dalton Trans.*, 2018, **47**, 9934–9974.
- 17 P. V. Simpson, I. Casari, S. Paternoster, B. W. Skelton, M. Falasca and M. Massi, *Chem. - A Eur. J.*, 2017, **23**, 6518–6521.
- 18 N. Agorastos, L. Borsig, A. Renard, P. Antoni, G. Viola, B. Spingler, P. Kurz and R. Alberto, *Chem. - A Eur. J.*, 2007, **13**, 3842–3852.
- 19 A. Kurzwernhart, W. Kandioller, C. Bartel, S. Bächler, R. Trondl, G. Mühlgassner, M. A. Jakupec, V. B. Arion, D. Marko, B. K. Keppler and C. G. Hartinger, *Chem. Commun.*, 2012, **48**, 4839–4841.
- 20 S. Imstepf, V. Pierroz, R. Rubbiani, M. Felber, T. Fox, G. Gasser and R. Alberto, *Angew. Chemie Int. Ed.*, 2016, **55**, 2792–2795.
- 21 E. Kottelat, V. Chabert, A. Crochet, K. M. Fromm and F. Zobi, *Eur. J. Inorg.*

- Chem.*, 2015, **2015**, 5628–5638.
- 22 A. Leonidova, V. Pierroz, R. Rubbiani, J. Heier, S. Ferrari and G. Gasser, *Dalt. Trans.*, 2014, **43**, 4287–4294.
- 23 A. Leonidova and G. Gasser, *ACS Chem. Biol.*, 2014, **9**, 2180–2193.
- 24 R. H. Shoemaker, *Nat. Rev. Cancer*, 2006, **6**, 813–823.
- 25 D. W. Zaharevitz, S. L. Holbeck, C. Bowerman and P. A. Svetlik, *J. Mol. Graph. Model.*, 2002, **20**, 297–303.
- 26 A. Cassidy-Stone, J. E. Chipuk, E. Ingeman, C. Song, C. Yoo, T. Kuwana, M. J. Kurth, J. T. Shaw, J. E. Hinshaw, D. R. Green and J. Nunnari, *Dev. Cell*, 2008, **14**, 193–204.
- 27 M. Niu, X. Dai, W. Zou, X. Yu, W. Teng, Q. Chen, X. Sun, W. Yu, H. Ma and P. Liu, *Transl. Neurosci.*, 2017, **8**, 37–48.
- 28 I. Tanida, T. Ueno and E. Kominami, Humana Press, Albuquerque, NM, 2008, pp. 77–88.
- 29 M. Boyce, K. F. Bryant, C. Jousse, K. Long, H. P. Harding, D. Scheuner, R. J. Kaufman, D. Ma, D. M. Coen, D. Ron and J. Yuan, *Science*, 2005, **307**, 935–939.
- 30 K. Pakos-Zebrucka, I. Koryga, K. Mnich, M. Ljujic, A. Samali and A. M. Gorman, *EMBO Rep.*, 2016, **17**, 1374–1395.
- 31 B. F. Teske, S. A. Wek, P. Bunpo, J. K. Cundiff, J. N. McClintick, T. G. Anthony and R. C. Wek, *Mol. Biol. Cell*, 2011, **22**, 4390–405.
- 32 J. B. DuRose, D. Scheuner, R. J. Kaufman, L. I. Rothblum and M. Niwa, *Mol. Cell. Biol.*, 2009, **29**, 4295–307.
- 33 S. R. Kimball, *Int. J. Biochem. Cell Biol.*, 1999, **31**, 25–29.
- 34 E. K. Schmidt, G. Clavarino, M. Ceppi and P. Pierre, *Nat. Methods*, 2009, **6**, 275–277.
- 35 H. Matsumoto, S. Miyazaki, S. Matsuyama, M. Takeda, M. Kawano, H. Nakagawa, K. Nishimura and S. Matsuo, *Biol. Open*, 2013, **2**, 1084–1090.
- 36 J. W. Brewer and J. A. Diehl, *Proc. Natl. Acad. Sci.*, 2000, **97**, 12625–12630.
- 37 D. R. Beriault and G. H. Werstuck, *Biochim. Biophys. Acta - Mol. Cell Res.*, 2013, **1833**, 2293–2301.
- 38 M. J. Chow, C. Licon, G. Pastorin, G. Mellitzer, W. H. Ang and C. Gaiddon, *Chem. Sci.*, 2016, **7**, 4117–4124.
- 39 M. J. Chow, M. V. Babak, K. W. Tan, M. C. Cheong, G. Pastorin, C. Gaiddon and W. H. Ang, *Mol. Pharm.*, 2018, **15**, 3020–3031.
- 40 F.-Y. Wang, X.-M. Tang, X. Wang, K.-B. Huang, H.-W. Feng, Z.-F. Chen, Y.-N. Liu and H. Liang, *Eur. J. Med. Chem.*, 2018, **155**, 639–650.
- 41 X. Wang, Q. Guo, L. Tao, L. Zhao, Y. Chen, T. An, Z. Chen and R. Fu, *Mol. Carcinog.*, 2017, **56**, 218–231.
- 42 S. Mandal, D. K. Poria, R. Ghosh, P. S. Ray and P. Gupta, *Dalton Trans.*, 2014, **43**, 17463–17474.
- 43 T.-L. Lam, K.-C. Tong, C. Yang, W.-L. Kwong, X. Guan, M.-D. Li, V. Kar-Yan Lo, S. Lai-Fung Chan, D. Lee Phillips, C.-N. Lok and C.-M. Che, *Chem. Sci.*, 2019, **10**, 293–309.
- 44 J. Zhao, S. Li, X. Wang, G. Xu and S. Gou, *Inorg. Chem.*, 2019, **58**, 2208–

- 2217.
- 45 W.-L. Kwong, R. Wai-Yin Sun, C.-N. Lok, F.-M. Siu, S.-Y. Wong, K.-H. Low and C.-M. Che, *Chem. Sci.*, 2013, **4**, 747–754.
- 46 K.-B. Huang, F.-Y. Wang, X.-M. Tang, H.-W. Feng, Z.-F. Chen, Y.-C. Liu, Y.-N. Liu and H. Liang, *J. Med. Chem.*, 2018, **61**, 3478–3490.
- 47 Y. Wang, J. Hu, Y. Cai, S. Xu, B. Weng, K. Peng, X. Wei, T. Wei, H. Zhou, X. Li and G. Liang, *J. Med. Chem.*, 2013, **56**, 9601–9611.
- 48 S. Tardito, C. Isella, E. Medico, L. Marchiò, E. Bevilacqua, M. Hatzoglou, O. Bussolati and R. Franchi-Gazzola, *J. Biol. Chem.*, 2009, **284**, 24306–19.
- 49 P. Kurz, B. Probst, B. Spingler and R. Alberto, *Eur. J. Inorg. Chem.*, 2006, 2966–2974.
- 50 J. M. Smieja and C. P. Kubiak, *Inorg. Chem.*, 2010, **49**, 9283–9289.
- 51 Y. Yuan, W. Dong, X. Gao, H. Gao, X. Xie and Z. Zhang, *J. Org. Chem.*, 2018, **83**, 2840–2846.
- 52 2015.
- 53 G. M. Sheldrick, *Acta Crystallogr. Sect. A Found. Crystallogr.*, 2015, **71**, 3–8.
- 54 G. M. Sheldrick, *Acta Crystallogr. Sect. C Struct. Chem.*, 2015, **71**, 3–8.
- 55 G. M. Sheldrick, *Acta Crystallogr. Sect. A Found. Crystallogr.*, 2008, **64**, 112–122.
- 56 P. Müller, *Crystallogr. Rev.*, 2009, **15**, 57–83.
- 57 O. V Dolomanov, L. J. Bourhis, R. J. Gildea, J. A. K. Howard and H. Puschmann, *J. Appl. Crystallogr.*, 2009, **42**, 339–341.
- 58 A. M. Brouwer, *Pure Appl. Chem.*, 2011, **83**, 2213–2228.
- 59 A. K. Godwin, A. Meister, P. J. O’Dwyer, C. S. Huang, T. C. Hamilton and M. E. Anderson, *Proc. Natl. Acad. Sci.*, 1992, **89**, 3070–3074.

CHAPTER 5

Exploring the In Vivo and In Vitro Anticancer Activity of Rhenium Isonitrile Complexes

Sierra C. Marker,* A. Paden King,* Samantha Granja, Brett Vaughn, Joshua J.
Woods, Eszter Boros, and Justin J. Wilson. *Submitted*, 2020.

*Denotes Equal Contribution

Introduction

In Chapter 4, we reported that the TRIP complex [Re(dmphen)(CO)₃(p-tol-ICN)]⁺ (**TRIP-1a**) is a potent anticancer agent that operates by inducing endoplasmic reticulum (ER) stress. This compound is one of a relatively new, promising class of anticancer agents that target endoplasmic reticulum (ER) stress pathways.¹⁻⁴ As discussed in Chapter 1, cancer cells and tumors often exhibit heightened levels of ER stress compared to normal cells due to their increased burden of reactive oxygen species (ROS) and higher rates of protein misfolding.⁵⁻⁷ To compensate for this stress, cancer cells will upregulate the unfolded protein response (UPR) pathway, which helps manage protein homeostasis. This upregulation renders cancer cells sensitive to compounds that induce ER stress,⁸⁻¹¹ leading to ER stress-mediated apoptosis, autophagy, or paraptosis.¹²⁻¹⁵ The strategy of targeting the UPR and triggering ER stress is highlighted by the clinical approval of the anticancer agents bortezomib and carfilzomib, which cause ER stress by inhibiting the proteasome.¹⁶ To better understand **TRIP-1a**, we designed a small library of related rhenium tricarbonyl complexes bearing various equatorial polypyridyl and axial isonitrile ligands in order to probe structure-activity relationships (SARs) for this compound class. In this Chapter, we describe the synthesis and characterization of 10 new analogs to **TRIP-1a** and an evaluation of their anticancer activities and ER stress-inducing properties. Through these studies, we have found that complexes with more hydrophobic and electron-donating ligands have higher cytotoxicities. Furthermore, we describe in vivo studies that elucidate the biodistribution of **TRIP-1a** and its ^{99m}Tc analog, as well as its anticancer activity in an ovarian cancer xenograft model. Collectively, this Chapter

demonstrates the viability of TRIP complexes as a new class of metal-based ER stress-inducing agents with promising in vitro and in vivo anticancer properties.

Results and Discussion

Library Design.

The modular coordination environment of the TRIP complexes makes them amenable for making systematic modifications to tune their properties. Both the hydrophobicity and electron-donating properties of the TRIP ligands alter the biological and physical properties of these complexes. To assess the role of the ligands on these attributes, we designed a library to modify both the equatorial polypyridyl ligands and the axial isonitrile ligands. We chose the equatorial ligands dmphen (**1**), 1,10-phenanthroline (**2**), 2,2'-bipyridine (**3**), 4,4'-dimethyl-2,2'-bipyridine (**4**), 4,4'-dimethoxy-2,2'-bipyridine (**5**), 4,4'-bis(trifluoromethyl)-2,2'-bipyridine (**6**), and 4,4'-di-*tert*-butyl-2,2'-bipyridine (**7**) based on their different steric, hydrophobic, and electronic properties. These equatorial ligands were paired with the *para*-tolyl isonitrile (ICN) axial ligand **a** to obtain the seven complexes **TRIP-1a**, **TRIP-2a**, **TRIP-3a**, **TRIP-4a**, **TRIP-5a**, **TRIP-6a**, and **TRIP-7a** (**Chart 5.1**). To probe the role of ICN ligand, we prepared another series of TRIP complexes that keep the polypyridyl ligand constant (**1**), while varying the axial ligand through addition of either *para*-tolyl ICN (**a**), 2,6-dimethylphenyl ICN (**b**), 3,5-dimethylphenyl (**c**), *para*-methoxyphenyl ICN (**d**), or *para*-chlorophenyl ICN (**e**). Thus, an additional 4 TRIP complexes, **TRIP-1b**, **TRIP-1c**, **TRIP-1d**, and **TRIP-1e**, comprise this subset of the library. A total of 11 complexes was incorporated into our full complex library (**Chart**

5.1).

These TRIP complexes were synthesized using a modification of a previously reported procedure.¹⁷ Briefly, 1 equiv. of *fac*-[Re(CO)₃(NN)Cl], where NN = polypyridyl ligand, was refluxed with 1 equiv. of AgOTf (OTf = trifluoromethanesulfonate) in dry tetrahydrofuran (THF) for 3 h to abstract the chloride ligand. Solid AgCl was removed by filtration, and an excess (4 equiv.) of the desired ICN ligand was added. After refluxing overnight, the products were isolated in moderate yields, and purified either by repeated recrystallization or column chromatography. The products were yellow to off-white powders, with more strongly donating equatorial ligands giving rise to whiter products. These 11 complexes were characterized by ¹H (Figures S5.1–S5.10, Supplementary Information (SI)) and ¹³C NMR (Figures S5.11–S5.19) spectroscopy, high resolution electrospray ionization mass spectrometry (HR-ESI-MS), and Fourier-transform infrared (FTIR) spectroscopy (Figures S5.20–S5.29), and their purities were verified with high-performance liquid chromatography (HPLC, Figures S5.30–S5.39) and elemental analysis.

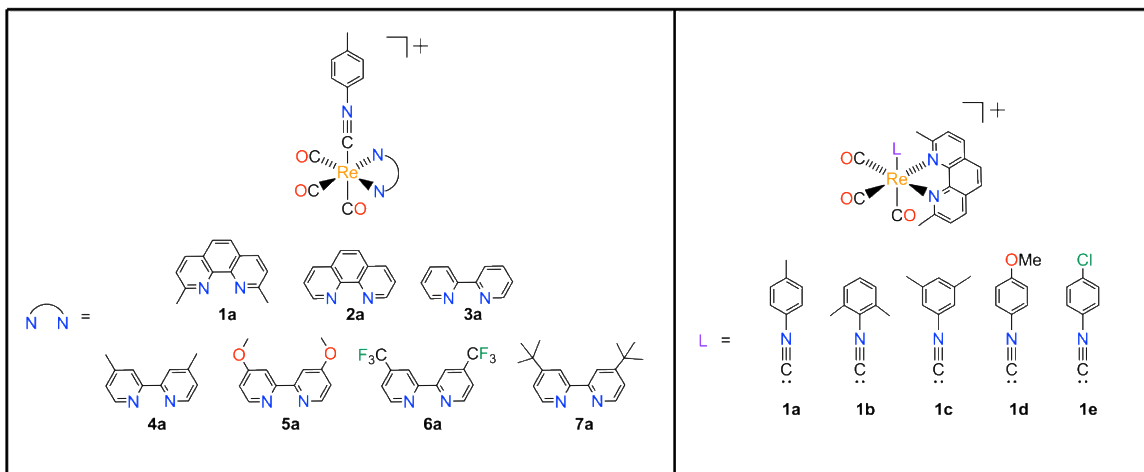


Chart 5.1. TRIP derivatives explored in this Chapter.

Physical Characterization.

The physical properties of the complexes were evaluated using several techniques, including FTIR spectroscopy, single-crystal X-ray diffraction (XRD), cyclic voltammetry (CV), and ^1H – ^{15}N -HMBC (Heteronuclear Multiple Bond Correlation) NMR spectroscopy. Within the IR spectra, 3 $\text{C}\equiv\text{O}$ stretching modes are observed, consistent with the C_s symmetry of these complexes. Additionally, a diagnostic $\text{C}\equiv\text{N}$ stretching mode in the energy range of 2155 – 2186 cm^{-1} was also detected, confirming the incorporation of this axial ligand. In comparing **TRIP-1a**–**TRIP-1e**, complexes which all bear the same equatorial dmphen ligand but different ICNs, the 3 $\text{C}\equiv\text{O}$ stretching frequencies are relatively invariant and span a narrow range of 2033 – 2036 , 1957 – 1967 , and 1926 – 1941 cm^{-1} . The $\text{C}\equiv\text{N}$ stretching frequency does predictably change depending on the type of substituents that are present on the ICN ligand. ICN ligands with more electron-donating substituents give rise to lower energy $\text{C}\equiv\text{N}$ stretches, than those with less electron-donating groups. For example, the

C≡N stretching frequency for **TRIP-1d**, which bears an electron-donating *p*-methoxy ICN, is found at 2179 cm⁻¹, whereas for **TRIP-1e** with an electron-withdrawing *p*-chloro ICN this mode occurs at 2185 cm⁻¹. A notable outlier in this series is that of **TRIP-2a**. For this complex, the C≡N stretch occurs at a 2155 cm⁻¹, an energy that is significantly lower than that of the other complexes. Structural data, obtained via X-ray crystallography (vide infra), indicate that the ICN ligand has a pronounced bend in this complex, providing a rationale for the lower energy C≡N stretch in **TRIP-2a**. As the equatorial ligand is varied over **TRIP-1a–TRIP-7a**, changes in the energy of the C≡O stretching modes are apparent with more electron-donating ligands giving rise to lower energy vibrations. This trend is most apparent for complexes **TRIP-3a–TRIP-6a**, which all contain derivatives of the 2,2'-bipyridine (bpy) ligand. For instance, **TRIP-6a**, which bears the electron-withdrawing 4,4'-bis(trifluoromethyl)-2,2'-bipyridine ligand, has relatively high-energy C≡O stretching frequencies at 2045, 1976, and 1944 cm⁻¹, whereas **TRIP-7a**, with the electron-donating 4,4'-di-*tert*-butyl-2,2'-bipyridine ligand, exhibits lower-energy C≡O stretching frequencies at 2028, 1959, and 1931 cm⁻¹. For these complexes, more electron-donating ligands give rise to more electron-rich metal centers that engage in more extensive π-back-bonding with the CO ligands, resulting in a weaker C≡O bond. As shown by the relative lack of variability in the C≡O stretching frequencies of complexes **TRIP-1a–TRIP-1e**, the equatorial polypyridyl ligand has a larger effect on the electron-richness of the metal center than the ICN axial ligand.

Single crystals of **TRIP-2a**, suitable for XRD analysis, were grown by diffusion of diethyl ether into a dichloromethane (DCM) solution. Crystallographic

refinement and data collection parameters and relevant interatomic distances and angles are reported in **Table S5.1** and **S5.2**, respectively. The structural metrics of this complex are generally comparable to those of **TRIP-1a** and other related rhenium tricarbonyl isonitrile structures.^{17–22} A key difference between these structures is the Re–C4–N3 bond angle of the ICN. This angle in **TRIP-2a** is noticeably bent at 169.4(3)° (**Figure 5.1a**). By contrast, the same angle in **TRIP-1a** is close to being linear at 176.1(3)° (**Figure 5.1b**),¹⁷ consistent with other reported rhenium isonitrile complexes, which have bond angles ranging from 173.6(3)–176.1(3)°. The deviation from linearity in **TRIP-2a** may be a consequence of increased back-bonding from the Re center to the ICN ligand. This type of interaction populates the π^* orbital of the ICN ligand, leading to an effective decrease in C \equiv N bond order and a shift in hybridization of the carbon atom closer to sp^2 . As noted above, this hypothesis is supported by the significantly lower energy C \equiv N stretching frequency of 2155 cm⁻¹ observed via IR spectroscopy for **TRIP-2a** relative to the other derivatives, which exhibit C \equiv N stretching frequencies between 2171–2186 cm⁻¹. The C \equiv N stretching frequency for two previously reported and crystallographically-characterized rhenium isonitrile complexes, *fac*-[Re(CO)₃(1,10-phenanthroline)(*ortho*-methoxyphenylICN)](PF₆) and *fac*-[Re(CO)₃(bpy)(2,6-dimethylphenylICN)]OTf, are 2173 and 2181 cm⁻¹, respectively. These two structures show only moderate deviations from linearity with Re–C_{ICN}–N_{ICN} bond angles of 175.8(3) and 173.6(3)°, respectively.^{18,21} However, for more electron-rich, low-valent metal complexes, the bending of the ICN ligands can give rise to angles of less than 135°,^{23,24} indicating that the effects observed for **TRIP-2a** are relatively modest.

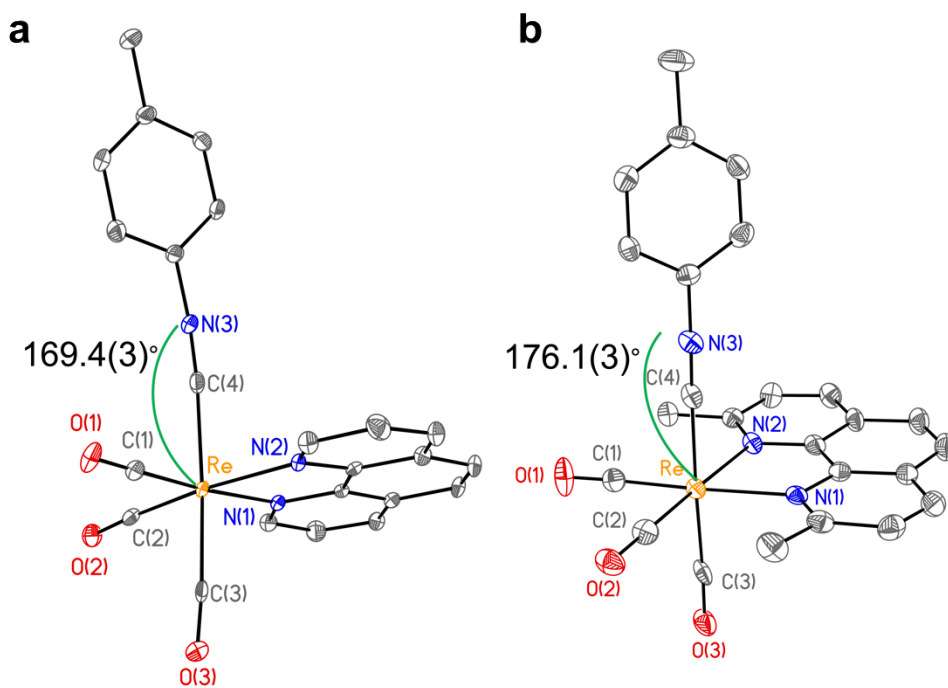


Figure 5.1. (a) X-ray crystal structure of **TRIP-2a**. The Re–C4–N3 interatomic angle is $169.4(3)^\circ$ and the C4–N3 distance is $1.132(4)$ Å. Selected interatomic distances and angles: Re–C(1) $1.944(3)$; Re–C(2) $1.933(3)$; Re–C(3) $1.986(3)$; Re–C(4) $2.081(3)$; Re–N(1) $2.183(2)$; Re–N(2) $2.137(2)$. (b) X-ray crystal structure of **TRIP-1a** taken from reference 66. Selected interatomic distances and angles: Re–C(1) $1.908(4)$; Re–C(2) $1.931(4)$; Re–C(3) $1.960(4)$; Re–C(4) $2.083(4)$; Re–N(1) $2.221(3)$; Re–N(2) $2.216(3)$. Ellipsoids are drawn at 50% probability. Hydrogen atoms and counterions are omitted for clarity.

To probe the electronic properties of these complexes, we employed ^1H – ^{15}N -HMBC NMR spectroscopy. Although the low gyromagnetic ratio and 0.37% natural abundance of ^{15}N makes it difficult to detect directly in unenriched samples, magnetization transfer from other nuclei, such as ^1H , can allow for signal enhancement via 2D NMR spectroscopic methods including HMBC.²⁵ Heteronuclear NMR spectroscopy is especially useful for analyzing metal-based anticancer agents because NMR-active nuclei, such as ^{15}N and ^{31}P , are often directly bound to the metal center of interest.²⁶ Based on this precedence, we used ^1H – ^{15}N HMBC NMR

spectroscopy to determine the ^{15}N chemical shifts of **TRIP-3a–TRIP-7a**, the complexes bearing bpy ligands. The ^{15}N chemical shifts of the bpy nitrogen atoms of these complexes span approximately 40 ppm, beginning at 202 ppm for **TRIP-5a** and ranging up to 237 ppm for **TRIP-6a** (Table 5.1, Figures S5.40–S5.45). These shifts are comparable to those previously reported for the ^{15}N nuclei within bpy and 1,10-phenanthroline (phen) ligands that are present within a series of Pd(II) and Pt(II) complexes. The ^{15}N chemical shifts for these complexes also hover around 200 ppm, ranging from 203 to 218 ppm and 201 to 216 ppm for Pd and Pt, respectively.²⁷ These ^{15}N chemical shifts are related to the electron-donating properties of the equatorial ligands. Stronger donors, like 4,4'-dimethoxy-2,2'-bipyridine in **TRIP-5a**, give rise to more upfield shifts, and weaker donors, like 4,4'-bis(trifluoromethyl)-2,2'-bipyridine in **TRIP-6a**, give rise to downfield shifts. Although in principle detecting the ^{15}N resonance of the ICN ligands should be possible as well, we generally found this signal to be undetectable within a time span of less than 4 h. Only for a highly concentrated sample of **TRIP-4a** were we able to observe a ^{15}N , ^1H crosspeak resonating at 175 ppm in the ^{15}N channel. Although we could not reliably measure the ^{15}N resonance of the isonitrile ligands, our data for the equatorial bpy ligands indicates that these chemical shifts can be used as a reporter of the electronic properties of these complexes.

Table 5.1. Physical properties of TRIP derivatives.

Compound	¹⁵ N chemical shift (ppm) ^b	E _{pc} (V vs SCE)	λ, nm (ε, M ⁻¹ cm ⁻¹)	λ, nm (Φ, %)	τ (μs)	τ _{N2} ^d (μs)
TRIP-1a	223.7	-1.25	230 (39900 ± 2000), 261 (44800 ± 2200), 282 (33800 ± 1600), 306 (21000 ± 900), 369 (2000 ± 100) ^c	505 (3.1 ± 0.3) ^c	1.1 ^c	3.5
TRIP-2a	222.3	-1.18	270 (46600 ± 1200), 301 (16200 ± 300), 364 (3000 ± 100)	512 (5.3 ± 0.4)	1.8	10.9
TRIP-3a	225.8	-1.18	244 (31000 ± 700), 260 (39100 ± 1800), 306 (17200 ± 700), 317 (16500 ± 1400), 332 (6100 ± 400)	523 (6.3 ± 0.2)	0.7	1.0
TRIP-4a	217.6	-1.30	244 (34400 ± 700), 261 (43200 ± 900), 303 (18600 ± 400), 314 (18400 ± 400), 333 (6800 ± 200)	516 (6.7 ± 0.1)	0.8	1.3
TRIP-5a	201.8	-1.33	223 (33900 ± 2100), 260 (41200 ± 2500), 303 (14100 ± 800), 332 (6600 ± 400)	525 (3.9 ± 0.3)	0.4	0.7
TRIP-6a	236.8	-0.75	260 (35600 ± 1700), 297 (17800 ± 600), 324 (11900 ± 700), 365 (3800 ± 100)	584 (0.8 ± 0.1)	0.1	0.1
TRIP-7a	n.d.	-1.30	260 (44200 ± 1200), 304 (19800 ± 100), 315 (18800 ± 900), 334 (7300 ± 100)	518 (7.7 ± 0.2)	0.7	1.6
TRIP-1b	n.d.	-1.28	259 (39100 ± 1600), 283 (31200 ± 1200), 305 (19400 ± 900), 370 (2000 ± 300)	503 (2.7 ± 0.3)	1.2	6.8
TRIP-1c	n.d.	-1.27	261 (36100 ± 800), 283 (29600 ± 500), 305 (18900 ± 800), 367 (2500 ± 60)	504 (1.6 ± 0.1)	1.1	5.3
TRIP-1d	n.d.	-1.26	268 (58200 ± 1700), 283 (46700 ± 1700), 306 (27900 ± 900), 2369 (600 ± 300)	506 (2.8 ± 0.3)	1.0	4.0
TRIP-1e	n.d.	-1.29	264 (44400 ± 2300), 284 (34600 ± 1700), 305 (21400 ± 1200), 369 (2000 ± 30)	501 (2.3 ± 0.1)	1.3	5.6

^an.d. = not determined.

^bReferenced to the internal standard acetonitrile at 240 ppm vs. liquid NH₃ at 0 ppm.

^cReported in reference 66.

^dLuminescence lifetime measured in nitrogen-saturated PBS (pH 7.4).

Because redox processes often play a critical role in mediating the anticancer activities of metal-based drug candidates,^{28,29} the electrochemical properties of the TRIP compounds were investigated using cyclic voltammetry (CV) in acetonitrile

(**Table 1, Figures S5.46–S5.56**). The cyclic voltammograms of these complexes all display a prominent irreversible reduction peak at potentials spanning -0.75 to -1.33 V vs SCE. Based on prior electrochemical studies of rhenium tricarbonyl complexes with polypyridyl and isonitrile ligands, these peaks in the voltammograms are assigned to ligand-based reductions.³⁰ Notably, all of these reduction events occur at potentials that are outside of the biologically relevant range. However, the values of these reduction potentials can be used as a readout on the electronic properties of these complexes. These potentials correlate, as expected, with the electron-donating properties of the diimine ligands. For example, **TRIP-6a**, which bears the most electron-deficient polypyridyl ligand, has the most positive reduction potential. The redox potentials for **TRIP-3a–TRIP-6a** also correlate with the ^{15}N chemical shifts of the diimine ligands with an R^2 value of 0.71 (**Figure S5.57, SI**). This correlation reflects the fact that both parameters provide a complementary measure for the electron-donating strengths of the diimine ligands.

Because rhenium tricarbonyl complexes have been extensively used as cellular imaging agents,^{31,32} we investigated the photophysical properties of these TRIP complexes to assess their suitability for this application. The absorbance (**Figures S5.58–S5.67**) and emission (**Figures S5.68–S5.77**) spectra for all complexes were collected in phosphate-buffered saline (PBS, pH 7.4) containing $\leq 1\%$ DMSO (**Table 5.1**). The absorbance and emission profiles of **TRIP-1a–TRIP-1e**, complexes containing the same dmphen equatorial ligand but different axial ICN ligands, are all nearly identical with only small differences in emission quantum yields and lifetimes. By contrast, when the equatorial ligands are varied across **TRIP-1a–TRIP-7a**,

significant differences in the absorbance and emission energies are observed. As the equatorial polypyridyl ligands become more electron-withdrawing, the lowest energy absorbance maxima, which are attributed to metal-to-ligand charge transfer (MLCT) transitions, undergo a red-shift. Likewise, the emission of these complexes, which is attributed to a relaxation of the $^3\text{MLCT}$ excited state, also undergoes a red-shift as the ligands contain more electron-withdrawing substituents. For instance, the emission maximum of **TRIP-6a**, with the electron-withdrawing 4,4'-bis(trifluoromethyl)-2,2'-bipyridine ligand, is at 584 nm, whereas for **TRIP-5a**, which bears the donating 4,4'-dimethoxy-2,2'-bipyridine ligand, this maximum occurs at 525 nm. Both the lack of effect of the axial ICN ligands and the importance of electron-withdrawing substituents on the equatorial ligands are consistent with the MLCT nature of these excited states in which the accepting ligand π^* orbital resides solely on the diimine.³³ However, for related complexes with large aromatic ICN axial ligands, MLCT states featuring these ligands are accessible.

The emission quantum yields (Φ), measured relative to quinine sulfate as a standard, range from 1 to 8% in air-equilibrated PBS. As expected, these values are generally correlated to the energy of the excited state, following the well-known energy-gap law.³⁴ **TRIP-6a**, for example, has the lowest quantum yield (0.8%), which coincides with it also having the lowest energy absorbance and emission energies in the series. The emission quantum yields are generally higher for complexes containing derivatives of bpy (**TRIP-3a–TRIP-7a**) compared to those that contain derivatives of phen, which is somewhat surprising because the phen ligands have higher energy emission maxima. The luminescence lifetimes of the complexes (**Figures S5.78–**

S5.87) range from 0.1 to 2 μ s in air-equilibrated PBS. Furthermore, these lifetimes increase by a factor of 1.5 to 5 in an atmosphere of N₂. These results provide further confirmation that the emission arises from an O₂-sensitive ³MLCT excited state. In general, the complexes containing derivatives of phen as equatorial ligands (**TRIP-1a–1e** and **TRIP-2a**) exhibit much larger changes in their luminescence lifetimes in response to the presence of O₂, which may also account for their lower Φ in air-equilibrated buffer compared to the bpy derivatives. The relatively high emission quantum yields of these complexes in aqueous buffer suggest that they could be valuable for various biological imaging applications. Like other, similar Re complexes bearing ICN ligands, these complexes are highly emissive with long excited state lifetimes.^{30,35,36} Within these studies, they show a similar trend with the TRIP derivatives in that the greater donating-capacity of the equatorial ligand results in a blue shift in the emission maxima, withdrawing equatorial ligands decrease the emission quantum yields, and that the axial ICN ligand has little effect on the emissive properties of the complexes.

Anticancer Activity and Intracellular Luminescence.

With the physical properties of the TRIP complexes thoroughly investigated, we next sought to evaluate their in vitro anticancer activities. The cytotoxicities of all 11 complexes in HeLa cells were tested with the colorimetric 3-(4,5-dimethylthiazol-2-yl)-2,5-tetrazolium bromide (MTT) assay. The concentration required to inhibit 50% of the cell population (IC₅₀ value) was determined for all of the TRIP derivatives (**Table 5.2, Figures S5.88–S5.97**). The IC₅₀ values of these complexes range from 1.2

to 53 μM , demonstrating that this class of complexes is cytotoxic. The relative activities of these complexes appear to be related to the electron-donating properties of the polypyridyl ligand. For example, **TRIP-6a**, which contains the strongly withdrawing 4,4'-bis(trifluoromethyl)-2,2'-bipyridine ligand, is the least active complex with an IC_{50} value of 53 μM (**Figure S5.92**). The more electron-rich **TRIP-5a**, on the other hand, has a much lower IC_{50} value of 8.4 μM (**Figure S5.91**).

Table 5.2. IC_{50} values of TRIP derivatives in HeLa Cells.

Compound	IC_{50} (μM)
TRIP-1a ^a	1.4 \pm 0.2
TRIP-2a	5.8 \pm 0.5
TRIP-3a	27.5 \pm 0.6
TRIP-4a	7.6 \pm 0.3
TRIP-5a	8.4 \pm 1.9
TRIP-6a	53.1 \pm 1.6
TRIP-7a	1.2 \pm 0.5
TRIP-1b	1.8 \pm 0.1
TRIP-1c	6.8 \pm 0.1
TRIP-1d	5.0 \pm 1.5
TRIP-1e	9.3 \pm 3.7

^aReported in reference 66.

As discussed above, the $\text{C}\equiv\text{O}$ stretching frequencies and ^{15}N chemical shifts of these complexes also correlate with the electron-donating strengths of the equatorial ligands. As such, it is reasonable that these parameters may serve as predictors of potency of these compounds. **Figure 5.2a** shows a plot of the ^{15}N chemical shifts versus $\log(1/\text{IC}_{50})$ for the complexes that contain bpy-ligand derivatives, **TRIP-3a–TRIP-7a**. If **TRIP-7a** is excluded as an outlier, a linear correlation ($R^2 = 0.77$) shows that complexes with upfield ^{15}N chemical shifts, like **TRIP-5a**, exhibit higher potency against HeLa cells. The need to remove **TRIP-7a** from this trend may be a

consequence of its unusual steric profile compared to other compounds in this series. Correlations between ^{13}C NMR chemical shifts and biological activities of compounds is a surprisingly common phenomenon.³⁷ The trend involving the ^{15}N NMR chemical shifts observed within the TRIP series shows that these types of relationships may also apply to other nuclei. A similar plot of the highest energy $\text{C}\equiv\text{O}$ stretching frequency versus $\log(1/\text{IC}_{50})$ for complexes bearing bpy-ligand derivatives, **TRIP-3a–TRIP-7a**, also yields a clear linear correlation with $R^2 = 0.90$ (**Figure 5.2b**). These two correlations illustrate how experimentally measured physical properties can be used in a predictive sense for determining the anticancer potential of this class of compounds. More specifically, these results indicate that more electron-rich TRIP complexes, which can be ascertained from their IR and NMR spectroscopic signatures, exhibit higher cytotoxicity toward HeLa cells. Although these correlations only use a subset of the TRIP complexes ($n = 5$ for both plots), the observed trends indicate that the activities of this class of compounds may be predicted on the basis of their physical properties. In order to develop a complete SAR for the whole library of complexes, more subtle variations need to be explored when varying the equatorial and axial ligands. In addition, a larger library of compounds could also provide stronger support for this SAR.

To analyze the role of the ICN ligand, we can compare the activities of complexes **TRIP-1a–TRIP-1e**, which contain the same equatorial dmphen ligand, but different axial ligands. Overall, the nature of the ICN ligands has a smaller effect on the cytotoxicity of the compounds, as evidenced by the smaller range of IC_{50} values that span from 1.4 to 9.3 μM . Upon analysis of the different physical properties of

these complexes, it is apparent that these activities, $\log(1/IC_{50})$, correlate with the $C\equiv N$ stretching frequencies, as shown in **Figure 5.2c**. Complexes with greater $C\equiv N$ stretching energies exhibit lower cytotoxicity. As noted above, the relative energies of the $C\equiv N$ stretching frequencies themselves are related to the presence of electron-donating or -withdrawing groups on the ICN ligand. This trend may arise because more strongly donating ICNs bind more tightly to the metal center, inhibiting ligand exchange that might lead to detoxification of the compounds. A further validation of this hypothesis might be gleaned by synthesizing complexes at the extremes of donating capacity, such as complexes bearing withdrawing $-CF_3$ or donating $-NMe_2$ substituents on the ICN ligand.

In addition to electronic effects, sterics and lipophilicity also appear to play a role in mediating the cytotoxic activities of the complexes. For example, **TRIP-7a**, which bears a bulky and lipophilic 4,4'-di-*tert*-butyl-2,2'-bipyridine, is more active than **TRIP-5a**, which bears a diimine of equal electron-donating capabilities. Surprisingly, none of these TRIP derivatives exhibited significantly greater activity than the parent complex, **TRIP-1a**, which has an IC_{50} value of 1.4 μM in HeLa cells. Notably, we have previously identified the complex *fac*- $[Re(CO)_3(dmphen)(OH_2)]^+$ to be more active than related rhenium tricarbonyl complexes bearing axial water ligands.³⁸ Thus, the use of this diimine ligand with rhenium tricarbonyl complexes appears to give rise to favorable anticancer properties.

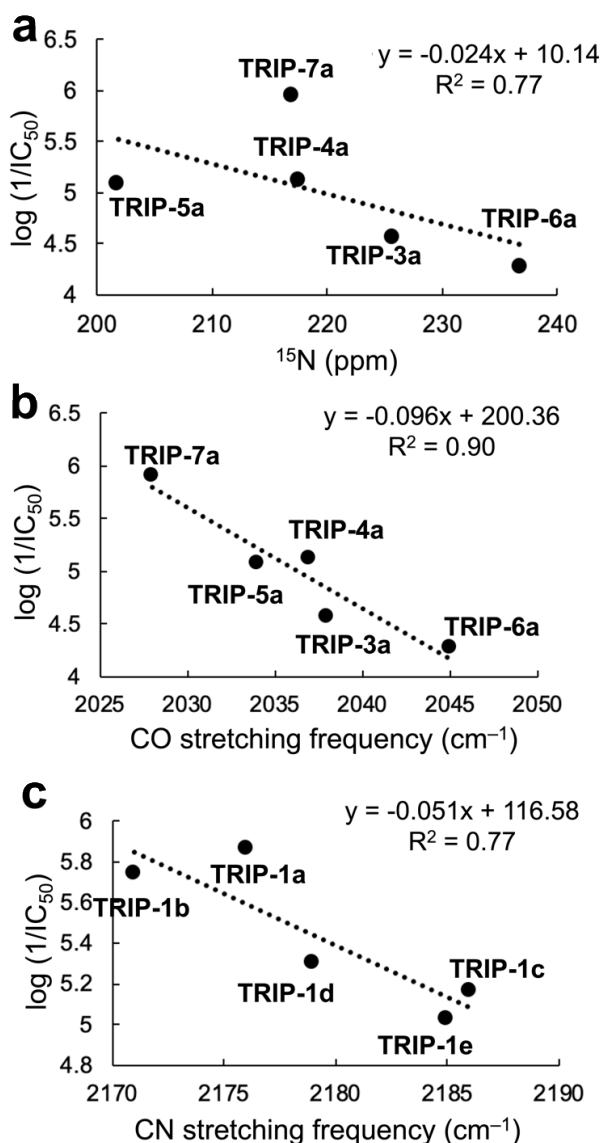


Figure 5.2. (a) Correlation of ^{15}N chemical shift (ppm) vs the $\log(1/\text{IC}_{50})$ values in HeLa cells of the bpy-derived TRIP complexes (**TRIP-3a–TRIP-6a**), excluding **TRIP-7a** in the fit. (b) Correlation of the highest $\text{C}\equiv\text{O}$ stretching frequency (cm^{-1}) vs the $\log(1/\text{IC}_{50})$ values in HeLa cells of the bpy-derived TRIP complexes (**TRIP-3a–TRIP-7a**). (c) Correlation of the $\text{C}\equiv\text{N}$ stretching frequency (cm^{-1}) vs the $\log(1/\text{IC}_{50})$ values in HeLa cells of the dmphen-bearing TRIP complexes (**TRIP-1a–TRIP-1e**). The $\log(1/\text{IC}_{50})$ were determined by using the IC_{50} values in units of M.

In addition to testing the *in vitro* anticancer activity of the TRIP derivatives, we explored their potential for use as intracellular imaging agents via confocal

fluorescence microscopy. The reasonably high aqueous emission quantum yields and long lifetimes of rhenium tricarbonyl compounds make them useful agents for biological imaging, enabling their intracellular localization to be tracked.^{31,32,39,40} Confocal fluorescence microscopy experiments were performed on HeLa cells treated with 10 μ M of the TRIP derivatives for 2 h. The total emission intensity emanating from the cells was quantified to assess the suitability of using these compounds as photoluminescent imaging agents. With the exception of **TRIP-7a**, all of the complexes gave rise to intracellular luminescence intensity that was 3–8 times that of the autofluorescence of the untreated control (**Figure S5.98**). Notably, cells treated with **TRIP-7a** were approximately 16 times brighter than the untreated control. As shown in **Table 5.1**, **TRIP-7a** has the largest emission quantum yield of the series, a property that may account for its efficacy as an intracellular imaging agent. Other factors, such as cellular uptake and environmental sensitivity of photophysical properties, also likely play a role in mediating the bright intracellular photoluminescence of these compounds. In comparing the fluorescence microscopy images, it is apparent that the complexes have different intracellular localization patterns. For instance, the photoluminescence of **TRIP-1a** and **TRIP-1e** is primarily localized around the nucleus in a punctate pattern. By contrast, **TRIP-7a** and **TRIP-1c** are distributed evenly throughout the cytoplasm. Interestingly, none of the complexes appear to localize to the nucleus. This result may indicate that these complexes do not target the nucleus. However, caution should be exercised in interpreting localization of these compounds based on fluorescence microscopy because the photoluminescence of the rhenium tricarbonyl complexes is highly sensitive to environmental factors. For

example, previous studies have shown how intracellular localization of rhenium tricarbonyl complexes as determined by inductively coupled plasma mass spectrometry (ICP-MS) and optical emission spectroscopy (ICP-OES) does not match that obtained via fluorescence microscopy.⁴¹⁻⁴⁴

ER Stress-Inducing and UPR-Activation Properties.

The parent complex in this series, **TRIP-1a**, increases the level of misfolded proteins in cells, which triggers ER stress. Subsequently, activation of the UPR and apoptosis ultimately lead to cell death. Based on these results, we aimed to determine if the other TRIP complexes in this library act via a similar mechanism of action. One of the key early phenotypic responses of cells treated with **TRIP-1a** is mitochondrial fission and accumulation of misfolded proteins, processes that happen within the first 30 min of exposure. To determine the importance of mitochondrial fission for the other TRIP complexes, we first tested the most and least toxic complexes within this library. Prior to confocal fluorescence microscopy and exposure to 10 μ M of a TRIP derivative, HeLa cells were treated with the mitochondria-specific dye, MitoTracker Red, to image the morphology of this organelle, and the nuclear stain Hoechst to identify viable cells. **TRIP-1b**, one of the most cytotoxic complexes in the series, induced rapid rounding of the mitochondria and loss of intensity of the MitoTracker Red dye within several minutes, features that are consistent with mitochondrial fission. Conversely, the least active compounds, **TRIP-3a** and **TRIP-6a**, did not give rise to any changes in mitochondrial morphology over the same time period with an equivalent dose (**Figure 5.3a**). To more quantitatively analyze these morphological

changes, we used an established procedure for counting the number of individual mitochondria with ImageJ.⁴⁵ After mitochondrial fission, the number of distinct mitochondria within the cells will increase. The number of mitochondria were quantified at 0, 14, and 30 min in the complex-treated and untreated cells. As shown in **Figure 5.3b**, of these three complexes only **TRIP-1b**, the most cytotoxic compound, was able to cause an increase (2-fold) in the number of mitochondria after a 14-min treatment period. These results illustrate that the cytotoxicities of these compounds is related to their ability to cause mitochondrial fission. Furthermore, the phenotypic similarity between the parent complex **TRIP-1a** and the new analog **TRIP-6a** show that structural modifications to these compounds do not change their mechanisms of action.

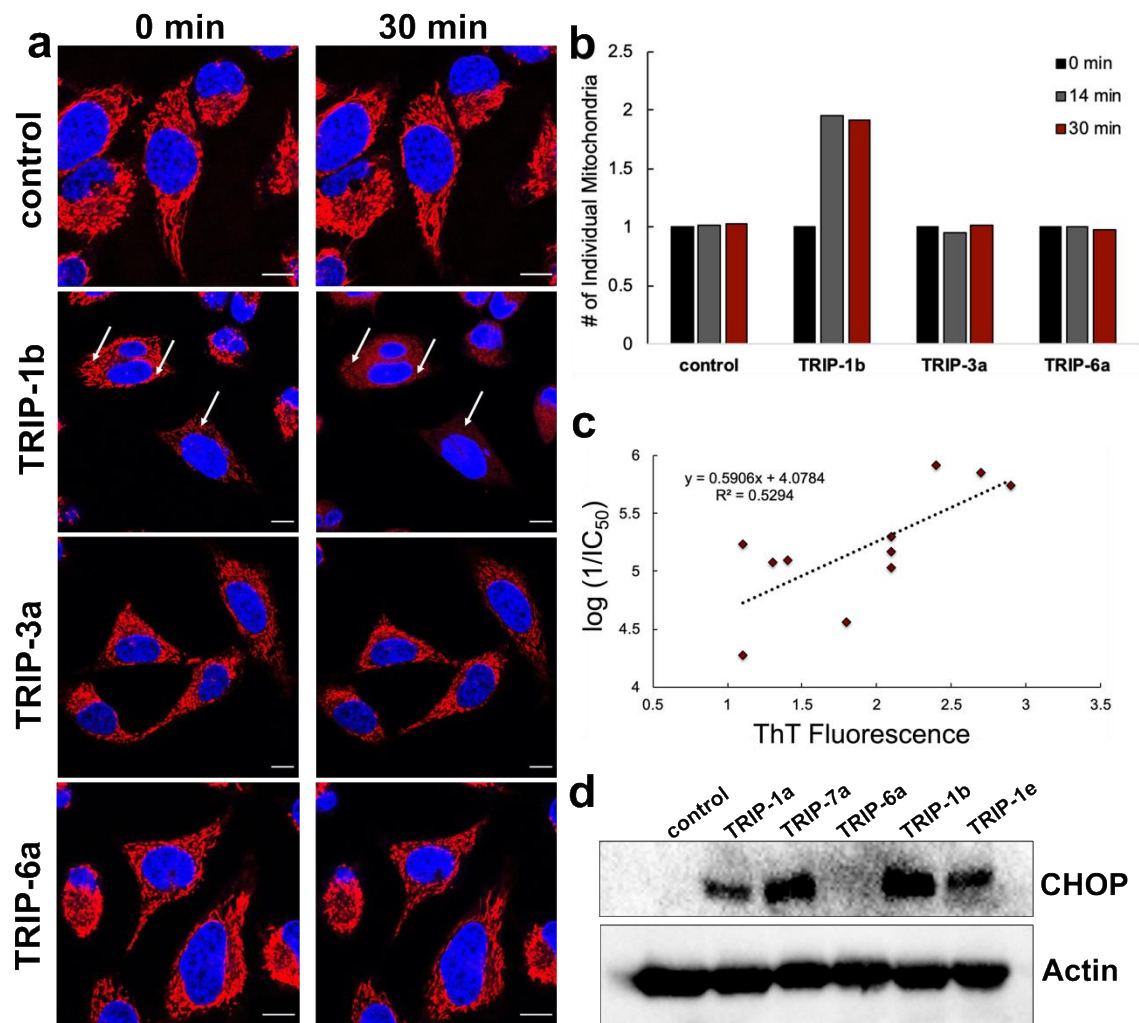


Figure 5.3. (a) HeLa cells stained with MitoTracker Red (red channel) and Hoechst (blue channel) before (0 min) and after (30 min) exposure to 10 μ M of a TRIP complex. (b) Quantification of the number of individual mitochondria after treatment with 10 μ M of a TRIP complex at 0, 14, and 30 min using ImageJ. (c) Correlation of ThT fluorescence in HeLa cells upon treatment with the TRIP derivatives vs the anticancer activity. (d) CHOP Western blot of selected TRIP derivatives after 24 h treatment in HeLa cells.

To determine if these compounds can cause the accumulation of misfolded or aggregated proteins like **TRIP-1a**, we employed Thioflavin T (ThT), a compound that undergoes an increase in fluorescence upon binding to protein aggregates.⁴⁶ This dye is commonly used to detect amyloid beta plaques in postmortem brains of Alzheimer's

Disease patients.^{47,48} HeLa cells were treated with ThT for 2 h prior to being exposed to 10 μ M of each of the 11 TRIP derivatives. Changes in fluorescence intensity was monitored at 0 and 30 min post-treatment (**Figure S5.99**) using confocal fluorescence microscopy. The results show that the 3 most cytotoxic species, **TRIP-1a**, **TRIP-7a**, and **TRIP-1b**, give rise to a 2-fold or greater increase in ThT fluorescence, demonstrating that these compounds cause protein aggregation. For comparison, the least active compound, **TRIP-6a**, was unable to change the ThT fluorescence levels relative to untreated cells. In analyzing all 11 compounds, a positive linear correlation between the cytotoxicity and the enhancement of ThT fluorescence intensity is apparent ($R^2 = 0.53$, **Figure 5.3c**). This relationship suggests that the cytotoxic activity of this class of complexes is related to their ability to cause the formation of intracellular protein aggregates. Furthermore, these data show that almost all these complexes induce protein aggregation within 30 min. Thus, this phenotypic response appears to be a general feature of this class of compounds.

As observed previously for **TRIP-1a**, the accumulation of misfolded or aggregated proteins causes cells to shutdown translation and initiate the proapoptotic wing of the ER stress response via activation of the UPR and expression of CHOP.^{49–}⁵¹ For **TRIP-1a**, activation of the PERK arm of the UPR occurs, resulting in phosphorylation of eIF2 α . This phosphorylation causes global protein synthesis inhibition, activation of the transcription factor ATF4 and CHOP, and finally apoptosis.⁵² Thus, we sought to verify that this process proceeds in the same manner for the newly reported TRIP analogs. Translation inhibition was investigated in HeLa cells with the puromycin incorporation assay. Puromycin is a tyrosine mimic that is

incorporated into newly synthesized proteins in place of tyrosine. This unnatural amino acid can be detected via Western blot, and its relative amounts present in cells scale with the rate of protein translation.⁵³ The HeLa cells were treated with 10 μ M of each TRIP complex for 2 h, after which puromycin was added. The most potent compounds, **TRIP-1a** and **TRIP-7a**, cause the most efficient inhibition of protein synthesis, as evidenced by the low levels of puromycin incorporation into the proteome. Conversely, the least active complexes, **TRIP-3a** and **TRIP-6a**, have the greatest amount of puromycin incorporation, with levels comparable to that of the untreated cells (**Figure S5.100**), indicating that these compounds are not effective translation inhibitors. Thus, these data show that protein translation inhibition is related to the cytotoxic properties of these compounds. Furthermore, protein translation inhibition is likewise related to the formation of intracellular protein aggregates as measured by the ThT assay. As a final confirmation on the ER stress-inducing properties of this class of compounds, we investigated a small subset of these complexes to probe their ability to induce CHOP expression. HeLa cells were treated with 10 μ M of either **TRIP-1a**, **TRIP-6a**, **TRIP-7a**, **TRIP-1b**, or **TRIP-1e** for 24 h, prior to analyzing cell lysates for CHOP expression via Western blotting. We found that all complexes tested, except for the least cytotoxic compound **TRIP-6a**, induce CHOP expression after 24 h. In conjunction with the results discussed above, these data collectively show that these TRIP analogs all cause the same ER stress phenotype in cancer cells. Importantly, the cytotoxicities of these complexes is correlated with their abilities to induce this phenotype, indicating that the ER stress response is a key feature of their mechanisms of action.

*In vivo Biodistribution and Anticancer Activity of **TRIP-1a**.*

A valuable aspect for the development of rhenium-based anticancer agents is the availability of the imaging radionuclide ^{99m}Tc .^{54,55} The chemistries of technetium and rhenium are largely similar, and therefore direct structural analogs of complexes of these metal ions can be prepared.^{56–58} In the context of developing new rhenium-based anticancer agents, the corresponding ^{99m}Tc analogs can be used as diagnostic partners to more easily ascertain pharmacokinetic properties of the parent drug candidate. Isonitrile ligands exhibit high affinity for Tc, and several Tc complexes containing ICN ligands have been reported as novel agents for biological imaging.^{59–64} To evaluate the potential use of ^{99m}Tc analogs of these TRIP complexes, we sought to synthesize the ^{99m}Tc analog of the parent compound **TRIP-1a**. The ^{99m}Tc analog of this compound, *fac*-[$^{99m}\text{Tc}(\text{CO})_3(\text{dmphen})(\text{ptolICN})$]⁺, called technetium tricarbonyl isonitrile polypyridyl or **TTIP**, was synthesized using an established approach from *fac*-[$^{99m}\text{Tc}(\text{CO})_3(\text{H}_2\text{O})_3$]⁺.⁶⁵ Briefly, an aqueous solution of the ^{99m}Tc starting material was heated at 60 °C for 1 h in the presence of a large excess of the dmphen ligand in water (pH 7). The *ptolICN* ligand was then added, and the mixture was further heated at 60 °C for 90 minutes to yield the product, **TTIP**, which was purified by HPLC. The purity and identity of the product were analyzed via radio-HPLC (**Figure S5.101**), which revealed a single peak in the chromatogram with a retention time that matched that of the non-radioactive rhenium analog **TRIP-1a**.

To evaluate the suitability of **TTIP** as a diagnostic analog for **TRIP-1a**, we carried out biodistribution studies of these complexes in mice. In general,

biodistribution studies of drug candidates are important for determining their in vivo localization and excretion pathways, and they may help identify potential off-target accumulation sites. Furthermore, a comparison of the biodistributions of **TRIP-1a** and **TTIP** is needed to assess their suitability as a matched therapeutic and diagnostic pair. Both of these complexes were administered simultaneously in BALB/c mice via tail vein injection to determine their biodistribution. Cohorts of mice were sacrificed at 0.5, 2, and 4 h, their organs were excised, and then either digested with HNO₃ and analyzed by ICP-OES for Re or subjected to gamma counting for quantifying ^{99m}Tc. The results of this biodistribution study are shown in **Figure 5.4**. Overall, the distribution of the two complexes is similar, with both exhibiting large kidney and moderate liver uptake. Uptake in these organs suggests that these compounds are undergoing renal and hepatobiliary excretion, similar to other previously reported Re and Tc tricarbonyl complexes.⁶⁶ Both **TRIP-1a** and **TTIP** also accumulate in the heart and lungs. The relatively high cardiac uptake may be due to the positive charge of the complexes, which is often observed in ^{99m}Tc complexes, such as the homoleptic isonitrile complex Cardiolite® that is used for myocardial perfusion imaging.^{67,68} Furthermore, analogous ^{99m}Tc complexes to **TTIP** with the general formula *fac*- [^{99m}Tc(CO)₃(NN)(ICN)]⁺, where NN are different bpy and phen derivatives and ICN are different isonitriles, exhibit high cardiac uptake, consistent with our observations.⁶⁹ The major significant difference in the distribution of the Re and ^{99m}Tc compounds lies in the spleen. **TRIP-1a** is taken up to a much higher extent in this organ compared to **TTIP**. The spleen is known to be a site of accumulation for macromolecular structures and aggregates.⁷⁰⁻⁷² Therefore, high Re uptake in this organ may suggest

that the compound is forming aggregates in vivo. The much lower concentrations of administered ^{99m}Tc would prevent aggregation of **TTIP**. Collectively, this comparison between the biodistribution of **TRIP-1a** and **TTIP** demonstrates that these compounds exhibit largely similar organ uptake profiles and suggests that ^{99m}Tc analogs of these TRIP complexes are useful partner diagnostic or imaging agents.

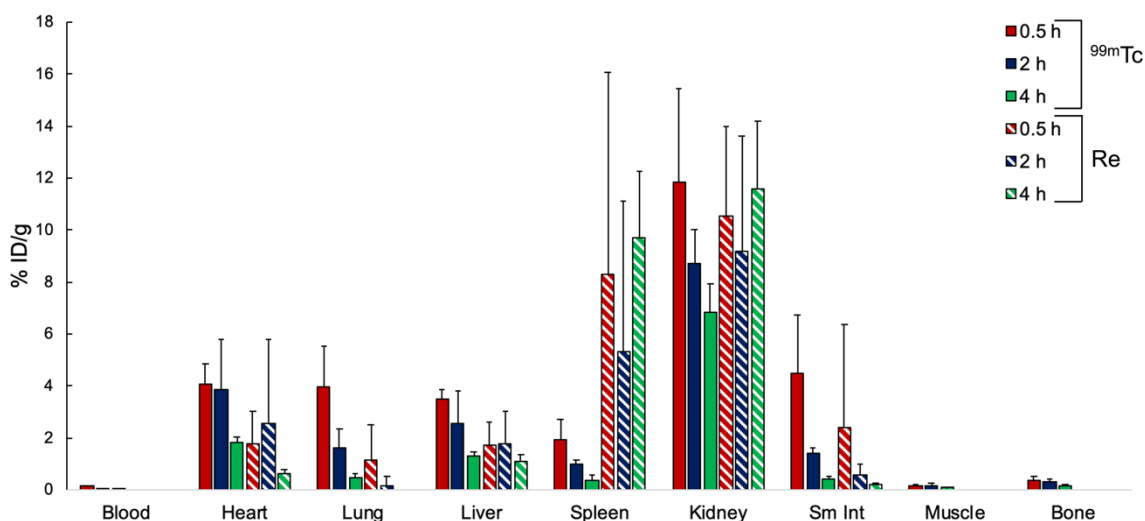


Figure 5.4. Biodistribution in BALB/c mice of **TRIP-1a** (striped) and **TTIP** (solid). The rhenium content for the blood, muscle, and bone were below detectable levels by ICP-OES.

Based on the promising in vitro anticancer activities of these complexes and favorable biodistribution, we sought to evaluate the in vivo antitumor activity of **TRIP-1a** in mice bearing A2780 ovarian cancer xenografts. These mice were treated with 5, 10, or 20 mg/kg of this complex, administered in 20% DMSO/PBS solutions via tail vein injection, twice weekly. Their tumor growth rates and overall health were monitored over 27 days (**Figure 5.5**). For several mice in this study, dosing was discontinued due to weight loss or necrosis at the injection site. The exact dosing

schedule and survival time for each mouse in the study is reported in **Table S5.3**. The lower doses (5 and 10 mg/kg) of **TRIP-1a** have no effect on tumor growth rate. At 20 mg/kg, **TRIP-1a** significantly inhibits tumor growth as shown in **Figure 5.5a**. From days 10 to 20 after beginning treatment, the 20 mg/kg cohort exhibited tumors with less than half the average volume of the vehicle-treated group. Thus, although **TRIP-1a** was not able to entirely eradicate these tumors, it was able to markedly decrease the tumor growth rate, demonstrating that its anticancer activity is also retained in vivo. These in vivo data can also be analyzed by comparing the survival time of the treated mice relative to the untreated control. Such survival data may be more useful than tumor volumes in comparing the efficacy of drug candidates because different tumor types undergo a wide range of growth rates. The effects of **TRIP-1a** on mouse survival were thus analyzed. In these experiments, mice were sacrificed and did not “survive” if their body weight decreased by 25% or if their tumor burden increased beyond 5500 mm³. As shown in **Figure 5.5b**, 20 mg/kg of **TRIP-1a** prolonged the survival of the tumor-bearing mice by 150% relative to the control group. These results demonstrate that this compound is able to significantly increase mice survival to levels that are comparable to several clinically investigated Ru anticancer agents.⁷³ These data represents only the fifth example in the literature where the in vivo anticancer activity of a rhenium tricarbonyl complex is demonstrated,^{42,74–77} and it supports the continued investigation of this interesting class of compounds as antitumor agents.

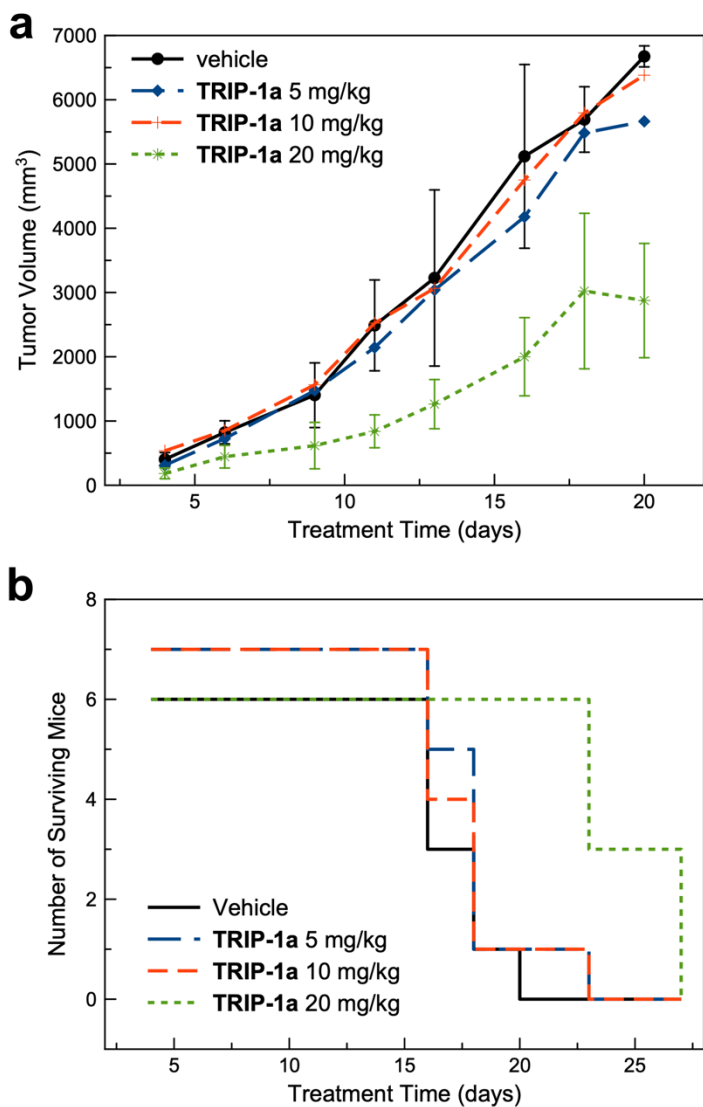


Figure 5.5. (a) Tumor volume of mice bearing A2780 ovarian cancer xenografts. **(b)** Kaplan-Meier survival plot of mice treated with **TRIP-1a** throughout the duration of the study.

Because side effects and off-target toxicity constitute two of the main hurdles to clinical success for novel drug candidates, we performed necropsies on all mice from the tumor xenograft study to assess the *in vivo* toxicity of **TRIP-1a**. All major organs including kidneys, liver, heart, brain, and spleen were cryosectioned, stained with hematoxylin and eosin (H&E), and submitted for analysis by a trained

pathologist.⁷⁸ These analyses revealed that there were no obvious morphological changes to these organs in mice treated with any of the three administered doses of **TRIP-1a** compared to the untreated mice. This result suggests that **TRIP-1a** is not causing any significant organ damage. This result is in contrast to H&E staining carried out for cisplatin and related platinum-based drugs, where their nephrotoxicity manifests in significant morphological changes to kidney sections.⁷⁹ Another indication of acute toxicity is mouse body weight. Acutely toxic compounds, like cisplatin, cause a decrease in body weight when administered at therapeutically relevant concentrations.⁸⁰ The body weights of all mice in this study were therefore monitored throughout its duration, as shown in **Figure S5.102** Mice treated with 5 and 10 mg/kg of **TRIP-1a** did not show any decrease in body weight. However, the body weight of mice treated with 20 mg/kg of **TRIP-1a** decreased by approximately 20% until day 16, when administration of **TRIP-1a** was ceased. The decrease in body weight was somewhat surprising given that no visible organ damage was observed. An additional limiting side effect that was observed was necrosis at the tail vein injection site in mice that were treated with **TRIP-1a** at all dose concentrations. As noted above, the severity of the inflammation required us to cease treatment for some mice (**Table S5.3**) In a few cases, the tails fell off due to extreme inflammatory effects. We hypothesize that this severe local effect may be a consequence of the formulation of **TRIP-1a** in a DMSO/PBS (20% DMSO) mixture. Because this effect is only present at the site of injection, it is likely that it is triggered by precipitation upon contact with the bloodstream. This hypothesis is also consistent with our biodistribution studies that show uptake in the spleen, a common site for the accumulation of aggregated species.

Although these studies demonstrate that this class of compounds possess in vivo antitumor activity, clearly work will be needed to improve their formulations for biological administration.

Conclusions

The ER has emerged as a promising target for cancer therapy, and, as summarized in Chapter 1, a number of recent studies have shown that many metal complexes are effective at triggering ER stress-induced cancer cell death. In this context, the TRIP compounds reported in this Chapter comprise a novel class of metal-based anticancer agents that operate via this mechanism of action. As demonstrated here, the physical and biological properties of these TRIP complexes can be modulated by altering the supporting ligands. From this small library of 11 complexes, our SAR analysis shows that more electron-rich compounds are more cytotoxic. Because a number of spectroscopic features of these complexes are related to their electronic properties, it is possible to identify direct correlations between physical and biological properties. Thus, correlations between spectroscopic methods, such as C≡O and C≡N IR stretching energies and ¹⁵N NMR chemical shifts, and cytotoxic activity are apparent. These results highlight the potential predictive power of physical characterization methods for use in biological SARs of novel metal-based anticancer agents.⁸¹⁻⁸⁵

An important assumption that is required for the development of SARs is that all compounds in the library act via a similar mechanism of action. The 11 complexes tested in this Chapter all trigger cell death by inducing ER stress. Furthermore, the ER

stress-inducing capacity of the compounds relates to their cytotoxicity, as more cytotoxic complexes elicit greater ER stress responses at equivalent dosing concentrations. These results stand in contrast to a number of other studies on metal anticancer agents, in which subtle ligand modifications led to significant changes in anticancer mechanisms.⁸⁶⁻⁸⁹ Although such mechanistic changes are interesting, they present practical challenges in improving and optimizing these types of metal-based drug candidates. Based on the consistent ER stress induction across the TRIP series, modifications of these complexes to optimize important pharmacokinetic properties, such as solubility and clearance rates, can be accomplished without compromising their novel mechanism of anticancer activity.

The promising *in vitro* anticancer activity and novel mechanism of action of **TRIP-1a**, detailed in Chapter 4, prompted us to further explore its activity *in vivo*. The use of the ^{99m}Tc analog, **TTIP**, revealed that the biodistribution of both complexes is comparable, suggesting that these compounds may constitute a theranostic pair. Furthermore, experiments conducted on mice bearing ovarian cancer xenografts indicate that **TRIP-1a** retains anticancer activity *in vivo*. The activity of this compound is limited because it slows tumor growth, but does not eradicate the tumor mass in its entirety. Furthermore, difficulties in the formulation and administration of this complex that gave rise to severe local inflammation need to be addressed. As noted above, the structural modification of this class of compounds do not lead to a change in the mechanism of action and can therefore be applied to overcome these issues associated with formulation. Together, the high potency, distinct mechanism of action, broad tunability, and *in vivo* efficacy of these complexes

establish the TRIP scaffold to be a promising class of anticancer agents.

Experimental

Methods and Materials

Rhenium carbonyl was purchased from Pressure Chemicals (Pittsburgh, Pennsylvania, USA). $\text{Re}(\text{CO})_5\text{Cl}$ was synthesized as previously described.⁹⁰ The diimine ligands, 2,9-dimethyl-1,10-phenanthroline (dmphen, Cayman Chemical, Ann Arbor, MI), 1,10-phenanthroline (phen, Sigma Aldrich, St. Louis, MO), 2,2'-bipyridine (bpy, Alfa Aesar, Ward Hill, MA), 4,4'-dimethyl-2,2'-bipyridine (dmbpy, Chem-Impex International Inc., Wood Dale, IL), 4,4'-dimethoxy-2,2'-bipyridine (dmobpy, Sigma Aldrich, St. Louis, MO), 4,4'-di-tert-butyl-2,2'-bipyridine (*t*butylbpy, Sigma Aldrich, St. Louis, MO), and 4,4'-bis(trifluoromethyl)-2,2'-bipyridine (CF_3bpy , Sigma Aldrich, MO), were used as received. The *fac*- $[\text{Re}(\text{CO})_3(\text{NN})\text{Cl}]$ complexes, where NN is the diimine ligand, were synthesized using previously reported procedures.^{91,92} The isonitrile ligands, *para*-tolyl ICN (*ptol*ICN), 2,6-dimethylphenyl ICN (2,6-dmphenylICN), 3,5-dimethylphenyl (3,5-dmphenylICN), *para*-methoxyphenyl ICN (*p*-methoxyphenylICN, Sigma Aldrich, St. Louis, MO), and *para*-chlorophenyl ICN (*p*-chlorophenylICN), were purchased or synthesized from their respective aniline species using a previously reported procedure.⁹³ *fac*- $[\text{Re}(\text{CO})_3(\text{dmphen})(\text{ptolICN})\text{OTf}]$ (**TRIP-1a**) was synthesized as previously reported.¹⁷ All solvents were ACS grade or higher.

Physical Measurements

NMR samples were prepared as solutions using CDCl_3 , methanol- d_4 , DMSO- d_6 , or acetone- d_6 as the solvent. ^1H and $^{13}\text{C}\{^1\text{H}\}$ NMR spectra were acquired on a Bruker 500 MHz spectrometer and ^{15}N HMBC spectra were acquired on a Varian Inova 600 MHz spectrometer. ^1H and $^{13}\text{C}\{^1\text{H}\}$ NMR chemical shifts were referenced to TMS at 0 ppm and ^{15}N HMBC NMR chemical shifts were referenced to acetonitrile as internal standard (240 ppm vs liquid NH_3 at 0 ppm). Samples for IR spectroscopy were prepared as KBr pellets and were analyzed on a Nicolet Avatar 370 DTGS (ThermoFisher Scientific, Waltham, MA). Analytical chromatography was carried out on a LC-20AT pump with a SPD-20AV UV-vis detector monitored at 270 and 220 nm (Shimadzu, Japan) using an Ultra Aqueous C18 column (100 Å, 5 μm , 250 mm \times 4.6 mm, Restek, Bellefonte, PA) at a flow rate of 1 mL/min with a mobile phase containing 0.1% trifluoroacetic acid (TFA) in H_2O or MeOH. The method consisted of 5 min at 10% MeOH, followed by a linear gradient to 100% MeOH over 20 min. High-resolution mass spectra (HRMS) were recorded on an Exactive Orbitrap mass spectrometer in positive ESI mode (ThermoFisher Scientific, Waltham, MA) with samples injected as acetonitrile/water solutions with 1% formic acid. Elemental analyses (C, H, N) were performed by Atlantic Microlab Inc. (Norcross, Georgia, USA). UV-visible spectra were recorded on a Cary 8454 UV-vis (Agilent Technologies, Santa Clara, CA) or a Beckman Coulter DU800 UV-vis using 1-cm quartz cuvettes. Fluorescence spectra and photoluminescent quantum yield measurements were carried out on a Beckman Coulter DU800 UV-vis and Varian Eclipse Fluorometer. Electrochemical measurements were carried out using a Pine WaveNow potentiostat with a three-electrode setup consisting of a glassy carbon

working electrode, a platinum counter electrode, and an Ag wire quasi-reference electrode. Complexes were dissolved in anhydrous acetonitrile with 0.10 M $[\text{Bu}_4\text{N}][\text{PF}_6]$ (TBAP) as the supporting electrolyte. Potentials were referenced using an internal standard of the ferrocene/ferricenium couple at 0.45 V vs. the saturated calomel electrode (SCE).

Synthesis of fac-[Re(CO)₃(phen)(ptolICN)]OTf (TRIP-2a)

fac-[Re(CO)₃(phen)Cl] (0.200 g, 0.41 mmol) was dissolved in dry THF (40 ml) and AgOTf (0.106 g, 0.41 mmol) was added. The mixture was heated at reflux for 3 h, after which the resulting yellow suspension was filtered. To the filtrate, *ptol*ICN (0.2 g, 1.7 mmol) was added, and the mixture was heated at reflux overnight. The resulting yellow precipitate is filtered and washed with ~25 ml of diethyl ether to yield a yellow solid. Yield: 0.126 g (43%). ¹H NMR (500 MHz, DMSO-*d*₆): δ 9.55 (d, *J* = 5.2 Hz, 2H), 9.07 (d, *J* = 8.3 Hz, 2H), 8.39 (s, 2 H), 8.19 (dd, *J* = 8.3, 5.2 Hz, 2H), 7.23 – 7.18 (m, 4H), 2.26 (s, 3H). ¹³C{¹H} NMR (126 MHz, DMSO-*d*₆): δ 191.5, 188.3, 155.3, 146.3, 141.2, 139.9, 130.7, 129.9, 127.8, 127.0, 126.9, 20.8. IR (KBr, cm⁻¹): 2155 m (C≡N), 2036 s (C≡O), 1973 s (C≡O), 1966 s (C≡O). HR-ESI-MS (positive ion mode): *m/z* 568.0646 ([M]⁺, calcd 568.0671). Anal. Calcd for [Re(CO)₃(phen)(*ptol*ICN)]OTf (ReC₂₄H₁₅F₃N₃O₆S): C, 40.22; H, 2.11; N, 5.86. Found: C, 40.15; H, 2.06; N, 5.37.

Synthesis of fac-[Re(CO)₃(bpy)(ptolICN)]OTf (TRIP-3a)

fac-[Re(CO)₃(bpy)Cl] (0.100 g, 0.22 mmol) was dissolved in dry THF (20 ml) and AgOTf (0.056 g, 0.22 mmol) was added. The mixture was heated at reflux for 3 h, after which the resulting yellow suspension was filtered. To the filtrate, *p*tolICN (0.1 g, 0.85 mmol) was added, and the mixture was heated at reflux overnight. The resulting orange solution was evaporated to dryness under vacuum. To the crude solid, 2 ml of toluene was added and the undissolved solid was filtered and washed with ~15 ml of diethyl ether to yield a pale-yellow solid. Yield: 0.069 g (45%). ¹H NMR (500 MHz, CDCl₃): δ 9.03 (d, *J* = 8.2 Hz, 2H), 8.97 (d, *J* = 5.4 Hz, 2H), 8.38 (t, *J* = 7.9 Hz, 2H), 7.69 (t, *J* = 6.5 Hz, 2H), 7.18 – 7.14 (m, 4H), 2.34 (s, 3H). ¹³C{¹H} NMR (126 MHz, CDCl₃): δ 191.3, 187.6, 156.4, 153.1, 142.2, 141.7, 130.5, 128.4, 127.1, 126.8, 21.6. IR (KBr, cm⁻¹): 2175 m (C≡N), 2038 s (C≡O), 1971 s (C≡O), 1930 s (C≡O). HR-ESI-MS (positive ion mode): *m/z* 544.0636 ([M]⁺, calcd 544.0671). Anal. Calcd for [Re(CO)₃(bpy)(*p*tolICN)]OTf (ReC₂₂H₁₅F₃N₃O₆S): C, 38.15; H, 2.18; N, 6.07. Found: C, 38.41; H, 2.19; N, 6.09.

*Synthesis of fac-[Re(CO)₃(dmobpy)(p*tolICN)]OTf (TRIP-4a)

fac-[Re(CO)₃(dmobpy)Cl] (0.130 g, 0.27 mmol) was dissolved in dry THF (25 ml) and AgOTf (0.068 g, 0.27 mmol) was added. The mixture was heated at reflux for 3 h, after which the resulting yellow suspension was filtered. To the filtrate, *p*tolICN (0.1 g, 0.85 mmol) was added, and the mixture was heated at reflux overnight. The resulting orange solution was evaporated. The crude residue was then purified using silica gel column chromatography (98% DCM: 2% MeOH). Fractions containing the desired product were pooled, and the solvent was removed under reduced pressure.

The product was isolated as a pale yellow solid. Yield: 0.080 g (41%). ^1H NMR (500 MHz, CDCl_3): δ 8.91 (s, 2H), 8.73 (d, $J = 5.7$ Hz, 2H), 7.40 (d, $J = 5.6$ Hz, 2H), 7.18 – 7.14 (m, 4H), 2.71 (s, 6H), 2.34 (s, 3H). $^{13}\text{C}\{^1\text{H}\}$ NMR (126 MHz, CDCl_3): δ 191.5, 187.9, 156.0, 154.7, 152.3, 142.1, 130.5, 129.0, 127.2, 127.1, 21.7. IR (KBr, cm^{-1}): 2176 m ($\text{C}\equiv\text{N}$), 2037 s ($\text{C}\equiv\text{O}$), 1958 s ($\text{C}\equiv\text{O}$), 1934 s ($\text{C}\equiv\text{O}$). HR-ESI-MS (positive ion mode): m/z 572.0941 ($[\text{M}]^+$, calcd 572.0984). Anal. Calcd for $[\text{Re}(\text{CO})_3(\text{dmbpy})(\text{ptolICN})]\text{OTf}$ ($\text{ReC}_{24}\text{H}_{19}\text{F}_3\text{N}_3\text{O}_6\text{S}$): C, 40.00; H, 2.66; N, 5.83. Found: C, 40.42; H, 2.75; N, 5.83.

Synthesis of fac- $[\text{Re}(\text{CO})_3(\text{dmobpy})(\text{ptolICN})]\text{OTf}$ (TRIP-5a)

fac- $[\text{Re}(\text{CO})_3(\text{dmobpy})\text{Cl}]$ (0.100 g, 0.19 mmol) was dissolved in dry THF (20 ml) and AgOTf (0.049 g, 0.19 mmol) was added. The mixture was heated at reflux for 3 h, after which the resulting yellow suspension was filtered. To the filtrate, *ptolICN* (0.1 g, 0.85 mmol) was added, and the mixture was heated at reflux overnight. The solvent was then removed under reduced pressure. To the crude solid, 2 ml of toluene was added and the undissolved solid was filtered and washed with ~15 ml of diethyl ether to yield a pale yellow solid. Yield: 0.115 g (81%). ^1H NMR (500 MHz, CDCl_3): δ 8.62 (d, $J = 6.4$ Hz, 2 H), 8.48 (d, $J = 2.5$ Hz, 2 H), 7.19 – 7.15 (m, 4 H), 7.07 – 7.05 (m, 2 H), 4.27 (s, 6 H), 2.35 (s, 3 H). $^{13}\text{C}\{^1\text{H}\}$ NMR (126 MHz, CDCl_3): δ 169.4, 158.9, 153.2, 142.1, 130.5, 127.1, 116.8, 110.7, 58.2, 21.7. IR (KBr, cm^{-1}): 2179 m ($\text{C}\equiv\text{N}$), 2034 s ($\text{C}\equiv\text{O}$), 1957 s ($\text{C}\equiv\text{O}$), 1924 s ($\text{C}\equiv\text{O}$). HR-ESI-MS (positive ion mode): m/z 604.0842 ($[\text{M}]^+$, calcd 604.0882). Anal. Calcd for $[\text{Re}(\text{CO})_3(\text{dmobpy})(\text{ptolICN})]\text{OTf}$ ($\text{ReC}_{24}\text{H}_{19}\text{F}_3\text{N}_3\text{O}_8\text{S}$): C, 38.30; H, 2.54; N, 5.58.

Found: C, 38.54; H, 2.60; N, 5.72.

Synthesis of fac-[Re(CO)₃(CF₃bpy)(ptolICN)]OTf (TRIP-6a)

fac- [Re(CO)₃(CF₃bpy)Cl] (0.072 g, 0.117 mmol) was dissolved in dry THF (8 ml) and AgOTf (0.032 g, 0.41 mmol) was added. The mixture was heated at reflux for 3 h, after which the resulting yellow suspension was filtered. To the filtrate, *ptol*ICN (0.100 g, 0.085 mmol) was added, and the mixture was heated at reflux overnight. The resulting solution was evaporated under reduced pressure. The crude product was dissolved in a minimum amount of DCM (~5 ml), and this concentrated solution was added to di-isopropyl ether (>100 mL) with rapid stirring. The product that precipitated out was collected by filtration. This process was repeated two more times to obtain analytically pure compound. Yield: 0.030 g (31%). ¹H NMR (500 MHz, acetone-*d*₆): δ 9.67 (d, *J* = 5.3 Hz, 2 H), 9.44 (s, 2 H), 8.31 (d, *J* = 6.0 Hz, 2 H), 7.29 – 7.25 (m, 4 H), 2.33 (s, 3 H). IR (KBr, cm⁻¹): 2180 m (C≡N), 2045 s (C≡O), 1976 s (C≡O), 1944 s (C≡O). HR-ESI-MS (positive ion mode): 680.0413 *m/z* ([M]⁺, calcd 680.0419). Anal. Calcd for [Re(CO)₃(CF₃bpy)(*ptol*ICN)]Otf (ReC₂₄H₁₃F₉N₃O₆S): C, 34.79; H, 1.58; N, 5.07. Found: C, 35.04; H, 1.48; N, 4.96. The ¹³C NMR spectra could not be collected due to poor solubility of the complex.

*Synthesis of fac-[Re(CO)₃(*t*butylbpy)(*ptol*ICN)]OTf (TRIP-7a)*

fac- [Re(CO)₃(*t*butylbpy)Cl] (0.132 g, 0.23 mmol) was dissolved in dry THF (12 mL) and AgOTf (0.060 g, 0.23 mmol) was added. The mixture was heated at reflux for 3 h, after which the resulting yellow suspension was filtered. To the filtrate,

*ptol*ICN (0.130 g, 1.1 mmol) was added, and the mixture was heated at reflux overnight. The resulting solution was evaporated under reduced pressure, and the crude product was recrystallized from DCM and ether. The material could not be purified sufficiently by recrystallization due to its high solubility. The crude material was purified by preparatory HPLC (50 to 100% MeOH in H₂O containing 0.1% TFA over 30 minutes) to yield a yellow powder. Elemental analysis data indicates that this complex was isolated with a mixture of TFA (25%) and OTf (75%) counterions (see below). Yield: 0.023 g (12%). ¹H NMR (500 MHz, MeOH-*d*₄): δ 9.04 (d, *J* = 6.0 Hz, 2 H), 8.71 (s, 2 H), 7.82 (d, *J* = 6.0 Hz, 2 H), 7.22 (m, 4 H), 2.34 (s, 3 H), 1.51 (s, 18 H). ¹³C{¹H} NMR (126 MHz, CDCl₃): δ 191.5, 187.9, 166.2, 156.3, 152.7, 141.7, 130.24, 127.2, 125.4, 123.0, 36.2, 30.2, 21.5. IR (KBr, cm⁻¹): 2175 m (C≡N), 2028 s (C≡O), 1959 s (C≡O), 1931 s (C≡O). HR-ESI-MS (positive ion mode): *m/z* 656.1882 ([M]⁺, calcd 656.1923). Anal. Calcd for [Re(CO)₃(*t*butylbpy)(*ptol*ICN)](OTf)_{0.75}(TFA)_{0.25} (ReC_{30.25}H₃₁F₃N₃O_{5.75}S_{0.75}): C, 45.65; H, 3.93; N, 5.28. Found: C, 45.69; H, 4.03; N, 5.31.

Synthesis of fac-[Re(CO)₃(dmphen)(2,6-dmphenylICN)]OTf (TRIP-1b)

fac- [Re(CO)₃(dmphen)Cl] (0.200 g, 0.38 mmol) was dissolved in dry THF (40 ml) and AgOTf (0.100 g, 0.38 mmol) was added. The mixture was heated at reflux for 3 h, after which the resulting yellow suspension was filtered. To the filtrate, 2,6-dmphenylICN (0.2 g, 1.5 mmol) was added, and the mixture was heated at reflux overnight. The THF is removed by rotary evaporation and the crude solid was dissolved in 2 ml of DCM. The DCM solution was then added dropwise to 50 ml of

diethyl ether to precipitate out a pale yellow solid, which was then collected via vacuum filtration and washed with ~20 ml of ether to yield the pure product. Yield: 0.230 g (80%). ^1H NMR (500 MHz, CDCl_3): δ 8.79 (d, $J = 8.3$ Hz, 2 H), 8.19 (s, 2 H), 8.07 (d, $J = 8.3$ Hz, 2 H), 7.15 – 6.96 (m, 3 H), 3.34 (s, 6 H), 1.76 (s, 6 H). $^{13}\text{C}\{^1\text{H}\}$ NMR (126 MHz, CDCl_3): δ 190.9, 188.1, 164.9, 147.9, 141.0, 135.5, 130.7, 129.8, 128.5, 127.8, 31.8, 18.0. IR (KBr, cm^{-1}): 2171 m ($\text{C}\equiv\text{N}$), 2033 s ($\text{C}\equiv\text{O}$), 1967 s ($\text{C}\equiv\text{O}$), 1929 s ($\text{C}\equiv\text{O}$). HR-ESI-MS (positive ion mode): 610.1136 m/z ($[\text{M}]^+$, calcd 610.1140). Anal. Calcd for $[\text{Re}(\text{CO})_3(\text{dmphen})(2,6\text{-dmphenylICN})]\text{OTf}$ ($\text{ReC}_{27}\text{H}_{21}\text{F}_3\text{N}_3\text{O}_6\text{S}$): C, 42.74; H, 2.79; N, 5.54. Found: C, 42.88; H, 2.65; N, 5.56.

Synthesis of fac-[Re(CO)₃(dmphen)(3,5-dmphenylICN)]OTf (TRIP-1c)

fac- $[\text{Re}(\text{CO})_3(\text{dmphen})\text{Cl}]$ (0.220 g, 0.41 mmol) was dissolved in dry THF (20 mL) and AgOTf (0.110 g, 0.43 mmol) was added. The mixture was heated at reflux for 3 h, after which the resulting yellow suspension was filtered. To the filtrate, 3,5-dmphenylICN (0.200 g, 1.5 mmol) was added, and the mixture was heated at reflux overnight. The resulting solution was evaporated under reduced pressure. The crude product was dissolved in a minimum amount of THF (~5 ml), and this concentrated solution was added to diethyl ether (>100 mL) with rapid stirring. The product that precipitated out was collected by filtration. This process was repeated two more times to obtain analytically pure compound. ^1H NMR (500 MHz, CDCl_3): δ 8.75 (d, $J = 8.3$ Hz, 2 H), 8.16 (s, 2 H), 8.04 (d, $J = 8.4$ Hz, 2 H), 7.00 – 6.72 (m, 3 H), 3.32 (s, 6 H), 2.22 (s, 6 H). $^{13}\text{C}\{^1\text{H}\}$ NMR (126 MHz, CDCl_3): δ 190.9, 187.6, 164.8, 147.9, 140.9, 140.2, 133.2, 129.7, 127.8, 124.6, 119.7, 31.9, 21.0. IR (KBr, cm^{-1}): 2186 m ($\text{C}\equiv\text{N}$),

2036 s (C≡O), 1963 sh (C≡O), 1941 s (C≡O). HR-ESI-MS (positive ion mode): 610.1138 m/z ($[M]^+$, calcd 610.1140). Anal. Calcd for $[\text{Re}(\text{CO})_3(\text{dmphen})(3,5\text{-dmphenylICN})]\text{OTf}\cdot 0.5\text{CH}_3\text{CH}_2\text{OCH}_2\text{CH}_3$ ($\text{ReC}_{29}\text{H}_{26}\text{F}_3\text{N}_3\text{O}_{6.5}\text{S}$): C, 43.77; H, 3.29; N, 5.28. Found: C, 43.84; H, 2.90; N, 5.79.

Synthesis of fac-[Re(CO)₃(dmphen)(p-methoxyphenylICN)]OTf (TRIP-1d)

fac- $[\text{Re}(\text{CO})_3(\text{dmphen})\text{Cl}]$ (0.200 g, 0.41 mmol) was dissolved in dry THF and AgOTf (0.110 g, 0.43 mmol) was added. The mixture was heated at reflux for 3 h, after which the resulting yellow suspension was filtered. To the filtrate, *p*-methoxyphenylICN (0.240 g, 1.8 mmol) was added, and the mixture was heated at reflux overnight. The resulting solution was evaporated under reduced pressure. The crude product was dissolved in a minimum amount of THF (~5 ml), and this concentrated solution was added to diethyl ether (>100 mL) with rapid stirring. The product that precipitated out was collected by filtration and dissolved in methanol (20 mL). The resulting solution was reduced to <1 mL, and water (10 mL) was added. The mixture was lyophilized to yield a yellow powder Yield: 0.170 g (77%). ^1H NMR (500 MHz, CDCl_3): δ 8.63 (d, $J = 8.4$ Hz, 2 H), 8.07 (s, 2 H), 7.95 (d, $J = 8.4$ Hz, 2 H), 6.98 – 6.74 (m, 4 H), 3.72 (s, 3 H), 3.29 (s, 3 H). $^{13}\text{C}\{^1\text{H}\}$ NMR (126 MHz, $\text{DMSO-}d_6$): δ 191.7, 187.9, 165.2, 160.6, 147.1, 138.7, 128.9, 128.8, 127.5, 126.9, 114.8, 55.7, 31.5. IR (KBr, cm^{-1}): 2179 m (C≡N), 2036 s (C≡O), 1960 s (C≡O), 1929 s (C≡O). HR-ESI-MS (positive ion mode): 612.0928 m/z ($[M]^+$, calcd 612.0933). Anal. Calcd for $[\text{Re}(\text{CO})_3(\text{dmphen})(p\text{-methoxyphenylICN})]\text{Otf}$ ($\text{ReC}_{26}\text{H}_{19}\text{F}_3\text{N}_3\text{O}_7\text{S}$): C, 41.05; H, 2.52; N, 5.52. Found: C, 41.15; H, 2.60; N, 5.37.

Synthesis of fac-[Re(CO)₃(dmphen)(p-chlorophenylICN)]OTf (TRIP-1e)

fac- [Re(CO)₃(dmphen)Cl] (0.160 g, 0.31 mmol) was dissolved in dry THF and AgOTf (0.080 g, 0.34 mmol) was added. The mixture was heated at reflux for 3 h, after which the resulting yellow suspension was filtered. To the filtrate, *p*-chlorophenylICN (0.160 g, 1.16 mmol) was added, and the mixture was heated at reflux overnight. The resulting solution was evaporated under reduced pressure. The crude product was dissolved in a minimum amount of THF (~5 ml), and this concentrated solution was added to diethyl ether (>100 mL) with rapid stirring. The product that precipitated out was collected by filtration. This process was repeated two more times to obtain analytically pure compound. Yield: 0.110 g (42%). ¹H NMR (500 MHz, CDCl₃): δ 8.68 (d, *J* = 8.4 Hz, 2 H), 8.11 (s, 2 H), 8.01 (d, *J* = 8.3 Hz, 2 H), 7.30 (d, *J* = 8.7 Hz, 2 H), 7.15 (d, *J* = 8.8 Hz, 2 H), 3.32 (s, 6 H). ¹³C{¹H} NMR (126 MHz, CDCl₃): δ 190.7, 187.5, 165.0, 147.9, 140.7, 137.5, 130.3, 129.7, 128.7, 127.8, 127.7, 31.9. IR (KBr, cm⁻¹): 2185 m (C≡N), 2034 s (C≡O), 1957 s (C≡O), 926 s (C≡O). HR-ESI-MS (positive ion mode): 616.0425 *m/z* ([M]⁺, calcd 616.0438). Anal. Calcd for [Re(CO)₃(dmphen)(*p*-chlorophenyl-ICN)]OTf·0.25CH₃CN (ReC_{25.5}H_{16.75}ClF₃N_{3.25}O₆S): C, 39.50; H, 2.13; N, 5.87. Found: C, 39.90; H, 2.09; N, 5.79.

X-ray Crystallography

Low temperature (100 K) X-ray diffraction data was collected on a Rigaku XtaLab Synergy diffractometer equipped with a 4-circle Kappa goniometer and HyPix

6000HE Hybrid Photon Counting (HPC) detector with monochromated Mo $K\alpha$ radiation ($\lambda = 0.71073 \text{ \AA}$). Diffraction images were processed using CrysAlisPro software.⁹⁴ The structure was solved through intrinsic phasing using SHELXT⁹⁵ and refined against F^2 on all data by full-matrix least-squares with SHELXL⁹⁶ following established strategies.⁹⁷ All non-hydrogen atoms were refined anisotropically. Hydrogen atoms were included in the model at geometrically calculated positions and refined using a riding model while allowing the torsion angle to refine using the appropriate HFIX command. The isotropic displacement parameters of these hydrogen atoms were set to 1.2 times the U_{eq} of the oxygen atom that they are linked to (1.5 for methyl groups). Details of the structure refinement and selected interatomic distances and angles are listed in **Tables S1** and **S2**.

Emission Quantum Yield

The luminescence quantum yields were measured relative to the standard quinine sulfate ($\Phi = 0.52$, 0.5 M H_2SO_4), which was cross-referenced in our lab to harmaline ($\Phi = 0.32$, 0.05 M H_2SO_4).⁹⁸ An excitation wavelength of 350 nm was used for the samples and standards. The compound was measured as a solution in pH 7.4 PBS containing $\leq 1\%$ DMSO with the absorbance maintained below 0.1 to prevent inner filter effects.⁹⁸ At least five different concentrations of the samples and standards were measured by UV-vis and fluorescence spectroscopy, and the absorbance at 350 nm was plotted versus the integrated emission intensity. The slopes of the resulting lines were used in equation 1:

$$(1) \quad \Phi_{sample} = \Phi_{ref} \frac{S_{sample} \eta_{sample}^2}{S_{ref} \eta_{ref}^2}$$

where Φ_{ref} is the quantum yield of the reference, quinine sulfate, and S is the slope of either the sample or the reference, and η is the refractive index.

Lifetime Measurements

Laser excitation for the phosphorescence lifetime measurements was provided by pulsing the 405 nm laser line from a four-line iChrome MLE laser (Toptica Photonics AG, Munich, Germany). The diode laser in the iChrome was triggered by a DG535 Digital Delay/Pulse Generator (Stanford Research, Sunnyvale, CA) at 100 KHz and delivered 100 ns FWHM 405 nm excitation pulses. The 405 nm pulses were fiber-delivered to a sample-filled cuvette and phosphorescence was collected at 90 degrees through second fiber for delivery to a Bialkali photomultiplier tube (HC125, Hamamatsu, Bridgewater, NJ) through a 470 nm long pass filter (HQ470lp, Chroma Technology, Bellows Falls, VT). The time-resolved photon counts were collected in 40 ns time bins using a SR430 Multi-channel scaler (Stanford Research, Sunnyvale, CA). Data was transferred to a PC via the SR430 GPIB bus and fit to the standard exponential decay model. Measurements were collected in PBS solutions at 10 μ M. For deoxygenated measurements, nitrogen gas was bubbled into the PBS solutions for 20 min and then the lifetime was determined. Lifetimes were calculated by fitting to a mono-exponential decay function using the Magic Plot Pro software.

Cell Culture and Cytotoxicity

The HeLa (cervical cancer) cell line were obtained from American Type Culture Collection (ATCC) and cultured using Dulbecco's Modified Eagle's Medium (DMEM) supplemented with 10% fetal bovine serum (FBS). HeLa cells were grown in a humidified incubator at 37 °C with an atmosphere of 5% CO₂. Cells were passed at 80–90% confluence using trypsin/EDTA. Cells were tested monthly for mycoplasma contamination with the Plasmotest™ mycoplasma detection kit from InvivoGen.

The compounds **TRIP-1a**, **TRIP-3a**, **TRIP-4a**, and **TRIP-5a** were dissolved in PBS (pH 7.4) to prepare 0.5–1 mM stock solutions. The compounds **TRIP-6a**, **TRIP-7a**, **TRIP-1b**, **TRIP-1c**, **TRIP-1d**, and **TRIP-1e** were dissolved in DMSO to prepare 5–20 mM stock solutions. **TRIP-2a** stock solutions were prepared in both PBS (pH 7.4) and DMSO and the IC₅₀ values were the same for both types of stock solutions, indicating that the stability of these complexes is the same in these solutions. For cell viability studies all cells were grown to 80–90% confluence, detached with trypsin/EDTA, seeded in 96-well plates at 4000 cells/well in 100 µL of growth media, and incubated for 24 h. The medium was removed and replaced with fresh medium (200 µL) containing varying dilutions of either the rhenium compounds or media. The cells were then incubated for 48 h. The additional 48 h incubation was performed to ensure that the cells were in the logarithmic growth phase and that the cells had adequate time to regrow after exposure to the complexes. The medium was removed from the wells, and 3-(4,5-dimethylthiazol-2-yl)-2,5-tetrazolium bromide (MTT) in DMEM (200 µL, 1 mg/mL) was added. After 4 h, the MTT/DMEM solution was removed, and the formazan crystals were dissolved in 200 µL of an 8:1 mixture of

DMSO and pH 10 glycine buffer. The absorbance at 570 nm in each well was measured using a BioTek Synergy HT plate reader. Cell viability was determined by normalizing the absorbance of the treated wells to untreated wells. The % viability data shown is an average of three independent experiments with six replicates per concentration.

Confocal Fluorescence Microscopy

A total of 1×10^5 HeLa cells were seeded onto 35 mm glass bottom dishes. After 24 h, the cells were treated with the rhenium compound (10 μ M) in DMEM media. After 2 h, the media was removed and the cells were washed with PBS and fresh media was added. Right before imaging, the media was removed and imaging buffer was added (20 mM HEPES pH 7.4, 135 mM NaCl, 5 mM KCl, 1.8 mM CaCl₂, 1 mM MgCl₂, 1 mg/mL glucose, and 1 mg/mL bovine serum albumin). The cells were imaged with a Zeiss LSM 800 or Zeiss LSM 880 confocal laser-scanning microscope. The rhenium complexes were imaged using a 405 nm laser excitation with a 410–550 nm emission filter and images were processed using ImageJ software. The cellular images were analyzed using ImageJ software and the corrected total cell fluorescence (CTCF) was determined using equation 2:

$$(2) \text{ CTCF} = \text{Integrated density} - (\text{area of cell} \times \text{mean fluorescence of background reading})$$

The average of at least ten cells was used to determine the average CTCF and the

red/green ratio.

Mitochondria Morphology Experiment

For time-lapse experiments, HeLa cells were incubated with MitoTracker Red FM (1 μ L of 1 mM dye) and Hoechst 33342 (1 μ L of 20 mM dye) for 30 min, respectively. After incubation with the dyes, the media was removed and the cells were washed with PBS and fresh media was added. At the microscope, the rhenium compounds were diluted in imaging buffer to reach a final concentration of 10 μ M and the cells were imaged over 2 min increments for a maximum of 30 min. MitoTracker Red FM was excited with a 561 nm laser with an emission filter from 630–700 nm. Hoechst 33342 was excited with a 405 nm laser with an emission filter of 410–550 nm. The cellular images were analyzed using ImageJ software and the mitochondrial morphology was analyzed using a previously reported procedure.⁴⁵

Thioflavin T (ThT) Assay

A total of approximately 1×10^5 HeLa cells were seeded onto 35 mm glass bottom dishes. After 24 h, the cells were treated with 5 μ M ThT for 2 h. After 2 h, the media was removed, cells were washed with 1 ml PBS and 1 ml of fresh media was added to the dishes. At the microscope, the rhenium complexes (10 μ M), were diluted in imaging buffer and imaged at 0 and 30 min. The cells were imaged using a 405 nm laser excitation with a 410–550 nm green emission filter. The cellular images were analyzed using ImageJ software and the CTCF was calculated using equation 2.

Immunoblotting

HeLa cells were treated with the vehicle control (DMSO) or the TRIP derivative (10 μ M) for 24 h. Cells were lysed in TBS buffer (50 mM Tris, pH7.5, 150 mM NaCl, 1 mM EDTA) containing 1% Triton X-100, 2 U/ml DNase and protease inhibitor cocktail tablet (Cell Signaling). The lysates were incubated on ice for 30 min, followed by heating for 10 min in SDS-PAGE sample buffer (50 mM Tris (pH6.8), 100 mM dithiothreitol, 2% SDS, 0.1% bromophenol blue, 10% glycerol). Proteins were separated on SDS-PAGE and transferred to PVDF membranes (Fisher). Membranes were blocked in TBS containing 5% bovine serum albumin and 0.1 % Tween-20 for 1 h, followed by incubation with the primary antibody CHOP (Cell Signaling) overnight at 4 °C. After incubation with the horseradish peroxidase-coupled secondary antibody at room temperature for 1 h, immunoblots were visualized using enhanced chemiluminescence (ECLPlus, GE Healthcare) and β -Actin antibody (Sigma-Aldrich) was used to quantify β -actin as a loading control.

Puromycin labeling of proteins

HeLa cells were treated with the vehicle control (DMSO) or the TRIP derivative (10 μ M) for 2 h. After 2 h, 10 μ M puromycin was added to the medium, and cells were harvested 10 min after the addition of puromycin. Cells were lysed in TBS buffer (50 mM Tris, pH 7.5, 150 mM NaCl, 1 mM EDTA) containing 1% Triton X-100, 2 U/ml DNase and protease inhibitor cocktail tablet (Cell Signaling). The lysates were incubated on ice for 30 min, followed by heating for 10 min in SDS-PAGE sample buffer (50 mM Tris (pH 6.8), 100 mM dithiothreitol, 2% SDS, 0.1% bromophenol blue,

10% glycerol). Proteins were separated on SDS-PAGE and transferred to PVDF membranes (Fisher). Membranes were blocked in TBS containing 5% non-fat milk and 0.1 % Tween-20 for 1 h. Puromycin-labeled polypeptides were then quantified by incubating membranes with anti-puromycin (Developmental Studies Hybridoma Bank, #PMY-2A4) overnight at 4 °C and then with horseradish peroxidase-coupled secondary antibodies at room temperature for 1 h. Immunoblots were visualized using enhanced chemiluminescence and β -Actin antibody (Sigma-Aldrich) was used to quantify β -actin as a loading control.

Synthesis of TTIP

General Methods

RadioHPLC analysis was carried out using a Shimadzu HPLC-20AR equipped with a binary gradient, pump, UV-Vis detector, autoinjector and Laura radiodetector. UV absorption was recorded at 254 and 280 nm, samples were analyzed using a C18 column (Phenomenex Gemini C18, 150 mm x 4.60 mm), 0.8 mL/min flow, with mobile phase method 1: Solvent A: 50 mM TEAP (tetraethylammonium phosphate, pH 2) in water, solvent B = MeOH. 0-2 min: 5% B; 2-14 min: 5-95% B; 14-19 min: 95% B; 19-19.5 min: 95-5% B; 19.5-25min: 5% B.

Purification of 2,9-dimethyl-1,10-phenantholine (dmphen). 2,9-dimethyl-1,10-phenantholine (98% purity) as received from Sigma-Aldrich was repurified using automated, reverse phase C18 chromatography. The identity of the product was confirmed with mass spectrometry.

Synthesis of TTIP

^{99m}Tc-labeling involved the initial synthesis of technetium tricarbonyl precursor, [^{99m}Tc(H₂O)₃(CO)₃]⁺. Sodium pertechnetate, Na[^{99m}TcO₄], was eluted from a ⁹⁹Mo/^{99m}Tc sterile generator as a 1.0 mL saline solution (0.9% v/v) and was provided by Triad Isotopes (Hicksville, NY). The radioactive solution was added to a sealed vial containing boranocarbonate (4 mg), sodium tartrate (7 mg), and sodium borate decahydrate (7 mg). The carbonylation was carried out under heating for 40 min at 100 °C using an oil bath. The solution was cooled to room temperature. A separate solution of ligand (10⁻⁴ M in MeOH) was prepared. To the aqueous [^{99m}Tc(H₂O)₃(CO)₃]⁺ solution (34.7 mCi, 1 mL) was added to 1 M HCl, (150-180 μL) to adjust the pH to 7. A 500 μL aliquot was removed and mixed with dmphen ligand stock solution (100 μL, 10 mM). The mixture was heated to 60 °C for 30 min under vigorous stirring in a sealed reaction vessel. The reaction was analyzed using analytical radioHPLC. Preparative purification of complexes was carried out using large volume HPLC injections followed by manual collection of the assigned product peak. 100 μL of 10 mM dmphen was added and the solution was heated 30 min at 60 °C. After confirmation of formation of the [^{99m}Tc(dmphen)(CO)₃(H₂O)]⁺ intermediate, the isonitrile (100 μL of 10 mM stock solution) was added and the reaction mixture was heated at 60 °C for 90 min to afford [^{99m}Tc(dmphen)(CO)₃(*ptol*ICN)]⁺ (**TTIP**) as confirmed by HPLC. Following purification by HPLC, the solvent was removed in vacuo and the product (1.525 mCi) was resuspended for injection in 1.35 mL PBS pH 7.4. The purified, final, non-decay-corrected radiochemical yield was 4.3%.

Biodistribution of TTIP

All animal experiments were conducted according to the guidelines of the Institutional Animal Care and Use Committee (IACUC) of Stony Brook University at the Department of Laboratory Animal Resources (DLAR), Stony Brook Medicine. Female balb/c mice (6 weeks old, Taconic Biosciences, Taconic NY) were intravenously injected with 51–104 μCi of **TTIP** and 0.2 μmol of **TRIP-1a** via a tail vein catheter in 10% EtOH/saline. Mice were sacrificed at 1, 2, and 4 hours post injection. The following organs were harvested and collected: Blood (obtained via cardiac puncture), heart, liver, lung, kidney, spleen, small intestine, muscle (thigh), bone (femur), urine. Urine was collected for metabolite analysis via bladder puncture. Radioactivity was counted using a gamma counter. Radioactivity associated with each organ was expressed as % ID/g. Metabolite analysis of blood and urine was carried out by fractionated collection of HPLC eluent and subsequent reconstruction of the chromatogram. For ICP-OES analysis of rhenium content, organs were incubated with nitric acid (3 mL) and the organs were left to digest for 20 h at 25 °C. 300 μL of organ digest was diluted with 3 mL of ICP diluent and subsequently analyzed for Re content using ICP-OES. 20 ppm of Tb was used as an internal standard. Percent injected dose per gram (% ID/g) was calculated based on injection volumes used for each animal (0.2 μmol for mouse 4; producing an administered Re dose was 10 $\mu\text{mol}/\text{kg}$ with 0.2 μmol (mouse)).

Supporting Information

Table S5.1. X-ray Crystallographic Data and Refinement Parameters.^a

zCompound	TRIP-2a	
Empirical Formula	C ₂₄ H ₁₅ F ₃ N ₃ O ₆ ReS	$R_1 = \frac{\sum F_o - F_c }{\sum F_o }$;
Formula Weight	716.65	$wR2 = \frac{\sum [w(F_o^2 - F_c^2)]}{\sum [w(F_o^2)]}$
<i>a</i> (Å)	14.2993(3)	
<i>b</i> (Å)	11.1080(2)	
<i>c</i> (Å)	15.4031(3)	
<i>α</i> (°)	90	
<i>β</i> (°)	99.902(2)	
<i>γ</i> (°)	90	
<i>V</i> (Å ³)	2410.12(9)	
<i>Z</i>	4	
Crystal System	Monoclinic	
Space Group	<i>P</i> 2 ₁ / <i>c</i>	
ρ_{calc} (Mg/m ³)	1.975	
μ (mm ⁻¹)	5.199	
F(000)	1384	
T (K)	99.97(15)	
Wavelength (Å)	0.71073	
2 θ range (°)	2.272 – 26.371	
Reflections Collected	25835	
Independent Reflections	4830	
Completeness to theta (%)	99.9	
<i>R</i> _{int}	0.0365	
Number of Parameters	344	
Largest diff. peak and hole (e/Å ⁻³)	1.321/−0.982	
GoF	1.047	
R1/wR2 (all data)	0.0289/0.0425	
R1/wR2 (<i>I</i> > 2 σ)	0.0194/0.0412	

$$F_c^2) / \sum_w [(F_o^2)^2]^{1/2}$$

GoF = $\{\sum [w(F_o^2 - F_c^2)] / (n - p)\}^{1/2}$, where *n* is the number of data and *p* is the number of refined parameters.

Table S5.2. Selected Interatomic Distances (Å) Angles (°).^a

Selected Interatomic Distances (Å)	
Re(1)-N(1)	2.183(2)
Re(1)-N(2)	2.137(2)
Re(1)-C(1)	1.944(3)
Re(1)-C(2)	1.933(3)
Re(1)-C(3)	1.986(3)
Re(1)-C(4)	2.081(3)
<hr/>	
N(1)-Re(1)-N(2)	82.69(9)
N(1)-Re(1)-C(1)	175.06(10)
N(2)-Re(1)-C(1)	92.73(10)
C(1)-Re(1)-C(3)	82.88(11)
C(1)-Re(1)-C(4)	89.74(11)
N(1)-Re(1)-C(2)	88.08(10)
N(2)-Re(1)-C(2)	170.62(11)
C(1)-Re(1)-C(2)	96.55(12)
C(2)-Re(1)-C(3)	89.00(11)
C(2)-Re(1)-C(4)	93.91(11)
N(1)-Re(1)-C(3)	98.96(10)
N(2)-Re(1)-C(3)	90.81(10)
C(3)-Re(1)-C(4)	172.33(12)
N(1)-Re(1)-C(4)	88.24(10)
N(2)-Re(1)-C(4)	87.47(9)

^aAtoms are labeled as shown in **Figure 5.1** of the main text. Numbers in parentheses are the estimated standard deviations for the last significant figure.

Table S5.3. Mouse Treatment Schedule and Survival Times.

Mouse Number	Treatment Group	Last Dose Received (day)	Survival Time (days)
1	5 mg/kg	9	16
9	5 mg/kg	20	18
15	5 mg/kg	13	18
17	5 mg/kg	13	16
23	5 mg/kg	20	23
28	5 mg/kg	13	18
36	5 mg/kg	13	18
2	10 mg/kg	9	16
9	10 mg/kg	20	18
14	10 mg/kg	9	13
18	10 mg/kg	16	20
24	10 mg/kg	16	18
32	10 mg/kg	13	18
34	10 mg/kg	13	18
3	20 mg/kg	16	27
16	20 mg/kg	9	23
19	20 mg/kg	13	25
20	20 mg/kg	9	25
33	20 mg/kg	13	27
35	20 mg/kg	16	23
5	Vehicle	N/A	16
7	Vehicle	N/A	18
12	Vehicle	N/A	20
21	Vehicle	N/A	18
25	Vehicle	N/A	13
31	Vehicle	N/A	16

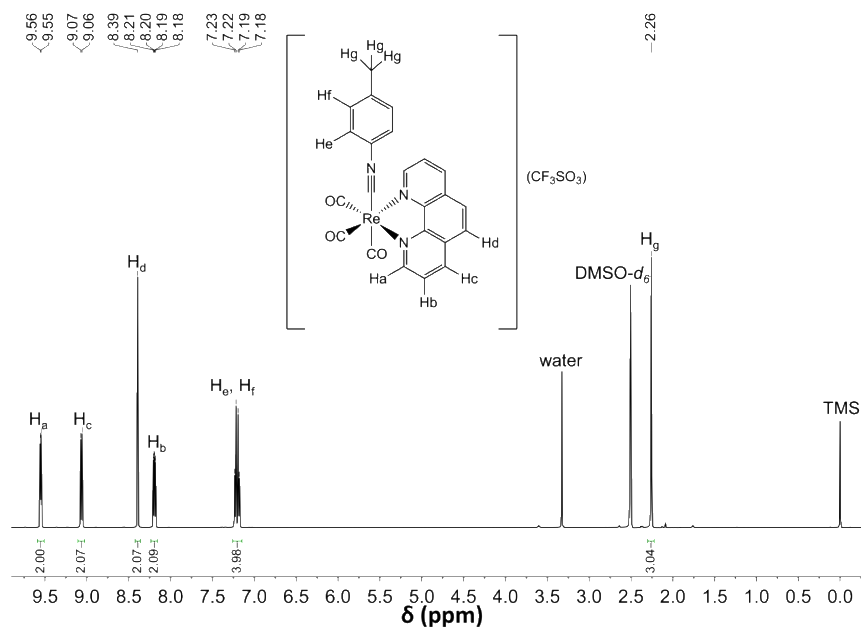


Figure S5.1. ^1H NMR spectrum of **TRIP-2a** ($\text{DMSO-}d_6$, 500 MHz) at 25 °C.

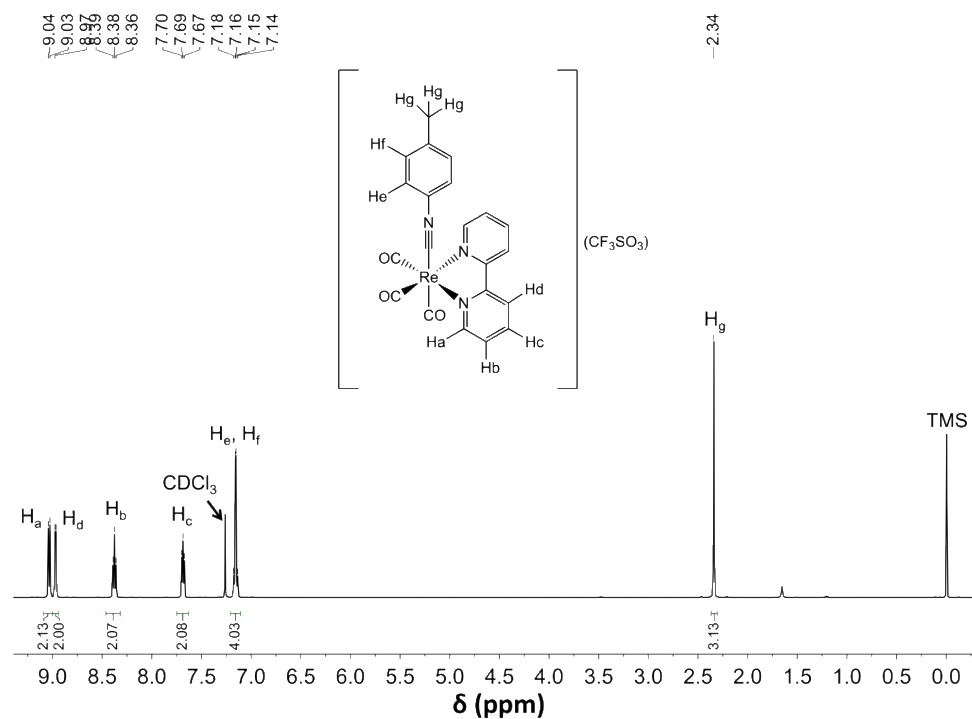


Figure S5.2. ^1H NMR spectrum of **TRIP-3a** (CDCl_3 , 500 MHz) at 25 °C.

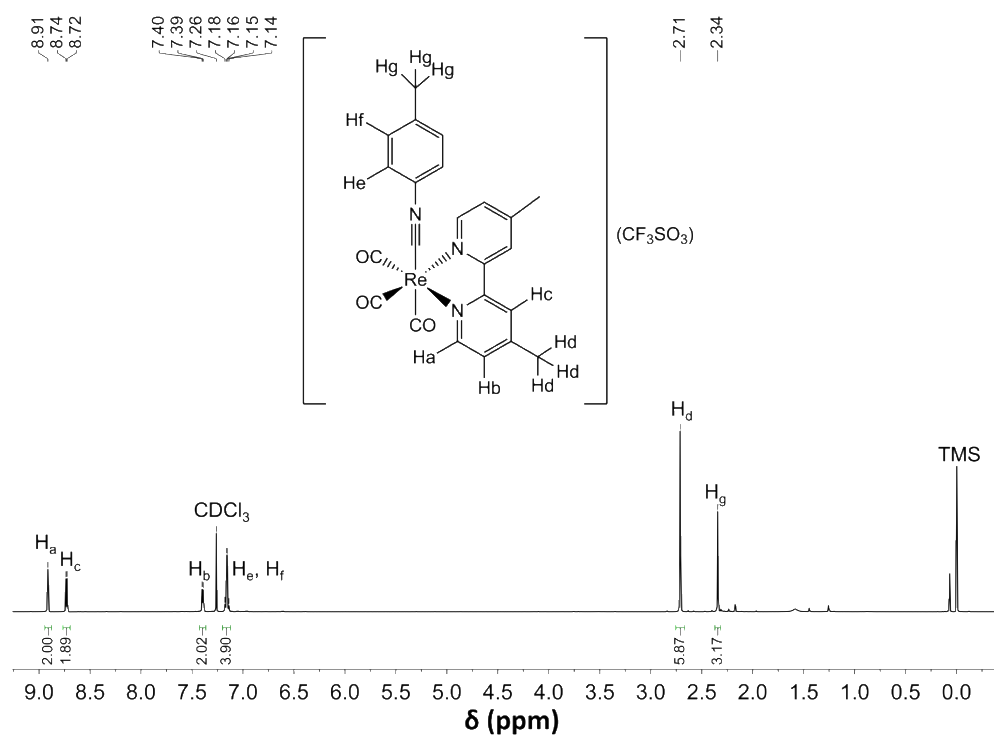


Figure S5.3. ¹H NMR spectrum of **TRIP-4a** (CDCl₃, 500 MHz) at 25 °C.

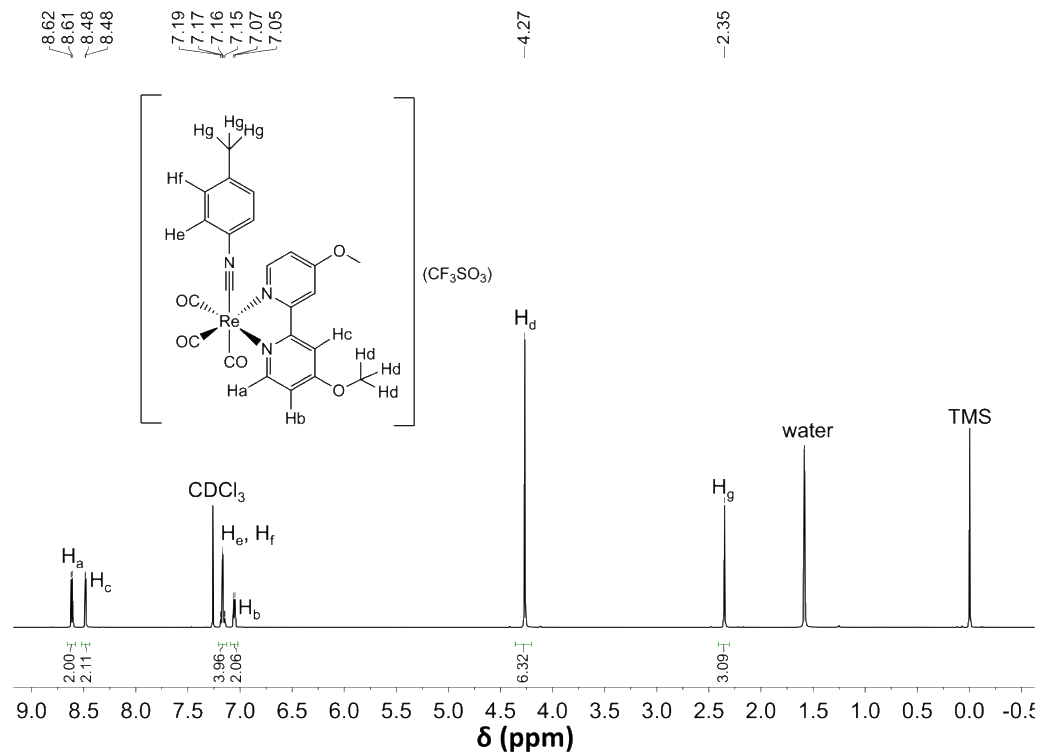


Figure S5.4. ¹H NMR spectrum of **TRIP-5a** (CDCl₃, 500 MHz) at 25 °C.

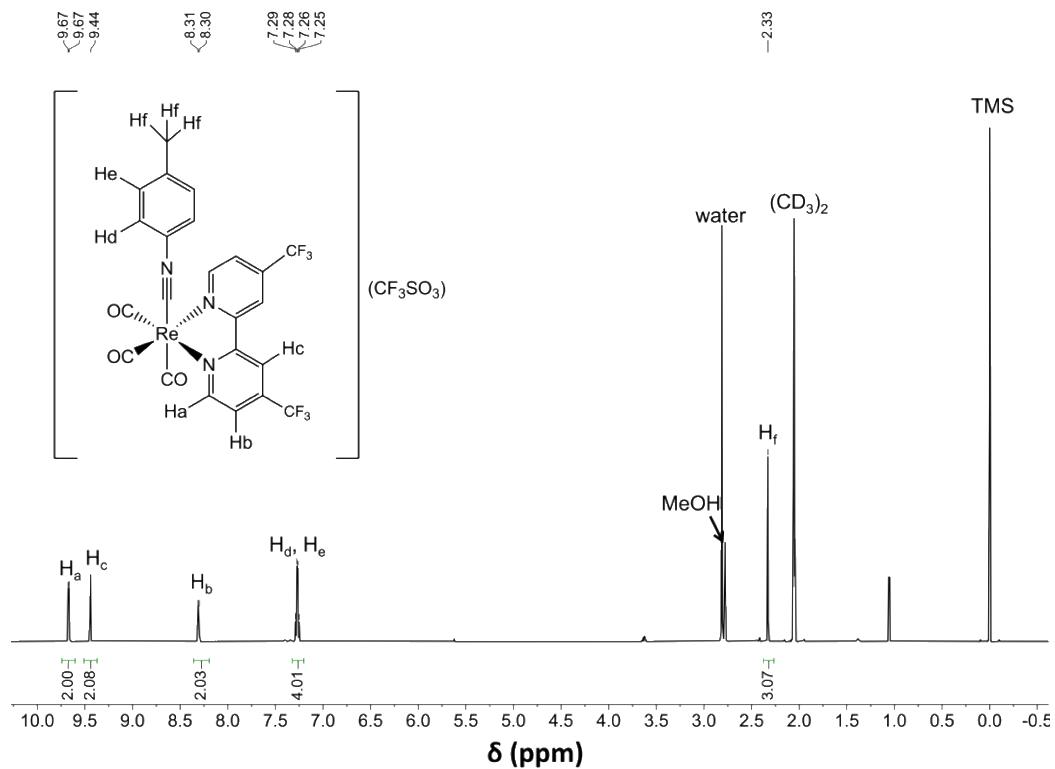


Figure S5.5. ^1H NMR spectrum of TRIP-6a ($\text{acetone-}d_6$, 500 MHz) at 25 °C.

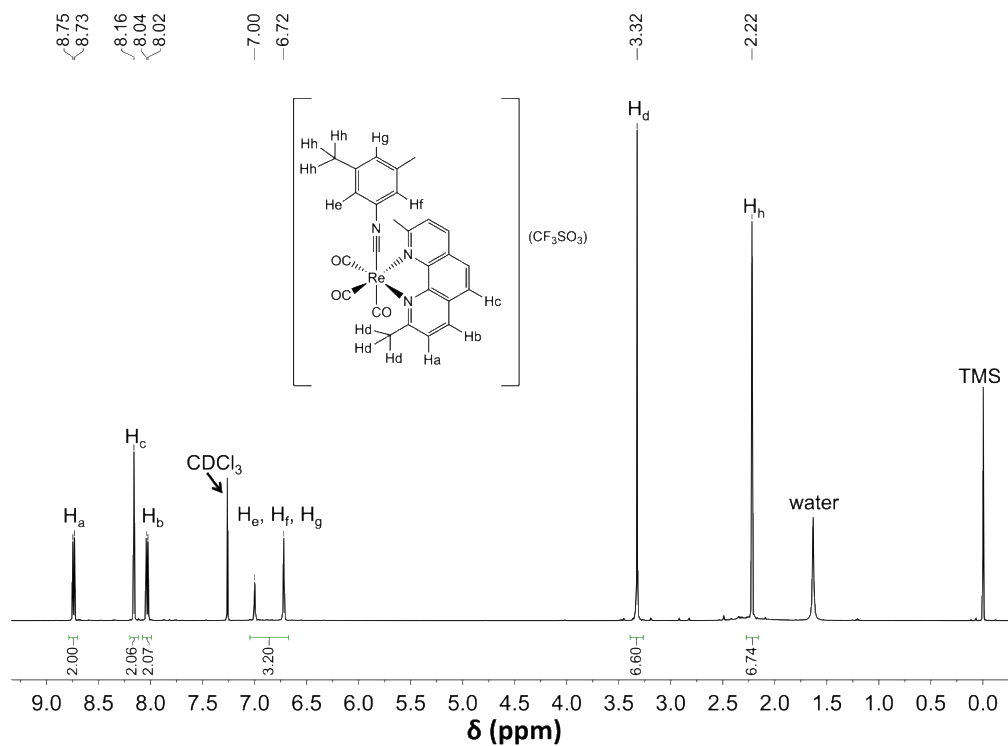


Figure S5.8. ^1H NMR spectrum of TRIP-1c (CDCl_3 , 500 MHz) at 25 $^\circ\text{C}$.

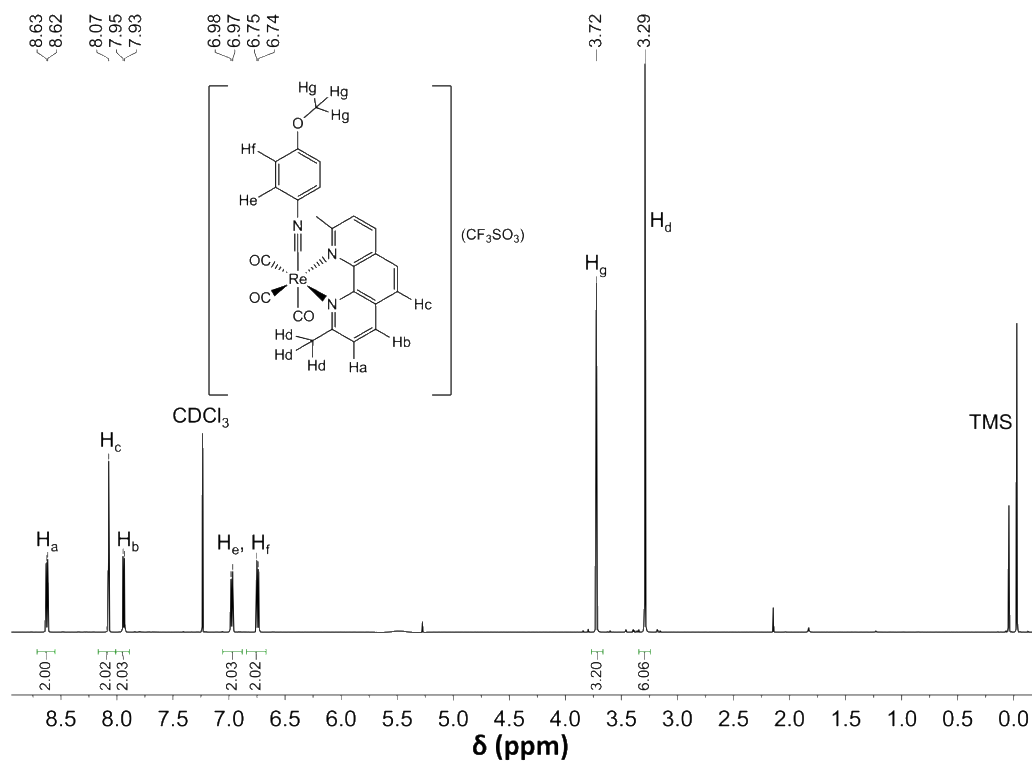


Figure S5.9. ^1H NMR spectrum of **TRIP-1d** (CDCl_3 , 500 MHz) at 25 °C.

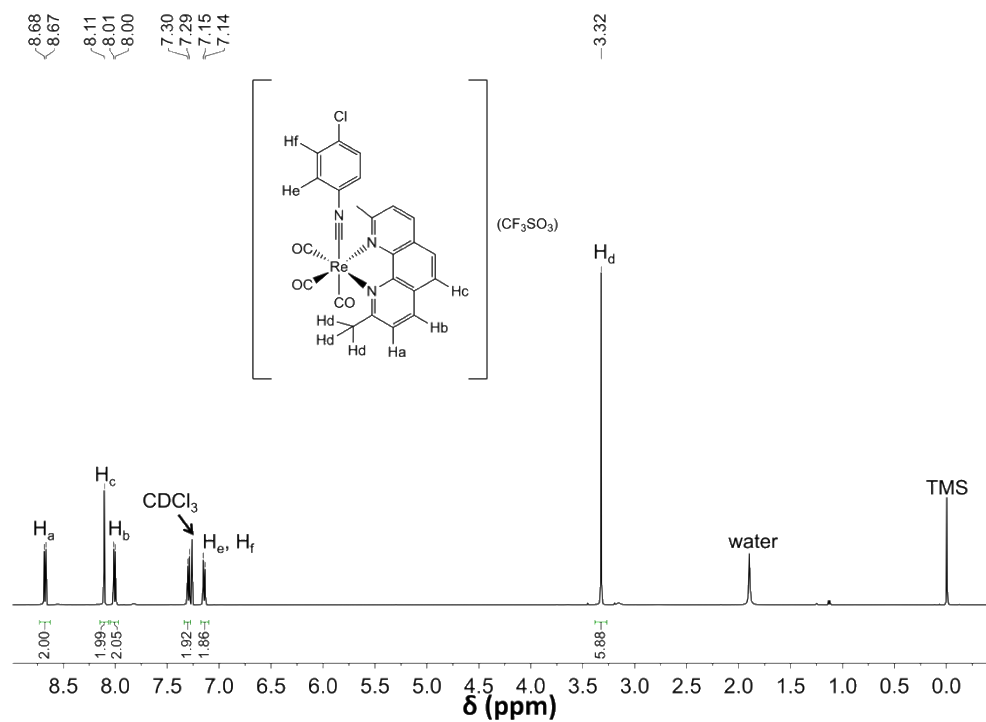


Figure S5.10. ^{13}C NMR spectrum of **TRIP-1e** (CDCl_3 , 500 MHz) at 25 °C.

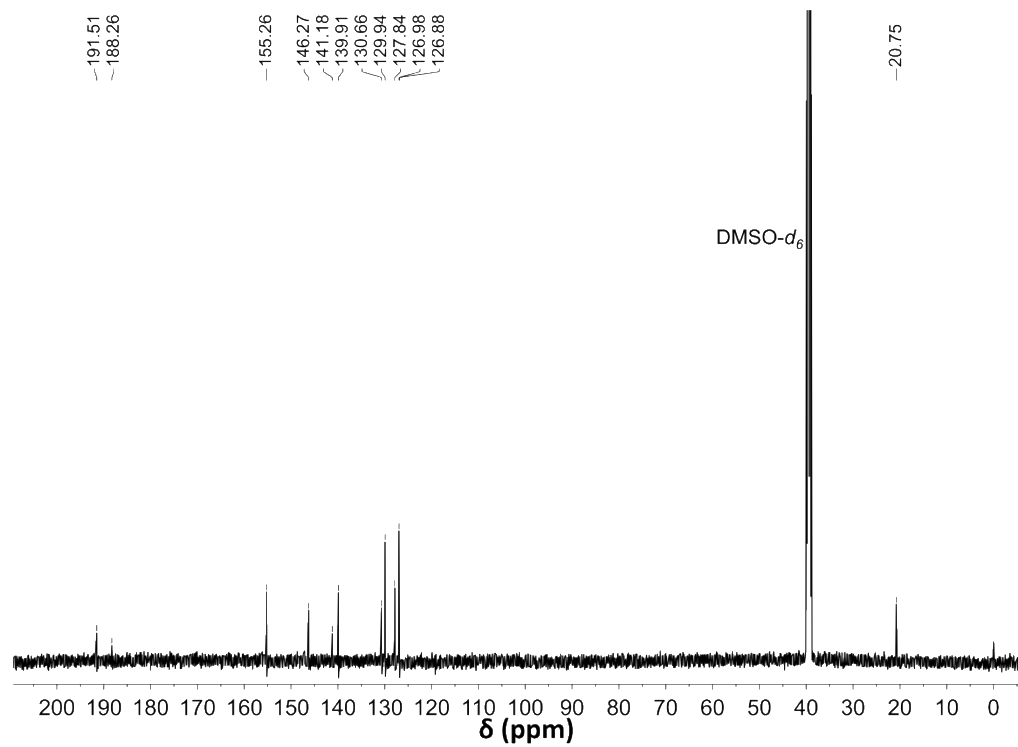


Figure S5.11. $^{13}\text{C}\{^1\text{H}\}$ NMR spectrum of **TRIP-2a** ($\text{DMSO-}d_6$, 126 MHz) at 25 °C.

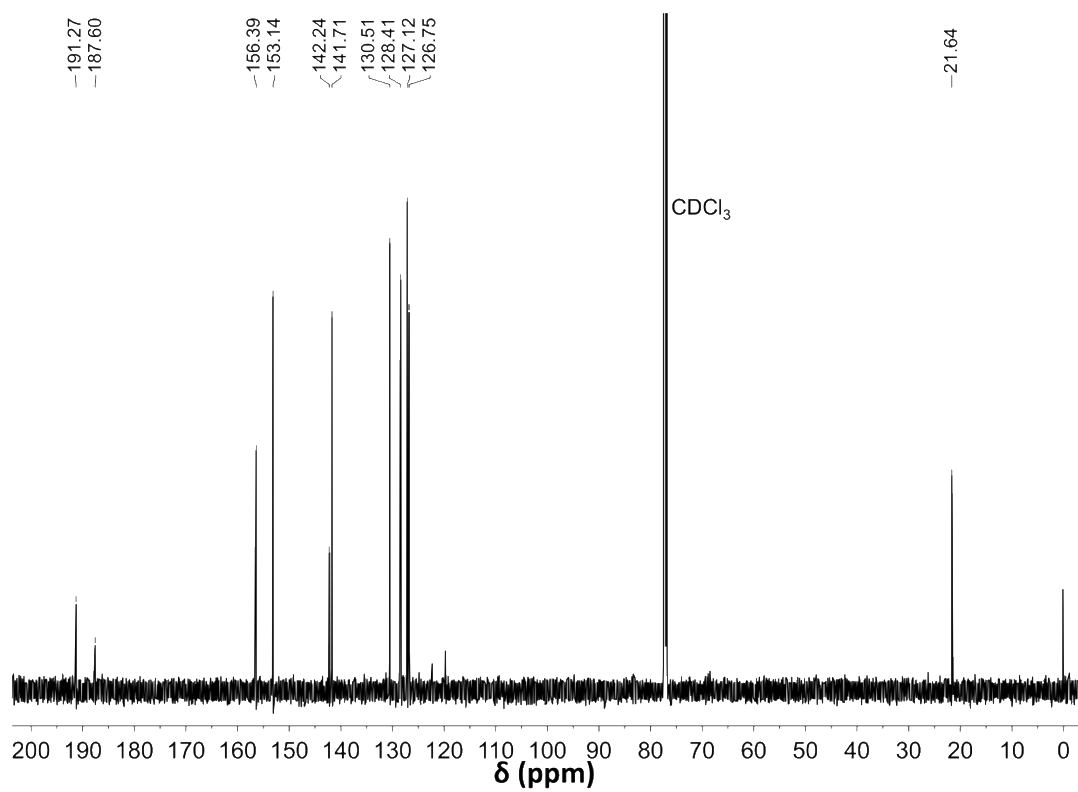


Figure S5.12. $^{13}\text{C}\{^1\text{H}\}$ NMR spectrum of **TRIP-3a** (CDCl_3 , 126 MHz) at 25 °C.

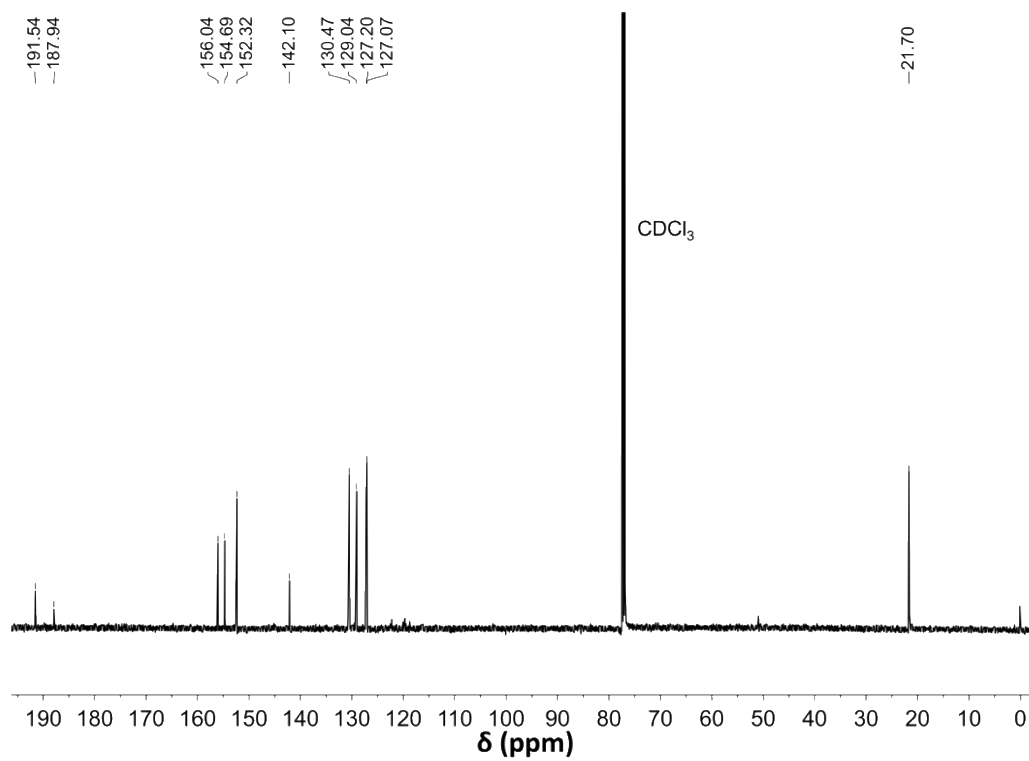


Figure S5.13. $^{13}\text{C}\{^1\text{H}\}$ NMR spectrum of **TRIP-4a** (CDCl_3 , 126 MHz) at 25 °C.

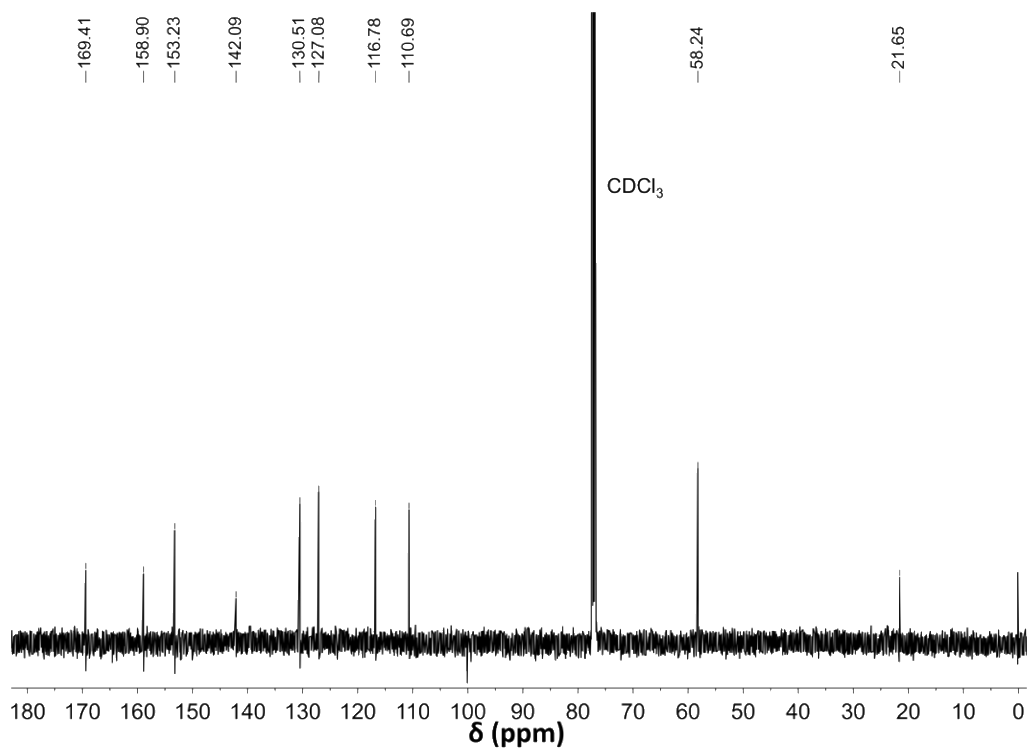


Figure S5.14. $^{13}\text{C}\{^1\text{H}\}$ NMR spectrum of **TRIP-5a** (CDCl_3 , 126 MHz) at 25 °C.

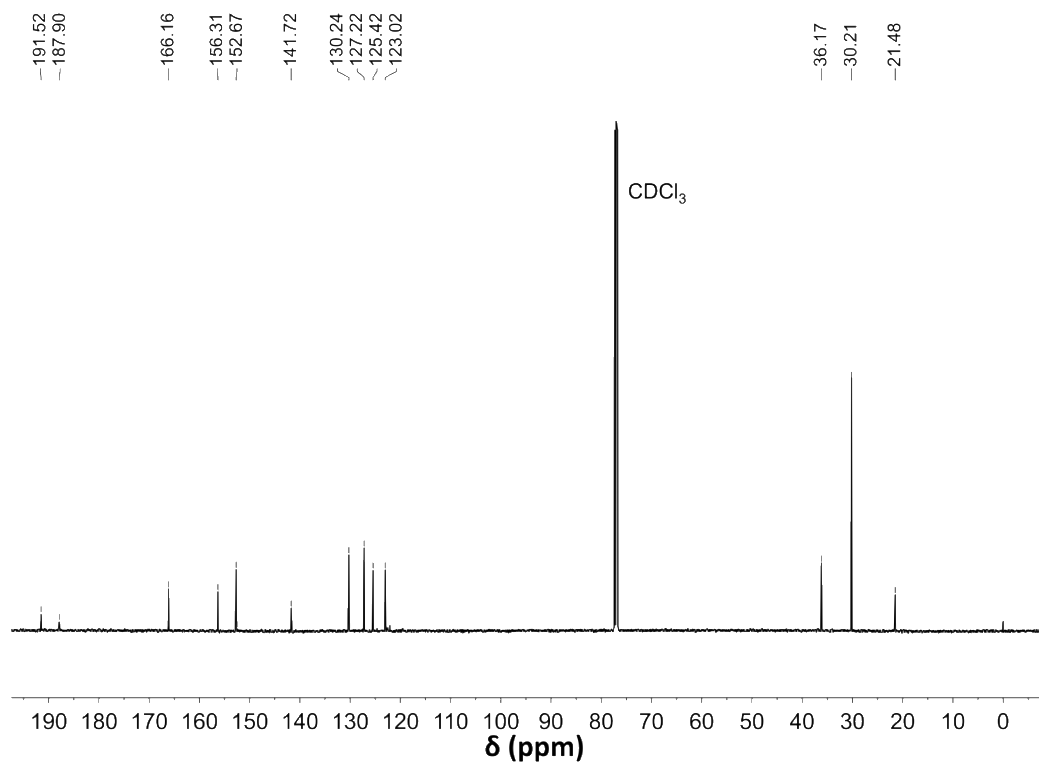


Figure S5.15. $^{13}\text{C}\{^1\text{H}\}$ NMR spectrum of **TRIP-7a** (CDCl_3 , 126 MHz) at 25 °C.

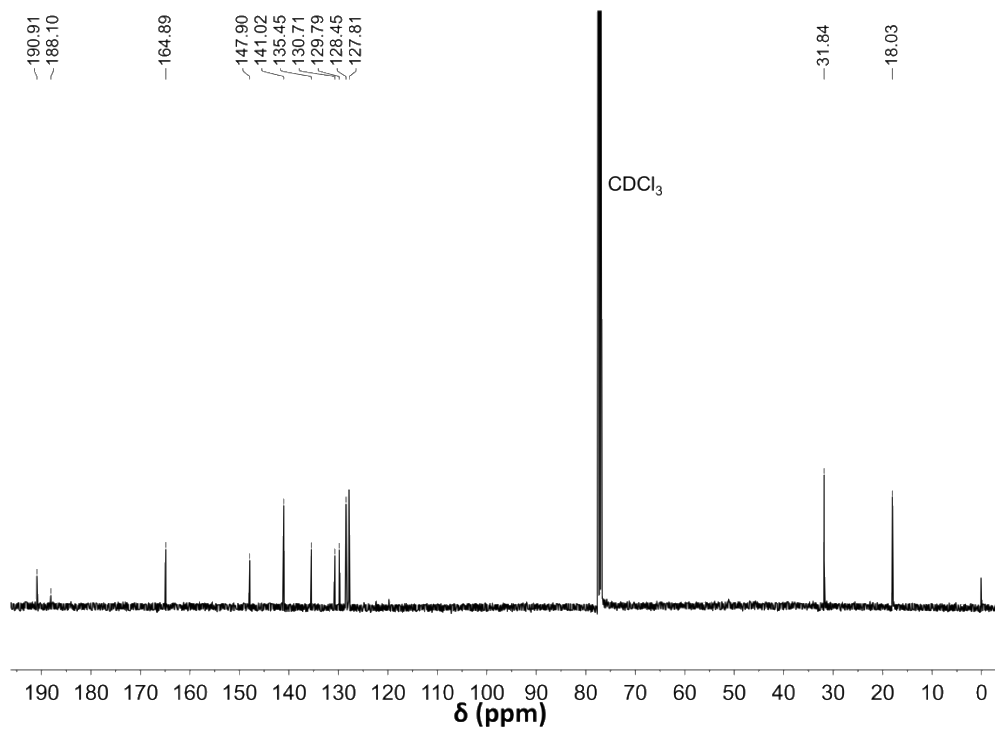


Figure S5.16. $^{13}\text{C}\{^1\text{H}\}$ NMR spectrum of **TRIP-1b** (CDCl_3 , 126 MHz) at 25 °C.

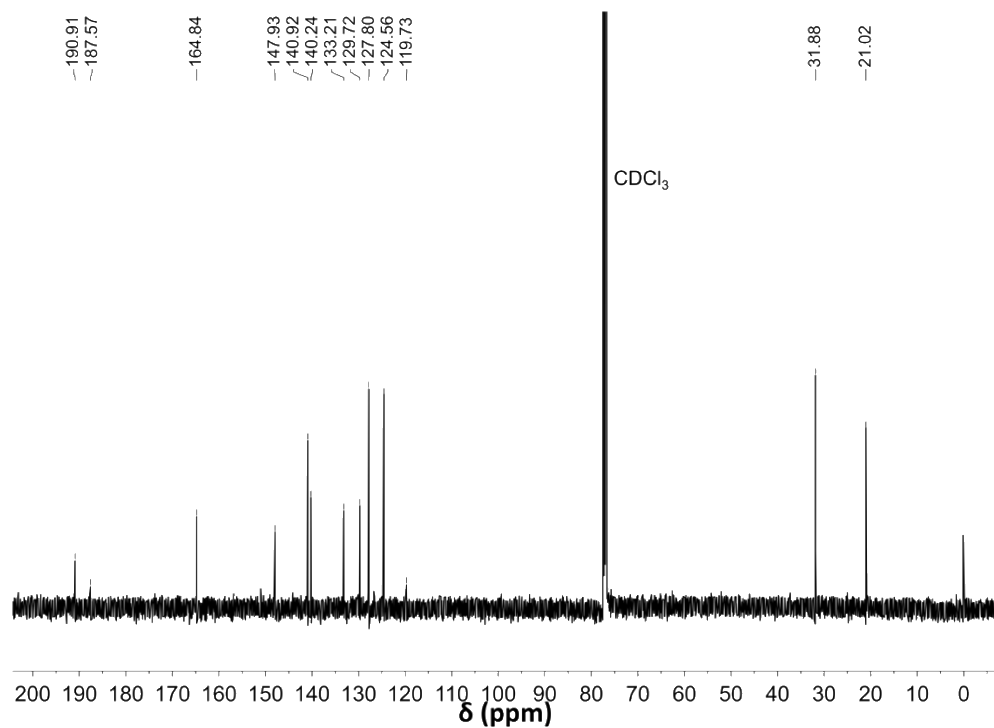


Figure S5.17. $^{13}\text{C}\{^1\text{H}\}$ NMR spectrum of **TRIP-1c** (CDCl_3 , 126 MHz) at 25 °C.

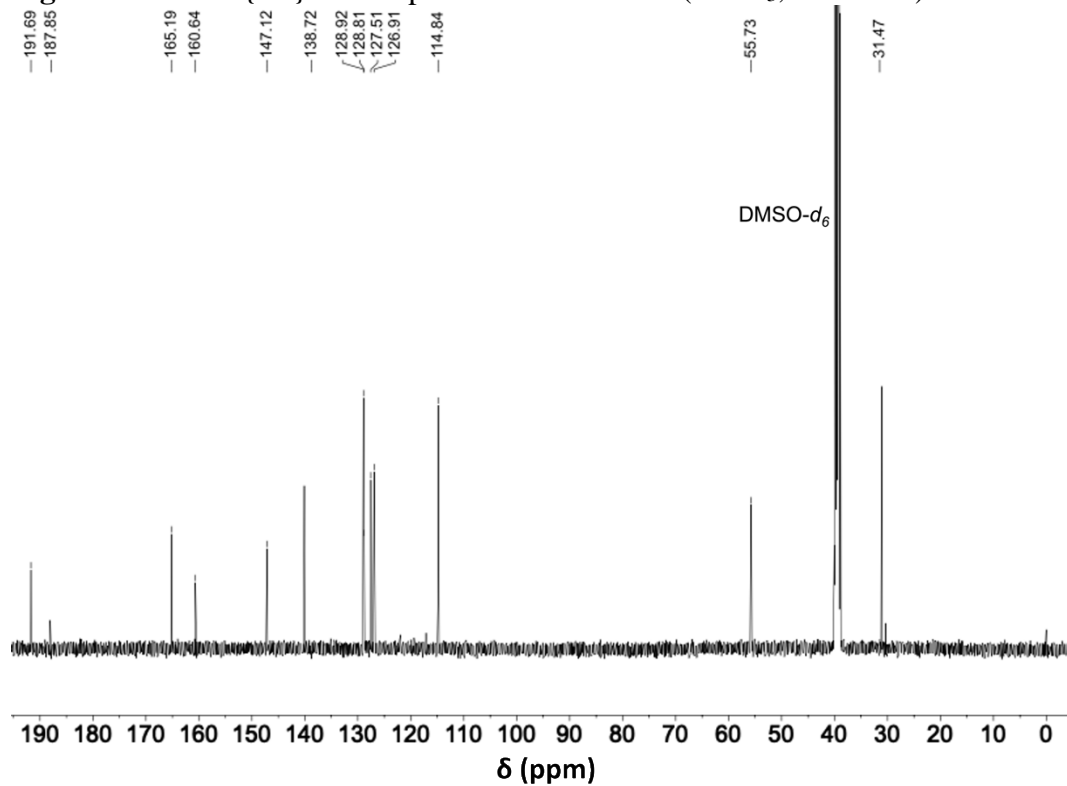


Figure S5.18. $^{13}\text{C}\{^1\text{H}\}$ NMR spectrum of **TRIP-1d** ($\text{DMSO-}d_6$, 126 MHz) at 25 °C.

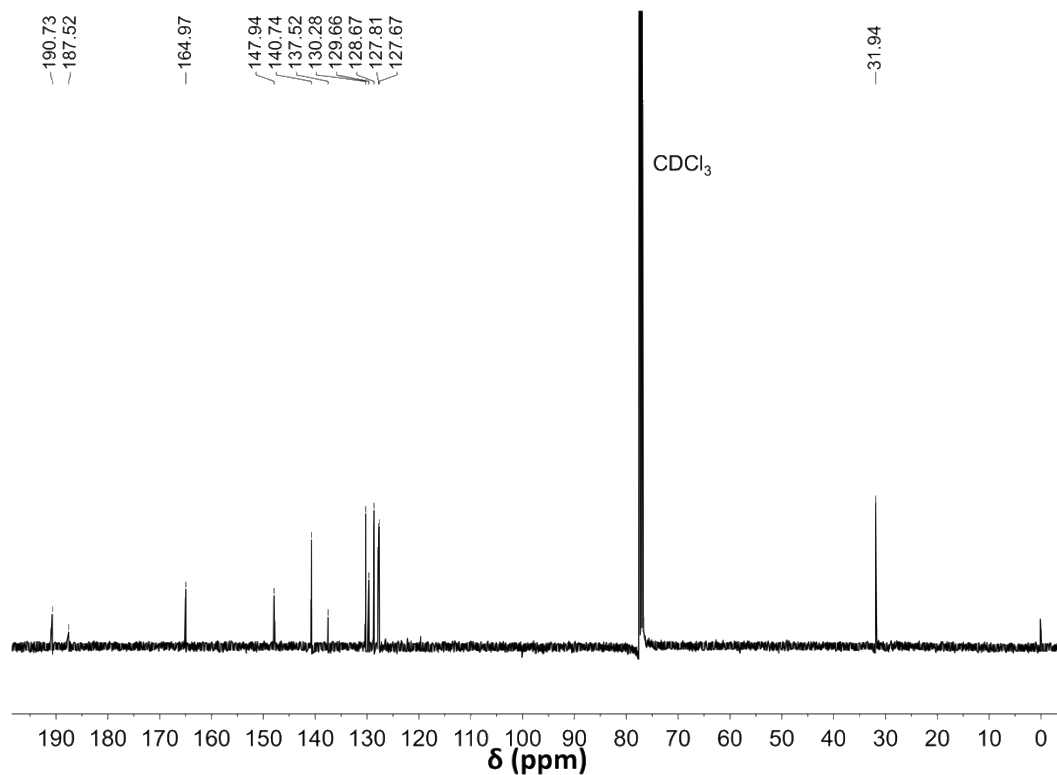


Figure S5.19. $^{13}\text{C}\{^1\text{H}\}$ NMR spectrum of **TRIP-1e** (CDCl_3 , 126 MHz) at 25 °C.

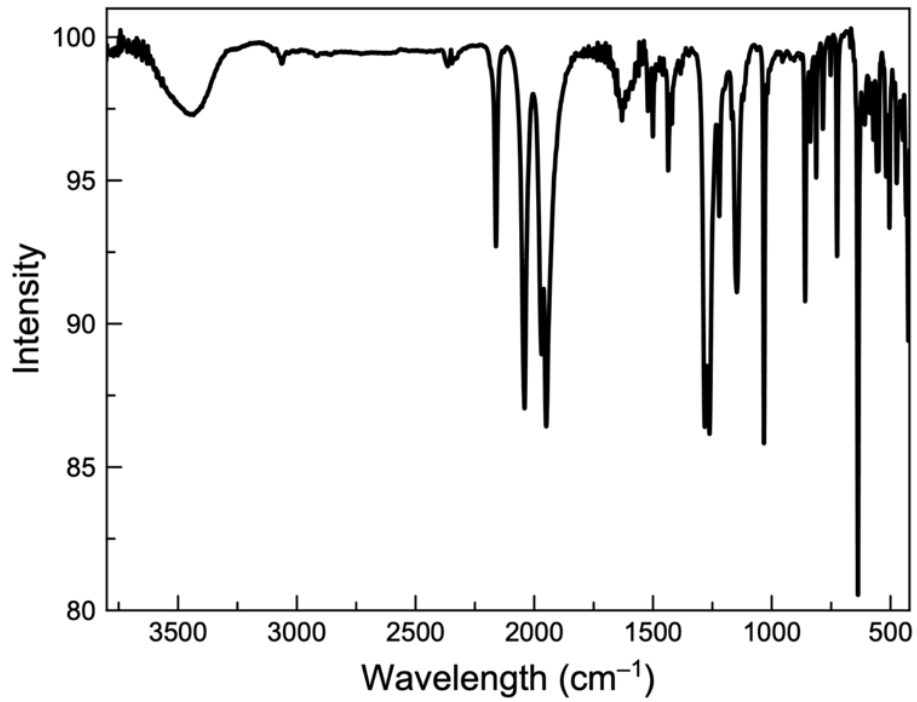


Figure S5.20. IR spectrum of TRIP-2a.

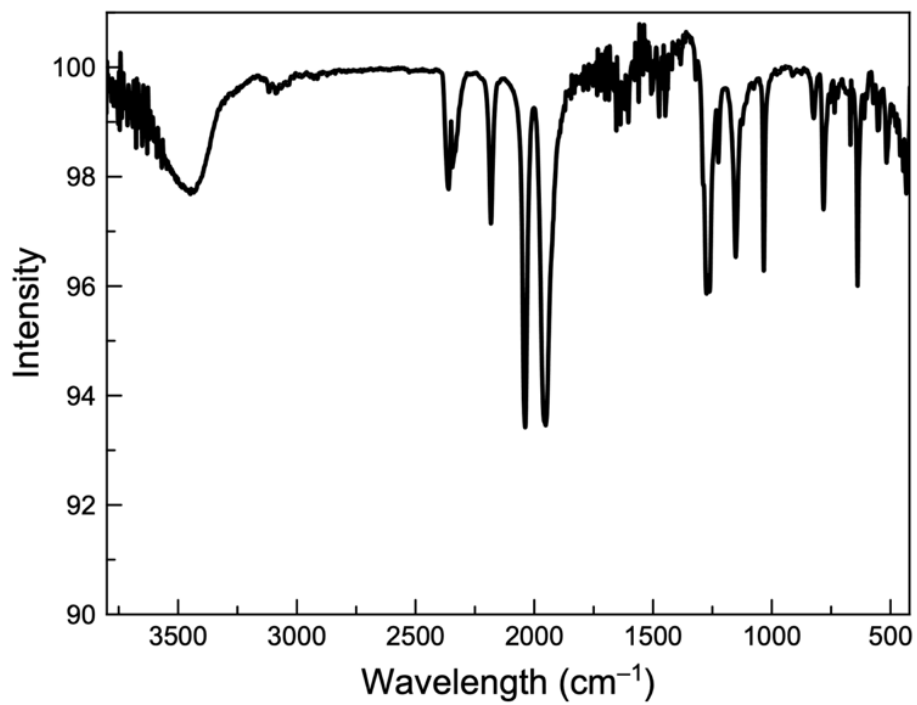


Figure S5.21. IR spectrum of TRIP-3a.

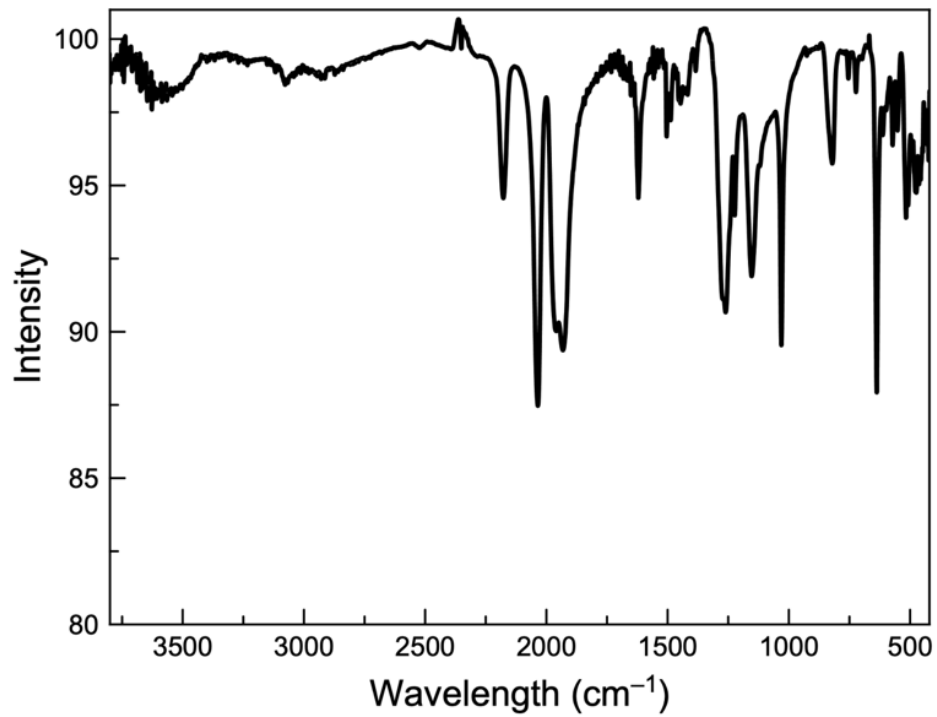


Figure S5.22. IR spectrum of TRIP-4a.

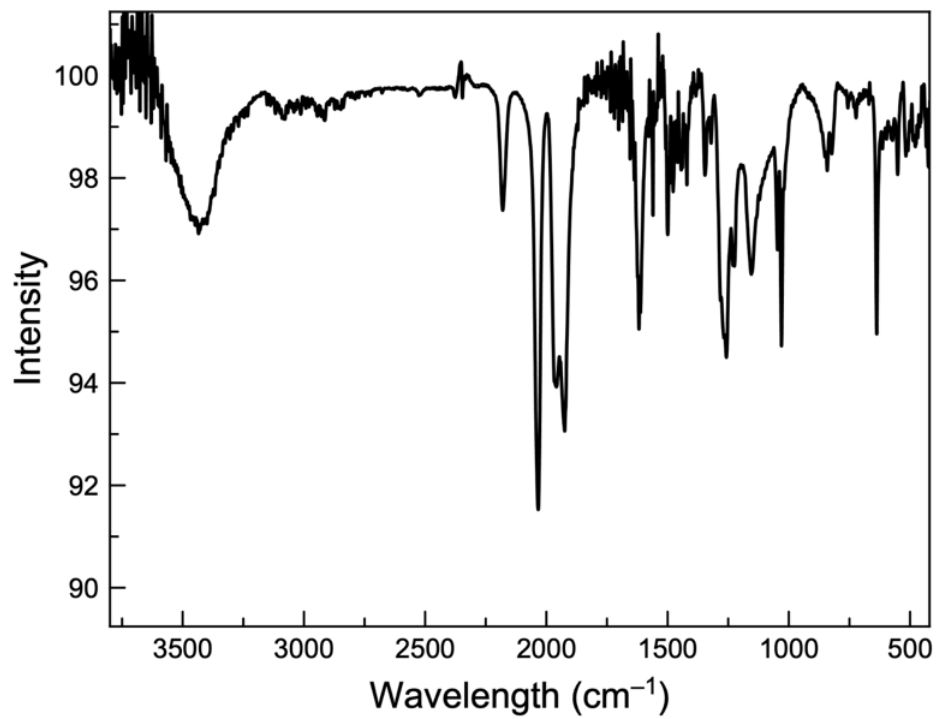


Figure S5.23. IR spectrum of TRIP-5a.

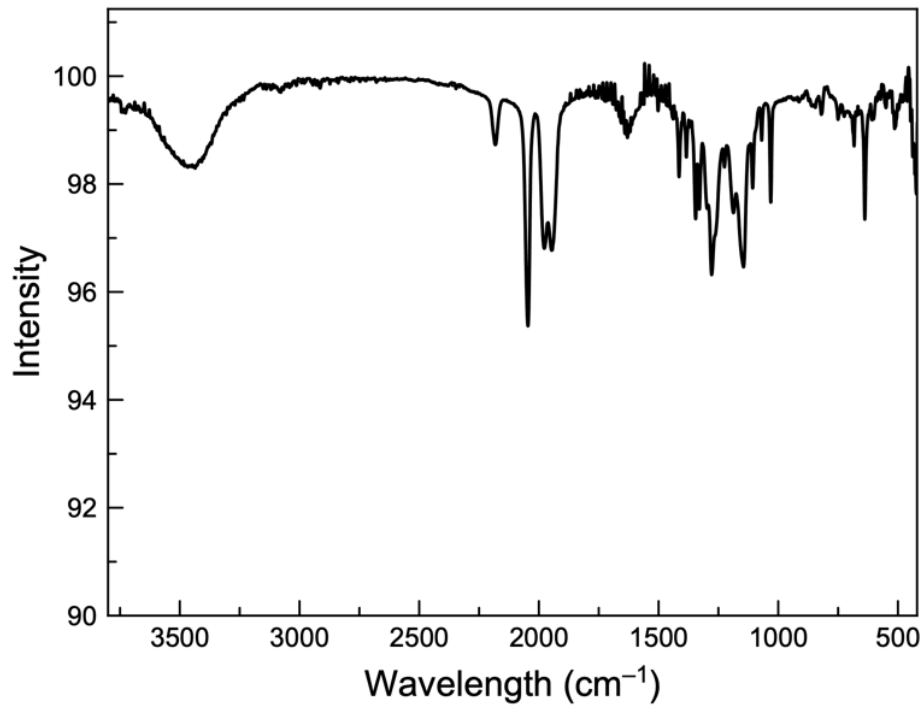


Figure S5.24. IR spectrum of TRIP-6a.

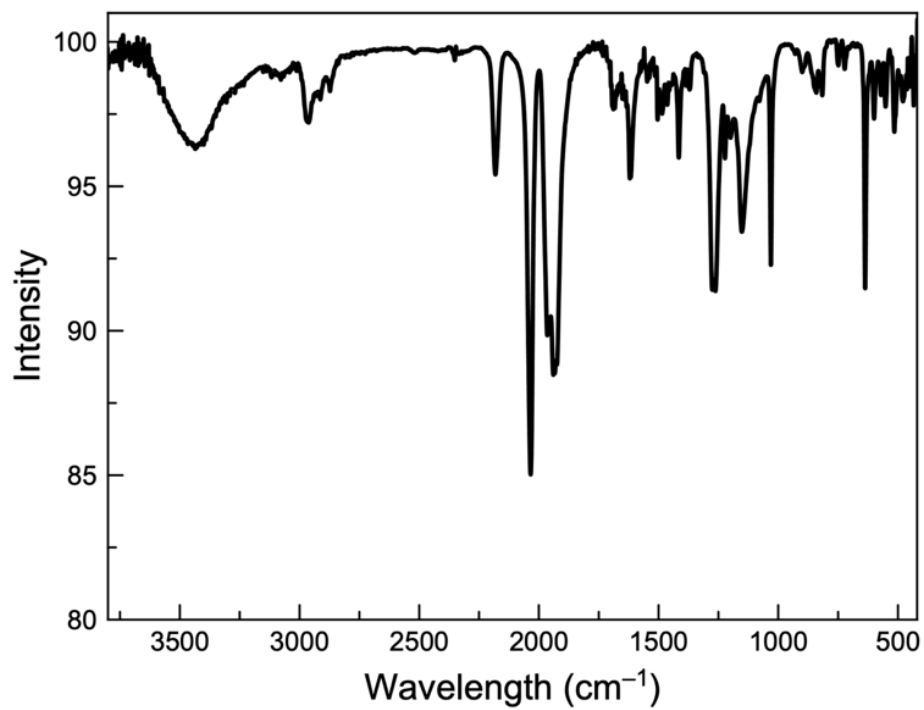


Figure S5.25. IR spectrum of TRIP-7a.

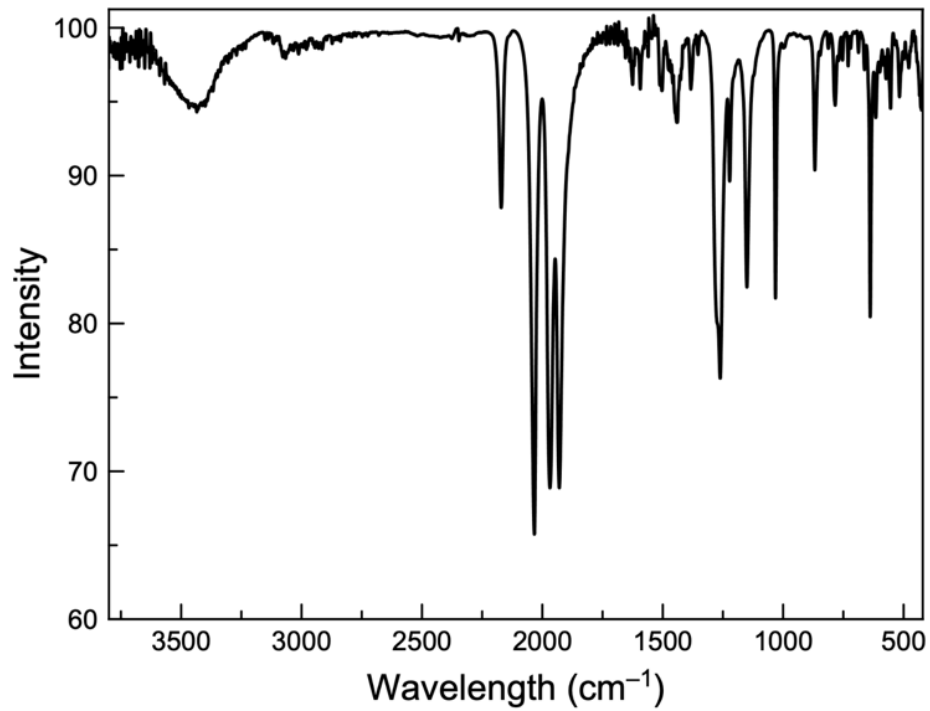


Figure S5.26. IR spectrum of TRIP-1b.

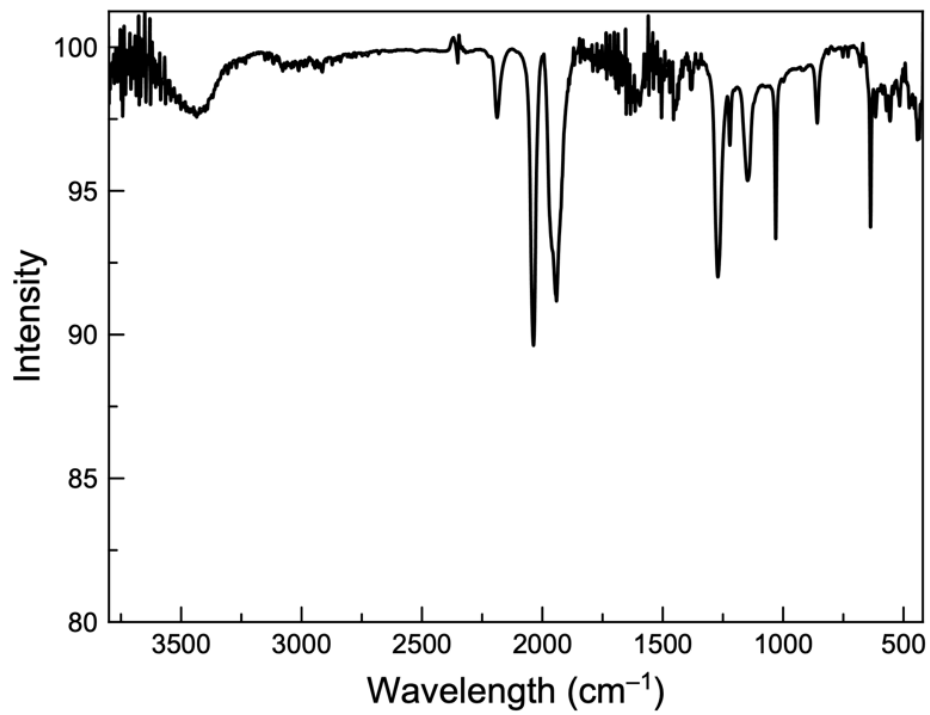


Figure S5.27. IR spectrum of TRIP-1c.

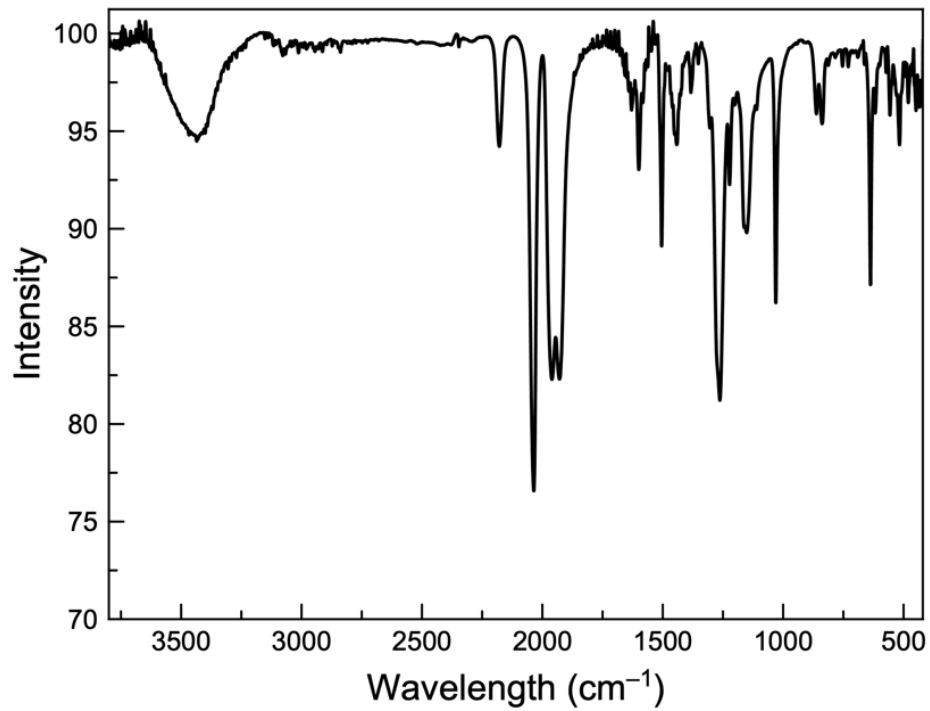


Figure S5.28. IR spectrum of TRIP-1d.

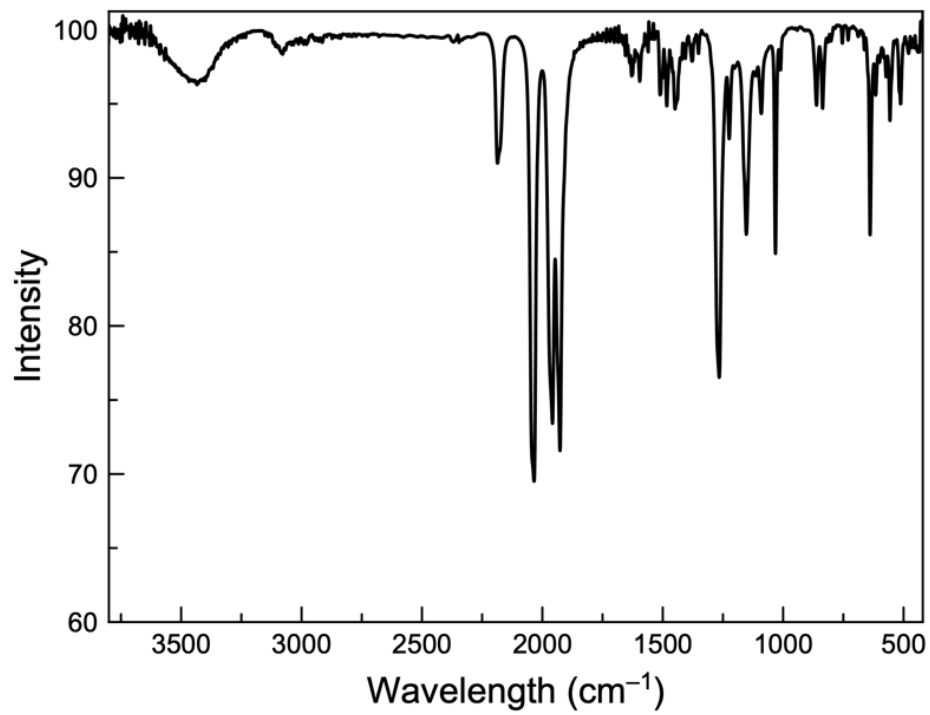


Figure S5.29. IR spectrum of TRIP-1e.

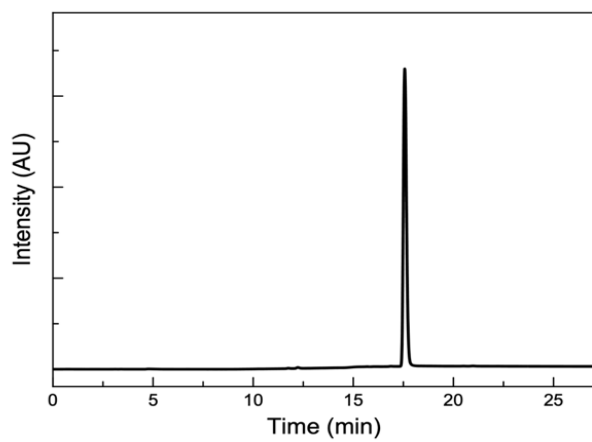


Figure S5.30. HPLC chromatogram of **TRIP-2a**.

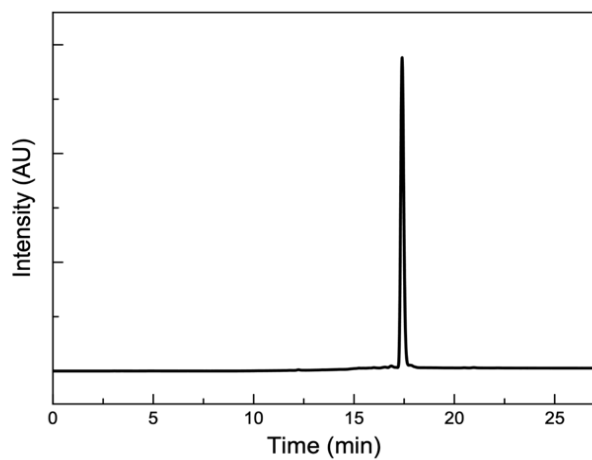


Figure S5.31. HPLC chromatogram of **TRIP-3a**.

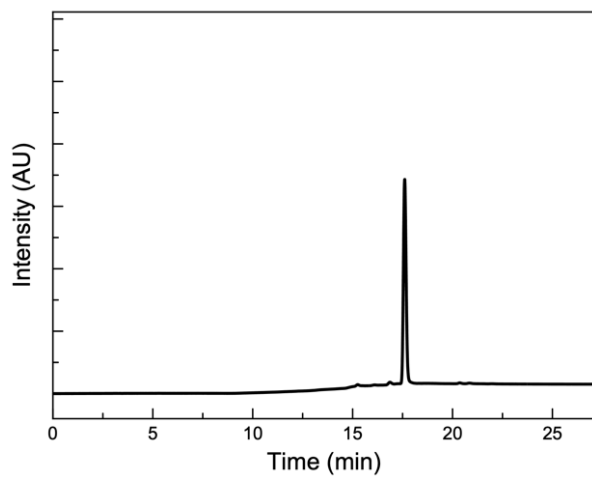


Figure S5.32. HPLC chromatogram of **TRIP-4a**.

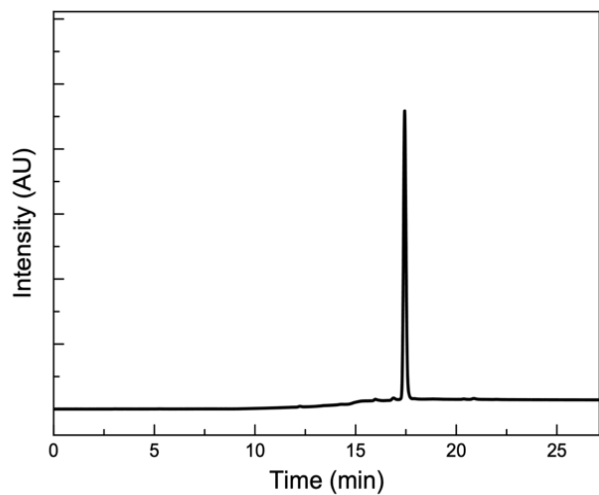


Figure S5.33. HPLC chromatogram of **TRIP-5a**.

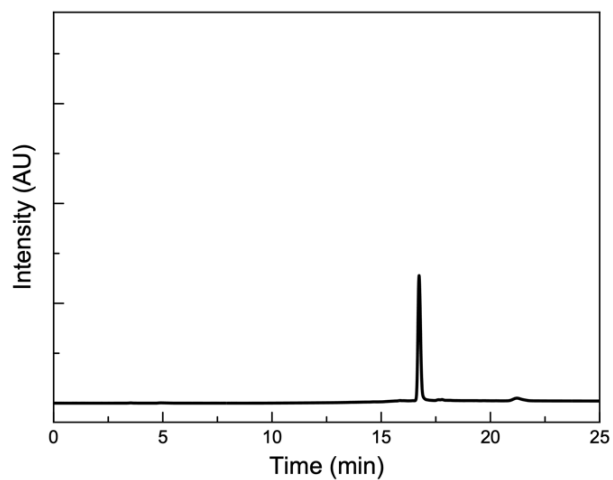


Figure S5.34. HPLC chromatogram of **TRIP-6a**.

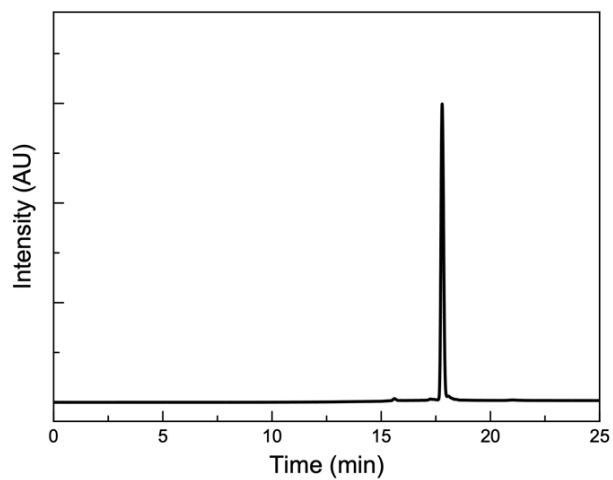


Figure S5.35. HPLC chromatogram of **TRIP-7a**.

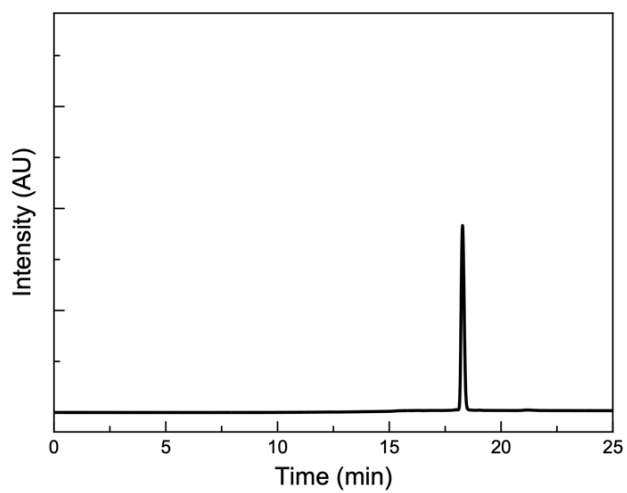


Figure S5.36. HPLC chromatogram of **TRIP-1b**.

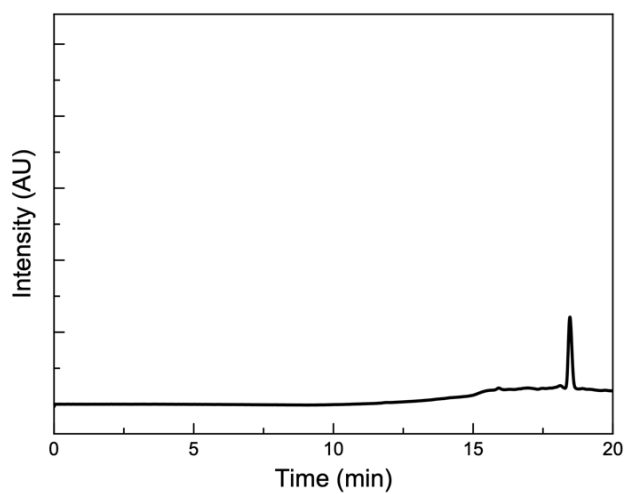


Figure S5.37. HPLC chromatogram of **TRIP-1c**.

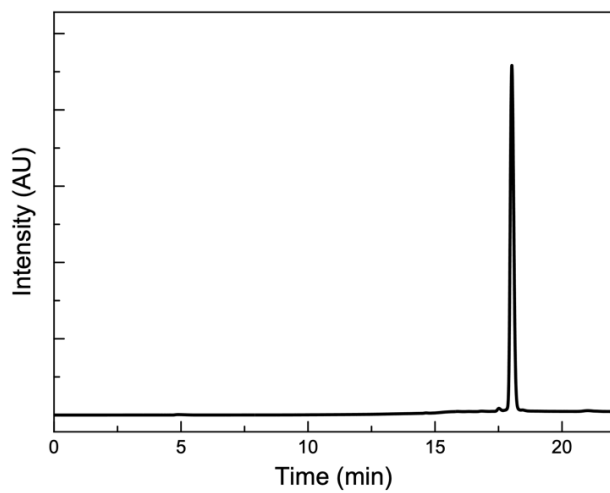


Figure S5.38. HPLC chromatogram of **TRIP-1d**.

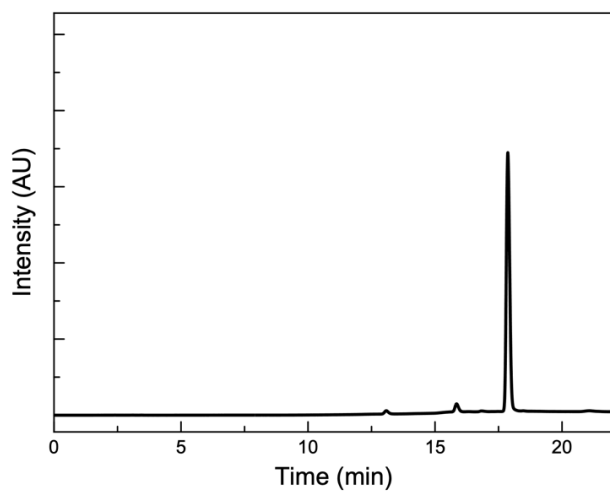


Figure S5.39. HPLC chromatogram of **TRIP-1e**.

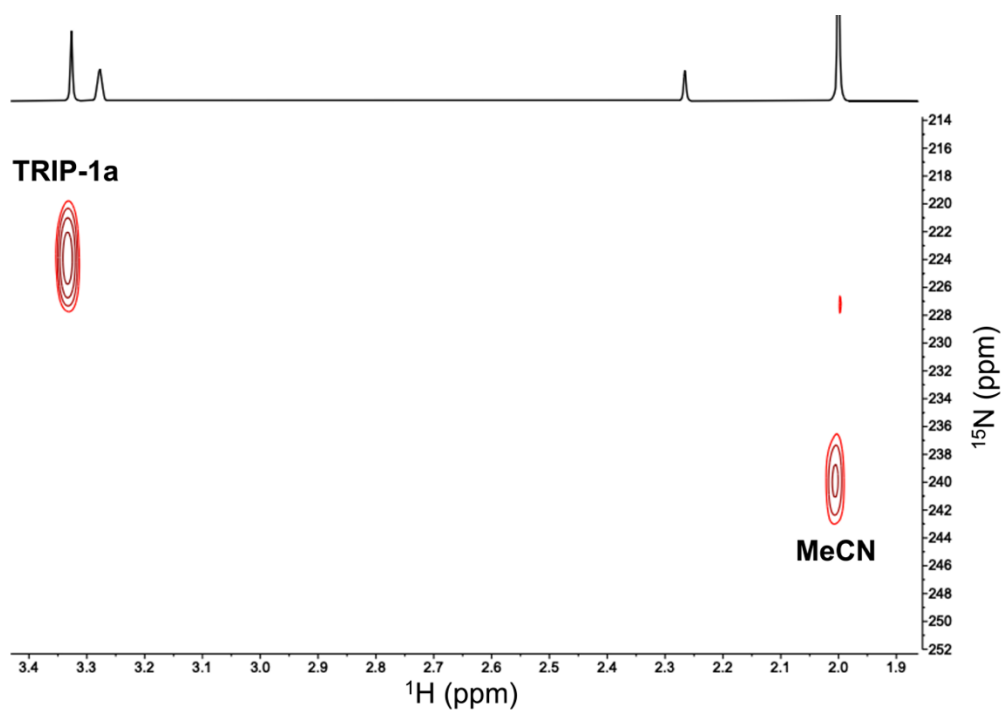


Figure S5.40. ¹⁵N HMBC NMR spectrum (f1 = 600 MHz, f2 = 61 MHz) of **TRIP-1a** (CD₃OD) at 25 °C, referenced to internal standard MeCN at 240 ppm vs liquid NH₃ at 0 ppm.

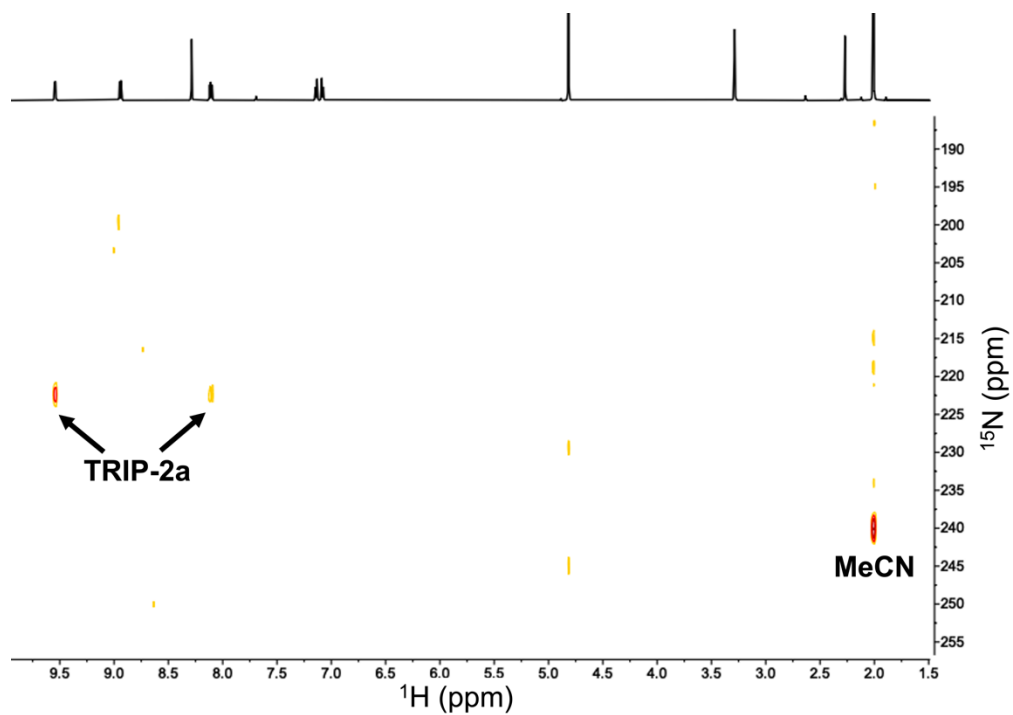


Figure S5.41. ^{15}N HMBC NMR spectrum (f1 = 600 MHz, f2 = 61 MHz) of **TRIP-2a** (CD_3OD) at 25 $^\circ\text{C}$, referenced to internal standard MeCN at 240 ppm vs liquid NH_3 at 0 ppm.

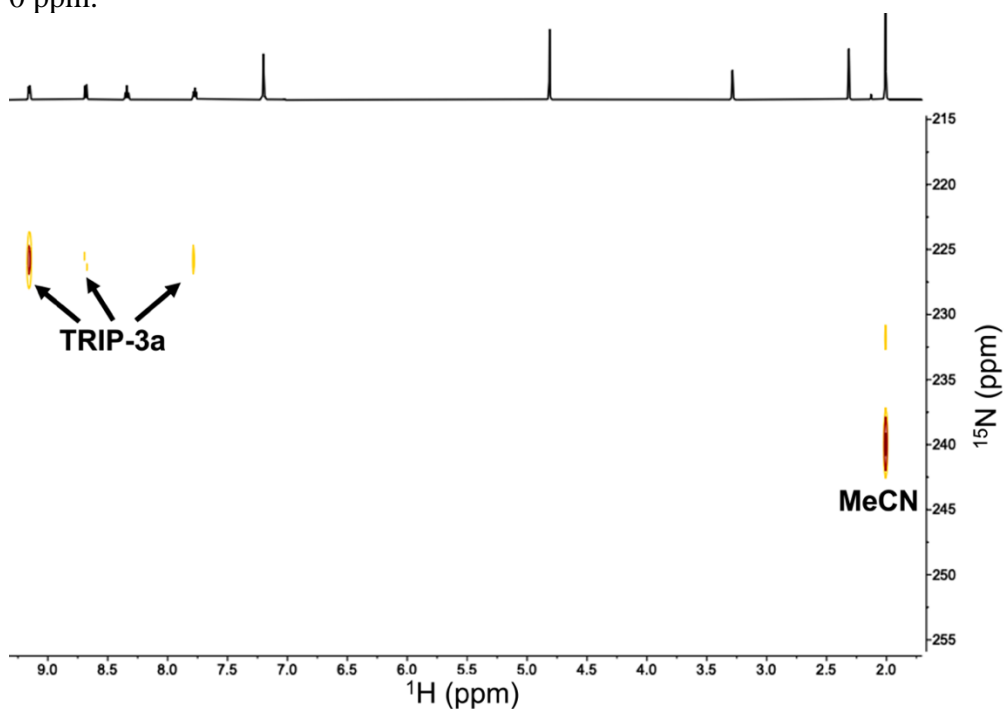


Figure S5.42. ^{15}N HMBC NMR spectrum (f1 = 600 MHz, f2 = 61 MHz) of **TRIP-3a** (CD_3OD) at 25 $^\circ\text{C}$, referenced to internal standard MeCN at 240 ppm vs liquid NH_3 at 0 ppm.

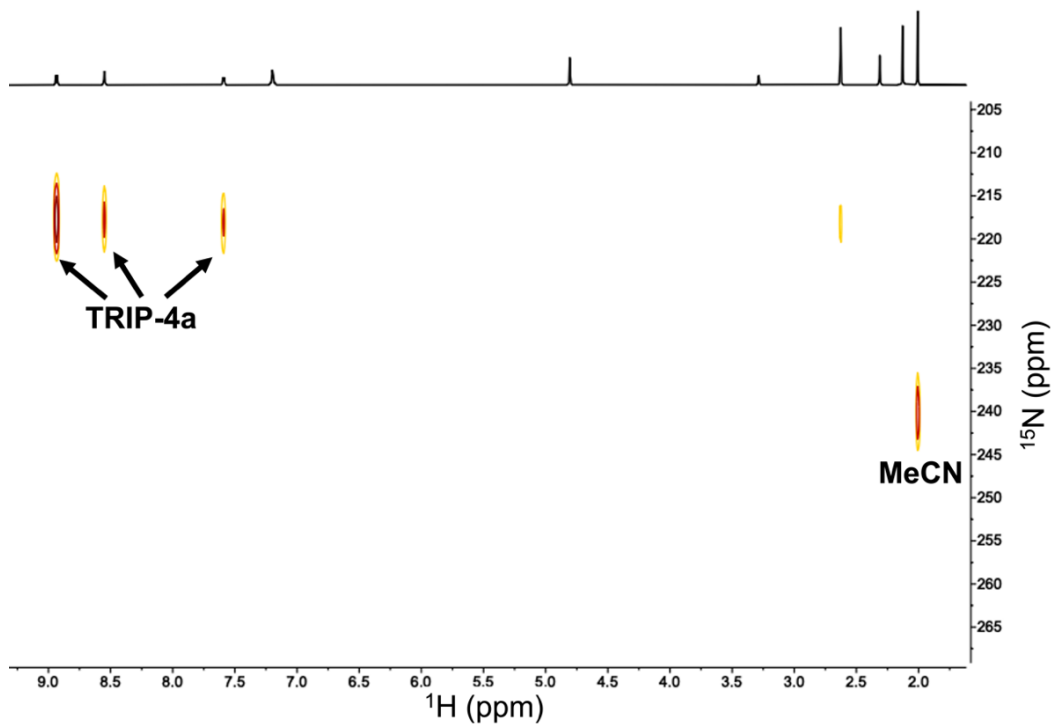


Figure S5.43. ^{15}N HMBC NMR spectrum (f1 = 600 MHz, f2 = 61 MHz) of **TRIP-4a** (CD_3OD) at 25 $^\circ\text{C}$, referenced to internal standard MeCN at 240 ppm vs liquid NH_3 at 0 ppm.

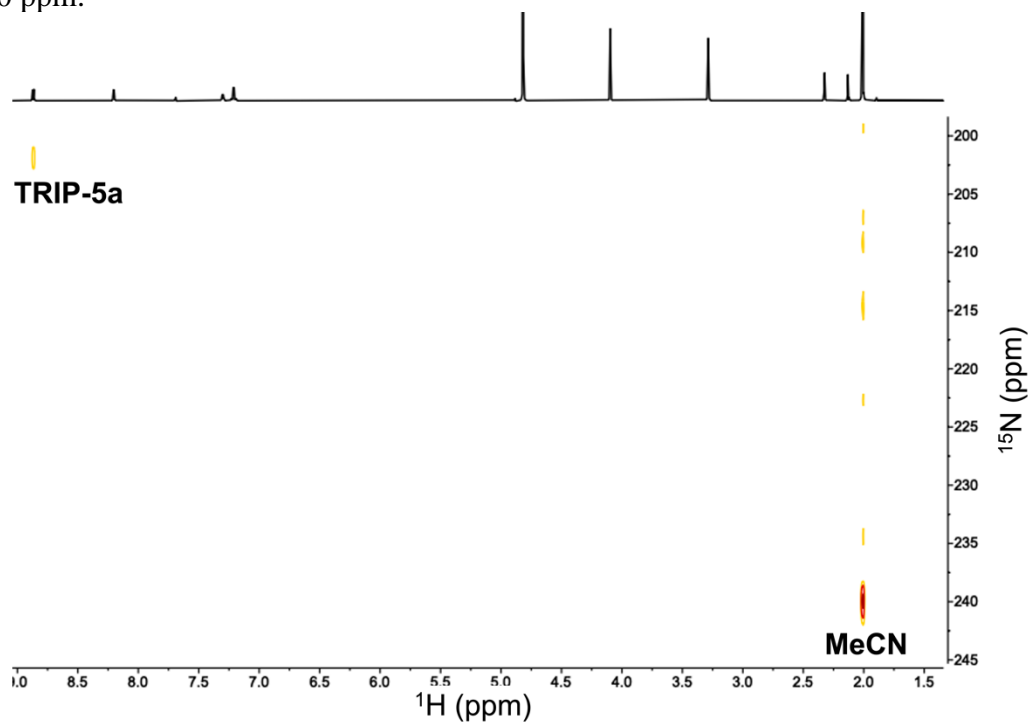


Figure S5.44. ^{15}N HMBC NMR spectrum (f1 = 600 MHz, f2 = 61 MHz) of **TRIP-5a** (CD_3OD) at 25 $^\circ\text{C}$, referenced to internal standard MeCN at 240 ppm vs liquid NH_3 at 0 ppm.

0 ppm.

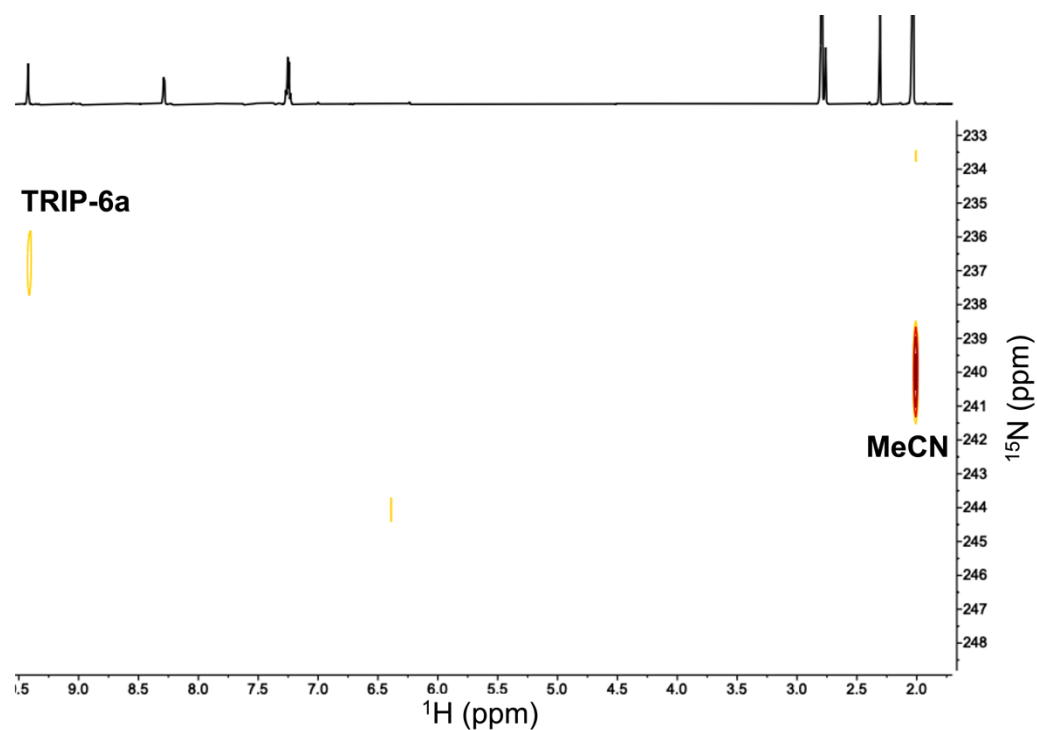


Figure S5.45. ^{15}N HMBC NMR spectrum (f1 = 600 MHz, f2 = 61 MHz) of **TRIP-6a** (CD_3OD) at 25 °C, referenced to internal standard MeCN at 240 ppm vs liquid NH_3 at 0 ppm.

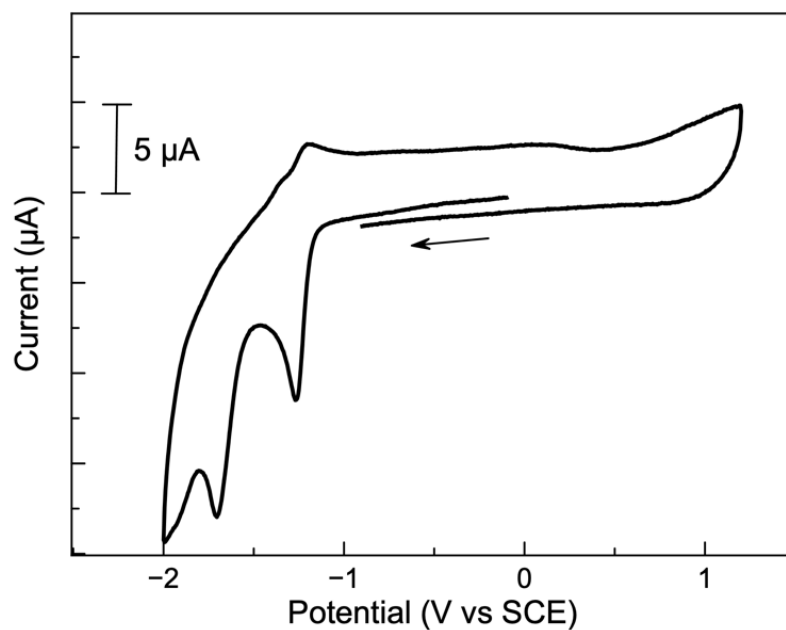


Figure S5.46. Cyclic voltammogram of **TRIP-1a** in MeCN with 0.1 M TBAP at 25

°C and 0.1 V/s scan rate.

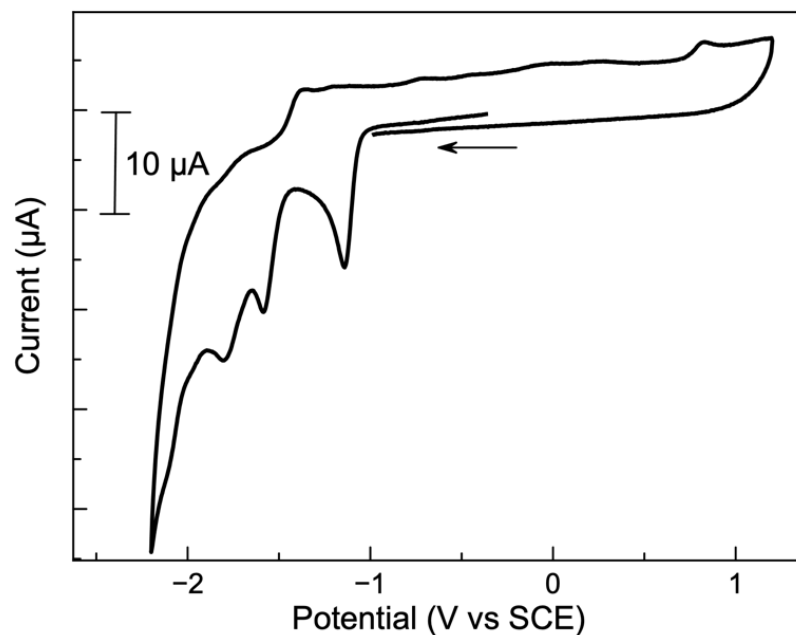


Figure S5.47. Cyclic voltammogram of **TRIP-2a** in MeCN with 0.1 M TBAP at 25 °C and 0.1 V/s scan rate.

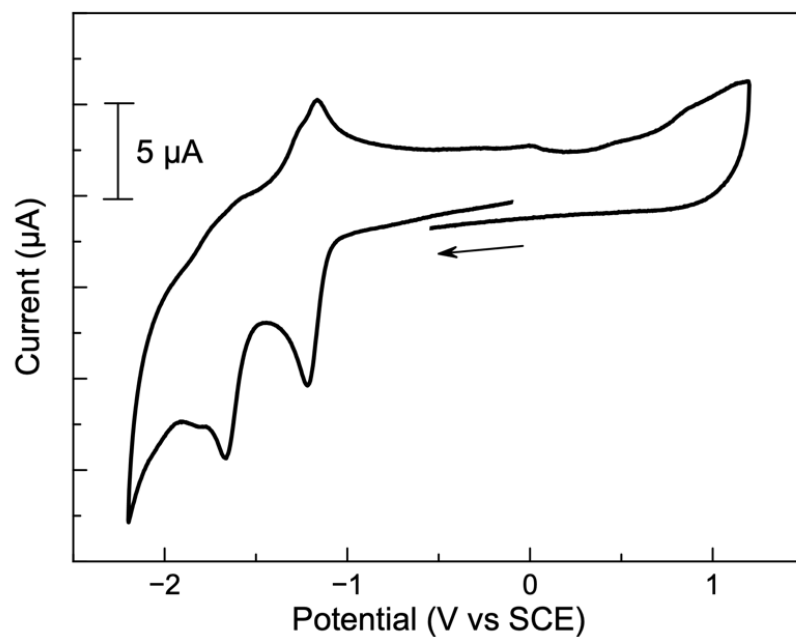


Figure S5.48. Cyclic voltammogram of **TRIP-3a** in MeCN with 0.1 M TBAP at 25 °C and 0.1 V/s scan rate.

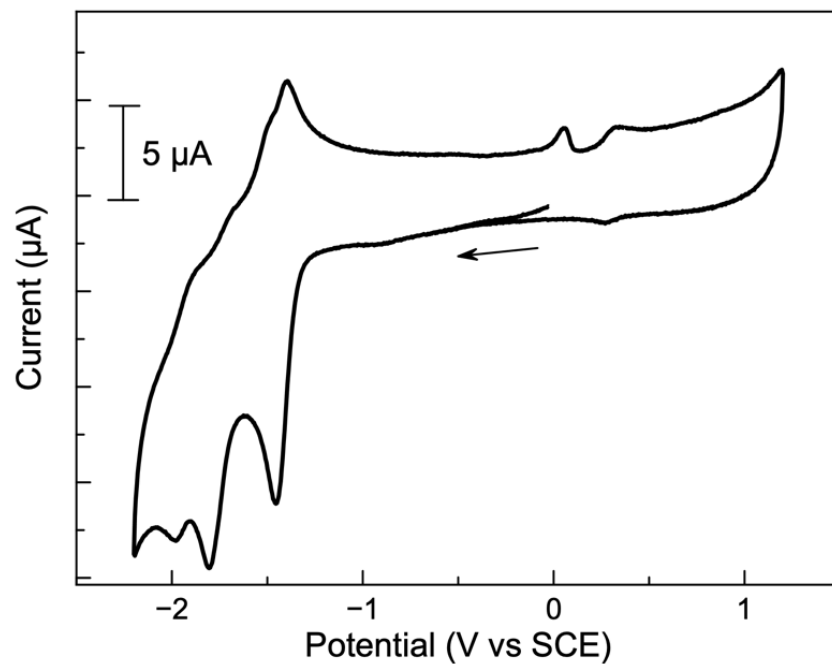


Figure S5.49. Cyclic voltammogram of **TRIP-4a** in MeCN with 0.1 M TBAP at 25 °C and 0.1 V/s scan rate.

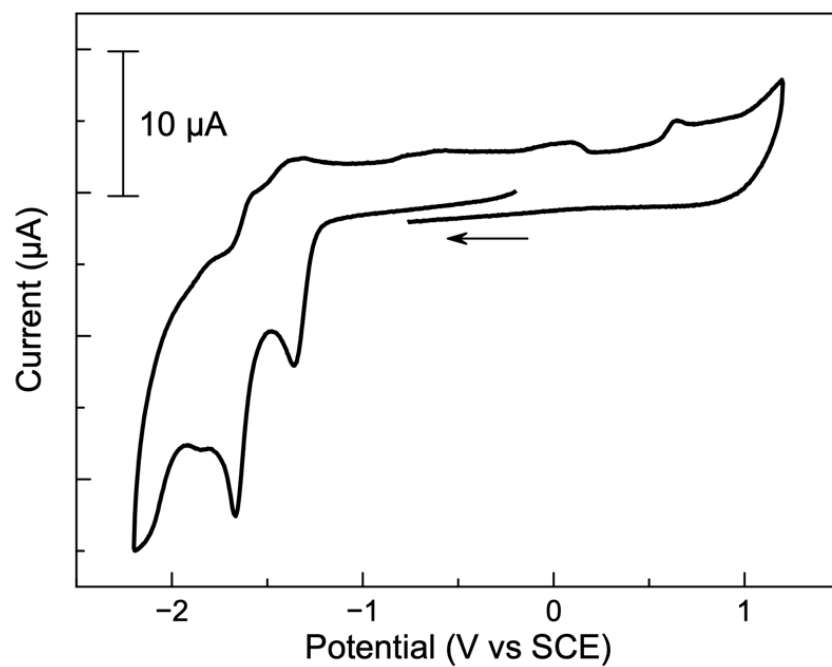


Figure S5.50. Cyclic voltammogram of **TRIP-5a** in MeCN with 0.1 M TBAP at 25 °C and 0.1 V/s scan rate.

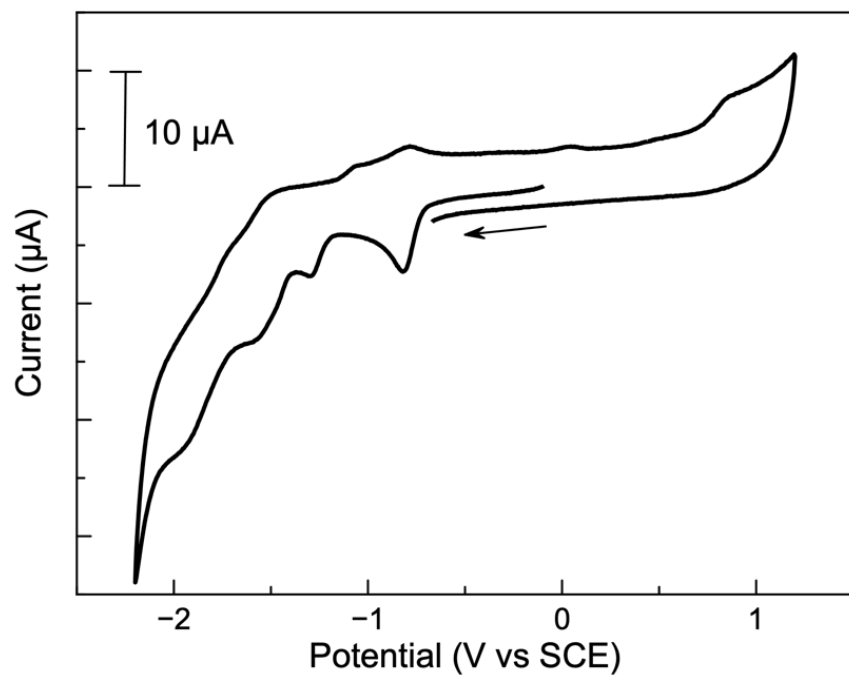


Figure S5.51. Cyclic voltammogram of **TRIP-6a** in MeCN with 0.1 M TBAP at 25 °C and 0.1 V/s scan rate.

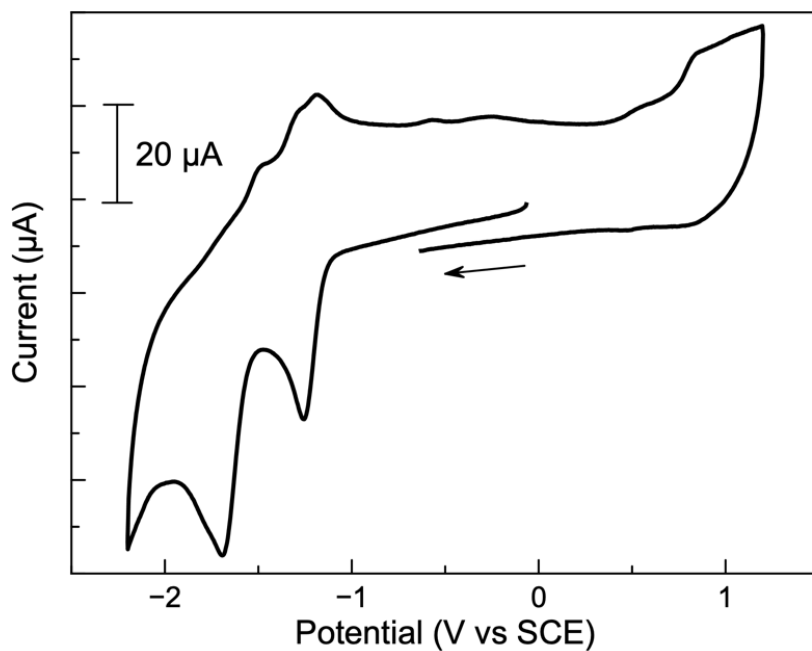


Figure S5.52. Cyclic voltammogram of **TRIP-7a** in MeCN with 0.1 M TBAP at 25 °C and 0.1 V/s scan rate.

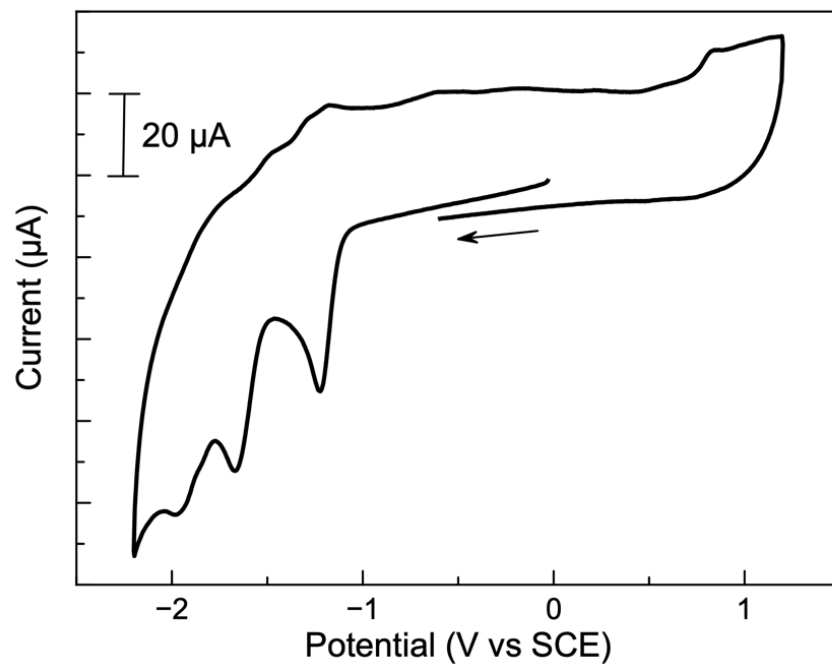


Figure S5.53. Cyclic voltammogram of **TRIP-1b** in MeCN with 0.1 M TBAP at 25 °C and 0.1 V/s scan rate.

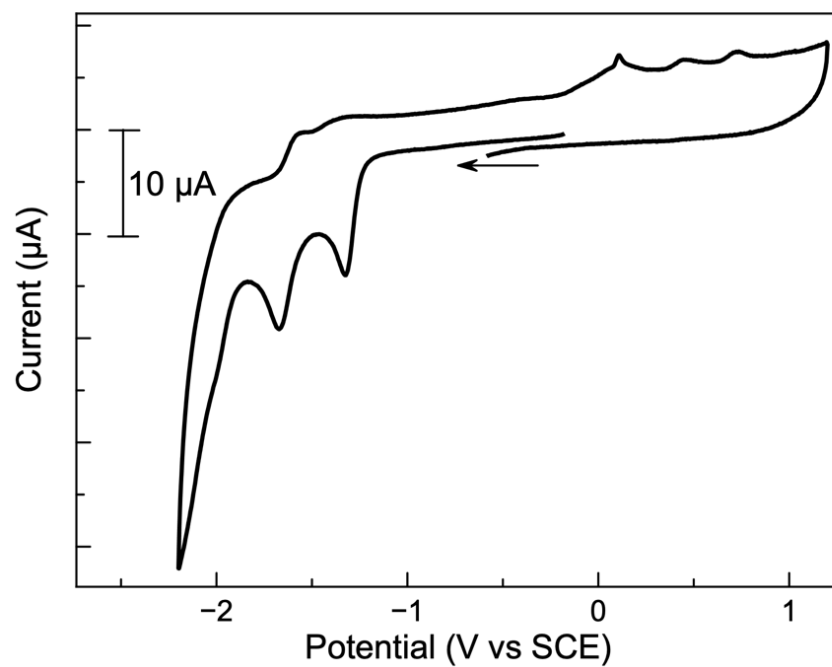


Figure S5.54. Cyclic voltammogram of **TRIP-1c** in MeCN with 0.1 M TBAP at 25 °C and 0.1 V/s scan rate.

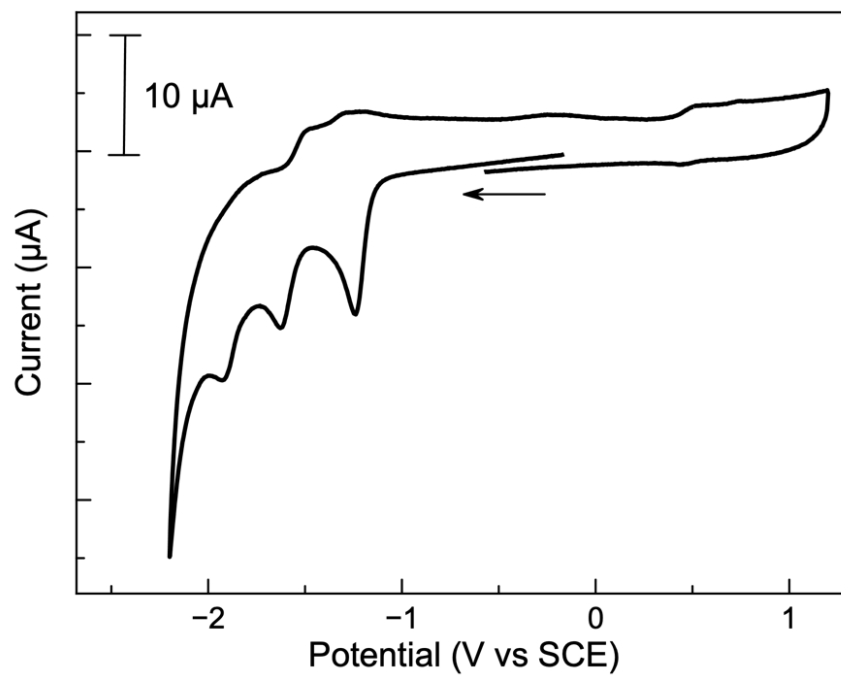


Figure S5.55. Cyclic voltammogram of **TRIP-1d** in MeCN with 0.1 M TBAP at 25 °C and 0.1 V/s scan rate.

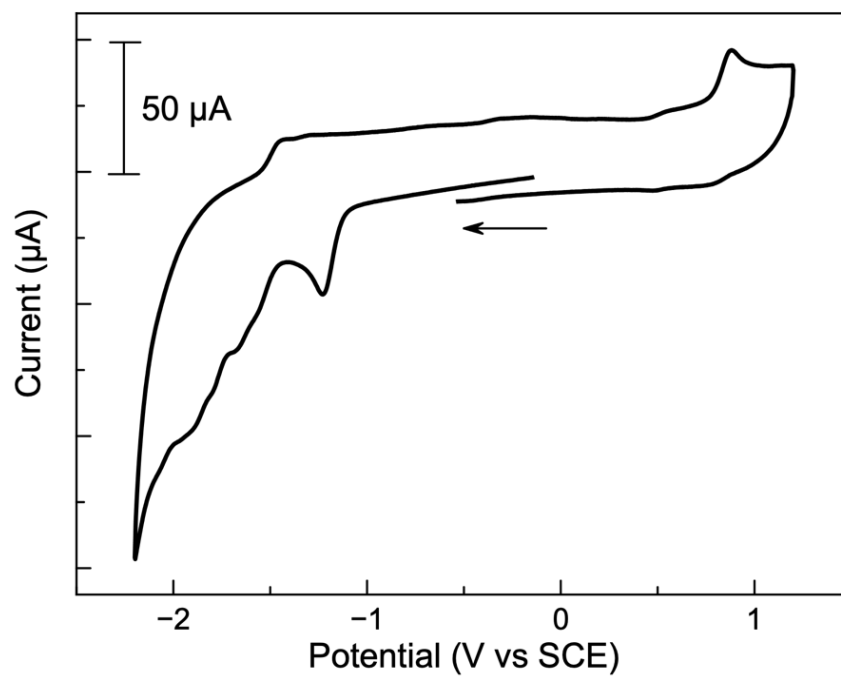


Figure S5.56. Cyclic voltammogram of **TRIP-1e** in MeCN with 0.1 M TBAP at 25 °C and 0.1 V/s scan rate.

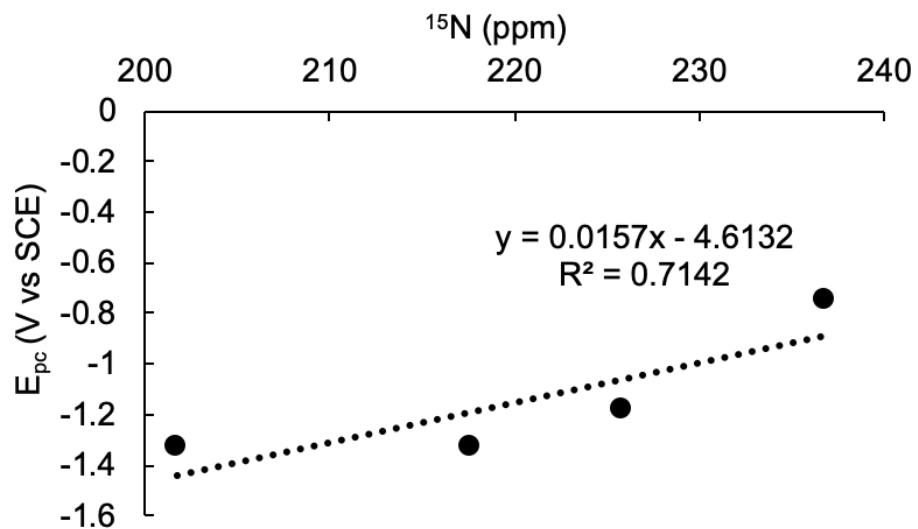


Figure S5.57. Scatter plot of ^{15}N chemical shifts (ppm) vs the first reduction potential (E_{pc} , V) of **TRIP-3a**, **TRIP-4a**, **TRIP-5a**, and **TRIP-6a**.

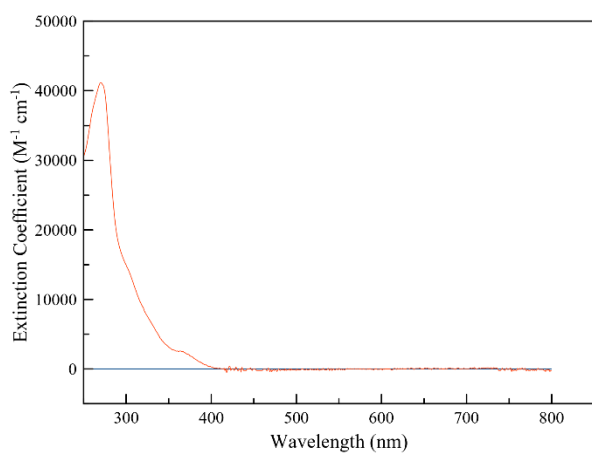


Figure S5.58. UV-vis absorption spectrum of **TRIP-2a** (15 μM) in PBS (pH 7.4) with $\leq 1\%$ DMSO at 25 $^{\circ}\text{C}$.

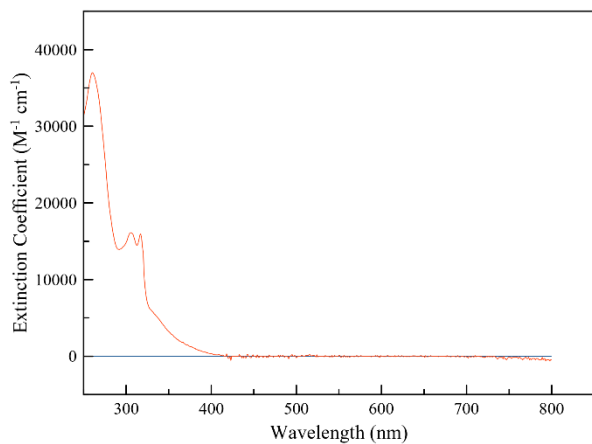


Figure S5.59. UV-vis absorption spectrum of **TRIP-3a** (15 μM) in PBS (pH 7.4) and $\leq 1\%$ DMSO at 25 $^{\circ}\text{C}$.

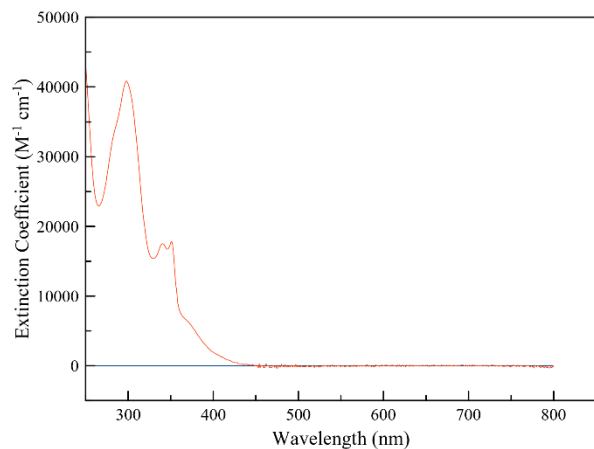


Figure S5.60. UV-vis absorption spectrum of **TRIP-4a** (15 μM) in PBS (pH 7.4) and $\leq 1\%$ DMSO at 25 $^{\circ}\text{C}$.

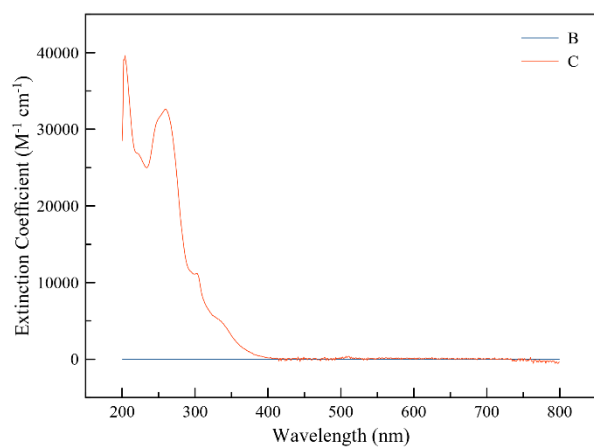


Figure S5.61. UV-vis absorption spectrum of **TRIP-5a** (15 μM) in PBS (pH 7.4) and $\leq 1\%$ DMSO at 25 $^{\circ}\text{C}$.

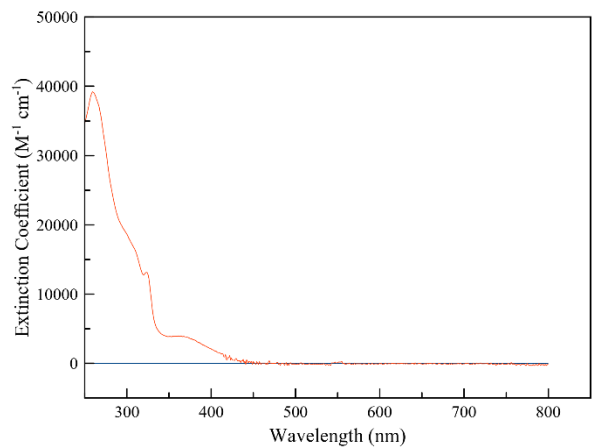


Figure S5.62. UV-vis absorption spectrum of **TRIP-6a** (15 μM) in PBS (pH 7.4) and $\leq 1\%$ DMSO at 25 $^{\circ}\text{C}$.

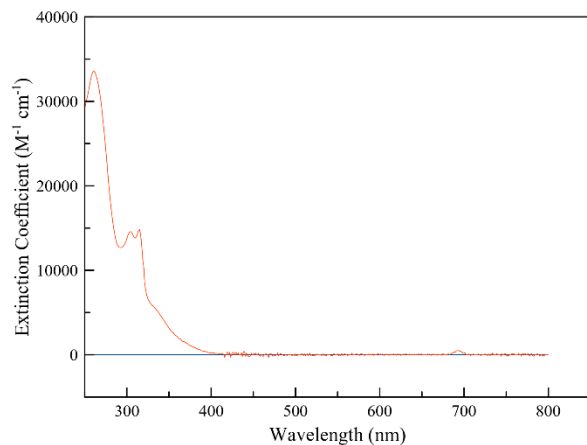


Figure S5.63. UV-vis absorption spectrum of **TRIP-7a** (15 μM) in PBS (pH 7.4) and $\leq 1\%$ DMSO at 25 $^{\circ}\text{C}$.

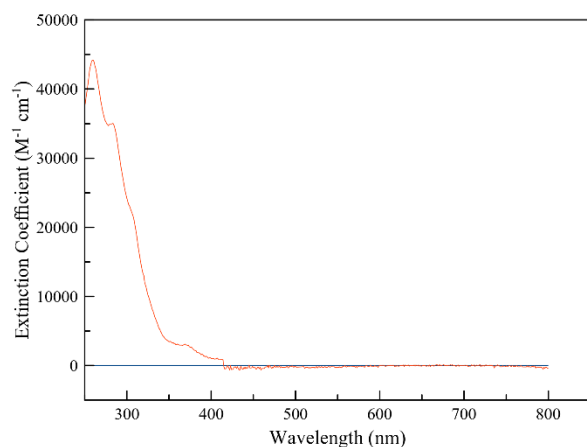


Figure S5.64. UV-vis absorption spectrum of **TRIP-1b** (15 μM) in PBS (pH 7.4) and $\leq 1\%$ DMSO at 25 $^{\circ}\text{C}$.

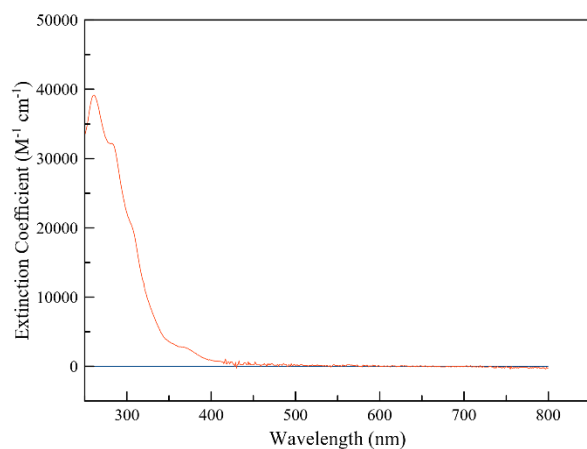


Figure S5.65. UV-vis absorption spectrum of **TRIP-1c** (15 μM) in PBS (pH 7.4) and $\leq 1\%$ DMSO at 25 $^{\circ}\text{C}$.

$\leq 1\%$ DMSO at 25 °C.

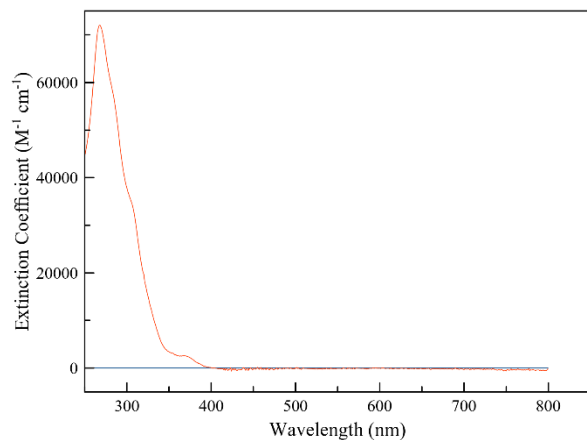


Figure S5.66. UV-vis absorption spectrum of **TRIP-1d** (15 μM) in PBS (pH 7.4) and $\leq 1\%$ DMSO at 25 °C.

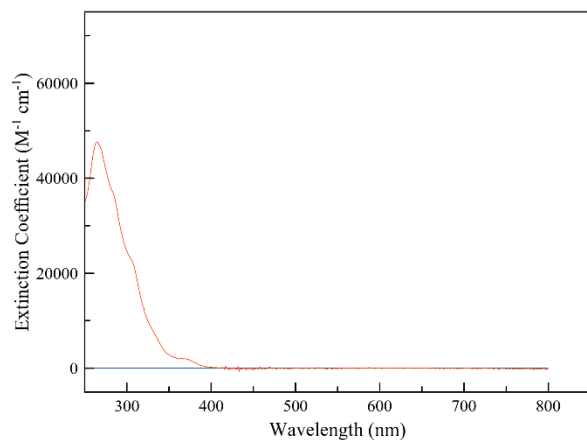


Figure S5.67. UV-vis absorption spectrum of **TRIP-1e** (15 μM) in PBS (pH 7.4) and $\leq 1\%$ DMSO at 25 °C.

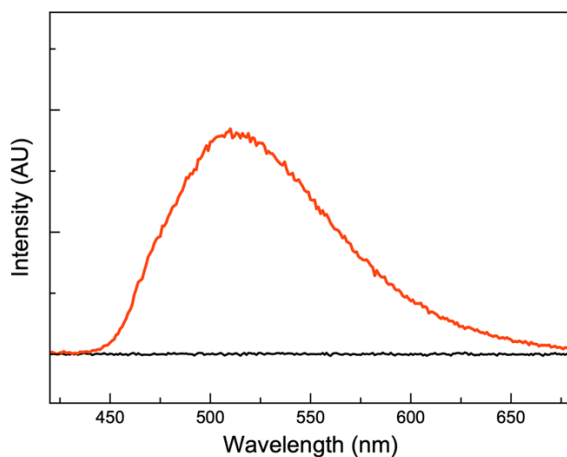


Figure S5.68. Emission spectrum of **TRIP-2a** (15 μM) in PBS (pH 7.4) and $\leq 1\%$

DMSO at 25 °C. Excitation wavelength: 350 nm.

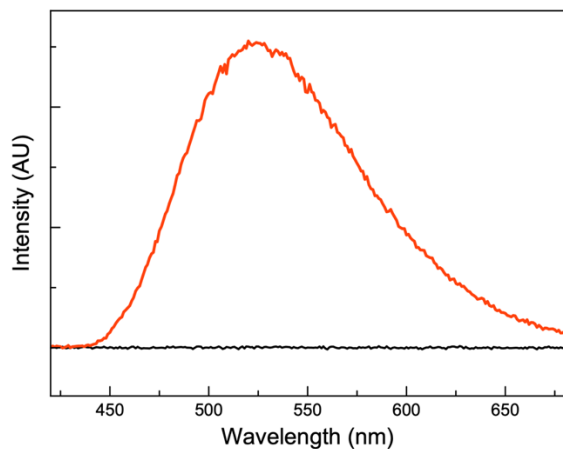


Figure S5.69. Emission spectrum of **TRIP-3a** (15 μM) in PBS (pH 7.4) and $\leq 1\%$ DMSO at 25 °C. Excitation wavelength: 350 nm.

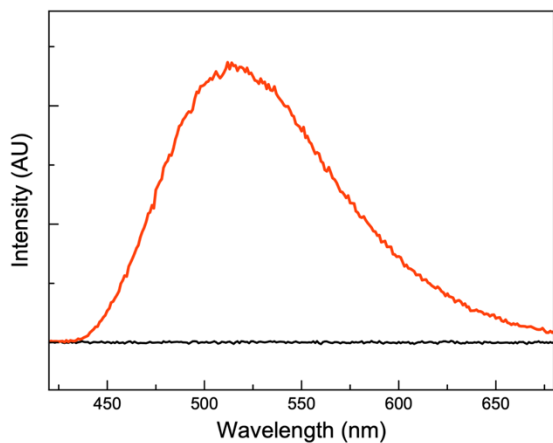


Figure S5.70. Emission spectrum of **TRIP-4a** (15 μM) in PBS (pH 7.4) and $\leq 1\%$ DMSO at 25 °C. Excitation wavelength: 350 nm.

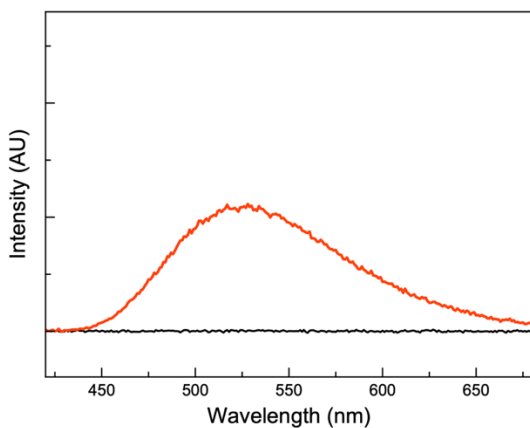


Figure S5.71. Emission spectrum of **TRIP-5a** (15 μM) in PBS (pH 7.4) and $\leq 1\%$ DMSO at 25 °C. Excitation wavelength: 350 nm.

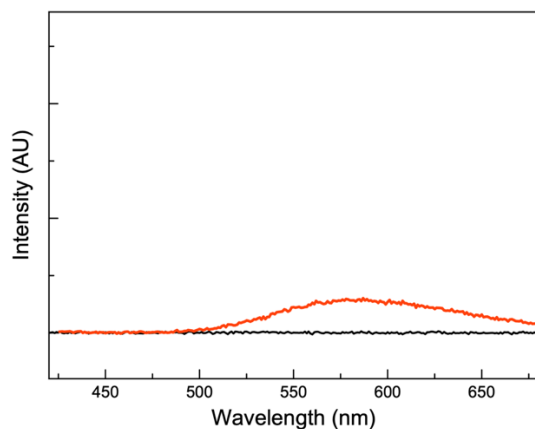


Figure S5.72. Emission spectrum of **TRIP-6a** (15 μM) in PBS (pH 7.4) and $\leq 1\%$ DMSO at 25 $^{\circ}\text{C}$. Excitation wavelength: 350 nm.

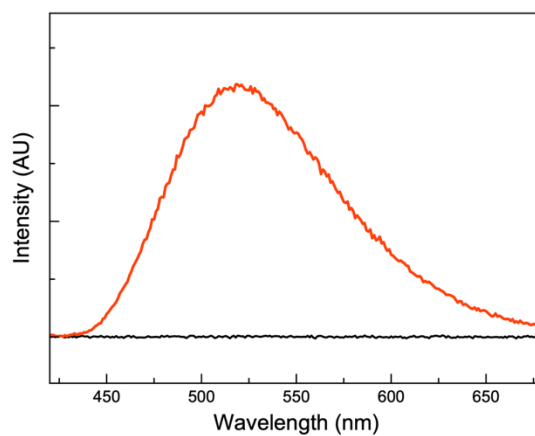


Figure S5.73. Emission spectrum of **TRIP-7a** (15 μM) in PBS (pH 7.4) and $\leq 1\%$ DMSO at 25 $^{\circ}\text{C}$. Excitation wavelength: 350 nm.

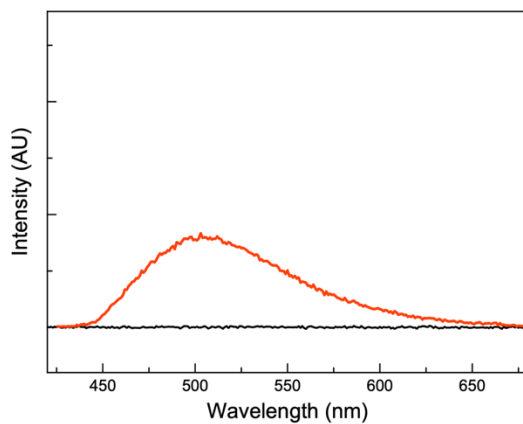


Figure S5.74. Emission spectrum of **TRIP-1b** (15 μM) in PBS (pH 7.4) and $\leq 1\%$ DMSO at 25 $^{\circ}\text{C}$. Excitation wavelength: 350 nm.

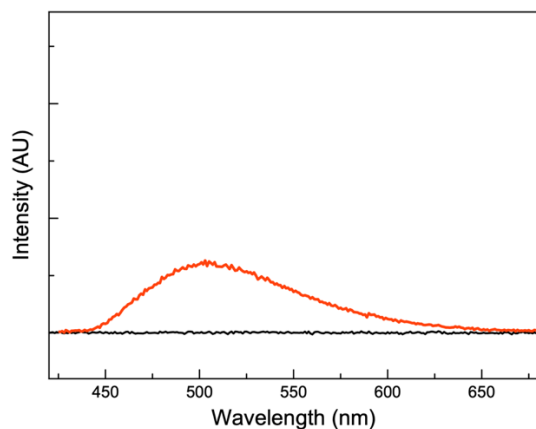


Figure S5.75. Emission spectrum of **TRIP-1c** (15 μM) in PBS (pH 7.4) and $\leq 1\%$ DMSO at 25 $^{\circ}\text{C}$. Excitation wavelength: 350 nm.

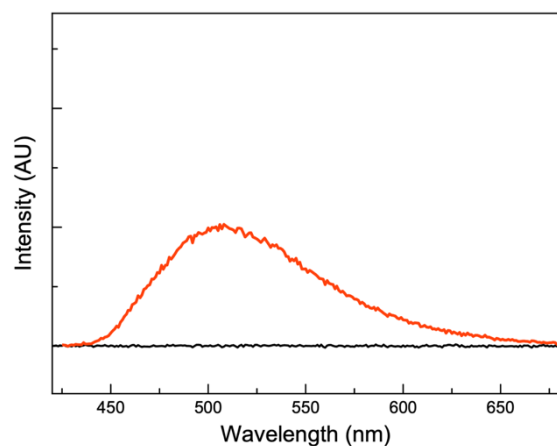


Figure S5.76. Emission spectrum of **TRIP-1d** (15 μM) in PBS (pH 7.4) and $\leq 1\%$ DMSO at 25 $^{\circ}\text{C}$. Excitation wavelength: 350 nm.

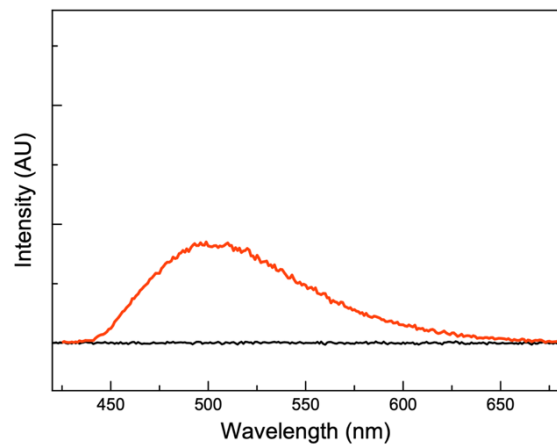


Figure S5.77. Emission spectrum **TRIP-1e** (15 μM) in PBS (pH 7.4) and $\leq 1\%$ DMSO at 25 $^{\circ}\text{C}$. Excitation wavelength: 350 nm.

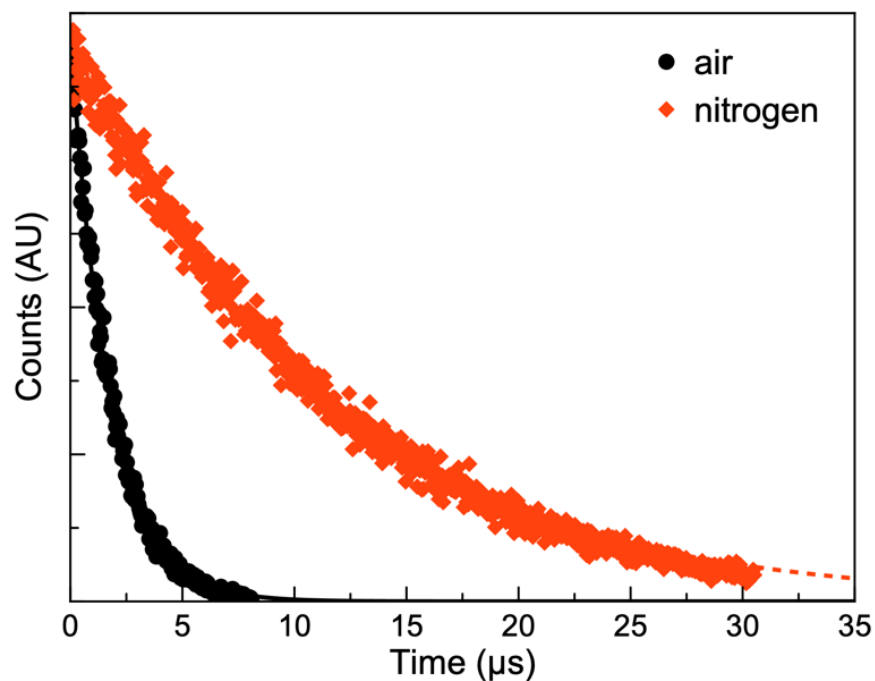


Figure S5.78. Transient emission decay profile of **TRIP-2a** (10 μM) in PBS (pH 7.4) at 25 $^{\circ}\text{C}$ under ambient conditions (black, fit = solid line) and under nitrogen (red, fit = dashed line). Excitation wavelength: (405 nm).

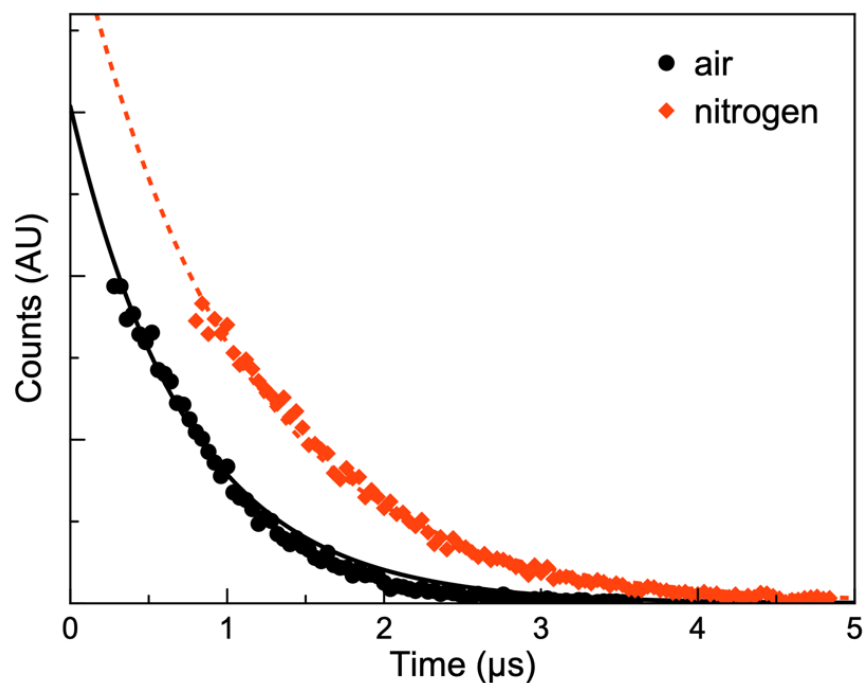


Figure S5.79. Transient emission decay profile of **TRIP-3a** (10 μM) in PBS (pH 7.4) at 25 $^{\circ}\text{C}$ under ambient conditions (black, fit = solid line) and under nitrogen (red, fit =

dashed line). Excitation wavelength: (405 nm).

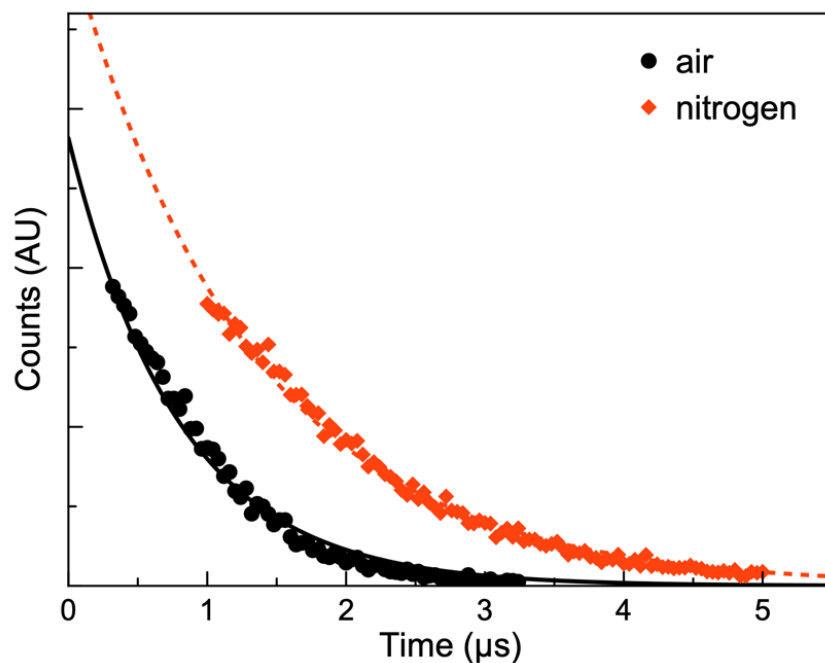


Figure S5.80. Transient emission decay profile of **TRIP-4a** (10 μM) in PBS (pH 7.4) at 25 °C under ambient conditions (black, fit = solid line) and under nitrogen (red, fit = dashed line). Excitation wavelength: (405 nm).

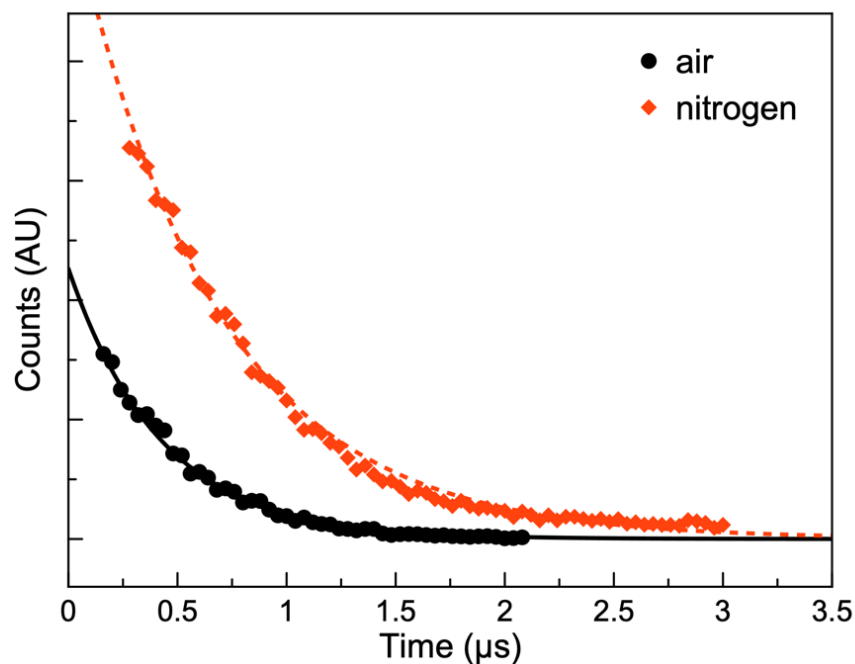


Figure S5.81. Transient emission decay profile of **TRIP-5a** (10 μM) in PBS (pH 7.4) at 25 °C under ambient conditions (black, fit = solid line) and under nitrogen (red, fit =

dashed line). Excitation wavelength: (405 nm).

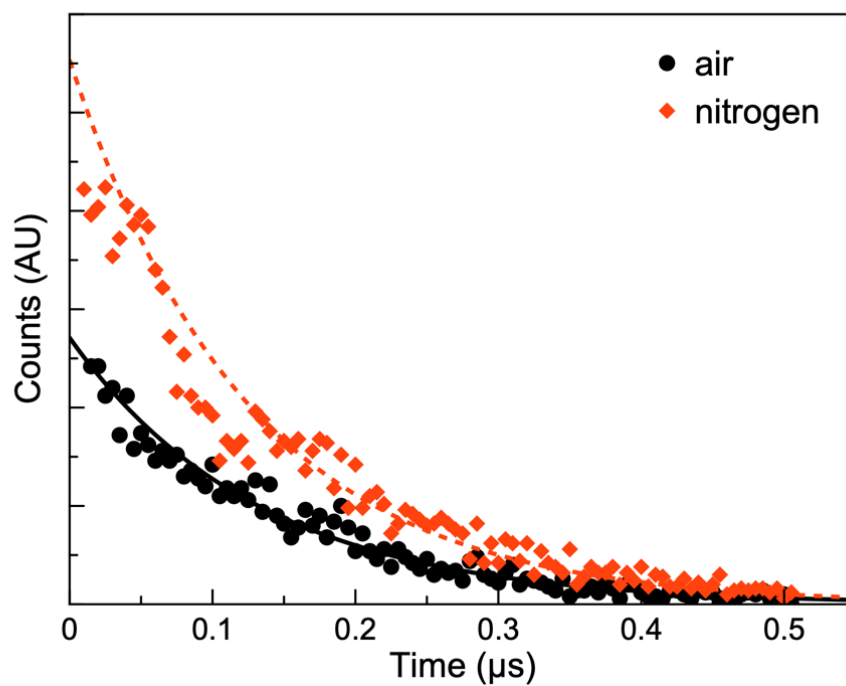


Figure S5.82. Transient emission decay profile of **TRIP-6a** (10 μM) in PBS (pH 7.4) at 25 °C under ambient conditions (black, fit = solid line) and under nitrogen (red, fit = dashed line). Excitation wavelength: (405 nm).

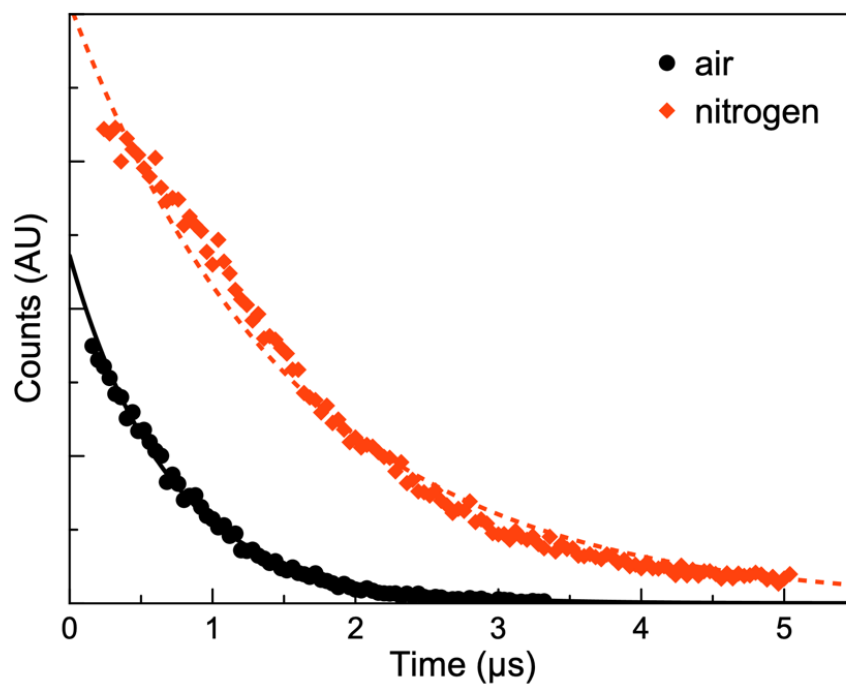


Figure S5.83. Transient emission decay profile of **TRIP-7a** (10 μM) in PBS (pH 7.4)

at 25 °C under ambient conditions (black, fit = solid line) and under nitrogen (red, fit = dashed line). Excitation wavelength: (405 nm).

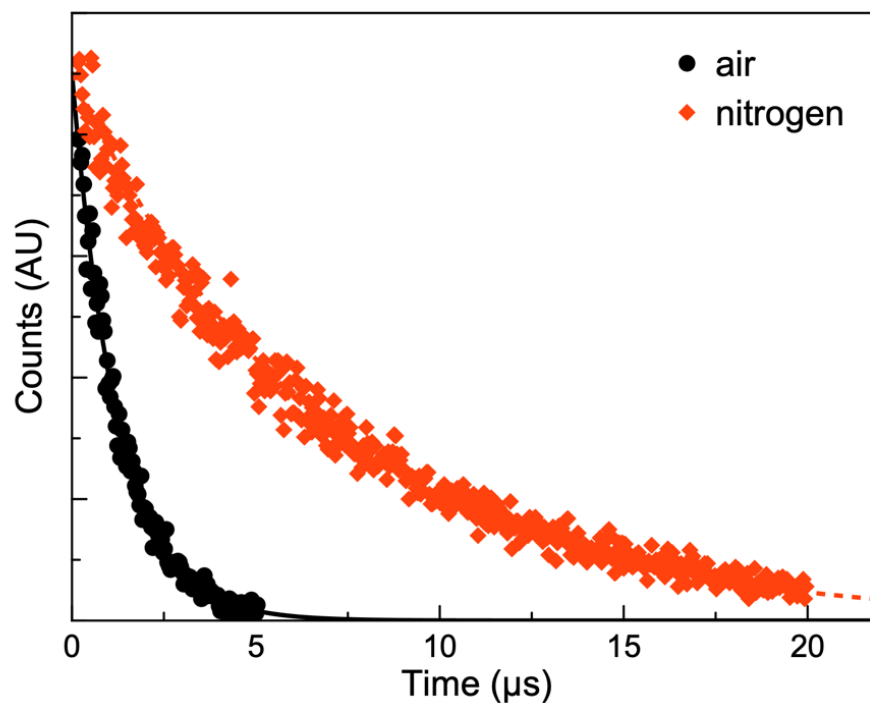


Figure S5.84. Transient emission decay profile of **TRIP-1b** (10 μM) in PBS (pH 7.4) at 25 °C under ambient conditions (black, fit = solid line) and under nitrogen (red, fit = dashed line). Excitation wavelength: (405 nm).

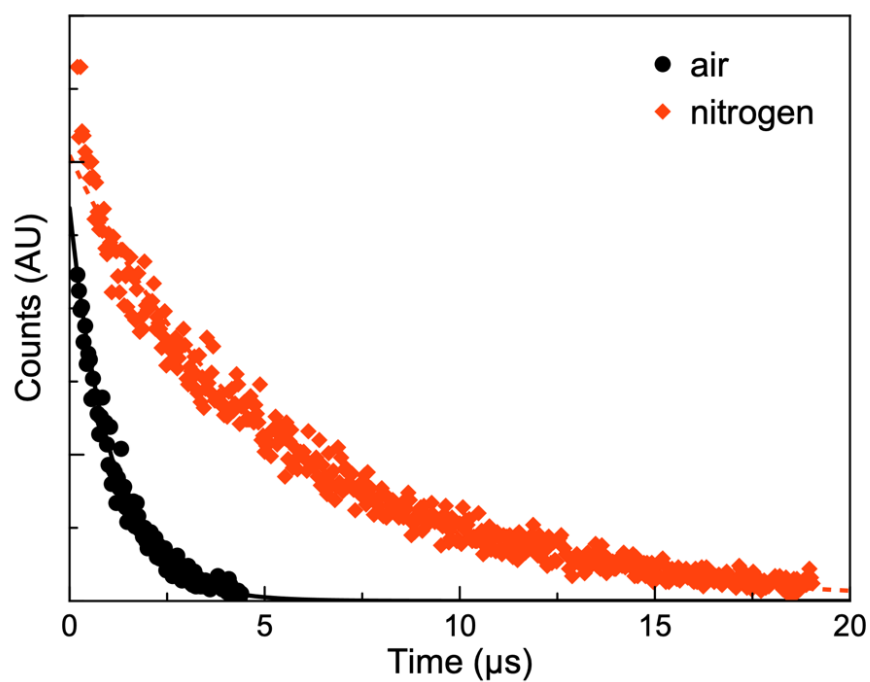


Figure S5.85. Transient emission decay profile of **TRIP-1c** (10 μM) in PBS (pH 7.4) at 25 $^{\circ}\text{C}$ under ambient conditions (black, fit = solid line) and under nitrogen (red, fit = dashed line). Excitation wavelength: (405 nm).

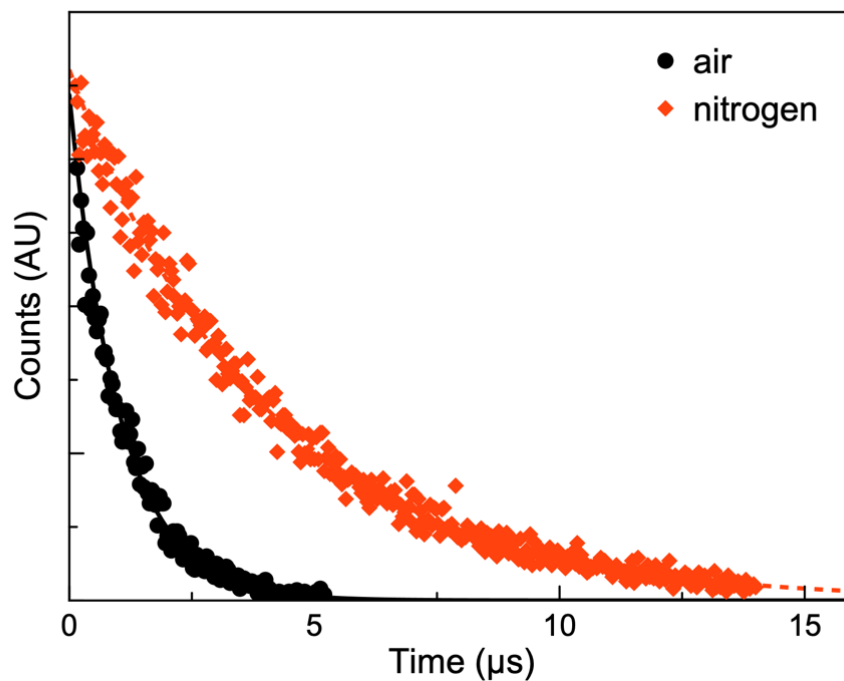


Figure S5.86. Transient emission decay profile of **TRIP-1d** (10 μM) in PBS (pH 7.4) at 25 $^{\circ}\text{C}$ under ambient conditions (black, fit = solid line) and under nitrogen (red, fit = dashed line). Excitation wavelength: (405 nm).

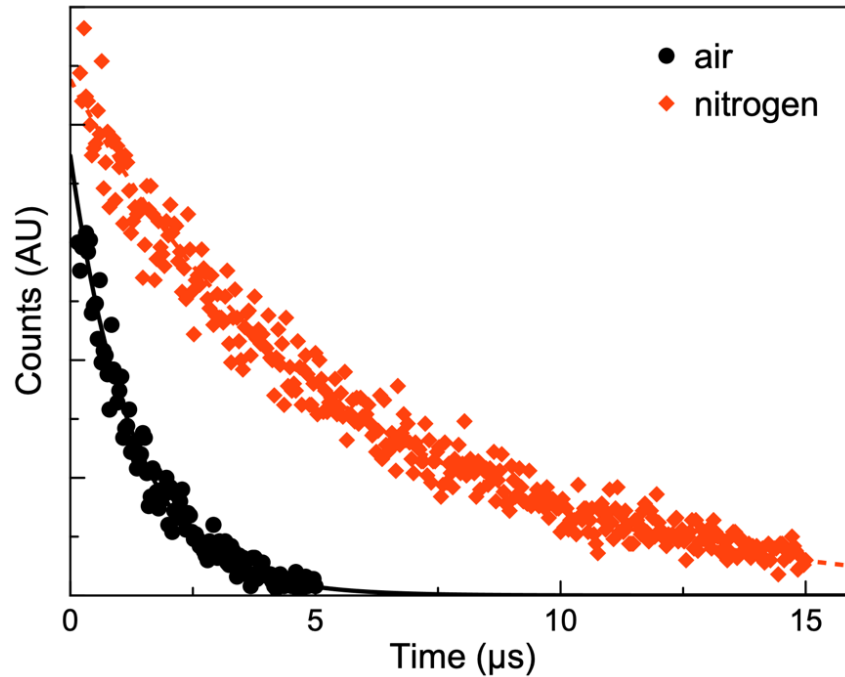


Figure S5.87. Transient emission decay profile of **TRIP-1e** (10 μM) in PBS (pH 7.4) at 25 $^{\circ}\text{C}$ under ambient conditions (black, fit = solid line) and under nitrogen (red, fit = dashed line). Excitation wavelength: (405 nm).

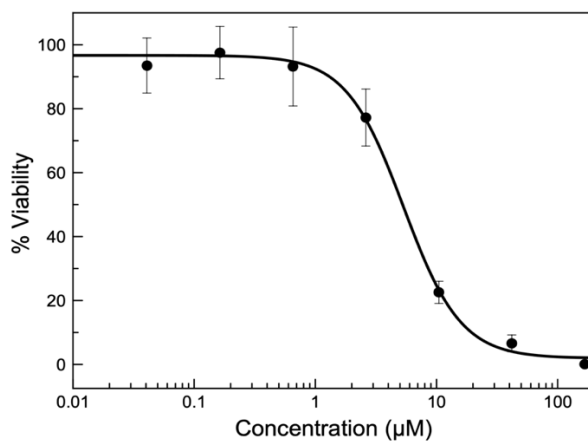


Figure S88. Dose-response curve for **TRIP-2a** in HeLa cells.

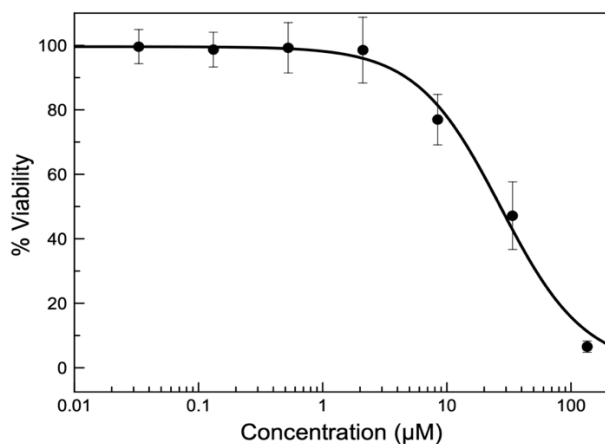


Figure S5.89. Dose-response curve for **TRIP-3a** in HeLa cells.

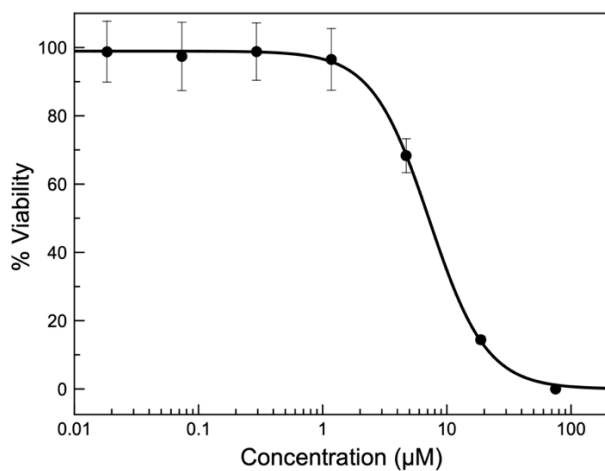


Figure S5.90. Dose-response curve for **TRIP-4a** in HeLa cells.

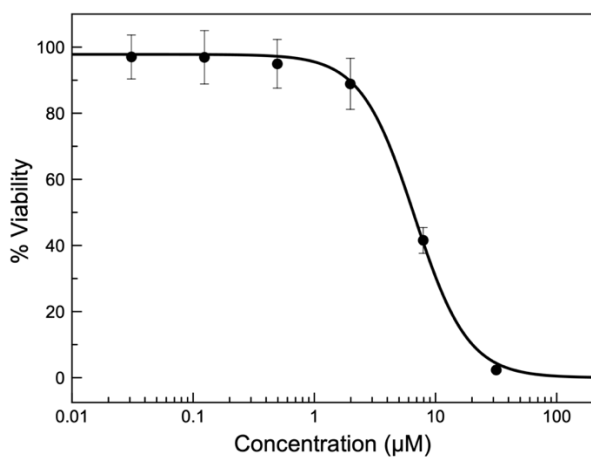


Figure S5.91. Dose-response curve for **TRIP-5a** in HeLa cells.

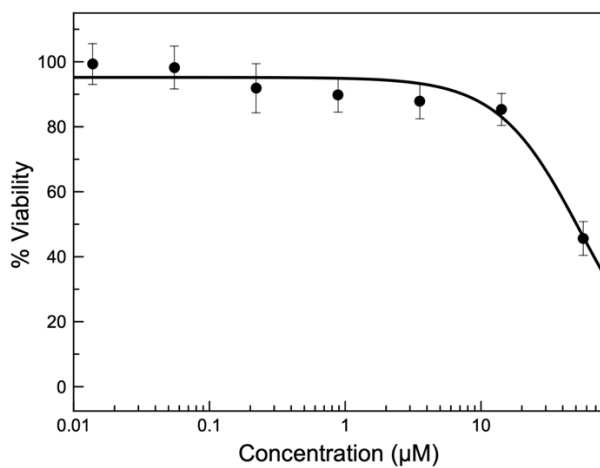


Figure S5.92. Dose-response curve for **TRIP-6a** in HeLa cells.

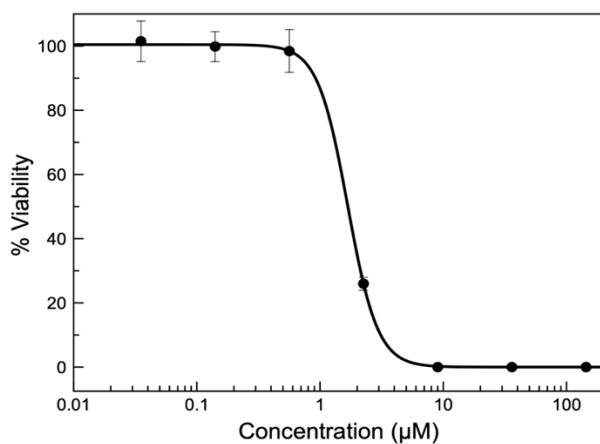


Figure S5.93. Dose-response curve for **TRIP-7a** in HeLa cells.

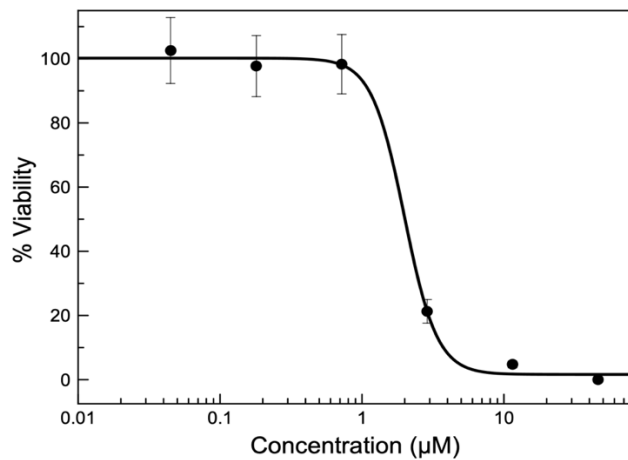


Figure S5.94. Dose-response curve for **TRIP-1b** in HeLa cells.

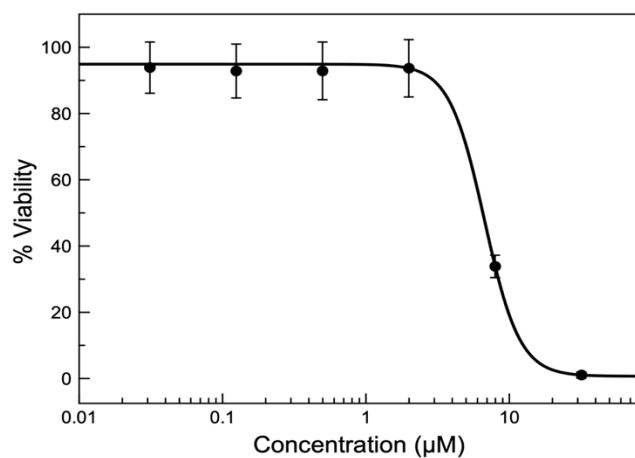


Figure S5.95. Dose-response curve for **TRIP-1c** in HeLa cells.

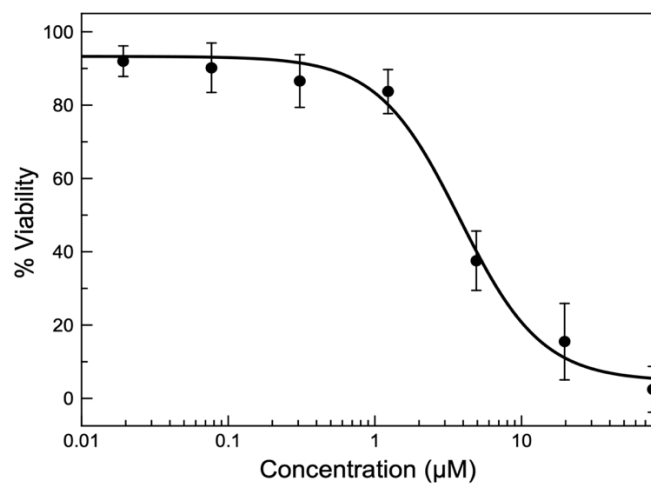


Figure S5.96. Dose-response curve for **TRIP-1d** in HeLa cells.

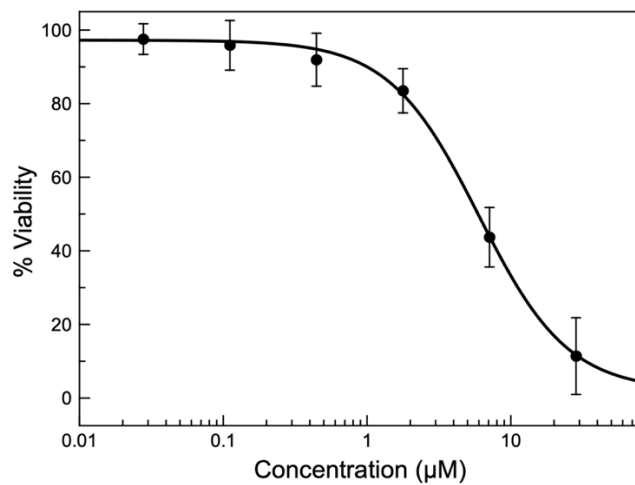


Figure S5.97. Dose-response curve for **TRIP-1e** in HeLa cells.

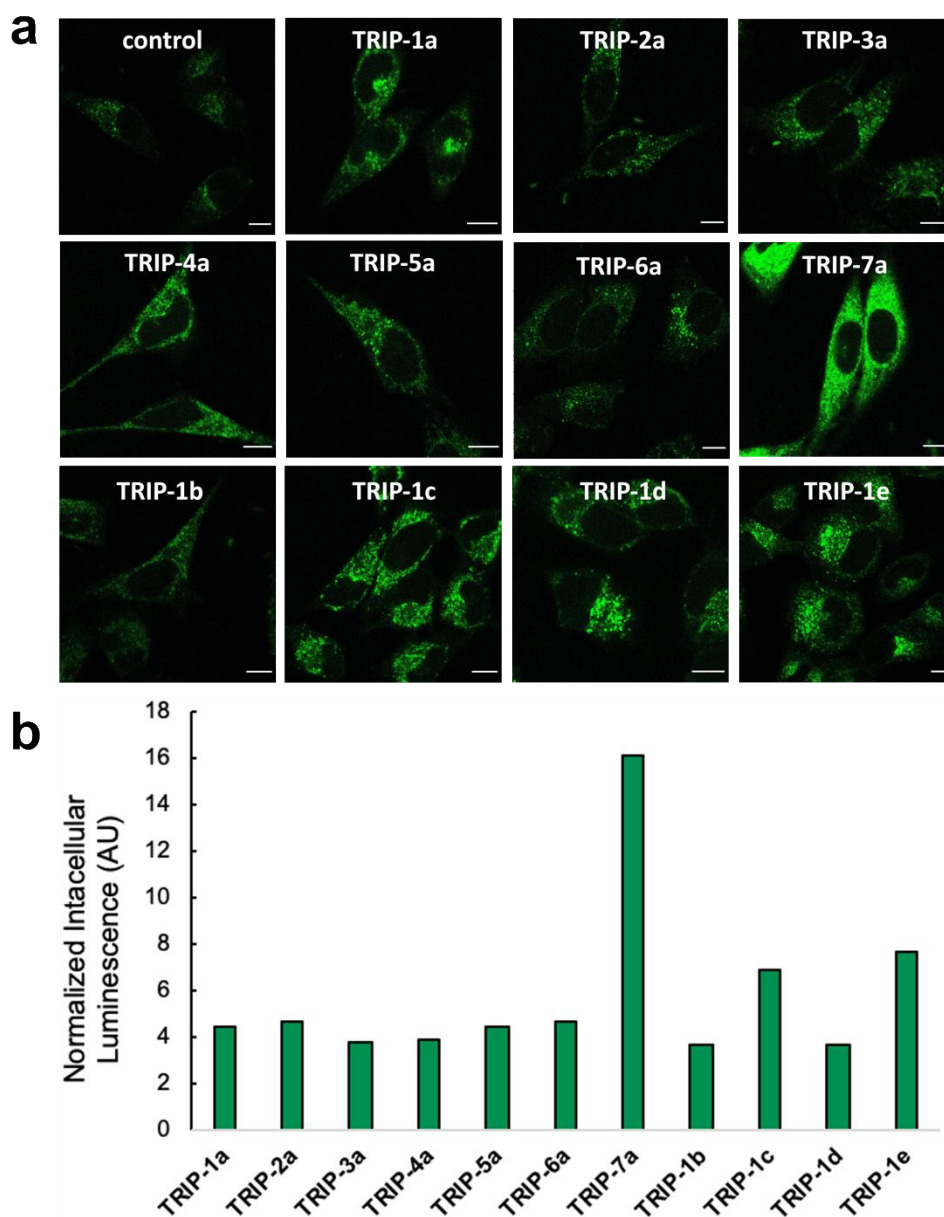


Figure S5.98. (a) Confocal fluorescence microscopy images of TRIP derivatives (10 μ M) in HeLa cells after 2 h incubation with the complexes. (b) Intracellular luminescence of TRIP complexes normalized to untreated cells and analyzed using ImageJ. Scale bar = 10 microns.

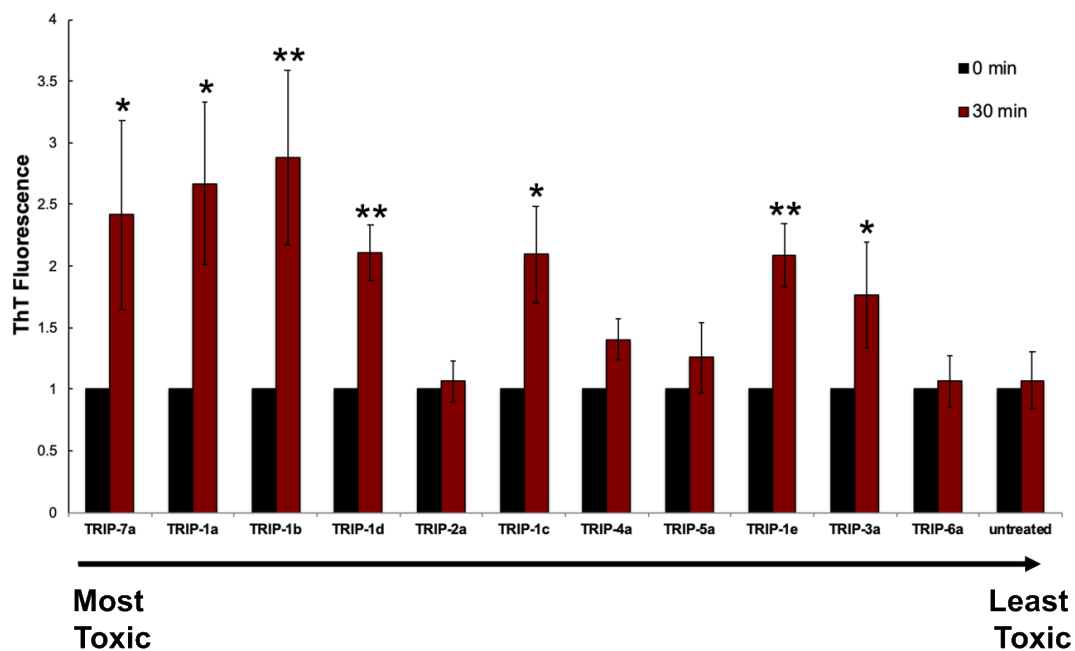


Figure S5.99. ThT fluorescence intensity of HeLa cells treated with TRIP derivatives (10 μM) normalized to fluorescence at time 0 min (black).

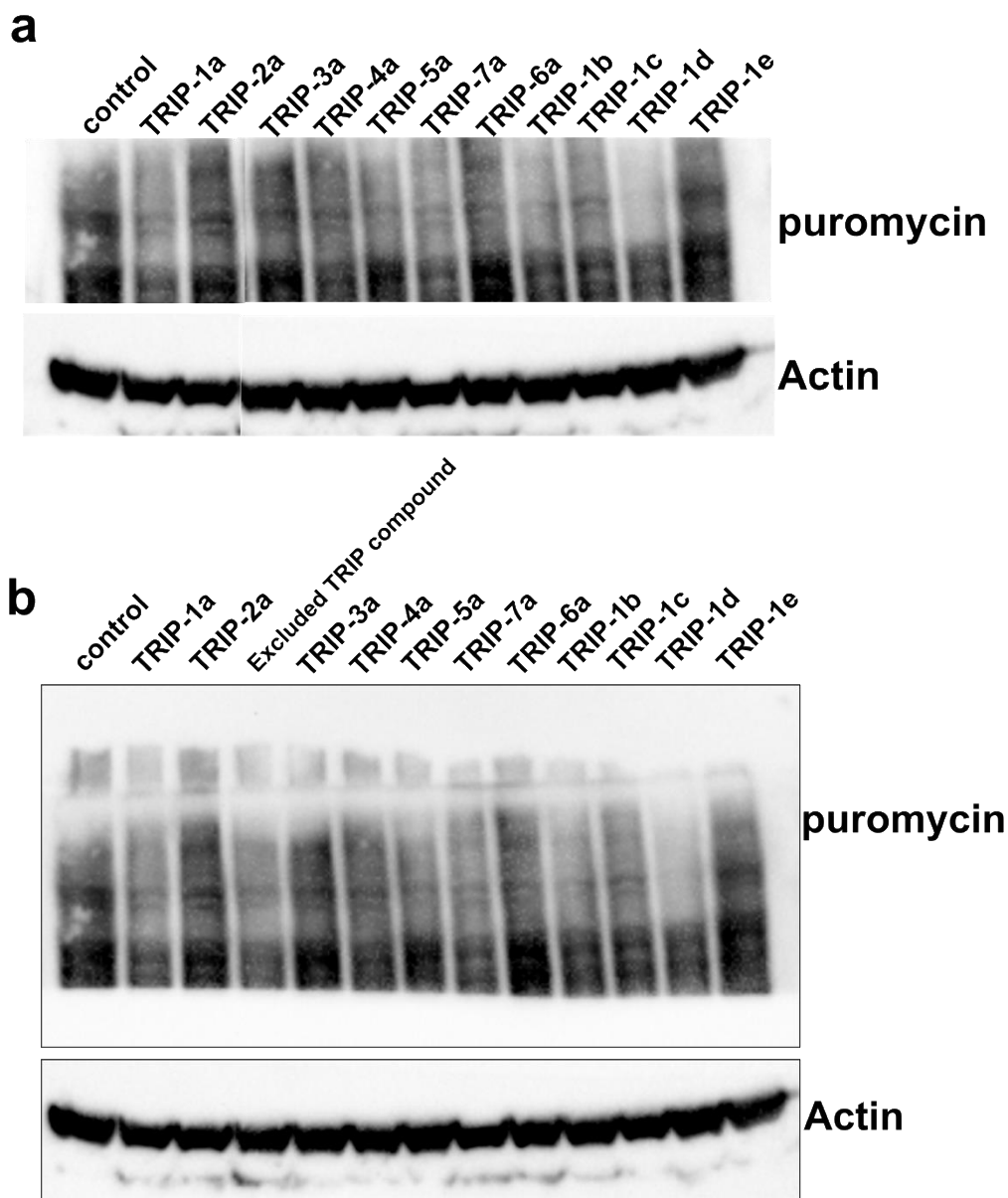


Figure S5.100. (a) Cut puromycin Western blot of HeLa cell lysates treated with TRIP derivatives (10 μ M) for 2 h. This blot has been cut between **TRIP-2a** and **TRIP-3a** to remove a compound that is no longer being investigated in this Chapter. (b) Original Western blot image.

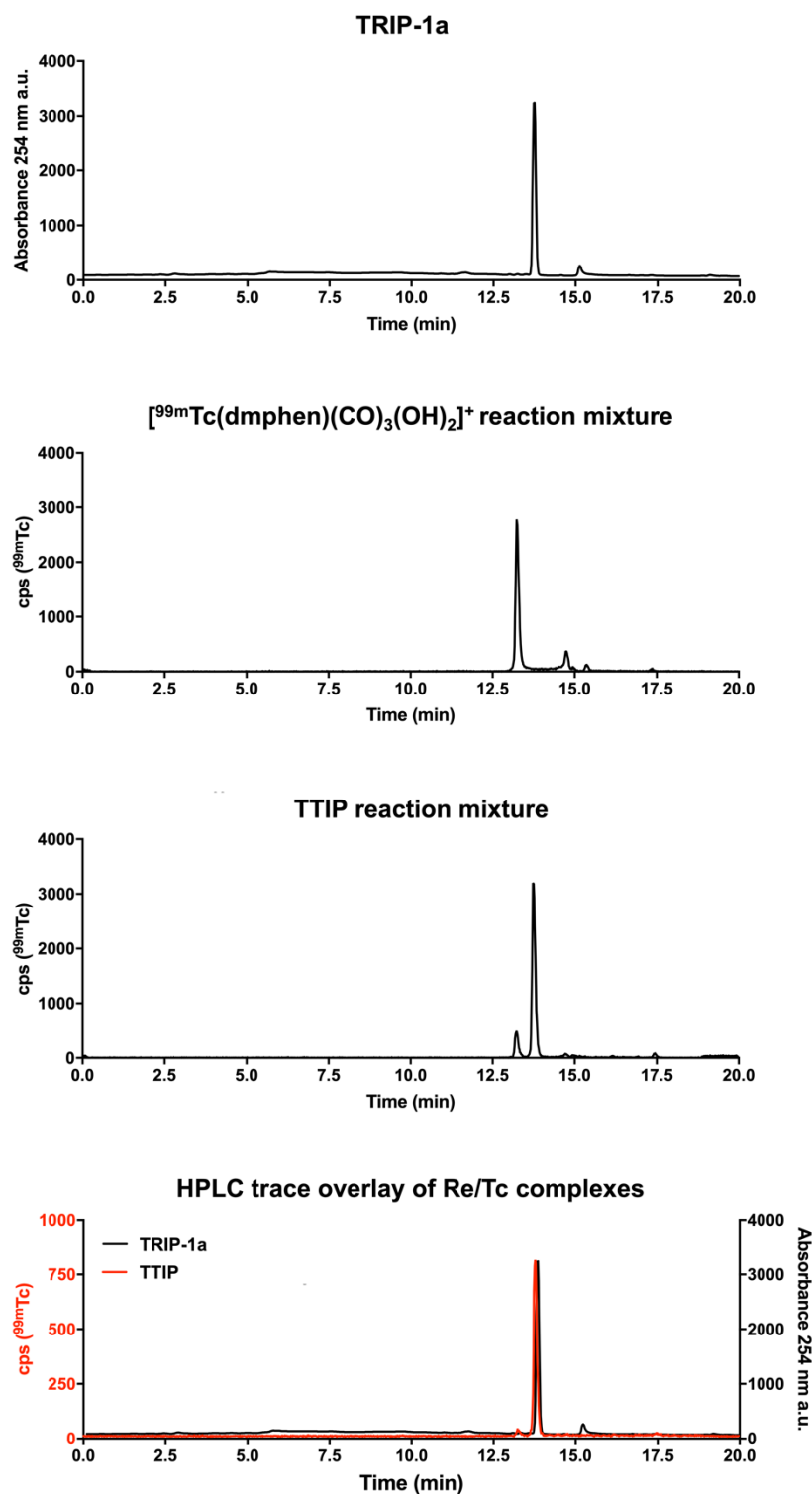


Figure S5.101. HPLC chromatograms of **TRIP-1a** (top), the starting Tc reaction mixture prior to ICN ligand addition (top middle), the final **TTIP** reaction mixture after purification by preparatory HPLC, and the overlay of **TRIP-1a** (black trace) and **TTIP** (red) (bottom).

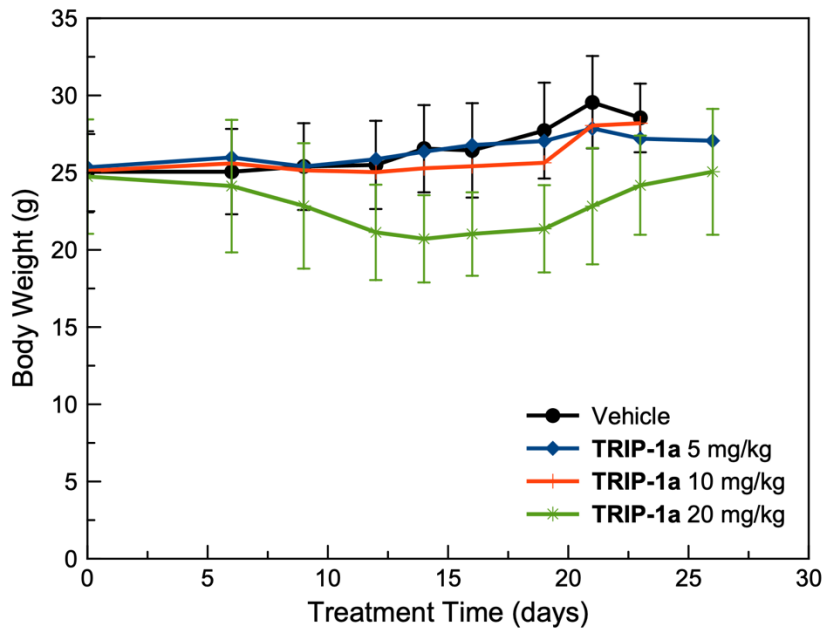


Figure S5.102. Body weight of mice treated with **TRIP-1a** throughout the duration of the study.

References

- 1 S. J. M. Healy, A. M. Gorman, P. Mousavi-Shafaei, S. Gupta and A. Samali, *Eur. J. Pharmacol.*, 2009, **625**, 234–246.
- 2 Y. Liu and Y. Ye, *Cell Res.*, 2011, **21**, 867–883.
- 3 L. Vincenz, R. Jäger, M. O'Dwyer and A. Samali, *Mol. Cancer Ther.*, 2013, **12**, 831–843.
- 4 S. Banerjee and W. Zhang, *ChemBioChem*, 2018, **19**, 2341–2343.
- 5 Y.-P. Vandewynckel, D. Laukens, A. Geerts, E. Bogaerts, A. Paridaens, X. Verhelst, S. Janssens, F. Heindryckx and H. Van Vlierberghe, *Anticancer Res.*, 2013, **33**, 4683–4694.
- 6 R. K. Yadav, S.-W. Chae, H.-R. Kim and H. J. Chae, *J. Cancer Prev.*, 2014, **19**, 75–88.
- 7 A. Walczak, K. Gradzik, J. Kabzinski, K. Przybylowska-Sygut and I. Majsterek, *Oxid. Med. Cell. Longev.*, 2019, **2019**, 5729710.
- 8 M. J. Mann and L. M. Hendershot, *Cancer Biol. Ther.*, 2006, **5**, 736–740.
- 9 R. Riha, P. Gupta-Saraf, P. Bhanja, S. Badkul and S. Saha, *Oncomedicine*, 2017, **2**, 156–167.
- 10 D. Xu, S. Q. Liang, H. Yang, U. Lüthi, C. Riether, S. Berezowska, T. M. Marti, S. R. R. Hall, R. Bruggmann, G. J. Kocher, R. A. Schmid and R. W. Peng, *Br. J. Cancer*, 2018, **119**, 65–75.
- 11 Y. Lin, M. Jiang, W. Chen, T. Zhao and Y. Wei, *Biomed. Pharmacother.*, 2019, **118**, 109249.
- 12 A. Fribley, K. Zhang and R. J. Kaufman, in *Methods in Molecular Biology. Humana Press, (Totowa, N.J.)*, 2009, vol. 559, pp. 191–204.
- 13 R. Sano and J. C. Reed, *Biochim. Biophys. Acta - Mol. Cell Res.*, 2013, **1833**, 3460–3470.
- 14 S. S. Cao and R. J. Kaufman, *Antioxid. Redox Signal.*, 2014, **21**, 396–413.
- 15 H.-O. Rashid, R. K. Yadav, H.-R. Kim and H.-J. Chae, *Autophagy*, 2015, **11**, 1956–1977.
- 16 E. A. Obeng, L. M. Carlson, D. M. Gutman, W. J. Harrington, K. P. Lee and L. H. Boise, *Blood*, 2006, **107**, 4907–4916.
- 17 A. P. King, S. C. Marker, R. V. Swanda, J. J. Woods, S. Qian and J. J. Wilson, *Chem. – A Eur. J.*, 2019, **25**, 9206–9210.
- 18 S. R. Stoyanov, J. M. Villegas, A. J. Cruz, L. L. Lockyear, J. H. Reibenspies and D. P. Rillema, *J. Chem. Theory Comput.*, 2005, **1**, 95–106.
- 19 L. Huynh, Z. Wang, J. Yang, V. Stoeva, A. Lough, I. Manners and M. A. Winnik, *Chem. Mater.*, 2005, **17**, 4765–4773.
- 20 J. M. Villegas, S. R. Stoyanov, C. E. Moore, D. M. Eichhorn and D. P. Rillema, *Acta Crystallogr. Sect. E Struct. Reports Online*, 2005, **61**, m533–m534.
- 21 C. C. Ko, C. O. Ng and S. M. Yiu, *Organometallics*, 2012, **31**, 7074–7084.
- 22 N. Saleh, M. Srebro, T. Reynaldo, N. Vanthuyne, L. Toupet, V. Y. Chang, G. Muller, J. A. G. Williams, C. Roussel, J. Autschbach and J. Crassous, *Chem. Commun.*, 2015, **51**, 3754–3757.
- 23 I. Ugi, *Isonitrile Chemistry*, Academic Press, Cambridge, MA, 1971.

- 24 J. M. Bassett, D. E. Berry, G. K. Barker, M. Green, J. A. K. Howard and F. G. A. Stone, *J. Chem. Soc. Dalt. Trans.*, 1979, 1003–1011.
- 25 G. E. Martin and C. E. Hadden, *J. Nat. Prod.*, 2000, **63**, 543–585.
- 26 T. Zou and P. J. Sadler, *Drug Discov. Today Technol.*, 2015, **16**, 7–15.
- 27 L. Pazderski, E. Szłyk, J. Sitkowski, B. Kamiński, L. Kozerski, J. Toušek and R. Marek, *Magn. Reson. Chem.*, 2006, **44**, 163–170.
- 28 I. Romero-Canelón and P. J. Sadler, *Inorg. Chem.*, 2013, **52**, 12276–12291.
- 29 P. Zhang and P. J. Sadler, *Eur. J. Inorg. Chem.*, 2017, **2017**, 1541–1548.
- 30 C.-C. Ko, L. T.-L. Lo, C.-O. Ng and S.-M. Yiu, *Chem. - A Eur. J.*, 2010, **16**, 13773–13782.
- 31 K. K.-W. Lo, *Acc. Chem. Res.*, 2015, **48**, 2985–2995.
- 32 L. C.-C. Lee, K.-K. Leung and K. K.-W. Lo, *Dalton Trans.*, 2017, **46**, 16357–16380.
- 33 J. M. Favale, E. O. Danilov, J. E. Yarnell and F. N. Castellano, *Inorg. Chem.*, 2019, **58**, 8750–8762.
- 34 J. V. Caspar and T. J. Meyer, *J. Phys. Chem.*, 1983, **87**, 952–957.
- 35 John M. Villegas, Stanislav R. Stoyanov, and Wei Huang and D. P. Rillema, *J. Chem. Theo. Comp.*, 2005, **1**, 95-106.
- 36 S. R. Stoyanov, J. M. Villegas, A. J. Cruz, L. L. Lockyear, J. H. Reibenspies and D. P. Rillema, *Inorg. Chem.*, 2005, **44**, 2297–2309.
- 37 R. P. Verma and C. Hansch, *Chem. Rev.*, 2011, 111, 2865–2899.
- 38 K. M. Knopf, B. L. Murphy, S. N. MacMillan, J. M. Baskin, M. P. Barr, E. Boros and J. J. Wilson, *J. Am. Chem. Soc.*, 2017, **139**, 14302–14314.
- 39 V. Fernández-Moreira, F. L. Thorp-Greenwood and M. P. Coogan, *Chem. Commun.*, 2010, 46, 186–202.
- 40 Q. Zhao, C. Huang and F. Li, *Chem. Soc. Rev.*, 2011, **40**, 2508–2524.
- 41 S. Imstepf, V. Pierroz, P. Raposinho, M. Bauwens, M. Felber, T. Fox, A. B. Shapiro, R. Freudenberg, C. Fernandes, S. Gama, G. Gasser, F. Motthagay, I. R. Santos and R. Alberto, *Bioconjug. Chem.*, 2015, **26**, 2397–2407.
- 42 C. C. Konkankit, A. P. King, K. M. Knopf, T. L. Southard and J. J. Wilson, *ACS Med. Chem. Lett.*, 2019, **10**, 822–827.
- 43 G. Gasser, S. Neumann, I. Ott, M. Seitz, R. Heumann and N. Metzler-Nolte, *Eur. J. Inorg. Chem.*, 2011, **2011**, 5471–5478.
- 44 S. Imstepf, V. Pierroz, R. Rubbiani, M. Felber, T. Fox, G. Gasser and R. Alberto, *Angew. Chemie Int. Ed.*, 2016, **55**, 2792–2795.
- 45 A. J. Valente, L. A. Maddalena, E. L. Robb, F. Moradi and J. A. Stuart, *Acta Histochem.*, 2017, **119**, 315–326.
- 46 D. R. Beriault and G. H. Werstuck, *Biochim. Biophys. Acta - Mol. Cell Res.*, 2013, **1833**, 2293–2301.
- 47 P. S. Vassar and C. F. Culling, *Arch. Pathol.*, 1959, **68**, 487–98.
- 48 M. Biancalana and S. Koide, *Biochim. Biophys. Acta - Proteins Proteomics*, 2010, 1804, 1405–1412.
- 49 A. Chakrabarti, A. W. Chen and J. D. Varner, *Biotechnol. Bioeng.*, 2011, **108**, 2777–2793.
- 50 C. Hetz, *Nat. Rev. Mol. Cell Biol.*, 2012, **13**, 89–102.

- 51 C. J. Adams, M. C. Kopp, N. Larburu, P. R. Nowak and M. M. U. Ali, *Front. Mol. Biosci.*, 2019, **6**, 11.
- 52 H. Matsumoto, S. Miyazaki, S. Matsuyama, M. Takeda, M. Kawano, H. Nakagawa, K. Nishimura and S. Matsuo, *Biol. Open*, 2013, **2**, 1084–1090.
- 53 E. K. Schmidt, G. Clavarino, M. Ceppi and P. Pierre, *Nat. Methods*, 2009, **6**, 275–277.
- 54 M. U. Akbar, M. R. Ahmad, A. Shaheen and S. Mushtaq, *J. Radioanal. Nucl. Chem.*, 2016, **310**, 477–493.
- 55 A. Boschi, L. Uccelli and P. Martini, *Appl. Sci.*, 2019, **9**, 2526.
- 56 P. Nunes, G. R. Morais, E. Palma, F. Silva, M. C. Oliveira, V. F. C. Ferreira, F. Mendes, L. Gano, H. V. Miranda, T. F. Outeiro, I. Santos and A. Paulo, *Org. Biomol. Chem.*, 2015, **13**, 5182–5194.
- 57 A. J. North, D. J. Hayne, C. Schieber, K. Price, A. R. White, P. J. Crouch, A. Rigopoulos, G. J. O'Keefe, H. Tochon-Danguy, A. M. Scott, J. M. White, U. Ackermann and P. S. Donnelly, *Inorg. Chem.*, 2015, **54**, 9594–9610.
- 58 J. E. Baumeister, K. M. Reinig, C. L. Barnes, S. P. Kelley and S. S. Jurisson, *Inorg. Chem.*, 2018, **57**, 12920–12933.
- 59 E. Barbarics, J. F. Kronauge, C. E. Costello, G. A. J̄anokp, B. L. Holman, A. Davison and A. G. Jones, *Nucl. Med. Biol.*, 1994, **21**, 583–591.
- 60 H. J. Pietzsch, A. Gupta, R. Syhre, P. Leibnitz and H. Spies, *Bioconjug. Chem.*, 2001, **12**, 538–544.
- 61 X. Z. Zhang, X. B. Wang and J. M. Zhou, *Appl. Radiat. Isot.*, 2003, **59**, 231–5.
- 62 L. Fuks, E. Gniazdowska, P. Kozminski, M. Lyczko, J. Mieczkowski and J. Narbutt, *Appl. Radiat. Isot.*, 2010, **68**, 90–95.
- 63 T. R. Hayes, A. S. Powell, C. L. Barnes and P. D. Benny, *J. Coord. Chem.*, 2015, **68**, 3432–3448.
- 64 Y. Mizuno, T. Uehara, H. Hanaoka, Y. Endo, C. W. Jen and Y. Arano, *J. Med. Chem.*, 2016, **59**, 3331–3339.
- 65 R. Alberto, R. Schibli, A. Egli, A. P. Schubiger, U. Abram and T. A. Kaden, *J. Am. Chem. Soc.*, 1998, **120**, 7987–7988.
- 66 A. Yazdani, N. Janzen, L. Banevicius, S. Czorny and J. F. Valliant, *Inorg. Chem.*, 2015, **54**, 1728–1736.
- 67 A. L. Baggish and C. A. Boucher, *Circulation*, 2008, **118**, 1668–1674.
- 68 O. Manabe, T. Kikuchi, A. J. H. A. Scholte, M. El Mahdiui, R. Nishii, M.-R. Zhang, E. Suzuki and K. Yoshinaga, *J. Nucl. Cardiol.*, 2018, **25**, 1204–1236.
- 69 B. L. Ellis, N. I. Gorshkov, A. A. Lumpov, A. E. Miroslavov, A. N. Yalfimov, V. V. Gurzhiy, D. N. Suglobov, R. Braddock, J. C. Adams, A.-M. Smith, M. C. Prescott and H. L. Sharma, *J. Label. Compd. Radiopharm.*, 2013, **56**, 700–707.
- 70 X. Liu, C. Jiang, Y. Li, W. Liu, N. Yao, M. Gao, Y. Ji, D. Huang, Z. Yin, Z. Sun, Y. Ni and J. Zhang, *J. Pharm. Sci.*, 2015, **104**, 215–222.
- 71 L. Yang, H. Kuang, W. Zhang, Z. P. Aguilar, H. Wei and H. Xu, *Sci. Rep.*, 2017, **7**, 3303.
- 72 N. Waegeneers, A. Brasseur, E. Van Doren, S. Van der Heyden, P. J. Serreyn, L. Pussemier, J. Mast, Y. J. Schneider, A. Ruttens and S. Roels, *Toxicol. Reports*, 2018, **5**, 632–638.

- 73 S. M. Meier-Menches, C. Gerner, W. Berger, C. G. Hartinger and B. K. Keppler, *Chem. Soc. Rev.*, 2018, **47**, 909–928.
- 74 P. Collery, A. Mohsen, A. Kermagoret, S. Corre, G. Bastian, A. Tomas, M. Wei, F. Santoni, N. Guerra, D. Desmaële and J. D'Angelo, *Invest. New Drugs*, 2015, **33**, 848–860.
- 75 L. He, Z. Y. Pan, W. W. Qin, Y. Li, C. P. Tan and Z. W. Mao, *Dalton Trans.*, 2019, **48**, 4398–4404.
- 76 F. X. Wang, J. H. Liang, H. Zhang, Z. H. Wang, Q. Wan, C. P. Tan, L. N. Ji and Z. W. Mao, *ACS Appl. Mater. Interfaces*, 2019, **11**, 13123–13133.
- 77 M. S. Capper, M. Rehkämper and H. Packman, *ChemBioChem*, 2020, **21**, doi:10.1002/cbic.202000117.
- 78 T. A. Azevedo Tosta, L. A. Neves and M. Z. do Nascimento, *Informatics Med. Unlocked*, 2017, **9**, 35–43.
- 79 M. A. Mashhadi, M. R. Arab, F. Azizi and M. R. Shahraki, *Gene, Cell Tissue*, 2014, **1**, 21536.
- 80 W. J. Aston, D. E. Hope, A. K. Nowak, B. W. Robinson, R. A. Lake and W. J. Lesterhuis, *BMC Cancer*, 2017, **17**, 684.
- 81 P. Gramatica, E. Papa, M. Luini, E. Monti, M. B. Gariboldi, M. Ravera, E. Gabano, L. Gaviglio and D. Osella, *J. Biol. Inorg. Chem.*, 2010, **15**, 1157–1169.
- 82 H. P. Varbanov, M. A. Jakupec, A. Roller, F. Jensen, M. Galanski and B. K. Keppler, *J. Med. Chem.*, 2013, **56**, 330–344.
- 83 A. Gutiérrez, L. Gracia-Fleta, I. Marzo, C. Cativiela, A. Laguna and M. C. Gimeno, *Dalton Trans.*, 2014, **43**, 17054–17066.
- 84 J. Yellol, S. A. Pérez, A. Buceta, G. Yellol, A. Donaire, P. Szumlas, P. J. Bednarski, G. Makhloufi, C. Janiak, A. Espinosa and J. Ruiz, *J. Med. Chem.*, 2015, **58**, 7310–7327.
- 85 L. Tabrizi and H. Chiniforoshan, *Dalton Trans.*, 2017, **46**, 2339–2349.
- 86 K. Suntharalingam, T. C. Johnstone, P. M. Bruno, W. Lin, M. T. Hemann and S. J. Lippard, *J. Am. Chem. Soc.*, 2013, **135**, 14060–14063.
- 87 R.-R. Ye, C.-P. Tan, M.-H. Chen, L. Hao, L.-N. Ji and Z.-W. Mao, *Chem. - A Eur. J.*, 2016, **22**, 7800–7809.
- 88 M. J. Chow, C. Licon, G. Pastorin, G. Mellitzer, W. H. Ang and C. Gaiddon, *Chem. Sci.*, 2016, **7**, 4117–4124.
- 89 C. Li, K.-W. Ip, W.-L. Man, D. Song, M.-L. He, S.-M. Yiu, T.-C. Lau and G. Zhu, *Chem. Sci.*, 2017, **8**, 6865–6870.
- 90 S. C. Marker, S. N. MacMillan, W. R. Zipfel, Z. Li, P. C. Ford and J. J. Wilson, *Inorg. Chem.*, 2018, **57**, 1311–1331.
- 91 P. Kurz, B. Probst, B. Spingler and R. Alberto, *Eur. J. Inorg. Chem.*, 2006, 2966–2974.
- 92 J. M. Smieja and C. P. Kubiak, *Inorg. Chem.*, 2010, **49**, 9283–9289.
- 93 Y. Yuan, W. Dong, X. Gao, H. Gao, X. Xie and Z. Zhang, *J. Org. Chem.*, 2018, **83**, 2840–2846.
- 94 *CrysalisPro*, Rigaku, OD: The Woodlands, TX, 2015.
- 95 G. M. Sheldrick, *Acta Crystallogr. Sect. A Found. Crystallogr.*, 2015, **71**, 3–8.
- 96 G. M. Sheldrick, *Acta Crystallogr. Sect. C Struct. Chem.*, 2015, **71**, 3–8.

- 97 P. Müller, *Crystallogr. Rev.*, 2009, **15**, 57–83.
98 A. M. Brouwer, *Pure Appl. Chem.*, 2011, **83**, 2213–2228.

CHAPTER 6

Development of Conjugation Strategies for Bifunctional Rhenium Anticancer Agents

Introduction

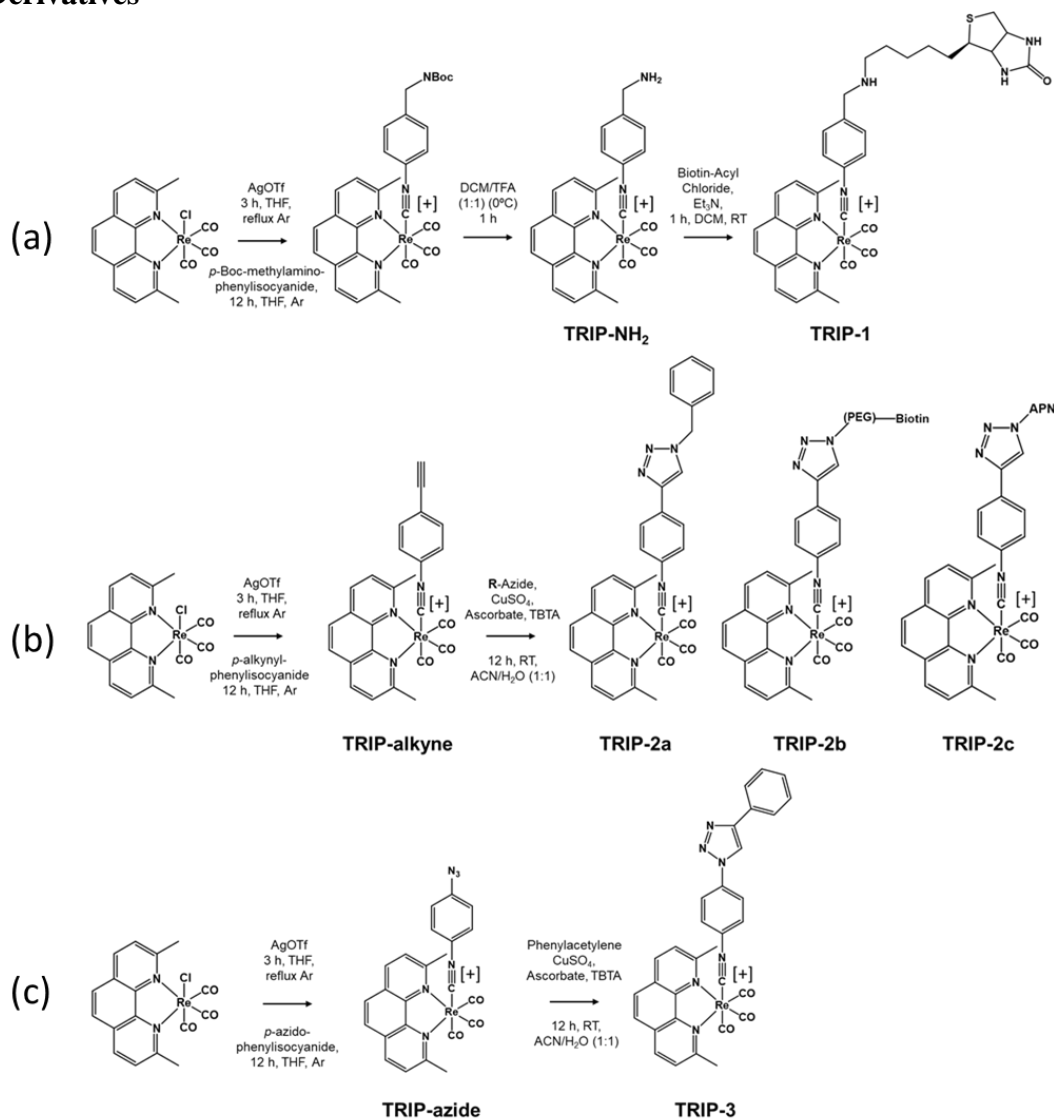
Chapters 4 and 5 of this work detail the development of tricarbonyl rhenium isonitrile polypyridyl (TRIP) complexes as anticancer agents that induce endoplasmic reticulum (ER) stress.¹ Although the TRIP complexes have potent cytotoxicity that is comparable to those of established anticancer drugs, the selectivity of these compounds is limited because they only select for tumors over normal cells by inducing ER stress, to which cancer cells are more sensitive. Furthermore, discrete molecular targets of TRIP remain unknown. Both of these shortcomings may be resolved through the development of bifunctional complexes that link the cytotoxic rhenium payload to a cancer-targeting vector or affinity pull-down tag, such as biotin. The ability to conjugate these types of different functionalities to the TRIP core could give rise to significantly improved anticancer agents.

The original lead molecule contains no functional groups that are amenable to conjugation. In order to synthesize a bifunctional complex, we first needed to synthesize a TRIP analog containing a handle suitable for bioconjugation reactions. The preparation of such complexes is complicated by the harsh reagents necessary for the synthesis of the isonitrile functionality. Isonitriles can be prepared by dehydration of formamides, which requires a strong electrophile such as phosphoryl chloride or phosgene. These reagents are incompatible with typical biological functionalities such as amines, amides, and alcohols. Alternatively, isonitriles may be synthesized from amines by exposing them to chloroform in the presence of strong base. However, the extremely basic conditions required for this reaction are incompatible with many functionalities such as esters and other electrophiles. Finally, isonitriles are easily

hydrolyzed in presence of acid and are reactive toward nucleophiles. These hurdles necessitate first synthesizing a TRIP complex with the isonitrile bound to rhenium as a protecting group, then performing conjugation chemistry to attach the other moiety of interest.

In order to develop bifunctional TRIP complexes, we have prepared three new TRIP derivatives containing reactive groups that are amenable to bioconjugation reactions. One complex, **TRIP-NH₂**, bears a methylamino group *para* to the isonitrile that can be used as a nucleophile for carboxylic acid-amine coupling reactions or for direct nucleophilic substitution reactions (**Scheme 6.1a**).^{2,3} Two of the complexes bear alkyne (**TRIP-alkyne**) (**Scheme 6.1b**) and azide (**TRIP-azide**) (**Scheme 6.1c**) handles, respectively, which are suitable for conjugation via click chemistry.^{4,5} In particular, we sought to develop a biotin conjugate of TRIP. Conjugation of biotin to biologically active molecules can enable discovery of their molecular targets, for the biotin motif binds with extremely high affinity to streptavidin. Thus, the molecule of interest may be exposed to cancer cells or cell extracts, then incubated with streptavidin immobilized on beads.^{6,7} The compound, bound to target proteins or small molecules, will attach to the beads via the biotin linker and can be analyzed via HPLC-MS or other methods. These techniques have been employed previously to identify the targets of metal anticancer agents with great success.^{8,9} To perform these experiments, we synthesized two bifunctional TRIP complexes containing biotin.

Scheme 6.1. Synthetic Strategy for the Preparation of Amine-Conjugated TRIP Derivatives



In the process of developing bifunctional TRIP derivatives via click chemistry approaches, we prepared azide- and alkyne-labeled TRIP complexes that could react with one another. We realized that such reactivity might allow for the synthesis of a dinuclear complex. Dinuclear complexes have attracted special attention as anticancer agents, for their biological activities are often enhanced significantly or altered in

comparison to the related mononuclear versions.¹⁰⁻¹² For this reason, we synthesized and characterized a dinuclear TRIP complex using click chemistry.

Results and Discussion

Through a combination of established and newly developed methods, we were able to synthesize several bifunctional TRIP complexes. The synthetic scheme for the development of these complexes is outlined in **Scheme 6.1**. The requisite isocyanide ligands were synthesized as described previously. 4-ethynylphenyl isocyanide, 4-Boc-aminomethyl-phenyl isocyanide, and 4-azidophenyl isocyanide were synthesized from the corresponding anilines using the Hoffman carbonylamine reaction, in which the anilines were stirred with chloroform under strongly basic conditions.¹³ The TRIP complexes were then synthesized from *fac*-[Re(dmphen)(CO)₃Cl] by first abstracting the chloride ligand with AgOTf, then adding the desired isocyanide, as reported previously.^{1,14} The alkynyl and azido isocyanide complexes were purified by recrystallization from DCM and ether. The 4-Boc-methylamino-phenylisocyanide complex was first deprotected using DCM and trifluoroacetic acid, then purified by preparatory HPLC. All complexes were obtained in moderate yields. With these conjugable TRIP derivatives in hand, we began exploring synthetic methods for the development of bifunctional complexes.

The modified TRIP complexes were attached to biotin in order to develop bifunctional complexes for pull-down experiments. We first synthesized **TRIP-1** using **TRIP-NH₂** and biotin acyl chloride. Although the synthesis proceeded smoothly, direct biotin attachment to the TRIP center is not ideal for pull-down experiments, for

a spacer group is often needed to allow the biotin moiety the freedom to bind streptavidin. After several attempts, installation of a spacer group proved unfeasible due to difficulties performing amine-carboxylate conjugation chemistry using **TRIP-NH₂**.

As an alternative, we considered whether click chemistry approaches might prove suitable for the synthesis of conjugated TRIP complexes. Thus, we synthesized **TRIP-alkyne** and **TRIP-azide** and investigated their suitability for conjugation. We first explored simple test substrates with each of these molecules. We tested the reaction of benzyl azide with **TRIP-alkyne** and phenylacetylene with **TRIP-azide**. Both reactions were performed using identical conditions, with CuSO₄ as the copper source, ascorbate as a reductant, and tris(benzyltriazolylmethyl)amine (TBTA) as a chelator to stabilize the Cu(I) catalyst. The conditions used for these reactions were similar to those reported previously for click-chemistry derivatization of a rhenium tricarbonyl complex.¹⁵ Both reactions proceeded smoothly, leading to products **TRIP-2a** and **TRIP-3**, respectively. Encouraged by these results, we used these reaction conditions to prepare another biotin conjugate. **TRIP-alkyne** and commercially available biotin-PEG-N₃ were used to synthesize the biotin conjugate, **TRIP-2b**, which contains a poly(ethylene)glycol (PEG) spacer. Pull-down experiments are currently underway using this conjugate.

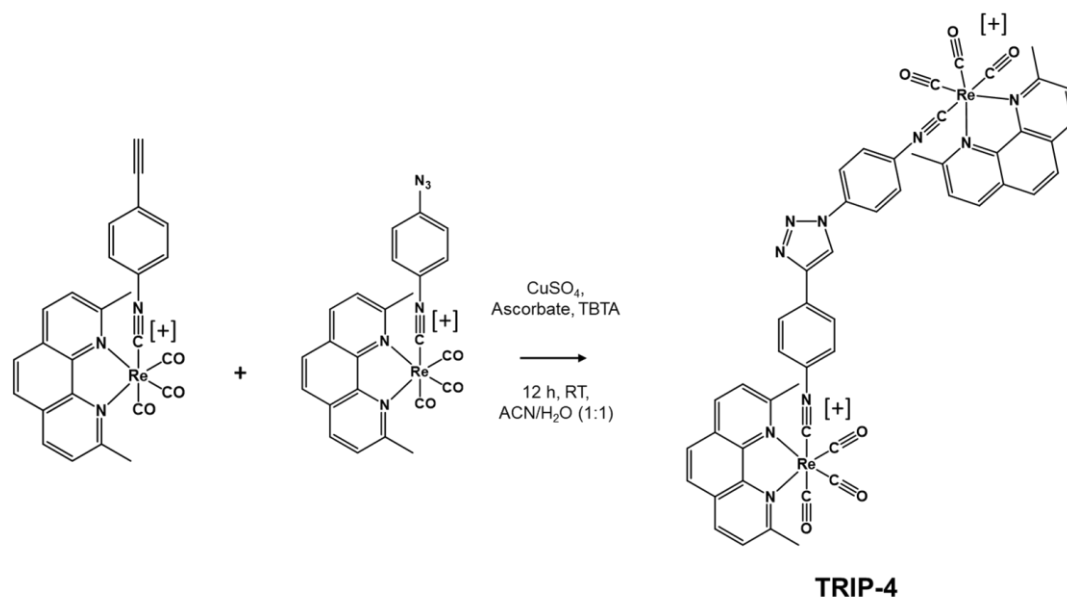
The facile synthesis of the biotin-conjugated TRIP complex via click chemistry led us to consider other potential conjugates of interest. Because azides and alkynes are rare in biomolecules, we sought to install a reactive linker with a broader substrate scope into the TRIP scaffold. We chose the recently established arylpropionitrile

(APN) moiety as a broader conjugation handle. The APN group reacts rapidly, selectively, and irreversibly with thiols to form stable conjugates.¹⁶ These linkers are ideal for conjugation with biomolecules such as the cysteine residues of proteins. An APN molecule bearing an azide functionality, APN-N₃, was attached to **TRIP-alkyne** via the previously outlined click chemistry approach. The resulting conjugate, **TRIP-2c**, is suitable for reactions with biological thiols. We are currently exploring conjugation reactions with this molecule.

Our efforts to synthesize TRIP conjugates via click chemistry yielded both an alkyne- and azide-tagged TRIP derivative. Because dinuclear complexes often show drastically different activities than their mononuclear counterparts, we sought to combine **TRIP-alkyne** and **TRIP-azide**. Using the previously discussed click reaction conditions, we synthesized **TRIP-4**, a dinuclear TRIP complex bridged via the axial isonitrile ligands, as shown in **Scheme 6.2**. It should be noted that this complex is asymmetric, for one TRIP moiety is bound to a nitrogen atom of the triazole bridge, and the other is bound to a carbon. The two components of the bridge are well-resolved via NMR spectroscopy, indicating that they have significantly different electronic properties. We have now begun investigating the biological properties of this dinuclear complex, particularly its capacity to bind DNA, which appears much greater than that of the mononuclear analogs. However, **TRIP-4** exhibits extremely poor solubility in aqueous systems, especially at neutral or basic pH values. The complex also appears to aggregate in aqueous solution, as solutions of the compound precipitate from multiple aqueous buffers even after filtration through a 0.2 μm syringe filter, as has been observed for other poorly soluble metal anticancer agents.¹⁷

This tendency to aggregate makes investigation of the compounds' physical properties difficult, as aggregation may occlude the observed results. We are currently further investigating this compounds' behavior in aqueous solution to determine whether it may prove useful despite this property.

Scheme 6.2. Synthesis of Dinuclear TRIP Complex



Conclusions

This chapter details several synthetic methods for the development of conjugated rhenium tricarbonyl isonitrile complexes. Both amine conjugation reactions and azide-alkyne click reactions have been successfully applied to rhenium isonitriles, and both these methods led to biotin-conjugated complexes. Click chemistry approaches have proven especially useful for conjugation of these complexes, and both azide- and alkyne-bearing TRIP derivatives participate rapidly and cleanly in Cu-catalyzed click reactions. This approach has led to several clean complexes and can provide very high yields. Furthermore, these methods can be used to synthesize dinuclear complexes with drastically different properties from their mononuclear counterparts. These efforts may lead to both identification of the molecular mechanism of action of these compounds, and they will allow for the

synthesis of multifunctional derivatives. Finally, the synthetic strategies used herein for rhenium isonitriles may also be applied to its congener technetium, which has similar reactivity. Thus, these methods may prove suitable for the synthesis of functionalized $^{99\text{m}}\text{Tc}$ complexes for molecular imaging.

Experimental

Materials and Methods

All solvents and reagents used were of ACS grade or higher. The starting material, $\text{Re}(\text{dmphen})(\text{CO})_3\text{Cl}$, was synthesized using a literature method.¹⁸ The *p*-alkynyl phenyl isonitrile and *p*-azido phenyl isonitrile ligands were synthesized according to a previously reported procedure.¹³ *p*-Boc-amino aniline was also synthesized as reported in the literature.¹⁹ Biotin-PEG-N₃ was purchased from Cayman Chemical. APN-Azide was purchased from Sigma Aldrich.

p-Boc-amino-phenyl isonitrile

p-Boc amino aniline (5.64 g, 25 mmol) was dissolved in DCM (35 mL) along with $[\text{NEt}_3\text{Bn}]\text{Cl}$ (1.2 g) and CHCl_3 (2 mL) was added. This solution was added dropwise with rapid stirring to a solution of KOH in water (35 mL, 1 g/mL) on ice. The mixture was stirred for 5 h. The DCM was then removed by rotary evaporation and the remaining aqueous solution was extracted 3x with ether. The combined ether fractions were then extracted with 0.1 M HCl to remove unreacted aniline. The ether fraction was then dried over Na_2SO_4 . The mixture was filtered and the solvent was removed under reduced pressure to yield the product as a red brown powder (3 g,

54%). Though NMR analysis indicates the product was not completely pure, this crude material was used for the synthesis of **TRIP-NH₂**. ¹H NMR (500 MHz, CDCl₃) δ 7.31 (m, 4H), 5.31 (t, *J* = 2.5 Hz, 2H), 4.31 (t, *J* = 2.5 Hz, 2H), 1.43 (s, 12H).

[Re(dmphen)(CO)₃(p-aminomethyl-phenyl isonitrile)]TFA (**TRIP-NH₂**)

Re(dmphen)(CO)₃Cl (428 mg, 0.83 mmol) was dissolved in 15 mL dry THF and AgOTf (230 mg, 0.89 mmol) was added. The mixture was sparged with Ar and refluxed under Ar for 3 h. The mixture was filtered to remove AgCl precipitate and *p*-Boc-amino-phenyl isonitrile (0.8 g, 3.47 mmol) was added. The mixture was refluxed overnight, and the solvent was removed by rotary evaporation. The residue was dissolved in a 50:50 mixture of DCM and TFA and stirred on ice for 1 hour. The solvents were removed by rotary evaporation, and the crude material was dissolved in 16 mL of 50:50 MeOH:H₂O and purified by preparatory HPLC (50-100% methanol in H₂O containing 0.1% TFA over 30 minutes). The fractions containing the product were reduced in volume by rotary evaporation and lyophilized from water to yield a yellow powder. Yield 442 mg (71%). ¹H NMR (500 MHz, Methanol-D₄) δ 8.74 (d, *J* = 8.4 Hz, 2H), 8.17 (s, 2H), 8.09 (d, *J* = 8.4 Hz, 2H), 7.45 (d, *J* = 8.6 Hz, 2H), 7.27 (d, *J* = 8.6 Hz, 2H), 4.09 (s, 2H), 3.36 (s, 6H).

[Re(dmphen)(CO)₃(p-biotin-phenyl isonitrile)]TFA (**TRIP-1**)

Biotin-acyl chloride was prepared by adding neat thionyl chloride (2.5 mL) to solid biotin (120 mg, 0.5 mmol) and stirring under inert atmosphere at room temperature. The biotin initially dissolved and then a white precipitate formed after 10

minutes. The mixture was filtered and the white solid product was washed with copious toluene, followed by hexanes.

TRIP-NH₂ (40 mg, 0.05 mmol) was dissolved in DMF with triethylamine (50 mg, 0.5 mmol) and biotin-acyl chloride (30 mg, 0.11 mmol) in 1 mL DMF was added. The mixture was stirred at room temperature, and the solvent was removed by rotary evaporation. The residue was purified using preparatory HPLC (30-100% ACN in H₂O containing 0.1% TFA over 30 minutes). Yield: 7 mg, (14%) ¹H NMR (600 MHz, DMSO-*d*₆) δ 8.87 (d, *J* = 8.7 Hz, 2H), 8.34 (t, *J* = 6.0 Hz, 1H), 8.25 (s, 2H), 8.19 (d, *J* = 8.3 Hz, 2H), 7.27 – 7.20 (m, 4H), 6.39 (s, 1H), 6.35 (s, 1H), 4.29-4.25 (m, 1H), 4.19 (d, *J* = 6.0 Hz, 2H), 4.10 (dd, *J* = 7.9, 4.5 Hz, 1H), 3.06-3.04 (m, 1H), 2.79 (dd, *J* = 12.4, 5.1 Hz, 1H), 2.09 (t, *J* = 7.4 Hz, 2H), 1.60-1.56 (m, 1H), 1.52-1.37 (m, 2H), 1.33-1.19 (m, 2H).

*[Re(dmphen)(CO)₃(*p*-alkynyl-phenyl isonitrile)]OTf* (**TRIP-alkyne**)

Re(dmphen)(CO)₃Cl (115 mg, 0.22 mmol) was dissolved in 10 mL dry THF and AgOTf (58 mg, 0.22 mmol) was added. The mixture was sparged with Ar and refluxed under Ar for 3 h. The mixture was filtered to remove AgCl precipitate and *p*-alkynyl-phenyl isonitrile (120 mg, 0.85 mmol) was added. The mixture was refluxed overnight, and the solvent was removed by rotary evaporation. The residue was dissolved in minimal THF and added to ether with rapid stirring. The resultant precipitate was isolated by filtration, washed with ether, and crystallized twice more using the same process. Yield: 80 mg, yellow powder (48%). ¹H NMR (600 MHz, Acetone-*d*₆) δ 8.87 (d, *J* = 8.3 Hz, 2H), 8.27 (s, 2H), 8.21 (d, *J* = 8.4 Hz, 2H), 7.48 (d,

$J = 8.7$ Hz, 2H), 7.31 (d, $J = 8.8$ Hz, 2H), 3.91 (s, 1H), 3.45 (s, 6H).

[Re(dmphen)(CO)₃(p-benzyltriazolyl-phenyl isonitrile)]TFA (TRIP-2a)

TRIP-alkyne (50 mg, 0.066 mmol) was dissolved in ACN (2.5 mL) along with benzyl azide (25 mg, 0.188 mmol) and TBTA (36 mg, 0.068 mmol). Sodium ascorbate (13.6 mg, 0.069 mmol) dissolved in H₂O (2.5 mL) was added, followed by CuSO₄ (17.1 mg, 0.064 mmol). The mixture immediately turned green, and a small amount of precipitate formed. The reaction mixture was stirred in a sealed vial at room temperature overnight. The resulting suspension was then filtered through a PTFE syringe filter and purified via preparatory HPLC (30-100% ACN in H₂O containing 0.1% TFA over 30 minutes). The fractions containing product were combined. The volume was reduced using rotary evaporation and lyophilized from water. Yield: 8 mg white powder (14%). ¹H NMR (600 MHz, DMSO-*d*₆) δ 8.87 (d, $J = 8.9$ Hz, 2H), 8.72 (s, 1H), 8.26 (s, 2H), 8.21 (d, $J = 11.8$ Hz, 2H), 7.87 (d, $J = 8.4$ Hz, 2H), 7.41 (d, $J = 8.7$ Hz, 2H), 7.39-7.29 (m, 5H), 5.62 (s, 2H), 3.32 (s, 6H).

[Re(dmphen)(CO)₃(p-PEG-biotin-phenyl isonitrile)]TFA (TRIP-2b)

TRIP-alkyne (50 mg, 0.068 mmol) was dissolved in ACN (3 mL) along with biotin-PEG-N₃ (25 mg, 0.056 mmol). TBTA (30 mg, 0.056 mmol), sodium ascorbate (11.1 mg, 0.056 mmol) and CuSO₄ (14 mg, 0.056 mmol) in H₂O (3 mL total). The mixture immediately turned green, and a small amount of precipitate formed. The mixture was stirred in a sealed vial at room temperature overnight. Water was added (3 mL), and the reaction mixture was then filtered through a PTFE syringe and

purified via preparatory HPLC (30-100% ACN in H₂O containing 0.1% TFA over 30 minutes). The fractions containing product were combined. The volume was reduced using rotary evaporation and lyophilized from water. Yield: 33 mg, yellow powder (65%). ¹H NMR (600 MHz, Methanol-*d*₄) δ 8.73 (d, *J* = 8.4 Hz, 2H), 8.39 (s, 1H), 8.16 (s, 2H), 8.08 (d, *J* = 8.4 Hz, 2H), 7.80 (d, *J* = 8.3 Hz, 2H), 7.23 (d, *J* = 8.3 Hz, 2H), 4.58 (t, *J* = 5.0 Hz, 2H), 4.44 (dd, *J* = 7.9, 5.1 Hz, 1H), 4.24 (dd, *J* = 7.9, 4.5 Hz, 1H), 3.88 (t, *J* = 5.0 Hz, 2H), 3.61 – 3.53 (m, 5H), 3.51 (q, *J* = 2.9, 2.3 Hz, 2H), 3.46 (dd, *J* = 6.0, 3.3 Hz, 2H), 3.39 (t, *J* = 5.5 Hz, 2H), 3.22 (t, *J* = 5.5 Hz, 2H), 3.11 (dt, *J* = 9.6, 5.2 Hz, 1H), 2.86 (dd, *J* = 12.7, 5.0 Hz, 1H), 2.64 (d, *J* = 12.7 Hz, 1H), 2.09 (t, *J* = 7.4 Hz, 2H), 1.69 – 1.60 (m, 1H), 1.60-1.43 (m, 3H), 1.40-1.26 (m, 2H). HR-ESI-MS (positive ion mode): *m/z* 1050.3 ([M]⁺, calcd 1050.3).

[Re(dmphen)(CO)₃(p-APN-phenyl isonitrile)]TFA (TRIP-2c)

TRIP-alkyne (20 mg, 0.027 mmol) was dissolved in ACN (2 mL) along with APN (8 mg, 0.0475 mmol) and TBTA (18 mg, 0.051 mmol). Water (2 mL) was added. CuSO₄ (47.8 mg/mL, 0.167 mL, 0.032 mmol) dissolved in H₂O was added, followed by sodium ascorbate (82.5 mg/mL, 0.085 mL, 0.035 mmol) in H₂O. The mixture immediately turned green, and a small amount of precipitate formed. The mixture was stirred in a sealed vial at room temperature overnight. The reaction mixture was then filtered through a PTFE syringe and purified via preparatory HPLC (30-100% ACN in H₂O containing 0.1% TFA over 30 minutes). The fractions containing product were combined. The volume was reduced using rotary evaporation and lyophilized from water. Yield: 13 mg white powder, (52%). ¹H NMR (600 MHz, Acetone-*d*₆) δ 9.31 (s,

1H), 8.89 (d, $J = 6.7$ Hz, 2H), 8.29 (s, 2H), 8.23 (d, $J = 8.3$ Hz, 2H), 8.14 (d, $J = 8.3$ Hz, 2H), 8.03 (d, $J = 8.8$ Hz, 2H), 8.00 (d, $J = 8.3$ Hz, 2H), 7.42 (s, 2H), 3.48 (s, 6H).

*[Re(dmphen)(CO)₃(*p*-azido-phenyl isonitrile)]TFA (TRIP-azide)*

Re(dmphen)(CO)₃Cl (200 mg, 0.039 mmol) was dissolved in 20 mL dry THF and AgOTf (110 mg, 0.042 mmol) was added. The mixture was sparged with Ar and refluxed under Ar for 3 h. The mixture was filtered to remove AgCl precipitate and *p*-azido-phenyl isonitrile (approximately 200 mg, 1.3 mmol) was added. The mixture was refluxed overnight, and the solvent was removed by rotary evaporation. The residue was dissolved in minimal THF and added to ether with rapid stirring. The resultant precipitate was isolated by filtration, washed with ether, and crystallized twice more using the same process. Yield: 120 mg yellow powder (41%). ¹H NMR (600 MHz, DMSO-*d*₆) δ 8.86 (d, $J = 8.9$ Hz, 2H), 8.25 (s, 2H), 8.20 (d, $J = 7.5$ Hz, 2H), 7.36 (d, $J = 8.4$ Hz, 2H), 7.13 (d, $J = 8.9$ Hz, 2H), 3.32 (s, 6H).

*[Re(dmphen)(CO)₃(*p*-phenyltriazolyl-phenyl isonitrile)]TFA (TRIP-3)*

TRIP-azide (11 mg, 0.014 mmol) was dissolved in ACN (1 mL) along with phenylacetylene (10 mg, 0.11 mmol) and TBTA (7.6 mg, 0.022 mmol). Sodium ascorbate (0.017 mmol) dissolved in 0.5 mL H₂O was added, followed by CuSO₄ (0.010 mmol) in 0.5 mL H₂O. The mixture immediately turned green, and a small amount of precipitate formed. The mixture was stirred in a sealed vial at room temperature overnight. The reaction mixture was then filtered through a PTFE syringe and purified via preparatory HPLC (50-100% ACN in H₂O containing 0.1% TFA over

30 minutes). The fractions containing product were combined. The volume was reduced using rotary evaporation, and the product was lyophilized from water. Yield: 8 mg, white powder (63%) ^1H NMR (600 MHz, $\text{DMSO-}d_6$) δ 9.36 (s, 1H), 8.88 (d, J = 8.4 Hz, 2H), 8.27 (s, 2H), 8.22 (d, J = 7.2 Hz, 2H), 8.01 (d, J = 9.3 Hz, 2H), 7.90 (d, J = 6.4 Hz, 2H), 7.67 (d, J = 9.0 Hz, 2H), 7.49 (dd, J = 8.3, 8.2 Hz, 2H), 7.39 (t, J = 7.8 Hz, 1H), 3.34 (s, 6H).

Dinuclear Tricarbonyl Rhenium Isonitrile Polypyridyl (TRIP-4)

TRIP-alkyne (10 mg, 0.013 mmol), **TRIP-azide** (10 mg, 0.013 mmol), and TBTA (7.5 mg, 0.02 mmol) were dissolved together in ACN (2 mL). To this mixture were added CuSO_4 (0.014 mmol) and sodium ascorbate (0.017 mmol) in water (2 mL). The mixture was stirred at room temperature in a sealed vial overnight. The mixture was filtered through a PTFE syringe filter and purified via preparatory HPLC (30-100% ACN in H_2O containing 0.1% TFA over 30 minutes). The fractions containing the product were combined. The volume was reduced using rotary evaporation, and the product was lyophilized from water. Yield 7 mg of yellow powder (35%). ^1H NMR (600 MHz, $\text{DMSO-}d_6$) δ 9.43 (s, 1H), 8.87 (d, J = 8.2 Hz, 4H), 8.26 (s, 4H), 8.21 (d, J = 6.8 Hz, 4H), 7.97 (d, J = 8.6 Hz, 2H), 7.92 (d, J = 8.6 Hz, 2H), 7.65 (d, J = 8.6 Hz, 2H), 7.51 (d, J = 6.8 Hz, 2H), 3.35 (s, 12H).

Supporting Information for Chapter 6

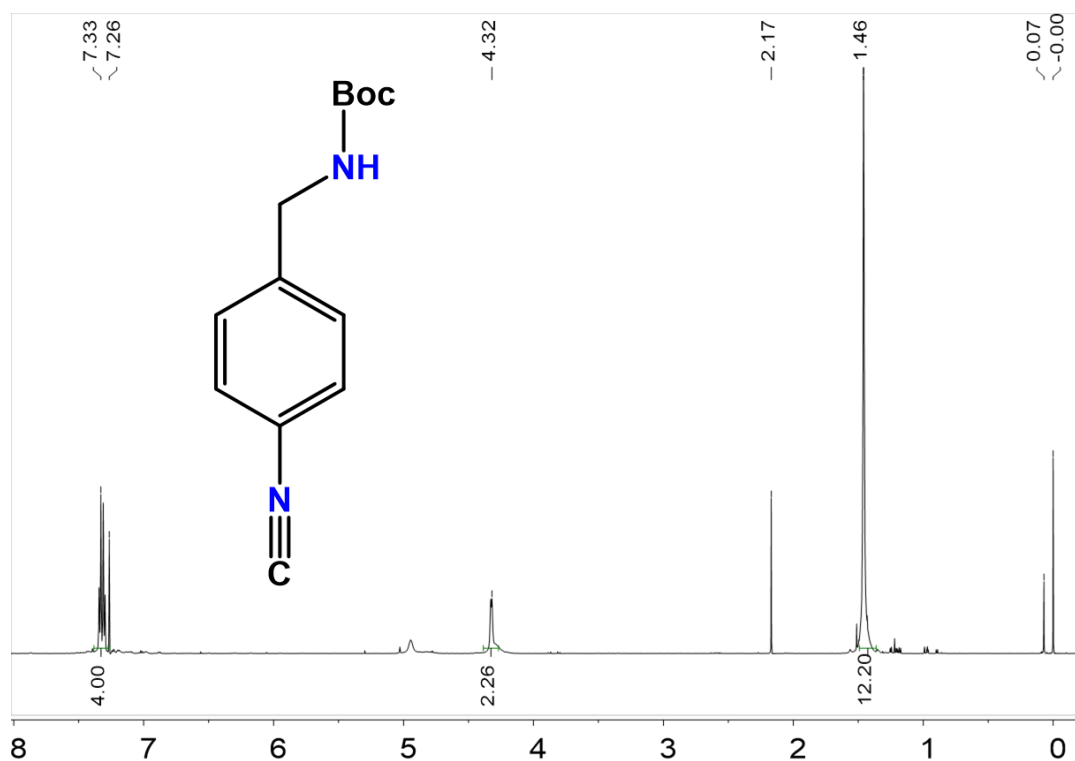


Figure S6.1. ^1H NMR spectrum of Boc-aminomethyl phenyl isocyanide (CDCl_3 , 600 MHz, 298 K).

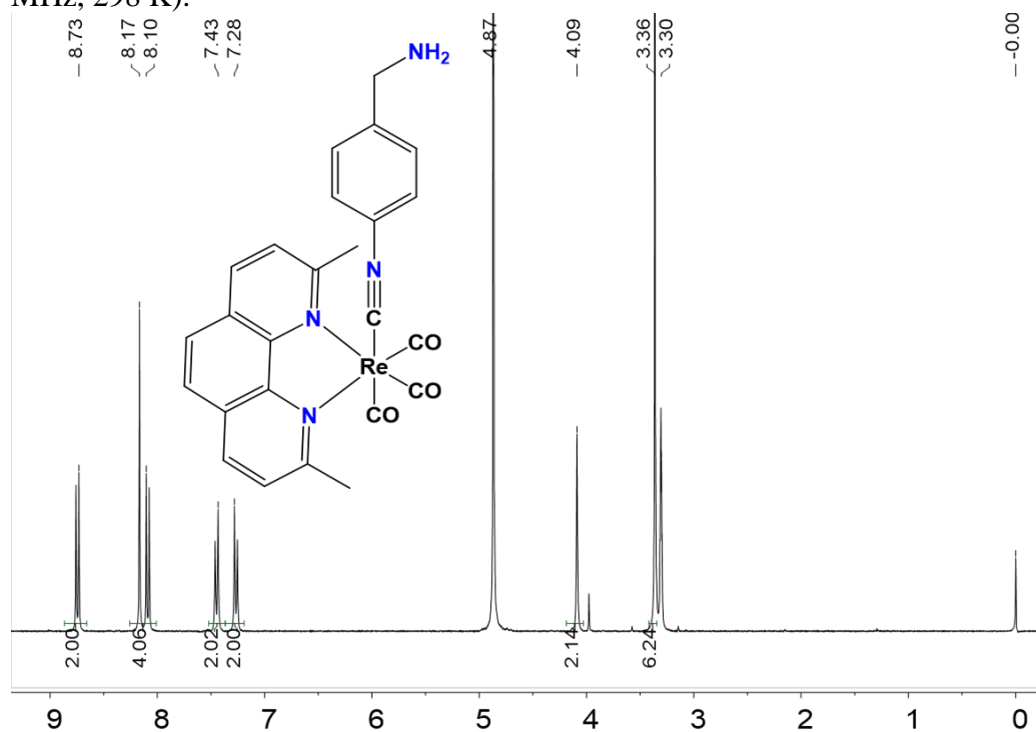


Figure S6.2. ^1H NMR spectrum of **TRIP-NH₂** (Methanol-*d*₄, 600 MHz, 298 K).

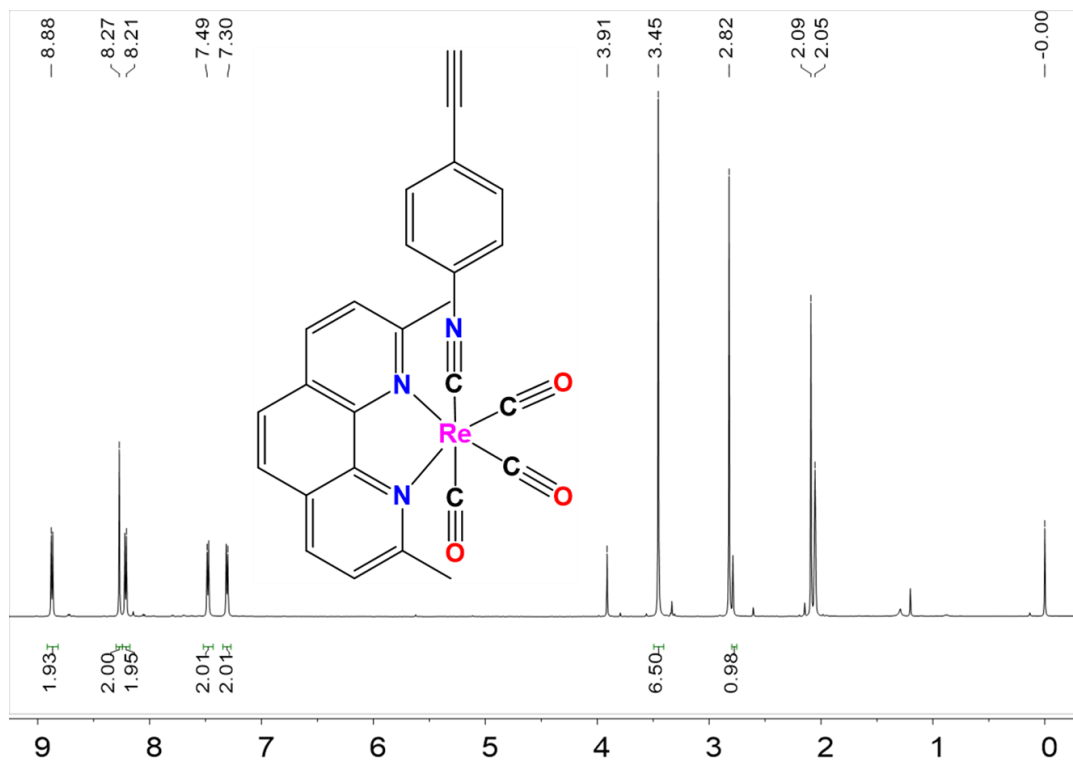


Figure S6.3. ^1H NMR spectrum of **TRIP-alkyne** (Acetone-*d*₆, 600 MHz, 298 K).

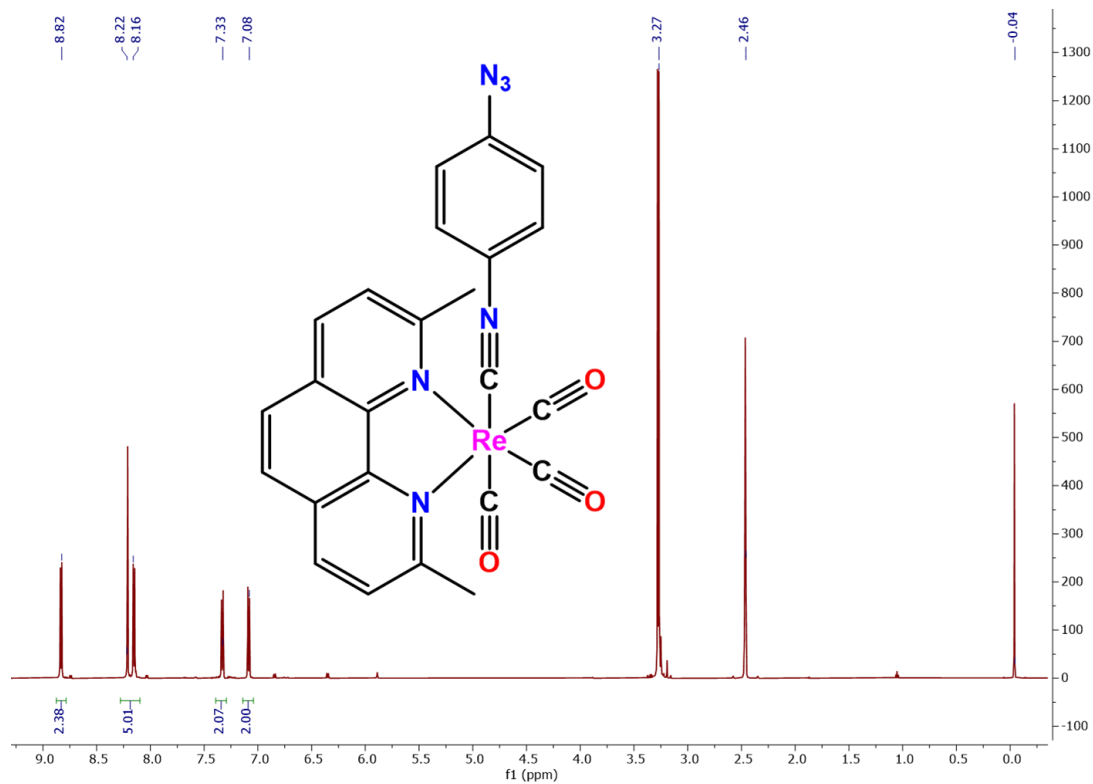


Figure S6.4. ^1H NMR spectrum of TRIP-azide (DMSO- d_6 , 600 MHz, 298 K).

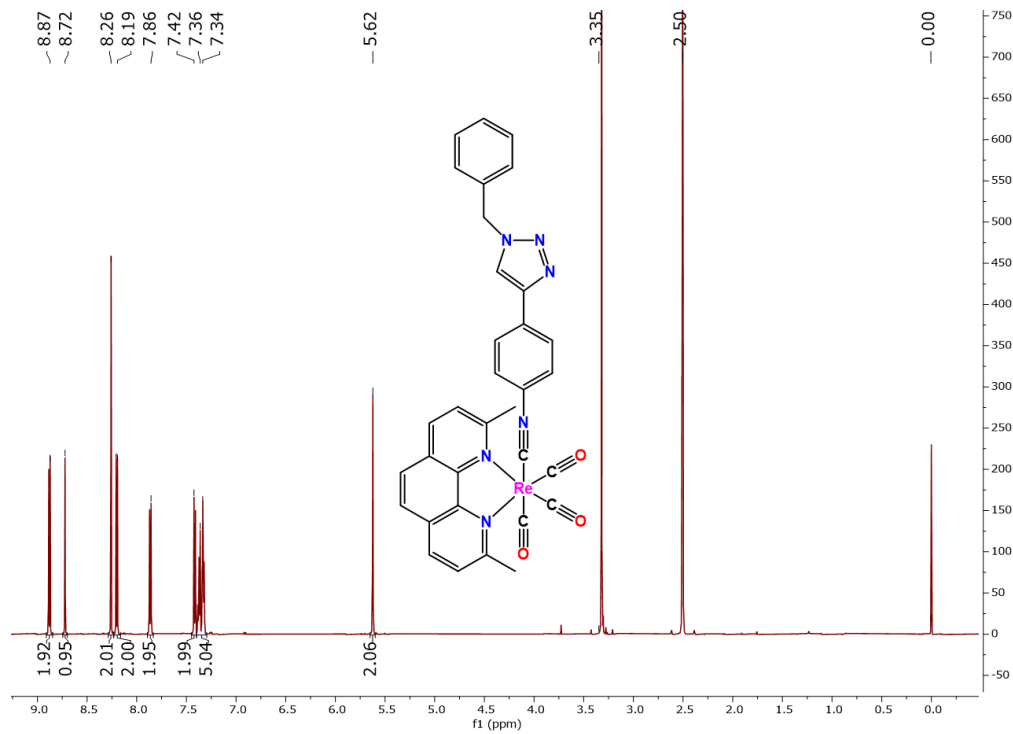


Figure S6.5. ^1H NMR spectrum of TRIP-2a (DMSO- d_6 , 600 MHz, 298 K).

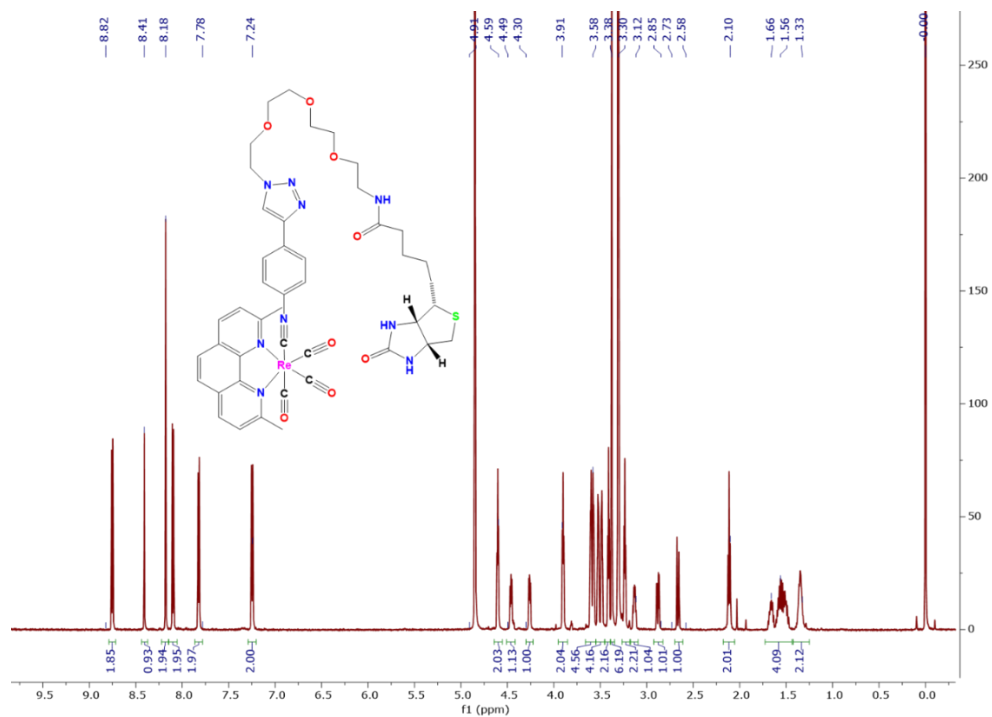


Figure S6.6. ^1H NMR spectrum of **TRIP-2b** (Methanol- d_4 , 600 MHz, 298 K).

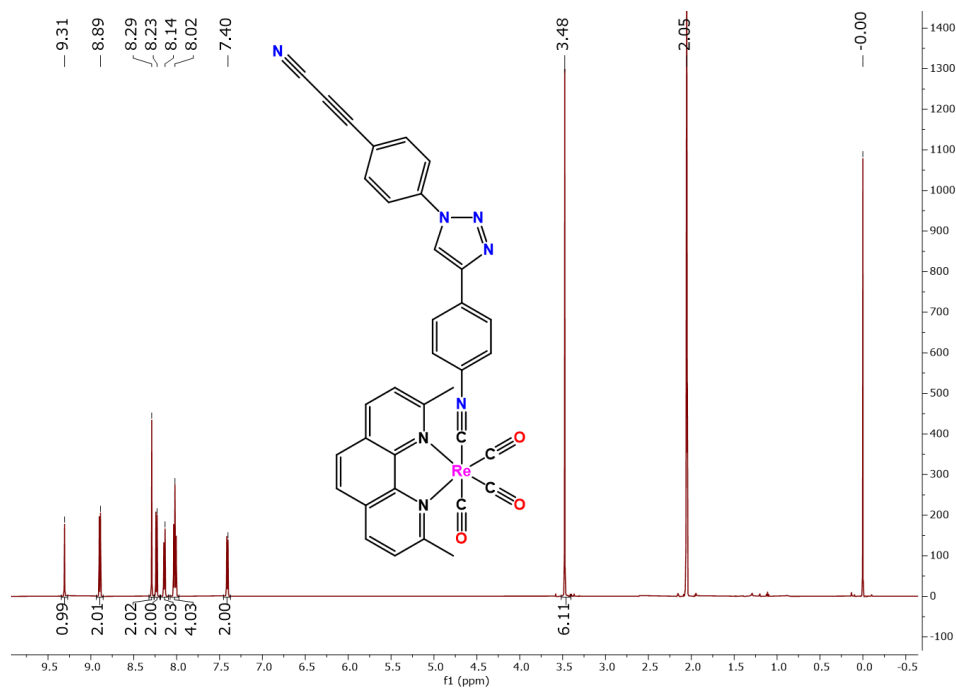


Figure S6.7. ^1H NMR spectrum of **TRIP-2c** (Acetone- d_6 , 600 MHz, 298 K).

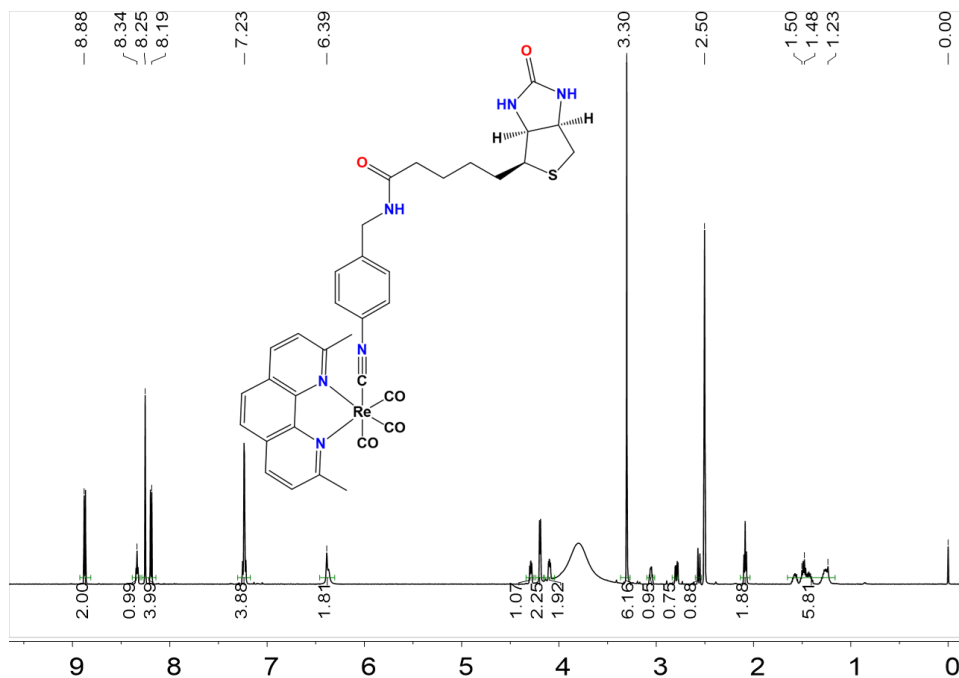


Figure S6.8. ^1H NMR spectrum of **TRIP-1** (DMSO- d_6 , 600 MHz, 298 K).

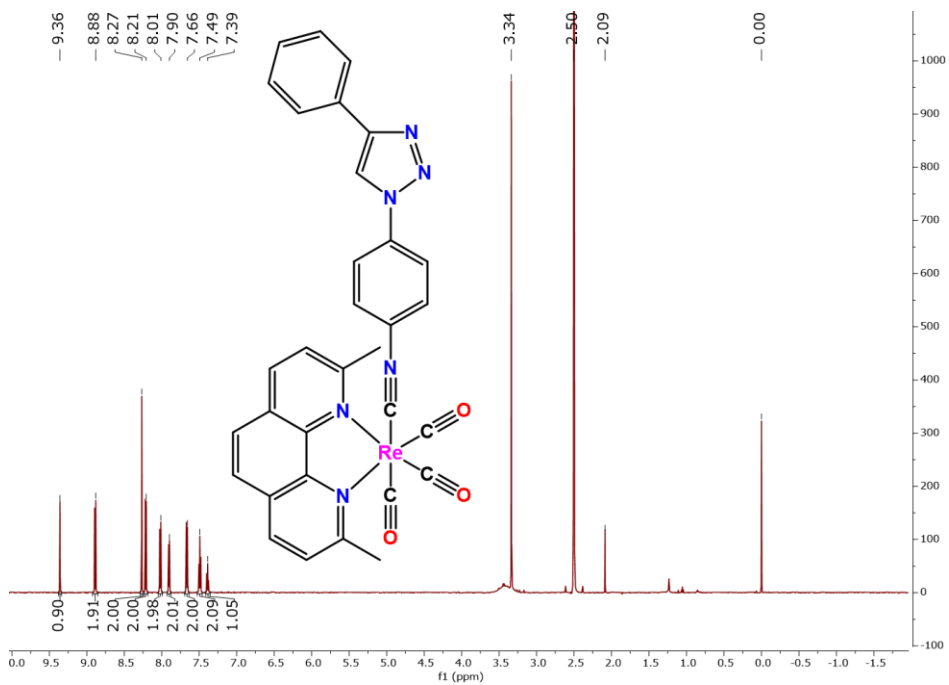


Figure S6.9. ^1H NMR spectrum of **TRIP-3** (DMSO- d_6 , 600 MHz, 298 K).

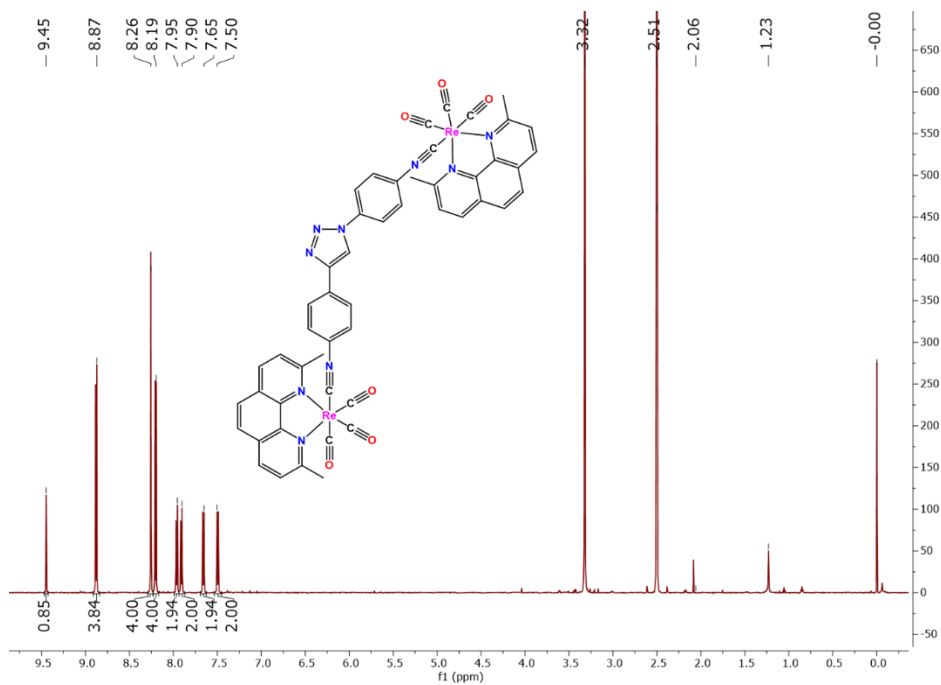


Figure S6.10. ^1H NMR spectrum of **TRIP-4** (DMSO- d_6 , 600 MHz, 298 K).

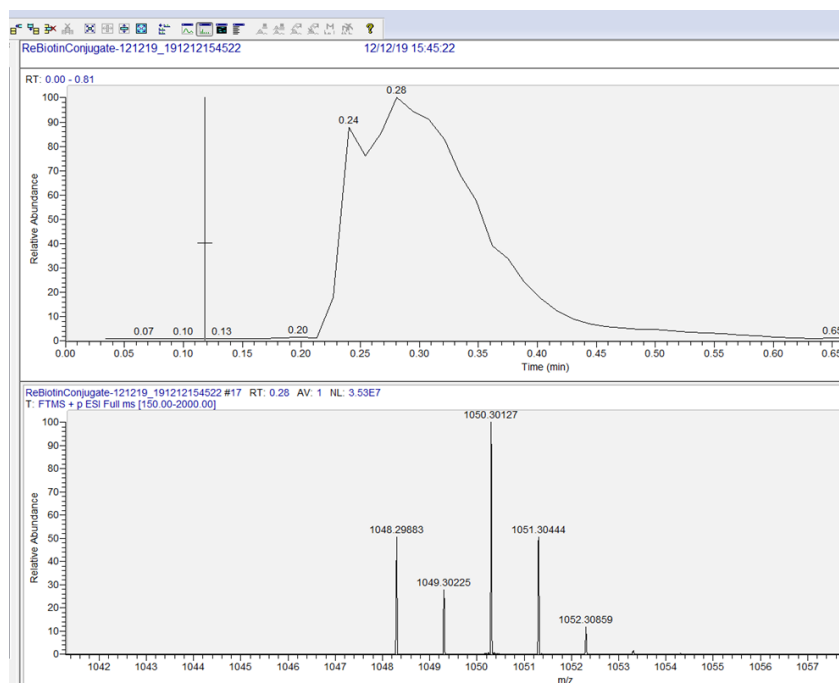


Figure S6.11. ESI-MS of **TRIP-1b**.

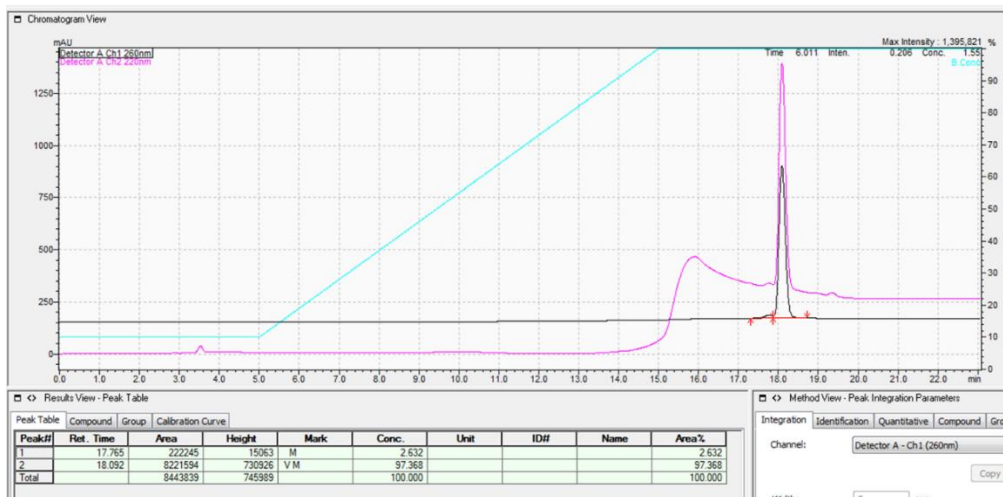


Figure S6.12. HPLC of TRIP-1b.

References

- 1 A. P. King, S. C. Marker, R. V. Swanda, J. J. Woods, S. Qian and J. J. Wilson, *Chem. – A Eur. J.*, 2019, **25**, 9206–9210.
- 2 J. M. Humphrey and A. R. Chamberlin, *Chem. Rev.*, 1997, **97**, 2243–2266.
- 3 H. Lundberg, F. Tinnis, N. Selander and H. Adolfsson, *Chem. Soc. Rev.*, 2014, **43**, 2714–2742.
- 4 H. C. Kolb and K. B. Sharpless, *Drug Discov. Today*, 2003, **8**, 1128–1137.
- 5 L. Liang and D. Astruc, *Coord. Chem. Rev.*, 2011, **255**, 2933–2945.
- 6 B. Lomenick, R. W. Olsen and J. Huang, *ACS Chem. Biol.*, 2011, **6**, 34–46.
- 7 M. Kawatani and H. Osada, *Medchemcomm*, 2014, **5**, 277–287.
- 8 S. M. Meier, D. Kreutz, L. Winter, M. H. M. Klose, K. Cseh, T. Weiss, A. Bileck, B. Alte, J. C. Mader, S. Jana, A. Chatterjee, A. Bhattacharyya, M. Hejl, M. A. Jakupec, P. Heffeter, W. Berger, C. G. Hartinger, B. K. Keppler, G. Wiche and C. Gerner, *Angew. Chemie Int. Ed.*, 2017, **56**, 8267–8271.
- 9 S. M. Meier-Menches, K. Zappe, A. Bileck, D. Kreutz, A. Tahir, M. Cichna-Markl and C. Gerner, *Metallomics*, 2019, **11**, 118–127.
- 10 R. W. Y. Sun, C. N. Lok, T. T. H. Fong, C. K. L. Li, Z. F. Yang, A. F. M. Siu and C. M. Che, *Chem. Sci.*, 2013, **4**, 1979–1988.
- 11 N. P. Farrell, *Chem. Soc. Rev.*, 2015, **44**, 8773–8785.
- 12 Y. Yang, L. Guo, Z. Tian, Y. Gong, H. Zheng, S. Zhang, Z. Xu, X. Ge and Z. Liu, *Inorg. Chem.*, 2018, [acs.inorgchem.8b01656](https://doi.org/10.1039/C8IN00165G).
- 13 G. Jia, N. C. Payne, J. J. Vittal and R. J. Puddephatt, *Organometallics*, 1993, **12**, 4771–4778.
- 14 S. R. Stoyanov, J. M. Villegas, A. J. Cruz, L. L. Lockyear, J. H. Reibenspies and D. P. Rillema, *J. Chem. Theory Comput.*, 2005, **1**, 95–106.
- 15 A. Leonidova, V. Pierroz, L. A. Adams, N. Barlow, S. Ferrari, B. Graham and G. Gasser, *ACS Med. Chem. Lett.*, 2014, **5**, 809–814.
- 16 O. Koniev, G. Leriche, M. Nothisen, J. S. Remy, J. M. Strub, C. Schaeffer-Reiss, A. Van Dorsselaer, R. Baati and A. Wagner, *Bioconjug. Chem.*, 2014, **25**, 202–206.
- 17 A. Notaro, G. Gasser and A. Castonguay, *ChemMedChem*, 2020, **15**, 345–348.
- 18 J. M. Smieja and C. P. Kubiak, *Inorg. Chem.*, 2010, **49**, 9283–9289.
- 19 M. Jörg, A. Glukhova, A. Abdul-Ridha, E. A. Vecchio, A. T. N. Nguyen, P. M. Sexton, P. J. White, L. T. May, A. Christopoulos and P. J. Scammells, *J. Med. Chem.*, 2016, **59**, 11182–11194.

Appendix 1
Synthesis and Characterization Data of Antibacterial Cobalt Complexes

Introduction

Although we originally investigated the cobalt(III) complexes reported in Chapters 2 and 3 as anticancer agents, a collaborative study with Dr. Angelo Frei and Dr. Mark Blaskovich at the University of Queensland revealed that these complexes possess potent activity against clinically relevant bacteria and fungi. The complexes were submitted to the Community for Open Antimicrobial Drug Discovery (CO-ADD) for screening against a panel of pathogens, and they exhibited powerful activity against several of the strains in the panel.¹ Some related thiosemicarbazone derivatives have previously been shown to exhibit antifungal activity, but these results represent the first examples of antibacterial or antifungal cobalt thiosemicarbazone complexes. In addition to their high activity against these pathogens, these cobalt complexes are relatively non-toxic toward healthy cells. Based on these promising results, we synthesized additional cobalt(III) complexes, as detailed in this Appendix. Together with our collaborators, we are currently performing detailed investigation of the antifungal activity of these complexes in order to better understand their potential as antibiotics, and we are currently preparing a manuscript to discuss our findings.

Materials and Methods

Synthesis of all cobalt complexes was carried out using modifications of previously reported procedures. 3-fluorosalicicylaldehyde, 3-fluorobenzylamine (3F-BnNH₂), *o*-phenylenediamine, thiosemicarbazide, diacetyl, and Co(NO)₃·(6H₂O) were of reagent grade and were obtained from commercial vendors. Solvents were of ACS grade or higher.² The synthesis of the ligands 3-fluorosalicicylaldehyde *o*-phenylenediamine (3F-salophen) and diacetyl thiosemicarbazone (ATS)³ were

performed according to literature procedures. The cobalt complexes:

[Co(ATS)(Im)₂]NO₃, [Co(GTS)(Im)₂]NO₃, [Co(tfacen)(Im)₂]NO₃, [Co(tfacen)(3F-BnNH₂)₂]Cl, and [Co(3F-salen)(3F-BnNH₂)₂]Cl were previously synthesized by our group and existing materials were used for these studies.^{4,5} The synthetic details for previously unreported cobalt complexes are outlined below.

Physical Measurements

NMR spectra were acquired on a 500 MHz Bruker AV 3HD-spectrometer equipped with a broadband Prodigy cryoprobe or a 400 MHz Varian spectrometer equipped with an auto-switchable probe. High-resolution mass spectrometry (HRMS) data were obtained using an Exactive Orbitrap mass spectrometer in positive ESI mode.

Experimental

[Co(3F-salophen)(3F-BnNH₂)₂]NO₃

3FSP (160 mg, 0.65 mmol) was dissolved in isopropanol (15 mL) and Co(NO₃)₂·6H₂O (190 mg, 0.65 mmol) was added, resulting in a green suspension that slowly turned reddish orange. The mixture was heated at reflux for 1 h, after which 3-fluorobenzylamine (3F-BnNH₂, 0.5 mL, mmol) was added. The mixture was stirred at room temperature overnight, filtered, and the precipitate was washed with isopropanol (20 mL) and diethyl ether (20 mL) to yield 210 mg (45%) of a dark red powder. ¹H NMR (500 MHz, DMSO-*d*₆) δ 8.86 (s, 2H), 8.44 – 8.28 (m, 2H), 7.48 (s, 4H), 7.32 (dd, J = 12, 11 Hz, 2H), 7.15 (q, J = 7.6 Hz, 2H), 6.94 (td, J = 8.7, 2.3 Hz, 2H), 6.83

(d, J = 9.6 Hz, 2H), 6.73 (d, J = 7.9 Hz, 2H), 6.67 – 6.60 (m, 2H), 4.15 (t, J = 6.3 Hz, 4H), 3.11 (t, J = 6.3 Hz, 4H). ^{19}F NMR (470 MHz, DMSO- d_6) δ -113.42 – -113.54 (m, 2F), -134.22 (d, J = 11 Hz, 2F). IR (KBr, cm^{-1}): 3070 br w, 1613 s, 1547 w, 1440 m, 1317 m, 1187 m, 1078 w, 904 w, 878 m, 723 s, 530 m. ESI-MS (positive ion mode): m/z $[\text{M}]^+$ 659.15, calcd 659.15.

[Co(3F-salophen)(NH₃)₂]NO₃

3FSP (160 mg, 0.65 mmol) was dissolved in methanol (8 mL) and Co(NO₃)₂·6H₂O (190 mg, 0.65 mmol) was added, resulting in a green suspension that slowly turned black. The mixture was heated at reflux for 1 h, after which 30% aqueous NH₄OH (1 mL) was added. The reflux was continued for 16 h, and then the resulting orange suspension was allowed to cool to room temperature, filtered, and the precipitate was washed with methanol (15 mL) and diethyl ether (30 mL) to yield 108 mg (22%) of a bright red powder. ^1H NMR (500 MHz, DMSO- d_6) δ 8.89 (s, 2H), 8.44 – 8.34 (m, 2H), 7.50 (dd, J = 6.4, 3.2 Hz, 2H), 7.46 (d, J = 7.7 Hz, 2H), 7.28 – 7.18 (m, 2H), 6.63 – 6.53 (m, 2H), 3.04 (s, 6H). ^{19}F NMR (470 MHz, DMSO) δ -133.26 (d, $J_{\text{F-H}}$ = 11 Hz, 2F). IR (KBr, cm^{-1}): 3078 br w, 1617 s, 1543 m, 1448 m, 1370 m, 1228 m, 1191 s, 735 s. ESI-MS (positive ion mode): m/z $[\text{M}]^+$ 443.07, calcd 443.07.

[Co(ATS)(DMAP)₂]NO₃

ATS (200 mg, 0.85 mmol) was dissolved in methanol (8 mL) and Co(NO₃)₂·6H₂O (250 mg, 0.85 mmol) was added, resulting in a green suspension that slowly turned black. The mixture was heated at reflux for 1 h, after which DMAP (1.4

g, 11.4 mmol) was added. The reflux was continued for 16 h, and then the resulting dark red suspension was allowed to cool to room temperature, filtered, and the precipitate was washed with methanol (30 mL) and diethyl ether (30 mL) to yield 400 mg (78%) of a dark red powder. $^1\text{H NMR}$ (400 MHz, DMSO-d_6) δ 7.66 (s, 4H), 7.60 (d, $J = 6.9$ Hz, 4H), 6.54 (d, $J = 6.9$ Hz, 4H), 2.97 (s, 12H), 2.59 (s, 6H). IR (KBr, cm^{-1}): 3417 w, 3286 m, 3178 m, 2913 w, 1626 s, 1539 m, 1439 s, 1378 m, 1230 s, 1060 w, 1017 m. ESI-MS (positive ion mode): m/z $[\text{M}]^+$ 533.14, calcd 533.14.

Supporting Information

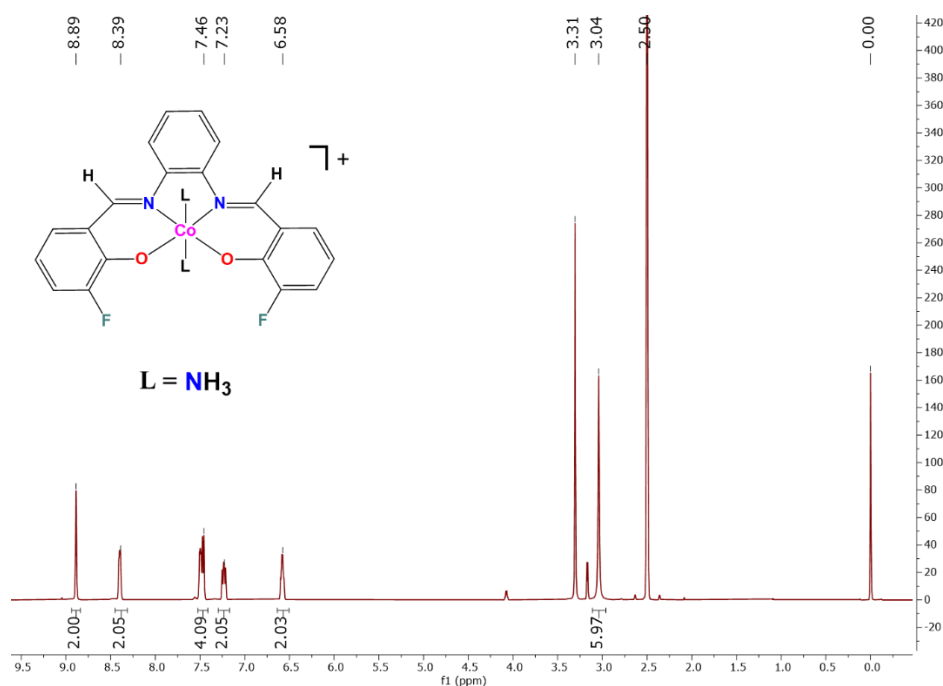


Figure A1. $^1\text{H NMR}$ (500 MHz) of $[\text{Co}(\text{3F-salophen})(\text{NH}_3)_2]\text{NO}_3$ in DMSO-d_6 .

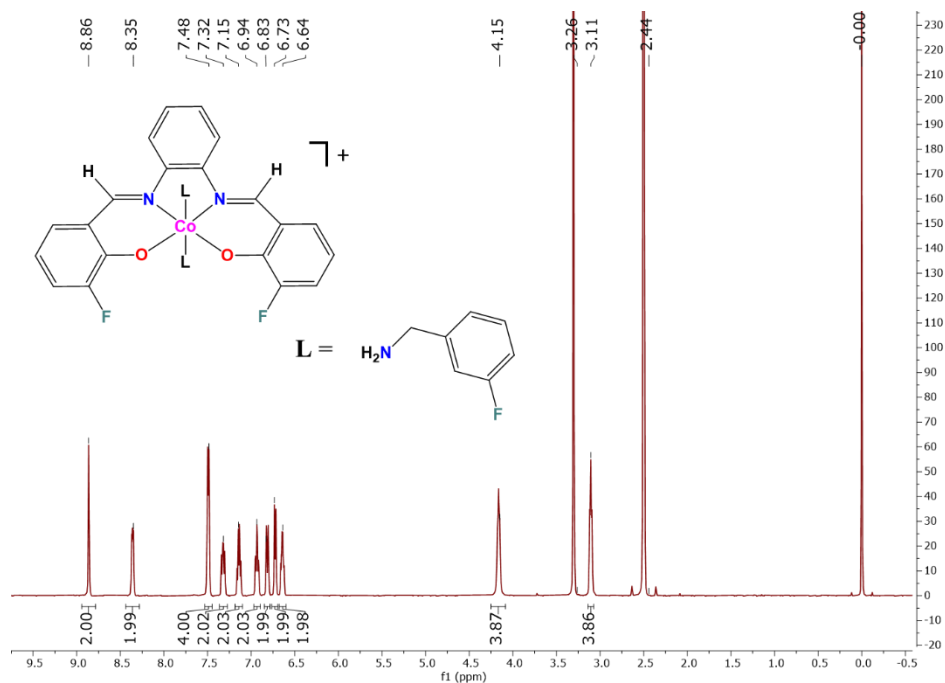


Figure A2. 1H NMR (500 MHz) of $[Co(3F\text{-salophen})(3F\text{-BnNH}_2)_2]NO_3$ in $DMSO\text{-}d_6$.

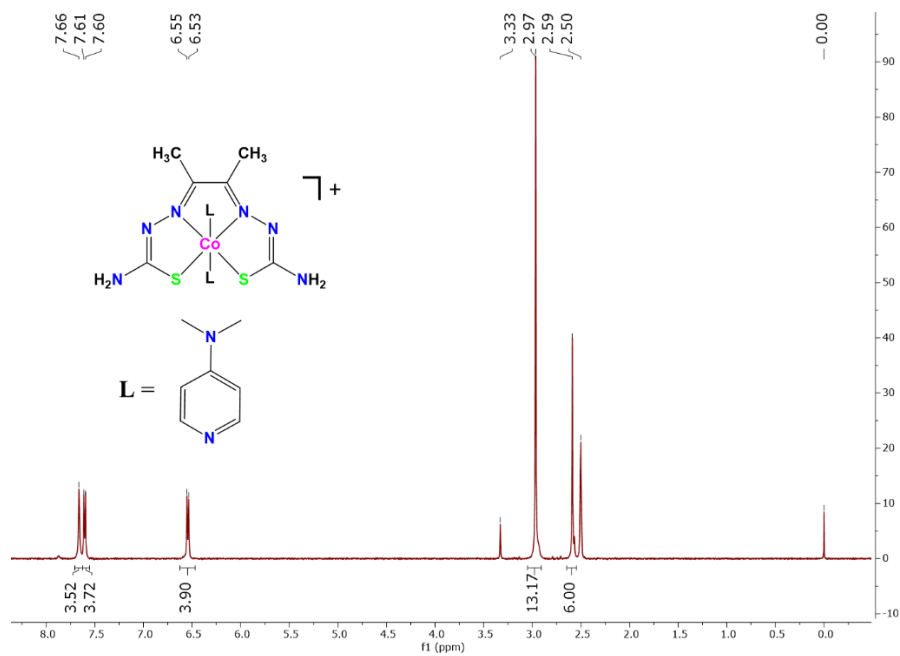


Figure A3. 1H NMR (400 MHz) of $[Co(ATS)(DMAP)_2]NO_3$ in $DMSO\text{-}d_6$.

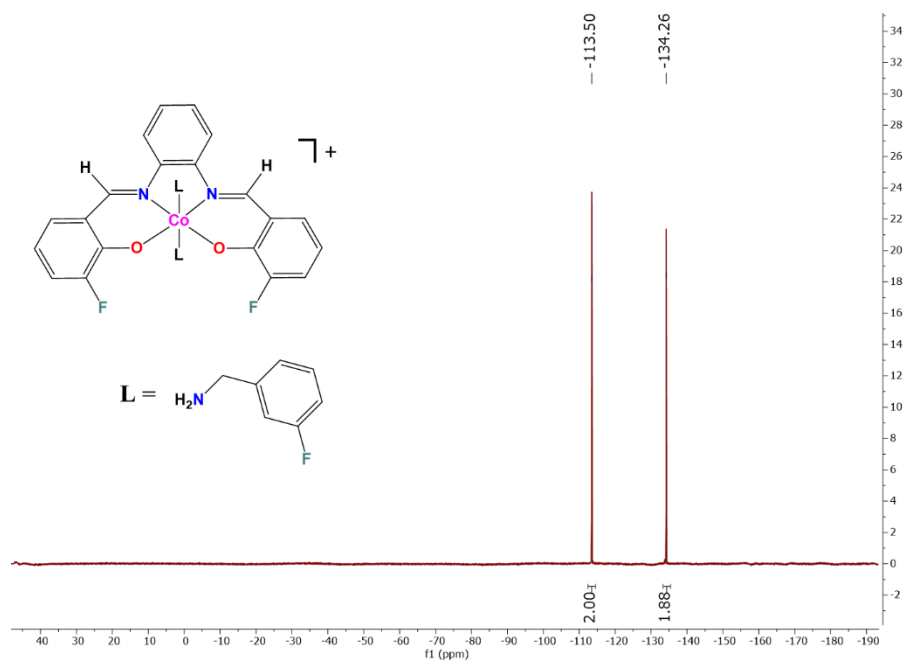


Figure A4. ^{19}F NMR (470 MHz) of $[Co(3F\text{-salophen})(3F\text{-BnNH}_2)_2]NO_3$ in $DMSO-d_6$.

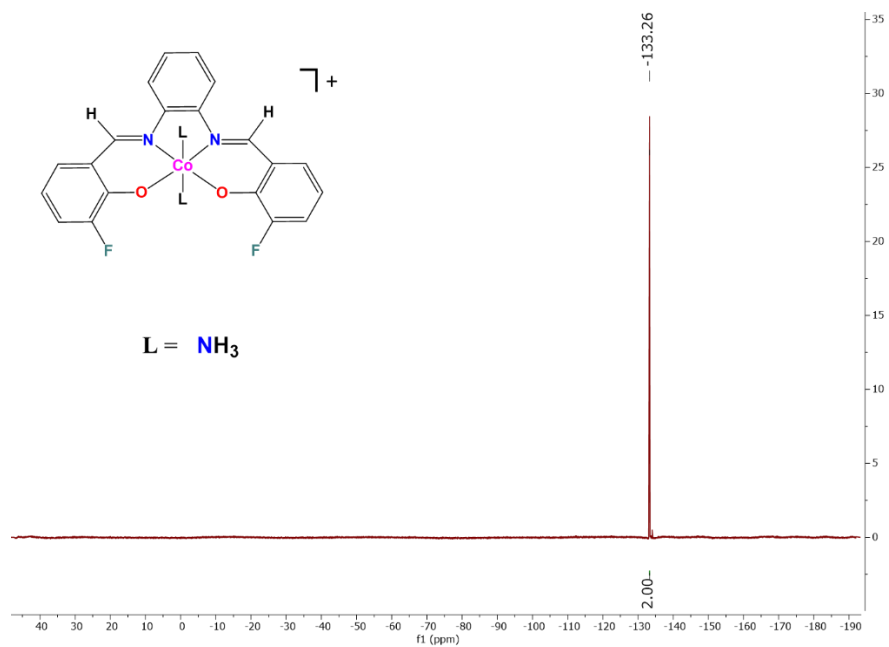


Figure A5. ^{19}F NMR (470 MHz) of $[Co(3F\text{-salophen})(NH_3)_2]NO_3$ in $DMSO-d_6$.

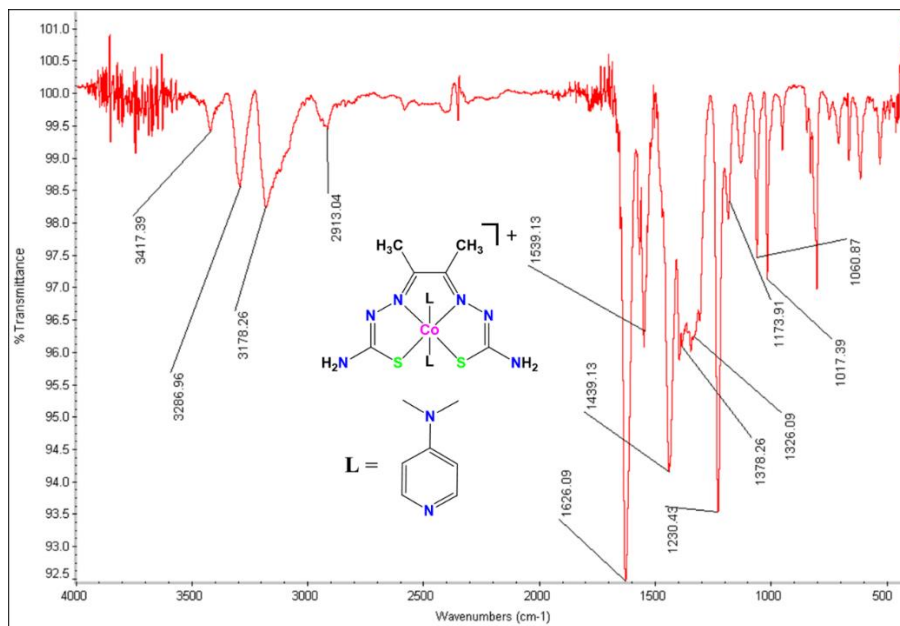


Figure A6. IR (KBr, cm^{-1}) of $[\text{Co}(\text{ATS})(\text{DMAP})_2]\text{NO}_3$.

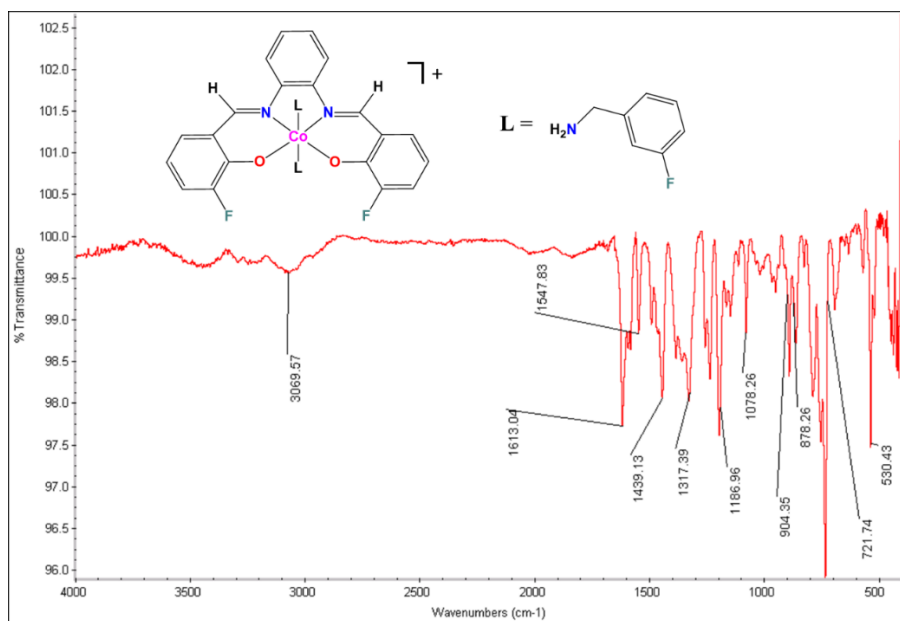


Figure A7. IR (KBr, cm^{-1}) of $[\text{Co}(3\text{F-salophen})(3\text{F-BnNH}_2)_2]\text{NO}_3$.

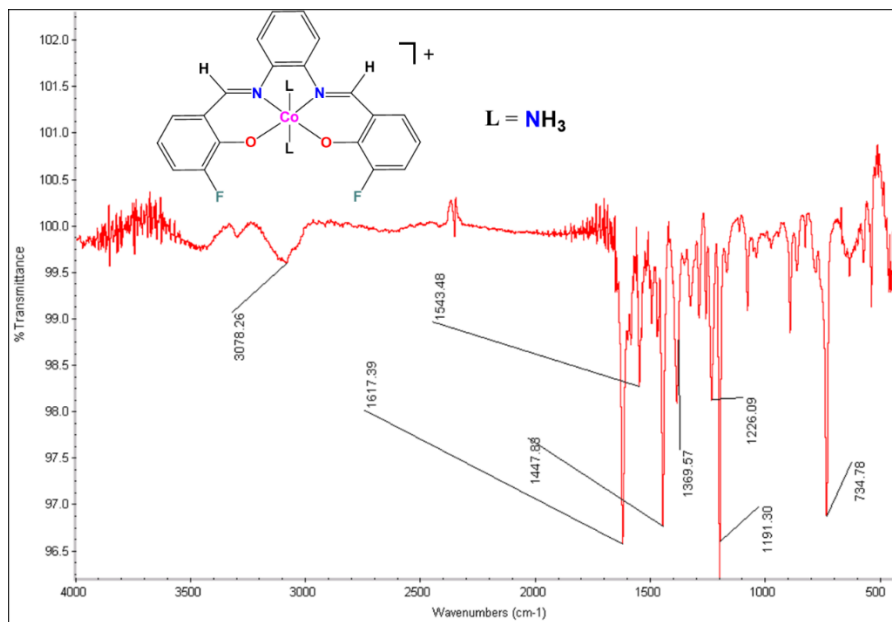


Figure A8. IR (KBr, cm^{-1}) of $[\text{Co}(\text{3F-salophen})(\text{NH}_3)_2]\text{NO}_3$.

References

- 1 A. Frei, J. Zuegg, A. G. Elliott, M. Baker, S. Braese, C. Brown, F. Chen, C. G. Dowson, G. Dujardin, N. Jung, A. P. King, A. M. Mansour, M. Massi, J. Moat, H. A. Mohamed, A. K. Renfrew, P. J. Rutledge, P. J. Sadler, M. H. Todd, C. E. Willans, J. J. Wilson, M. A. Cooper and M. A. T. Blaskovich, *Chem. Sci.*, 2020, **11**, 2627–2639.
- 2 S. R. Doctrow, K. Huffman, C. B. Marcus, G. Tocco, E. Malfroy, C. A. Adinolfi, H. Kruk, Keith Baker, N. Lazarowych, J. Mascarenhas and B. Malfroy, *J. Med. Chem.*, 2002, **45**, 4549–4558.
- 3 B. A. Gingras, T. Suprunchuk and C. H. Bayley, *Can. J. Chem.*, 1962, **40**, 1053–1059.
- 4 A. P. King, H. A. Gellineau, J.-E. Ahn, S. N. MacMillan and J. J. Wilson, *Inorg. Chem.*, 2017, **56**, 6609–6623.
- 5 A. P. King, H. A. Gellineau, S. N. Macmillan and J. J. Wilson, *Dalton Trans.*, 2019, **48**, 5987–6002.

Appendix 2
Synthesis of [⁵⁵Co(ATS)(NH₃)₂]Cl

Introduction

Bis(thiosemicarbazones) (BTSCs) are privileged radioligands with high affinity for first-row transition metals. In particular, the copper-BTSC complex, $^{64}\text{CuATSm}$, has shown promise as a hypoxia-targeting agent for tumor imaging.^{1,2} The positron-emitting $^{64}\text{Cu-ATSm}$ ($t_{1/2}$ 12.7 h) targets hypoxic tissues by virtue of the Cu(I)/Cu(II) redox couple, which allows selective reduction and trapping of the Cu(I) complex under hypoxic conditions. The success of BTSCs as high-affinity chelators for hypoxia-targeting copper complexes prompted us to investigate whether BTSC complexes of another first-row transition metal, cobalt, might display similar properties, as outlined in Chapter 2. The results of this study showed that Co(III)-BTSC complexes are powerful anticancer agents with modest hypoxia selectivity. Inspired by the anticancer activity and potential hypoxia selectivity of the non-radioactive Co(III)-BTSC complexes, we synthesized a radioactive $^{55}\text{Co-BTSC}$ complex. Similar to the clinically investigated ^{64}Cu ($t_{1/2}$ 12.7 h), ^{55}Co has a convenient half-life of 17.5 h and has a high positron yield of 77%, which make it an ideal isotope for PET imaging.^{3,4} These experiments resulted in the first report of a $^{55}\text{CoBTSC}$ complex.

Experimental

Materials and Methods

Diacetyl bis(thiosemicarbazone) (ATS) was synthesized through condensation of glyoxal with two equivalents of thiosemicarbazide as reported in Chapter 2. Stock solutions of ATS were prepared in N,N-dimethylformamide (DMF) and serially

diluted with HEPES buffer (pH 7.4) to working concentrations. $^{55}\text{CoCl}_2$ was obtained through cyclotron irradiation of a naturally-abundant Ni target as reported previously.⁴ All solvents were of reagent grade or higher and were used without further purification. Chelex 100 resin was obtained from Bio-Rad. Radio-TLC experiments were performed using a 1:1 MeOH/HEPES mixture at pH 7.4, and the results were analyzed by autoradiography using a Packard Cyclone Phosphor-Plate imaging system (Perkin Elmer).

Synthesis of $[^{55}\text{Co}(\text{ATS})(\text{NH}_3)_2]\text{Cl}$

A solution of ATS (0.35 mL, 20 μM) in HEPES buffer was added to a solution of $^{55}\text{CoCl}_2$ (0.15 mL, 900 μCi) in HEPES buffer, and the mixture was heated at 60 $^\circ\text{C}$ with shaking at 300 rpm for 1 h. A solution of NH_3 in HEPES buffer (50 μL , 5 mM) was added, and heating was continued for 20 h. An aliquot of the resulting solution (200 μL) was added to approximately 50 mg of Chelex resin, vortexed for 15 min, and centrifuged at 10,000 rpm for 15 min. Radio-TLC analysis of the resulting product revealed approximately 95% purity. Decay-corrected yield: 51%.

Results and Discussion

The ^{55}Co -containing complex $[^{55}\text{Co}(\text{ATS})(\text{NH}_3)_2]\text{Cl}$ was successfully synthesized in moderate yield using a modification of the procedure used for the non-radioactive analog. An excess of ATS ligand was added to the ^{55}Co solution in aqueous buffer and the two components were allowed to react for one hour, and then an aqueous NH_3 solution was added. The formation of the product upon addition of

the axial ligand proceeded slowly, requiring heating overnight for optimal yields. The radiolabeling experiment was performed at varying ratios of ligand to metal in order to find the optimal labeling conditions, as shown in **Figure A9**. At least 1 uM ATS was required to achieve suitable radiolabeling, which is a significant excess compared to the amount of ^{55}Co present in solution. Also shown in **Figure A9** are relevant control experiments conducted in the absence of NH_3 or ATS, indicating that the product contains NH_3 , ATS, and ^{55}Co .

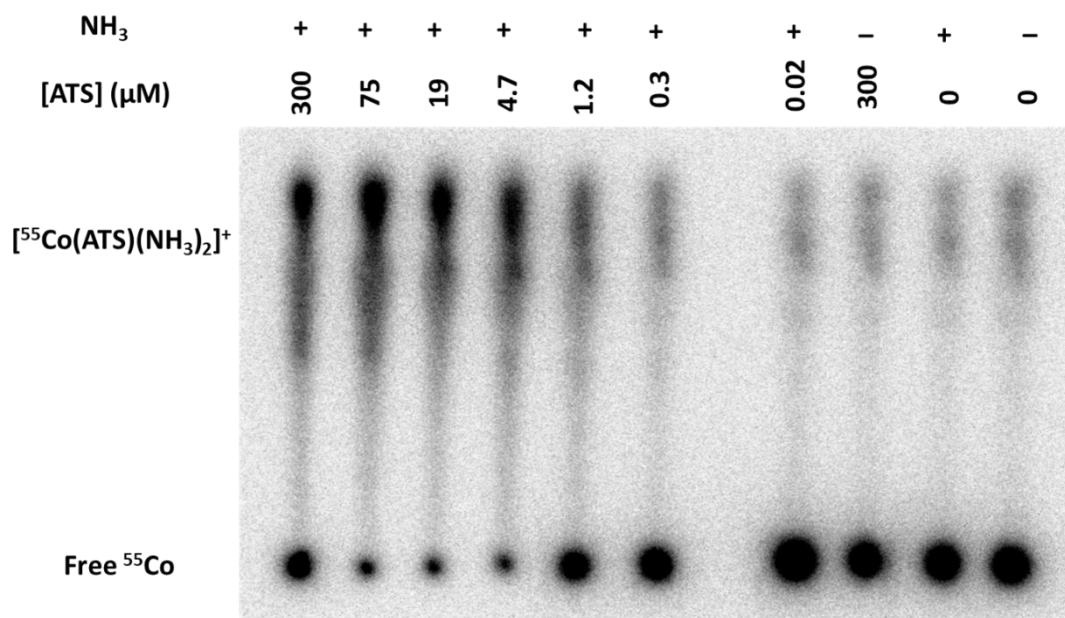


Figure A9. Radio-TLC image of $[\text{Co}(\text{ATS})(\text{NH}_3)_2]\text{Cl}$ synthesized using varying concentrations of ATS ligand and relevant control experiments. Other than ATS concentration, experimental conditions are the same as those reported in the experimental section, with the exception of the Chelex purification step, which was omitted.

Although the complex may be synthesized through an overnight reaction, the resulting material contains a large amount of uncomplexed ^{55}Co . The uncomplexed material may be removed through incubation with Chelex resin to yield the final

product, $[\text{Co}(\text{ATS})(\text{NH}_3)_2]^+$, in approximately 95% purity.

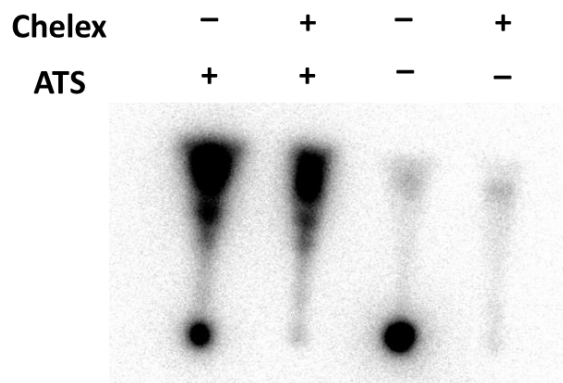


Figure A10. TLC image demonstration of purification of crude $[\text{Co}(\text{ATS})(\text{NH}_3)_2]^+$ using Chelex resin.

Conclusion

This Appendix details the synthesis of the first reported ^{55}Co -BTSC complex. The BTSC ligand effectively chelates the ^{55}Co , indicating that these complexes may be suitable for radiological imaging applications such as PET. Future experiments will involve the synthesis and characterization of other ^{55}Co -BTSC complexes containing diverse BTSC and axial ligands. We will also characterize the biological activity of these complexes to determine their stability in vitro and in vivo.

References

- 1 J. P. Holland, J. S. Lewis and F. Dehdashti, *Q. J. Nucl. Med. Mol. Imaging*, 2009, **53**, 193–200.
- 2 C. J. Anderson and R. Ferdani, *Cancer Biother. Radiopharm.*, 2009, **24**, 379–393.
- 3 T. Mastren, B. V Marquez, D. E. Sultan, E. Bollinger, P. Eisenbeis, T. Voller and S. E. Lapi, *Mol. Imaging*, 2015, **14**, 526–533.
- 4 H. F. Valdovinos, R. Hernandez, S. Graves, P. A. Ellison, T. E. Barnhart, C. P. Theuer, J. W. Engle, W. Cai and R. J. Nickles, *Appl. Radiat. Isot.*, 2017, **130**, 90–101.